High Density Plasma Heating in the Tokamak à Configuration Variable

THÈSE N^{O} 5012 (2011)

PRÉSENTÉE LE 29 AVRIL 2011

À LA FACULTÉ SCIENCES DE BASE

CRPP - PHYSIQUE DU TOKAMAK TCV

PROGRAMME DOCTORAL EN PHYSIQUE

ÉCOLE POLYTECHNIQUE FÉDÉRALE DE LAUSANNE

POUR L'OBTENTION DU GRADE DE DOCTEUR ÈS SCIENCES

PAR

Loïc CURCHOD

acceptée sur proposition du jury:

Prof. V. Savona, président du jury
Dr A. Pochelon, directeur de thèse
Dr S. Brunner, rapporteur
Prof. P. Chattopadhyay, rapporteur
Prof. H. Laqua, rapporteur

ÉCOLE POLYTECHNIQUE
FÉDÉRALE DE LAUSANNE

Suisse
2011

The figures in this dissertation are in color in the electronic version available for download from http://library.epfl.ch/theses/?nr=5012.

Please cite this work as:
L. Curchod, ***High density plasma heating in the Tokamak à Configuration Variable***, Ph.D. thesis, no. 5012, Ecole Polytechnique Fédérale de Lausanne (EPFL), CH-1015 Lausanne, Switzerland, March 2011.

n croit qu'on va faire un voyage, mais bientôt c'est le voyage qui vous fait, ou vous défait.

Nicolas Bouvier (*1929 – †1998)
dans ***L'Usage du monde*** (1963)

Résumé

Le Tokamak à Configuration Variable (TCV) est une expérience de fusion thermonucléaire par confinement magnétique de taille moyenne conçue pour l'étude des performances du plasma en fonction de sa forme. TCV est équipé d'un système de chauffage (ECH) et de génération de courant (ECCD) par ondes cyclotroniques électroniques très puissant et flexible. Jusqu'à 3 MW de puissance EC à la 2ème harmonique en mode ordinaire (O2) ou extraordinaire (X2) peuvent être injectés par le côté bas-champ via six lanceurs indépendamment orientables. Jusqu'à 1.5 MW d'ECH à la 3ème harmonique (X3) peuvent être injectés depuis le haut de TCV.
A haute densité, l'ECH est rendu impossible par une couche de coupure empêchant l'accès à la résonance EC au centre du plasma. En conséquence, moins de 50% du domaine d'opération en densité de TCV sont accessibles à l'ECH par X2 et X3. Les ondes de Bernstein électroniques (EBW) permettent de surmonter cette limite en densité. L'EBW est un mode électrostatique se propageant au-delà de la coupure, sans limite supérieure de densité. Puisqu'il ne se propage pas dans le vide, l'EBW doit être excité par conversion de mode d'ondes EC dans le plasma.
L'efficacité du chauffage (EBH) et de la génération de courant (EBCD) par EBW a été démontrée précédemment dans plusieurs expériences de fusion, en particulier dans le stellarator W7-AS et le tokamak sphérique MAST. Dans TCV, les conditions pour la conversion de mode O-X-B (i.e. un fort gradient de densité à la coupure O2) sont réunies au bord de plasmas à haut confinement (mode-H), caractérisés par un piédestal dans les profils de température et de densité électroniques. Des expériences menées dans TCV ont démontré le premier chauffage de plasmas de haute densité par EBH via O-X-B dans un tokamak à rapport d'aspect moyen.
Le travail de cette thèse se concentre sur plusieurs aspects de l'ECH et de l'EBH dans des plasmas de basse et haute densité. En premier lieu, l'optimum angulaire expérimental pour la conversion de mode O-X-B est comparée avec succès au résultat numérique du code AMR. L'implémentation de la géométrie du système ECRH de TCV dans AMR ainsi que le couplage de AMR avec le code quasi-linéaire Fokker-Planck LUKE pour le cas de TCV ont fait partie intégrante de ce travail.
Le lieu d'absorption d'EBH modulé est ensuite détecté à l'intérieur d'un plasma surdense grâce à l'analyse en oscillation du profil de rayons-X mous en utilisant la méthode de brisure-de-pente (BIS) ainsi qu'une méthode d'identification de la

réponse harmonique (HRIM), démontrant ainsi l'EBH résonant dans TCV. Les méthodes BIS and HRIM sont aussi utilisées avec succès pour la localisation au cours du temps des lieux de dépôt variables d'un, puis de deux faisceaux de puissance X2 simultanément. Les résultats expérimentaux sont en accords à 10% près avec les résultats des codes de tracé-de-rayon AMR et C3PO couplés à LUKE.
Le coefficient d'absorption de la puissance ECH modulée (MECH) est étudié par l'analyse HRIM de la réponse du flux toroïdal du plasma mesuré par la boucle diamagnétique (DML) de TCV. L'analyse d'expériences de MECH X2 et X3 révèle une perturbation majeure de la méthode par l'activité magnétohydrodynamique en dent-de-scie (DDS) au centre du plasma. En effet, une amélioration de l'absorption de la puissance X3 (jusqu'à 100%), asymétrique par rapport au signe de l'ECCD X2 préchauffant le plasma, a été observée ultérieurement dans TCV. Aucune simulation Fokker-Planck n'avait pu expliquer cet effet. Le présent travail permet d'attribuer cette asymétrie à une activité en dent de scie fortement déstabilisée par le co-ECCD X2 et se couplant au MECH X3.
La génération de courant par ondes de Bernstein électroniques (EBCD) dans TCV est étudiée avec les codes AMR-LUKE pour plusieurs positions poloïdales de l'injection des EBW. L'efficacité maximum d'EBCD maximum est obtenue quand les EBW sont injectées proche du plan médian du plasma de sorte que l'indice de réfraction parallèle de l'onde n'augmente que modérément et que les EBW sont absorbées au centre du plasma où la température est la plus élevée. Néanmoins, le niveau absolu de courant généré reste très faible (i.e. $\lesssim 1\%$ du courant ohmique).
Finalement, une antenne pour la détection des ondes hybrides inférieures (LH) générées par une instabilité paramétrique (PI) à la conversion de mode X-B a été conçue, construite et installée sur TCV. Une mesure rapide de l'évolution du spectre LHPI montre pour la première fois la corrélation entre l'amplitude des ondes LHPI avec le seuil de puissance LHPI estimé à partir des données de profil expérimentales. Grâce à un scan de puissance EBH, le seuil de puissance LHPI est estimé à $\lesssim 50$ kW, en accord avec les valeurs prédites. La cascade d'énergie des basses aux hautes bandes de fréquence LH avec l'augmentation de la puissance EBH est démontrée sur TCV.

Mots clefs : plasmas, haute densité, mode-H, chauffage, génération de courant, ondes cyclotroniques électroniques, ondes de Bernstein électroniques, O-X-B, conversion de mode, absorption de puissance, détecteur de rayons-X mous, DMPX, boucle diamagnétique, ondes hybrides inférieures, instabilité paramétrique, antenne, TCV, tokamak.

Abstract

The *Tokamak à Configuration Variable* (TCV) is a medium size magnetic confinement thermonuclear fusion experiment designed for the study of the plasma performances as a function of its shape. It is equipped with a high power and highly flexible electron cyclotron heating (ECH) and current drive (ECCD) system. Up to 3 MW of 2nd harmonic EC power in ordinary (O2) or extraordinary (X2) polarization can be injected from TCV low-field side via six independently steerable launchers. In addition, up to 1.5 MW of 3rd harmonic EC power (X3) can be launched along the EC resonance from the top of TCV vacuum vessel.

At high density, standard ECH and ECCD are prevented by the appearance of a cutoff layer screening the access to the EC resonance at the plasma center. As a consequence, less than 50% of TCV density operational domain is accessible to X2 and X3 ECH. The electron Bernstein waves (EBW) have been proposed to overcome this limitation. EBW is an electrostatic mode propagating beyond the plasma cutoff without upper density limit. Since it cannot propagate in vacuum, it has to be excited by mode conversion of EC waves in the plasma.

Efficient electron Bernstein waves heating (EBH) and current drive (EBCD) were previously performed in several fusion devices, in particular in the W7-AS stellarator and in the MAST spherical tokamak. In TCV, the conditions for an efficient O-X-B mode conversion (i.e. a steep density gradient at the O2 plasma cutoff) are met at the edge of high confinement (H-mode) plasmas characterized by the appearance of a pedestal in the electron temperature and density profiles. TCV experiments have demonstrated the first EBW coupling to overdense plasmas in a medium aspect-ratio tokamak via O-X-B mode conversion.

This thesis work focuses on several aspects of ECH and EBH in low and high density plasmas. Firstly, the experimental optimum angles for the O-X-B mode conversion is successfully compared to the full-wave mode conversion calculation of the AMR code. The implementation of TCV ECH system geometry in AMR and the coupling of AMR to the LUKE quasi-linear Fokker-Planck solver for the TCV environment were part of this work.

The power deposition location of modulated EBH is then detected inside the O2 plasma cutoff by oscillation analysis of the soft X-ray emission profile using the break-in-slope (BIS) analysis and a harmonic response identification method

(HRIM), which is the demonstration of resonant EBH in TCV. The BIS and HRIM methods are also used to successfully detect and track the time-varying deposition locations of one and then two X2 power beams simultaneously. All experimental results are in good agreement within 10% of the normalized plasma radius with numerical results of the AMR and C3PO ray-tracing codes coupled to LUKE.
The global power absorption coefficient of modulated ECH (MECH) is studied by HRIM analysis of the plasma toroidal flux response measured by TCV diamagnetic loop (DML). Analysis of earlier X3 MECH and new X2 MECH experiments reveals a major perturbation of the method by the sawtooth magnetohydrodynamic activity in the plasma center. Indeed, an asymmetric improvement of the X3 power absorption (up to 100%) with respect to the sign of the X2 ECCD pre-heating was observed in previous TCV experiments and remained unexplained by Fokker-Planck simulations until now. The present work allows to attribute this asymmetry to a sawtooth activity strongly destabilized by the central X2 co-ECCD locking to the X3 power modulation.
The performances of EBW current drive (EBCD) in TCV are studied with the AMR-LUKE codes for several poloidal positions of the EBW injection. The maximum EBCD efficiency is obtained when the EBW are injected close the plasma midplane such that the wave parallel refractive index upshift is moderate and the absorption takes place at the plasma center where the electron temperature is the highest. However, the absolute driven current remains small (i.e. $\lesssim 1\%$ of the Ohmic current).
Finally, a new loop-antenna for the detection of the lower-hybrid (LH) waves generated by a parametric instability (PI) at the X-B mode conversion was designed, built and installed in TCV torus. Fast monitoring of the LHPI spectrum allows to show for the first time the correlation of the amplitude of the detected waves with the local LHPI threshold power at the mode conversion region, estimated from the experimental profiles data. In an EBW power scan, the LHPI threshold power is estimated to be $\lesssim 50$ kW in good agreement with the value predicted from the experimental profiles data. The LHPI energy cascade from the low to the high LH frequency bands with increasing EBH power is shown for the first time in TCV.

Keywords: plasma, high density, H-mode, heating, current drive, electron cyclotron waves, ECW, ECH, ECCD, electron Bernstein waves, EBW, EBH, EBCD, O-X-B, mode conversion, power absorption, soft X-ray detector, DMPX, diamagnetic loop, DML, lower-hybrid waves, LH, parametric instability, PI, loop-antenna, TCV, tokamak.

Contents

List of Tables

Chapter 1

Introduction

1.1 Research context

At the dawn of the 21st century, the world demographic growth and continuously increasing energy consumption combine to urge for the development of new energy resources. Nuclear fusion is one potential solution for future multi-gigawatt power plants. Nuclear fusion research has been focusing on magnetically confined fusion, and especially on the tokamak concept since its invention in the 1950's by the Soviet physicists Igor Yevgenyevich Tamm and Andrei Sakharov.

The electron cyclotron heating (ECH) by resonant absorption of radio frequency (RF) power on the free electrons of the plasma is a widespread method for fusion plasma heating and has been a key aspect of the fusion plasma research for decades, as reviewed in references [1–3]. Indeed, ECH can provide high power densities in very localized regions. Moreover, the systems delivering the electron cyclotron waves (ECW) to the plasma are generally very flexible. In particular, most of EC power systems allow the generation of electron cyclotron current drive (ECCD). ECH and ECCD are therefore tools of primary importance for the study of the plasma confinement and transport properties, as well as the stabilization and control of fusion plasmas [4, 5].

On the other hand, a high plasma density will be beneficial to the fusion power yield in a thermonuclear reactor both directly, by increasing the reaction rate, and indirectly, by increasing the plasma confinement, according to well-established experimental observations. The investigation of the high-density plasma regime characteristics and performances is thus a major goal of experimental fusion devices nowadays, in preparation for the advanced scenarios in future demonstration fusion power plants.

However, the standard ECH and ECCD at the first and second harmonics of the electron cyclotron frequency are precluded in high density plasmas by the appearance of a cutoff layer screening the access to the EC resonance at the plasma center. This limitation is particularly severe in small and medium size experimental fusion devices with moderate magnetic field B_φ since the ECWs cutoff densities are proportional to B_φ^2 [3].

Various RF power heating schemes have been developed in order to circumvent this limitation. EC waves at higher harmonics allow the heating of higher density plasmas like the high confinement (H-mode) regime. However, they are still subject to a cutoff density limit and their absorption efficiency is lower than for the second harmonic EC waves [3].

At all densities above the plasma cutoff (i.e. in so-called "overdense" plasmas), the electron Bernstein wave (EBW) branch is a potential solution for plasma heating using EC power. EBW is an electrostatic wave first predicted by Ira B. Bernstein [6] and propagating beyond the plasma cutoff with no upper density limit. As a consequence of their electrostatic nature, EBWs cannot propagate in vacuum and several processes have been proposed to excite the EBWs by mode-conversion of externally launched ECWs, as summarized here and in figure 1.1.

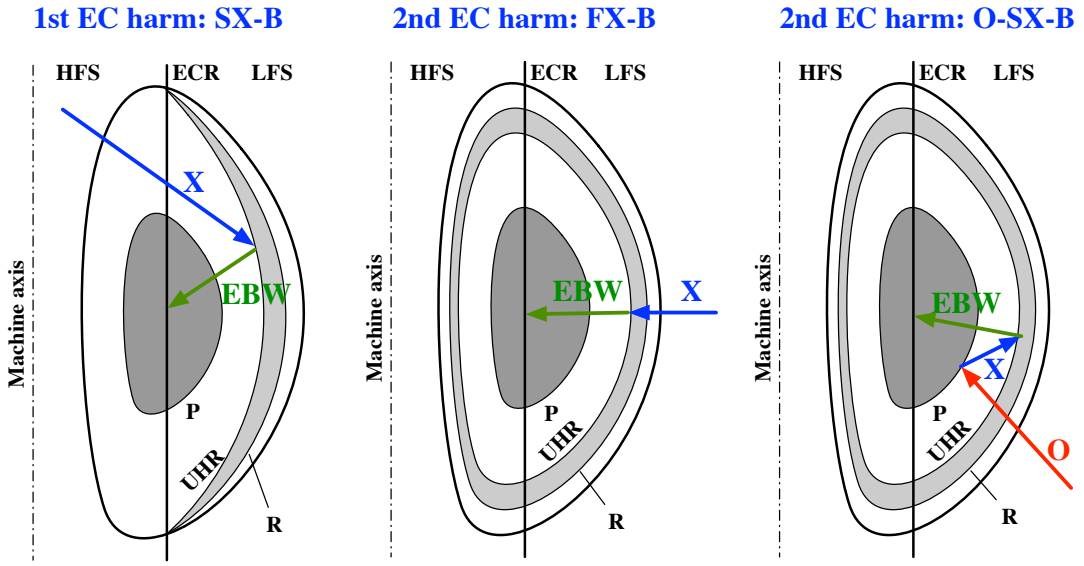

Figure 1.1: EBW excitation schemes. Schematics of three schemes for the excitation of electron Bernstein waves (EBW) by mode conversion of externally injected electromagnetic waves. **Left:** direct SX-Bernstein mode conversion from the high-field side, only possible for 1st harmonic electron cyclotron waves. **Center:** FX-Bernstein mode conversion from the low-field side. Efficient tunneling through the evanescent layer requires an extremely steep density gradient. **Right:** O-SX-Bernstein double mode conversion from the low-field side. The O-SX mode conversion requires a steep density gradient at the plasma cutoff and an optimum injection angle.

- **SX-B** mode-conversion of a slow EC wave in the extraordinary (SX) polarization injected from the plasma high-field side (HFS) is possible at the first EC harmonic. The X-mode wave reaches the upper-hybrid resonance (UHR) on the plasma low-field side (LFS), where it connects to the Bernstein branch [7,8]. The Bernstein wave then propagates back towards the plasma center where it is absorbed at the electron cyclotron resonance with a high efficiency. This scheme requires the X-mode wave to travel through the plasma center. As a consequence, the SX-B scheme is possible only in so-called "underdense" plasmas where the plasma center is not screened by the L-cutoff. Electron Bernstein wave heating via the SX-B mode conversion have been reported in the Versator II tokamak [9] and in the FT-1 tokamak [10], as well as EBCD in the COMPASS-D tokamak [11].

- **FX-B** mode conversion is performed by normal incidence of a fast X-wave (FX) injected from the LFS of the plasma. The FX wave tunnels through the evanescent layer between the R-cutoff and the UHR and connects to the EBW at the UHR. This scheme requires such a steep density gradient at the plasma edge (i.e. a density scale length of the order of the wavelength of the injected FX wave) that it has usually a poor mode-conversion efficiency. However, FX-B experiments from the LFS have shown efficient EBH in the TST-2 spherical tokamak where the FX wave propagation through the evanescent layer is helped by the presence of a local limiter around the injecting antenna [12].

- In the **O-SX-B** scheme, the EBW is excited by mode conversion of an EC wave in ordinary (O) polarization injected into the plasma from the LFS of the plasma [13, 14]. At an optimum oblique incidence, the O-mode wave converts into a SX wave at the plasma cutoff which propagates back towards lower density where its power is passed onto the Bernstein mode at the upper-hybrid resonance. The Bernstein wave finally propagates towards the plasma center where it is absorbed at the electron cyclotron resonance. The first demonstration of EBH in an overdense plasma via the O-X-B scheme was performed in the W7-AS stellarator [15–17]. Efficient electron Bernstein wave current drive (EBCD) was also achieved in the W7-AS stellarator [17, 18], as well as measurements of thermal electron Bernstein wave emission (EBE) via the B-SX-O inverse mode conversion process [16, 19]. EBH and EBE experiments were reported from MAST spherical tokamak [20].

The reader can find a recent review of EBW theory and experiments in reference [21].

1.2 Thesis motivations

The *Tokamak à Configuration Variable* (TCV) is equipped with a versatile and powerful EC power system at the second (X2/O2, $f_2 = 82.6$ GHz) and third (X3, $f_3 = 118$ GHz) harmonics of the EC frequency, providing ECH/ECCD over respectively $\sim$ 17% and $\sim$ 46% of TCV's operational domain in density ($n_e \lesssim 25 \cdot 10^{19}$ m^{-3}). Electron Bernstein waves can potentially extend the domain of TCV RF-heated plasmas to the high-density H-mode plasmas, up to 100% of its operational domain in density.
In TCV, the second harmonic EC power is injected from the plasma low-field side. Moreover, the wave frequency is high and the wavelength is small ($\lambda_2 = 3.628$ mm for the second harmonic). As a consequence, the extremely steep density gradients necessary for the FX-B mode conversion cannot be obtained in TCV plasma equilibria and the only possible Bernstein waves excitation scheme in TCV is the O-SX-B double mode conversion. Thanks to the flexibility of its magnetic coil and EC power systems, TCV offers the possibility to study EBH in a tokamak with medium aspect ratio and medium magnetic field. Indeed, the demonstrations of EBW power deposition and EBE via O-SX-B mode conversion in the overdense plasmas of a medium aspect ratio tokamak were performed in TCV [22–24].
The main goals of this thesis work are

- a detailed study of the physics of
  - the electron Bernstein wave excitation in TCV,
  - the possibilities of high power and central EBH/EBCD;
- the development of the analysis tools for
  - the interpretation of the EBH experiments in presence of the sawtooth activity,
  - the simulation of the EBW coupling, propagation and absorption in TCV.

More specifically, the following key aspects are investigated.

- **Wave-plasma coupling at high density.** Two features of the O-SX-B mode-conversion of O2 power in TCV overdense plasmas are examined:
  - The O-SX mode conversion is efficient only around an optimum injection angle. It is thus of primary importance to verify the existence and position of this optimum in the experimental conditions and to benchmark

the numerical simulation tool against the experimental results. In this work, the O-SX-B mode conversion efficiency in TCV EBH experiments is examined and compared to the results of the full-wave mode-conversion-calculation AMR code [25–27]. The implementation of the geometry of TCV EC system in the AMR code and thes subsequent benchmarks were part of this thesis work.

  - At the SX-B mode conversion, a non-linear coupling of the SX wave to lower-hybrid waves (LHW) via a parametric instability (LHPI) may appear and strongly deteriorate the overall EBH efficiency [28]. In order to investigate the emission of the LH waves during TCV EBH experiments, a new loop-antenna is designed, built and installed on TCV. The initial data are collected and interpreted, in particular the LHPI spectrum evolution with the plasma profile conditions and the injected EBH power.

- **Power deposition location:** The power deposition location is an important quantity to assess from the experimental data for the interpretation of plasma RF heating results and for the comparison of the experiments with simulations. However, the H-mode plasmas are generally perturbed by a strong magneto-hydrodynamic (MHD) sawtooth activity which can hamper the EBH power deposition analysis. In this thesis work, the Break-In-Slope (BIS) method is proposed to detect the power deposition location in presence of strong sawtooth activity and/or in time-varying conditions. The detection method is first tested in stationary X2 ECH experiments and used to track time-varying X2 power absorption locations. The method is then applied to an off-axis EBH experiment in a strongly sawtoothing H-mode plasma. The experimental results are compared to the numerical simulations of the C3PO [29] and AMR ray-tracing codes for the ECWs and EBWs, respectively.

- **Global power absorption.** A major part of this thesis work is dedicated to the experimental measurement of the global RF power absorption efficiency which is an essential quantity for the interpretation of the heating experiments, especially in TCV where X2 and X3 ECH are routinely used. In TCV, the absorption coefficient is estimated by analyzing the response of the plasma kinetic energy measured using the DiaMagnetic Loop (DML) diagnostic to modulated ECH (MECH). In this work, we examine the impact of the sawtooth MHD activity on the frequency response of the plasma kinetic energy to X2 and X3 MECH and the subsequent detremental perturbation on the power

absorption estimate.

- **EBCD via O-SX-B in a standard aspect ratio tokamak.** EBW can provide efficient current drive in overdense plasmas where ECCD is not possible. The possibilities of EBCD in TCV are explored with the AMR code coupled to the LUKE quasi-linear Fokker-Planck solver [30].

1.3 Thesis outline

A brief description of the scientific context and the motivations of this work were given in this chapter. Chapter 2 presents the TCV tokamak, its EC power system, as well as the principles and specifications of the diagnostics essential to this thesis. Section 2.4 is dedicated to a presentation of the high confinement (H-mode) regime obtained in the TCV tokamak for the EBH experiments.
Chapter 3 addresses the basic theory of linear plasma waves and of mode conversions which are of relevance for this work. The codes used in this thesis work are also briefly described. The O-SX-B mode conversion experiments and numerical results are discussed in chapter 4.
In chapter 5, the experimental deposition locations of X2 and EBW RF power is retrieved from high spatial and temporal resolution soft X-ray profiles using the BIS analysis and compared to ray-tracing simulations. Chapter 6 reports on the global power absorption measurements in X2, X3 and EBH experiments. In particular, the previously neglected impact of the sawtooth activity on the method is investigated. Chapter 7 presents the initial results of a systematic scan of AMR-LUKE simulations investigating the EBCD performances in TCV. Chapter 8 reports on the lower-hybrid parametric instability (LHPI) observations in high power EBH experiments in TCV. The design of the new loop-antenna for the detection of LH waves is described and the initial experimental results are presented. In particular, the time-evolution of the LHPI signal intensity is analyzed in coherence with the evolution of the plasma profiles and an EBH power scan allows a first estimate of the LHPI power threshold in TCV EBH experiments. Chapter 9 summarizes the main results and draws conclusions.
The dissertation ends with a number of appendices. Appendix A introduces the sign conventions, the coordinate systems and the definitions of the RF power injection angles used at TCV and implemented in the various codes. Appendix B presents the detailed derivation of the MHD integral relations necessary to the RF power absorption analysis of chapter 6, along with a summary of the various conventions

for the Shafranov integrals met in the literature. Appendix C addresses the equations for the energy anisotropy relaxation which are used in the modeling of the plasma response to modulated ECH in chapter 6.

Chapter 2

The TCV experiment

This chapter describes the *Tokamak à Configuration Variable* (TCV) of the *Centre de Recherches en Physique des Plasma* (CRPP) at the *Ecole Polytechnique Fédérale de Lausanne* (EPFL), along with its electron cyclotron heating system and the main diagnostics used in this thesis work. The reader can find introductions to the tokamak concept in references [31,32] and exhaustive discussions of the toroidal confinement problem in references [33,34].

2.1 The Tokamak à Configuration Variable

TCV is a medium-size magnetic-confinement experimental nuclear fusion device of the tokamak type, designed for the study of plasma performance as a function of its shape [35], in particular the impact of the plasma shape on the plasma magnetohydrodynamic (MHD) properties and the particle and energy confinement. A sketch of TCV's main components is given in figure 2.1. The magnetic field coils arrangement is described in the poloidal view of figure 2.2. TCV tokamak system and plasmas key parameters are listed in tables 2.1 and 2.2, respectively.
TCV has a rectangular stainless steel vacuum vessel of major radius $R_0 = 0.88$ m. The thickness of the vessel wall varies between 1.5 cm and 2 cm. The vessel is continuous in both poloidal and toroidal directions, yielding a low electrical resistance. It can thus passively contribute to the vertical stabilization of highly elongated plasmas. In order to prevent the penetration of high-Z impurities into the plasma, which would yield to substantial plasma cooling by radiation losses, about 90% of the vessel interior is covered with graphite tiles whose thickness varies between 2 cm and 2.4 cm. As a consequence of the graphite tiles, carbon is the main impurity in TCV plasmas. Taking into account the graphite tiles thickness, the inner minor radius

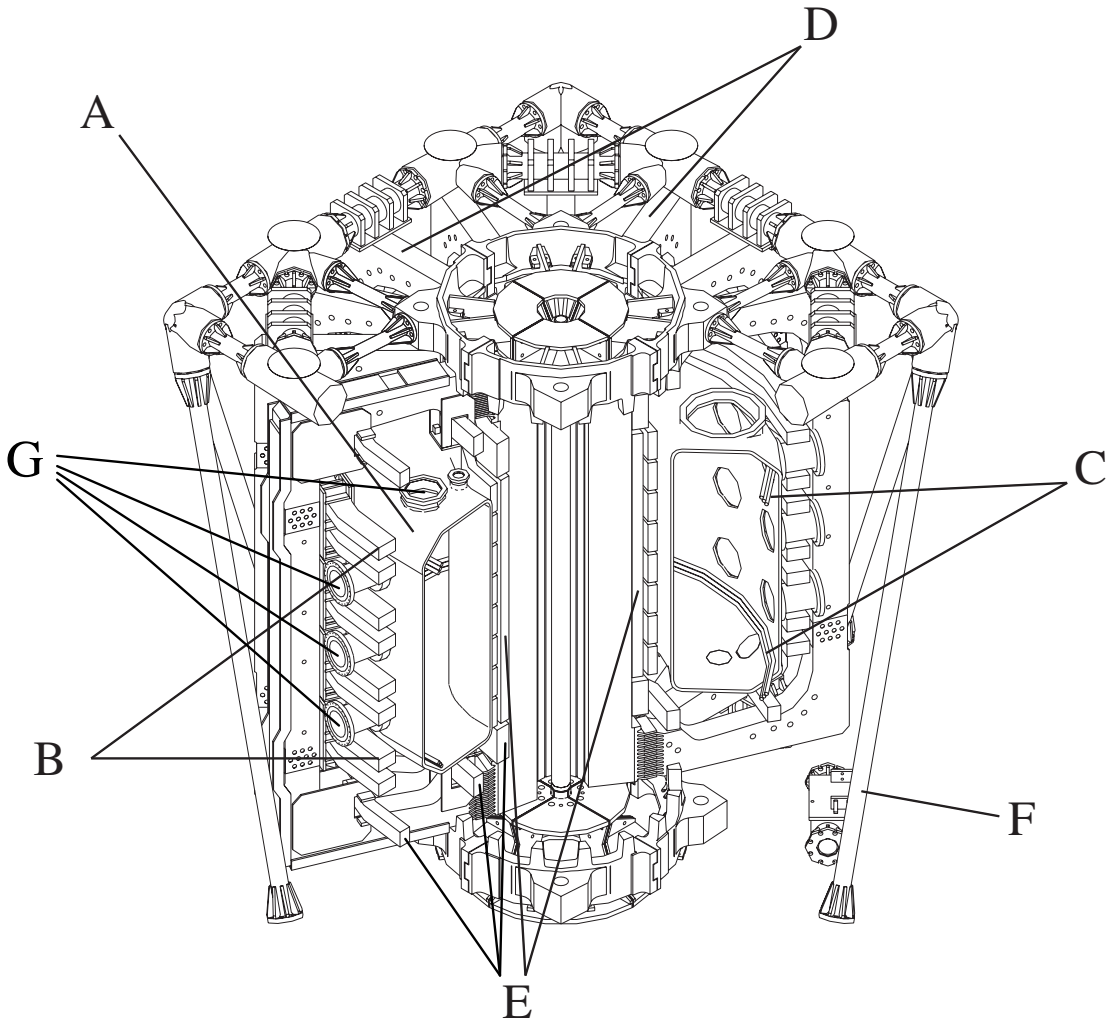

Figure 2.1: TCV tokamak. Drawing of the main components of TCV tokamak: (A) the vacuum vessel, (B) the 16 poloidal field coils for the plasma positioning and shaping, (C) the 6 fast internal coils for the plasma vertical stabilization, (D) the 16 coils for the generation of the main toroidal magnetic field, (E) the 7 primary coils of the transformer circuit driving the inductive plasma current, (F) the supporting structure, (G) the ports for the diagnostics and the ECH system access to the plasma (3 lateral ports per sector + top and bottom ports).

and half-height of the torus are $a_T = 0.255$ m and $b_T = 0.75$ m, respectively. The torus has thus a strong inner elongation $\kappa_T \equiv b_T/a_T \simeq 2.94$ and a medium aspect ratio $\epsilon \equiv R_0/a_T \simeq 3.45$.

TCV main toroidal magnetic field is produced by 16 toroidal field coils (TFC) around the torus. The TFC coils are evenly spaced in the toroidal direction, thus defining the 16 sectors of TCV. TCV sectors are numbered from 1 to 16 in the counter-clockwise direction (seen from the top), with the TFC coil between sectors 1 and 16 aligned with the west direction. This is the historical reason for the choice of the

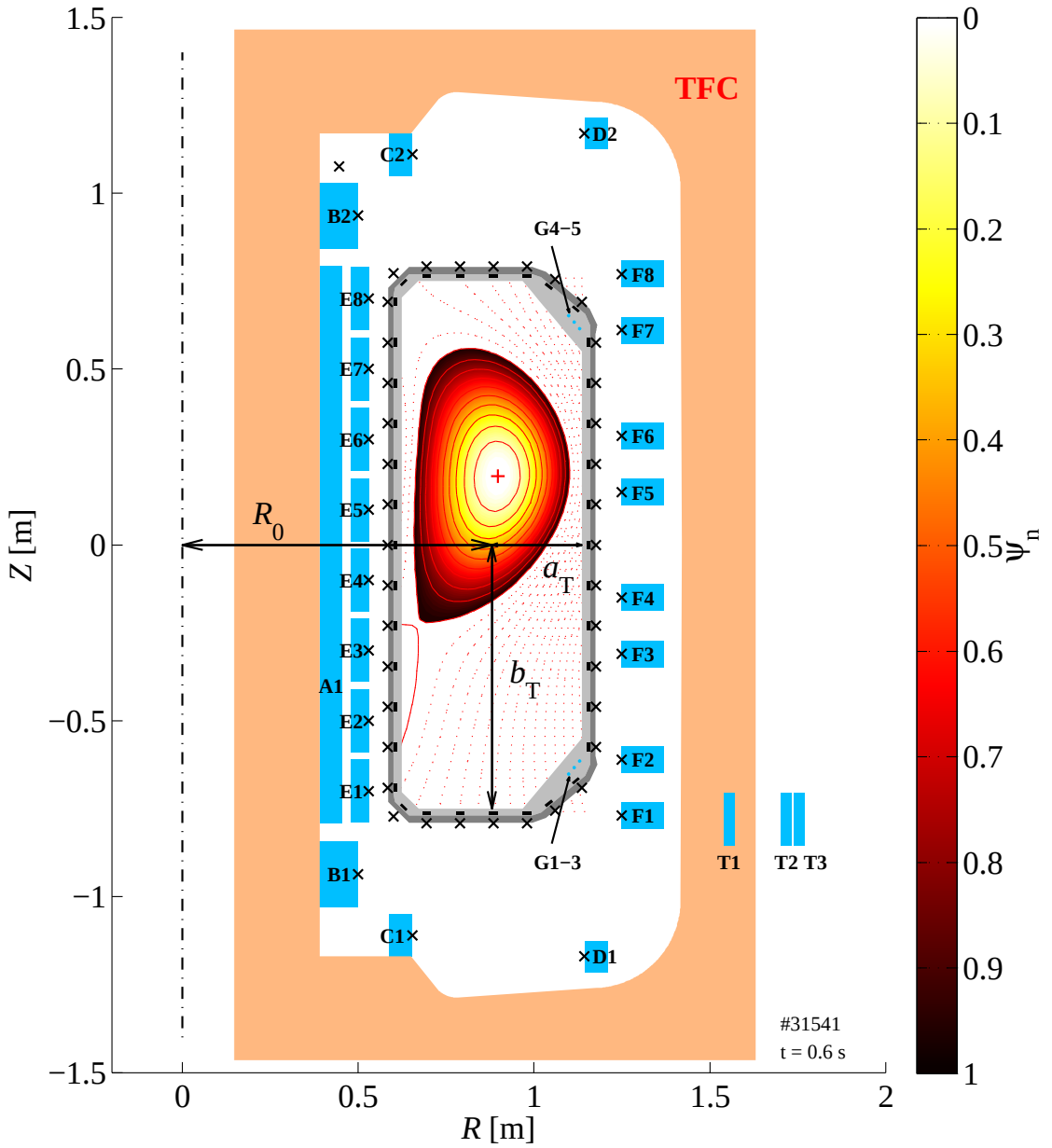

Figure 2.2: TCV magnetic coil system. TCV poloidal cross section showing the vacuum vessel (dark gray) with the graphite tiles (light gray), the 7 Ohmic transformer coils (A, B, C and D), the 16 poloidal field coils (E and F), the 6 internal fast coils (G), one of the 16 toroidal field coils (TFC), the bus bars (T1 and T2) connecting the toroidal field coils, and the return loop (T3). The position of the internal magnetic probes and external flux loops is indicated by small rectangles (▮) and crosses (×), respectively. In the vacuum vessel are also plotted contours and color map of the normalized poloidal flux ψ_n for a diverted high-current H-mode equilibrium of elongation $\kappa_a \simeq 1.76$ and triangularity $\delta_a \simeq 0.55$, typical of the EBW experiments presented in this work. The vertical dash-dotted line indicates the tokamak revolution axis. $R_0 = 0.88\,\mathrm{m}$, $a_T = 0.255$ m and $b_T = 0.75$ m are the vacuum vessel major radius, minor radius and half-height, respectively. TCV shot #31541 at $t = 0.6\,\mathrm{s}$.

counter-clockwise direction (seen from the top) as the definition of TCV positive toroidal direction. Other sign conventions and coordinate systems are defined in appendix A.

The inductive component of the plasma current (also called Ohmic current) is generated by the 7 primary coils of an air core transformer. The plasma position and shape are controlled by two groups of 8 poloidal field coils (PFC) arranged on the inner and outer sides of the TCV vacuum vessel, respectively. Finally, the plasma vertical stability is ensured by 6 fast internal coils installed at the top and bottom of TCV inside wall, behind the graphite tiles.

TCV tokamak		
Parameter	**Symbol**	**Value**
Torus major radius	R_0	0.88 m
Torus inner minor radius (with tiles)	a_T	0.28 m (0.255 m)
Torus inner half-height (with tiles)	b_T	0.77 m (0.75 m)
Torus inner elongation (with tiles)	$\kappa_\mathrm{T} \equiv b_\mathrm{T}/a_\mathrm{T}$	2.75 m (2.94 m)
Torus inner aspect ratio (with tiles)	$\epsilon \equiv R_0/a_\mathrm{T}$	3.14 (3.45)
Loop voltage	V_loop	≤ 10 V
Installed X2/O2 RF power (nominal)	P_RF	3 MW
Installed X3 RF power (nominal)	P_RF	1.5 MW
Toroidal magnetic field on vessel axis	$B_\varphi(R_0)$	≤ 1.54 T

Table 2.1: TCV tokamak key parameters. The values given in parentheses take into account the graphite tiles thickness.

Between the TFC and PFC coils on the lateral side of the vacuum vessel, as well as on the top and at the bottom of the torus, several tens of ports with various sizes allow the many diagnostics and the electron cyclotron heating (ECH) system to access the plasma.

The plasma current and the poloidal field coils generates the poloidal magnetic field $\mathbf{B}_\mathrm{p}$. The resulting nested flux surfaces are labelled either with the normalized poloidal-flux radius ρ_ψ or with the normalized volume radius ρ_vol defined as

$$\rho_\psi \equiv \sqrt{\frac{\psi - \psi_0}{\psi_a - \psi_0}} \qquad \text{and} \qquad \rho_\mathrm{vol} \equiv \sqrt{\frac{V}{V_a}}, \tag{2.1.1}$$

respectively, where

$$\psi = \frac{1}{2\pi} \int_A \mathbf{B}_\mathrm{p} \cdot \mathrm{d}\mathbf{A} \tag{2.1.2}$$

TCV plasmas		
Parameter	**Symbol**	**Value**
Plasma current	I_p	$\lesssim 1.1$ MA
Central electron density, L-mode	$n_{\mathrm{e}0} \equiv n_\mathrm{e}(\rho_\psi = 0)$	$\leq 5 \cdot 10^{19}$ m^{-3}
Central electron density, H-mode	$n_{\mathrm{e}0} \equiv n_\mathrm{e}(\rho_\psi = 0)$	$\leq 25 \cdot 10^{19}$ m^{-3}
Central electron temperature, OH	$T_{\mathrm{e}0} \equiv T_\mathrm{e}(\rho_\psi = 0)$	≤ 2 keV
Central electron temperature, ECH	$T_{\mathrm{e}0} \equiv T_\mathrm{e}(\rho_\psi = 0)$	$\lesssim 20$ keV
Central ion temperature	$T_{\mathrm{i}0} \equiv T_\mathrm{i}(\rho_\psi = 0)$	$\lesssim 1$ keV
Plasma minor radius	a	≤ 0.255 m
Plasma half-height	b	≤ 0.75 m
Plasma edge elongation	κ_a	$0.9 \leq \kappa_a \leq 2.8$
Plasma edge triangularity	δ_a	$-0.8 \leq \delta_a \leq 0.9$
Electron plasma frequency	$f_\mathrm{pe} \equiv \omega_\mathrm{pe}/2\pi$	89.8 GHz
Ion plasma frequency	$f_\mathrm{pi} \equiv \omega_\mathrm{pi}/2\pi$	1.5 GHz
Electron cyclotron frequency	$f_\mathrm{ce} \equiv \Omega_\mathrm{ce}/2\pi$	40.6 GHz
Ion cyclotron frequency	$f_\mathrm{ci} \equiv \Omega_\mathrm{ci}/2\pi$	11.1 MHz
Electron thermal velocity	$v_\mathrm{the} \equiv \sqrt{T_\mathrm{e}/m_\mathrm{e}}$	$1.33 \cdot 10^7$ m/s
Ion thermal velocity	$v_\mathrm{thi} \equiv \sqrt{T_\mathrm{i}/m_\mathrm{i}}$	$2.19 \cdot 10^5$ m/s
Electron Larmor radius	$r_\mathrm{Le} \equiv v_\mathrm{the}/\Omega_\mathrm{ce}$	$5.2 \cdot 10^{-5}$ m
Ion Larmor radius	$r_\mathrm{Li} \equiv v_\mathrm{thi}/\Omega_\mathrm{ci}$	$3.2 \cdot 10^{-3}$ m
Electron Debye length	$\lambda_\mathrm{De} \equiv v_\mathrm{the}/\omega_\mathrm{pe}$	$2.4 \cdot 10^{-5}$ m
Ion Debye length	$\lambda_\mathrm{Di} \equiv v_\mathrm{thi}/\omega_\mathrm{pi}$	$2.4 \cdot 10^{-5}$ m

Table 2.2: Range of TCV plasmas parameters. The second half of the table gives the plasma characteristic frequencies and lengths for the typical H-mode plasma parameters met in this work (temperatures $T_\mathrm{e} = T_\mathrm{i} = 1$ keV, particle number densities $n_\mathrm{e} = n_\mathrm{i} = 1 \cdot 10^{20}$ m^{-3}, magnetic field $B = 1.45$ T). Deuterium ions have been considered here. The plasma and cyclotron angular frequencies are defined as $\omega_{\mathrm{p}\alpha} \equiv \sqrt{(n_\alpha q_\alpha^2/m_\alpha \varepsilon_0)}$ and $\Omega_{\mathrm{c}\alpha} = q_\alpha B/m_\alpha$, respectively, where q_α and m_α are respectively the electric charge and the mass of the particle of species $\alpha = \mathrm{e}, \mathrm{i}$.

is the poloidal magnetic flux through a washer-shaped surface A on the horizontal plane passing through the magnetic axis. The integration constant can be chosen such that $\psi = 0$ on the magnetic axis or on the last closed flux surface. The latter convention is followed at TCV. In definitions 2.1.1, ψ_0 and ψ_a are the poloidal magnetic fluxes on the magnetic axis and at the plasma edge, respectively, and the V_a is the total plasma volume.

Thanks to its 16 independently driven poloidal field coils system, TCV offers the unique ability to vary the magnetic equilibrium over a wide range of plasma positions and shape parameters, in limited or diverted configurations, as indicated in table 2.2. The toroidal magnetic field and plasma current values, as well as the position of the plasma column and the shape of its cross section, can be programmed to change during the plasma discharge.
The first and second order poloidal plasma shaping parameters are the elongation and the triangularity defined as

$$\kappa \equiv b/a \qquad \text{elongation} \tag{2.1.3}$$

$$\delta \equiv -d/a \qquad \text{triangularity} \tag{2.1.4}$$

where a is the plasma minor radius at the plasma midplane, b is the plasma half-height and d is the radial shift of the flux surface vertical extremum with respect to the magnetic axis position, as illustrated in figure 2.3.

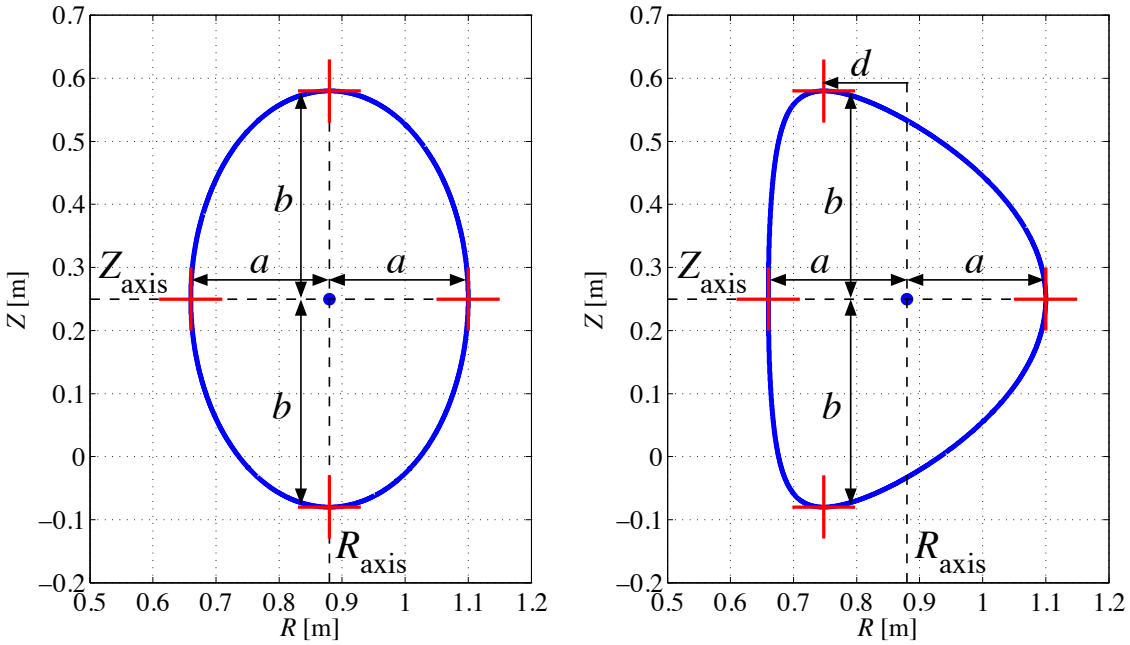

(a) Elongation $\kappa_a = b/a$.

(b) Triangularity $\delta_a = -d/a$.

Figure 2.3: Plasma shape parameters. Sketches of last closed flux surface contours illustrating the first and second order poloidal shaping moments, i.e. the elongation $\kappa_a \equiv b/a$ and the triangularity $\delta_a \equiv -d/a$, respectively. (a) $\kappa_a = 1.5$ and $\delta_a = 0$, i.e. $a = 0.22$ m and $b = 0.33$ m. (b) $\kappa_a = 1.5$ and $\delta_a = 0.6$, i.e. $a = 0.22$ m, $b = 0.33$ m and $d = -0.132$ m. In both examples, the plasma magnetic axis (indicated by a blue dot) is located at $R_{\text{axis}} = 0.88$ m and $Z_{\text{axis}} = 0.25$ m.

The plasma edge elongation κ_a and triangularity δ_a parametrize its poloidal contour

as:

$$R = R_0 + a\cos(\xi + \arcsin(\delta_a \sin(\xi))) \tag{2.1.5}$$

$$Z = Z_0 + \kappa_a a \sin(\xi) \tag{2.1.6}$$

where (R, Z) is the cartesian coordinate system in the poloidal plane as illustrated in figure 2.2 and ξ is an angle in the poloidal plane. (Note that ξ is not equal to the actual poloidal angle θ of the toroidal coordinate system.)
In limited plasmas, the intersection of the flux surfaces with a solid surface in the vacuum vessel defines the size of the plasma and thus the so-called last closed flux surface (LCFS). The solid surface can be either a dedicated "limiter" or the vessel wall protected by graphite tiles, as it is the case in TCV. In general, the plasma shape parameters κ_a and δ_a and the edge safety factor q_a are measured at the last closed flux surface. In diverted configurations, the flux surface delimiting the plasma passes through a null of the poloidal flux created by the poloidal field coil system (also called "X-point"), like in figure 2.2. This last flux surface is called "separatrix". At the separatrix, the safety factor q diverges. In this case, the edge safety factor q_{95} is usually evaluated at 95% of the normalized poloidal flux.
The unique flexibility of TCV magnetic coil system has been extensively used to investigate the plasma performances as a function of its shape. In particular, elongated plasmas allow to operate at higher plasma currents (than in circular plasmas) without breaking the limit of the ideal MHD stability requiring an edge safety factor $q_a > 2$ [36]. In turn, higher currents allow one to reach higher plasma densities as predicted by the Greenwald limit [37], which is overall beneficial to fusion power yield in a thermonuclear reactor. The most elongated plasma in ITER-like medium aspect ratio tokamaks has been achieved in TCV with $\kappa = 2.8$. TCV experiments also demonstrated that plasma elongation and triangularity improve the plasma MHD stability [38] and reduce the heat transport [39, 40].

2.2 TCV electron cyclotron heating system

TCV is equipped with a highly flexible electron cyclotron heating (ECH) and current drive (ECCD) system at the second and third harmonics of the electron cyclotron frequency, totalizing the highest EC power density and one of the highest EC power installed on a magnetic confinement fusion device. A detailed presentation of the TCV ECH hardware and control systems along with an exhaustive operation history is to be found in reference [41].

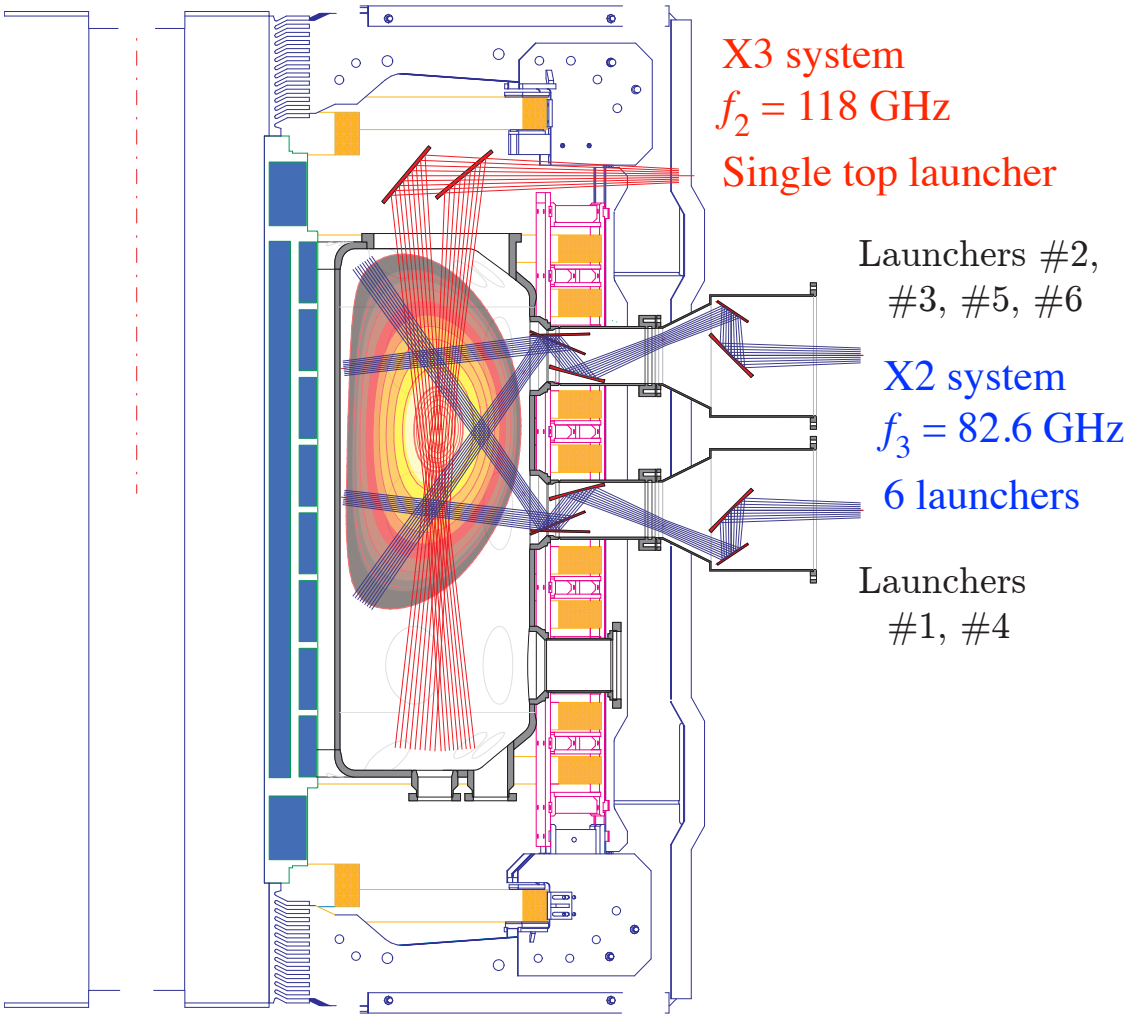

Figure 2.4: TCV X2 and X3 ECH system. Poloidal view of TCV cross section showing the mirror system of the 2nd and 3rd harmonics EC power launchers. The six X2/O2 steerable launchers are distributed amongst two equatorial ports (#1 and #4) and four upper lateral ports (#2, #3, #5 and #6). The X3 steerable launcher allows the injection of EC power from the top of TCV vacuum vessel along the quasi-vertical EC resonance. The blue and red rays indicate the range of poloidal beam trajectories (in vacuum) that can be achieved thanks to the steerable mirrors of the X2/O2 and X3 launchers, respectively. Since the X2/O2 launchers can rotate on their horizontal axis, the equatorial (respectively upper lateral) launchers can also inject the EC power with a downward (respectively upward) direction, in addition to toroidal directions as indicated in figure 2.5.

2.2.1 2nd harmonic ECH system

TCV 2nd harmonic ECH system consists of 2 clusters (A and B) of 3 gyrotrons each. The two clusters have independent power supplies (thus allowing two independent power modulation waveforms). The gyrotrons operate at a fixed vacuum wavelength $\lambda_2 = 3.628$ mm, i.e. at a frequency $f_2 = 82.6$ GHz, such that the corresponding electron cyclotron resonance is located close to the vessel center for plasmas with

standard toroidal field values around $B_{\varphi 0} = 1.43$ T [42]. Each gyrotron can deliver a nominal radio frequency (RF) power $P_{\mathrm{RF}} = 0.5$ MW during a maximum pulse length of 2 s. The individual gyrotron power calibration is performed by calorimetric measurement of the power absorption in a water load. The power amplitude of both clusters can be modulated independently.

The microwave power leaving the gyrotrons is passed through matching optic units (MOUs) which optimize the wave polarization (ellipticity and orientation of the ellipse major axis) for ordinary (O2) or extraordinary (X2) mode coupling to the plasma thanks to a pair of sinusoidally corrugated gratings. Corrugated waveguides bring the RF power to TCV over an average distance of 30 m. The waves are then injected into the plasma via 6 steerable transmitting antennas, referred to as "launchers", installed in equatorial ports (L1 and L4 with their longitudinal axis at $Z_{\mathrm{launcher}} = 0$ cm) and upper lateral ports (L2, L3, L5 and L6 with their longitudinal axis at $Z_{\mathrm{launcher}} = 45.5$ cm), as indicated in figure 2.4. The gyrotrons of cluster A are connected to launchers L1, L2 (in sector 2) and L3 (in sector 1), while the gyrotrons of cluster B are connected to launchers L4, L5 (in sector 6) and L6 (in sector 7), as indicated in figure 2.5. The overall power losses from the gyrotrons to the wave injection into the plasma are typically of the order of 7%.

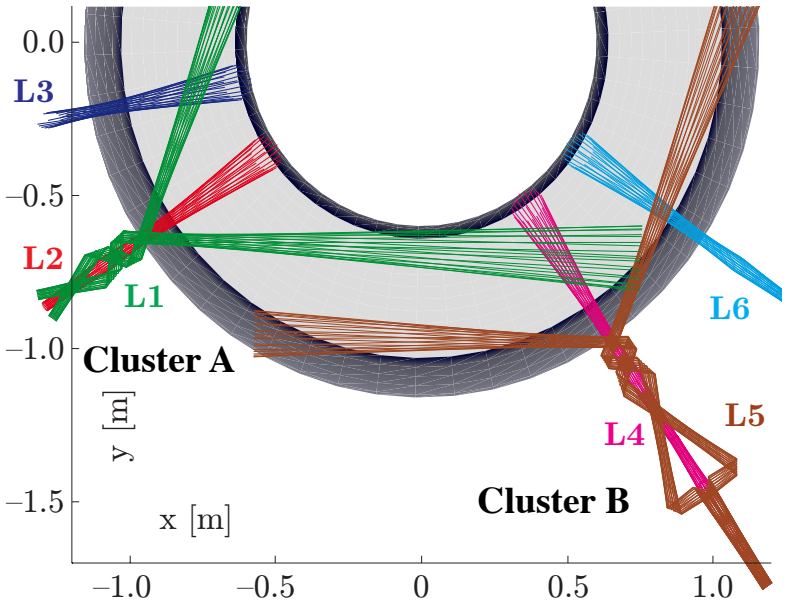

Figure 2.5: TCV X2 ECH system. Top view of TCV 2nd harmonics ECH launcher system. Launchers L1, L2 and L3 are connected to the gyrotrons of cluster A and distributed in sectors 1 and 2. Launchers L4, L5 and L6 are connected to the gyrotrons of cluster B and distributed in sectors 6 and 7. The rays leaving launchers L1 and L5 indicate the range of achievable toroidal angles.

The 6 X2/O2-power launchers are essentially identical. They each consist of 4 mirrors made of TZM molybdenum alloy. The detailed launcher mirror system is presented in figure 2.6. The mirrors M2 and M4 are planar while mirrors M1 and M3 are focusing, as can be observed on the X2/O2 ray paths in figure 2.4. The mirrors were designed such that the RF power leaves the launcher as a circular gaussian beam with a waist $w_0 = 18.3$ mm located at ~ 276 mm from the incident point on the last focusing mirror (M3). Each of the 6 launchers can be steered independently with 2 degrees of freedom, providing a full coverage of the plasma cross-section for on-axis and off-axis ECH for all plasma positions, as well as co-/counter-ECCD, as indicated in figures 2.4 and 2.5.

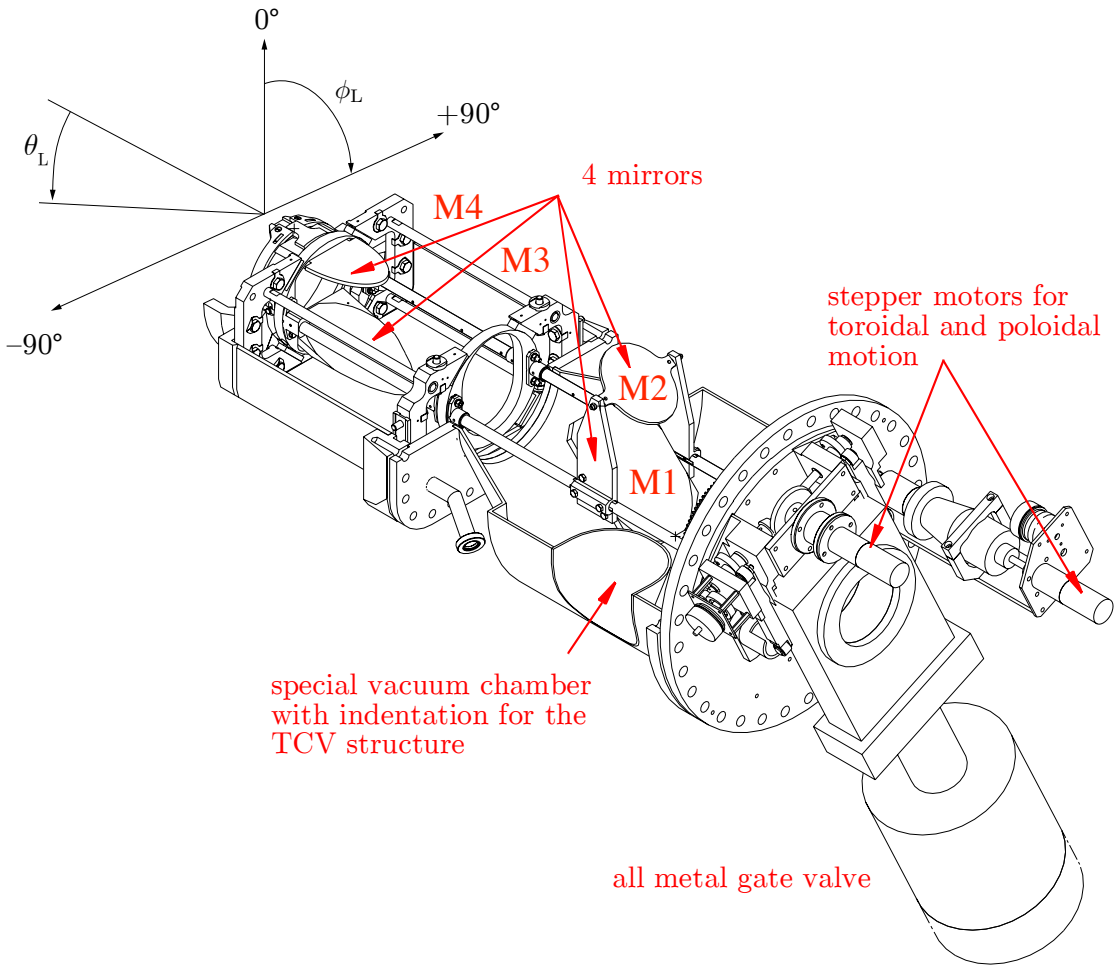

Figure 2.6: X2 EC power launcher. Drawing of TCV second-harmonic EC power launcher consisting of two focusing mirrors (M1 and M3) and two planar mirrors (M2 and M4). In between shots, the whole system can be rotated around its horizontal axis by a "toroidal launcher angle" $-180° \leq \phi_L \leq +180°$. The last mirror can be tilted such that the beam leaves the launcher with a "poloidal launcher angle" $7° \leq \theta_L \leq 55°$ with respect to the launcher axis. This latter angle can be programmed to change during the plasma discharge.

The two degrees of freedom of the launcher are illustrated on figure 2.6:

- The whole mirror system can fully rotate around its horizontal axis with an angle $-180^\circ \leq \phi_L \leq +180^\circ$ called the "toroidal launcher angle" since it allows oblique beam injections with non-zero parallel refractive index $N_\parallel$, which is necessary for ECCD and EBH experiments. The ϕ_L angle can be varied only in between plasma discharges.

- The mirror facing the plasma can be tilted such that the beam leaves the antenna with a "poloidal launcher angle" $7^\circ \leq \theta_L \leq 55^\circ$. This naming may be confusing since θ_L corresponds to the actual poloidal angle in the vertical plane of injection only in situations of pure ECH, i.e. for $\phi_L = 0^\circ$ (downward injection) and $\phi_L = \pm 180^\circ$ (upward injection). The θ_L angle can be swept during plasma discharges.

The conversion formulae between the launcher angles (θ_L, ϕ_L) and the effective injection angles $(\theta_{inj}, \phi_{inj})$ implemented in the codes and used in this thesis are given in appendix A.

2.2.2 3rd harmonic ECH system

TCV 3rd harmonic ECH system consists of one cluster of 3 gyrotrons with a common power supply. The gyrotrons operate at a fixed frequency $f_3 = 118$ GHz such that the corresponding EC resonance is located close to the center of TCV vacuum vessel at standard toroidal magnetic field $B_{\varphi 0} = 1.43$ T . Each gyrotron can deliver a nominal radio frequency (RF) power $P_{RF} = 0.45$ MW during 2 s. Only the X-mode polarization is available from the 3rd harmonic gyrotrons (X3) for maximum absorption.
At the beginning of the X3 ECH system exploitation (in 2002), a first X3 gyrotron was connected to the upper-lateral launcher L3 of the X2 ECH system [43]. During the 2003 TCV campaign, the X3 ECH system was made complete with its 3 gyrotrons. The EC power coming from the three X3 gyrotrons is injected from a unique launcher consisting of a single mirror and installed at the top of TCV vacuum vessel, as indicated on figure 2.4, in order to increase the wave trajectory length along the EC resonance and maximize the absorption [44]. The mirror radial position can be optimized between shots and a real-time control of the poloidal tilt has been implemented to adjust the X3 power injection to the EC resonance position during the plasma discharge [45].

2.3 Selected TCV diagnostics

TCV is equipped with a large ensemble of diagnostics for the experimental measurement of the plasma characteristics. This section provides a brief description of the diagnostics essential to this thesis and used in several chapters. The diamagnetic loop (DML) diagnostic for the measurement of the plasma toroidal magnetic flux is presented in details in chapter 6 focusing on the determination of the global RF power absorption coefficient. The new TCV loop-antenna for the detection of lower-hybrid waves (LHW) is introduced in chapter 8 treating of the LH parametric instability in TCV high-power electron Bernstein heating experiments.

2.3.1 Duplex Multiwire soft-X ray Proportional detector (DMPX)

Soft X-ray emission in plasmas

Plasma radiation emission in the soft X-ray range ($h\nu = 0.12 - 12$ keV) originates from three processes:

- the **Bremsstrahlung radiation** arising from free-free electron-ion Coulomb collisions,
- the **recombination radiation** arising from the capture of free electrons by ions in free-bound collisions,
- the **line radiation** arising from the transition of a bound electron from an excited state to a lower energy state.

The Bremsstrahlung and recombination radiation spectra are continuous in frequency where the line radiation spectrum is discrete: the emitted photon has a specific energy $h\nu = \Delta E$ where ΔE is the difference in energy of the two states involved in the transition.
A derivation of the spectral emissivity for these phenomena is given in references [46, 47]. Assuming a Maxwellian electron velocity distribution, the Bremsstrahlung spectral emissivity $j_{\mathrm{B}}(\nu)$ (power per unit solid angle per unit volume per unit energy of the emitted photons) writes [47]

$$j_{\mathrm{B}}(\nu) = g_{\mathrm{ff}} n_{\mathrm{e}}^2 Z_{\mathrm{eff}} \frac{e}{h} \left(\frac{e^2}{4\pi\epsilon_0}\right)^3 \frac{8\pi}{3\sqrt{3} m_{\mathrm{e}}^2 c^3} \left(\frac{2m_{\mathrm{e}}}{\pi e T_{\mathrm{e}}}\right)^{1/2} \mathrm{e}^{-\frac{h\nu}{T_{\mathrm{e}}}} \tag{2.3.1}$$

which evaluates to

$$j_{\mathrm{B}}(\nu) = 1.22 \cdot 10^{-39}\, g_{\mathrm{ff}} n_{\mathrm{e}}^2 Z_{\mathrm{eff}} \frac{1}{\sqrt{T_{\mathrm{e}}}} \mathrm{e}^{-\frac{h\nu}{T_{\mathrm{e}}}} \quad [\mathrm{W\ sr^{-1}\ m^{-3}\ eV^{-1}}] \tag{2.3.2}$$

where the electron density n_{e} is expressed in $[\mathrm{m}^{-3}]$, the electron temperature T_{e} and photon energy $h\nu$ are expressed in [eV], and the effective charge is defined as

$$Z_{\mathrm{eff}} \equiv \frac{\sum_{\mathrm{i}} Z_{\mathrm{i}}^2}{\sum_{\mathrm{i}} n_{\mathrm{i}} Z_{\mathrm{i}}}. \tag{2.3.3}$$

The temperature and frequency dependence of the Maxwell-averaged free-free Gaunt factor g_{ff} is weak and g_{ff} is assumed to be a constant [47]. After integration on the whole energy spectrum, the Bremsstrahlung power P_{B} emitted per unit solid angle and unit volume depends on the electron density, temperature and effective charge as

$$P_{\mathrm{B}} \equiv \int_0^\infty j_{\mathrm{B}}(\nu)\, \mathrm{d}\nu = 1.84 \cdot 10^{-6}\, g_{\mathrm{ff}} n_{\mathrm{e}}^2 Z_{\mathrm{eff}} \sqrt{T_{\mathrm{e}}} \quad [\mathrm{W\ sr^{-1}\ m^{-3}}]. \tag{2.3.4}$$

2.3.1.1 Soft X-rays detection in a wire-chamber detector

Soft X-ray photons interact with matter mainly by photo-electric absorption. During this process, the incident photon is absorbed by an atom which gets ionized. In a wire-chamber, the resulting free charges (negatively charged electron and positively charge ion) are used for the detection of the incident soft X-ray. A wire-chamber is composed of an array of thin wires (anodes) and two plane cathodes, one on each side of the wire array. An electrical field is applied between the anodes and the cathodes. An incident soft X-ray photon interacts with an atom of the detection gas filling the chamber, creating a pair of electron and ion which are then accelerated by the electrical field. While migrating towards the closest wire-anode, the primary electron will collide with detection gas atoms and ionize them, thus creating more electron-ion pairs which will in turn be accelerated and collide with neutral atoms... A chain-reaction (avalanche) takes place near the wire and the wire chamber measures a slight change in the tension on this wire due to the work of the free charges (mainly the ions) migrating in the electrical field. To prevent parasitic avalanches and continuous arcs which can seriously damage the wire-anodes, the detection gas is usually mixed with a bit of quenching gas absorbing a fraction of the secondary electrons.

DMPX hardware description

The Duplex Multiwire Proportional soft X-ray detector (DMPX) is a 64-channel soft X-ray profile diagnostic, offering both high radial and temporal resolutions and

covering most of TCV vessel cross section [48, 49]. It is sensitive to photons in the $h\nu = 1.5 - 30$ keV range, where ν is the emitted frequency and h is the Planck constant. In the TCV plasmas studied in this thesis work, the central electron temperature is typically $T_{e0} \gtrsim 1$ keV. The following condition is thus fulfilled:

$$T_{e0} \gg Z_{eff}^2 R_y \simeq 122 \text{ eV} \tag{2.3.5}$$

where $R_y \simeq 13.6$ eV is the Rydberg energy and $Z_{eff} \equiv \sum_i Z_i^2/n_e \simeq 3$ is the plasma effective charge (the quasi-neutrality condition $n_e = \sum_i n_i Z_i$ has been invoked here). As a consequence, the recombination radiation is negligible for all frequencies ν compared to the Bremsstrahlung radiation [47]. Moreover, the line radiation from light impurities (carbon, oxygen) is important only in the ultra-soft X-ray spectral range ($h\nu \leq 1$ keV). The DMPX diagnostic thus measures mainly Bremsstrahlung radiation.

The DMPX detector is installed at the bottom of TCV vacuum vessel (in sector 9) and views the plasma vertically, as indicated in figure 2.7.

The DMPX detector consists of two superimposed multiwire chambers referred to as "top" and "bottom" detectors. Both detectors are essentially identical and work on the wire-chamber principle developed at CERN [50] and briefly described here above. Each detector is made of an airtight aluminum box containing 64 parallel gold-plated tungsten anode-wires of 20 microns diameter and 32 mm length spaced by 2 mm. The wires are aligned with the toroidal direction. Parallel to the planes containing the wires are two plane-cathodes for each detector. For the top detector, these are two 50-micron-thick beryllium windows, one to let the incident photons in, one to let the non-absorbed photons leave the chamber. For the bottom chamber, the two plane-cathodes are one 50-micron-thick beryllium window to let the photons in and a 2-mm-thick stainless steel sheet. The Beryllium was chosen for its relative transparency to soft X-rays. Since there are less photons reaching the bottom detector (most of them are absorbed in the top wire-chamber and in the 10 mm of air between them), its wires are connected two by two to maximize the signal, reducing the number of its lines-of-sight to 32. The DMPX detector has high space resolution: the mean distance separating two lines-of-sight at the equatorial plane of TCV is of 7.9 mm and 16.3 mm for the top and bottom detectors, respectively. In our conventions, the DMPX lines-of-sight are numbered from 1 to 64 (or from 1 to 32 for the bottom detector) going from HFS to LFS.

The two wire-chambers are assembled with 10 mm of air in between. The whole system is connected to the bottom of TCV sector 9 with a 230-mm-long tube filled

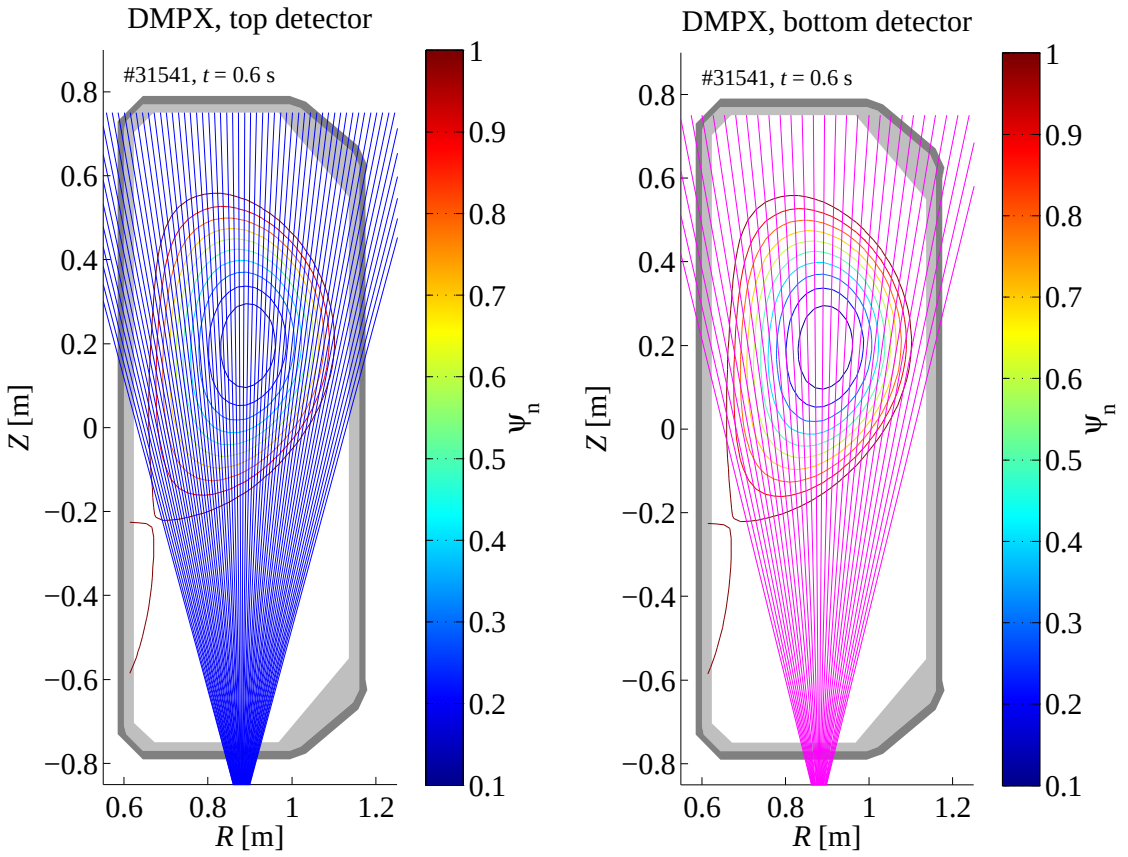

(a) DMPX: top detector lines-of-sight. **(b)** DMPX: bottom detector lines-of-sight.

Figure 2.7: High radial resolution soft X-ray detector (DMPX). TCV poloidal cross section showing the lines-of-sight of DMPX (a) top and (b) bottom detectors. The 64-channel top detector has a radial resolution of 7.9 mm at the vessel midplane. In the bottom detector, the channels are connected by pairs, yielding a radial resolution of 16.3 mm. #31541 at $t = 0.6\,\mathrm{s}$.

with a constant flux of Helium at atmospheric pressure. Helium is necessary to prevent air absorption of the soft X-rays. The soft X-rays emitted by the plasma can reach the DMPX via a 2-mm-thin slit (itself recovered by a 50-micron-thick Beryllium window) at the top of the Helium tube. Each wire thus sees only a trapezoidal volume of the plasma.

In order to detect the incident soft X-rays, a high voltage up to 2500 V is applied between the wires and the cathodes in each chambers independently, and the detection volumes are filled with a constant flux of detection gas at atmospheric pressure. The default gas used since 2002 is a mixture of 90% krypton (detection gas) and 10% methane for the quenching of parasitic avalanches. The wire-chambers operate in the proportional and continuous regime, that is the measured signal, integrated along the lines-of-sight, is proportional to the mean power of the incident soft X-

ray flux. The DMPX detector is sensitive to soft X-ray photons emitted in the $3 - 40$ keV energy range. The lower energy radiation (including the line radiation of light impurities like oxygen and carbon) is filtered by the Beryllium windows.
A movable absorber-holder is installed just below the slit to allow the addition of an extra absorber layer in front of both wire-chambers: 125 microns Beryllium, 550 microns Beryllium or 308 microns Aluminum. The operation of the DMPX can thus be extended to plasmas with a very intense soft X-ray flux or limited to the observation of higher energy part of the soft X-rays emission.
The DMPX has a high time resolution with a frequency bandwidth of 50 kHz. The measured signal is amplified, low-pass filtered at 70 kHz for anti-aliasing and stored in a DTACQ unit at an acquisition frequency of 200 kHz.
The pair of wire-chamber detectors was meant to extract the electron temperature profile from the ratio of the soft X-ray profiles from the top and bottom detector, using the so-called "absorber method", but needs further work to become reliable. In this thesis work, only the raw soft X-ray signal from the top detector is used.

2.3.2 Electron density and temperature diagnostics

Thomson Scattering (TS)

The Thomson scattering (TS) diagnostic measures the local profiles of electron temperature $T_e(\rho)$ and density $n_e(\rho)$ by spectral analysis of the fraction of a laser beam scattered by the plasma electrons. The scattered light is Doppler-shifted due to the electron motion. The width of the Doppler line broadening and the integral over the spectral peak determine the electron temperature and density, respectively.
TCV Thomson scattering diagnostic [51–55] is equipped with three powerful (1.5 J/pulse) Nd-Yag lasers in the near infrared spectrum (i.e. $\lambda = 1.064$ μm) offering a 20 Hz repetition rate. The light of the three lasers is injected along the same vertical path through the plasma at $R = 0.9$ m, as indicated in figure 2.8(a). The scattered light is collected by 26 optic fibers installed in three lateral ports of the TCV vacuum vessel. The lines-of-sight are evenly spaced and cover the whole plasma cross section with a spatial resolution of ~ 4 cm on the lasers path: this is the main TS system. Nine additional lines-of-sight installed in the upper lateral port aim at increasing the density of data points and thus the radial resolution at the plasma edge, especially for the measurement of H-modes pedestal profiles: this is the edge TS system.
In low-density plasmas, the three lasers are usually pulsed simultaneously to increase

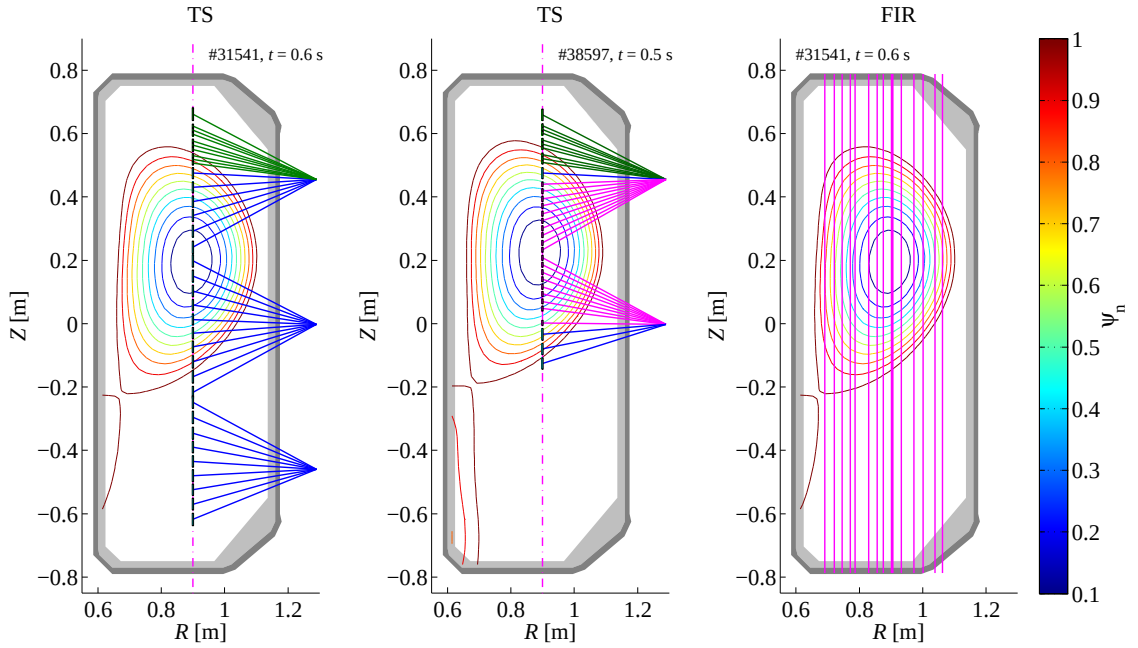

(a) TS: full coverage. **(b)** TS: high resolution. **(c)** FIR vertical chords.

Figure 2.8: Thomson Scattering (TS) and Far Infra-Red (FIR) interferometer lines-of-sight. (a) 2006 TS setup covering the whole vessel cross section: the 25 lines-of-sight of the main TS system (blue, $\Delta Z \simeq 35-41$ mm) and the 10 lines-of-sight of the edge TS system (green, $\Delta Z \simeq 12-13$ mm and $\Delta Z \simeq 40$ mm for the top chord) cross the beam path (vertical dash-dotted line) at $R \simeq 0.9$ m. **(b) 2009 high resolution TS setup:** the 23 main chords are divided in two groups, with low spatial resolution (blue, $\Delta Z \simeq 36-37$ mm) and high spatial resolution (magenta, $\Delta Z \simeq 16-17$ mm). The edge chords cover the plasma edge with high spatial resolution (green, $\Delta Z \simeq 12$ mm and $\Delta Z \simeq 36$ mm for the top chord). **(c) FIR interferometer:** 14 vertical chords. The central chord (#9, thick line, $R \simeq 0.9$ m) is used for the real-time control of the density during the plasma discharges.

the signal-to-noise ratio. In high-density plasmas ($n_e \geq 5 \cdot 10^{19}$ m^{-3}), the scattered light from one laser is sufficient to insure a proper profile measurement. In this case, the lasers can be pulsed sequentially, either with evenly spaced trigger times in order to increase the repetition rate to 60 Hz for a higher time resolution, or with 1-ms spaced triple pulses at a 20 Hz rate in order to increase the density of radial data points for a high-quality profile fitting. When available, the latter option was routinely chosen for the measurement of the H-modes profiles in this thesis work.

Multi-chord Far Infra-Red interferometer (FIR)

TCV Far Infra-Red (FIR) interferometer [56, 57] provides a line-integrated measurement of the electron density with an accuracy of 1% and a frequency response

up to 750 kHz (usually down-sampled to 20 kHz). The FIR system determines the phase shift between two laser beams ($\lambda = 214.6$ μm) from a coherent light source, the probing and reference beams traveling through the plasma and outside the tokamak, respectively. The measured phase shift $\Delta\phi$ is proportional to the line-integrated electron density along the probing beam path through the plasma [47]:

$$\Delta\phi \simeq \frac{\omega}{2cn_c}\int n_e dl \tag{2.3.6}$$

where $n_c = \frac{\varepsilon_0\omega^2 m_e}{e^2}$ is the cutoff density for beam of angular frequency ω.

2.4 H-mode plasmas in TCV

H-mode milestones

The high confinement (H-mode) regime was first observed in neutral-beam-heated diverted plasmas in ASDEX [58]. For the cost of only a small amount of additional power (either Ohmic or from auxiliary heating systems), the H-mode regime is characterized by high values of the particles and energy confinement times and a high normalized pressure β_p compared to the low confinement (L-mode) regime [59]. The improved confinement is provided by the appearance of a transport barrier at the edge of the plasma, thus generating a pedestal in the electron temperature and density profiles. The pedestal characteristics depend on the plasma parameters [60]. The H-mode regime is usually perturbed by a periodic relaxation of the pedestal profiles caused by an MHD instability at the edge of the plasma [61, 62]. This edge-localized-mode (ELM) can cause substantial losses of particles and energy in the form of short bursts. Several types of ELMs have been identified: dithering activity, type-III and type-I ELMs. The latter are large-amplitude ELMs observed in H-modes with dominant auxiliary heating, which may release up to 15% of the plasma thermal energy.

ELMy H-modes in TCV

In TCV, the H-mode regime was first reported in Ohmically heated diverted plasmas exhibiting both type-III and type-I-reminiscent ELMs [63]. High plasma currents $I_p \geq 250$ kA favor the L-H transition. To ensure MHD stability at high current, a plasma edge elongation $\kappa_a \geq 1.5$ is necessary. Ohmic H-mode regime is accessible in limited configurations for plasma currents in the range $360 - 600$ kA and at high elongation $\kappa_a = 1.7 - 1.9$. At $I_p = 360$ kA, the L-H transition is obtained provided

the edge triangularity exceeds $\delta_a \geq 0.25$, which indicates that a high δ_a (in addition to a high κ_a) favors the H-mode regime. H-mode operation was also achieved in X3 ECH heated plasmas with clear type-I ELM activity [64].

ELM-free H-modes in TCV

In all ELMy H-modes, the ELM activity regulates the plasma density and allows keeping stationary conditions during the whole current flattop. However, it has been observed that ELM crashes strongly relax the edge profiles and deteriorate the pedestal gradients [64, 65].

As presented in section 3.4, an efficient conversion of O2 power to Bernstein waves via the O-X-B double mode conversion process in TCV overdense plasmas requires a steep density gradient at the plasma cutoff. This condition is met at the edge of ELM-free overdense H-modes when the electron density pedestal height H_n exceeds the O2 cutoff density $n_{\mathrm{c,O2}} = 8.48 \cdot 10^{19}$ m^{-3}.

In TCV, ELM-free H-modes are obtained in diverted configuration with high plasma current $I_\mathrm{p} > 400$ kA, high triangularity $\delta_a = 0.5 - 0.6$ and medium elongation $\kappa_a = 1.7 - 1.8$ [63]. In absence of ELM activity, the H-mode is non-stationary, with the density continually increasing (in average) until the plasma disruption. The density usually exceeds $n_\mathrm{e} \geq 10 \cdot 10^{19}$ m^{-3} and can reach up to 100% of the Greenwald density limit for elliptical plasmas (evaluated for $I_\mathrm{p} = 0.5$ MA and $a = 0.25$ m) [37]:

$$\langle n_\mathrm{G} \rangle = \kappa_a \langle J \rangle = \frac{I_\mathrm{p}}{\pi a^2} \simeq 2.5 \cdot 10^{20} \text{ m}^{-3} \tag{2.4.1}$$

where $\langle n_\mathrm{G} \rangle$ is the maximum line-average density in units of [10^{20} m^{-3}], κ_a is the plasma elongation, $\langle J \rangle$ is the average plasma current density in [MA/m^2], I_p is the plasma current in [MA] and a is the plasma minor radius in [m]. As a consequence of the high plasma current, the edge safety factor is low, i.e. $q_{95} = 2.2 - 2.4$, and the plasma centre usually exhibits a strong sawtooth MHD activity with a large inversion radius.

Description of ELM-free H-modes profiles

In H-mode regime, the edge density and temperature profiles are well described by a modified hyperbolic tangent fit F through the experimental data points of the Thomson scattering system described in subsection 2.3.2 [55, 65]:

$$F(X) = a_5 - a_1 \tanh(X) - a_1 a_4 \frac{X \mathrm{e}^X}{\mathrm{e}^X + \mathrm{e}^{-X}} \tag{2.4.2}$$

with $X = (R - R_{\mathrm{LCFS}} - a_2)/a_3$ a normalized spatial coordinate where R is the major radius passing through the equilibrium axis and R_{LCFS} is the major radius at the last closed flux surface (LCFS).

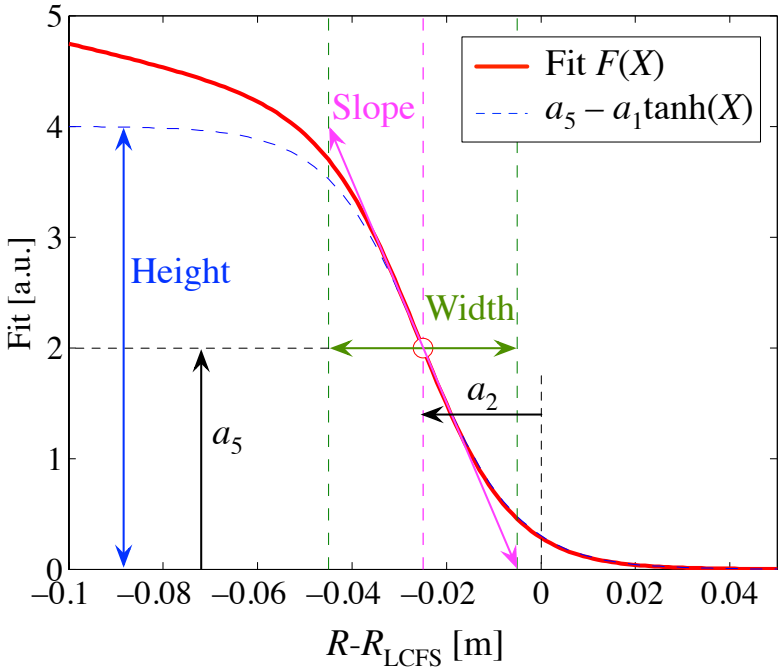

Figure 2.9: Modified hyperbolic tangent (2.4.2) for the pedestal profiles fitting. Example of modified tanh function $F(X)$ (solid red line) evaluated for $a_1 = a_5 = 2$, $a_2 = -0.025$ m, $a_3 = 0.02$ m and $a_4 = 0.1$. The F function maximum gradient and its location (red $\circ$) are only slightly modified with respect to the unmodified hyperbolic tangent function $a_5 - a_1 \tanh(X)$ (dashed blue line).

The fit parameters are linked to the unmodified tanh function properties as follows:

$$\text{Width:} \qquad W = 2a_3, \tag{2.4.3}$$

$$\text{Height:} \qquad H = a_1 + a_5, \tag{2.4.4}$$

$$\text{Maximum slope:} \qquad S = a_1/a_3. \tag{2.4.5}$$

Moreover, we note that a_2 is the distance from the LCFS to the maximum slope point of the unmodified tanh function

$$a_2 = R_{\max(\nabla n)} - R_{\mathrm{LCFS}} \tag{2.4.6}$$

and that a_5 is the tanh height at the maximum slope point. From these observations and equation (2.4.5), it is clear that the unmodified tanh function scale length at maximum gradient is given by

$$L_n(R_{\max(\nabla n)}) = a_5/S = a_5 a_3/a_1. \tag{2.4.7}$$

If the hyperbolic tangent modification parameter a_4 remains small (i.e. $a_4 \leq 0.1$), the tanh function maximum gradient (2.4.5) and its position (2.4.6) are only slightly modified by the exponential term in (2.4.2) and can be identified to the corresponding pedestal properties. An example of modified tanh function F is shown in figure 2.9 along with the pedestal parameters for $a_1 = a_5 = 2$, $a_2 = -0.025$, $a_3 = 0.02$ and $a_4 = 0.1$.

Figure 2.11 presents the time evolution of a typical TCV ELM-free H-mode obtained in electron Bernstein wave experiments ($Z_{\text{axis}} = 0.23$ m, $\kappa_a = 1.7$, $\delta_a = 0.54$, $I_\text{p} = 380$ kA, $q_{95} = 2.6$). The electron density and temperature profiles fitted on the experimental data from the main and edge Thomson scattering systems are given in figure 8.8. The corresponding time evolution of the density pedestal parameters are presented in figure 2.11. The L-H regime transition is defined by the appearance of a transport barrier at the plasma edge and is characterized by an abrupt drop in the emission intensity of the D_α recombination light due to a sudden rise of the edge temperature. After the L-H transition, the pedestal height develops and the edge density gradient becomes three times steeper than during the L-mode phase. In the meanwhile, the central electron density increases continuously, rapidly exceeding the O2 plasma cutoff density. The pedestal parameters of typical density and temperature profiles in ELM-free H-modes (corresponding to figures 2.12(a) and 2.12(b)) are indicated in tables 2.3 and 2.4, respectively.

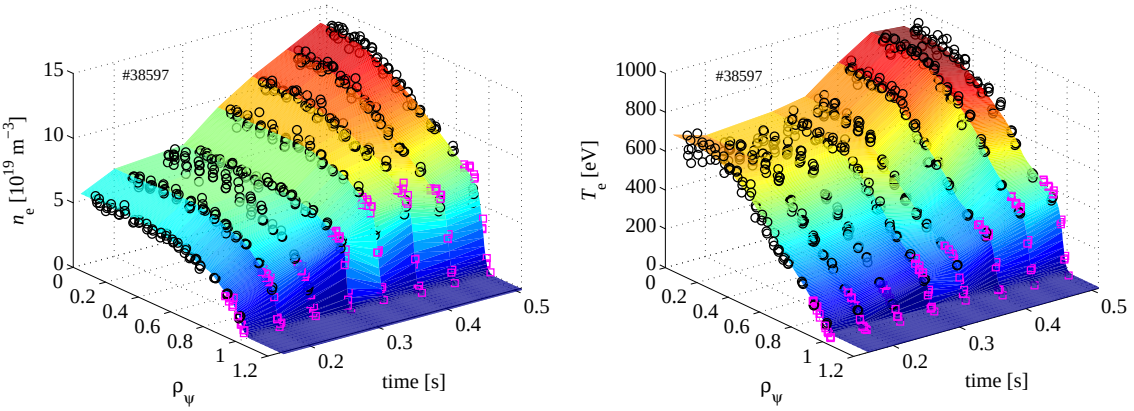

(a) Electron density profile evolution. **(b)** Electron temperature profile evolution.

Figure 2.10: Typical TCV ELM-free H-mode profiles. (a) Electron density and (b) electron temperature profiles versus time. The colour surfaces are the fits on the experimental data from the Thomson scattering central (○) and edge (□) lines-of-sight. The time evolution of the corresponding pedestal parameters is given in figure 2.11. #38597.

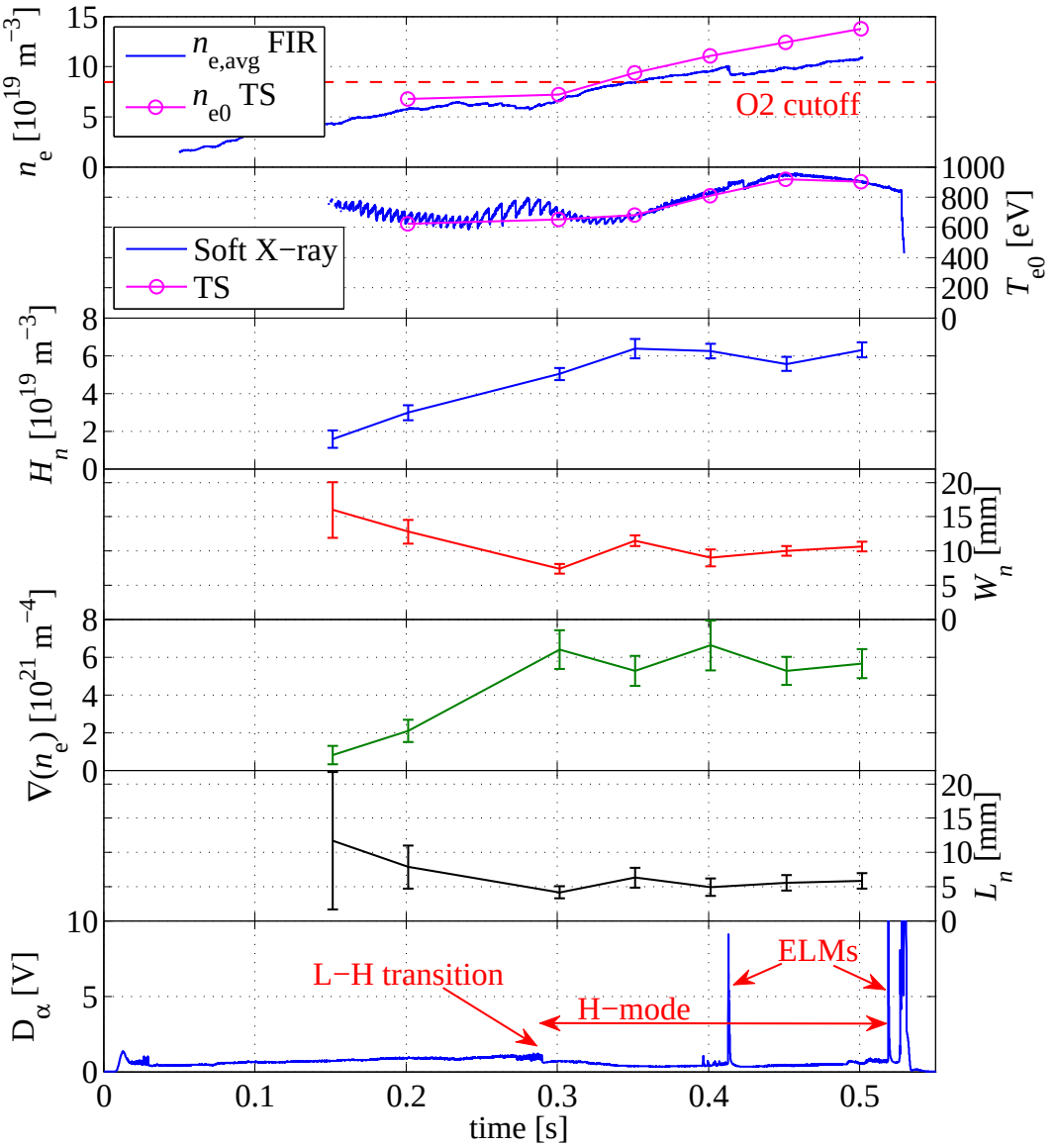

Figure 2.11: Typical TCV ELM-free H-mode plasma. From top to bottom: Central electron density from TS (∘) and line-averaged electron density from FIR, central electron temperature from TS (∘) and from soft X-ray signals, electron density pedestal height H_n, width W_n, maximum gradient ∇n_e and scale length at maximum gradient L_n, and D$_\alpha$ recombination light. The L-H transition is indicated by the characteristic drop in the emission intensity of the D$_\alpha$ recombination light. In the L-mode phase, the large errorbars on the edge profile parameters indicate that the pedestal is not well defined yet. In the ELM-free H-mode phase, the density profile develops and the edge gradient becomes three times steeper than during the L-mode phase. The sawtooth activity amplitude and period decrease with increasing density. The profile relaxation effect of the isolated ELM at $t \simeq 0.41$ s is still visible on the pedestal height and gradient measured by the TS diagnostics 35 ms after the ELM event. The central density increases continuously and exceeds the O2 plasma cutoff 30 ms after the L-H transition. Due to the high plasma current necessary to obtain the L-H transition in Ohmic regime, the plasma center is perturbed by a strong sawtooth activity whose amplitude reduces with increasing density, as indicated by the soft X-ray trace. #38597.

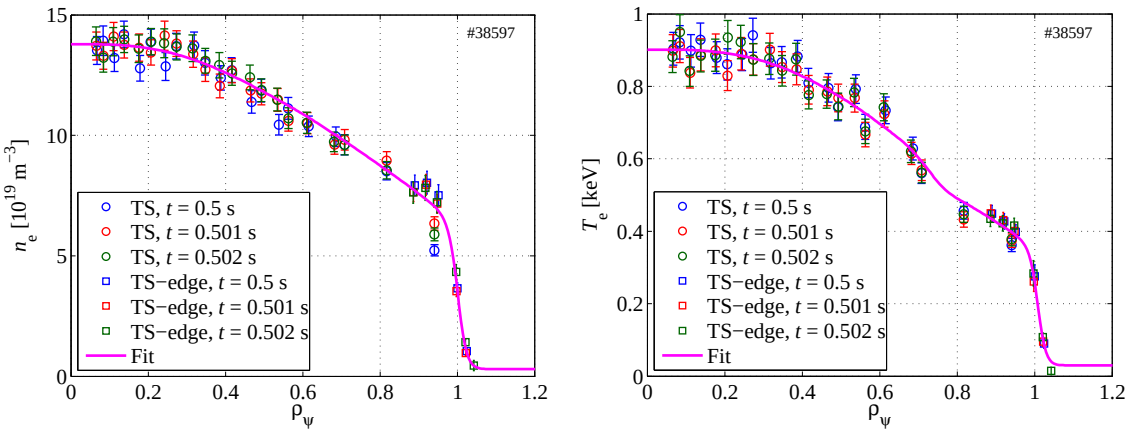

(a) Electron density profile fit at $t = 0.5$ s. **(b)** Electron temperature profile fit at $t = 0.5$ s.

Figure 2.12: Typical TCV ELM-free H-mode profiles. (a) Electron density and (b) electron temperature profiles fit (solid curves) on the experimental data from the main (○) and edge (□) lines-of-sight of the Thomson scattering diagnostics. The edge pedestal region ($\rho_\psi > 0.8$) is fitted using equation (2.4.2). The corresponding pedestal parameters are given in tables 2.3 and 2.4. #38597, $t = 0.5$ s.

	Electron density pedestal parameters			
	Height H_n [10^{19} m^{-3}]	Width W_n [mm]	Max. slope S_n [10^{21} m^{-4}]	Scale length L_n [mm]
H-mode ($t = 0.5$ s)	6.3 ± 0.4	10.6 ± 0.7	5.6 ± 0.8	5.8 ± 1.1
L-mode ($t = 0.2$ s)	3.0 ± 0.4	12.8 ± 1.7	2.1 ± 0.6	7.9 ± 3.1

Table 2.3: Typical density profile pedestal parameters in an ELM-free H-mode. For the sake of comparison, the fitted parameters are also given for a profile in the L-mode phase. #38597.

	Electron temperature pedestal parameters			
	Height H_T [eV]	Width W_T [mm]	Max. slope S_T [keV/m]	Scale length L_T [mm]
H-mode ($t = 0.5$ s)	348 ± 24	9.7 ± 1.4	32.9 ± 0.7	5.7 ± 1.6
L-mode ($t = 0.2$ s)	73 ± 16	4.5 ± 6.0	9.6 ± 16.1	5.3 ± 9.7

Table 2.4: Typical temperature profile pedestal parameters in an ELM-free H-mode. For the sake of comparison, the fitted parameters are also given for a profile in the L-mode phase. #38597.

Chapter 3

High frequency plasma waves

3.1 Introduction

This chapter presents the basic theory of linear plasma waves relevant to the sequel of this work. It treats only high-frequency waves such that the characteristic times of the variations in the plasma inhomogeneities don't affect the waves description. The theory presented here is valid in infinite homogeneous plasmas. The validity domain can be extended to real bounded inhomogeneous plasmas — as met in laboratories — if they satisfy the Wentzel-Kramer-Brillouin (WKB) approximation for slowly space-varying plasmas. Exhaustive linear wave theory derivations can be found in [66], [67] and [68].

3.2 Linear waves in an infinite homogeneous plasma

3.2.1 Maxwell's equations and constitutive relation

Considering only waves with a wavelength much larger than the Debye length, $\lambda \gg \lambda_{\mathrm{D}}$, propagating in a plasma such that a volume λ_{D}^3 contains a large number of particles, the wave is properly described by the Maxwell's equations for the macroscopic fields

$$\nabla \times \mathbf{E} + \frac{\partial \mathbf{B}}{\partial t} = 0 \qquad \text{Faraday's law} \tag{3.2.1}$$

$$\nabla \times \mathbf{B} - \varepsilon_0 \mu_0 \frac{\partial \mathbf{E}}{\partial t} = \mu_0 \mathbf{J} \qquad \text{Ampère-Maxwell's law} \tag{3.2.2}$$

$$\nabla \cdot \mathbf{E} = \frac{\rho}{\varepsilon_0} \qquad \text{Gauss's law} \tag{3.2.3}$$

$$\nabla \cdot \mathbf{B} = 0 \tag{3.2.4}$$

where $\mathbf{E}(\mathbf{x},t)$ and $\mathbf{B}(\mathbf{x},t)$ are the total electric and magnetic fields, $\mathbf{J}(\mathbf{x},t)$ and $\rho(\mathbf{x},t)$ are the total macroscopic current and charge densities, respectively. Taking the divergence of Ampère-Maxwell's law (3.2.2) and inserting Gauss's law (3.2.3) leads to the conservation of charge

$$\frac{\partial \rho}{\partial t} + \nabla \cdot \mathbf{J} = 0. \tag{3.2.5}$$

Taking the rotational of Faraday's law (3.2.1) and inserting Ampère-Maxwell's law (3.2.2) gives the wave equation for the electric field

$$\nabla \times \nabla \times \mathbf{E} + \varepsilon_0 \mu_0 \frac{\partial^2 \mathbf{E}}{\partial t^2} = -\mu_0 \frac{\partial \mathbf{J}}{\partial t}. \tag{3.2.6}$$

Maxwell's equations form a closed system only if $\mathbf{J}(\mathbf{x},t)$ and $\rho(\mathbf{x},t)$ are known. In the plasma, the current and charge densities are defined as moments of the distribution functions f_α summed over all species α:

$$\mathbf{J}(\mathbf{x},t) \equiv \sum_\alpha q_\alpha \iiint \mathrm{d}^3 v \ \mathbf{v} f_\alpha(\mathbf{x},\mathbf{v},t), \tag{3.2.7}$$

$$\rho(\mathbf{x},t) \equiv \sum_\alpha q_\alpha \iiint \mathrm{d}^3 v \ f_\alpha(\mathbf{x},\mathbf{v},t). \tag{3.2.8}$$

with $q_\alpha \equiv Z_\alpha e$ the electric charge of the particles of species α and Z_α their ionization state ($Z_\mathrm{e} = -1$ for electrons). The evolution of the distribution functions $f_\alpha(\mathbf{x},\mathbf{v},t)$ is governed by the Boltzmann equation

$$\frac{\partial f_\alpha}{\partial t} + \mathbf{v} \cdot \nabla f_\alpha + \frac{q_\alpha}{m_\alpha} \left[\mathbf{E} + \mathbf{v} \times \mathbf{B}\right] \cdot \frac{\partial f_\alpha}{\partial \mathbf{v}} = \left(\frac{\partial f_\alpha}{\partial t}\right)_{\mathrm{coll}}. \tag{3.2.9}$$

Equation (3.2.9) implies that the current and charge densities generating the fields are themselves modified by the presence of the fields via the dynamic of the distribution functions. The system is thus clearly non-linear and self-consistent.
When an electromagnetic wave is injected in the plasma, we can write the electric and magnetic fields

$$\mathbf{E}(\mathbf{x},t) = \mathbf{E}_0(\mathbf{x},t) + \mathbf{E}_1(\mathbf{x},t) \tag{3.2.10}$$

$$\mathbf{B}(\mathbf{x},t) = \mathbf{B}_0(\mathbf{x},t) + \mathbf{B}_1(\mathbf{x},t) \tag{3.2.11}$$

as sums of the slowly time-varying background fields (0 indices), verifying themselves the field and Boltzmann equations, and the wave contributions (1 indices). The presence of the wave fields generates perturbations ρ_1 and $\mathbf{J}_1$ of the background plasma charge and current densities:

$$\rho(\mathbf{x},t) = \rho_0(\mathbf{x},t) + \rho_1(\mathbf{x},t) \tag{3.2.12}$$

$$\mathbf{J}(\mathbf{x},t) = \mathbf{J}_0(\mathbf{x},t) + \mathbf{J}_1(\mathbf{x},t). \tag{3.2.13}$$

Maxwell's equations being linear, the wave fields $\mathbf{E}_1$ and $\mathbf{B}_1$ and the densities perturbations $\mathbf{J}_1$ and ρ_1 satisfy Maxwell's equations(*), and thus the wave equation (3.2.6) and the charge conservation (3.2.5):

$$\nabla \times \nabla \times \mathbf{E}_1 + \varepsilon_0 \mu_0 \frac{\partial^2 \mathbf{E}_1}{\partial t^2} = -\mu_0 \frac{\partial \mathbf{J}_1}{\partial t}, \tag{3.2.14}$$

$$\frac{\partial \rho_1}{\partial t} + \nabla \cdot \mathbf{J}_1 = 0. \tag{3.2.15}$$

The problem consists now in solving the wave equation (3.2.14) for the wave electric field to determine the plasma electromagnetic eigenmodes excited by the externally injected wave. To do so, we will linearize the Maxwell-Boltzmann system for small perturbations $f_{\alpha 1}(\mathbf{x}, \mathbf{v}\, t)$ around an equilibrium described by distribution functions $f_{\alpha 0}(\mathbf{x}, \mathbf{v}, t)$. Note that the linearization is not performed on the field equations, which allows the wave to carry a large power and its electric field $\mathbf{E}_1$ to take values larger than the background electric field $\mathbf{E}_0$.

3.2.2 Linearized system

The system can be linearized around a steady-state (or a slowly-time varying) equilibrium in absence of wave fields with distribution functions $f_{0\alpha}(\mathbf{x}, \mathbf{v}, t)$, such that the perturbations $f_{1\alpha}(\mathbf{x}, \mathbf{v}, t)$ linear in $\mathbf{E}_1$ are small

$$\left| \frac{f_{1\alpha}(\mathbf{x}, \mathbf{v}, t)}{f_{0\alpha}(\mathbf{x}, \mathbf{v}, t)} \right| \ll 1. \tag{3.2.16}$$

The total distribution function then writes

$$f_\alpha(\mathbf{x}, \mathbf{v}, t) \simeq f_{0\alpha}(\mathbf{x}, \mathbf{v}, t) + f_{1\alpha}(\mathbf{x}, \mathbf{v}, t) \tag{3.2.17}$$

for each species α. In consequence, the current and charge densities

$$\mathbf{J}_1(\mathbf{x}, t) \equiv \sum_\alpha q_\alpha \iiint \mathrm{d}^3 v\ \mathbf{v} f_{1\alpha}(\mathbf{x}, \mathbf{v}, t), \tag{3.2.18}$$

$$\rho_1(\mathbf{x}, t) \equiv \sum_\alpha q_\alpha \iiint \mathrm{d}^3 v\ f_{1\alpha}(\mathbf{x}, \mathbf{v}, t) \tag{3.2.19}$$

due to the wave fields are linear in $\mathbf{E}_1$ (via $f_{1\alpha}$). The constitutive relation between $\mathbf{J}_1$ and $\mathbf{E}_1$ can be formally written as a functional

$$\mathbf{J}_1(\mathbf{x}, t) = \int_{-\infty}^{t} \mathrm{d}t' \iiint \mathrm{d}^3 x'\ \mathbb{C}(\mathbf{x}, \mathbf{x}', t, t') \cdot \mathbf{E}_1(\mathbf{x}', t'). \tag{3.2.20}$$

(*) For the background fields and plasma current and charge densities to satisfy Maxwell's equation, one has also to consider the currents circulating in the coil system of the machine.

where $\mathbb{C}(\mathbf{x}, \mathbf{x}', t, t')$ is the conductivity tensor reflecting the plasma response to the wave perturbation. The time integral stops at time t for causality. The non-locality of $\mathbb{C}$ in time and space implicitly embodies the dispersive nature of the plasma due to the particles inertia and their trajectories with different thermal velocities. The latter thermal effect vanishes in the limit of cold plasma. As a consequence, we will see that the cold plasma conductivity tensor exhibits only a time dispersion (i.e. $\mathbb{C}$ is a function of the wave angular frequency ω only and not of the wave refraction index vector $\mathbf{N}$). We note that the dependence of the current density $\mathbf{J}_1$ on the wave magnetic field $\mathbf{B}_1$ in the linear relation (3.2.20) is implicitly embedded in $\mathbb{C}$. (Explicitly, Faraday's law is used to replace $\mathbf{B}_1$ with $\mathbf{E}_1$ in the linearized system.)
Finally, we shall mention under which conditions this linearization is valid. The wave electric field must be sufficiently small such that the particle collisions maintain the perturbed distribution functions f_α continuously close to the unperturbed equilibrium $f_{0\alpha}$. This is true if the wave electric field doesn't exceed the following critical value [66]:

$$E_{\text{crit}} \simeq 10^{-5} \frac{n_{\text{e}}^{5/6}}{T_{\text{e}}^{1/2}} \tag{3.2.21}$$

where E is in [V/m], n_{e} is in [m^{-3}] and T_{e} is in [keV]. With low density and high temperature values for TCV plasmas ($n_{\text{e}} = 10^{18}$ $\text{m}^{-3} = 10^{12}$ cm^{-3} and $T_{\text{e}} = 100$ keV), we obtain a conservative estimation $E_{\text{crit}} \simeq 10^9$ V/cm of this critical field amplitude.
We now evaluate the order of magnitude of the electric field of a microwave power beam of TCV ECRH system with radius $r_{\text{b}} = 2$ cm and power $P_{\text{b}} = 1$ MW. The beam energy density can be simply estimated by the energy density of a monochromatic plane waves in vacuum:

$$u = \frac{1}{2}\varepsilon_0 E^2. \tag{3.2.22}$$

The beam power is thus

$$P = cS_{\text{b}}u = \frac{1}{2}cS_{\text{b}}\varepsilon_0 E^2 \tag{3.2.23}$$

where $S_{\text{b}} = \pi r_{\text{b}}^2$ is the beam cross section. Finally, the wave electric field is

$$E = \frac{1}{r_{\text{b}}}\sqrt{\frac{2P}{c\pi\varepsilon_0}} \simeq 7.8 \cdot 10^5 \ \frac{\text{V}}{\text{m}} \tag{3.2.24}$$

which is more than three orders of magnitude smaller than the critical value estimated above. The Maxwell-Boltzmann system can thus be safely linearized even in the case of high power electron cyclotron heating in hot low-density plasmas where the collisionality is reduced.

In an infinite homogeneous and constant plasma, the conductivity depends only on the relative distance and time, and the constitutive relation (3.2.20) writes as a convolution

$$\mathbf{J}_1(\mathbf{x},t) = \int_{-\infty}^{t} \mathrm{d}t' \iiint \mathrm{d}^3x'\, \mathbb{C}(\mathbf{x}-\mathbf{x}', t-t') \cdot \mathbf{E}_1(\mathbf{x}', t'). \tag{3.2.25}$$

We can then Fourier-analyze Maxwell's equations, keeping only first-order terms

$$i\mathbf{k} \times \tilde{\mathbf{E}}_1(\mathbf{k},\omega) - i\omega\tilde{\mathbf{B}}_1(\mathbf{k},\omega) = 0 \tag{3.2.26}$$

$$i\mathbf{k} \times \tilde{\mathbf{B}}_1(\mathbf{k},\omega) + \varepsilon_0\mu_0 i\omega\tilde{\mathbf{E}}_1(\mathbf{k},\omega) = \mu_0\tilde{\mathbf{J}}_1(\mathbf{k},\omega) \tag{3.2.27}$$

$$i\mathbf{k} \cdot \tilde{\mathbf{E}}_1(\mathbf{k},\omega) = \frac{\tilde{\rho}_1(\mathbf{k},\omega)}{\varepsilon_0} \tag{3.2.28}$$

$$i\mathbf{k} \cdot \tilde{\mathbf{B}}_1(\mathbf{k},\omega) = 0 \tag{3.2.29}$$

where the Fourier transform $\tilde{Q}_1(\mathbf{k},\omega)$ of a quantity $Q_1(\mathbf{x},t)$ is defined as

$$\tilde{Q}_1(\mathbf{k},\omega) \equiv \frac{1}{(2\pi)^4} \int \mathrm{d}t \iiint \mathrm{d}^3x\; Q_1(\mathbf{x},t)\mathrm{e}^{-\mathrm{i}(\mathbf{k}\cdot\mathbf{x}-\omega t)}. \tag{3.2.30}$$

In other words, all perturbations $Q_1(\mathbf{x},t)$ are expressed as superpositions of harmonic plane waves

$$Q_1(\mathbf{x},t) = \int \mathrm{d}\omega \iiint \mathrm{d}^3k\; \tilde{Q}_1(\mathbf{k},\omega)\mathrm{e}^{\mathrm{i}(\mathbf{k}\cdot\mathbf{x}-\omega t)}. \tag{3.2.31}$$

Before taking the Fourier transform of the constitutive relation, we first extend the conductivity tensor to times $t' > t$ such that

$$\mathbb{C}(\mathbf{x}-\mathbf{x}', t-t') = 0 \qquad \forall t' > t. \tag{3.2.32}$$

The constitutive relation can then be integrated on the whole time axis

$$\mathbf{J}_1(\mathbf{x},t) = \int \mathrm{d}t' \iiint \mathrm{d}^3x'\, \mathbb{C}(\mathbf{x}-\mathbf{x}', t-t') \cdot \mathbf{E}_1(\mathbf{x}', t') \tag{3.2.33}$$

and Fourier-analyzed

$$\tilde{\mathbf{J}}_1(\mathbf{k},\omega) = (2\pi)^4\tilde{\mathbb{C}}(\mathbf{k},\omega) \cdot \tilde{\mathbf{E}}_1(\mathbf{k},\omega) = \mathbb{C}(\mathbf{k},\omega) \cdot \tilde{\mathbf{E}}_1(\mathbf{k},\omega) \tag{3.2.34}$$

where we have defined the conductivity tensor $\mathbb{C}$ in Fourier space as

$$\begin{aligned} \mathbb{C}(\mathbf{k},\omega) &\equiv (2\pi)^4\tilde{\mathbb{C}}(\mathbf{k},\omega) \\ &= \int \mathrm{d}t' \iiint \mathrm{d}^3x'\, \mathbb{C}(\mathbf{x}-\mathbf{x}', t-t')\mathrm{e}^{-\mathrm{i}[\mathbf{k}\cdot(\mathbf{x}-\mathbf{x}')-\omega(t-t')]} \\ &= \int_0^{+\infty} \mathrm{d}\tau \iiint \mathrm{d}^3\rho\, \mathbb{C}(\boldsymbol{\rho},\tau)\mathrm{e}^{-\mathrm{i}[\mathbf{k}\cdot\boldsymbol{\rho}-\omega\tau]}. \end{aligned} \tag{3.2.35}$$

with $\boldsymbol{\rho} = \mathbf{x} - \mathbf{x}'$ and $\tau = t - t'$. In the following, the notation $Q_{\mathbf{k},\omega} \equiv \tilde{Q}_1(\mathbf{k},\omega)$ will be used for the Fourier components of the perturbation of any quantity Q and blackboard bold letters like $\mathbb{T}$ will be used for tensors in Fourier space.

3.2.3 Dielectric tensor

Inserting $\mathbf{B}_{\mathbf{k},\omega}$ from Faraday's equation (3.2.26) and $\mathbf{J}_{\mathbf{k},\omega}$ from the constitutive equation (3.2.34) into Ampère's equation (3.2.27) — or by direct Fourier analysis of the wave equation (3.2.14) — we get the wave equation for the electric field in Fourier space

$$\mathbf{k} \times \mathbf{k} \times \mathbf{E}_{\mathbf{k},\omega} + \frac{\omega^2}{c^2} \mathbb{K} \cdot \mathbf{E}_{\mathbf{k},\omega} = 0 \tag{3.2.36}$$

where

$$\mathbb{K}(\mathbf{k}, \omega) \equiv \mathbb{I} + \mathbb{S}(\mathbf{k}, \omega) \tag{3.2.37}$$

is the dielectric tensor and

$$\mathbb{S}(\mathbf{k}, \omega) \equiv \frac{\mathrm{i}}{\varepsilon_0 \omega} \mathbb{C}(\mathbf{k}, \omega) \tag{3.2.38}$$

is the susceptibility tensor with $\mathbb{I}$ the identity matrix. We have used the relation $c^2 = 1/(\varepsilon_0 \mu_0)$. The wave equation (3.2.36) can be expressed in terms of the index of refraction defined as

$$\mathbf{N} \equiv \frac{c}{\omega} \mathbf{k} \tag{3.2.39}$$

yielding the wave equation

$$\boxed{\left(\mathbf{NN} - N^2 \mathbb{I}\right) \cdot \mathbf{E}_{\mathbf{k},\omega} + \mathbb{K} \cdot \mathbf{E}_{\mathbf{k},\omega} = \mathbb{D} \cdot \mathbf{E}_{\mathbf{k},\omega} = 0} \tag{3.2.40}$$

with

$$\mathbb{D}(\mathbf{N}, \omega) \equiv \mathbf{NN} - N^2 \mathbb{I} + \mathbb{K}(\mathbf{N}, \omega) \tag{3.2.41}$$

the definition of the dispersion tensor. Here, $\mathbf{NN}$ is the dyadic tensor defined as $(\mathbf{NN})_{ij} \equiv N_i N_j$. From the definition (3.2.18), we note that each species contribute separately to the current density. The conductivity and susceptibility tensors can thus be written as sums on all species contributions

$$\mathbb{S}(\mathbf{N}, \omega) \equiv \sum_\alpha \mathbb{S}_\alpha(\mathbf{N}, \omega) \qquad \text{with} \qquad \mathbb{S}_\alpha(\mathbf{N}, \omega) \equiv \frac{\mathrm{i}}{\varepsilon_0 \omega} \mathbb{C}_\alpha(\mathbf{N}, \omega) \tag{3.2.42}$$

and the dielectric tensor (3.2.37) writes

$$\mathbb{K} \equiv \mathbb{I} + \sum_\alpha \mathbb{S}_\alpha. \tag{3.2.43}$$

Onsager's relations ensure the following symmetry of the dielectric tensor with respect to the wave vector $\mathbf{k}$ and the background magnetic field $\mathbf{B}_0$ [66]:

$$K_{ij}(-\mathbf{N}, \omega, -\mathbf{B}_0) = K_{ji}(\mathbf{N}, \omega, \mathbf{B}_0). \tag{3.2.44}$$

These relations reduce the number of independent components of the dielectric tensor from nine to six. The Stix reference frame is such that the background magnetic field $\mathbf{B}_0$ lies along $\hat{\mathbf{z}}$ and the refractive index is in the $x-z$ plane, i.e.

$$\mathbf{B}_0 = B_0\hat{\mathbf{z}}, \tag{3.2.45}$$

$$\mathbf{N} = N_\perp\hat{\mathbf{x}} + N_\parallel\hat{\mathbf{z}} \qquad \text{with} \qquad N_\parallel \equiv \frac{\mathbf{N}\cdot\mathbf{B}_0}{B_0},\ N_\perp \equiv \mathbf{N} - N_\parallel\frac{\mathbf{B}_0}{B_0}, \tag{3.2.46}$$

as described in figure 3.1. In this coordinate system, the Onsager's relations write explicitly as

$$K_{yx} = -K_{xy} \qquad \text{and} \qquad K_{zx} = K_{xz} \qquad \text{and} \qquad K_{zy} = -K_{yz}. \tag{3.2.47}$$

The wave equation (3.2.40) becomes

$$\begin{pmatrix} K_{xx} - N_\parallel^2 & K_{xy} & K_{xz} + N_\perp N_\parallel \\ -K_{xy} & K_{yy} - N^2 & K_{yz} \\ K_{xz} + N_\perp N_\parallel & -K_{yz} & K_{zz} - N_\perp^2 \end{pmatrix} \begin{pmatrix} E_x \\ E_y \\ E_z \end{pmatrix} = 0. \tag{3.2.48}$$

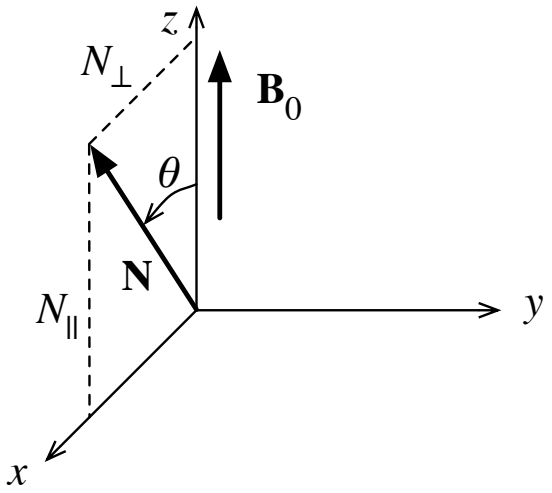

Figure 3.1: Stix reference frame. In this coordinate system, the $\hat{\mathbf{z}}$ direction is aligned with the background magnetic field direction $\mathbf{B}_0$ and the wave refractive index $\mathbf{N}$ lies in the $x-z$ plane, with θ the angle between $\mathbf{B}_0$ and $\mathbf{N}$.

3.2.4 Dispersion relation

Clearly, non-trivial solutions (i.e. with $\mathbf{E}_{\mathbf{k},\omega} \neq 0$) of the wave equation (3.2.40) exist only if the determinant of the dispersion tensor vanishes

$$\boxed{\mathcal{D}(\mathbf{N},\omega) \equiv \det|\mathbb{D}(\mathbf{N},\omega)| = \det|\mathbf{N}\mathbf{N} - N^2\mathbb{I} + \mathbb{K}(\mathbf{N},\omega)| = 0.} \tag{3.2.49}$$

This is the dispersion relation for linear waves in an infinite uniform plasma. One can express it as a quadratic equation for N^2

$$K_{ij}n_in_jN^4 - \left[\left(K_{ij}n_in_j\right)K_{kk} - K_{ik}K_{kj}n_in_j\right]N^2 + \det|\mathbb{K}(\mathbf{N},\omega)| = 0 \qquad (3.2.50)$$

where $\hat{\mathbf{n}} = \mathbf{N}/N$ is the unitary vector in the direction of $\mathbf{N}$ and summation is performed over repeated indices. This expression is independent of the coordinate system. Note that the coefficients of this equation generally depend on N via the dielectric tensor $\mathbb{K}$. Only in the cold plasma limit is the dielectric tensor independent of $\mathbf{N}$ and the dispersion relation is explicitly quadratic in N^2. Solutions $N^2(\hat{\mathbf{n}},\omega)$ to the dispersion relation represent eigenmodes propagating in the plasma at the angular frequency ω and in the direction $\hat{\mathbf{n}}$ (with two modes propagating in opposite direction for each $N^2 > 0$). In general, for a given real angular frequency ω, there can be one or more solutions with $N^2 < 0$, and thus an imaginary wave vector. Such modes are not propagating and are said to be evanescent. The transition between propagation and evanescence (i.e. the transition between $N^2 > 0$ and $N^2 < 0$) occurs at $N^2 = 0$ and $N^2 = \infty$.

Cutoffs

The case $N^2 \to 0$ at fixed $\omega \neq 0$ is called a cutoff. From (3.2.50), one can write the condition for a wave to be in cutoff as

$$\det|\mathbb{K}(\mathbf{N},\omega)| = 0. \qquad (3.2.51)$$

Resonances

The case $N^2 \to \infty$ at fixed $\omega \neq 0$ is called a resonance. From (3.2.50), one can write a necessary condition for the wave to meet a resonance as

$$K_{ij}n_in_j = 0. \qquad (3.2.52)$$

In the cold plasma model, the dielectric tensor K_{ij} is independent of N and the resonance condition above is sufficient.

WKB approximation

The whole difficulty resides now in the determination of the dielectric tensor (i.e. the susceptibility tensor) depicting the plasma response to the wave perturbation. The dielectric tensor is a function of $\mathbf{N}$ and ω but also depends on the plasma parameters: the background magnetic B_0, the species temperatures T_α and densities

n_α. As already mentioned, we focus our interest on high-frequency waves such than in presence of slow time variations of the equilibrium parameters

$$\omega \gg \frac{1}{B_0}\left|\frac{\mathrm{d}B_0}{\mathrm{d}t}\right|,\ \frac{1}{T_\alpha}\left|\frac{\mathrm{d}T_\alpha}{\mathrm{d}t}\right|,\ \frac{1}{n_\alpha}\left|\frac{\mathrm{d}n_\alpha}{\mathrm{d}t}\right| \qquad \forall\alpha \tag{3.2.53}$$

the wave equation (3.2.40) and the dispersion relation (3.2.49) are still valid locally in time.

In slightly non-homogeneous plasma with characteristic gradient scale-lengths much larger than the mode wavelength

$$\|\mathbf{k}\| \gg \frac{\|\nabla B_0\|}{B_0},\ \frac{\|\nabla T_\alpha\|}{T_\alpha},\ \frac{\|\nabla n_\alpha\|}{n_\alpha} \qquad \forall\alpha \tag{3.2.54}$$

and far from the singularities of the dispersion relation (cutoffs and resonances), i.e. if the wave vector varies slowly

$$\|\mathbf{k}\|^2 \gg \|\nabla k\|, \tag{3.2.55}$$

the wave equation (3.2.40) and the dispersion relation (3.2.49) are still valid locally in space. These conditions are the required assumptions underlying the Wentzel-Kramer-Brillouin (WKB) approximation allowing for a geometrical optics treatment of the wave propagation.

3.3 Cold plasma model

3.3.1 Dielectric tensor

It is interesting to study the plasma waves in the non-collisional cold plasma model since the validity conditions for the cold plasma approximation are satisfied even at very high temperature [66]. The cold dielectric tensor is derived by solving the colisionless equation of motion for the species α in the oscillating electric field $\mathbf{E}_1$:

$$\frac{\mathrm{d}\mathbf{u}_\alpha}{\mathrm{d}t} = \frac{q_\alpha}{m_\alpha}\left(\mathbf{E}_1 + \mathbf{u}_\alpha \times \mathbf{B}_0\right). \tag{3.3.1}$$

Choosing the $\hat{\mathbf{z}}$ axis along the magnetic field $\mathbf{B}_0$, the components of the cold sus-

ceptibility tensor $\mathbb{S}$ are given by [66]

$$S_{xx} = S_{yy} = -\sum_{\alpha} \frac{\omega_{\mathrm{p}\alpha}^2}{\omega^2 - \Omega_{\mathrm{c}\alpha}^2}, \tag{3.3.2}$$

$$S_{xy} = -S_{yx} = -\mathrm{i}\sum_{\alpha} \frac{\Omega_{\mathrm{c}\alpha}\omega_{\mathrm{p}\alpha}^2}{\omega\left(\omega^2 - \Omega_{\mathrm{c}\alpha}^2\right)}, \tag{3.3.3}$$

$$S_{zz} = -\sum_{\alpha} \frac{\omega_{\mathrm{p}\alpha}^2}{\omega^2}, \tag{3.3.4}$$

$$S_{xz} = S_{zy} = S_{yz} = S_{zy} = 0, \tag{3.3.5}$$

where the plasma frequency and cyclotron frequency are defined as, respectively,

$$\omega_{\mathrm{p}\alpha} \equiv \left(\frac{n_{0\alpha} q_\alpha^2}{\varepsilon_0 m_\alpha}\right)^{1/2} \qquad \text{and} \qquad \Omega_{\mathrm{c}\alpha} \equiv \frac{q_\alpha B_0}{m_\alpha} \tag{3.3.6}$$

Note that $q_\alpha \equiv Z_\alpha e$ with $Z_\mathrm{e} = -1$ and thus $\Omega_{\mathrm{ce}} < 0$ for electrons (if $B_0 > 0$). The dielectric tensor $\mathbb{K} = \mathbb{I} + \mathbb{S}$ writes

$$\mathbb{K} = \begin{pmatrix} S & -\mathrm{i}D & 0 \\ \mathrm{i}D & S & 0 \\ 0 & 0 & P \end{pmatrix}, \tag{3.3.7}$$

where we used the standard Stix notation

$$S \equiv \frac{1}{2}(R + L) = 1 - \sum_{\alpha} \frac{\omega_{\mathrm{p}\alpha}^2}{\omega^2 - \Omega_{\mathrm{c}\alpha}^2} = 1 - \sum_{\alpha} \frac{X_\alpha}{1 - Y_\alpha^2}, \tag{3.3.8}$$

$$D \equiv \frac{1}{2}(R - L) = \sum_{\alpha} \frac{\Omega_{\mathrm{c}\alpha}\omega_{\mathrm{p}\alpha}^2}{\omega\left(\omega^2 - \Omega_{\mathrm{c}\alpha}^2\right)} = \sum_{\alpha} \frac{Y_\alpha X_\alpha}{1 - Y_\alpha^2}, \tag{3.3.9}$$

$$P \equiv 1 - \sum_{\alpha} \frac{\omega_{\mathrm{p}\alpha}^2}{\omega^2} = 1 - \sum_{\alpha} X_\alpha, \tag{3.3.10}$$

$$R \equiv 1 - \sum_{\alpha} \frac{\omega_{\mathrm{p}\alpha}^2}{\omega\left(\omega + \Omega_{\mathrm{c}\alpha}\right)} = 1 - \sum_{\alpha} \frac{X_\alpha}{1 + Y_\alpha}, \tag{3.3.11}$$

$$L \equiv 1 - \sum_{\alpha} \frac{\omega_{\mathrm{p}\alpha}^2}{\omega\left(\omega - \Omega_{\mathrm{c}\alpha}\right)} = 1 - \sum_{\alpha} \frac{X_\alpha}{1 - Y_\alpha}, \tag{3.3.12}$$

with

$$X_\alpha \equiv \left(\frac{\omega_{\mathrm{p}\alpha}}{\omega}\right)^2 \qquad \text{and} \qquad Y_\alpha \equiv \frac{\Omega_{\mathrm{c}\alpha}}{\omega} \tag{3.3.13}$$

the normalized squared plasma frequency and the normalized cyclotron frequency, proportional to the particle density and the magnetic field strength, respectively. The expression for the cold dielectric tensor is worth a few comments:

- For the case of high-frequency waves in the electron cyclotron range ($\omega \simeq |\Omega_{ce}|$) injected in a high-density plasma ($\omega_{pe} \simeq \omega$), we have the relations

$$|Y_e| \simeq 1 \gg |Y_i| \qquad \text{and} \qquad X_e \simeq 1 \gg X_i \tag{3.3.14}$$

due to the small ratio $m_e/m_i \ll 1$. In the following, we will treat only waves in the electron cyclotron frequency range. We will thus neglect the ion contributions to the dielectric tensor.

- The cold plasma dielectric tensor $\mathbb{K}$, and thus $\mathbb{S}$ and $\mathbb{C}$, depend only on the wave angular frequency ω and not on the wave refraction index $\mathbf{N}$:

$$\mathbb{K} = \mathbb{K}(\omega) \qquad \text{for cold plasma.} \tag{3.3.15}$$

This implies that the direction of the magnetic field ($\hat{\mathbf{z}}$ in this instance) is a symmetry axis of $\mathbb{K}$ which has only three independent components (S, D and P). As a consequence, the expression (3.3.7) for the cold dielectric tensor is valid for arbitrary $\mathbf{N}$ directions (i.e. not only for $\mathbf{N}$ in the $x-z$ plane as in the Stix reference frame).

Moreover, it means that cold plasma waves don't exhibit any space dispersion. In other words, the constitutive relation is local in space and we can use the cold dielectric tensor for the case of non-homogeneous plasmas without further assumptions (of the WKB type). The space locality of the constitutive relation is directly seen from the inverse Fourier transform of the conductivity tensor $\tilde{\mathbb{C}}(\omega)$ following the rule (3.2.31):

$$\begin{aligned} \mathbb{C}(\mathbf{x}-\mathbf{x}', t-t') &= \int \mathrm{d}\omega \iiint \mathrm{d}^3k\, \tilde{\mathbb{C}}(\omega) \mathrm{e}^{\mathrm{i}[\mathbf{k}\cdot(\mathbf{x}-\mathbf{x}')-\omega(t-t')]} \\ &= (2\pi)^3 \mathbb{C}(t-t')\delta(\mathbf{x}-\mathbf{x}'). \end{aligned} \tag{3.3.16}$$

Inserting this result in the constitutive relation for homogeneous plasmas (3.2.25), one gets

$$\mathbf{J}_1(\mathbf{x}, t) = (2\pi)^3 \int_{-\infty}^{t} \mathrm{d}t'\, \mathbb{C}(t-t') \cdot \mathbf{E}_1(\mathbf{x}, t') \tag{3.3.17}$$

which is clearly local in space.

- The expression (3.3.7) of the cold dielectric tensor can be extended to the case of $\mathbf{B}_0$ having an arbitrary direction with respect to the axes (see reference [69]) by writing

$$K_{ij} = \delta_{ij} - \sum_{\alpha} \frac{X_\alpha}{1 - Y_\alpha^2} \left(\delta_{ij} - Y_{\alpha i} Y_{\alpha j} - \mathrm{i}\varepsilon_{ijk} Y_{\alpha k}\right) \tag{3.3.18}$$

with the vector $\mathbf{Y}_\alpha$ defined as

$$\mathbf{Y}_\alpha \equiv \frac{\mathbf{\Omega}_\alpha}{\omega} \equiv \frac{q_\alpha \mathbf{B}_0}{\omega m_\alpha}. \tag{3.3.19}$$

3.3.2 Dispersion relation

Since the cold dielectric tensor is independent of the wave vector direction, there is no need to keep $\mathbf{N}$ in the $x-z$ plane as specified by the Stix reference frame in (3.2.48). We can thus write the wave equation 3.2.40 for linear waves in a cold uniform magnetized plasma for an arbitrary wave refraction index $\mathbf{N} = (N_x, N_y, N_z)$:

$$\mathbb{D} \cdot \mathbf{E}_{\mathbf{k},\omega} = \begin{pmatrix} S - N_y^2 - N_z^2 & -\mathrm{i}D + N_x N_y & N_x N_z \\ \mathrm{i}D + N_y N_x & S - N_x^2 - N_z^2 & N_y N_z \\ N_z N_x & N_z N_y & P - N_x^2 - N_y^2 \end{pmatrix} \begin{pmatrix} E_x \\ E_y \\ E_z \end{pmatrix} = 0. \tag{3.3.20}$$

The dispersion relation 3.2.49 then writes

$$\det |\mathbb{D}| = \det \begin{vmatrix} S - N_y^2 - N_z^2 & -\mathrm{i}D + N_x N_y & N_x N_z \\ \mathrm{i}D + N_y N_x & S - N_x^2 - N_z^2 & N_y N_z \\ N_z N_x & N_z N_y & P - N_x^2 - N_y^2 \end{vmatrix} = 0 \tag{3.3.21}$$

which reduces to

$$P N_\parallel^4 + S N_\perp^4 + (P+S) N_\parallel^2 N_\perp^2 - 2PS N_\parallel^2 - (RL + PS) N_\perp^2 + PRL = 0 \tag{3.3.22}$$

where $N_\perp^2 \equiv N_x^2 + N_y^2$ and $N_\parallel^2 = N_z^2$. We note that the $\hat{\mathbf{z}}$ axis (i.e. the magnetic field direction) is a symmetry axis of the cold dispersion relation itself.
We can introduce the angle θ defined as the angle between $\mathbf{N}$ and $\mathbf{B}_0$

$$\theta \equiv \arccos\left(\frac{\mathbf{N} \cdot \mathbf{B}_0}{\|\mathbf{N}\| \|\mathbf{B}_0\|}\right) \tag{3.3.23}$$

such that $N_\parallel = N\cos(\theta)$ and $N_\perp = N\sin(\theta)$. Then the cold dispersion relation can be written as a quadratic equation for N^2

$$\boxed{\mathcal{D}(\mathbf{N}, \omega) = \det |\mathbb{D}(\mathbf{N}, \omega)| = AN^4 - BN^2 + C = 0} \tag{3.3.24}$$

with coefficients

$$A = S\sin^2(\theta) + P\cos^2(\theta) \tag{3.3.25}$$

$$B = RL\sin^2(\theta) + PS(1 + \cos^2(\theta)) \tag{3.3.26}$$

$$C = PRL. \tag{3.3.27}$$

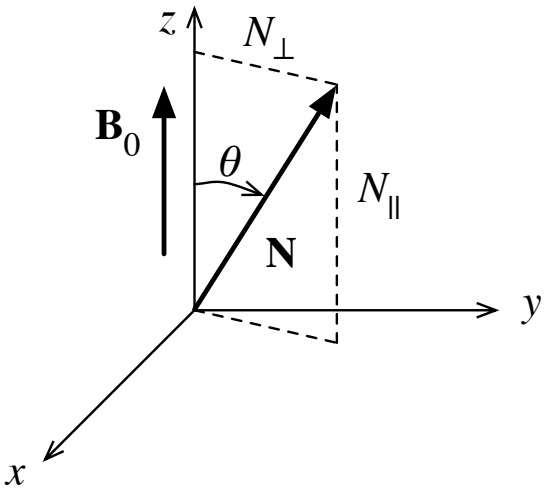

Figure 3.2: Reference frame for the cold plasma dispersion relation. In this coordinate system, the $\hat{\mathbf{z}}$ direction is aligned with the background magnetic field direction $\mathbf{B}_0$, and θ is the angle between $\mathbf{B}_0$ and the wave refractive index $\mathbf{N}$.

We recovered the standard expression usually derived in the Stix frame (with $\mathbf{N}$ in the $x-z$ plane). As expected from (3.2.50), the dispersion relation is independent of the coordinate system. Moreover, it does not depend on $\mathbf{N}$ but only on the relative direction of $\mathbf{N}$ with respect to $\mathbf{B}_0$ parametrized by θ (i.e. $\mathbf{B}_0$ is an axis of symmetry of the cold plasma dispersion relation), a special feature of the cold plasma model.

3.3.3 Cutoffs and resonances

According to the dispersion relation (3.2.50) and the definition of cutoffs (3.2.51), the cold plasma cutoffs are given by the condition

$$C = 0 \tag{3.3.28}$$

which is satisfied for

$$P = 0 \qquad \text{or} \qquad R = 0 \qquad \text{or} \qquad L = 0. \tag{3.3.29}$$

corresponding to

$$X_\mathrm{e} = 1 \qquad \text{and} \qquad X_\mathrm{e} = 1 + Y_\mathrm{e} \qquad \text{and} \qquad X_\mathrm{e} = 1 - Y_\mathrm{e} \tag{3.3.30}$$

respectively. These cutoffs are named the plasma cutoff, the R-cutoff and the L-cutoff respectively. They are independent of the propagation angle θ. According to the dispersion relation (3.2.50) and the definition of resonances (3.2.52), the cold plasma resonance, named upper-hybrid resonance (UHR), is given by the condition

$$A = 0 \qquad \text{equivalent to} \qquad X_\mathrm{e} = \frac{1 - Y_\mathrm{e}^2}{1 - \cos^2(\theta) Y_\mathrm{e}^2}. \tag{3.3.31}$$

Conversely to the cutoffs, the UHR resonance depends on the propagation angle θ. Note that when the ion dynamic is taken into account for lower frequency waves, a second resonance appears, named the lower-hybrid resonance (LHR).

3.3.4 Solution for N^2 as a function of θ

We can solve the dispersion relation (3.3.24) for N^2:

$$N_{\pm}^2(\theta) = \frac{B \pm \sqrt{\Delta}}{2A} \tag{3.3.32}$$

with

$$\Delta = B^2 - 4AC = (RL - PS)^2 \sin^4(\theta) + 4P^2 D^2 \cos^2(\theta) > 0. \tag{3.3.33}$$

Inserting explicit expressions for A, B, C, S, D, P, R, L and some algebra (see [69]) yields the solutions $N_{\pm}^2$ with explicit dependence on the propagation angle θ, the wave angular frequency ω and the plasma parameters X_e and Y_e:

$$N_{\pm}^2(\theta) = 1 + \frac{X_e}{2}\left[\frac{Y_e^2 \sin^2(\theta) - 2(1 - X_e) \pm \Gamma}{1 - X_e - Y_e^2 + X_e Y_e^2 \cos^2(\theta)}\right] \tag{3.3.34}$$

with

$$\Gamma = \left[Y_e^4 \sin^4(\theta) + 4(1 - X_e)^2 Y_e^2 \cos^2(\theta)\right]^{1/2}. \tag{3.3.35}$$

The discriminant Δ (or Γ) is always positive. Cold plasma waves are thus either purely propagative $N^2 > 0$ or purely evanescent $N^2 < 0$. The N_+ and N_- roots for $\theta = 90°$ (i.e. perpendicular propagation) are called the ordinary mode (O-mode) and extraordinary mode (X-mode) respectively. By extension, we will give the same names to the N_+ and N_- branches for oblique propagation with $0° \leq \theta < 90°$.
Another popular yet equivalent way to express the solutions $N_{\pm}^2(\theta)$ is obtained from (3.3.24) in the following manner:

$$AN^4 + AN^2 - AN^2 - BN^2 + C = 0 \quad \Rightarrow \quad N^2 = \frac{AN^2 - C}{AN^2 - B + A} \tag{3.3.36}$$

Inserting the expression (3.3.32) for $N_{\pm}^2$ in the latter relation, one writes

$$N_{\pm}^2 = 1 - \frac{2(A - B + C)}{2A - B \pm \sqrt{\Delta}}. \tag{3.3.37}$$

With explicit expressions, one gets the high-frequency collisionless Appleton-Hartree dispersion relation [67]:

$$N_{\pm}^2(\theta) = 1 - \frac{2X_e(1 - X_e)}{2(1 - X_e) - Y_e^2 \sin^2(\theta) \pm \Gamma}. \tag{3.3.38}$$

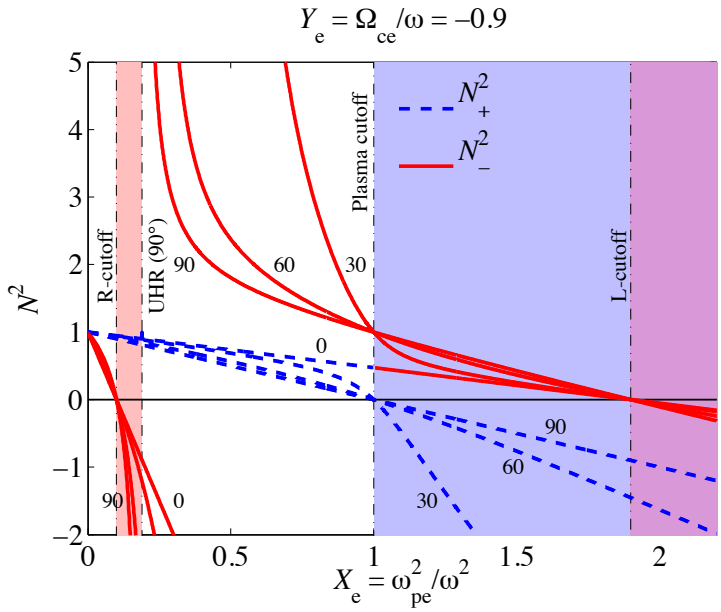

(a) Cold plasma dispersion roots N^2_+ and N^2_- for $Y_e = -0.9$.

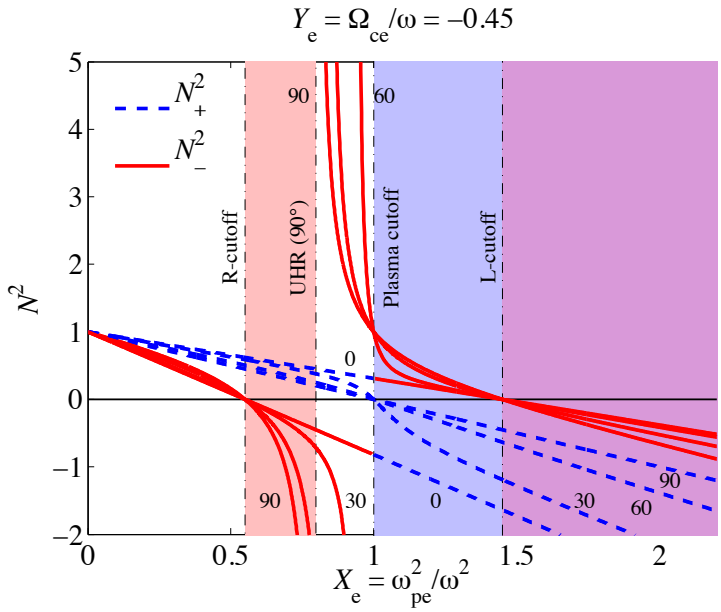

(b) Cold plasma dispersion roots N^2_+ and N^2_- for $Y_e = -0.45$.

Figure 3.3: Roots (3.3.34) of the cold plasma dispersion relation (3.3.24) for high-frequency waves. N^2_+ (dashed blue lines) and N^2_- (solid red lines) as functions of X_e for two values of Y_e and four values of the propagation angle $\theta = 0°, 30°, 60°, 90°$. For a given magnetic field, (a) $Y_e = -0.9$ and (b) $Y_e = -0.45$ correspond to first and second harmonic waves on the LFS of the EC resonance, respectively. The color bands are the regions of evanescence delimited by the cutoffs and the resonance. The N_+ branch (O-mode for $\theta = 90°$) is evanescent beyond the plasma cutoff (blue band covering $X_e \geq 1$). The N_- branch (X-mode for $\theta = 90°$) is evanescent between the R-cutoff and the UH resonance (red band) as well as beyond the L-cutoff. The UH resonance being dependent on the propagation angle, the UHR line drawn here is valid only for $\theta = 90°$, i.e. pure X-mode. Note that the N_+ and N_- branches connect at the plasma cutoff for $\theta = 0°$.

Figure 3.3 shows the roots $N_\pm^2$ as functions of $X_e = \omega_{pe}^2/\omega^2$ for two values of $Y_e = \Omega_{ce}/\omega$ and several propagation angles θ. For a given wave angular frequency ω (e.g. fixed by a microwave source as it is when applying ECRH from a gyrotron), X_e is proportional to the electron density n_e and the cases $Y_e = -0.9$ and $Y_e = -0.45$ represent respectively first and second harmonic waves on the low-field side of the electron cyclotron resonance (defined by $Y_e = -1$ and $Y_e = -0.5$ respectively).
Solutions of the dispersion relation on the low-field side of the resonance are of particular interest since most of the ECRH systems inject the microwaves from the low-field side (LFS) wall of the vessel, as it is the case for TCV second harmonic ECRH system. In figure 3.3, the evanescent regions for the N_+ and N_- branches are indicated as color bands delimited by the cutoffs (3.3.30) and the UH resonance (3.3.31). An important feature of the cold dispersion relation is that the O-mode branch cannot propagate at densities such that $X_e > 1$, except if the wave propagation is parallel to the magnetic field. In the latter case, it connects to the X-mode branch: this is the O-X mode conversion.

3.3.5 Perpendicular propagation: the O and X modes

Solution for θ as a function of N^2

It is useful to solve the dispersion relation (3.3.24) for θ by writing

$$AN^4 - BN^2 + C\underbrace{\left(\cos^2(\theta) + \sin^2(\theta)\right)}_{=1} = 0 \tag{3.3.39}$$

and dividing by $\cos^2(\theta)$ to extract

$$\tan^2(\theta) = \frac{-P(N^2 - R)(N^2 - L)}{S(N^2 - RL/S)(N^2 - P)}. \tag{3.3.40}$$

This expression allows the determination of the existing modes for a given propagation angle θ. In particular, for perpendicular propagation with $\theta = \pi/2$, we find simple expression of the dispersion relations for the ordinary mode (O-mode) and the extraordinary mode (X-mode):

$$N_O^2 = P \tag{3.3.41}$$

and

$$N_X^2 = \frac{RL}{S}. \tag{3.3.42}$$

The O-mode

For the propagation direction perpendicular to the static magnetic field, i.e. $\theta = \pi/2$, the N_+ branch (3.3.34) becomes

$$N_{\mathrm{O}}^2 = 1 - X_{\mathrm{e}}, \tag{3.3.43}$$

which is equivalent to the O-mode dispersion relation (3.3.41). Clearly, the O-mode has no resonance but it experiences a cutoff at the plasma frequency (the first of (3.3.30)):

$$X_{\mathrm{e}} = 1 \quad \Rightarrow \quad \omega = \omega_{\mathrm{pe}}. \qquad \text{O-mode cutoff (plasma cutoff)} \tag{3.3.44}$$

Solving the wave equation 3.3.20 for the electric field components with $N^2 = N_{\mathrm{O}}^2$ and $N_z = 0$ (i.e. perpendicular propagation), one finds

$$\mathbf{E} = (0, 0, E_z)\,, \tag{3.3.45}$$

i.e. the O-mode is a transverse wave with the electric field linearly polarized in the direction of the background magnetic field $\mathbf{B}_0$.

The X-mode

With $\theta = \pi/2$, the N_- branch (3.3.34) becomes

$$N_{\mathrm{X}}^2 = \frac{X_{\mathrm{e}}^2 - 2X_{\mathrm{e}} - Y_{\mathrm{e}}^2 + 1}{1 - X_{\mathrm{e}} - Y_{\mathrm{e}}^2}, \tag{3.3.46}$$

which is equivalent to the X-mode dispersion relation (3.3.42). The X-mode undergoes the R and L cutoffs (the second and third of (3.3.30)) given by

$$X_{\mathrm{e}} = 1 + Y_{\mathrm{e}} \quad \Rightarrow \quad \omega^2 + \omega\Omega_{\mathrm{ce}} - \omega_{\mathrm{pe}}^2 = 0, \qquad \text{X-mode cutoff (R-cutoff)} \tag{3.3.47}$$

$$X_{\mathrm{e}} = 1 - Y_{\mathrm{e}} \quad \Rightarrow \quad \omega^2 - \omega\Omega_{\mathrm{ce}} - \omega_{\mathrm{pe}}^2 = 0. \qquad \text{X-mode cutoff (L-cutoff)} \tag{3.3.48}$$

The X-mode meets the upper-hybrid (UH) resonance at

$$X_{\mathrm{e}} = 1 - Y_{\mathrm{e}}^2 \quad \Rightarrow \quad \omega^2 = \Omega_{\mathrm{ce}}^2 + \omega_{\mathrm{pe}}^2. \qquad \text{X-mode UH resonance} \tag{3.3.49}$$

Solving the wave equation 3.3.20 for the electric field components with $N^2 = N_{\mathrm{X}}^2$ and $N_z = 0$ (i.e. perpendicular propagation), one finds

$$E_z = 0 \tag{3.3.50}$$

and the polarization

$$\mathcal{P} \equiv \frac{\mathrm{i}E_x}{E_y} = \frac{-D}{S} = \frac{L - R}{L + R}, \tag{3.3.51}$$

i.e. the X-mode is generally elliptically polarized, although it becomes linearly polarized when approaching the UHR resonance ($S \to 0$), and circularly polarized at the cutoffs ($\mathcal{P} = \pm 1$ for $R, L = 0$).

3.3.6 Electron cyclotron resonance heating and accessibility

Wave absorption in a hot magnetized plasma

In the cold plasma model, the charged particles are treated as initially immobile. Hence, all kinetic effects linked to a finite temperature and having an impact on the plasma waves propagation and absorption are missing. In particular, the strong wave-particle resonances at the harmonics of the cyclotron frequencies due to the gyration of the charged particles around the magnetic field lines are at the base of electron cyclotron resonance heating (ECRH) and current drive (ECCD).

In order to describe the EC wave behavior at the vicinity of the EC resonance in a hot plasma, the cold plasma dielectric tensor is corrected by the kinetic theory accounting for the microscopic motion of the particles. Detailed derivations of the hot plasma dielectric tensor can be found in the literature [66,67]. The two solutions of the dispersion relation in a hot plasma are the electromagnetic electron cyclotron wave (ECW) and the electrostatic electron Bernstein wave (EBW) first described by Ira B. Bernstein in [6].

The diverging denominator of the hot dielectric tensor yields the EC resonance condition [66]

$$\omega = \frac{\ell|\Omega_{ce}|}{\gamma} + k_{\parallel} v_{\parallel} \tag{3.3.52}$$

where ω is the wave angular frequency, ℓ is the harmonic number, Ω_{ce} is the electron cyclotron frequency, $\gamma \equiv (1 - v^2/c^2)^{-1/2}$ is the usual relativistic factor $k_{\parallel} \equiv \omega N_{\parallel}/c$ is the wave vector component parallel to the magnetic field and $v_{\parallel}$ is the parallel velocity component of the electrons involved in the resonance.

ECRH accessibility

It is interesting to express the O-mode and X-mode cutoffs in the scope of ECRH applications in a toroidal magnetic fusion device with nominal central magnetic field B_0. If one wants to heat the plasma with wave-particle interaction at the electron cyclotron resonance, the gyrotrons frequencies must be chosen as harmonics of the electron cyclotron angular frequency $\Omega_{ce} = q_e B_0/m_e$, i.e. $\omega_\ell = \ell|\Omega_{ce}|$ where $\ell = 1, 2, 3, \ldots$ is the harmonic number. Evaluating the cutoff conditions (3.3.44), (3.3.47) and (3.3.48) with $\omega = \omega_\ell$ and $\Omega_{ce} = q_e B_0/m_e$ (i.e. at the resonance location), we find the cutoff densities above which the electron cyclotron resonance is screened

by the corresponding cutoff:

$$\text{P-cutoff:} \quad \omega_{\mathrm{pe}}^2 = \omega_\ell^2 \quad \Rightarrow \quad n_{\mathrm{P}\ell} = \frac{\varepsilon_0 m_\mathrm{e}}{q_\mathrm{e}^2}\omega_\ell^2 = \frac{\varepsilon_0}{m_\mathrm{e}}\ell^2 B_0^2 = 9.72\cdot 10^{18}\cdot \ell^2 B_0^2 \tag{3.3.53}$$

$$\text{R-cutoff:} \quad \omega_{\mathrm{pe}}^2 = \omega_\ell^2 + \omega_\ell \Omega_{\mathrm{ce}} \quad \Rightarrow \quad n_{\mathrm{R}\ell} = \frac{\varepsilon_0 m_\mathrm{e}}{q_\mathrm{e}^2}\left(1-\frac{1}{\ell}\right)\omega_\ell^2 = \frac{\varepsilon_0}{m_\mathrm{e}}\ell(\ell-1)B_0^2 \tag{3.3.54}$$

$$\text{L-cutoff:} \quad \omega_{\mathrm{pe}}^2 = \omega_\ell^2 - \omega_\ell \Omega_{\mathrm{ce}} \quad \Rightarrow \quad n_{\mathrm{L}\ell} = \frac{\varepsilon_0 m_\mathrm{e}}{q_\mathrm{e}^2}\left(1+\frac{1}{\ell}\right)\omega_\ell^2 = \frac{\varepsilon_0}{m_\mathrm{e}}\ell(\ell+1)B_0^2. \tag{3.3.55}$$

where the densities are given in $[\mathrm{m}^{-3}]$ and the magnetic field is given in [T].
In TCV, the ECRH systems consists of six gyrotrons at the second harmonics (O2/X2 at $\omega_2/2\pi = 82.6$ GHz) and three gyrotrons at the third harmonic (X3 at $\omega_3/2\pi = 118.0$ GHz). The corresponding cutoff densities n_{cutoff} calculated using the intermediate expressions with ω_ℓ in (3.3.53), (3.3.54) and (3.3.55) are given in table 3.1. The L-cutoff density is given for the sake of completeness since this cutoff cannot be reached for the second harmonic X-mode, neither from the low-field side (LFS), nor from the high-field side (HFS) of the resonance: it is completely surrounded by the R-cutoff.

Polarization	**Harmonic** ℓ	$\omega_\ell/2\pi$	**Cutoff**	n_c	$n_\mathrm{c}/\langle n_\mathrm{G}\rangle$
		[GHz]		$[10^{19}\ \mathrm{m}^{-3}]$	[%]
O	2	82.6	P	8.46	34
X	2	82.6	R	4.23	17
			L	12.70	51
X	3	118.0	R	11.52	46
			L	23.03	92

Table 3.1: Cutoff densities n_c for the TCV ECRH system.

These cutoff densities need to be compared to TCV operational domain in density whose maximum limit is well described by the Greenwald empirical limit [37]:

$$\langle n_\mathrm{G}\rangle = \kappa_a \langle J\rangle = \frac{I_\mathrm{p}}{\pi a^2} \tag{3.3.56}$$

where $\langle n_\mathrm{G}\rangle$ is the maximum line-average density in units of $[10^{20}\ \mathrm{m}^{-3}]$, κ_a is the plasma elongation, $\langle J\rangle$ is the average plasma current density in $[\mathrm{MA/m}^2]$, I_p is the

plasma current in [MA] and a is the plasma minor radius in [m]. The highest densities in TCV are achieved in ELM-free H-mode plasmas, as described in section 2.4, with typically $I_p = 0.5$ MA and $a = 0.25$ m, yielding $\langle n_G \rangle \simeq 2.5 \cdot 10^{20}$ m^{-3}. As a consequence, X2 and X3 can access only up to $\sim 17\%$ and $\sim 46\%$ of TCV operational domain in density. TCV ECRH accessibility is summed-up in the Clemmov-Mullaly-Allis (CMA) diagram given in figure 3.4.

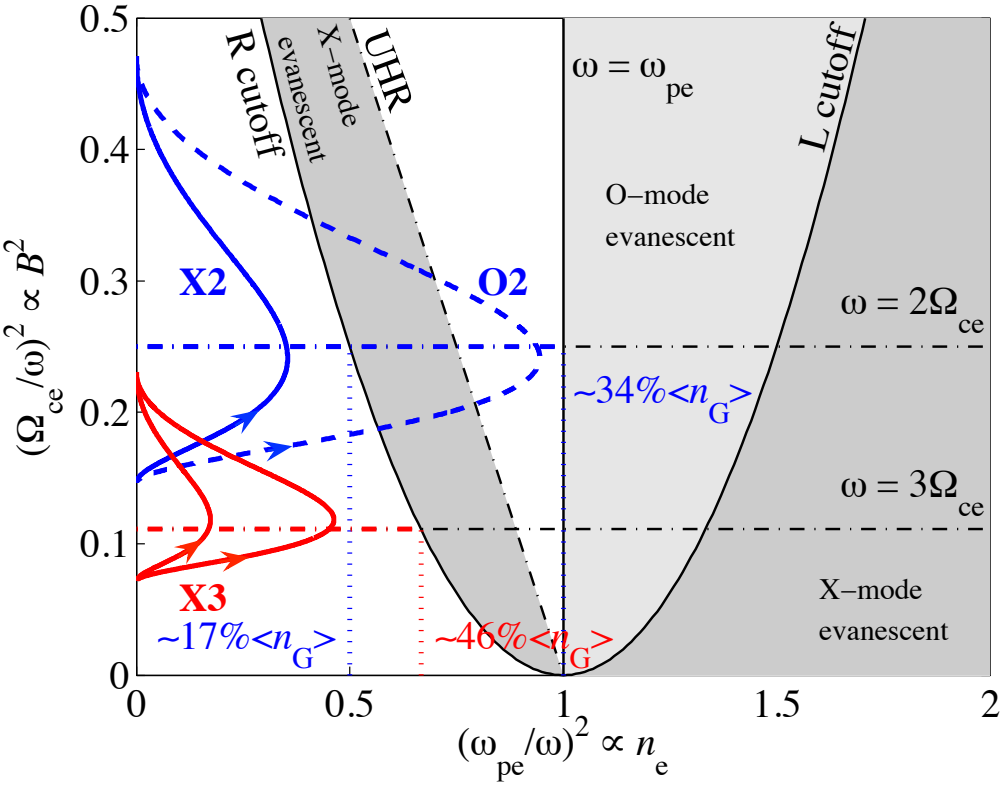

Figure 3.4: ECRH accessibility in the CMA diagram. CMA diagram for electron cyclotron waves propagating perpendicularly to the background magnetic field. The R and L cutoffs (solid black curves) as well as the upper-hybrid resonance (dash-dotted black curve) delimit the regions of evanescence for the X-mode (dark gray shade). The O-mode is evanescent on the right (light gray shade, $\omega < \omega_{pe}$) of the plasma cutoff (solid vertical line). The second and third electron cyclotron resonances are indicated by dash-dotted horizontal lines. The solid and dashed blue curves indicate the typical trajectories of 2nd harmonic X-mode and O-mode waves, respectively, injected horizontally from the LFS (i.e. from $\omega > 2\Omega_{ce}$) into a plasma with parabolic electron density profile, assuming the resonant field is located close to the plasma center where the density is maximum. The O-mode trajectory is given for a higher electron density. The solide red curves give the trajectories of 3rd harmonic X-mode waves injected from the LFS (i.e. from $\omega > 3\Omega_{ce}$) into plasmas which have the same density profiles than for the X2 and O2 cases. The maximum densities at which the EC resonance can be reached by the X2, O2 and X3 waves are indicated by vertical dotted lines, corresponding to 17%, 34% and 46% of TCV Greenwald density, respectively.

3.3.7 Solution for $N_\perp^2$ as a function of $N_\parallel^2$

In the case of ECRH, the wave angular frequency ω is fixed by the external power source and the initial wave vector is imposed by the antenna at the injection. If the plasma can be considered as a plane-stratified medium with gradients perpendicular to the homogeneous magnetic field (i.e. we use the so-called slab geometry), Snell's law [70] ensures that the parallel wave vector $k_\parallel$ is conserved. It is then natural to solve the dispersion relation (3.3.22) for the perpendicular index of refraction $N_\perp^2$ as a function of the parallel index of refraction $N_\parallel^2$:

$$A_\perp N_\perp^4 - B_\perp N_\perp^2 + C_\perp = 0 \tag{3.3.57}$$

with

$$A_\perp = S \tag{3.3.58}$$
$$B_\perp = PS + RL - (P+S)N_\parallel^2 \tag{3.3.59}$$
$$C_\perp = P\left(N_\parallel^2 - R\right)\left(N_\parallel^2 - L\right). \tag{3.3.60}$$

Explicitly in terms of $N_\parallel^2$ and fixed angular frequency ω and plasma parameters X_e and Y_e, one gets

$$N_{\perp\pm}^2(N_\parallel) = 1 - N_\parallel^2 - X_\mathrm{e} - \frac{X_\mathrm{e}Y_\mathrm{e}}{2}\frac{Y_\mathrm{e}\left(1+N_\parallel^2\right) \pm \sqrt{\Gamma_\perp}}{1 - X_\mathrm{e} - Y_\mathrm{e}^2} \tag{3.3.61}$$

with

$$\Gamma_\perp = Y_\mathrm{e}^2\left(1 - N_\parallel^2\right)^2 + 4N_\parallel^2\left(1 - X_\mathrm{e}\right). \tag{3.3.62}$$

For positive $N_\parallel^2$, the last term in $\Gamma_\perp$ is negative beyond the plasma cutoff where $X_\mathrm{e} > 1$, and $\Gamma_\perp$ itself can be negative. As a consequence, the two roots $N_{\perp\pm}^2$ can be complex conjugate. For a fixed value of $N_\parallel$, each value of $N_\perp$ (when varying X_e and Y_e) correspond to a different value of the propagation angle θ. It is also important to notice that for a given value of $N_\parallel$, the $N_{\perp+}$ and $N_{\perp-}$ branches don't necessarily belong to the O-mode and X-mode respectively.

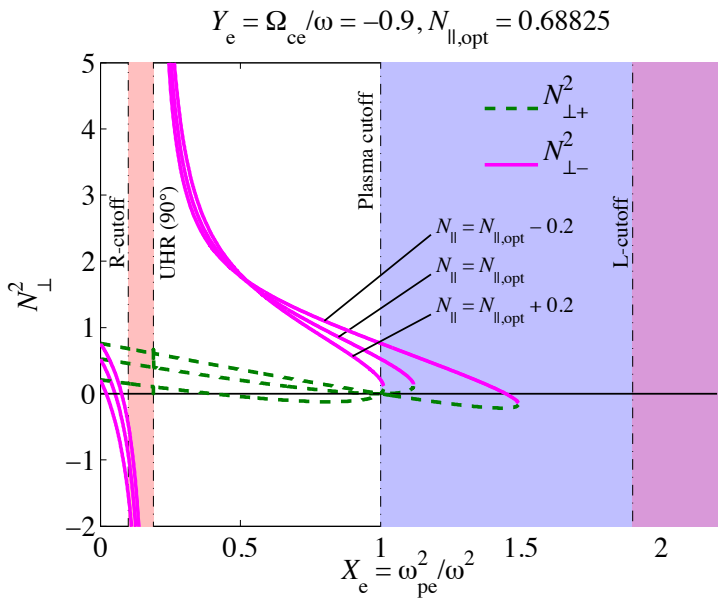

(a) Cold plasma dispersion roots $N^2_{\perp+}$ and $N^2_{\perp-}$ for $Y_e = -0.9$.

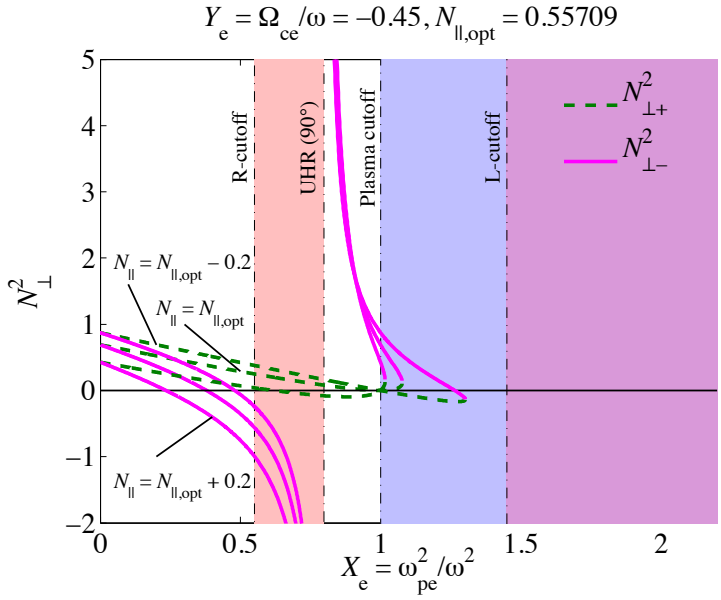

(b) Cold plasma dispersion roots $N^2_{\perp+}$ and $N^2_{\perp-}$ for $Y_e = -0.45$.

Figure 3.5: Roots (3.3.61) of the cold plasma dispersion relation (3.3.22) for high-frequency waves. $N^2_{\perp+}$ (dashed green lines) and $N^2_{\perp-}$ (solid magenta lines) are given as a function of the normalized electron plasma frequency X_e for the normalized electron cyclotron frequencies (a) $Y_e = -0.9$ and (b) $Y_e = -0.45$ and three values of the parallel refraction index: $N_\parallel = N_{\parallel,opt}$ and $N_\parallel = N_{\parallel,opt} \pm 0.2$ with $N_{\parallel,opt} \equiv \sqrt{Y_e/(Y_e - 1)}$. The color bands represent the evanescent regions of the O-mode and X-mode as described in figure 3.3. Both propagating $N_{\perp+}$ and $N_{\perp-}$ branches at $X_e > 1$ belong to the X-mode (but for different values of θ) since no O-mode can propagate beyond the plasma cutoff. For $N_\parallel = N_{\parallel,opt}$, the O-mode connects to the X-mode propagating beyond the plasma cutoff $X_e = 1$ without excursion into the evanescent layer, and thus a 100% efficiency. This is the O-X mode conversion.

This fact is illustrated by the roots $N_{\perp\pm}^2$ represented in figure 3.5 for the same two values of Y_e as in figure 3.3 (but with different colors to avoid confusion with the N_+ and N_- branches) and three values of $N_\parallel$. For densities below the plasma cutoff (i.e. $X_e < 1$) the branches $N_{\perp+}$ and $N_{\perp-}$ correspond to the branches N_+ (O-mode) and N_- (X-mode). But for $X_e > 1$, both propagating roots with $N_{\perp\pm}^2 > 0$ belong to the N_- (X-mode) branch since no propagating N_+ (O-mode) branch can exist in this region (see figure 3.3). The point is that these two solutions have different values of the propagation angle θ, except at the confluence point at the maximum X_e reached.

For the optimum value

$$N_{\parallel,\mathrm{opt}} \equiv \left(\frac{Y_e}{Y_e - 1}\right)^{1/2} \tag{3.3.63}$$

of the parallel refractive index, the O-mode reaches $N_{\perp+}^2 = 0$ (i.e. $\theta = 0$) at the plasma cutoff and propagates beyond the plasma cutoff without any excursion in the evanescent region ($N_{\perp\pm}^2 < 0$ region) by direct connection to the X-mode, that is the $N_{\perp+}$ branch for $X_e > 1$. This direct and smooth connection of the propagating O-mode to the propagating X-mode at the plasma cutoff $X_e = 1$ if $\theta = 0$ can also be seen in figure 3.3. It is called the ***O-X mode conversion***. For non-optimum values of the parallel refractive index as shown on figure 3.5, the O-mode wave energy needs to tunnel through an evanescent layer to connect to the X-mode beyond the plasma cutoff. In this case, the mode conversion efficiency cannot be 100%.

3.4 O-X mode conversion theory

3.4.1 Optimum parallel refractive index

When ECRH is applied in a fusion plasma, the wave angular frequency ω and the vacuum wave vector $\mathbf{k}_0$ are fixed by the power generator and the injection antenna respectively. In a tokamak equilibrium, we can consider the density gradient to be normal to the nested flux surfaces and thus to the magnetic field on each point. Moreover, the wavelength of microwaves in the electron cyclotron range ($\lambda_0 \simeq 3.6$ mm for $\omega/2\pi = 82.6$ GHz in TCV) is much smaller than the flux surfaces curvature radius, except close to the magnetic axis. We can then consider the plasma as a plane-layered medium in slab geometry with gradients perpendicular to the magnetic field. As a consequence of Snell's law, the wave vector component parallel to the magnetic field will be conserved along the wave trajectory.

As previously mentioned in subsection 3.3.7, it is then sound to solve the homogeneous cold plasma dispersion relation for $N_\perp$ as a function of $N_\parallel$, ω and the plasma parameters. As seen on figure 3.5, the $N_\perp^2$ solution exhibits an optimum value $N_{\parallel,\mathrm{opt}}$ of the parallel refractive index such that the O-mode root connects to the X-mode root at the plasma cutoff without experiencing any evanescence. The O-X mode conversion is the wave energy transfer from the O-mode propagating at densities below the plasma cutoff to the X-mode propagating beyond the plasma cutoff. When $N_\parallel$ departs from the optimum value $N_{\parallel,\mathrm{opt}}$, the wave energy must tunnel through an evanescent layer around the plasma cutoff and the mode conversion efficiency η is not 100%.

The solution (3.3.34) of the dispersion relation and figure 3.3 show that roots N_+^2 and N_-^2 coalesce when $\Gamma = 0$, which happens when both $X_\mathrm{e} = 1$ and $\theta = 0$. To calculate the corresponding parallel refractive index, we first look at the solution for $\theta = 0$ [71]:

$$N_{\parallel,\pm}^2 = \begin{cases} 1 + \dfrac{X_\mathrm{e}}{\mp Y_\mathrm{e} - 1} & \text{for} \quad X_\mathrm{e} > 1 \\ \\ 1 + \dfrac{X_\mathrm{e}}{\pm Y_\mathrm{e} - 1} & \text{for} \quad X_\mathrm{e} < 1 \end{cases} \tag{3.4.1}$$

where the upper and lower signs are for O-mode and X-mode respectively. Here, we remind that $Y_\mathrm{e} < 0$ (because $q_\mathrm{e} = -e$ for electrons). To ensure that $N_\parallel^2 > 0$ (i.e. the wave is propagating) on both sides of the plasma cutoff, we need to select the upper sign for $X_\mathrm{e} < 1$ (corresponding to the O-mode) and the lower sign for $X_\mathrm{e} > 1$ (corresponding to the X-mode). With $X_\mathrm{e} \to 1$, both solutions yield

$$N_{\parallel,\mathrm{opt}}^2 \equiv \left(\frac{Y_\mathrm{e}}{Y_\mathrm{e} - 1} \right). \tag{3.4.2}$$

We remind that the dispersion relations in section 3.3, and thus this initial discussion, are valid only for homogeneous plasmas. We invoked inhomogeneous plasmas only to justify the need of solving the dispersion relation for $N_\perp^2$ with fixed $N_\parallel^2$.

Now, two questions arise for the case of non-uniform plasmas:

1. What are the optimum angles at injection for the O-mode wave energy to be transferred to the X-mode beyond the cutoff ?

2. How does the transmission efficiency behave around this optimum ?

3.4.2 Full-wave equations for non-homogeneous cold plasmas

We study the propagation of a monochromatic electromagnetic wave

$$\mathbf{E}_1(\mathbf{x},t) = \tilde{\mathbf{E}}_1(x,k_y,k_z,\omega)\mathrm{e}^{\mathrm{i}(k_y y + k_z z - \omega t)} \tag{3.4.3}$$

in the electron cyclotron frequency range in a cold plasma slab with the static magnetic field in the z direction and the gradients (density, static magnetic field) in the x direction:

$$\mathbf{B}_0 = B_0\hat{\mathbf{z}} \qquad \text{and} \qquad \nabla n_\mathrm{e}, \nabla B_0 \parallel \hat{\mathbf{x}}, \tag{3.4.4}$$

as described in figure 3.6.

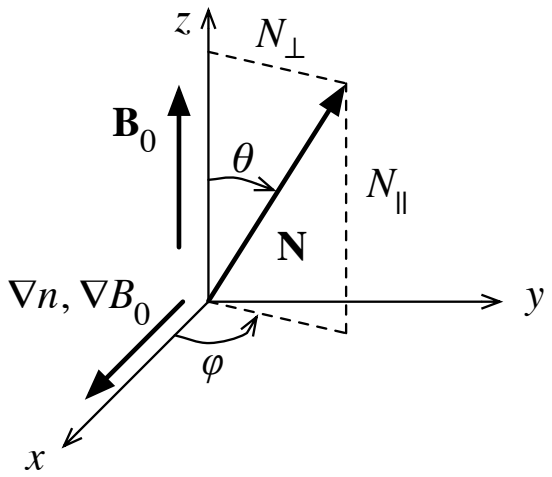

Figure 3.6: Reference frame of the plasma slab. In this coordinate system, the $\hat{\mathbf{z}}$ direction is aligned with the background magnetic field direction $\mathbf{B}_0$ and the $\hat{\mathbf{x}}$ direction is aligned with the gradients.

Snell's law ensures that neither k_y nor k_z depend on x. The information of the wave propagation along x is embedded in $\tilde{\mathbf{E}}_1(x,k_y,k_z,\omega)$. In this case, we need to reconsider the full-wave equation (3.2.14):

$$\nabla(\nabla\cdot\mathbf{E}_1) - \nabla^2\mathbf{E}_1 + \frac{1}{c^2}\frac{\partial^2\mathbf{E}_1}{\partial t^2} + \mu_0\frac{\partial\mathbf{J}_1}{\partial t} = 0. \tag{3.4.5}$$

Inserting (3.4.3) and the constitutive relation (3.2.34) in Fourier space

$$\tilde{\mathbf{J}}_1(\mathbf{k},\omega) = \mathbb{C}(\omega)\cdot\tilde{\mathbf{E}}_1(\mathbf{k},\omega), \tag{3.4.6}$$

the three components of the wave equation (3.4.5) in Fourier space become

$$\begin{aligned}\mathrm{i}k_y\frac{\mathrm{d}\tilde{E}_{1y}}{\mathrm{d}x} + \mathrm{i}k_z\frac{\mathrm{d}\tilde{E}_{1z}}{\mathrm{d}x} + \left[k_y^2 + k_z^2 - \frac{\omega^2}{c^2}\right]\tilde{E}_{1x} \\ - \mathrm{i}\omega\mu_0\left[C_{xx}\tilde{E}_{1x} + C_{xy}\tilde{E}_{1y} + C_{xz}\tilde{E}_{1z}\right] = 0\end{aligned} \tag{3.4.7}$$

$$\mathrm{i}k_y\frac{\mathrm{d}\tilde{E}_{1x}}{\mathrm{d}x} - k_yk_z\tilde{E}_{1z} - \frac{\mathrm{d}^2\tilde{E}_{1y}}{\mathrm{d}x^2} + \left[k_z^2 - \frac{\omega^2}{c^2}\right]\tilde{E}_{1y} - \mathrm{i}\omega\mu_0\left[C_{yx}\tilde{E}_{1x} + C_{yy}\tilde{E}_{1y} + C_{yz}\tilde{E}_{1z}\right] = 0 \tag{3.4.8}$$

$$\mathrm{i}k_z\frac{\mathrm{d}\tilde{E}_{1x}}{\mathrm{d}x} - k_yk_z\tilde{E}_{1y} - \frac{\mathrm{d}^2\tilde{E}_{1z}}{\mathrm{d}x^2} + \left[k_y^2 - \frac{\omega^2}{c^2}\right]\tilde{E}_{1z} - \mathrm{i}\omega\mu_0\left[C_{zx}\tilde{E}_{1x} + C_{zy}\tilde{E}_{1y} + C_{zz}\tilde{E}_{1z}\right] = 0. \tag{3.4.9}$$

Note that the constitutive relation (3.2.34) as well as the cold susceptibility tensor and the cold dielectric tensor are valid for the case of a non-uniform cold plasma since the cold conductivity tensor $\mathbb{C}$ is local in space. We can write the full-wave equations in a more compact form, giving up the tildes and 1 indices:

$$\mathrm{i}N_yE_y' + \mathrm{i}N_zE_z' + \left(N_y^2 + N_z^2 - K_{xx}\right)E_x - K_{xy}E_y - K_{xz}E_z = 0 \tag{3.4.10}$$

$$\mathrm{i}N_yE_x' - K_{yx}E_x - E_y'' + \left(N_z^2 - K_{yy}\right)E_y - \left(N_yN_z + K_{yz}\right)E_z = 0 \tag{3.4.11}$$

$$\mathrm{i}N_zE_x' - K_{zx}E_x - E_z'' + \left(N_y^2 - K_{zz}\right)E_z - \left(N_yN_z + K_{yz}\right)E_y = 0 \tag{3.4.12}$$

where we used the definition (3.2.38) of the susceptibility tensor $\mathbb{S}$, the definition of the dielectric tensor $K_{mn} = \delta_{mn} + \frac{\mathrm{i}}{\omega\varepsilon_0}S_{mn}$ and the notation $E' \equiv \frac{\mathrm{d}E}{\mathrm{d}\xi}$ with the normalized distance $\xi \equiv x\omega/c$. In this set of equations, the cold dielectric tensor $\mathbb{K}$ depends on x via the plasma parameter profiles X_e and Y_e, i.e. $n_\mathrm{e}(x)$ and $B_0(x)$.

3.4.3 WKB approximation and analytical solutions

The set (3.4.10)–(3.4.12) of ordinary differential equations (ODE) must be solved numerically. But for the case of slightly non-uniform plasmas, the system can be solved in the WKB approximation (3.2.54) for electron cyclotron waves in cold plasmas:

$$k_0 \gg L_B^{-1},\ L_n^{-1} \tag{3.4.13}$$

where the characteristic lengths of the plasma inhomogeneities are defined by

$$L_B \equiv \left[\frac{1}{B_0}\frac{\mathrm{d}B_0}{\mathrm{d}x}\right]^{-1} \qquad \text{and} \qquad L_n \equiv \left[\frac{1}{n_\mathrm{e}}\frac{\mathrm{d}n_\mathrm{e}}{\mathrm{d}x}\right]. \tag{3.4.14}$$

A direct consequence of the WKB approximation is that not only the cold plasma dielectric tensor is valid locally in space, but also the cold plasma dispersion relation. Since $N_z(=N_\parallel)$ and N_y are conserved in the plasma slab, the optimum parallel refractive index at the injection is thus equal to the optimum parallel refractive index at the mode conversion location (3.4.2) and we write

$$N_{\parallel,\mathrm{opt}}^2 = N_{z,\mathrm{opt}}^2 \equiv \left(\frac{Y_\mathrm{e}|_{X_\mathrm{e}=1}}{Y_\mathrm{e}|_{X_\mathrm{e}=1} - 1}\right) \tag{3.4.15}$$

where it is specified that the normalized electron cyclotron frequency Y_e must be evaluated at the cutoff $X_e = 1$. There is one optimum injection in the direction of the field and one in the opposite direction. Since we must have $N_\perp^2 = N_x^2 + N_y^2 = 0$ at the conversion location, $N_\perp = 0$ and $N_\parallel = 0$ at $X_e = 1$. Since N_y is conserved, the optimum N_y at the injection is

$$N_{y,\mathrm{opt}}^2 = 0. \tag{3.4.16}$$

In addition to the angle θ between the wave refractive index $\mathbf{N}$ and the magnetic field $\mathbf{B}_0$ defined in (3.3.23), one can introduce the angle φ between the plane defined by $\mathbf{N}$ and $\mathbf{B}_0$ and the direction of the plasma inhomogeneities such that

$$N_x = N\sin(\theta)\cos(\varphi), \tag{3.4.17}$$

$$N_y = N\sin(\theta)\sin(\varphi), \tag{3.4.18}$$

$$N_z = N\cos(\theta). \tag{3.4.19}$$

Since $N = 1$ at the injection (from vacuum), the optimum wave injection angles pairs for the O-X mode conversion in the WKB limit are given by

$$(\theta_{\mathrm{opt}}, \varphi_{\mathrm{opt}}) = \left(\arccos\left[\pm\sqrt{\frac{Y_e|_{X_e=1}}{Y_e|_{X_e=1} - 1}}\right], 0\right). \tag{3.4.20}$$

As reviewed in reference [72], several authors have solved the O-X conversion problem in the WKB limit $k_0 L_n \gg 1$ for plasmas with non-uniform density but uniform magnetic field. In particular, Preinhaelter and Kopecký studied the case $N_y = 0$ in [13] which Preinhaelter generalized to arbitrary N_y in reference [14]. The resulting wave energy transmission coefficient (or O-X mode conversion efficiency) writes

$$\eta_{\mathrm{P}} = \exp\left\{-\pi k_0 L_n \sqrt{\frac{-Y_e}{2}}\left[\frac{(1-Y_e)^2}{(-2Y_e)}\left(N_{z,\mathrm{opt}}^2 - N_z^2\right)^2 + N_y^2\right]\right\} \tag{3.4.21}$$

where all quantities must be evaluated at the plasma cutoff $X_e = 1$. Starting from the dielectric tensor (3.3.18), Mjølhus extended the discussion to the case of the uniform magnetic field making an arbitrary angle α with the density gradient, see [73]. For the situation of our interest, $\alpha = \pi/2$ and Mjølhus's energy transmission coefficient is

$$\eta_{\mathrm{M}} = \exp\left\{-\pi k_0 L_n \sqrt{\frac{-Y_e}{2}}\left[2\,(1-Y_e)\left(N_{z,\mathrm{opt}} - N_z\right)^2 + N_y^2\right]\right\}. \tag{3.4.22}$$

Both transmission coefficients (3.4.21) and (3.4.22) represent gaussian-like angular windows around the optimum angles (3.4.20). They differ in the N_z dependence

but match each other very well close to $N_{z,\mathrm{opt}}$. A comparison of these analytical solutions to numerical simulations of the full-wave ODEs system (3.4.10)–(3.4.12) was performed in [72] for $Y_\mathrm{e} = 0.9$ (corresponding to first harmonic waves on the low-field side of the EC resonance) and different density profiles, i.e. different values of the WKB parameter $k_0 L_n$. The best agreement between analytical and numerical solutions is obtained for η_M.

3.5 The AMR-LUKE simulation tool

The Antenna–Mode-conversion–Ray-tracing (AMR) simulation tool is a code for the mode conversion, propagation, absorption and emission of the electron Bernstein waves. It was written by Jakub Urban and Josef Preinhaelter, Euratom/IPP.CR Association, Institute of Plasma Physics, Prague, Czech Republic. In the sequel of this work, we will use the AMR code [26,27] to calculate the angular window of mode conversion efficiency and the ray-tracing of the EBW with linear damping. The ray trajectory is then passed to the 3D Fokker-Planck code LUKE [30] which calculates the quasi-linear wave-particle interaction along the ray path. The LUKE code is developed by J. Decker and Y. Peysson, Euratom/CEA Association, Cadarache, France.

3.5.1 The AMR code

The AMR code includes two main modules, the mode conversion and the ray-tracing modules.

Mode conversion calculation module

The O-X-B mode conversion efficiency is calculated by a full-wave numerical solver. It solves the set of second-order ordinary differential equations (3.4.10)–(3.4.12) for a cold magnetized 1D plasma slab model along the density inhomogeneity direction x. It uses a finite elements method (FEM) with zeroth and first order cubic Hermite polynomials for the function discretization and an adaptive mesh refinement.
Since waves are injected from vacuum, the 1D slab comprises the UHR and a weak collision term ν is added to the equation of motion (3.3.1) to avoid the singularity at the UHR [25, 66, 72]:

$$\frac{\mathrm{d}\mathbf{u}_\alpha}{\mathrm{d}t} = \frac{q_\alpha}{m_\alpha}\left(\mathbf{E}_1 + \mathbf{u}_\alpha \times \mathbf{B}_0\right) - \nu \mathbf{u}_\alpha. \tag{3.5.1}$$

The components of the cold dielectric tensor are thus modified as follow:

$$K_{xx} = K_{yy} \equiv 1 - \sum_{\alpha} \frac{X_\alpha (1 + \mathrm{i} Z_\nu)}{(1 + \mathrm{i} Z_\nu)^2 - Y_\alpha^2}, \tag{3.5.2}$$

$$K_{xy} = -K_{yx} \equiv \mathrm{i} \sum_{\alpha} \frac{Y_\alpha X_\alpha}{(1 + \mathrm{i} Z_\nu)^2 - Y_\alpha^2}, \tag{3.5.3}$$

$$K_{zz} \equiv 1 - \sum_{\alpha} \frac{X_\alpha}{1 + \mathrm{i} Z_\nu}, \tag{3.5.4}$$

with $Z_\nu \equiv \nu/\omega$. Moreover, a gaussian peak is added around the upper hybrid resonance (UHR) in the initial mesh density. AMR also offers the possibility to calculated the O-X mode conversion efficiency using Preinhaelter's analytical solution (3.4.21). The collisional damping at the UHR gives the wave energy transmitted to the Bernstein mode.

Ray-tracing module

The ray-tracing part of the code [74] calculates the wave trajectory using a non-relativistic electrostatic hot plasma dispersion relation. The ray-tracing starts with the X-mode at the mode conversion region, beyond the plasma cutoff. The wave propagates back to the UHR layer where it connects to the Bernstein wave branch. It has been shown that relativistic effects can be neglected for the wave propagation but are necessary for a sound description of the wave absorption [75]. A weakly relativistic correction is thus implemented on the linear damping in AMR to account for the relativistic shift of the resonance.

3.5.2 The LUKE code

LUKE is a fully relativistic quasi-linear 3D bounce-averaged Fokker-Plank solver (formerly named DKE). It is coupled with the C3PO ray-tracing code for EC waves [29]. This code is mainly devoted to study the effect of the heating and current drive by RF power on the electron distribution function. Electron dynamics is studied in a reduced 3D phase-space: the momentum in direction parallel and perpendicular to the magnetic field, and the radial direction.

3.5.3 AMR-LUKE implementation in TCV environnement

The integration of the AMR code in the TCV environment was part of this thesis work in close collaboration with J. Urban and J. Decker. In particular, the launcher angles needed to be translated into the AMR effective injection geometry

defined around the major radius axis passing through the beam waist, as described in appendix A.

At TCV, the AMR code is called via the LUKE interface. LUKE takes as input the magnetic equilibrium data (in the form of an EQDSK file) and the electron temperature and density profiles measured by the Thomson scattering diagnostic, as well as the ion temperature and density profiles and the effective charge as provided by the charge exchange diagnostic. In the implementation of the AMR-LUKE coupling in the TCV environment, special attention was given to the treatment of the magnetic fields and plasma currents, since TCV, the equilibrium EQDSK files and the AMR-LUKE codes do not share the same definition of the positive toroidal direction, as pictured in figure 3.7.

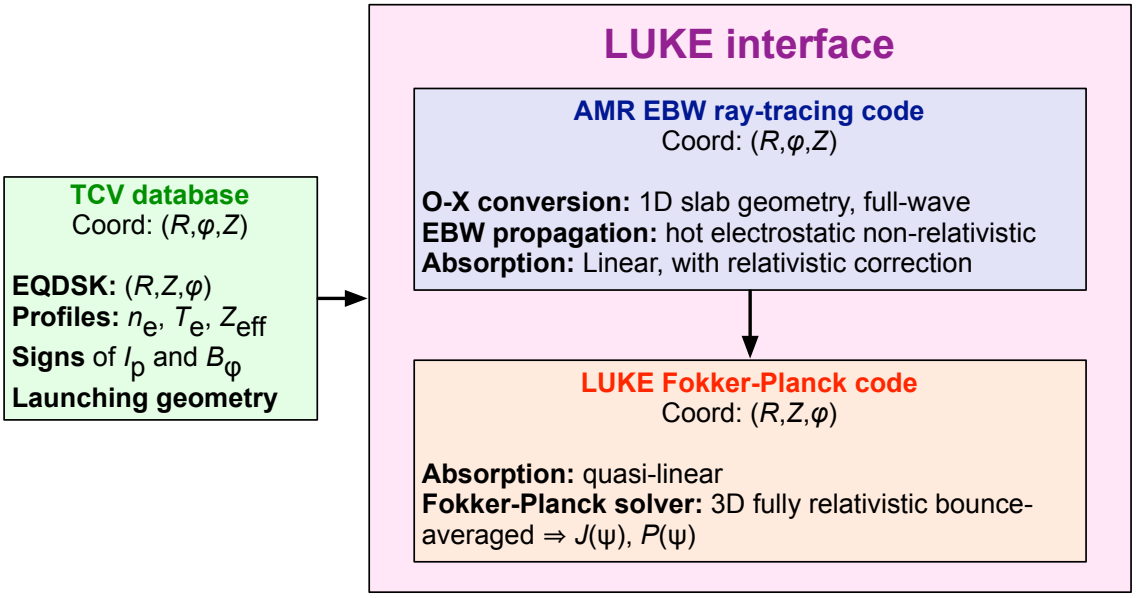

Figure 3.7: AMR-LUKE code coupling in the TCV environment.

Chapter 4

O-X-B mode conversion in TCV

4.1 Introduction

In this chapter, we study the EBW-plasma coupling via O-X-B mode conversion of O2 power launched in TCV H-modes. According to the mode conversion theory reviewed in section 3.4, for given magnetic equilibrium position and relative wave injection location, there are two optimum injection directions to reach the O-X-B mode conversion, one in each toroidal direction. Each injection direction can be parametrized by a pair of optimum toroidal and poloidal angles, expressed in terms of either effective geometry or launching antenna geometry.

Here, we investigate the poloidally oblique injection of O2 power from below the plasma midplane. In practice, this is performed by injecting the microwaves from an equatorial launcher into a plasma located in the upper half of TCV vessel ($Z_{\mathrm{axis}} > 10$ cm). In such a launching scheme, the EBW mode undergoes a strong upshift of its parallel index of refraction, as will be shown by ray-tracing simulations with the AMR code. As a consequence, the wave undergoes a strong Doppler-shift and the power is absorbed far off-axis (with the EC resonance located close to the magnetic axis).

In section 4.2, the angular window of mode conversion efficiency is first calculated using the full-wave AMR code. The sensitivity of the AMR results to the density gradient at the mode conversion region and to the plasma vertical position is tested. In section 4.3, the numerical results are compared to the experimental position of the angular optimum obtained by analysis of the wave-plasma coupling in a shot-to-shot scan of the O2 power injection direction in overdense H-mode plasmas. A discussion of the results and the conclusions are given in section 4.4.

4.2 Simulations of O-X mode conversion

The O-X mode-conversion is calculated for an equilibrium in H-mode regime located in the upper half of TCV vacuum vessel at $Z_{\text{axis}} = 12.6$ cm. At this time of TCV operation, the edge Thomson scattering system for the measurement of pedestal profiles was not yet available. Typical TCV H-mode density and temperature profiles from a later discharge will thus be used in this case. The electron temperature and density experimental data from the Thomson scattering diagnostic are given in figure 4.1(a) and 4.1(b) respectively, along with the fitted profiles used in the simulation. The density is corrected using the absolutely calibrated measurements from the far-infrared interferometer (FIR). The O2 mode cutoff is located in the steep edge density gradient region, at $\rho_\psi \simeq 0.96$.

A detailed view of the edge electron density profile with pedestal width $W_{n,0} = 1.44$ cm is given in figure 4.2(a) along with artificially modified profiles having half pedestal width $W_n = 0.5W_{n,0}$ and double pedestal width $W_n = 2W_{n,0}$. The edge density profiles are mapped on the major radius passing through the magnetic axis (figure 4.2(b)) to calculate the edge density gradient and scale length (figures 4.2(c) and 4.2(d), respectively). The resulting density profile pedestal parameters are given in table 4.1. For this high density H-mode, the electron to ion temperatures ratio is assumed to be $T_e/T_i = 1$ [32, 76] and a flat $Z_{\text{eff}} = 3$ profile is chosen.

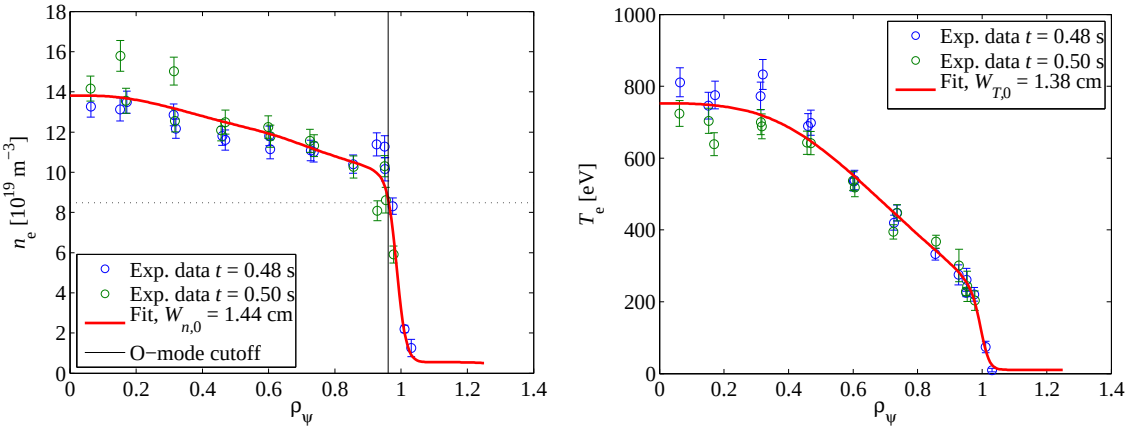

(a) Electron density data and profile. **(b)** Electron temperature data and profile.

Figure 4.1: TCV ELM-free H-mode electron density and temperature profiles. Thomson scattering experimental data (○) and fitted profiles (solid curve) of (a) electron density and (b) temperature used in the O-X mode conversion efficiency calculation with the AMR code. The O2 mode cutoff density (dotted line) is located at $\rho_\psi \simeq 0.96$ (vertical line), at the edge in the steep pedestal gradient region. #31541.

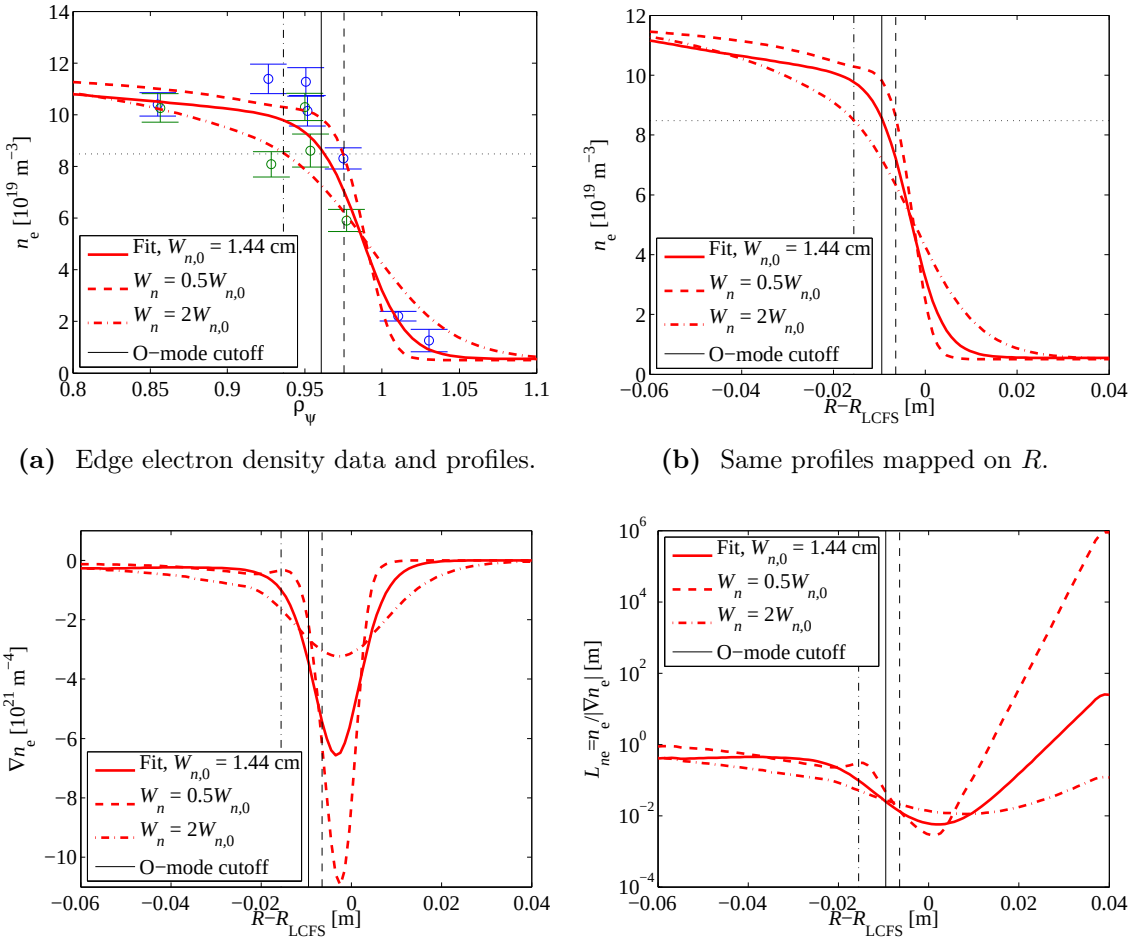

(a) Edge electron density data and profiles.

(b) Same profiles mapped on R.

(c) Edge electron density gradients.

(d) Edge electron density scale lengths.

Figure 4.2: Edge electron density profiles, gradients and scale lengths. Edge density profiles used in the O-X mode conversion efficiency calculations with the AMR code. The original profile (solid curve) with pedestal width $W_{n,0} = 1.44$ cm is artificially modified for $W_n = 0.5W_{n,0}$ (dashed curve) and $W_n = 2W_{n,0}$ (dash-dotted curve). The corresponding O2 mode cutoffs are indicated (vertical lines). The profiles of (a) are mapped on the major radius in (b) to calculate the edge density gradients (c) and scale lengths (d). TCV shot #31541, $t = 0.49$ s.

O-X mode conversion efficiency calculations and sensitivity study

The injection angles window of O-X mode conversion efficiency is calculated with the AMR code around the optimum injection for the counter-clockwise toroidal direction. For each pair of "poloidal" and "toroidal" launcher angles (θ_L, ϕ_L), a single ray of second harmonic EC waves in O-mode polarization (abbreviated O2) with power $P_{EC} = 500$ kW is injected from TCV equatorial launcher L4, as indicated in figure 4.4. The resulting angular window for the original density pedestal width $W_{n,0} = 1.44$ cm and magnetic axis vertical position $Z_{axis} = 12.0$ cm is shown in figure 4.5(b).

		At maximum slope		At O2 mode cutoff	
Height H_n [10^{19} m^{-3}]	Width W_n [mm]	Slope S_n [10^{21} m^{-4}]	Scale length L_n [mm]	Slope S_n [10^{21} m^{-4}]	Scale length L_n [mm]
	14.4 ± 1.3	6.3 ± 0.8	8.0 ± 1.3	3.4	2.5
9.6 ± 0.3	7.2	10.9	4.5	6.2	13.8
	28.8	3.2	15.6	1.7	51.3

Table 4.1: ELM-free H-mode edge density profile parameters. The top line corresponds to the original pedestal width. The second and third line give the pedestal parameters for twice smaller and larger widths, respectively, at constant pedestal height. #31541, $t = 0.49$ s.

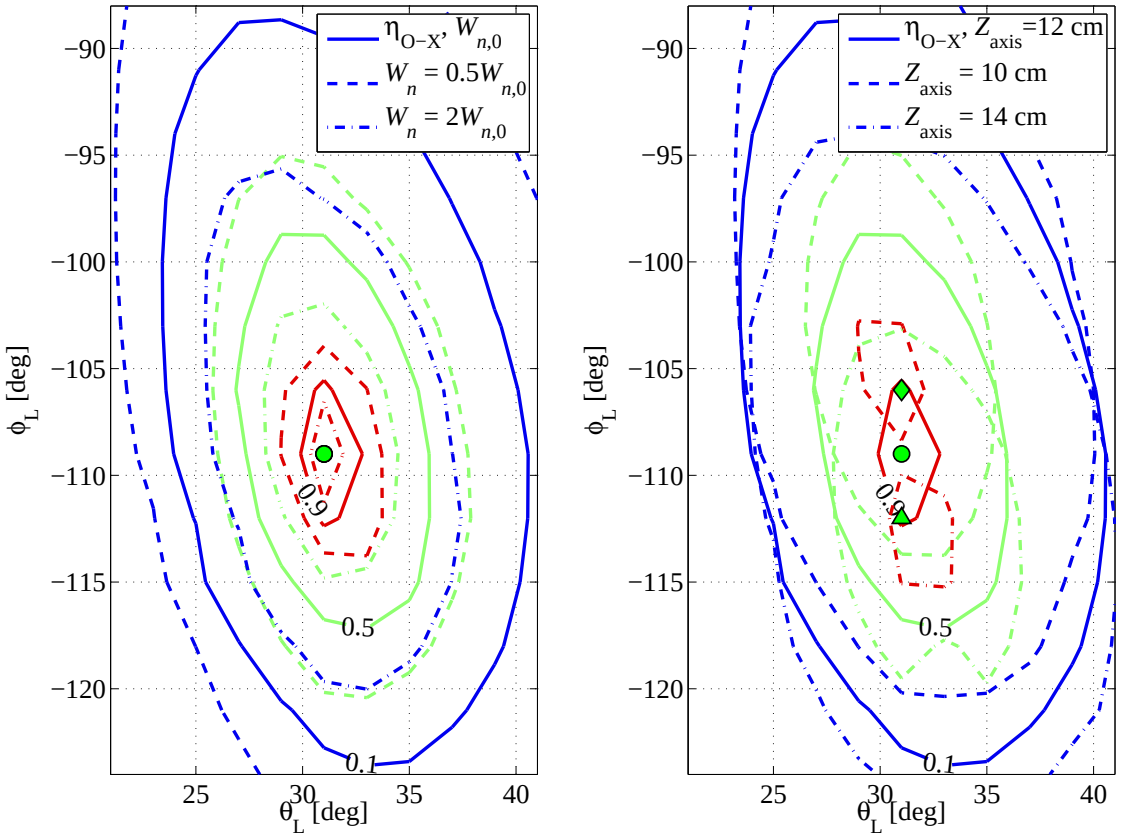

(a) Sensitivity on density pedestal width W_n. **(b)** Sensitivity on magnetic axis position Z_{axis}.

Figure 4.3: O-X mode conversion efficiency sensitivity on (a) the pedestal width and (b) the magnetic axis vertical position. Superimposed contour plots of the AMR O-X mode conversion efficiencies $\eta_{\text{O-X}}$ (blue = 10%, green for = 50% and red for = 90%) for (a) different density pedestal widths (see figure 4.5) and (b) different magnetic axis positions (see figure 4.6) for the case of poloidally oblique injection. In (a), the dashed and dash-dotted contours correspond to the dashed and dash-dotted profiles of figure 4.2. TCV shot #29005 at $t = 0.81$ s with profiles from #31541 at $t = 0.49$ s.

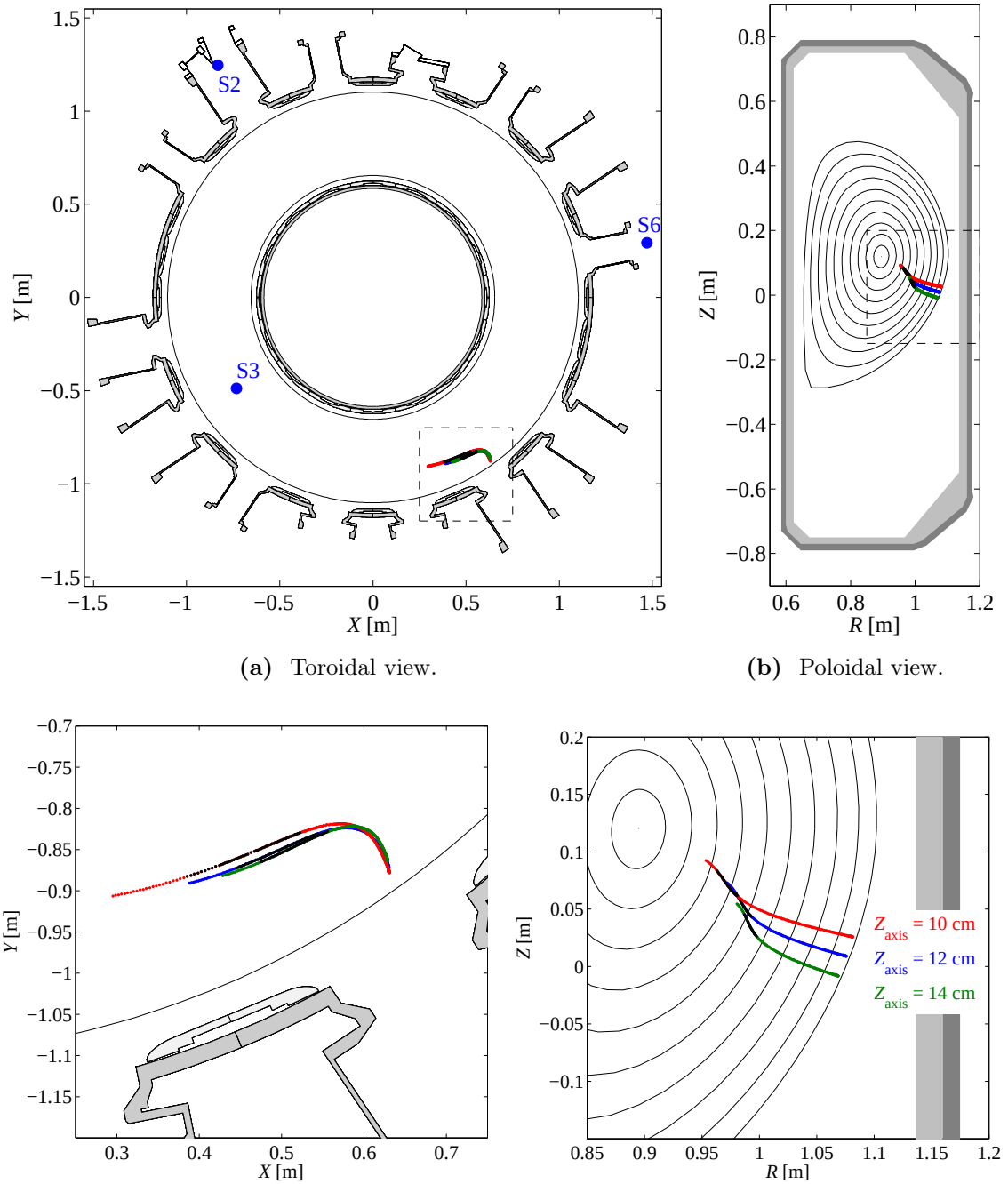

(a) Toroidal view.

(b) Poloidal view.

(c) Details of the toroidal view.

(d) Details of the poloidal view.

Figure 4.4: AMR ray-tracing trajectories. (a) Toroidal and (b) poloidal views of the ray trajectories calculated by the AMR ray-tracing code for the equilibrium at its original vertical position $Z_{\text{axis}} = 12.0$ cm (blue) and for equilibria artificially displaced to $Z_{\text{axis}} = 10.0$ cm (red) $Z_{\text{axis}} = 14.0$ cm (green). On the toroidal view, the stray diodes position is denoted by three blue •. The dashed frames define the detail views on the ray trajectories given in (c) and (d). Black dots indicate the power absorption location along the rays. TCV shot #29005 at $t = 0.81$ s with profiles from #31541 at $t = 0.49$ s.

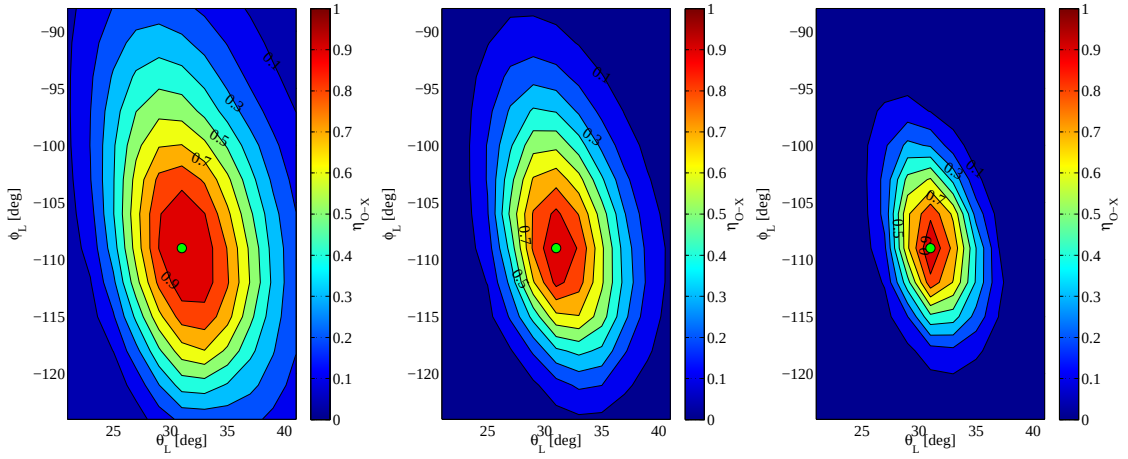

(a) $W_n = 0.5W_{n,0}$. **(b)** $W_{n,0} = 1.44$ cm. **(c)** $W_n = 2W_{n,0}$.

Figure 4.5: Sensitivity of O-X mode conversion efficiency on density pedestal width. AMR calculations of the O-X mode conversion efficiency $\eta_{\text{O-X}}$ as a function of the launcher injection angles $(\theta_{\text{L}}, \phi_{\text{L}})$ for (b) the original density pedestal width $W_{n,0} = 1.44$ cm, (a) a half density pedestal width $W_n = 0.5W_{n,0}$ and (c) a double density pedestal width $W_n = 2W_{n,0}$. The magnetic axis is located at $Z_{\text{axis}} = 12.0$ cm. The optimum mode conversion $\eta_{\text{O-X}} = 1$ (green •) is obtained for the same angle pair $(\theta_{\text{L,opt}}, \phi_{\text{L,opt}}) = (31.0°, -109.0°)$ in all cases. TCV shot #29005 at $t = 0.81$ s with profiles from #31541 at $t = 0.49$ s.

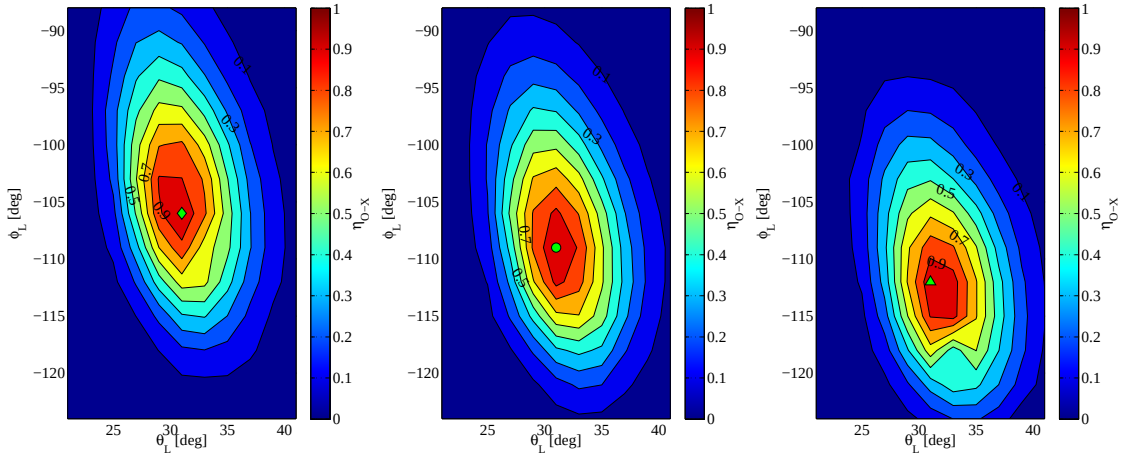

(a) $Z_{\text{axis}} = 10.0$ cm. **(b)** $Z_{\text{axis}} = 12.0$ cm. **(c)** $Z_{\text{axis}} = 14.0$ cm.

Figure 4.6: Sensitivity of O-X mode conversion efficiency on magnetic axis position. AMR calculations of the O-X mode conversion efficiency $\eta_{\text{O-X}}$ as a function of the launcher injection angles $(\theta_{\text{L}}, \phi_{\text{L}})$ for (b) the original magnetic axis vertical position $Z_{\text{axis}} = 12.0$ cm, (a) the equilibrium artificially displaced to $Z_{\text{axis}} = 10$ cm and (c) to $Z_{\text{axis}} = 14$ cm. The density pedestal width is $W_{n,0} = 1.44$ cm. The corresponding optimum injection angles and optimum O-X mode conversion efficiencies are (b) $\eta_{\text{O-X}} = 1$ (green •) for $(\theta_{\text{L,opt}}, \phi_{\text{L,opt}}) = (31.0°, -109.0°)$, (a) $\eta_{\text{O-X}} = 0.99$ (green ♦) for $(\theta_{\text{L,opt}}, \phi_{\text{L,opt}}) = (31.0°, -106.0°)$ and (c) $\eta_{\text{O-X}} = 0.98$ (green ▲) for $(\theta_{\text{L,opt}}, \phi_{\text{L,opt}}) = (31.0°, -112.0°)$. TCV shot #29005 at $t = 0.81$ s with profiles from #31541 at $t = 0.49$ s.

The optimum pair of injection angles is found to be $(\theta_{\mathrm{L,opt}}, \phi_{\mathrm{L,opt}}) = (31.0°, -109.0°)$. Similar mode conversion windows are calculated for the modified density pedestal profiles (see figure 4.2) with pedestal widths $W_n = 0.5W_{n,0}$ and $W_n = 2W_{n,0}$ resulting in figures 4.5(a) and 4.5(c), respectively. For the sake of comparison, all three mode conversion angular windows are superimposed as contour plots in figure 4.3(a). As expected, the steeper the density gradient at the O2 mode cutoff, the wider the mode conversion angular window. Conversely, the value of the optimum injection angles does not depend on the gradient.

The sensitivity of the O-X mode conversion efficiency on the plasma equilibrium vertical position with respect to the injection antenna has been tested by artificially displacing the equilibrium by $\Delta Z \pm 2$ cm, resulting in the angular windows of figures 4.3(b) and 4.6. Varying the plasma position, the width of the angular window is essentially constant. Conversely, the optimum "toroidal" launcher angle $\phi_{\mathrm{L,opt}}$ is very sensitive to the plasma vertical position and varies by $\mp 3°$. As it is presented in the next section, the experimental optimum angle is in excellent agreement with the AMR simulation. The high sensitivity of the simulated optimum to the plasma-antenna relative position confirms that this is a successful benchmark of the AMR code against the experiment.

4.3 Experimental angle scans

Experimental setup

A scan of the L4 launcher angles was performed on shot to shot basis in TCV H-mode overdense plasmas to test the existence and the position of the optimum injection angles for the O2 power to convert to X-mode, then to EBWs and to finally be absorbed at the EC resonance. As a preparation to these experiments, the optimum launcher angles were determined for the target plasma conditions using the ART (Another-Ray-Tracing) code [19, 77] — the EBW simulation tool used at CRPP prior to the AMR code — as described in [22–24]. The ART mode conversion efficiency calculation is based on Mjølhus's formula (3.4.22). The experimental angle scan was then performed around the calculated optimum, first scanning the toroidal launcher angle while keeping the poloidal launcher angle constant at a measured value of $\theta_{\mathrm{L}} = 28.0 \pm 0.0°$. The scan of the poloidal launcher angle was then performed keeping the toroidal launcher angle at the value which seemed to previously exhibit a minimum stray power level, i.e. $\phi_{\mathrm{L}} = -110.2 \pm 0.1°$.

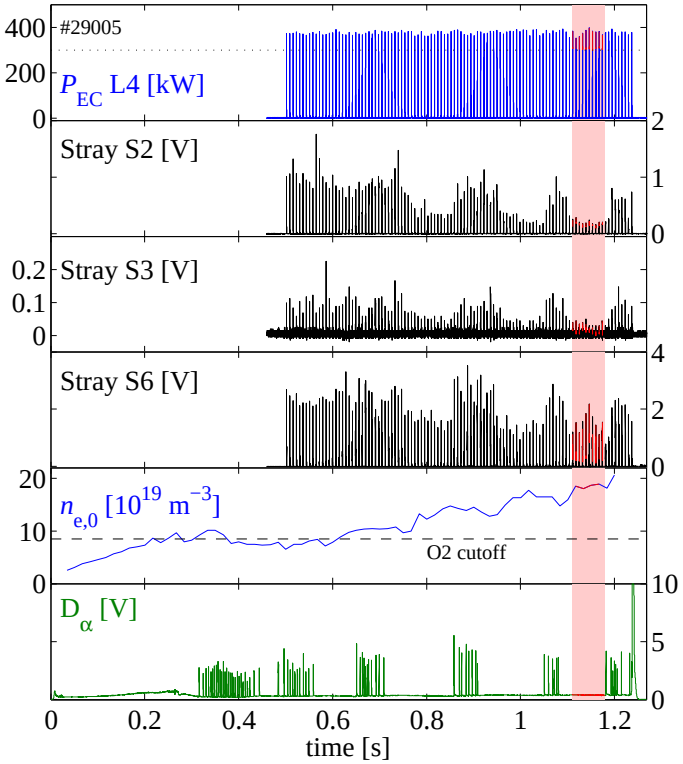

(a) Stray power measurement during modulated EBH.

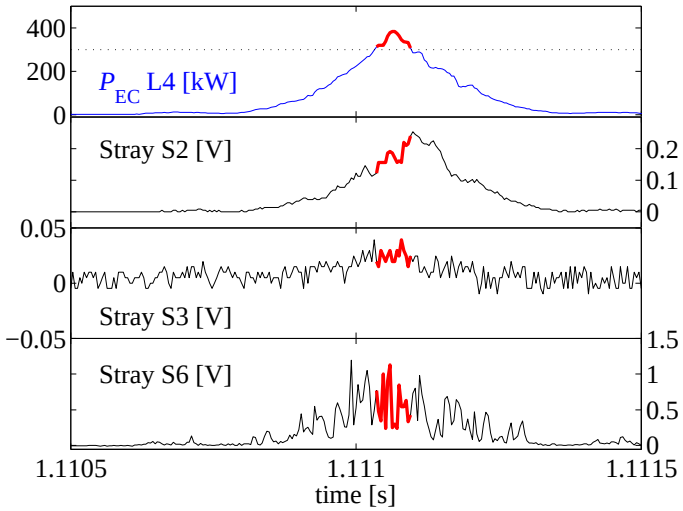

(b) Detailed view of one EBW power pulse.

Figure 4.7: O-X-B mode conversion experiment in TCV. (a). From top to bottom: modulated O2 power, stray EC power measured by diode S2, S3 and S6 (whose positions are given in figure 4.4(a)), central electron density (Thomson scattering) and D-α recombination light. The latter signal indicated that the H-mode has alternating ELM-free/ELMy phases. The evaluation of the stray EC power level is performed during the ELM-free phase with the highest density (indicated by the vertical red surface), i.e. when the best conditions for the O-X-B mode conversion are met. (b) The stray signal is taken into account for averaging only when the EC power is on ($P_{EC} \geq 300$ kW) during the short (< 1 ms) EBW power pulses. #29005.

In these initial EBW experiments in TCV, the O2 EC power was injected as short pulses ($\sim$ 1 ms) at a frequency $f_{\mathrm{mod}} = 143$ Hz (i.e. $< 10\%$ duty-cycle) to avoid the risk of any damage caused to diagnostics by high levels of stray power for non-absorbing angles. The quality of wave-plasma coupling is estimated using the signal of three stray power detectors, a decrease of the stray power level indicating an improvement of the mode conversion and wave absorption.

The stray power detectors were located at different toroidal locations around the vessel torus as follows: S2 detector in sector 14 (omnidirectional detector on the concrete pillar next to the DNBI); S3 detector in sector 2 (sniffer below TCV); S6 detector in sector 9 (at the vessel equator, beside the glow antenna). The equatorial launcher L4 is located in sector 6 (on a total of 16 TCV sectors) and the angle scans were performed for counter-clockwise injection (seen from the top).

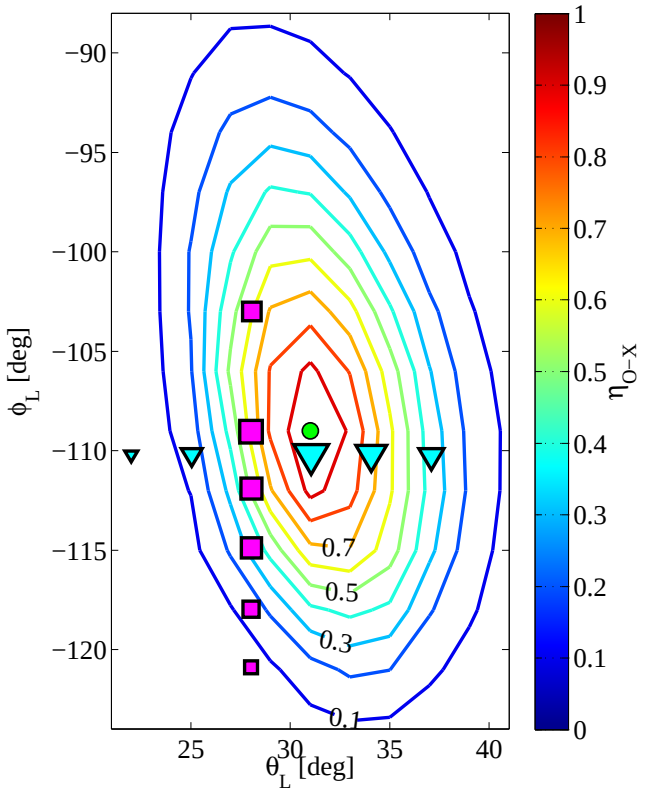

Figure 4.8: Experiment-simulation comparison of the O-X mode conversion efficiency. Experimental toroidal angle scan (magenta ■) and poloidal angle scan (cyan ▼) superimposed on the contour plot of the AMR O-X mode conversion efficiency $\eta_{\text{O-X}}$. The markers size is inversely proportional to the corresponding stray power level (S2 detector). The simulated optimum launcher angles $(\theta_{\mathrm{L,opt}}, \phi_{\mathrm{L,opt}}) = (31.0°, -109.0°)$ (green •) are in perfect agreement with the experimental optimum launcher angles from the toroidal and poloidal scans. TCV shot numbers: see caption of figures 4.5 and 4.9.

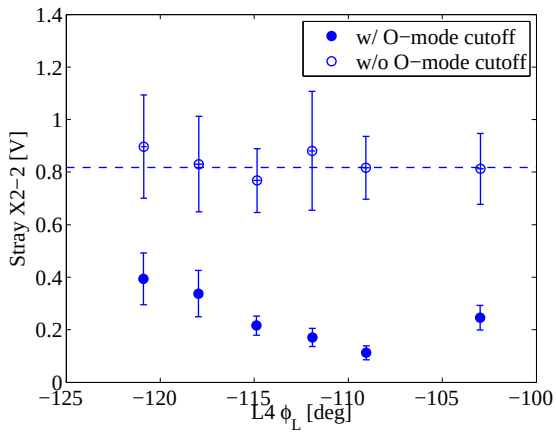

(a) Toroidal launcher angle scan, detector S2.

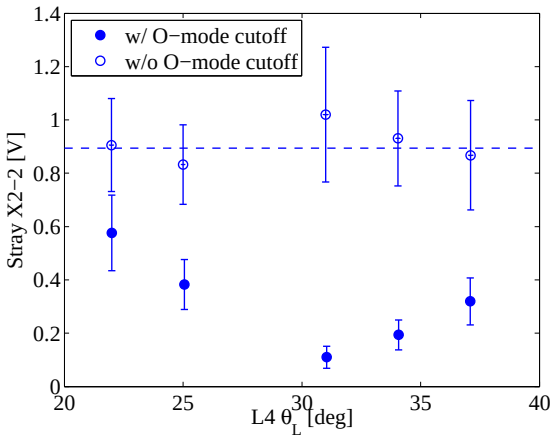

(b) Poloidal launcher angle scan, detector S2.

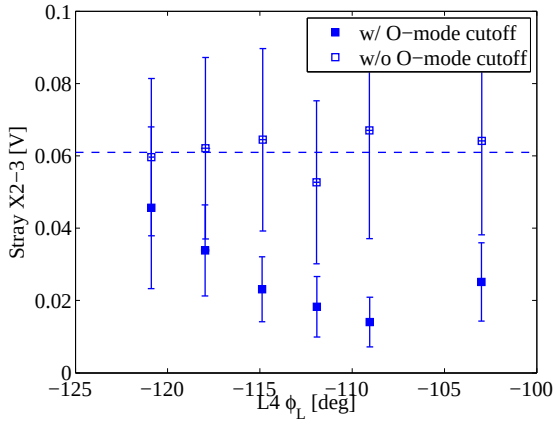

(c) Toroidal launcher angle scan, detector S3.

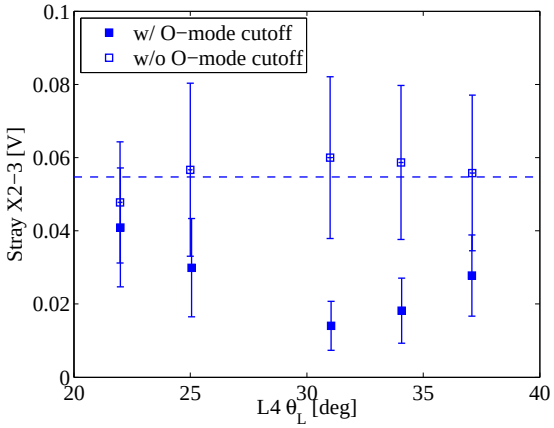

(d) Poloidal launcher angle scan, detector S3.

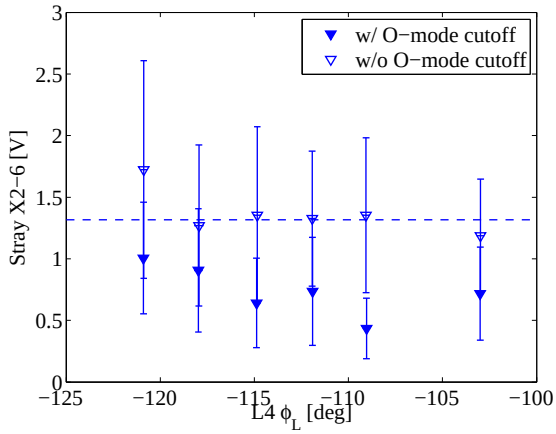

(e) Toroidal launcher angle scan, detector S6.

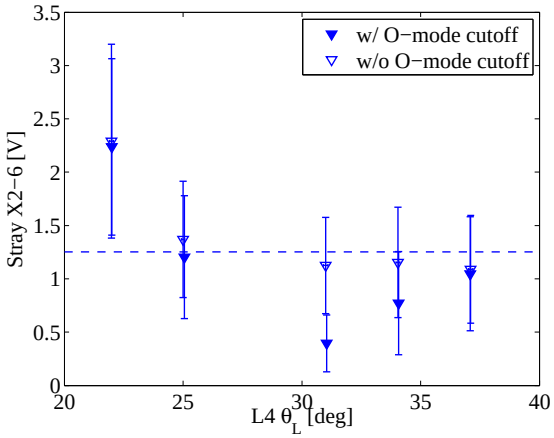

(f) Poloidal launcher angle scan, detector S6.

Figure 4.9: Experimental angle scan of the O2 power injection. Stray power level (full symbols) versus toroidal launcher angle ϕ_L with constant poloidal launcher angle $\theta_L = 28.0 \pm 0.0°$ (left column) and versus θ_L with constant $\phi_L = -110.2 \pm 0.1°$ (right column) for detectors (a)-(b) S2, (c)-(d) S3 and (e)-(f) S6. For each angle, the stray power level at non-optimal O-X mode conversion conditions is indicated (empty symbols) and averaged over the angle scans (dashed lines). TCV shots #29005-29009 and #29011 (ϕ_L-scan), #29012-29015 and #29020 (θ_L-scan).

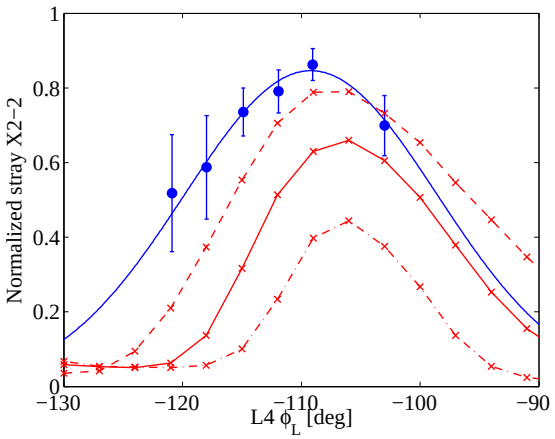

(a) Toroidal launcher scan, detector S2.

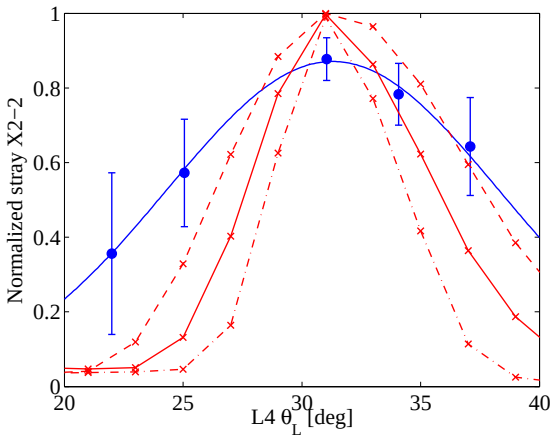

(b) Poloidal launcher scan, detector S2.

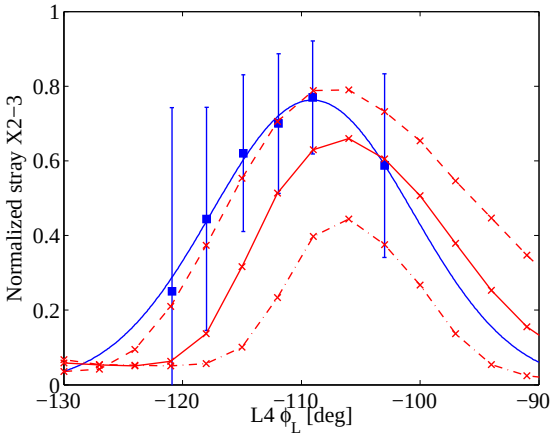

(c) Toroidal launcher scan, detector S3.

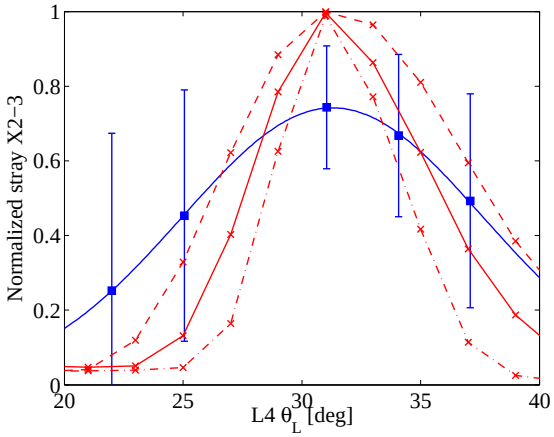

(d) Poloidal launcher scan, detector S3.

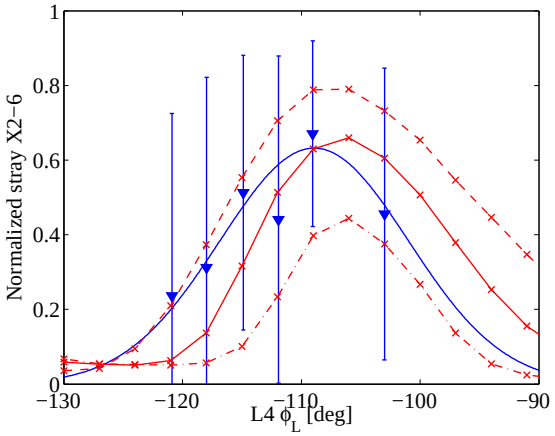

(e) Toroidal launcher scan, detector S6.

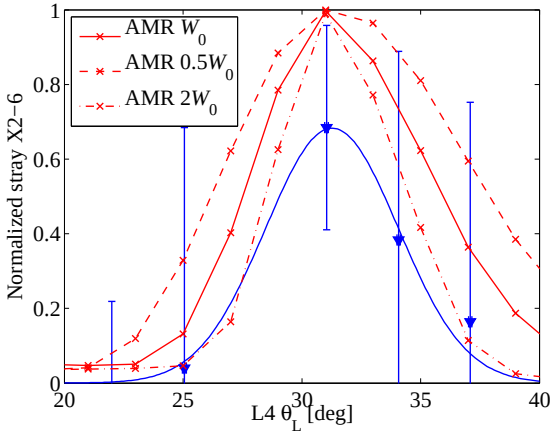

(f) Poloidal launcher scan, detector S6.

Figure 4.10: Experiment-simulation comparison of the angular window width. Normalized stray power level (full symbols) versus toroidal launcher angle ϕ_L with constant poloidal launcher angle $\theta_L = 28.0 \pm 0.0°$ (left column) and versus θ_L with constant $\phi_L = -110.2 \pm 0.1°$ (right column) for detectors (a)-(b) S2, (c)-(d) S3 and (e)-(f) S6. The experimental results are compared to AMR simulations for the original (solid line), half (dashed line) and double (dash-dotted line) density pedestal widths. TCV shot numbers: as in caption of figures 4.5 and 4.9.

The time windows for the stray power level averaging are selected such that similar conditions are met for all shots : typically 100-millisecond-long ELM-free H-mode phase (i.e. typically a dozen of EC power pulses) with mean plasma vertical position and volume-averaged electron density (FIR measurements) $Z_{\text{axis}} = 12.7 \pm 0.0$ cm and $n_e = (13.5 \pm 0.2) \cdot 10^{19}$ m^{-3}, respectively. The stray signal is taken into account for averaging only when the EC power is on ($P_{\text{EC}} \geq 300$ kW) during the short power pulses.

Full symbols in figure 4.9 show the averaged stray power level for both angle scans and the three detectors. Detectors S3 and detector S6 provide low amplitude and noisy signals, respectively, yielding large errorbars. Nevertheless, all stray power detectors exhibit a clear variation of the average stray power level with the injection angles. The minimum stray power is reached at $\phi_{\text{L}} = -109.0 \pm 0.2°$ and at $\theta_{\text{L}} = 31.0 \pm 0.1°$ for all detectors independently from their toroidal position around the tokamak. The optimum angles determined experimentally are thus in perfect agreement with the optimum angles obtained from the post-shot AMR numerical simulations for the original vertical position of the plasma magnetic axis $Z_{\text{axis}} = 12.0$ cm and the original density pedestal width $W_{n,0} = 1.44$ cm, as shown in figure 4.8. This is a remarkable result given the sensitivity of the optimum angles on the plasma vertical position as shown in figure 4.6.

For the sake of comparison with the width of the simulated angular window, the experimental measurements need to be normalized between their minimum and maximum values. Of course, a zero stray signal would indicate a 100% mode conversion and power absorption. Conversely, one can evaluate the zero level of mode-conversion by measuring the stray power level when the O-X mode-conversion conditions are not met. This is done for each shot in the angle scan (empty symbols in figure 4.9) and an average maximum stray level is calculated (dashed lines in figure 4.9). One can then normalize the raw stray signal between these maximum and minimum values, fit the data with a Gaussian function and compare with AMR mode conversion efficiencies calculated along the experimental angles for the various pedestal profiles, see figure 4.10.

In contrast to the optimum angles, the width of the experimental angular window seems to depend on the detector. Nevertheless, the experimental angular windows are in reasonable agreement with the simulated window, though slightly wider. This discrepancy can come from a density gradient at the mode-conversion layer actually steeper than the measured profile. Indeed, the AMR simulations for a half density pedestal width has a better match with the experimental measurements. The com-

bined effects of the finite EC power beam width and its k-spectrum can also yield a broader angular window with reduced mode conversion efficiency. This is consistent with the finite minimum stray power level observed experimentally. The effect of the beam divergence and size has been tested in AMR simulations with the injection of 13-ray bundles. The resulting angular windows are however very similar to the single-ray calculations, with central mode conversion efficiency reduced by only less than 1%.

4.4 Discussion and conclusions

The O-X-B mode conversion experiments presented here were previously analyzed and published in [22–24]. In these references, the experimental optimum angles are in good agreement (within 3°) with the optimum angles of Mjølhus's analytical mode conversion window η_M of equation (3.4.22) calculated by the ART mode-conversion and ray-tracing code, as indicated in the figure 4.11 reprinted from [22].

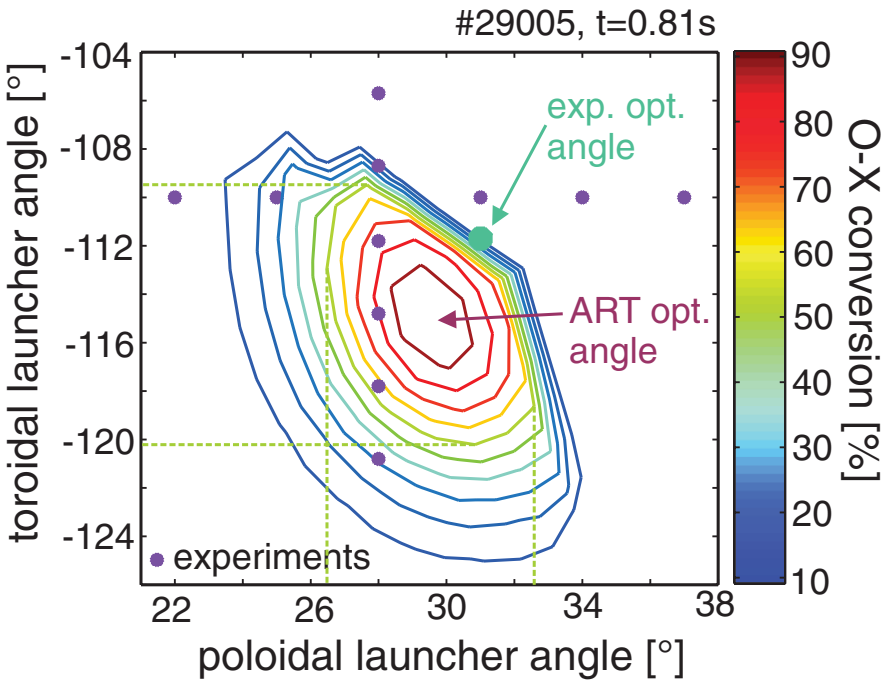

Figure 4.11: Mjølhus's analytical angular window. In this former analysis of the O-X-B mode conversion experiments, the experimental scan points (magenta •) are superimposed on the contour plot of Mjølhus's mode conversion window η_M of equation (3.4.22) calculated by the ART code. The simulated optimum angles $(\theta_L, \phi_L) = (29.0°, -115.0°)$ are in agreement within 3° with the experimental optimum angles $(\theta_L, \phi_L) = (31.0°, -112.0°)$. In the new analysis of the experimental data performed in this thesis work, the experimental optimum is corrected to $(\theta_{L,opt}, \phi_{L,opt}) = (31.0°, -109.0°)$. Reprinted from [22].

However, the analytical mode conversion window is strongly asymmetric and drops rapidly from 100% at its optimum $(\theta_L, \phi_L) = (29.0°, -115.0°)$ down to 10% at the experimental optimum $(\theta_L, \phi_L) = (31.0°, -112.0°)$. In this sense, the comparison of the simulation with the experiment was not fully satisfactory.
Moreover, at the time of this first analysis, the temperature and density pedestal profile fitting on the edge-Thomson-scattering data was not available. The profiles used then yielded an underestimated density gradient. This effect, combined to the asymmetric distortion of the analytical solution far from the optimum, can explain that the mode conversion window calculated by ART is narrower than the full-wave ARM result in figure 4.8. Indeed, the toroidal and poloidal widths at half maximum are $\Delta\theta_L \simeq 6.0°$ and $\Delta\phi_L \simeq 11.0°$ for ART and $\Delta\theta_L \simeq 9.0°$ and $\Delta\phi_L \simeq 18.5°$ for AMR.
Finally, the new analysis of the O-X-B experiments presented in this chapter brings a correction of $+3°$ on the position of the experimental optimum toroidal angle $\phi_{L,opt}$ with respect to the older analysis. Indeed, the stray power level at this angle point was erroneously evaluated in the older analysis. This correction increases the discrepancy between the experimental result and the analytical ART calculation. On the other hand, this correction yields excellent agreement with the full-wave AMR calculation, which is a successful benchmark of the implementation of TCV EC system geometry in the AMR code and of the full-wave mode conversion calculation.

Chapter 5

Detection of RF power deposition location

5.1 Introduction

The assessment of the RF power deposition profile from experimental data is of primary importance for the interpretation of plasma auxiliary heating results and for the comparison of the experiments with simulations. In particular, local temperature and current profile tailoring with electron cyclotron resonant heating (ECRH) and current drive (ECCD) allows the control of the sawtooth instability [4, 78] and the suppression of neo-classical tearing modes (NTMs) in tokamak plasmas [5, 79]. The understanding of the involved stabilization mechanism requires a precise knowledge of the power deposition location (either absolute or relative to the mode location). A widely spread method to retrieve the absorbed power profile is to analyze the plasma response to modulation of the injected power amplitude. Many analysis methods have lead to conclusive results in previous heating and transport studies in stationary conditions: Fourier analysis [22, 80] or harmonic response identification methods (HRIM) [81] of the plasma response (with or without suppression of the sawtooth perturbation using singular value decomposition and system identification, SI-SVD), as well as correlation of the plasma response with the modulation waveform [82]. In non-stationary conditions, a high time-resolution estimate of the EC beam(s) absorption location(s) is necessary, for example in cases where the microwave injection angles are controlled by a real-time feedback loop [83]. But Fourier and correlation methods need a finite number of power modulation cycles to yield a significant result. Conversely, the break-in-slope (BIS) method is based on the estimation of the instantaneous change in the time derivative of the plasma

kinetic energy at the power switch-on/off times [84], thus providing an estimated power deposition profile for each power step in the modulation, that is, with high temporal resolution.

Moreover, natural plasma oscillations like the sawtooth activity can heavily hamper the use of Fourier analysis methods, especially when frequency locking occurs between the power modulation and the sawtooth. In such cases, the BIS method allows to select and analyze individual power modulations avoiding the time of the sawtooth crash and the related heat pulse propagation.

In this chapter, the experimental RF power deposition location of X2 modulated ECH (MECH) and O2 modulated EBH (MEBH) is retrieved using the BIS method applied to the soft X-ray profiles from a fast and high radial resolution wire-chamber camera (DMPX). The deposition location is defined as the location of the maximum in the power deposition profile. Since soft X-ray signals are used (no electron temperature diagnostics with comparable temporal and spatial resolutions is available at TCV), the actual full power deposition profile information is not retrieved here and the question of the total absorbed power is treated in chapter 6 using the diamagnetic loop diagnostic. The BIS method results are compared to the results of the HRIM analysis and of numerical simulations.

The chapter is structured as follows. Section 5.2 introduces the two plasma response analysis methods used in this chapter. Subsection 5.2.1 presents the HRIM method which is also intensively used to analyze the diamagnetic loop diagnostic (DML) response to modulated ECH and EBH in chapter 6. In subsection 5.2.2, it is shown under which conditions the simplest form of the BIS analysis can be applied. In section 5.3, the BIS method is applied to the case of X2 MECH in stationary conditions as a validation step. Section 5.4 then focuses on the unique ability of the BIS method to retrieve the location of the maximum power deposition at each power step, that is, with high time resolution. Off-line BIS analysis is used to monitor the power deposition locations of one or two simultaneous EC power beams injected in plasmas programmed to sweep vertically down in front of the launching antennas. In section 5.5, EBH via O-X-B mode-conversion in TCV is demonstrated by retrieving the power deposition location inside the O2 cutoff, that is in an overdense H-mode plasma. Conclusions and outlooks are given in section 5.6.

5.2 Plasma response analysis methods

5.2.1 The harmonic response identification method (HRIM)

In modulated ECH experiments, the injected RF power is composed of a sinusoidally modulated part $\tilde{P}_{\mathrm{RF}}(t)$ at the frequency $f_{\mathrm{mod}} = \omega/2\pi$, superimposed on a stationary part $\langle P_{\mathrm{RF}} \rangle_t$:

$$P_{\mathrm{RF}}(t) = \langle P_{\mathrm{RF}} \rangle_t + \tilde{P}_{\mathrm{RF}}(t) \qquad \text{with} \qquad \tilde{P}_{\mathrm{RF}}(t) = \hat{P}_{\mathrm{RF}} \mathrm{e}^{\mathrm{i}\omega t} \tag{5.2.1}$$

where $\hat{P}_{\mathrm{RF}}$ is a complex amplitude carrying both phase and amplitude informations:

$$\hat{P}_{\mathrm{RF}} = |\hat{P}_{\mathrm{RF}}| \mathrm{e}^{\mathrm{i}\phi_{\mathrm{RF}}}. \tag{5.2.2}$$

Of course, the RF power excitation is generally not a pure monochromatic sinusoid but rather a sum of N sinusoids at different frequencies

$$\tilde{P}_{\mathrm{RF}}(t) = \sum_{n=1}^{N} \hat{P}_n \mathrm{e}^{\mathrm{i}\omega_n t} \tag{5.2.3}$$

where $\hat{P}_n$ is the complex amplitude at the angular frequency ω_n. For example, in most of the MECH experiments presented in this work, the EC power is modulated with a square waveform with fundamental angular frequency ω and a 50% duty-cycle. In this case, mainly the odd harmonic numbers $\omega_n = n\omega$ with $n = 1, 3, 5, \ldots$ are excited.

The modulated ECH induces oscillations of the electron temperature at the same angular frequency ω than the excitation (and possibly at other frequencies if the system is non-linear) such that the electron temperature evolution also splits into stationary and modulated parts:

$$T_{\mathrm{e}}(t) = \langle T_{\mathrm{e}} \rangle_t + \tilde{T}_{\mathrm{e}}(t) \qquad \text{with} \qquad \tilde{T}_{\mathrm{e}}(t) = \hat{T}_{\mathrm{e}} \mathrm{e}^{\mathrm{i}\omega t}. \tag{5.2.4}$$

The complex amplitude $\hat{S}(\omega)$ of any experimental signal $S(t)$ can be estimated by the standard Fourier transform:

$$\hat{S}(\omega) = \int_{-\infty}^{+\infty} S(t) \mathrm{e}^{\mathrm{i}\omega t} \mathrm{d}t. \tag{5.2.5}$$

But in practical MECH experiments, the number of modulation cycles available for the oscillation analysis is finite and not necessarily integer, which will cause truncation problems in a standard Fourier analysis. Moreover, the fast modulation of the plasma response induced by the EC power modulation is often superimposed

on a slow drift of the signal, which will strongly bias the Fourier components of the signal, in particular if the number of modulation cycles is small. A harmonic response identification method (HRIM) accounting for these effects is presented in appendix A.1 of reference [81] and in appendix 3 of reference [85]. It consists in expressing the signal $S(t)$ in the form

$$S'(t') = \mathcal{R}\left[\left\langle \hat{S} \right\rangle_t\right] \cos(\omega t') - \mathcal{I}\left[\left\langle \hat{S} \right\rangle_t\right] \sin(\omega t') + \langle S \rangle_t + \left\langle \frac{\mathrm{d}S}{\mathrm{d}t} \right\rangle_t (t - t') \tag{5.2.6}$$

for a time interval $t' = \left[t \pm \frac{\Delta T}{2}\right]$ around the time t, where the real and imaginary parts $\mathcal{R}\left[\left\langle \hat{S} \right\rangle_t\right]$ and $\mathcal{I}\left[\left\langle \hat{S} \right\rangle_t\right]$ of the time average complex amplitude $\hat{S}(\omega)$, as well as the time averages $\langle S \rangle_t$ and $\left\langle \frac{\mathrm{d}S}{\mathrm{d}t} \right\rangle_t$ of the signal $S(t)$ and of its time derivative are assumed to remain constant in the time interval considered. The parameters $\mathcal{R}\left[\left\langle \hat{S} \right\rangle_t\right]$, $\mathcal{I}\left[\left\langle \hat{S} \right\rangle_t\right]$, $\langle S \rangle_t$ and $\left\langle \frac{\mathrm{d}S}{\mathrm{d}t} \right\rangle_t$ are adjusted by minimizing the cost function

$$\frac{1}{\Delta T} \int_{1-\frac{\Delta T}{2}}^{1+\frac{\Delta T}{2}} \left(S(t') - S'(t')\right)^2 \mathrm{d}t'. \tag{5.2.7}$$

After time discretization, the minimization procedure is expressed in matrix form and yields an estimate of the signal complex amplitude at the angular frequency ω without truncation and drift errors. For an infinite time interval (i.e. $\Delta T \to \infty$), the solution tends to the Fourier coefficients. If the experimental conditions are not stationary and the parameters in equation (5.2.6) are expected to vary, the total time interval during which MECH is applied can be divided into M time intervals $t' = \left[t_m \pm \frac{\Delta T}{2}\right]$ centered on t_m with $m = 1, \ldots, M$ and the complex amplitude $\hat{S}(\omega)$ is evaluated for each t_m. The time interval division can be performed with or without overlapping, i.e. for $\Delta T > t_m - t_{m+1}$ or for $\Delta T \leq t_m - t_{m+1}$, respectively.
Finally, if the RF power modulation waveform is a combination of several harmonics of the fundamental excitation frequency (e.g. a square modulation), the HRIM analysis (5.2.6) can be performed for each harmonic frequency independently, or for all harmonics at once (both methods yielding essentially the same result):

$$S'(t') = \sum_{n=1}^{N} \mathcal{R}\left[\left\langle \hat{S}_n \right\rangle_t\right] \cos(n\omega t') - \mathcal{I}\left[\left\langle \hat{S}_n \right\rangle_t\right] \sin(n\omega t') + \langle S \rangle_t + \left\langle \frac{\mathrm{d}S}{\mathrm{d}t} \right\rangle_t (t - t'). \tag{5.2.8}$$

5.2.2 The break-in-slope (BIS) analysis method

The BIS model to determine the auxiliary power absorbed by a given species α is based on the energy density conservation equation for that particular species:

$$\frac{\partial \varepsilon_\alpha}{\partial t} + \nabla \cdot (\varepsilon_\alpha \mathbf{u}_\alpha) = Q_\alpha - \mathbb{P}_\alpha : \nabla \mathbf{u}_\alpha - \nabla \cdot \mathbf{q}_\alpha \tag{5.2.9}$$

with

$$\varepsilon_\alpha(\rho,t) \equiv \frac{3}{2} n_\alpha(\rho,t) T_\alpha(\rho,t) \tag{5.2.10}$$

the local kinetic energy density, $\mathbf{u}_\alpha$ the fluid velocity, Q_α the power density term accounting for the particles energy equipartition as well as for the power sources (like the external heating $P_{\text{ext}} = P_{\text{aux}} + P_{\text{OH}} + \cdots$) and sinks (like the radiation losses P_{rad}), $\mathbb{P}_\alpha$ the pressure tensor, $\mathbf{q}_\alpha$ the heat flux density and $\nabla \equiv \partial/\partial\mathbf{x}$ the spatial partial derivative operator. All quantities in equation (5.2.9) are functions of the radial coordinate ρ (i.e. $P_{\text{aux}}(\rho,t)$, etc...) Assuming that the convective, diffusive and viscous terms as well as the equipartition power, the losses and the Ohmic source all have a typical evolution time longer than one period of the auxiliary power modulation, the energy density conservation equation (5.2.9) can be simplified to [86]

$$\frac{\partial \varepsilon_\alpha}{\partial t} \simeq P_{\text{aux}}. \tag{5.2.11}$$

If in addition the density profile remains mainly constant around the power step happening at time t_0 (except for longer time scales due to the electron density pump-out by the ECRH), i.e. $n_\alpha(\rho,t) = n_\alpha(\rho,t_0) \equiv n_{\alpha 0}(\rho)$, equation (5.2.11) can be further simplified to

$$\frac{3}{2} n_{\alpha 0} \frac{\partial T_\alpha}{\partial t} \simeq P_{\text{aux}} \tag{5.2.12}$$

yielding a linear time evolution for $T_\alpha(\rho,t)$. In other words, the simplest form of the BIS analysis assumes that, if the heating power modulation is fast enough, the plasma temperature profile has a prompt linear response to the breaks in the auxiliary heating power amplitude. Linear fits can then be performed on the $T_\alpha(\rho,t)$ time traces before and after the power step $\Delta P_{\text{aux}}(\rho)$ at time t_0:

$$\begin{cases} T_{\alpha,1} = a_1(t-t_0) + b_1 & \text{for} \quad t < t_0, P_{\text{aux},1} \\ T_{\alpha,2} = a_2(t-t_0) + b_2 & \text{for} \quad t > t_0, P_{\text{aux},2} = P_{\text{aux},1} + \Delta P_{\text{aux}} \end{cases} \tag{5.2.13}$$

where $a_{1,2}$ and $b_{1,2}$ are functions of ρ. According to (5.2.12), the variation $\Delta P_{\text{aux}}(\rho)$ in the locally absorbed power is then proportional to the jump in the slope of the fits at time t_0:

$$\Delta P_{\text{aux}} \simeq \frac{3}{2} n_{\alpha 0} \Delta \left(\frac{\partial T_\alpha}{\partial t} \right) \Big|_{t_0} \simeq \frac{3}{2} n_{\alpha 0} \left(a_2 - a_1 \right). \tag{5.2.14}$$

Applied to the signals of a temperature diagnostic with multiple channels or lines-of-sight viewing at different flux surfaces, the BIS analysis thus provides an estimated heating profile for each power step i.e. at a frequency of the order of the power modulation frequency (typically a few 100 Hz), which is particularly well-suited

for fast time-varying scenarios. Since it assumes that the break in the slope of the plasma response is simultaneous with the power steps, the simple BIS method reveals the direct heating location of the species of interest (e.g. the electrons in the case of ECH). Any temperature response which is not in phase with the power modulation (e.g. indirect collisional heating) is averaged-out.
The BIS analysis can be improved to retrieve and take into account the delay of the breaks in the slope of the analyzed signal with respect to the times of power step (BIS* method) [87]. This BIS* profile then reveals both the direct heating and the indirect heating of the species of interest, similarly to a Fourier amplitude profile.
In case of a slow power modulation or a single power step, an effective loss term accounting for the various energy sources and losses (diffusion, radiation, equipartition) can be retained in equation (5.2.11) to account for the saturation in the plasma response. The simplified energy density conservation equation becomes

$$\frac{\partial \varepsilon_\alpha}{\partial t} = P_{\text{aux}} - \frac{\varepsilon_\alpha}{\tau_\alpha}. \tag{5.2.15}$$

Around the power step time t_0, the solution to this new equation is an exponential:

$$\varepsilon_\alpha(\rho, t) = \varepsilon_{\alpha 0} \exp\left(-\frac{t-t_0}{\tau_\alpha}\right) + P_{\text{aux}}\tau_\alpha \left[1 - \exp\left(-\frac{t-t_0}{\tau_\alpha}\right)\right] \tag{5.2.16}$$

where $\varepsilon_{\alpha 0}(\rho) = \varepsilon_\alpha(\rho, t_0)$ is the kinetic energy density profile at the time t_0 and $P_{\text{aux}}(\rho)$ and $\tau_\alpha(\rho)$ are the parameters to be determined from the exponential fits performed on the data before and after the auxiliary power jump at time t_0. The change in the absorbed auxiliary power is then estimated by the slope jump of the exponential fits at time t_0.

5.3 Detection of stationary X2 ECH location

Experimental setup

In this section, the BIS method to estimate the power deposition location is tested for the case of X2 MECH in stationary conditions. The experiment analyzed here aimed at studying the X2 and X3 ECH synergy by injecting one X2 power beam in a limited L-mode plasma with low toroidal magnetic field $B_\varphi(R_0) = 1.18$ T at the machine axis. Thanks to the reduced magnetic field, the X2 beam crosses the 3rd ECR harmonic ($\omega = 3\Omega_{\text{ce}}$) on the LFS and the 2nd ECR harmonic ($\omega = 2\Omega_{\text{ce}}$) on the HFS as indicated by the ray-tracing trajectories in figure 5.2. After a first plateau, the magnetic field is further lowered to 1.11 T in a 300-ms ramp-down, see figure 5.1.

As a consequence, the X2 and X3 EC resonances move outwards and inwards the plasma, respectively. At some time, the Doppler-shifted X2 and X3 absorptions take place on the same flux surface and a synergy is expected to enhance both absorption efficiencies, yielding the generation of fast electrons and the emission of hard X-ray. During the magnetic field ramp-down, the plasma current is also reduced from $I_\mathrm{p} \simeq 230$ kA to 217 kA in order to maintain the edge safety factor at a constant value $q_a \simeq 3.7$. Analyses of the X2/X3 synergy and of the observed hard X-ray emission can be found in reference [88]. We will now focus on the analysis of the power deposition location.

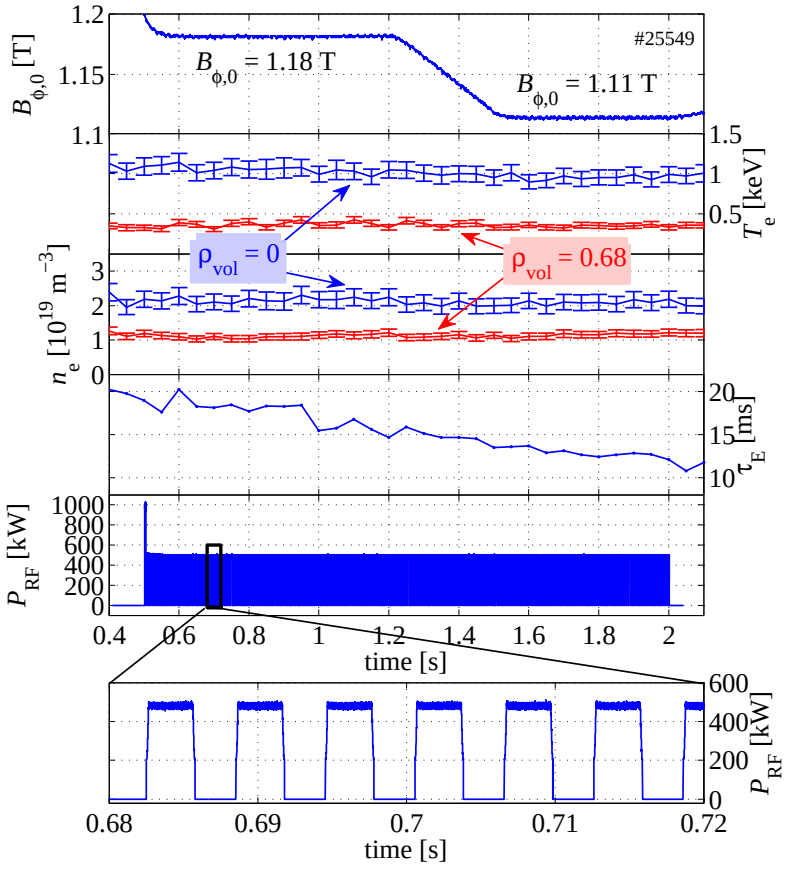

Figure 5.1: Typical X2/X3 synergy experiment used for the test of the BIS method. From top to bottom: time evolution of the toroidal magnetic field, the electron temperature and density at $\rho_\mathrm{vol} = 0$ and 0.68 (Thomson scattering, corrected by FIR), the electron energy confinement time and the injected X2 power modulated at $f_\mathrm{mod} = 166$ Hz with a duty cycle $d_\mathrm{c} = 50\%$. The black rectangle defines the zoom region on the square power modulation shown in the bottom subplot. The toroidal magnetic field is swept down from $B_{\varphi 0} = 1.18$ T to 1.11 T in the time interval $t = [1.2; 1.5]$ s. #25549.

The plasma is located at $R_\mathrm{axis} \simeq 0.90$ m and $Z_\mathrm{axis} \simeq 0.09$ m, i.e. close to the machine equator. The X2 power beam is injected from the equatorial launcher L1

with un upward poloidal angle $\theta_{\text{inj}} \simeq 5^\circ$ in the vertical plane of injection and a clockwise toroidal angle $\phi_{\text{inj}} \simeq -19^\circ$. The power amplitude is modulated between $P_{\text{RF}} = 0$ kW and ~ 500 kW with a 50% duty-cycle square waveform at a frequency $f_{\text{mod}} \simeq 166$ Hz. The power amplitude was programmed to be doubled with a second X2 beam injected from launcher L4, but the gyrotron stopped after the first pulse, as can be seen on the RF power trace in figure 5.1.

Ray-tracing and Fokker-Planck simulations

For both magnetic field values achieved in the experiment, the beam propagation and linear absorption are calculated for a 12-ray bundle with the C3PO ray-tracing code for the EC waves using the experimental equilibrium and profiles data. The resulting trajectories are shown in figures 5.2(a)-(c). The power absorption and the current generation are calculated by the quasi-linear Fokker-Planck code LUKE. The power absorption profiles are shown in figures 5.2(d)-(e). Due to the low electron temperature at the plasma edge ($T_{\text{e}} \simeq 400$ eV, as indicated in figure 5.1), the X2 power is not fully absorbed and the driven current is very small. The magnetic field ramp-down yields a radial shift of the power deposition peak from $\rho_{\text{vol}} \simeq 0.68$ to $\rho_{\text{vol}} \simeq 0.84$ and a decrease of the total power absorption from $\eta \simeq 21\%$ to 21%, with 1% of absorbed power at the 3rd EC resonance. In the meanwhile the driven current drops from $I_{\text{CD}} \simeq 1$ kA to 0 kA.

BIS analysis of the line-integrated soft X-ray profiles

The BIS analysis is applied to the line-integrated signal coming from the multi-wire proportional soft X-ray detector (DMPX) located under TCV vacuum vessel as described in section 2.3.1 and indicated in figure 5.3(a). This soft X-ray camera has both high time and radial resolutions (200 kHz acquisition frequency, 64 lines-of-sight with 7.9 mm average spacing at TCV midplane). As previously discussed in chapter 2, the DMPX detector is mainly sensitive to soft X-rays from Bremsstrahlung emission whose power density per unit solid angle is

$$P_{\text{B}} \propto n_{\text{e}}^2 Z_{\text{eff}} \sqrt{T_{\text{e}}} \quad [\text{W sr}^{-1} \text{ m}^{-3}]. \tag{5.3.1}$$

If both the electron density and the plasma effective charge vary on a slower time scale than the heating modulation, as it is the case in this experiment, an estimate of the power deposition location can be inferred by applying the BIS method on the soft-X flux profiles at each power step.

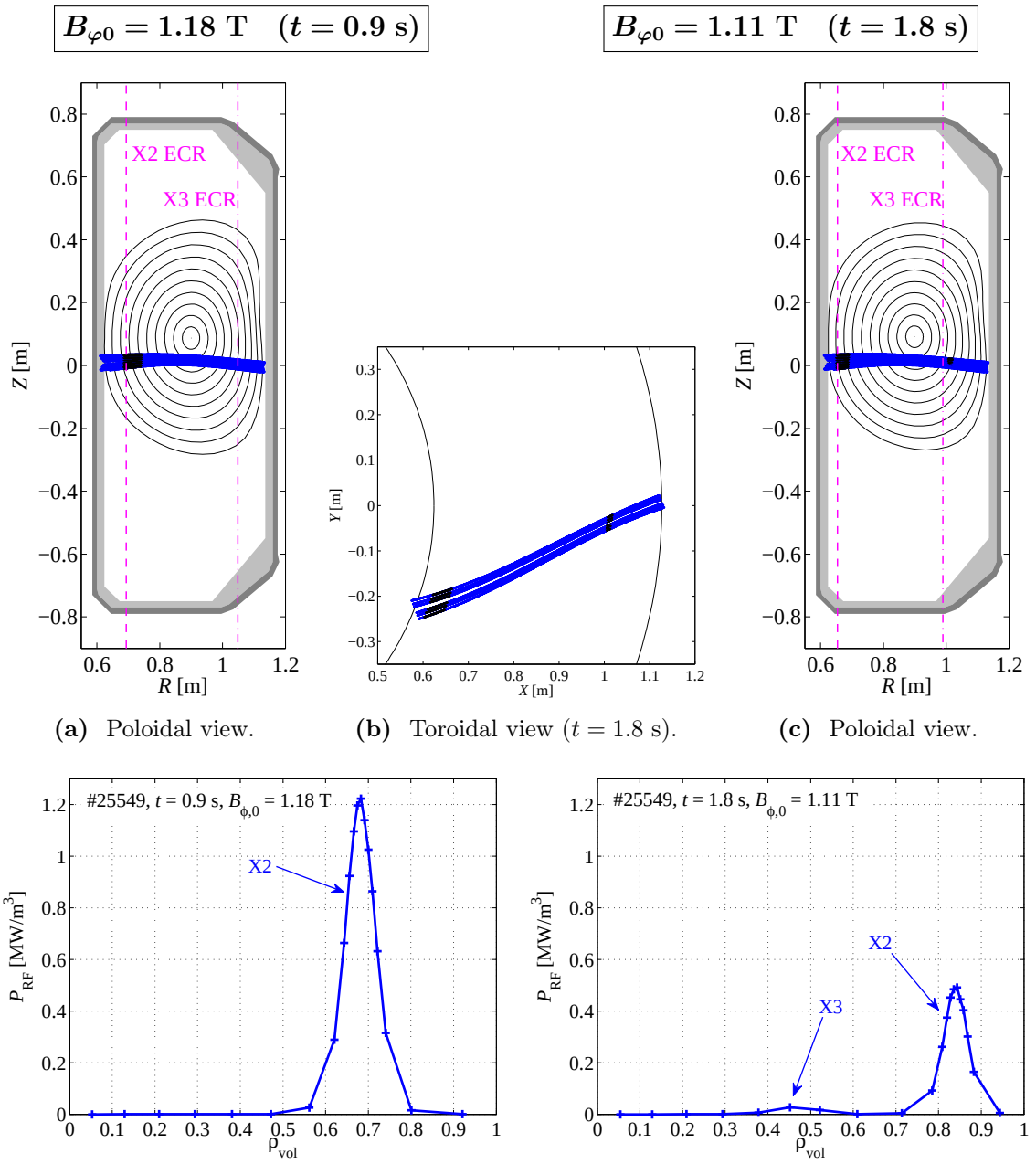

(a) Poloidal view. **(b)** Toroidal view ($t = 1.8$ s). **(c)** Poloidal view.

(d) Power deposition profile for $B_{\varphi 0} = 1.18$ T. **(e)** Power deposition profile for $B_{\varphi 0} = 1.11$ T.

Figure 5.2: Beam trajectory and absorption profile simulation for both magnetic field values. Left figures: $B_{\varphi 0} = 1.18$ T at $t = 0.9$ s. Right figures: $B_{\varphi 0} = 1.11$ T at $t = 1.8$ s. (a)-(c): C3PO ray-tracing trajectories of a 12-ray bundle injected from launcher L1, superimposed on contour plots of constant ρ_{vol}. The vertical lines indicate the X2 and X3 cold EC resonances. The resonances move from $R_{\mathrm{X2}} \simeq 0.69$ m and $R_{\mathrm{X3}} \simeq 1.05$m to $R_{\mathrm{X2}} \simeq 0.65$ m and $R_{\mathrm{X3}} \simeq 0.99$ m when the magnetic field is reduced. (d) and (e): corresponding profiles of absorbed power density (quasi-linear LUKE calculation). As a consequence of the magnetic field ramp-down, the power deposition moves from $\rho_{\mathrm{vol}} \simeq 0.68$ to $\rho_{\mathrm{vol}} \simeq 0.84$ and the total (X2 + X3) power absorption drops from $\eta \simeq 51\%$ to 21% (with 1% of the power absorbed at the 3rd harmonic at $\rho_{\mathrm{vol}} \simeq 0.45$). Calculated using the equilibrium and profiles data from #25549.

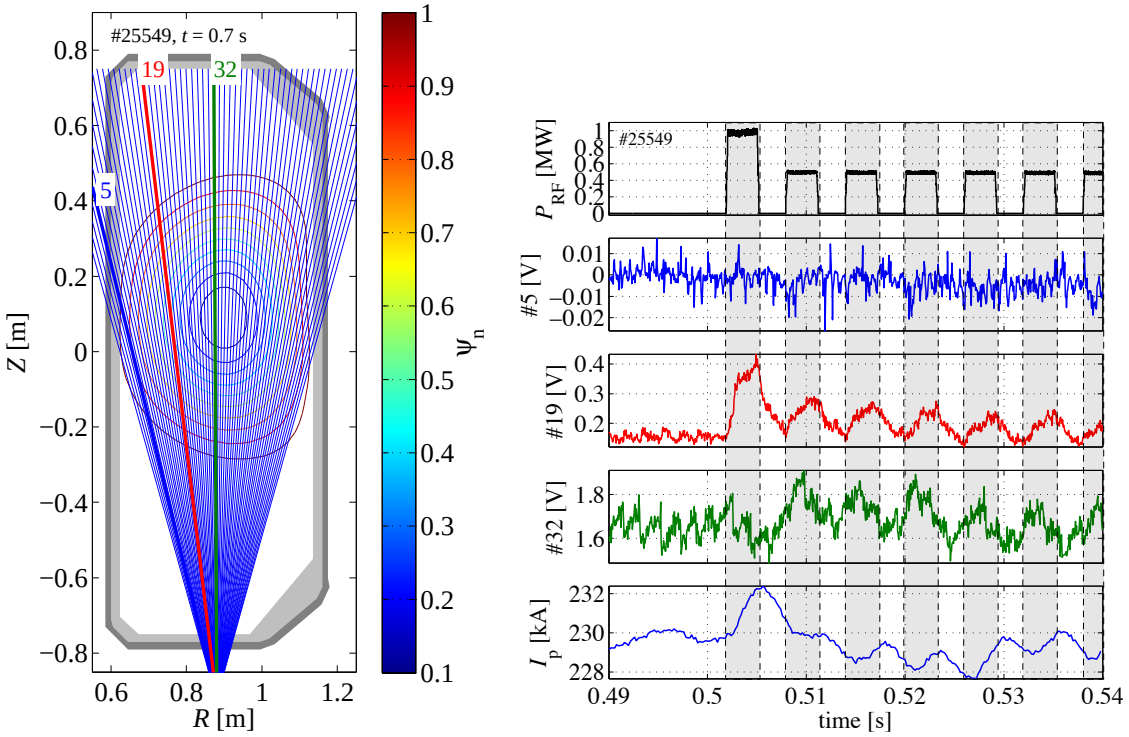

(a) DMPX lines-of-sight. **(b)** Modulation of soft X-ray traces.

Figure 5.3: Soft X-ray profile response to the X2 MECH. (a) Lines-of-sight of the multi-wire proportional soft-X ray detector (DMPX) superimposed on normalized poloidal flux contours. Lines-of-sight #5, 19 and 32 are highlighted in blue, red and green, respectively. (b). Corresponding raw soft X-ray traces, along with the modulated ECH traces and the plasma current. Grey surfaces indicate the times when the ECH power is on. The mid-radius soft X-ray signal is modulated in phase with the ECH perturbation. #25549.

Indeed, when the X2 MECH starts, an oscillation in phase with the ECH modulation is observed on the raw soft X-ray signal coming from the plasma mid-radius where the X2 power absorption is taking place, as indicated in figure 5.3(b). Unexpectedly, a modulation is also observed on the soft X-ray signal coming from the plasma center. This oscillation is not in phase with the MECH perturbation, which indicates it is an indirect consequence of the off-axis X2 MECH. It is believed to be caused by the TCV feedback control system in reaction to the modulated ECH and ECCD. The detailed analysis of this mechanism is not the scope of this work. More importantly, we will see that the BIS analysis reveals only the direct off-axis X2 heating and not the indirect central modulation.

The plasma center is also perturbed by a sawtooth activity. The sawtooth frequency and inversion radius are estimated by analyzing the soft X-ray profiles from the DMPX camera during the Ohmic and ECH phases, yielding $f_{\mathrm{st}} \simeq 584 \pm 77$ Hz and

$\rho_{\mathrm{vol,inv}} \simeq 0.25 \pm 0.02$. Both sawtooth frequency and inversion radius are not changed by the off-axis heating.

Before the BIS analysis is applied to the soft X-ray data, each of the 64 line-integrated DMPX signals is band-pass filtered to remove the fast MHD activity perturbations and the slow time-varying component of the signal by using a first-order zero-phase Butterworth filter with cutoff frequencies at $f_{\mathrm{mod}}/2 = 83$ Hz and $2f_{\mathrm{mod}} = 332$ Hz. The resulting signal is the modulated part of the soft X-ray traces: $\tilde{I}_{\mathrm{SX}}(t) = I_{\mathrm{SX}}(t) - \langle I_{\mathrm{sx}} \rangle_t$. Since we are here using soft X-ray signals instead of electron temperature signals, the density and effective charge profiles will distort the estimated power deposition profile. In order to alleviate this difficulty, the signal is normalized along the time dimension such that all 64 soft-X traces take values between 0 and 1.

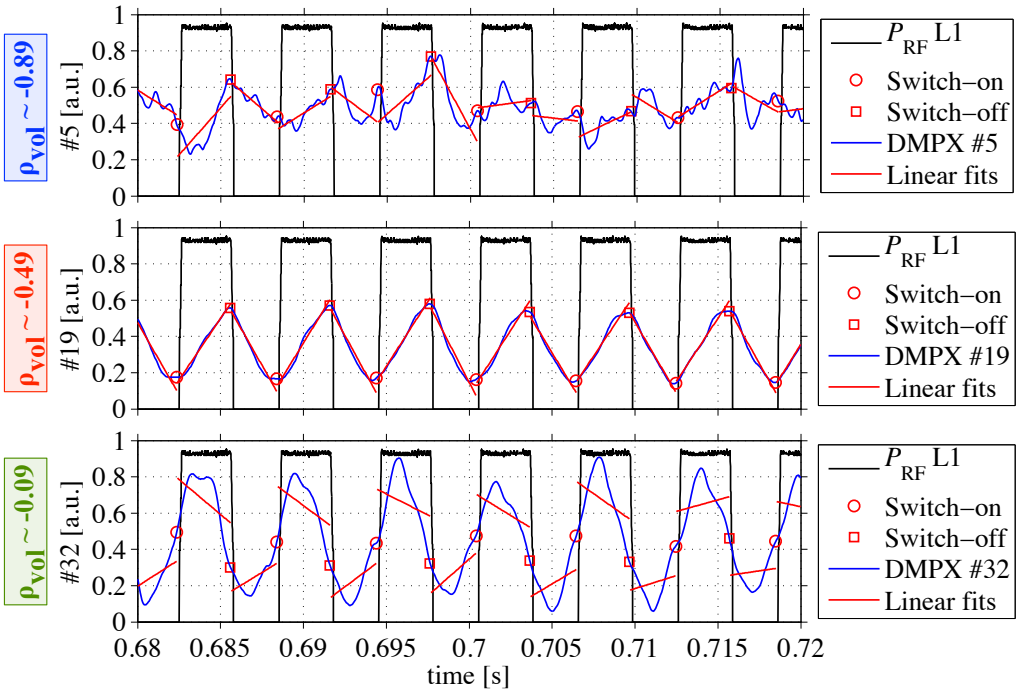

Figure 5.4: BIS analysis of the soft X-ray traces. Filtered and normalized soft X-ray signals (in blue) from DMPX lines-of-sight #5, 19 and 32, as indicated in figure 5.3(a), superimposed on the MECH trace (in black). The soft X-ray traces are labeled with the ρ_{vol} coordinate of the flux surface to which the DMPX lines-of-sight are tangential, negative values indicating HFS viewing lines-of-sight. The red ∘ and □ indicate the ECH switch-on and switch-off times, respectively. Linear fits of the soft X-ray data (in red) are performed between these times. The largest break-in-slope takes place at mid-radius where the modulation is in phase with the MECH perturbation. #25549.

In this modulated ECRH (MECH) experiments, the period of the power modulation is $\tau_{\mathrm{mod}} = 6$ ms, which is smaller than the typical energy confinement time $\tau_{\mathrm{E}} > 10$ ms

as indicated in figure 5.1. As a consequence, the plasma response is close to being linear and the simple BIS analysis based on linear fits can be used. Figure 5.4 shows the linear fits performed on the filtered and normalized soft X-ray traces between all EC power step-up and step-down times. The slope break in the linear fits is then calculated at each power step-up time for each soft X-ray trace, providing BIS amplitude profiles at a $f_{\mathrm{mod}} = 166$ Hz rate. In a similar way, the BIS information can be deduced at the power step-down times, thus doubling the information rate to $2f_{\mathrm{mod}} = 332$ Hz.

The largest slope jumps happen on the signal of the mid-radius-viewing chord #19 where the modulation is in phase with the MECH perturbation. At the edge (trace #5), the soft X-ray signal is dominated by random fluctuations and the break-in-slope at the power switch-on times is small. In the plasma center (trace #32), the modulation is dephased with respect to the MECH and the break-in-slope at the power switch-on times is negative.

Figure 5.5 presents the BIS amplitude profile averaged on the first magnetic field plateau $B_{\varphi 0} = 1.18$ T, along with the oscillation amplitude and phase retrieved by HRIM analysis of the same soft X-ray signals. Here and in figure 5.4, the soft X-ray traces are labeled with the ρ_{vol} coordinate of the flux surface to which the DMPX lines-of-sight are tangential, negative values indicating HFS viewing lines-of-sight. The average location of the maximum BIS amplitude is $\rho_{\mathrm{vol,dep}} \simeq 0.70 \pm 0.02$, which indicates the experimental location of direct ECH. It is in good agreement with the LUKE simulation within the experimental errrorbar. On the other hand, the width $\Delta\rho_{\mathrm{vol}} \simeq 0.4$ at half maximum of the BIS amplitude peak is much larger than the width $\Delta\rho_{\mathrm{vol}} \simeq 0.1$ of the power deposition peak calculated by LUKE. This is an effect of the line-integration of the soft X-ray signal, as will be seen from the analysis of the inverted data. Finally, the central off-phase modulation is quasi averaged out, as expected from figure 5.4.

The oscillation amplitude and phase from the HRIM analysis exhibit local maxima and minima, respectively, at the power deposition location, in agreement with the BIS analysis and the LUKE simulation. Conversely to the BIS analysis, the central modulation is revealed by the HRIM analysis (as it would be by any other Fourier-like analysis). The jump on the phase profile confirms that this central modulation is not due to the propagation of the heat pulse from the off-axis ECH to the plasma center. It is rather an indirect consequence of the modulated ECH. Note that only the BIS analysis yields an unambiguous estimate of the direct power deposition profile, excluding the indirect plasma response to the perturbation.

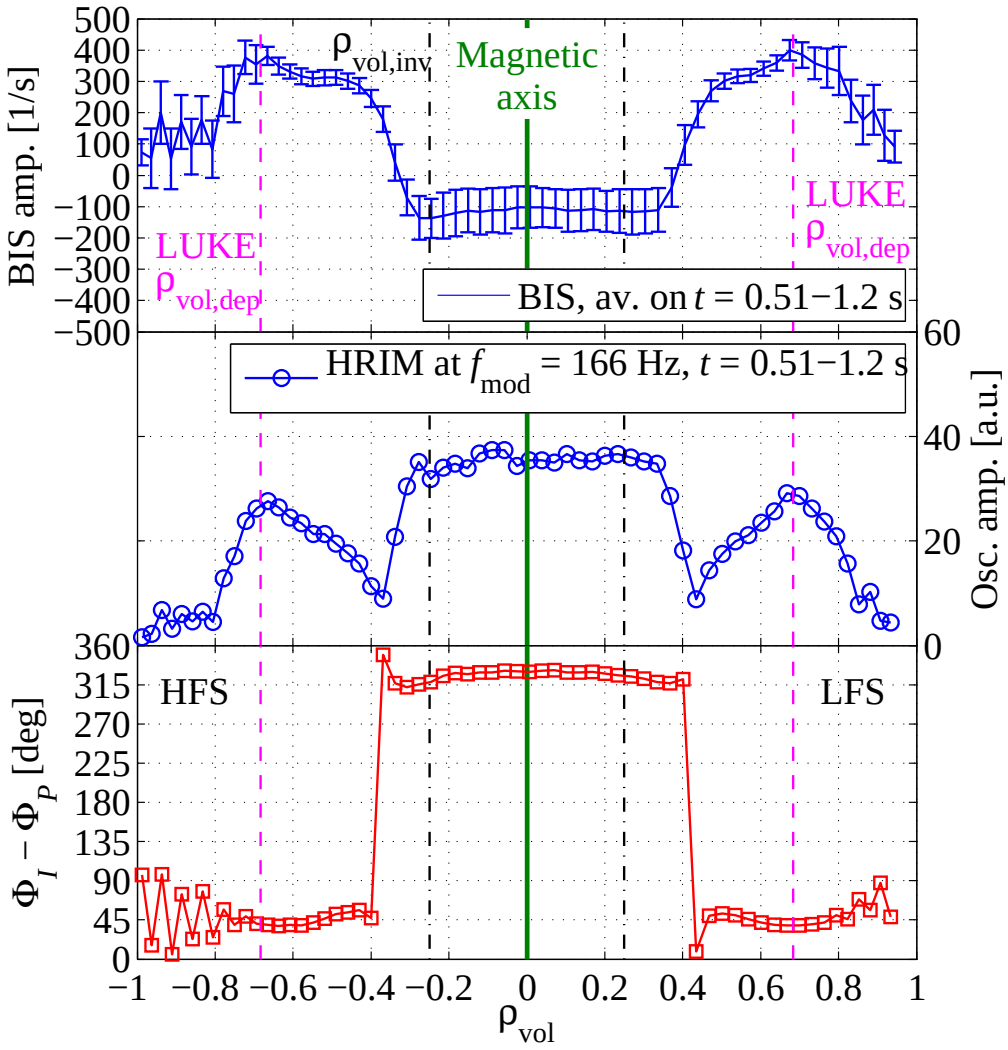

Figure 5.5: Power deposition location from BIS and HRIM analyses of the soft X-ray profiles. From top to bottom: Average BIS amplitude, oscillation amplitude and phase of the line-integrated soft X-ray profile during the first magnetic field plateau $B_{\varphi 0} = 1.18$ T. The maxima of BIS amplitude at $\rho_{\mathrm{vol,dep}} \simeq \pm 0.68$ on both HFS and LFS indicate the experimental location of direct EC heating, in perfect agreement with the LUKE simulation (vertical dashed lines). The indirect (off-phase) modulation at the plasma center is averaged out. The HRIM analysis also exhibits local amplitude maxima and phase minima at the power deposition location. #25549.

Another intrinsic advantage of the BIS analysis is that it provides an estimate of the power deposition location at the same rate than the ECH modulation, i.e. at $f_{\mathrm{mod}} = 166$ Hz in the present example, which can be doubled to $2f_{\mathrm{mod}} = 332$ Hz if the power switch-off times are also used in the analysis. Figure 5.6 shows the BIS amplitude profiles at the successive power switch-on times covering the two B-field plateaus. The maximum BIS amplitude shifts from $\rho_{\mathrm{vol,dep}} \simeq 0.70 \pm 0.02$ to $\rho_{\mathrm{vol,dep}} \simeq 0.82 \pm 0.02$ during the B-field ramp-down. Within the errorbars, the

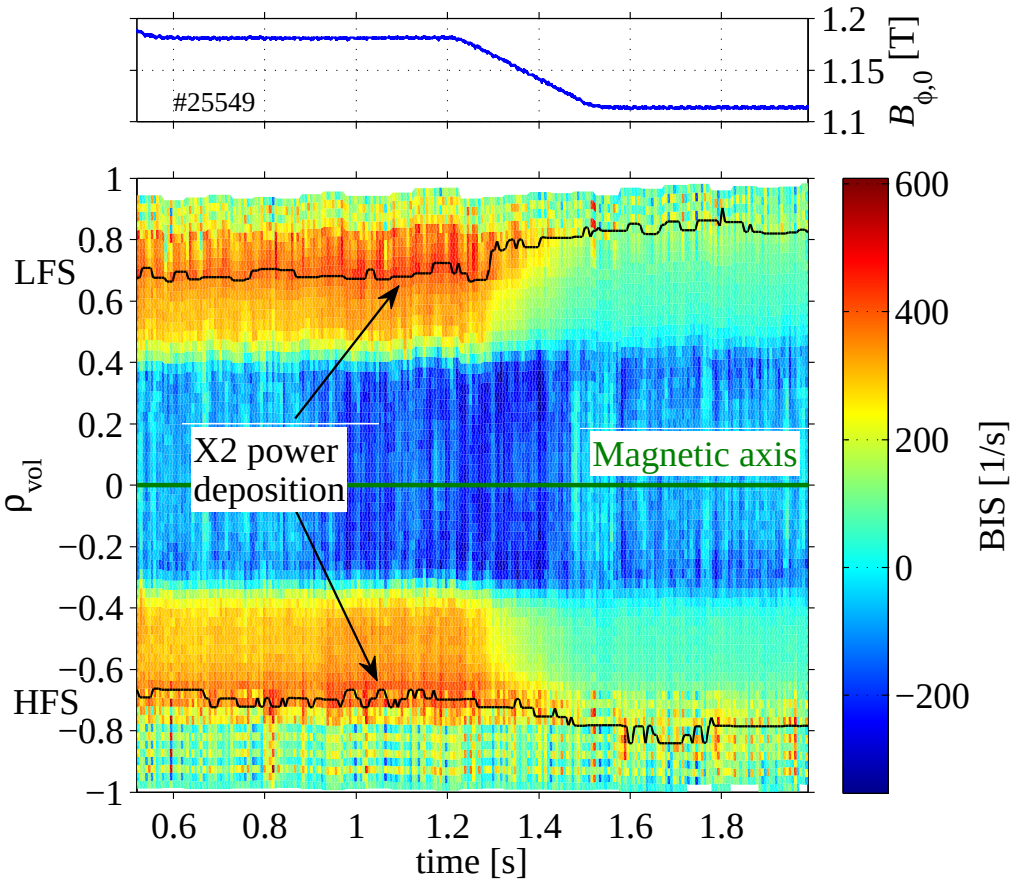

Figure 5.6: ECH tracking in *B*-field ramp-down with the BIS analysis. Top: magnetic field time trace. The field amplitude is decreased from $B_\varphi(R_0) = 1.18$ T to 1.11 T in $t = [1.3; 1.5]$ s. Bottom: Colormap of the soft X-ray BIS amplitude versus time and ρ_{vol}. The superimposed black traces indicate a 7-time-point median time-average of the maximum BIS amplitude location. The latter allow to track the ECH location which shifts from $\rho_{\text{vol,dep}} \simeq 0.70 \pm 0.02$ to $\simeq 0.82 \pm 0.02$ during the *B*-field ramp-down. #25549.

experimental results are in very good agreement with the LUKE predictions of figure 5.2. Another consequence of the *B*-field ramp-down is the dramatic BIS amplitude drop, as expected from the calculated absorption efficiency reduction.

BIS analysis of the local soft X-ray profiles

The local soft X-ray profiles are retrieved from line-integrated data using a tomographic-like inversion based on Fisher-information minimization. The BIS analysis is then performed on the inverted soft X-ray profiles. Despite the noisy inversion procedure, the resulting averaged local BIS profile compares well with the local power density profile from LUKE simulation in figure 5.7.

On the local profile, the BIS amplitude peak has a width $\Delta\rho_{\text{vol}} \simeq 0.2$ at half maxi-

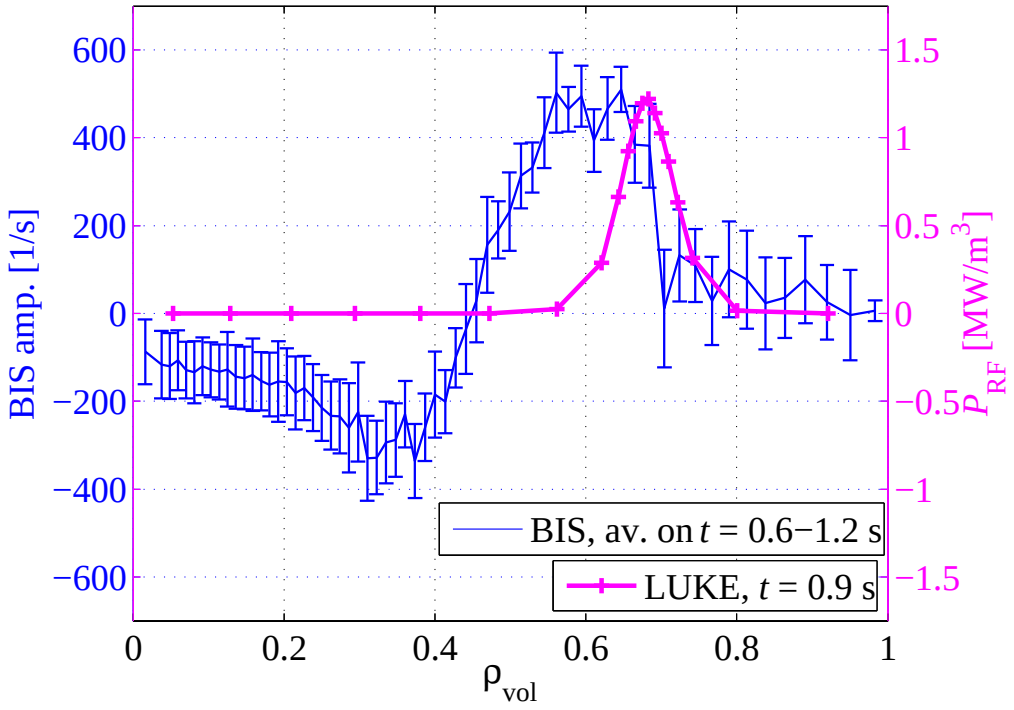

Figure 5.7: Average BIS amplitude of the local soft X-ray profiles after tomographic inversion. BIS amplitude profile of the local soft X-ray profiles averaged on the first B-field plateau (blue errorbars), compared to the absorbed RF power density calculated by LUKE (magenta). #25549.

mum, which is twice less wide than the BIS amplitude peak for the line-integrated signal as observed in figure 5.5. This confirms that line-integration of the soft X-ray signal along the DMPX camera chords may strongly deform the shape of power deposition profile. As another consequence of the signal tomographic inversion, the average location of the maximum BIS amplitude has moved toward the plasma center to $\rho_{\mathrm{vol,dep}} \simeq 0.61 \pm 0.04$, which is still in fair agreement with the LUKE numerical prediction at $\rho_{\mathrm{vol}} \simeq 0.68$.

Summary

The break-in-slope (BIS) method is a simple analysis of the plasma response to modulated ECH, aiming at determining the experimental power deposition profile. Applied to the signal of TCV high radial and time resolution soft X-ray camera, the BIS analysis is able to assess the power deposition location of X2 MECH partially absorbed at the very edge of a low magnetic field plasma, where the signal to noise ratio is low. The experimental results are in very good agreement with the numerical simulation. Moreover, only the direct heating location is revealed with the BIS

method, discarding indirect off-phase plasma responses to the MECH perturbation. Finally, since the BIS analysis provides an estimated power deposition profile at each power step time, the ECH location can be tracked along time. Dedicated experiments testing this particular advantage of the BIS analysis are presented in the next section.

5.4 Tracking of non-stationary X2 ECH location

The present section focuses on the ability of the BIS method to retrieve the location of the maximum power deposition at each power step and thus to track time-varying deposition locations. This is tested in subsections 5.4.1 and 5.4.2 where off-line BIS analysis is applied to the soft X-ray signals from the DMPX camera to track the power deposition locations of one and then two simultaneous X2 power beams injected in plasmas programmed to sweep vertically in front of the launching antennas. The experimental results are compared to ray-tracing and Fokker-Planck simulations. Conclusions are summarized in subsection 5.4.3.

5.4.1 Single X2 power deposition location

Experimental setup

As described in chapter 2, the toroidal magnetic field value, the position of the plasma column as well as the shape of its cross section can be programmed to change during a TCV plasma discharge. The flexibility of the plasma shaping is provided by 16 independent poloidal field coils [35]. TCV 2nd harmonic ECH system (at $f = 82.7$ GHz) is equipped with 2 clusters of 3 gyrotrons of 0.5 MW nominal power each [42]. The power amplitude of both clusters can be modulated independently. The power in ordinary (O) or extraordinary (X) mode polarization is then injected in the plasma via 6 steerable launchers having 2 angles of freedom, one of which can be varied during the plasma discharge. Launchers #2, 3, 5 and 6 are located at the upper lateral side of TCV vacuum vessel (with their longitudinal axis at $Z_{\text{launcher}} = 45.5$ cm). Launchers #1 and 4 are located at the equatorial side (with their longitudinal axis at $Z_{\text{launcher}} = 0.0$ cm), see figure 2.4. The flexibility of both TCV plasma magnetic configuration and ECH system allows the variation of the normalized minor radius at which the EC wave-particule resonance takes place.
In this experiment, the equilibrium is a limited plasma with medium shaping ($\kappa_a \simeq 1.55$, $\delta_a \simeq 0.45$) and low plasma current $I_p \simeq 135$ kA yielding a high edge safety

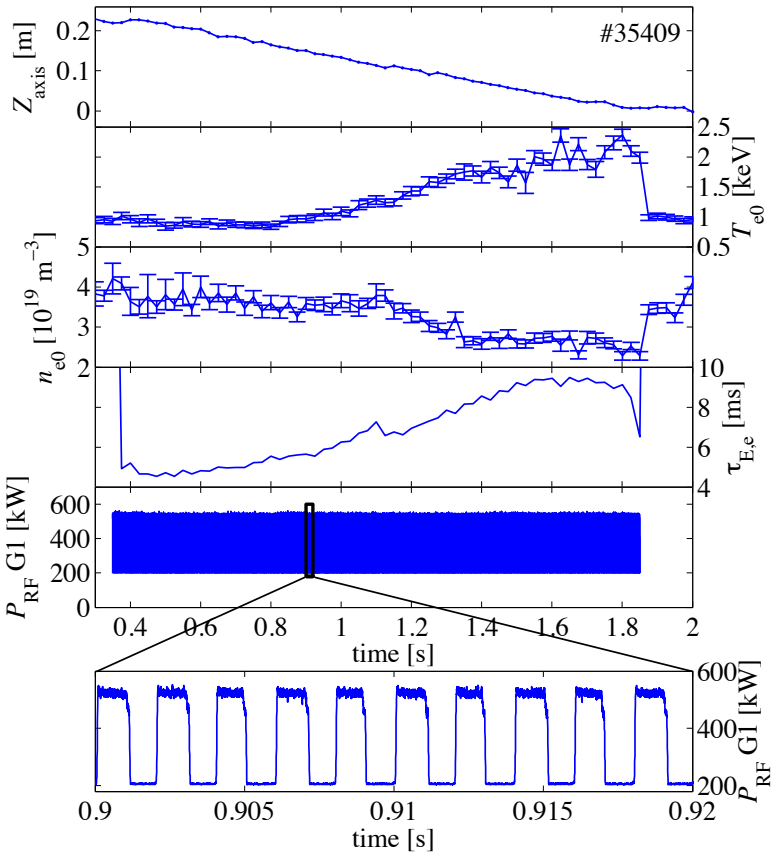

Figure 5.8: Plasma vertical position sweep. From top to bottom: time evolution of the magnetic axis vertical position (LIUQE reconstruction code), the central electron temperature and density (Thomson scattering, corrected by FIR), the electron energy confinement time and the EC power injected from launcher 1, modulated at $f_{\mathrm{mod}} = 500$ Hz with a duty cycle $d_{\mathrm{c}} = 50\%$. The black rectangle defines the zoom region on the square power modulation shown in the bottom subplot. The confinement time, increasing while the deposition is getting more central, is calculated for an average ECH power $\bar{P}_{\mathrm{EC}} = 365$ kW. The toroidal magnetic field and the plasma current are maintained constant at $B_\varphi = 1.45$ T and $I_{\mathrm{p}} \simeq 135$ kA respectively while the plasma vertical position is swept down from $Z_{\mathrm{axis}} = 24$ cm to 0 cm in the time interval $t = [0.2; 2.0]$ s. #35409.

factor value $q_a > 9$ and a central safety factor marginally above $q_0 = 1$. This results in a fast ($f_{\mathrm{st}} \simeq 470$ Hz) and small amplitude sawtooth activity. When the off-axis MECH starts at $t = 0.35$ s, the sawtooth activity becomes quasi indistinguishable on the soft X-ray traces. Hence, the sawtooth perturbation on the BIS estimate is negligible. As we will see later on, this assumption is true as long as the X2 power is not deposited in the plasma center. The nominal value of the magnetic field is $B_\varphi = 1.45$ T such that the second harmonic ECR is located close to the plasma axis at $R \simeq 0.85$ m as indicated on the poloidal views in figure 5.9.

All parameters of the magnetic equilibrium are kept constant, except for the magnetic axis vertical position, which is programmed to sweep down from $Z_{\mathrm{axis}} = 24$ cm

to $Z_{\text{axis}} = 0$ cm in the time interval $t = [0.2; 2.0]$ s in front of the equatorial launcher L1 injecting one X2 EC power beam, see figure 5.8. The power amplitude is modulated at a frequency $f_{\text{mod}} = 500$ Hz with a square waveform, a depth $\Delta P_{\text{RF}} = 320$ kW (between 205 kW and 525 kW) and a duty-cycle $d_{\text{c}} = 50\%$. The launcher angles are kept fixed for a quasi-horizontal injection in the poloidal plane ($\phi_{\text{L}} \simeq 180°$, i.e. $\phi_{\text{inj}} \simeq 0°$) with a $\theta_{\text{L}} \simeq \theta_{\text{inj}} \simeq 9°$ upward poloidal angle.

Ray-tracing and Fokker-Planck simulations

Due to the displacement of the plasma in front of the EC power launcher, the beam absorption location is expected to move from off-axis to central normalized minor radius when the plasma sweeps down in front of the launcher. Indeed, simulations from the C3PO ray-tracing code [29] and the LUKE quasi-linear Fokker-Planck-equation solver code [30] for successive equilibria along the plasma discharge indicate a displacement of the beam-plasma resonant interaction from $\rho_{\text{vol}} = 0.63$ to $\rho_{\text{vol}} = 0.07$, see figures 5.9 and 5.11. All simulations were performed with $Z_{\text{eff}} = 3$, $T_{\text{e}}/T_{\text{i}} = 6$ and 500 kW of injected EC power.

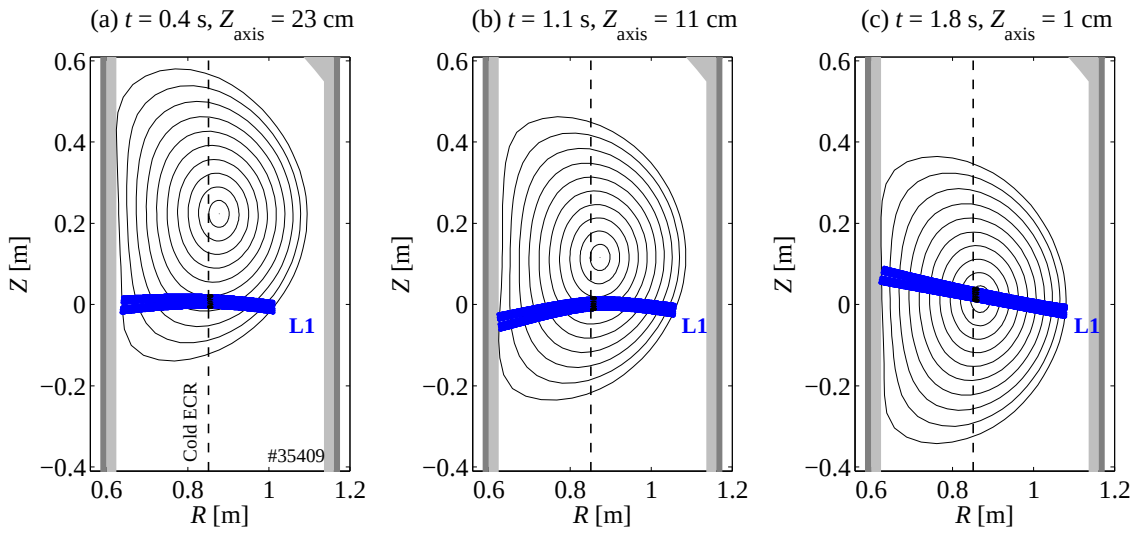

Figure 5.9: Time-varying deposition location. Poloidal trajectory of X2 ray-tracing simulations with the C3PO code [29] for a 12-ray beam injected from the equatorial launcher L1, at times (a) $t = 0.4$ s, (b) 1.1 s and (c) 1.8 s when the plasma magnetic axis is located at $Z_{\text{axis}} = 23$ cm, 11 cm and 1 cm respectively. The vertical dashed-line indicates the 2nd harmonic cold EC resonance location. The location of the beam-plasma resonant interaction (black dots) moves from mid-radius to the plasma core, i.e. $\rho_{\text{vol}} = 0.63$, 0.35 and 0.07, respectively. #35409.

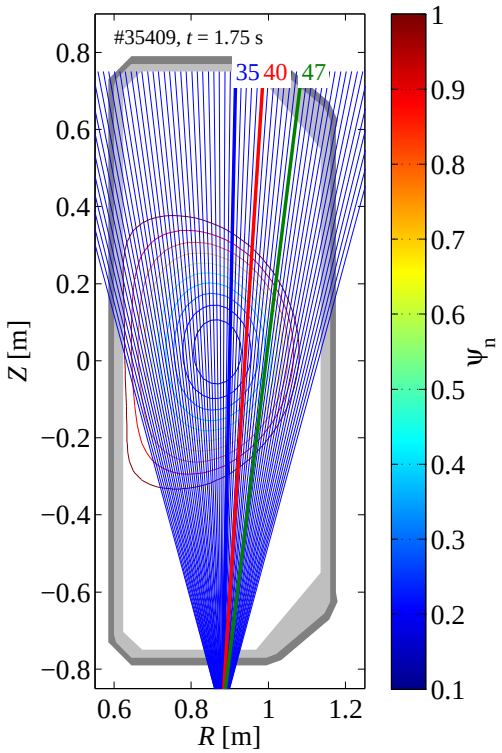

(a) High resolution soft X-ray camera.

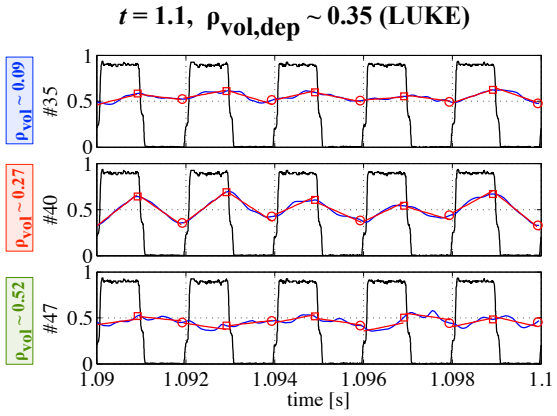

(b) BIS: mid-radius X2 power deposition.

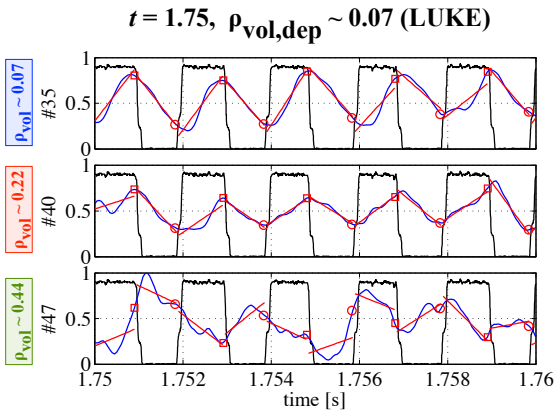

(c) BIS: central X2 power deposition.

Figure 5.10: Displacement of the maximum slope jump amplitude. (a) Lines-of-sight of the multi-wire proportional soft-X ray detector (DMPX) superimposed on normalized poloidal flux contours. Lines-of-sight #35, 40 and 47 are highlighted in blue, red and green, respectively. (b)-(c) BIS analysis of the corresponding soft X-ray signals at $t = 1.1$ s and $t = 1.75$ s, respectively. The filtered and normalized soft X-ray signals (in blue) are plotted on top of the X2 square waveform (in black). Linear fits (in red) are performed between the EC power step-up and step-down times (indicated by red circles and squares). At times $t = 1.1$ s and $t = 1.75$ s, the largest slope jumps take place at the mid-radius-viewing chord #40 ($\rho_{\rm vol} \simeq 0.27$) and at the central-viewing chord #35 ($\rho_{\rm vol} \simeq 0.07$), respectively, as expected from the simulations in figure 5.9. #35409.

BIS analysis of the soft X-ray profiles

Before the BIS analysis is applied to the 64 line-integrated DMPX signals, the data is filtered and normalized as in the previous experiment. The signal is band-pass filtered to remove the fast MHD activity perturbations and the slow time-varying component of the signal using a first-order zero-phase Butterworth filter with cutoff frequencies at $f_{\mathrm{mod}}/2 = 250$ Hz and $f_{\mathrm{mod}} = 500$ Hz. The resulting oscillatory signal component is then normalized along the time dimension such that all 64 soft-X traces take values between 0 and 1.

In these modulated ECRH (MECH) experiments, the auxiliary power modulation period $\tau_{\mathrm{mod}} = 2$ ms is smaller than the typical electron energy confinement time $\tau_{\mathrm{E,e}} > 5$ ms as shown in figure 5.8. As a consequence, the plasma response is close to linear and the simple BIS analysis based on linear fits can be used. It is applied to all DMPX channels independently: linear fits are performed on the DMPX traces between all EC power step-up and step-down times, see figure 5.10. The slope break in the linear fits is then calculated at each power step-up time for each DMPX chord, providing BIS amplitude profiles at a $f_{\mathrm{mod}} = 500$ Hz rate. In a similar way, the BIS information can be deduced at the power step-down times, thus doubling the information rate to $2f_{\mathrm{mod}} = 1$ kHz.

With mid-radius deposition (at time $t = 1.1$ s, see figure 5.10(b)), the largest slope jumps take place at the mid-radius-viewing chord #40 ($\rho_{\mathrm{vol}} \simeq 0.27$) as expected from the simulation on figure 5.9(b) indicating power deposition at $\rho_{\mathrm{vol}} = 0.35$. With central deposition (at time $t = 1.75$ s, see figure 5.10(c)), the strongest slope jump region moves to the central-viewing chord #35 ($\rho_{\mathrm{vol}} \simeq 0.07$), as expected from the simulation on figure 5.9(c) indicating power deposition at $\rho_{\mathrm{vol}} = 0.07$.

The colour map in figure 5.11 shows the successive BIS amplitude profiles versus time. Only the LFS part of the profiles is shown. In the same figure, the color contours give the local power deposition profiles calculated by the C3PO-LUKE codes. For the sake of comparison with the simulation, the BIS amplitude profiles are projected on the normalized minor radius ρ_{vol} to which the DMPX lines-of-sight are tangential. Positive and negative ρ_{vol} values are attributed to LFS and HFS viewing lines-of-sight, respectively. The maximum BIS amplitude location is tracked along time and filtered using a 7-time-point median average, yielding an estimated time evolution of the power deposition location. As expected, the location of maximum BIS amplitude clearly moves from far off-axis to central minor radius when the plasma vertical position decreases. The simulated and experimental power deposition locations are all superimposed in the last subplot of figure 5.11.

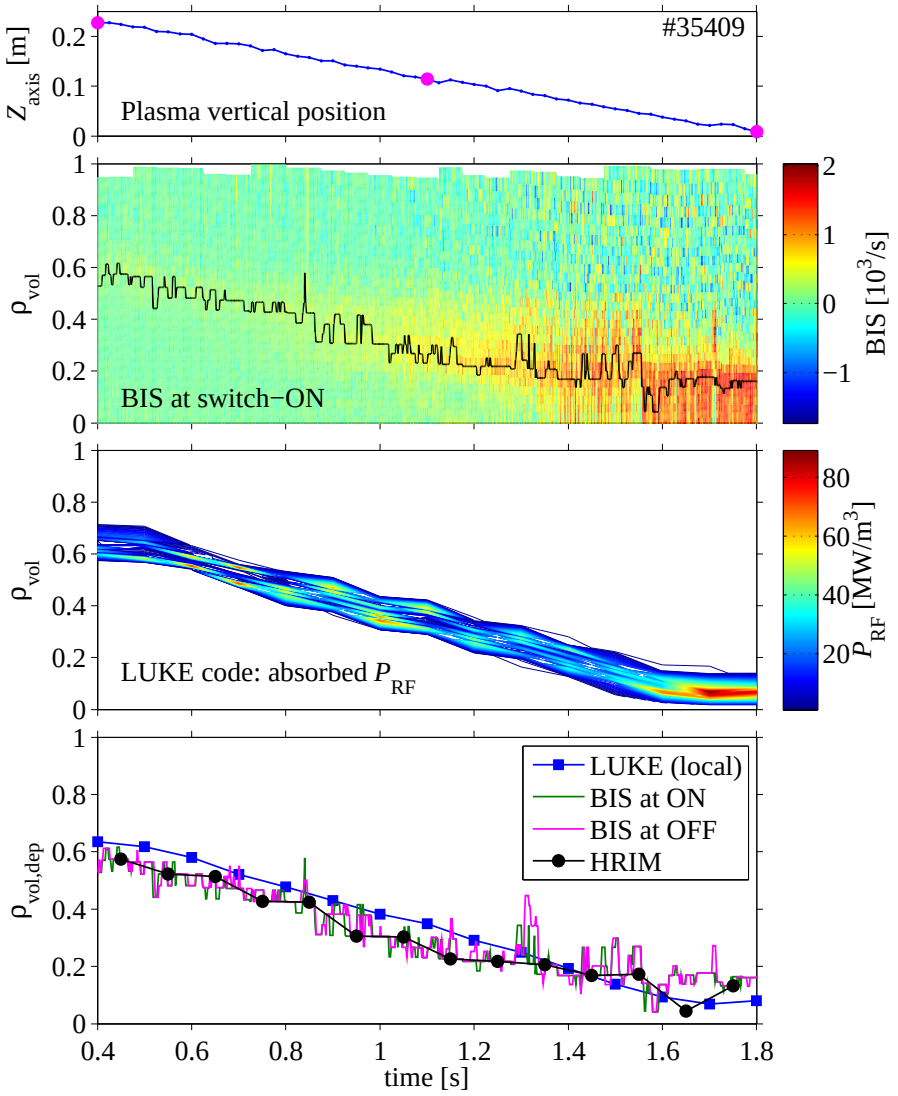

Figure 5.11: X2 power deposition location tracking. From top to bottom: plasma vertical position versus time (pink dots indicate the times corresponding to the C3PO simulations in figure 5.9); BIS amplitude of line-integrated soft X-ray profiles versus time and normalized minor radius ρ_{vol} (only the LFS part of the BIS profiles is shown and the black line is a 7-time-point median average of the maximum BIS amplitude location); local absorbed EC power density versus time and normalized minor radius ρ_{vol} from LUKE simulations; superimposed EC power deposition locations from LUKE (blue ■), from BIS analysis of the soft X-ray profiles at both EC power switch-on (green trace) and switch-off times (magenta trace), and from HRIM analysis of the soft X-ray profiles (black •). Both analysis methods are in excellent agreement with each other and within 10% of ρ_{vol} with the numerical simulation. #35409.

The experimental power deposition location inferred from BIS at the EC power switch-on and switch-off times are in excellent agreement with each other, with a time average difference $\langle|\rho_{dep,ON} - \rho_{dep,OFF}|\rangle_t \simeq 2.3\%$, during the whole position sweep.

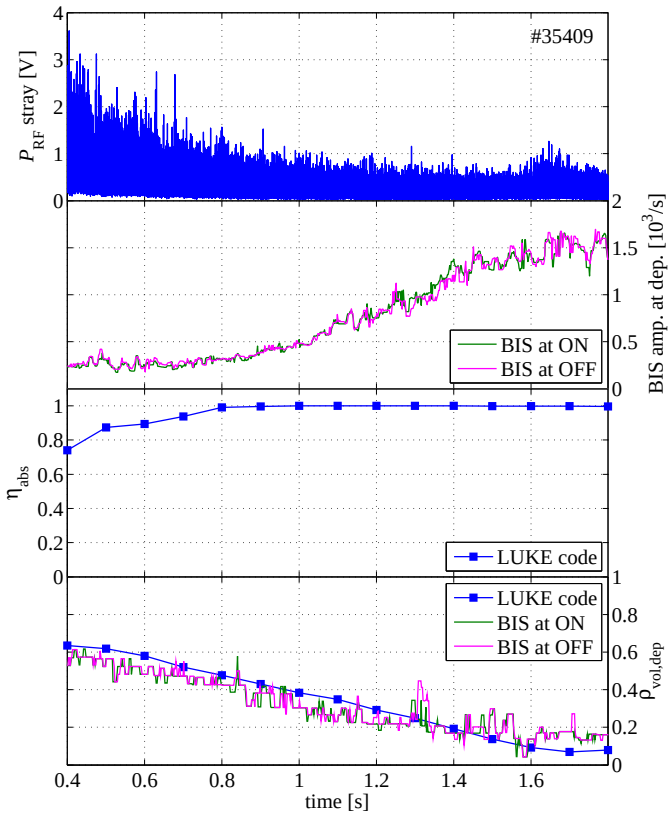

Figure 5.12: EC power absorption efficiency. From top to bottom: stray EC power level, maximum BIS amplitude at power switch-on and switch-off times, X2 EC power absorption efficiency calculated by the LUKE code, and power deposition location from BIS analysis and simulations. Since BIS amplitudes at switch-on and switch-off times have opposite signs, the latter is multiplied by -1. The X2 power absorption increases from 74% when the beam power is deposited at the edge where the temperature is low, to 100% for central deposition. Both the level of stray EC power and the maximum BIS amplitude follow the same trend. #35409.

For off-axis deposition ($\rho_{\mathrm{vol,dep}} \gtrsim 0.2$, $t < 1.3$ s), the experimental results are in fair agreement with the simulated power deposition location, that is $\langle|\rho_{\mathrm{dep,ON}} - \rho_{\mathrm{dep,LUKE}}|\rangle_t \simeq 8.4\%$ more inside than the simulation result. This slight discrepancy can be explained by the fact that the BIS analysis is applied to line-integrated soft X-ray data, whereas the simulated deposition profiles are local. A tomographic inversion of the soft X-ray data will cause a slight outward shift of the experimental power deposition location [89], which should improve the agreement with the ray-tracing calculation. In stationary scenarios, the DMPX profile can be inverted off-line using a Fisher-information minimization algorithm, mapping both HFS and LFS viewing chords on one local profile. In the present non-stationary scenarios where the flux surfaces cross different lines-of-sight as a function of time, the signal/noise ratio after inversion is poor and the modulation information is lost. Note that the

inversion of the soft-X ray profiles is not necessary if the same diagnostic is used to determine both the location of the power deposition and the aim point of the beam, e.g. in the case of NTM tracking and stabilization with EC power. In this case, relative position information is sufficient.

For central deposition ($\rho_{\mathrm{vol,dep}} \lesssim 0.2$, $t > 1.3$ s), the experimental deposition location is more outward than expected from the simulation and it undergoes larger fluctuations. Both effects may be caused by the resurgence of the sawtooth activity or a similar periodic profile relaxation triggered by the modulated ECH when it reaches the plasma center.

Although this type of experiment is designed rather for the fast tracking of the EC power deposition location than for a quantitative estimation of the absorption efficiency, the maximum BIS amplitude is compared qualitatively to the power absorption efficiency calculated by LUKE in figure 5.12. Note that the BIS amplitude at the power switch-off times is simply multiplied by -1 to compare the information of BIS amplitude at switch-on and switch-off times. At the beginning of the plasma vertical sweep, the X2 beam power is deposited at the edge where the electron temperature is low and the EC power is not fully absorbed (74% absorption according to LUKE), as confirmed by the high level of stray EC power which provides a qualitative indication of the non-absorbed power fraction. At the end of the plasma position sweep, central deposition and full absorption are reached. The maximum BIS amplitude follows the same trend, increasing with more central deposition radius $\rho_{\mathrm{vol,dep}}$.

HRIM analysis of the soft X-ray profiles

The harmonic response identification analysis is performed on the same filtered and normalized soft X-ray profiles used in the BIS analysis. The complex amplitude at $f_{\mathrm{mod}} = 500$ Hz is calculated for each of the 64 soft X-ray traces in 14 successive 100-ms-long time intervals. The resulting amplitude and phase profiles are given in figures 5.13(a) and 5.13(b), respectively. Note that the HRIM analysis provides one amplitude profile per 100-ms interval whereas the BIS analysis yields 100 amplitude profiles in the same time (thanks to 50 power switch-on events and 50 power switch-off events).

The location of maximum soft X-ray oscillation amplitude inferred from the HRIM analysis is shown in the bottom subplot of figure 5.11. It is in excellent agreement with the results of the BIS analysis, with difference averaged on the whole sweep time $\langle|\rho_{\mathrm{dep,ON}} - \rho_{\mathrm{dep,HRIM}}|\rangle_t \simeq 3.1\%$. The soft X-ray oscillation phase exhibits a

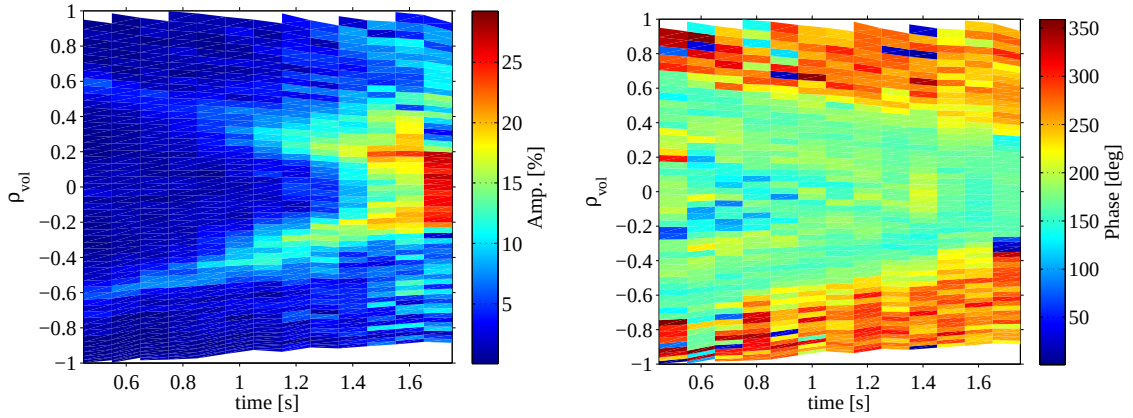

(a) Oscillation amplitude. **(b)** Oscillation phase.

Figure 5.13: HRIM analysis of the power deposition location. HRIM analysis of the 500-Hz component of the 64 soft X-ray signals from the DMPX is performed in successive 100-ms-long time intervals comprising 50 modulation cycles. (a)-(b) Amplitude and phase of the resulting complex amplitudes versus time and ρ_{vol}. Negative ρ_{vol} values represent lines-of-sight viewing on the HFS. #35409.

local minimum which also follows the power deposition location. Figures 5.14(a), (b) and (c) presents successive amplitude and phase profiles for decreasing $\rho_{\mathrm{vol,dep}}$. The rather shallow local minima in the phase profiles at $t = 0.95$ s and $t = 1.35$ s indicate a fast radial propagation of the ECH heat pulse. At $t = 1.75$ s, the X2 power is deposited at the plasma centre. There is no clear amplitude maxima at the power deposition location, but rather a flat profile. Moreover, the phase profile exhibits 90° jumps. These effects is the clear signature that a periodic profile relaxation with inversion radius is dominating the heat pulse propagation. This confirms that central heating trigs a MHD instability which in turn induces perturbations in the analysis of the plasma response to MECH, increasing the error on the power deposition location estimate.

5.4.2 Double X2 power deposition location

The natural next step toward real-time applications of the BIS analysis method is to test the potential of simultaneous tracking of multiple power deposition locations. For this purpose, a similar plasma target is repeated where, in addition to the EC power beam from the equatorial launcher L1, a second beam is injected in the poloidal plane ($\phi_{\mathrm{L}} \simeq 0°$, i.e. $\phi_{\mathrm{inj}} \simeq 0°$) from the upper lateral launcher L5 with a $\theta_{\mathrm{inj}} \simeq -30°$ downward poloidal angle. When the plasma vertical position is swept down, the power deposition location of the first beam is thus expected to move from

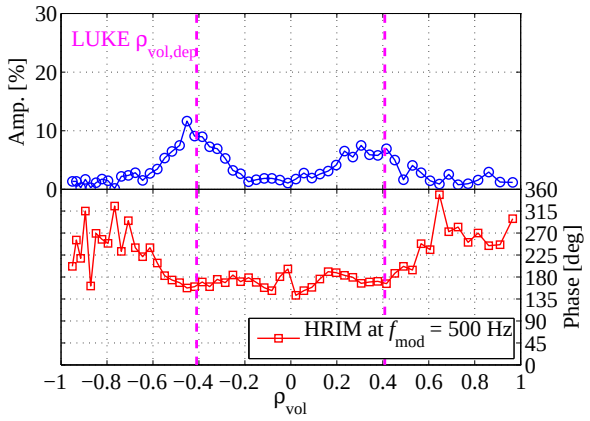

(a) HRIM at $f_{\mathrm{mod}} = 500$ Hz on $t = 0.9 - 1.0$ s.

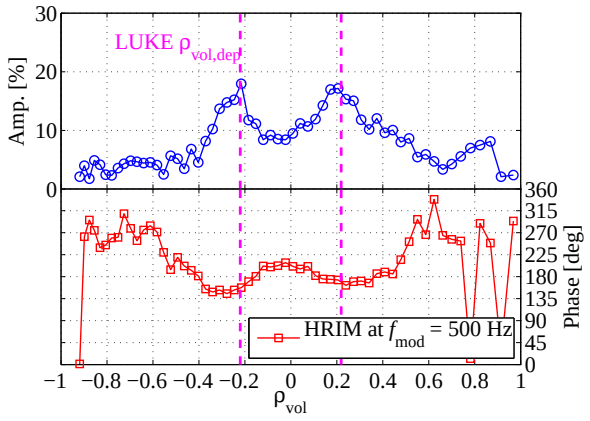

(b) HRIM at $f_{\mathrm{mod}} = 500$ Hz on $t = 1.3 - 1.4$ s.

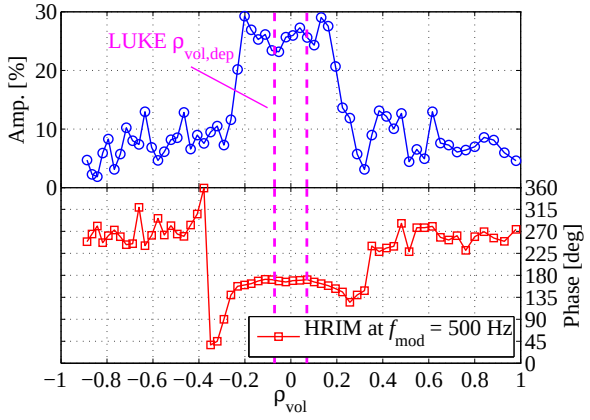

(c) HRIM at $f_{\mathrm{mod}} = 500$ Hz on $t = 1.7 - 1.8$ s.

Figure 5.14: Effect of central relaxation on amplitude and phase profiles. Amplitude and phase of the 500-Hz component of the soft X-ray profiles for decreasing $\rho_{\mathrm{vol,dep}}$ (indicated by the vertical dashed lines). For (a) $t = 0.95$ s and (b) $t = 1.35$ s, the amplitude is maximum and the phase exhibits a local minimum at the power deposition location. (c) At $t = 1.75$ s, i.e. when the power is absorbed inside $\rho_{\mathrm{vol}} \simeq 0.2$, the phase profile exhibits a 90° jump, which is the standard signature of a perturbation of the heat pulse transport by some periodic profile relaxation. #35409

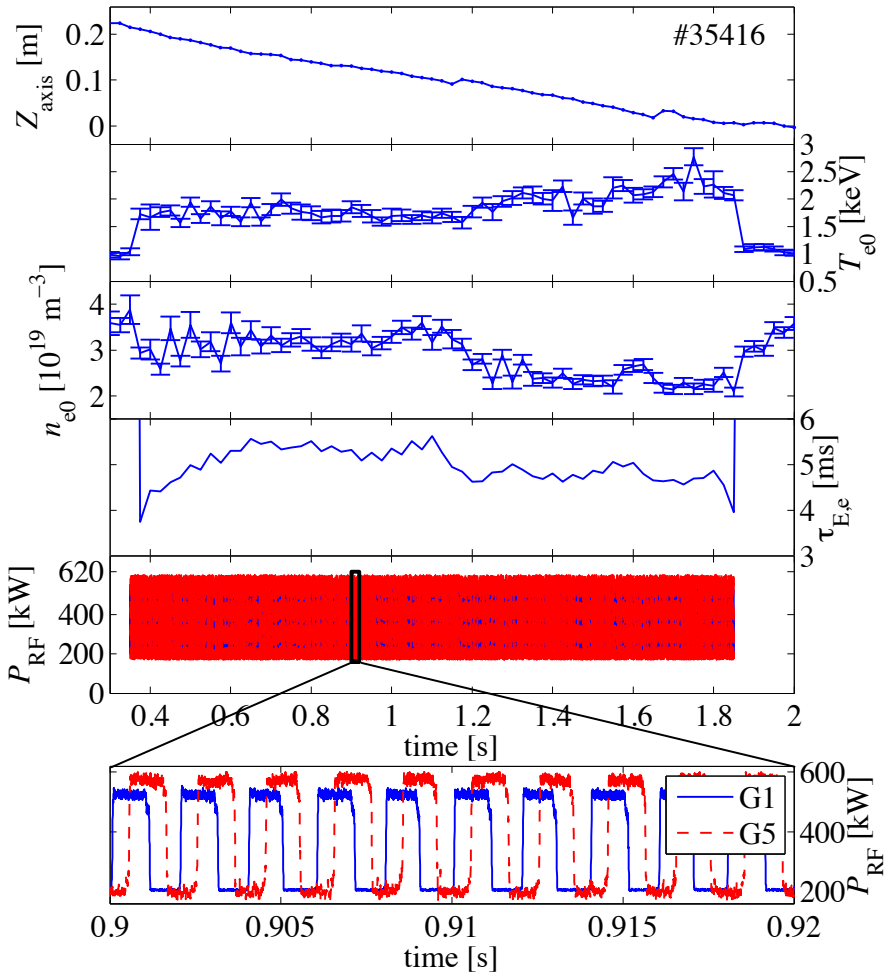

Figure 5.15: Plasma vertical sweep and double beam modulation. From top to bottom: same as in figure 5.8. In addition to the X2 EC power beam injected from the equatorial launcher L1 (blue solid P_{EC} trace), a X2 EC power beam is injected from the upper lateral launcher L5 (red dashed P_{EC} trace). Both EC power traces are square modulated at $f_{mod} = 500$ Hz with a duty-cycle $d_c = 50\%$, but with a relative phase of $\pi/2$. The confinement time was calculated for an average ECH power $\bar{P}_{EC} = 750$ kW. The toroidal magnetic field and the plasma current are maintained constant at $B_\varphi = 1.45$ T and $I_p \simeq 160$ kA respectively while the plasma vertical position is swept down from $Z_{axis} = 24$ cm to 0 cm in the time interval $t = [0.2; 2.0]$ s. #35416.

mid-radius to the center of the plasma and vice-versa for the second beam, as shown by C3PO ray-tracing simulations in figure 5.16. In order to perform independent but simultaneous BIS analysis of the beam absorption locations, both power amplitudes are modulated with the same 500 Hz square waveform as in the previous experiment, but with a phase difference of $\pi/2$, see figure 5.15. The difference in the modulation depths — $\Delta P_{RF} = 320$ kW for L1 and $\Delta P_{RF} = 375$ kW for L5 (between 200 kW and 575 kW) — is due to the different individual efficiencies of the gyrotrons response to the same applied voltage.

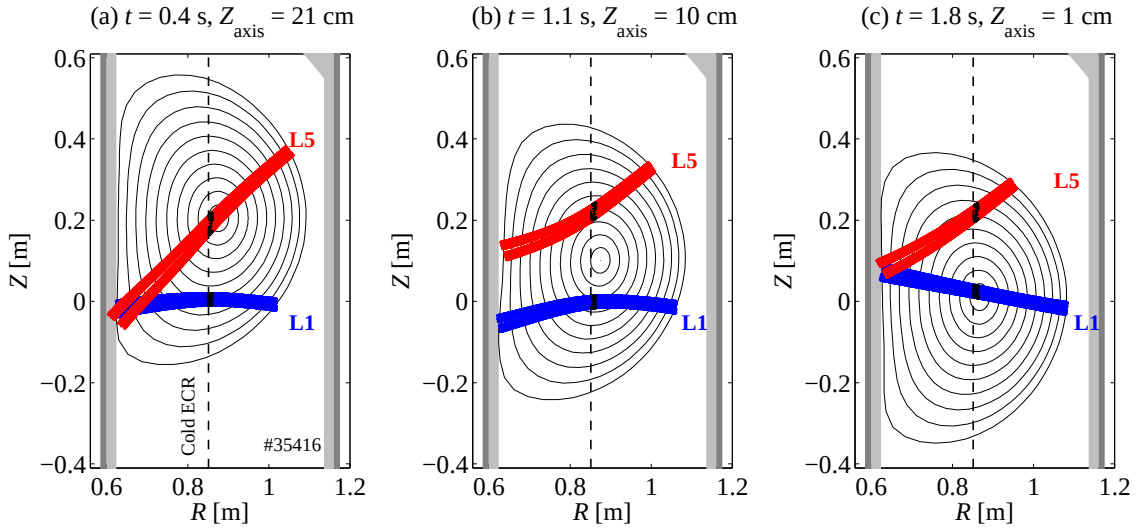

Figure 5.16: Double time-varying deposition locations. Poloidal trajectory of X2 ray-tracing simulations with the C3PO code [29] for 12-ray beams injected from the equatorial launcher L1 (blue) and from the upper lateral launcher L5 (red), at times (a) $t = 0.4$ s, (b) 1.1 s and (c) 1.8 s when the plasma magnetic axis is located at $Z_{\text{axis}} = 21$ cm, 10 cm and 1 cm respectively. The vertical dashed-line indicates the 2nd harmonic cold EC resonance location. The beam-plasma resonant interaction location (black dots) moves from mid-radius to the plasma core for the beam coming from L1 and vice-versa for the beam coming from L5. TCV shot #35416.

In this somewhat more delicate experiment to retrieve the deposition location, the best discrimination between the two beam absorption locations is obtained when the DMPX signal is not band-pass filtered (neither low-pass filtered nor detrended) but only normalized along time, to ensure the highest signal dynamics. The linear fits are then performed between the power step-up and step-down times of the beams coming from launchers L1 and L5 separately and an estimate of the power deposition location can be drawn for each beam at a 500 Hz rate, see figures 5.17 and 5.18.

In this double beam case, the signal/noise ratio is lower and the discrepancy with the simulations is larger than for the single beam experiment since the power modulation of one beam perturbs the analysis of the response to the other beam modulation. The double beam experiment was repeated with slower modulation frequencies (137 Hz and 237 Hz instead of 500 Hz) in order to improve the discrimination between the two beam deposition locations by performing the linear fits on quarters of the modulation period ($\tau_{\text{mod}}/4$ instead of $\tau_{\text{mod}}/2$) around the power steps of one gyrotron such as to avoid the perturbation due to the power steps of the other gyrotron. But similar results were obtained and no clear improvement was observed.

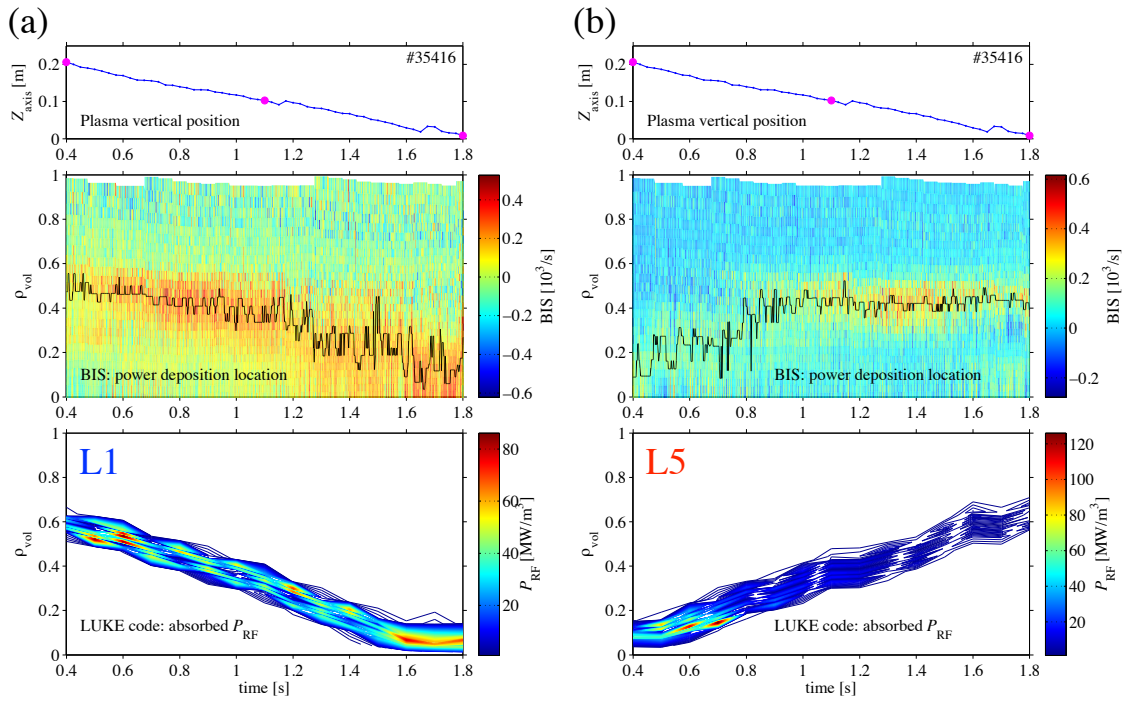

Figure 5.17: Simultaneous X2 power deposition tracking. Same as in figure 5.11 but for the EC power beams from (a) launcher L1 and (b) launcher L5 simultaneously. The pink dots indicate the times corresponding to the C3PO simulations in figure 5.16(a-c). #35416.

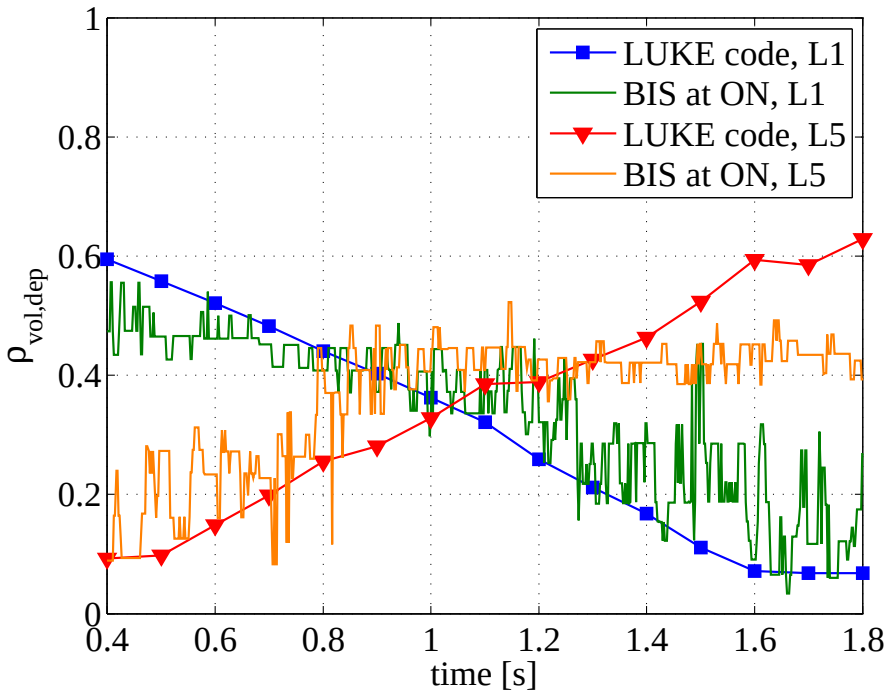

Figure 5.18: Simultaneous X2 power deposition tracking. LUKE simulated power deposition locations for the beams from launcher L1 (blue ■) and launcher L5 (red ▼), superimposed on the BIS estimated power deposition locations for L1 (green trace) and L5 (orange trace). #35416.

5.4.3 Summary

The time-varying power deposition location of one X2 power beam is successfully tracked at a high time rate (1 kHz) by BIS analysis of high radial resolution soft X-ray profiles. The experimental results and the power absorption profiles simulated by the C3PO-LUKE code are in very good agreement, i.e. within 10% of the normalized minor radius ρ_{vol}, except for the central deposition. Harmonic response identification analysis of the soft X-ray profiles indicates that the latter discrepancy is caused by the resurgence of periodic profile relaxations when the X2 MECH is deposited in the plasma center, i.e. within $\rho_{\mathrm{vol}} \simeq 0.2$. The BIS analysis is thus a candidate of choice for ECH power deposition detection in real-time applications.
Orthogonal power modulation waveforms allow to track the power deposition locations of two X2 power beams simultaneously. The experimental results compare satisfactorily with the simulation, but the discrepancy is larger than in the single beam case due to the mutual disturbance of the two heating modulations.
This part of the thesis work has been submitted for publication as ***Multiple EC power deposition locations tracking by break-in-slope analysis in TCV plasmas*** in *Plasma Physics and Controlled Fusion*, 2011.

5.5 EBW deposition detection

Experimental setup

The BIS and HRIM methods have been successfully used to detect and track both stationary and time-varying X2 power deposition locations in the previous sections. In this section, the location of resonant EBW absorption is determined using the same methods.
In this EBW heating experiment, the target plasma is an ELM-free H-mode plasma located in the upper half of TCV vacuum vessel ($R_{\mathrm{axis}} \simeq 89.7$ cm, $Z_{\mathrm{axis}} \simeq 19.5$ cm, $\kappa_a \simeq 1.76$, $\delta_a \simeq 0.55$). The time evolution of the plasma parameters is given in figure 5.19. The L-H confinement transition is obtained in Ohmic regime thanks to a high Ohmic power input obtained with a high plasma current $I_{\mathrm{p}} \simeq 420$ kA. In absence of ELM activity, the electron density rises dramatically, and the density pedestal height and gradient grow rapidly. Hence, the conditions for an efficient O-X-B mode conversion are met shortly after the L-H transition. In the meanwhile, the central electron temperature decreases with increasing density.
As a consequence of the high plasma current, the edge safety factor is low ($q_{95} \simeq$

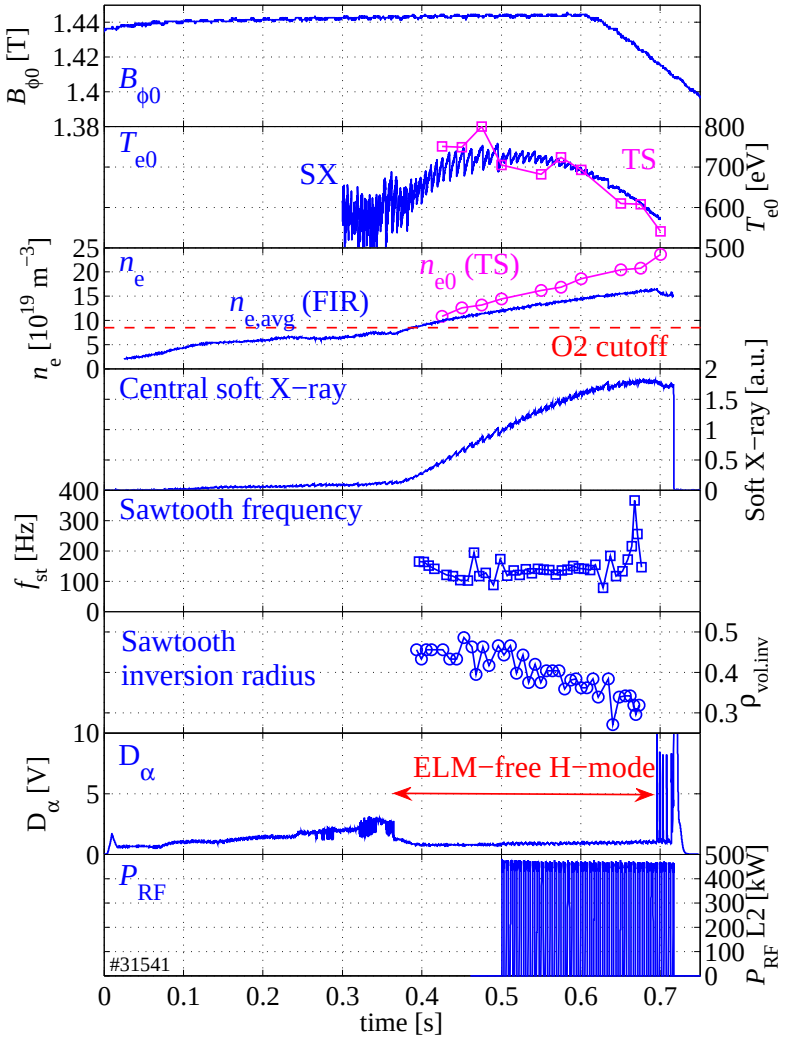

Figure 5.19: EBH experiment in ELM-free H-mode. From top to bottom: toroidal magnetic field, central electron temperature from profile fitting of the Thomson scattering data (TS, □) and from soft X-ray signals, central electron density from TS (∘) along with the volume averaged density from FIR measurements, central soft X-ray emission (line-integrated), sawtooth frequency and inversion radius calculated from the soft X-ray profiles after tomographic inversion (DMPX), D_α recombination light intensity and modulated O2 power. The L-H transition is indicated by the characteristic intensity drop in the D_α light emission. In absence of ELM activity, the electron density increases dramatically, rapidly exceeding the O2 cutoff density (dashed line). Efficient O-X-B mode conversion is thus expected. #31541.

2.4) and the plasma center undergoes strong sawtooth activity with frequency $f_{\rm st} \simeq$ 140Hz. The sawtooth crashes have a wide inversion radius $\rho_{\rm vol,inv} > 0.3$, decreasing with increasing density, as determined from tomographic inversion of the soft X-ray emission profiles measured by the DMPX diagnostic.

The O2 power is modulated between $P_{\rm RF} = 0$ kW and 450 kW with a 50% duty-cylce square waveform. The modulation frequency $f_{\rm mod} = 181$ Hz is chosen to lie

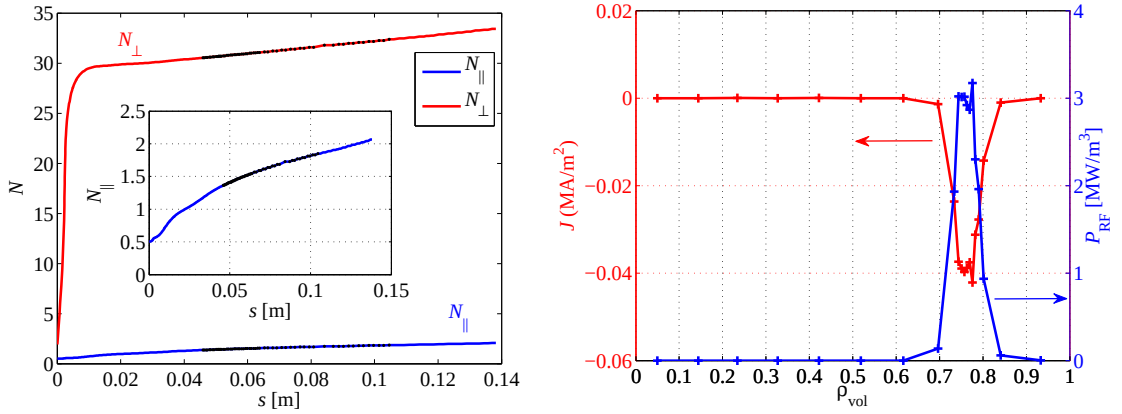

(a) Details of the poloidal view. **(b)** Details of the toroidal view.

Figure 5.20: $N_\parallel$-upshift and power deposition profile. (a) Evolution of the parallel and perpendicular refractive indices along the central ray propagation coordinate s, calculated by AMR. (b). Absorbed power density profile and driven current density profile, calculated by LUKE. #31541 at $t = 0.69$ s.

between the fundamental and the second harmonic of the sawtooth frequency. The O2 power is injected from the upper lateral launcher L2. The optimum launcher angles $(\theta_\mathrm{L}, \phi_\mathrm{L}) \simeq (43.1°, -40.8°)$ were determined prior to the experiment using the ART code. These launcher angles correspond to a downward poloidal injection angle $\theta_\mathrm{inj} \simeq -31.1°$ and a counter-clockwise toroidal injection angle $\phi_\mathrm{inj} \simeq 31.4°$. With such a poloidally oblique launching geometry, the EBWs penetrate the plasma high above its magnetic axis and a strongly Doppler-shifted off-axis resonant absorption is expected. A toroidal magnetic field ramp-down from $B_\varphi = 1.44$ T to 1.29 T was programmed in order to displace the absorption location, which would be an additional signature that resonant absorption is at play, but the plasma disruption happened before the field sweep was completed.

Numerical simulation of the EBW trajectory and absorption profile

Figure 5.21 shows the post-shot calculation of the EBW trajectory performed for a 7-ray bundle using the AMR code with the experimental equilibrium and profiles data for the time $t = 0.69$ s when the magnetic field is the lowest, i.e. $B_\varphi = 1.42$ T. The calculated O-X-B mode-conversion efficiency is 82.3%. As indicated in figure 5.20(a), the EBW undergoes an upshift of the parallel refractive index up to $N_\parallel \simeq 1.6$ at the absorption. The EBW trajectory is passed to the LUKE Fokker-Planck code in order to calculate the quasi-linear power absorption profile and the generated current density given in figure 5.20(b). As a consequence of the high $N_\parallel$, the mode-converted

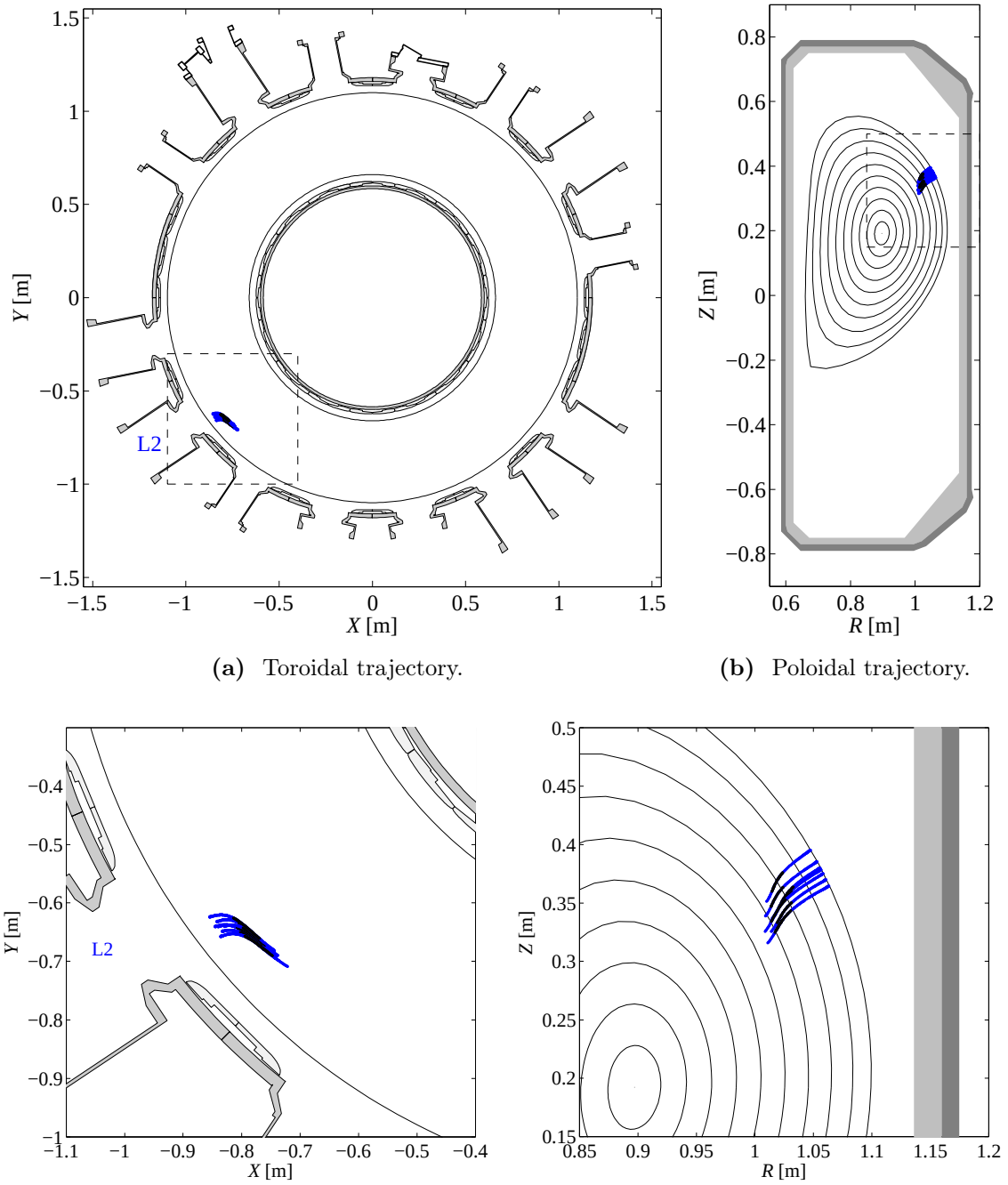

(a) Toroidal trajectory.

(b) Poloidal trajectory.

(c) Detail view of the toroidal trajectory.

(d) Detail view of the poloidal trajectory.

Figure 5.21: Oblique EBW beam injection and O-X-B trajectory. (a) Toroidal and (b) poloidal trajectories of a 7-ray EBW bundle calculated by the AMR ray-tracing code using the experimental equilibrium and profiles data of #31541 at $t = 0.69$ s. The dashed frames define the detail views on the ray trajectories given in (c) and (d). Black dots along the rays indicate the power absorption location, which takes place far off-axis. The corresponding deposition profile and refractive index evolution are given in figures 5.20.

power is fully absorbed far off-axis at $\rho_{\mathrm{vol,dep}} \simeq 0.76$, i.e. inside the plasma cutoff

but far from the strong central sawtooth perturbation. The driven counter-current is low, i.e. $I_{CD} \simeq -1.2$ kA.

BIS and HRIM analyses of the experimental EBW deposition

The EBW power deposition location is inferred from the local soft X-ray emission profiles obtained after tomographic inversion of the line-integrated signal measured by the DMPX camera.

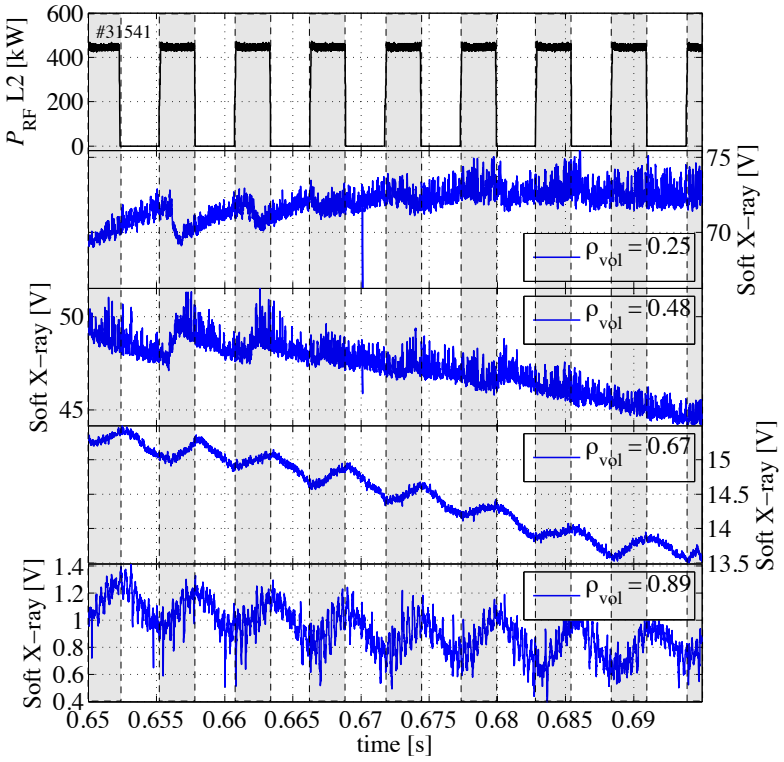

Figure 5.22: Local (inverted) soft X-ray profile response to modulated EBH. Soft X-ray traces after tomographic inversion of the line-integrated signal from the DMPX, along with the modulated RF power trace. Grey surfaces indicate the times when the ECH power is on. The plasma center is perturbed by the sawtooth activity (which is inverted outside $\rho_{vol,inv} \simeq 0.32$), while the traces at the plasma edge are dominated by an oscillation in phase with the EBH modulation. #31541.

In order to minimize the perturbation due to the sawtooth activity, the soft X-ray profile response to the modulated EBH is analyzed on the last five RF power modulations before the plasma disruption, when the amplitude of the sawtooth activity is the lowest and its inversion radius is the smallest, as indicated in figures 5.22 and 5.19, respectively. The data are band-pass filtered (between $f_{mod}/2 = 90.5$ Hz and $2f_{mod} = 362$ Hz) and normalized in this time interval. The BIS analysis is then performed as indicated in figure 5.4, as well as the HRIM oscillation analysis.

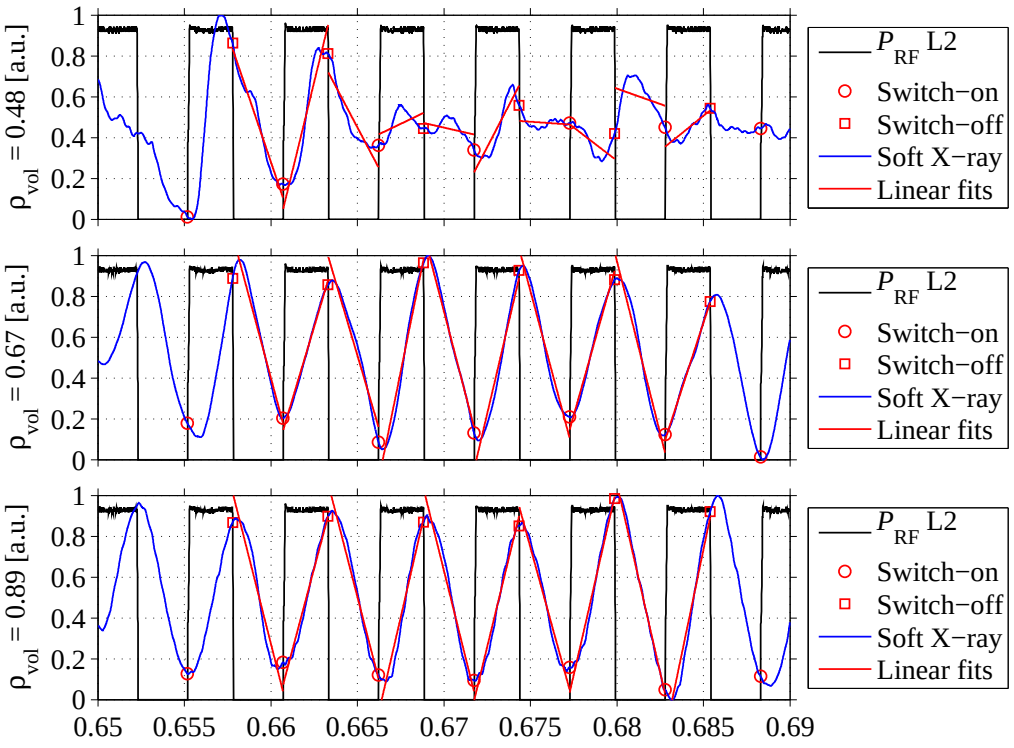

Figure 5.23: BIS analysis of the local (inverted) soft X-ray emission. Filtered and normalized soft X-ray emission (in blue) at $\rho_{\text{vol}} \simeq 0.48$, 0.67 and 0.89, superimposed on the modulated EBH trace (in black). The red ∘ and □ indicate the RF power switch-on and switch-off times, respectively. Linear fits of the soft X-ray data (in red) are performed between these times. The largest break-in-slope takes place at the plasma edge where the modulation is in phase with the modulated EBH. #31541.

The resulting average amplitude and phase profiles are given in figure 5.24. One peak is observed on the BIS and HRIM amplitude profiles at $\rho_{\text{vol}} = 0.68$. Since this peak in the plasma response is situated far from the region of the strongest sawtooth perturbation ($\rho_{\text{vol,inv}} \simeq 0.32 \pm 0.02$) and well inside the O2 cutoff layer located at $\rho_{\text{vol}} = 0.92 - 0.96$, it can be safely attributed to the resonant absorption of EBW power. It is in agreement with the numerical results within 8% of ρ_{vol}. The detailed view in figure 5.25 indicates that the HRIM phase profile has a local minimum at the same normalized minor radius, which confirms this is the location EBH.

Both the BIS and HRIM amplitude profiles exhibit a second peak at the cutoff layer, which could be explained by several effects: some collisional damping of the wave around the X-B mode conversion layer, absorption of the decay waves from the lower-hybrid parametric instability or edge absorption of the non-converted power fraction after multiple reflections between the plasma cutoff and the vessel wall.

Finally, the third peak observed on the BIS amplitude profile (and, to a lesser extent, on the HRIM amplitude profile) at $\rho_{\text{vol}} \simeq 0.4$ is due to the sawtooth oscillation

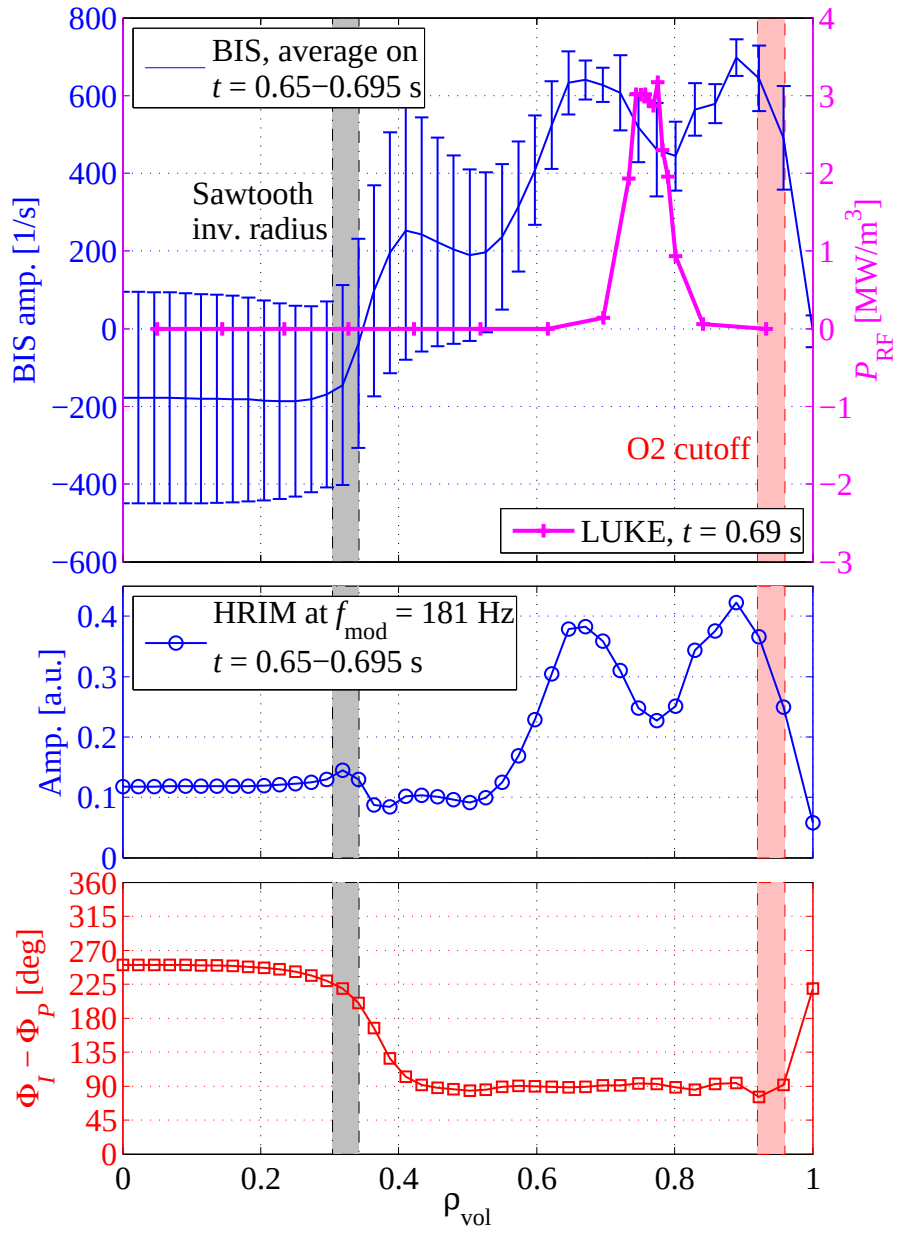

Figure 5.24: Detection of resonant EBH at the plasma edge. Top figure: BIS amplitude profile of the local (inverted) soft X-ray emission averaged over five EBH pulses, superimposed on the power density profile calculated by LUKE. Center and bottom figures: oscillation amplitude and phase profiles of the local soft X-ray emission inferred from the HRIM analysis at the modulation frequency $f_{\mathrm{mod}} = 181$ Hz. The average O2 cutoff location and sawtooth inversion radius are indicated by red and grey surfaces, respectively. The amplitude peak at $\rho_{\mathrm{vol}} = 0.68$ indicates the location of resonant EBW absorption. A local minimum is observed on the phase profile at the same location, as indicated by the detailed view in figure 5.25. #31541.

outside the inversion radius. The large errorbars indicate that the amplitude and position of this third peak are subject to strong fluctuations.

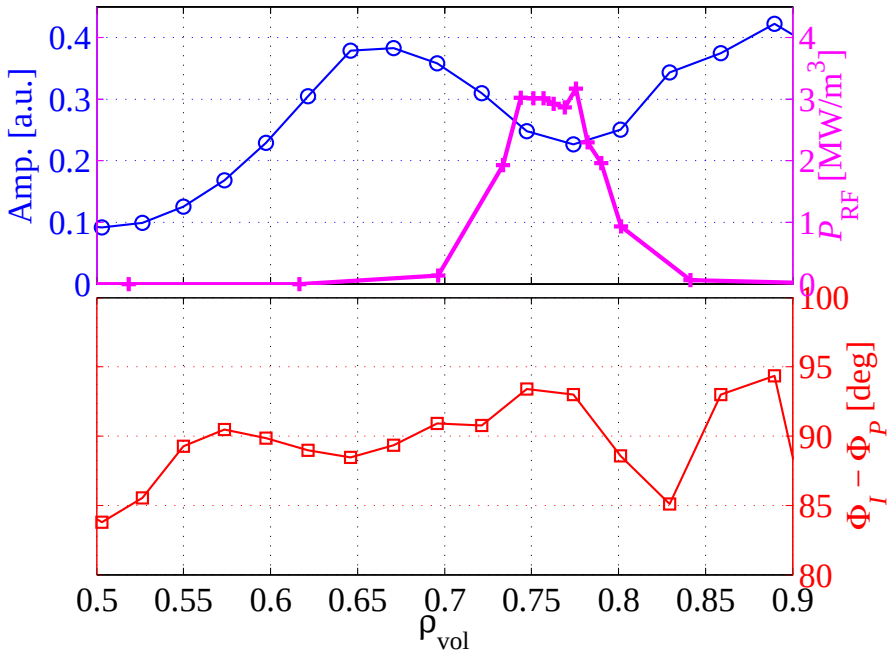

Figure 5.25: Local minimum of the oscillation phase at the EBH location. Amplitude profile (top) and phase profile (bottom) of the local (inverted) soft X-ray oscillation retrieved by HRIM analysis at the RF power modulation frequency $f_{\mathrm{mod}} = 181$ Hz, compared to the absorbed RF power density calculated by LUKE (magenta). The phase profile exhibits a local minimum at the same normalized minor radius than the maximum amplitude, indicating direct EBH. #31541.

5.6 Conclusion and outlook

Modulation of the amplitude of injected RF power is a frequent tool used to estimate the absorbed power profile in the experiment. Amongst the many methods proposed to analyze the plasma response to the power modulation, the simple break-in-slope (BIS) analysis is the only one that provides an estimated power deposition profile at each power step-up and step-down time, thus with a high temporal resolution. It has been successfully tested and compared to other methods in previous experiments in stationary conditions.

In this chapter, the deposition location of modulated RF power is retrieved by BIS analysis of the soft X-ray profiles measured by the high radial and time resolution DMPX camera. It is compared to the results of a harmonic response identification method (HRIM) applied to the same experimental data, and to the numerical results of the C3PO (for X2) and AMR (for EBW) ray-tracing codes coupled to the Fokker-Planck solver LUKE.

The direct deposition location of partially absorbed X2 power at the edge of the plasma where the signal to noise ratio is low is successfully determined by both the

BIS and the HRIM analyses. Conversely to the HRIM, the BIS analysis is able to discard the indirect plasma center response to the MECH, revealing only the direct edge ECH. The experimental results are in good agreement with the numerical simulation of C3PO-LUKE within 7% of ρ_{vol}.

Using the unique flexibility of both TCV magnetic coil system and ECH system, the ability of the BIS analysis to track the X2 power deposition location with a high time resolution is demonstrated in TCV experiments with time-varying EC resonance when either the toroidal magnetic field is varied or the plasma position relative to the injecting antenna is swept during the plasma discharge. The BIS analysis provides estimated power deposition profiles with a high time resolution (i.e. $2f_{\mathrm{mod}} = 1$ kHz if both power step-up and step-down times are used in the analysis). The experimental results are in agreement within 10% of ρ_{vol} with the evolution of the absorbed power profile described by the C3PO-LUKE simulations. Choosing orthogonal power modulation waveforms allows different time-varying power deposition locations of two X2 beams to be tracked simultaneously.

The absorption location of O-X-B mode-converted O2 power is detected at the edge of a strongly sawtoothing ELM-free H-mode plasma by BIS and HRIM analyses of the local soft X-ray emission, in good agreement with the AMR-LUKE simulation within 8% of normalized minor radius, thus demonstrating the resonant absorption of EBWs in TCV overdense plasmas. A second absorption peak is observed at the plasma cutoff, which can be due to multi-pass absorption of the non-converted power fraction. It may also indicate a non-negligible fraction of collisional damping of the EBW at the mode-conversion layer where the temperature is low. In future work, the importance of the collisional damping can be assessed with the help of the AMR code.

Chapter 6

RF power absorption measurements using the DiaMagnetic Loop (DML) diagnostic

6.1 Introduction

The experimental deposition location of injected RF power is determined in chapter 5 with the BIS analysis method. For a complete information about the RF power deposition profile, the global absorption coefficient need to be assessed. The experimental results can then be compared to the numerical results from ray-tracing and mode-conversion calculation codes for X2/X3 ECH and EBH, respectively.

The absorption efficiency η of auxiliary power injected in the plasma is defined as the ratio of the power P_{abs} actually absorbed by the plasma and the power P_{inj} injected into the plasma (i.e. the power leaving the injection system, taking into account possible losses in the transmission lines from the power sources to the vacuum vessel):

$$\eta = \frac{P_{\text{abs}}}{P_{\text{inj}}}. \tag{6.1.1}$$

The absorption efficiency η is of primary importance to compare the efficiency of different auxiliary heating techniques. It is also an important quantity to retrieve from the measurements for the interpretation of plasma auxiliary heating results, in particular in heat transport studies, and for the comparison of the experiments with simulations.

The experimental methods for the measurement of the auxiliary power absorption divide into two categories:

- direct measurements of the non-absorbed power fraction;
- perturbative methods based on the modulation of the heating power intensity.

The first method consists in measuring the stray power reflected and transmitted by the plasma. It has the advantage that no modulation of the power source strength is needed. However, the main inconvenient of this method is that the locations where to instal the detectors to ensure a total stray power detection strongly depend on the beam trajectory, i.e. on reflection and refraction effects and on the launching geometry. A fixed set of detectors would provide a valid measurement for only one launching geometry and a very narrow range of plasma parameters. This method is thus not applicable in most experiments, and in particular in TCV where both the plasma configuration and the EC heating conditions vary largely, due to the high flexibility offered by the coil system and the heating system.

The second method consists in analyzing the dynamic response of the plasma energy to total or partial modulation of the auxiliary power intensity. The power modulation wave form is typically sinusoidal or square with abrupt switch-on/off jumps. Of course, this method is not restricted to RF heating and is applicable to all types of auxiliary heating, including NBI. As recalled in [90], there are many techniques for the determination of the auxiliary power absorption coefficient from the plasma response to the modulation: instantaneous time derivative of the plasma energy at the power switch-on/off time (i.e. the so-called break-in-slope method); fitting the plasma energy time evolution after an isolated power switch-on/off; fitting the plasma energy as a function of the auxiliary power using a confinement time scaling model; oscillation analysis of both the injected power and the plasma energy response. In the present work, the latter method is used.

This chapter presents analyses of global power absorption of RF heating experiments in TCV using the diamagnetic loop (DML) diagnostic measuring the plasma toroidal magnetic flux. The three types of RF heating available at TCV are studied: X2 ECRH, X3 ECRH and EBWH via O-X-B mode conversion. The section 6.2 introduces TCV DML diagnostic. In section 6.3, it is shown how the plasma toroidal flux is linked to the plasma perpendicular kinetic energy. A model for the transfer function between the RF power and the plasma perpendicular kinetic energy is introduced and the oscillation analysis is presented, along with a system transfer identification method. In section 6.4, a new light is cast on earlier experimental results for X3 modulated ECH (MECH) in presence of X2 ECCD pre-heating, disclosing an important perturbation of the measurement by the sawtooth activity,

which was not revealed in the first analysis of these experiments. As important drawbacks are met for the X3 power absorption measurements, the method is tested in scenarios simpler to interpret, i.e. X2 MECH experiments, which are discussed in section 6.5. Modulated EBW heating experiments are then presented and discussed in section 6.6. Conclusions and outlooks are given in section 6.7.

6.2 TCV DML diagnostic

TCV is equipped with a diamagnetic loop (DML) diagnostic for the measurement of the plasma toroidal flux. A detailed presentation of the diagnostic system is given in [91], along with an exhaustive description of the analog and software signal processing. The important features of the system are summarized in this section.

6.2.1 DML hardware

The plasma contribution to the toroidal magnetic flux through a poloidal surface S is defined as

$$\Phi_{\rm pl} \equiv \int_S B_{\varphi \rm pl}\, {\rm d}S \qquad \text{with} \qquad B_{\varphi \rm pl} \equiv B_\varphi - B_{\varphi \rm v} \tag{6.2.1}$$

where B_φ is the total toroidal magnetic field, $B_{\varphi \rm pl}$ is the plasma contribution and $B_{\varphi \rm v}$ is the vacuum contribution provided by the toroidal field coils. The plasma toroidal flux $\Phi_{\rm pl}$ is also called "plasma diamagnetic flux" even though the net plasma effect can be either diamagnetic with $\text{sign}(B_{\varphi \rm pl}) = -\text{sign}(B_{\varphi \rm v})$ (for $\beta_{\rm p} > 1$) or paramagnetic with $\text{sign}(B_{\varphi \rm pl}) = \text{sign}(B_{\varphi \rm v})$ (for $\beta_{\rm p} < 1$) as it is seen in subsection 6.3.1.
In TCV, $\Phi_{\rm pl}$ is measured by the DML diagnostic consisting of four principal loops, as illustrated in figure 6.1:

- **Loop A** (also named DML2) is a single-turn loop tightly wound on the outer surface of the vacuum vessel. This loop was first meant for the compensation of the toroidal flux due to vessel image currents. It is now used as the default main diamagnetic loop instead of loop D since it is expected to undergo much smaller displacements relative to the vacuum vessel.

- **Loop B** is an 80-turn loop mounted on one of the 16 toroidal field coils in order to measure parasitic fluxes due to current diffusion in the toroidal coil.

- **Loop C** is an 80-turn loop meant for the compensation of the externally applied vacuum field from the toroidal coils.

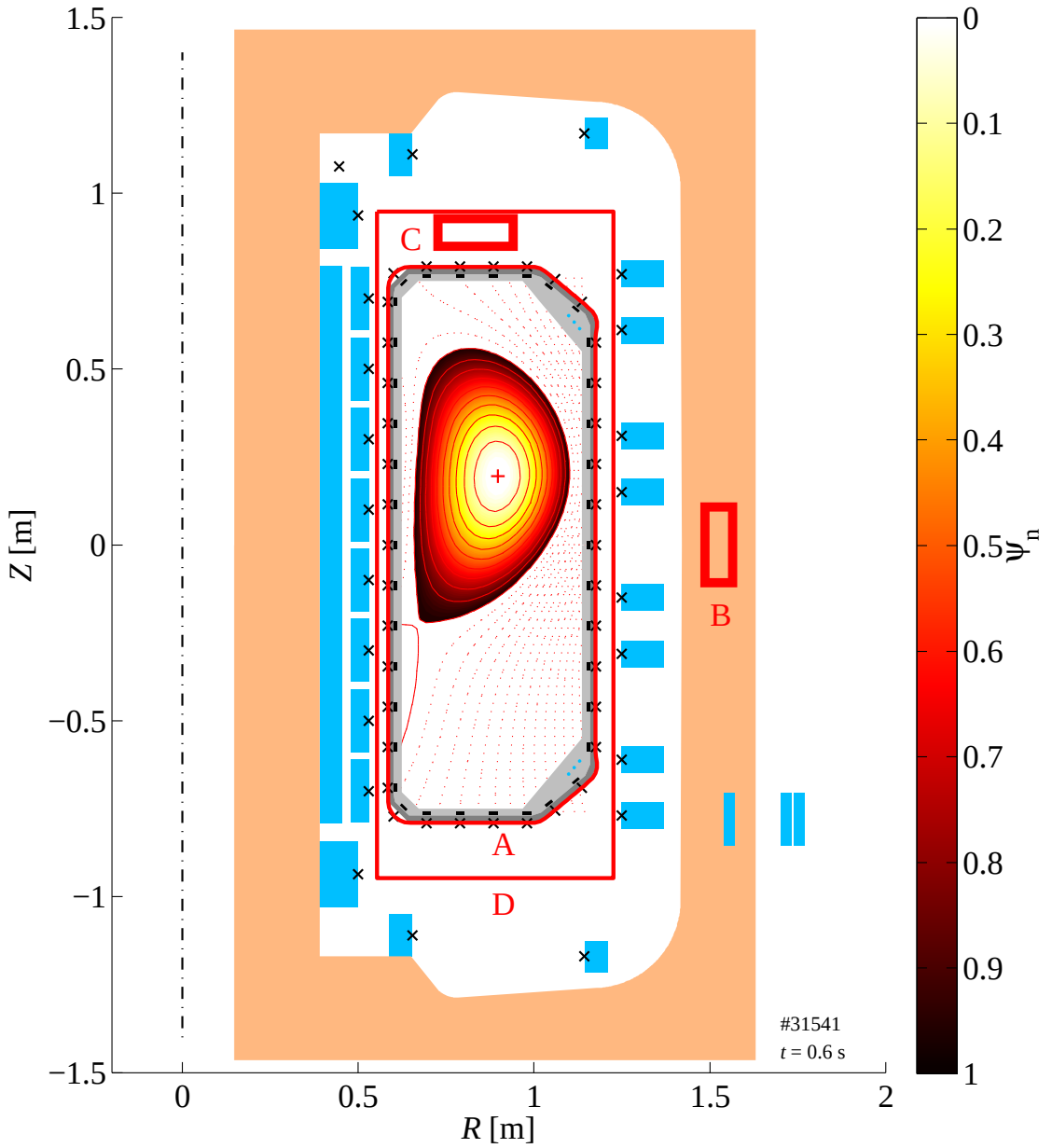

Figure 6.1: TCV DML loops. TCV poloidal cross section showing the DML diagnostic single-turn loops A and D (also called respectively DML2 and DML1) and multi-turn loops B and C, as well as one of the 16 toroidal field coils (orange), the Ohmic transformer coils and the poloidal field coils (light blue), along with the flux loops (×) and the magnetic probes (▮) as in figure 2.2. TCV shot #31541 at $t = 0.6\,\mathrm{s}$.

- **Loop D** (also named DML1) is a single-turn loop, mechanically independent from the vacuum vessel. It was first used as the main diamagnetic loop but is now used for the compensation of the vessel image currents.

All loops are located in TCV sector #16, with the loop B mounted on the toroidal field coil between sectors #1 and #16.

6.2.2 Signal processing and compensations

As it will be seen in subsection 6.3.1, the plasma toroidal flux Φ_{pl} to be measured with the DML diagnostic takes values between typically 0.4 mWb (at low plasma currents) and 40 mWb (at high plasma currents). However, the diamagnetic loop A (as well as loop D) also measures the flux produced by the toroidal field coils which is of the order of 2 Wb. A careful compensation of this external flux and other parasitic fluxes is thus needed.

Moreover, the study of fast modulated ECH (MECH) and of fast MHD activity like EMLs requires a DML diagnostic bandwidth extending up to frequencies of the order of 1 kHz. But TCV vacuum vessel is a one-piece conductor with low electrical resistance in both poloidal and toroidal directions for the passive stabilization of the vertical position of highly elongated plasmas. Fast variations of the plasma toroidal flux are thus screened by image currents induced in the conducting vacuum vessel, with a characteristic vessel time constant $\tau_v = 5.3$ ms [91]. A proper compensation of the fluxes produced by these vessel currents is then of primary importance to obtain adequate plasma toroidal flux measurements at high frequency, e.g. for the MECH applications which are the scope of this chapter.

The processing of the DML signal is performed as follows. In a first step before the signal digitalization, the raw voltages from loops A (DML2), C and D (DML1) are combined, amplified, integrated and filtered in order to subtract all toroidal fluxes which are not produced by the plasma. A set of 10 digital compensations (also called back-off signals) is then applied to the analog-corrected toroidal flux signal Φ_{DML2} from the DML2 loop (or Φ_{DML1} from the DML1 loop) in order to compensate for remaining parasitic fluxes. The subtraction of the total back-off flux Φ_{BO} results in a measurement of the plasma toroidal flux Φ_{pl} (also named DMLCOR)

$$\Phi_{pl} = \Phi_{DML2} - \Phi_{BO} \tag{6.2.2}$$

with an absolute accuracy of 0.05 mWb and a bandwidth of ~ 10 kHz [91].

The 10 software compensations are:

- **Compensation of residual parasitic *toroidal fluxes* from an imperfect analog compensation:** linear and non-linear terms for the toroidal coils current (VAR-TOR-LIN and FIX-TOR-NONLIN), one term for the vessel eddy currents (VAR-TOR-VESSEL), one term due to the presence of ferromagnetic material close to the DML loops (VAR-TOR-FERRO) and one term for the compensation of current diffusion in the toroidal field coils (FIX-TOR-DIFF);

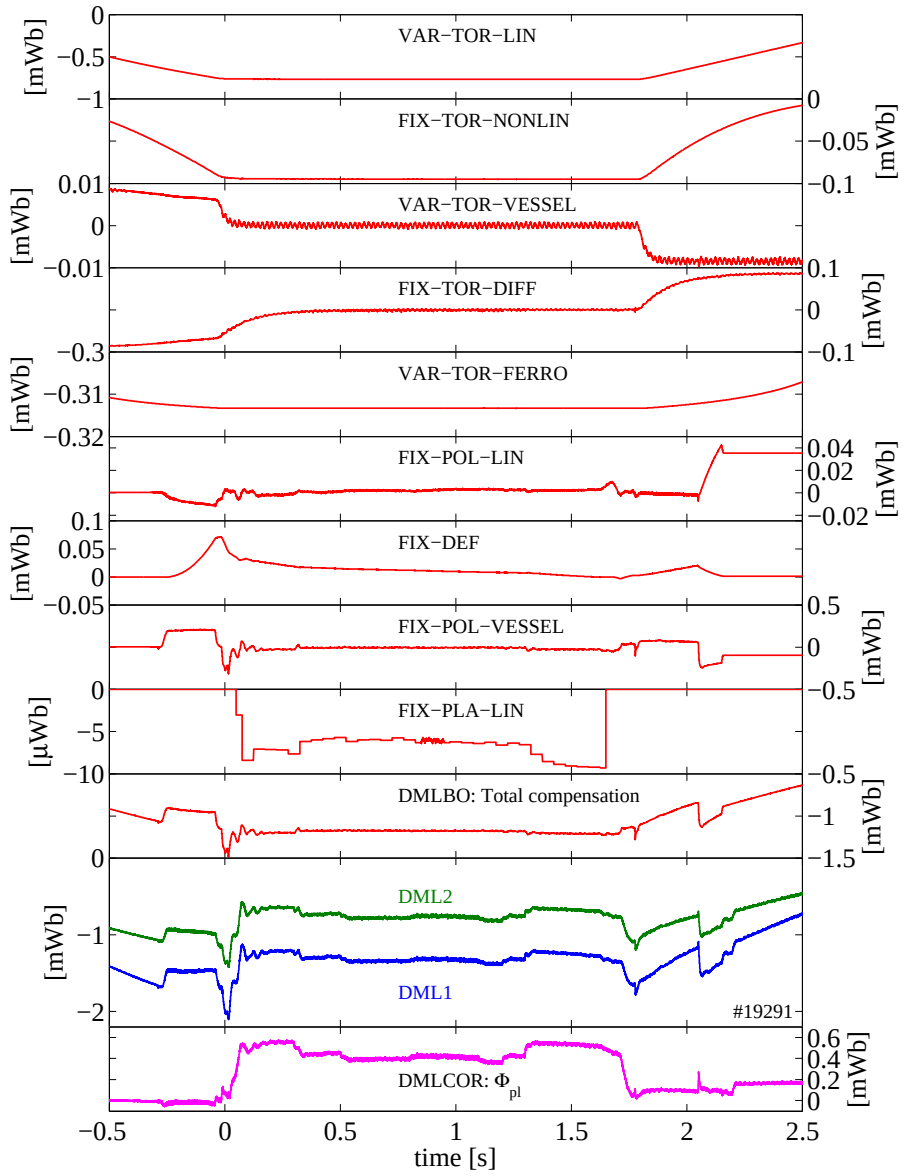

Figure 6.2: DML compensations and corrected signal. From top to bottom: the 9 software DML back-off signals calculated for the DML2 loop, the total back-off signal, the uncorrected plasma toroidal fluxes from DML1 and DML2 loops (blue and green), and the corrected plasma toroidal flux Φ_{pl} calculated from the DML2 loop signal. TCV shot #19291, see also figure 6.7.

- **Compensation of parasitic *poloidal fluxes* picked-up due to a slight misalignment of the main DML loop in the poloidal plane:** one term for the current in the 16 poloidal shaping coils and the Ohmic transformer coils (FIX-POL-LIN), one term for the vessel eddy currents (FIX-POL-VESSEL), one term due to the presence of large vessel ports near the DML loops (FIX-POL-PORT) and one term for the pick-up of poloidal flux produced by the plasma current itself (FIX-PLA-LIN). The FIX-POL-PORT term is now embedded in the FIX-POL-VESSEL term;

- **Compensation of flux variations due to a DML loop deformation:** one term for the mechanical and thermal stresses (FIX-DEF).

All software compensation signals listed above are plotted in figure 6.2 for a shot which is part of the X3 MECH frequency scan presented in section 6.4. Clearly, the total compensation signal is not negligible: during the discharge flattop, the sum of all 10 back-off corrections totalizes a higher amplitude ($|\Phi_{\mathrm{BO}}| > 1$ mWb) than the uncorrected toroidal plasma magnetic flux from DML2 loop ($|\Phi_{\mathrm{DML2}}| < 1$ mWb), such that the toroidal plasma flux measurement (DMLCOR) acquires its a proper sign only after the corrections are applied. Indeed, this plasma discharge has $\beta_{\mathrm{p}} < 1$ and $B_\varphi > 0$ such that one expects $\Phi_{\mathrm{pl}} > 0$, see equation (6.3.20).

6.3 DML signal analysis

6.3.1 MHD integral relations

In this subsection, one shows how the plasma toroidal flux Φ_{pl} defined in (6.2.1) and measured by the DML diagnostic is linked to the different plasma energies, and in particular to the perpendicular plasma kinetic energy $W_{\mathrm{kin}\perp}$. A full derivation of the MHD integral relations linking the various plasma energies is given in appendix B with the corresponding references.
Starting from the momentum conservation equation for an MHD equilibrium

$$\nabla \cdot \mathbb{T} = 0 \tag{6.3.1}$$

with the stress tensor

$$\mathbb{T} \equiv \rho_{\mathrm{m}} \mathbf{u}\mathbf{u} + \left(p_\perp + \frac{B^2}{2\mu_0} \right) \mathbb{I} - \sigma \frac{\mathbf{B}\mathbf{B}}{\mu_0} \tag{6.3.2}$$

and the anisotropy parameter

$$\sigma \equiv 1 - \frac{\mu_0 \left(p_\parallel - p_\perp \right)}{B^2}, \tag{6.3.3}$$

one can show that for a toroidally axisymmetric plasma the perpendicular kinetic energy

$$W_{\mathrm{kin}\perp} \equiv \frac{1}{2} \int_V 2 p_\perp \, \mathrm{d}V \tag{6.3.4}$$

is linked to the plasma toroidal magnetic energy

$$W_{\mathrm{M}} \equiv \int_V \frac{B_\varphi^2 - B_{\varphi \mathrm{v}}^2}{2\mu_0} \, \mathrm{d}V \tag{6.3.5}$$

through the relation

$$W_{\mathrm{kin}\perp} = \frac{1}{2}\left[S_1 + \delta_R S_2\right] - W_{\mathrm{rot}} + W_{\mathrm{rot}\varphi} - W_{\mathrm{M}} \tag{6.3.6}$$

where W_{rot} is the plasma fluid rotation energy defined as

$$W_{\mathrm{rot}} \equiv \int_V \frac{1}{2}\rho_{\mathrm{m}} u^2 \,\mathrm{d}V \tag{6.3.7}$$

with $\mathbf{u}$ the fluid rotation velocity and ρ_{m} the mass density. Here, $p_\parallel$ and $p_\perp$ are the pressures in the parallel and perpendicular directions to the total magnetic field, respectively. $B_{\varphi\mathrm{v}}$ is the vacuum contribution (produced by the tokamak coil system) to the total toroidal magnetic field B_φ. In equation (6.3.6), $W_{\mathrm{rot}\varphi}$ is the toroidal component of W_{rot}, and S_1 and S_2 are the (unnormalized) Shafranov integrals [92] given by

$$S_1 \equiv \frac{1}{\mu_0}\oint_{\partial V}\left[\frac{B_{\mathrm{p}}^2}{2}\hat{\mathbf{n}}\cdot\rho\hat{\boldsymbol{\rho}} - (\hat{\mathbf{n}}\cdot\mathbf{B}_{\mathrm{p}})(\mathbf{B}_{\mathrm{p}}\cdot\rho\hat{\boldsymbol{\rho}})\right]\,\mathrm{d}A \tag{6.3.8}$$

and

$$S_2 \equiv \frac{1}{\mu_0}\oint_{\partial V}\left[\frac{B_{\mathrm{p}}^2}{2}\hat{\mathbf{n}}\cdot R'\hat{\mathbf{R}} - (\hat{\mathbf{n}}\cdot\mathbf{B}_{\mathrm{p}})(\mathbf{B}_{\mathrm{p}}\cdot R'\hat{\mathbf{R}})\right]\,\mathrm{d}A. \tag{6.3.9}$$

Here, $\mathbf{B}_{\mathrm{p}}$ is the poloidal magnetic field, ρ is the radial coordinate of a polar coordinate system in the poloidal plane centered on the arbitrarily chosen major radius R', $\mathrm{d}A$ is the surface element on the boundary δV of the toroidal volume V encompassing the whole plasma volume V_{pl}, see figure B.1. The volume V is obtained by revolution of a poloidal surface S around the plasma vertical axis. Finally, $\hat{\mathbf{n}}$ is the normal unit vector on $\mathrm{d}A$ and δ_R is a normalized radial shift defined as

$$\delta_R \equiv \frac{R' - R_T}{R'} \qquad \text{with} \qquad R_T \equiv \frac{\displaystyle\int_S g 2\pi R \,\mathrm{d}S}{\displaystyle\int_S g 2\pi \,\mathrm{d}S} \tag{6.3.10}$$

where R_T is a major radius averaged on the plasma configuration and g is the weighting factor

$$g \equiv \rho u_\varphi^2 + p_\parallel + \frac{B_{\mathrm{p}}^2}{2\mu_0} - \frac{B_{\mathrm{p}}^2\left(p_\parallel - p_\perp\right)}{B^2} - \frac{B_\varphi^2 - B_{\varphi\mathrm{v}}^2}{2\mu_0}. \tag{6.3.11}$$

In the derivation of (6.3.6), it is assumed that the pressure, the fluid velocity and the plasma contribution to the toroidal field vanish outside the plasma: $B_\varphi = B_{\varphi\mathrm{v}}$, $p_\parallel = p_\perp = 0$ and $\mathbf{u} = 0$ in $V \setminus V_{\mathrm{pl}}$. Moreover, a small term associated to the pressure anisotropy is neglected even for anisotropic plasmas, see equations (B.4.9) and (B.4.10) in section B.4.1.

Of course, one can write an equation equivalent to (6.3.6) in terms of normalized plasma energies:

$$\beta_{\mathrm{p}\perp} = \frac{1}{2}\left[s_1 + \delta_R s_2\right] - w + w_\varphi - \mu \tag{6.3.12}$$

where $\beta_{\mathrm{p}\perp}$, s_1, s_2, w, w_φ and the diamagnetism μ are equal, respectively, to $W_{\mathrm{kin}\perp}$, S_1, S_2, W_{rot}, $W_{\mathrm{rot}\varphi}$ and W_{M} normalized by a factor $N \equiv 2\mu_0/V\bar{B}_{\mathrm{p}}^2$ with $\bar{B}_{\mathrm{p}}$ a contour-averaged poloidal field on the boundary of the poloidal surface S. In TCV LIUQE magnetic equilibrium reconstruction code, this normalization factor is evaluated in the cylindrical limit: $N = 4/(R_0\mu_0 I_\varphi^2)$ where $R_0 = 0.88$ m is TCV major radius, see table B.2.

Static plasma limit

In the limit of a static plasma, the fluid rotation energy vanishes ($W_{\mathrm{rot}} = 0$) and the relation (6.3.6) thus reduces to

$$W_{\mathrm{kin}\perp} = \frac{1}{2}\left[S_1 + \delta_R S_2\right] - W_{\mathrm{M}} \tag{6.3.13}$$

or

$$\beta_{\mathrm{p}\perp} = \frac{1}{2}\left[s_1 + \delta_R s_2\right] - \mu \tag{6.3.14}$$

in terms of normalized quantities. In TCV plasmas, both toroidal and poloidal fluid rotation velocities are of the order of $u \simeq 10$ km/s [93]. The energy stored in the macroscopic fluid rotation of a TCV deuterium plasma of major radius $R = 0.88$ m, minor radius $a = 0.25$ m and elongation $\kappa = 1.5$ (i.e. a volume $V \simeq 1.6$ m^3) with density $n = 1 \cdot 10^{20}$ m^{-3} is thus estimated to be

$$W_{\mathrm{rot}} \simeq \frac{1}{2} n m_{\mathrm{D}} V \left(u_\varphi^2 + u_\theta^2\right) \simeq 50 \text{ J} \tag{6.3.15}$$

where the electron fluid rotation energy is neglected in view of the small $m_{\mathrm{e}}/m_{\mathrm{i}}$ ratio. Assuming an homogeneous (isotropic) plasma pressure $p = 16$ kPa (corresponding to a temperature $T = 1$ keV) for both electrons and ions, the plasma perpendicular kinetic energy is

$$W_{\mathrm{kin}\perp} = 2 p_\perp V \simeq 50 \text{ kJ} \tag{6.3.16}$$

where the factor 2 comes from the contribution of both the electrons and the ions. The fluid rotation energy is thus typically 3 orders of magnitude smaller than the perpendicular kinetic energy and can be safely neglected. Of course, this assumption would break in presence of an external momentum source like neutral beam injection (NBI) heating. In this case, the fluid rotation energy must be accounted for in order to draw a proper kinetic energy measurement from the DML diagnostic.

Small diamagnetism approximation

In standard tokamak operation, the plasma contribution to the toroidal magnetic flux is small compared to the vacuum field contribution. (This is the so-called small diamagnetism approximation.) In this case one has

$$|B_{\varphi\mathrm{pl}}| = |B_\varphi - B_{\varphi\mathrm{v}}| \ll |B_{\varphi\mathrm{v}}| \qquad \text{small diamagnetism approximation} \tag{6.3.17}$$

where $B_{\varphi\mathrm{pl}}$ is the toroidal field produced by the plasma. The relation (6.3.13) further simplifies to

$$\boxed{W_{\mathrm{kin}\perp} \simeq \frac{1}{2}\left[S_1 + \delta_R S_2\right] - \frac{2\pi}{\mu_0} R B_{\varphi\mathrm{v}} \Phi_{\mathrm{pl}}} \tag{6.3.18}$$

where R is the major radius coordinate. The second term of this estimate of the perpendicular kinetic energy can be fully determined from magnetic measurements.

Cylindrical limit

In terms of normalized quantities, equation (6.3.13) writes:

$$\beta_{\mathrm{p}\perp} = \frac{1}{2}\left[s_1 + \delta_R s_2\right] - \mu. \tag{6.3.19}$$

In the cylindrical limit (straight cylinder with circular cross section), one has $\delta_R = 0$ and $s_1 = 2$ [94], the average poloidal field $\bar{B}_{\mathrm{p}}^2$ in the normalization factor N can be directly evaluated from Ampère's law (see subsection B.5.3), and the small diamagnetism appoximation yields

$$\Phi_{\mathrm{pl}} \simeq \frac{\mu_0^2 I_\varphi^2}{8\pi B_{\varphi\mathrm{v}}}(1 - \beta_{\mathrm{p}\perp}) \qquad \text{cylindrical, small diamagnetism.} \tag{6.3.20}$$

From this last relation, it is clear that Φ_{pl} has the sign of $B_{\varphi\mathrm{v}}$ when $\beta_{\mathrm{p}\perp} < 1$ and the opposite sign when $\beta_{\mathrm{p}\perp} > 1$. In other words, the presence of the plasma increases (respectively decreases) the toroidal magnetic field amplitude when $\beta_{\mathrm{p}} < 1$ (respectively > 1). In the first case the plasma has a net paramagnetic effect, and in the second case the plasma has a net diamagnetic effect.

Both situations are illustrated in figures 6.3 and 6.4 for plasmas with $B_{\varphi\mathrm{v}} > 0$. The diamagnetic plasma is a low-current X2-heated L-mode with an electron internal transport barrier (eITB). The presence of the plasma decreases the toroidal magnetic field by up to $B_{\varphi\mathrm{pl}} \simeq -3.5$ mT in the plasma center. The paramagnetic plasma is a high-current high-density EBW-heated H-mode. In this case, the plasma contribution increases the toroidal magnetic field by up to $B_{\varphi\mathrm{pl}} \simeq +33$ mT in the plasma center. The resulting radial excursions of the second harmonic cold electron

cyclotron resonance for the frequency $\omega/2\pi = 82.7$ GHz at the magnetic axis vertical position are of the order of $\Delta R \simeq -2$ mm and $\Delta R \simeq +20$ mm, for the paramagnetic and the diamagnetic plasmas respectively.

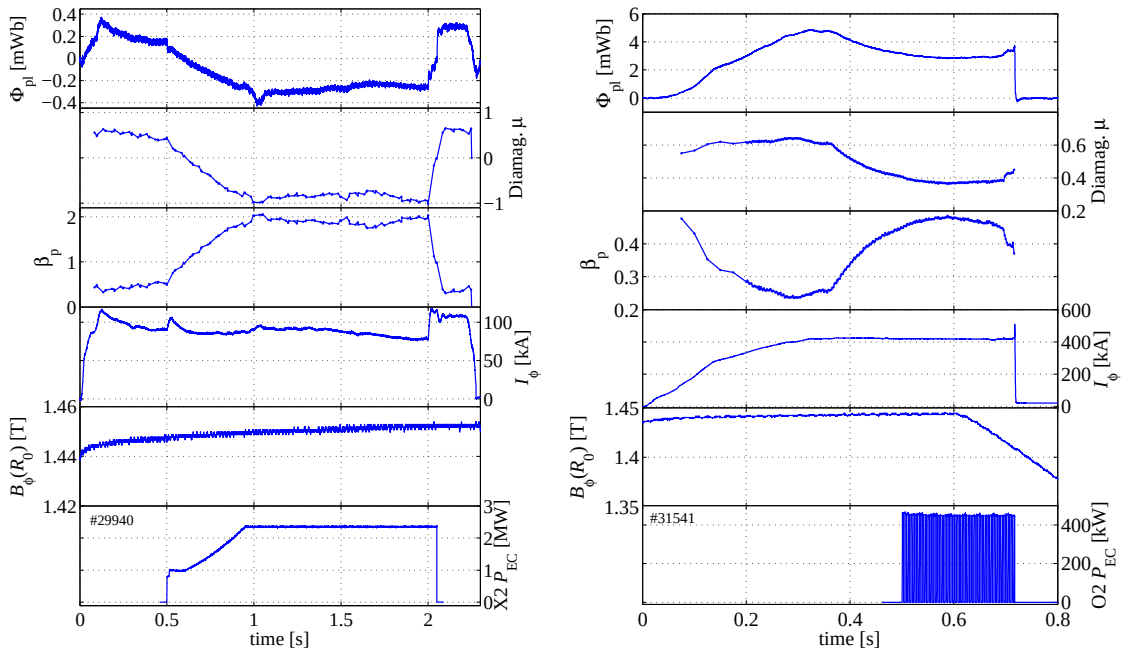

(a) Diamagnetic plasma. X2-heated L-mode plasma with eITB. #29940.

(b) Paramagnetic plasma. H-mode plasma with EBH.#31541.

Figure 6.3: Diamagnetic and paramagnetic plasmas toroidal flux. From top to bottom: Plasma toroidal flux $\Phi_{\rm pl}$, diamagnetism μ, poloidal beta $\beta_{\rm p}$, plasma current I_φ and vacuum toroidal field B_φ at $R = R_0$ for (a) the diamagnetic L-mode plasma and (b) the paramagnetic H-mode plasma introduced in figure 6.4. The L-mode plasma becomes diamagnetic, i.e. $\Phi_{\rm pl} < 0$ and $\mu < 0$, between $t = 0.6$ s and $t = 2$ s, when X2 ECH is injected and the plasma pressure is increased above $\beta_{\rm p} > 1$. But for such a low plasma current ($I_\varphi < 100$ kA), the plasma toroidal flux remains very small ($|\Phi_{\rm pl}| < 0.4$ mWb).

It is also clear from equation (6.3.20) that the amplitude of the plasma toroidal flux has a quadratic dependence on the plasma current I_φ. At the highest TCV plasma current ($I_\varphi = 1$ MA, $B_{\varphi \rm v} = 1.45$ T), the plasma toroidal flux is of the order $\Phi_{\rm pl} \simeq 40$ mWb. At low plasma current ($I_\varphi = 100$ kA, $B_{\varphi \rm v} = 1.45$ T), the plasma toroidal flux is of the order $\Phi_{\rm pl} \simeq 0.40$ mWb. The plasma diamagnetism is thus very small compared to the vacuum magnetic flux produced by the toroidal field coils ($\Phi_{\rm v} \simeq 2$ Wb) and the small diamagnetism approximation is valid for the case of TCV plasmas. At very low plasma currents ($I_\varphi \leq 100$ kA), a relevant measurement of $\Phi_{\rm pl}$ may even become difficult.

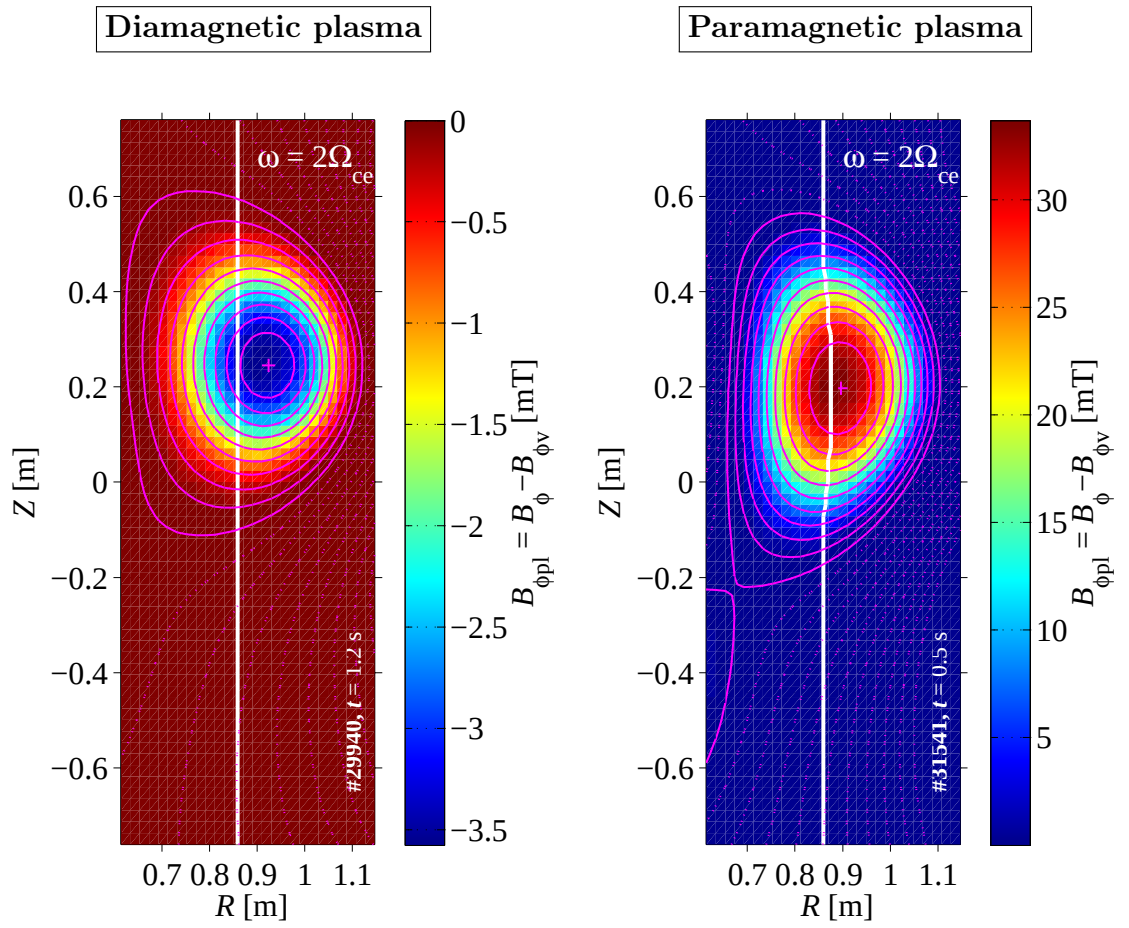

(a) Plasma toroidal field $B_{\varphi \mathrm{pl}}$.

(b) Plasma toroidal field $B_{\varphi \mathrm{pl}}$.

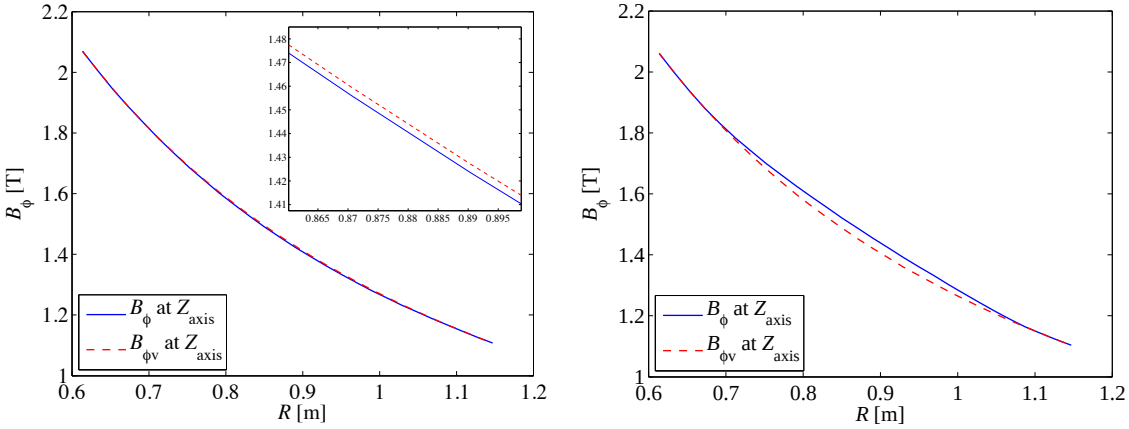

(c) Profiles of total toroidal field B_φ (blue) and vacuum toroidal field $B_{\varphi \mathrm{v}}$ (red dashed).

(d) Profiles of total toroidal field B_φ (blue) and vacuum toroidal field $B_{\varphi \mathrm{v}}$ (red dashed).

Figure 6.4: Diamagnetic and paramagnetic plasmas. (a)-(b) Poloidal map of the plasma toroidal field $B_{\varphi \mathrm{pl}} = B_{\varphi \mathrm{v}} - B_{\varphi \mathrm{v}}$ with superimposed normalized poloidal flux contours (magenta) and magnetic axis position (+). The thick line is the second harmonic cold EC resonance for the frequency $\omega/2\pi = 82.7$ GHz. (c)-(d) Profiles of the total and vacuum toroidal fields at $Z = Z_{\mathrm{axis}}$. The relevant physical traces of the diamagnetic plasma with $\beta_{\mathrm{p}} > 1$ (left column) and the paramagnetic plasma with $\beta_{\mathrm{p}} < 1$ (right column) are given in figure 6.3. Both plasmas have $B_{\varphi \mathrm{v}} > 0$. TCV shots #29940 at $t = 1.2$ s and #31541 at $t = 0.5$ s.

6.3.2 Plasma response modeling

Energy evolution equations

In the sequel of this text, the "kin" index of the kinetic energy variables is dropped for the sake of a lighter notation. A model for the response of the perpendicular kinetic energy (6.3.18) to modulations in the auxiliary power is derived from the evolution equations for the perpendicular and parallel kinetic energies of a three component plasmas, i.e. bulk isotropic ions, bulk isotropic electrons and anisotropic RF-heated electrons:

$$\frac{\mathrm{d}W_\perp}{\mathrm{d}t} = -\frac{W_\perp}{\tau_{\mathrm{inc}}} + \eta P_{\mathrm{RF}} - \frac{2}{3}\frac{1}{\tau_{\mathrm{a}}^{\mathrm{e}*}}\left(\frac{1}{2}W_\perp - W_\parallel\right) \tag{6.3.21}$$

$$\frac{\mathrm{d}W_\parallel}{\mathrm{d}t} = -\frac{W_\parallel}{\tau_{\mathrm{inc}}} + P_{\mathrm{OH}} + \frac{2}{3}\frac{1}{\tau_{\mathrm{a}}^{\mathrm{e}*}}\left(\frac{1}{2}W_\perp - W_\parallel\right). \tag{6.3.22}$$

Here, it is assumed that the Ohmic power P_{OH} and the absorbed RF power P_{RF} increase mainly the parallel and perpendicular energies, respectively, with η the RF power absorption efficiency ($0 \leq \eta \leq 1$). According to a single-electron model [3], the perpendicular power absorption is valid for pure X-mode heating (i.e. perpendicular wave propagation without any ECCD fraction).

The first term on the right-hand side of both (6.3.21) and (6.3.22) is an effective loss term accounting for transport and radiation losses. The energy incremental confinement time τ_{inc} is defined as [90]

$$\tau_{\mathrm{inc}} \equiv \frac{\partial W}{\partial\left(P_{\mathrm{tot}} - \frac{\mathrm{d}W}{\mathrm{d}t}\right)} \tag{6.3.23}$$

where W is the total plasma kinetic energy

$$W = W_\perp + W_\parallel \tag{6.3.24}$$

and $P_{\mathrm{tot}} = \eta P_{\mathrm{RF}} + P_{\mathrm{OH}} + \cdots$ is the sum of all external heating powers multiplied by their corresponding absorption coefficients. The incremental energy confinement time is shorter than the global energy confinement time

$$\tau_{\mathrm{inc}} < \tau_E \equiv \frac{W}{\left(P_{\mathrm{tot}} - \frac{\mathrm{d}W}{\mathrm{d}t}\right)}. \tag{6.3.25}$$

The incremental confinement time is assumed to be identical in both perpendicular and parallel directions.

The last term on the right-hand side of both (6.3.21) and (6.3.22) treats of the energy transfer from the perpendicular direction to the parallel direction due to the Coulomb collisions of the anisotropic heated electrons on all species (including the

self-collisions). This term is derived in appendix C taking the appropriate moments of the Fokker-Planck equation (neglecting collective effects) with bi-Maxwellian velocity distribution functions. This model is valid for the perpendicular relaxation of a fully ionized plasmas with one anisotropic constituent. The characteristic energy anisotropy relaxation time of the hot electrons by collisions on themselves, the bulk electrons and the bulk ions writes

$$\tau_{\mathrm{a}}^{\mathrm{e}^*} = \left[\frac{1}{\tau_{\mathrm{a}}^{\mathrm{e}^*/\mathrm{e}^*}} + \frac{1}{\tau_{\mathrm{a}}^{\mathrm{e}^*/\mathrm{e}}} + \frac{1}{\tau_{\mathrm{a}}^{\mathrm{e}^*/\mathrm{i}}}\right]^{-1}. \tag{6.3.26}$$

and is a complicated function of the temperature anisotropy. Here, we assume that the level of the anisotropy and thus $\tau_{\mathrm{a}}^{\mathrm{e}^*}$ are maintained constant by the time-averaged ECRH power, neglecting the effect of the power amplitude modulation.
In general, the incremental confinement time τ_{inc} also depends on the heating power. The RF power absorption coefficient η can as well depend on P_{RF} and ω via the plasma temperature, in particular for the cases where $\eta \leq 1$ is expected, e.g. high harmonic ECH (like X3 in TCV) and ICRH [90]. Here, $1/\tau_{\mathrm{inc}}$ and η are assumed to be independent of the mean RF power level and equations (6.3.21)-(6.3.22) are linear in P_{RF} and ω.

Transfer functions

In modulated ECH experiments, the injected RF power is composed of sinusoidally modulated part $\tilde{P}_{\mathrm{RF}}(t)$ at the frequency $f = \omega/2\pi$, superimposed on a stationary part $\langle P_{\mathrm{RF}} \rangle$:

$$P_{\mathrm{RF}}(t) = \langle P_{\mathrm{RF}} \rangle_t + \tilde{P}_{\mathrm{RF}}(t) \qquad \text{with} \qquad \tilde{P}_{\mathrm{RF}}(t) = \hat{P}_{\mathrm{RF}} \mathrm{e}^{\mathrm{i}\omega t} \tag{6.3.27}$$

where $\hat{P}_{\mathrm{RF}}$ is a complex amplitude carrying both phase and amplitude informations:

$$\hat{P}_{\mathrm{RF}} = |\hat{P}_{\mathrm{RF}}| \mathrm{e}^{\mathrm{i}\phi_{\mathrm{RF}}}. \tag{6.3.28}$$

Of course, the RF power excitation is often not a pure monochromatic sinusoid but rather a sum of N sinusoids at different frequencies

$$\tilde{P}_{\mathrm{RF}}(t) = \sum_{n=1}^{N} \hat{P}_n \mathrm{e}^{\mathrm{i}\omega_n t} \tag{6.3.29}$$

where $\hat{P}_n$ is the complex amplitude at the angular frequency ω_n. For example, in most of the MECH experiments presented in this work, the EC power is modulated with a square waveform with fundamental angular frequency ω and a 50% duty-cycle. In this case, mainly the odd harmonic numbers $\omega_n = n\omega$ with $n = 1, 3, 5, \ldots$ are excited.

Consistently with the linear equations (6.3.21) and (6.3.22), the plasma is assumed to be a linear system. The RF power modulation thus induces a plasma response (i.e. $W_\perp(t)$, $W_\parallel(t)$ and $P_{\mathrm{OH}}(t)$) of the same form and at the same frequency, superimposed on a stationary or slowly drifting signal. The energy conservation equations (6.3.21) and (6.3.22) become

$$\mathrm{i}\omega\hat{W}_\perp = -\frac{\hat{W}_\perp}{\tau_{\mathrm{inc}}} + \eta\hat{P}_{\mathrm{RF}} - \frac{1}{\tau_{\mathrm{a}}}\left[\frac{\hat{W}_\perp}{2} - \hat{W}_\parallel\right] \tag{6.3.30}$$

$$\mathrm{i}\omega\hat{W}_\parallel = -\frac{\hat{W}_\parallel}{\tau_{\mathrm{inc}}} + \hat{P}_{\mathrm{OH}} + \frac{1}{\tau_{\mathrm{a}}}\left[\frac{\hat{W}_\perp}{2} - \hat{W}_\parallel\right]. \tag{6.3.31}$$

where we have defined $1/\tau_{\mathrm{a}} \equiv 2/(3\tau_{\mathrm{a}}^{\mathrm{e}^*})$ for the sake of simplicity. If the RF power excitation contains several components at different frequencies ω_n like in (6.3.29), the linearity of equations (6.3.30) and (6.3.31) ensures that such a system can be written for each angular frequency ω_n.

An expression for $\hat{W}_\parallel$ is obtained from equation (6.3.31):

$$\hat{W}_\parallel = \frac{\hat{W}_\perp/2\tau_{\mathrm{a}} + \hat{P}_{\mathrm{OH}}}{\mathrm{i}\omega + 1/\tau_{\mathrm{inc}} + 1/\tau_{\mathrm{a}}}. \tag{6.3.32}$$

Assuming the Ohmic power is small compared to the perpendicular kinetic energy modulation ($|\hat{P}_{\mathrm{OH}}| \ll |\hat{W}_\perp/2\tau_{\mathrm{a}}|$), the latter expression is inserted in equation (6.3.30) to retrieve an expression for $\hat{W}_\perp$:

$$\hat{W}_\perp\left[\mathrm{i}\omega + \frac{1}{\tau_{\mathrm{inc}}} + \frac{1}{2\tau_{\mathrm{a}}} - \frac{\tau_{\mathrm{inc}}}{2\tau_{\mathrm{a}}\left(\mathrm{i}\omega\tau_{\mathrm{a}}\tau_{\mathrm{inc}} + \tau_{\mathrm{a}} + \tau_{\mathrm{inc}}\right)}\right] = \eta\hat{P}_{\mathrm{RF}}. \tag{6.3.33}$$

By definition, the system transfer function at the modulation frequency is the ratio of the complex amplitudes of the perpendicular kinetic energy and the RF power modulation:

$$H(\omega) \equiv \frac{\hat{W}_\perp}{\hat{P}_{\mathrm{RF}}} = \left|\frac{\hat{W}_\perp}{\hat{P}_{\mathrm{RF}}}\right| \mathrm{e}^{i\left(\phi_{W_\perp} - \phi_{\mathrm{RF}}\right)}. \tag{6.3.34}$$

The above model yields a transfer function of the form

$$H_2 \equiv \eta\frac{2\tau_{\mathrm{inc}}\left(\tau_{\mathrm{a}} + \tau_{\mathrm{inc}}\right) + 2\tau_{\mathrm{a}}\tau_{\mathrm{inc}}^2(\mathrm{i}\omega)}{2\tau_{\mathrm{a}} + 3\tau_{\mathrm{inc}} + \left[4\tau_{\mathrm{a}}\tau_{\mathrm{inc}} + 3\tau_{\mathrm{inc}}^2\right](\mathrm{i}\omega) + 2\tau_{\mathrm{a}}\tau_{\mathrm{inc}}^2(\mathrm{i}\omega)^2}. \tag{6.3.35}$$

In the limit of very small anisotropy relaxation time compared to the modulation angular period $\tau = 1/\omega$, the transfer function H_2 reduces to

$$H_2 \xrightarrow[\tau_{\mathrm{a}}\omega\to 0]{} H_1 \equiv \frac{2}{3}\frac{\eta}{\frac{1}{\tau_{\mathrm{inc}}} + \mathrm{i}\omega} \tag{6.3.36}$$

which is valid only when both τ_{inc} and $1/\omega$ are much greater than τ_{a}. The factor 2/3 comes from the fact that H_1 is a transfer function between the RF power and the

perpendicular (not the total) kinetic energy, see definition (6.3.34). The expression (6.3.36) for H_1 can actually be derived from the energy conservation equation for plasma with isotropic temperatures

$$\frac{\mathrm{d}W}{\mathrm{d}t} = -\frac{W}{\tau_{\mathrm{inc}}} + \eta P_{\mathrm{RF}} + P_{\mathrm{OH}} \tag{6.3.37}$$

noting that $W = 3/2 W_\perp$ and neglecting the Ohmic power modulation compared to the RF power modulation ($|\hat{P}_{\mathrm{OH}}| \ll |\eta \hat{P}_{\mathrm{RF}}|$).
The transfer function H_1 can be further simplified assuming a very long confinement time compared to the modulation period:

$$H_1 \xrightarrow[\tau_{\mathrm{inc}}\omega \to \infty]{} H_0 \equiv \frac{2}{3}\frac{\eta}{\mathrm{i}\omega} \tag{6.3.38}$$

which is valid for $1/\tau_{\mathrm{inc}} \ll \omega \ll 1/\tau_{\mathrm{a}}$. The simple transfer function H_0 can be directly derived from the energy conservation equation for isotropic plasma, assuming negligible transport and radiation losses, as well as a negligible Ohmic power modulation compared to the RF power modulation ($|\hat{P}_{\mathrm{OH}}| \ll |\eta \hat{P}_{\mathrm{RF}}|$):

$$\frac{\mathrm{d}W}{\mathrm{d}t} = \eta P_{\mathrm{RF}} + P_{\mathrm{OH}}. \tag{6.3.39}$$

Another important limit of the transfer function H_2 is obtained for very high modulation angular frequency of the RF power amplitude, i.e. when both the anisotropy relaxation time τ_{a} and the incremental confinement time τ_{inc} are large compared to a modulation period:

$$H_2 \xrightarrow[\omega \to \infty]{} \frac{\eta}{\mathrm{i}\omega}. \tag{6.3.40}$$

A plot of the model transfer function H_2 for the perpendicular kinetic energy response to RF heating is given in figures 6.5 and 6.6, along with its limits H_1 and H_0 for typical values of the physical parameters: $\eta = 0.9$, $\tau_{\mathrm{inc}} = 5$ ms and $\tau_{\mathrm{a}} = 0.3$ ms. At large modulation frequency $\omega \gg 1/\tau_{\mathrm{a}}$, the phase and amplitude of the model transfer function H_2 saturate at $\phi_{W_\perp} - \phi_{\mathrm{RF}} = -90°$ and $|\omega H| = \eta$, respectively. Clearly, both H_1 and H_0 models assuming isotropic plasma are not valid in this frequency domain. At such high frequencies, the DML diagnostic sees an anisotropic plasma with all the absorbed RF power stored in the perpendicular direction. Assuming an isotropic electron distribution function would yield an overestimation of the absorption coefficient by a factor 3/2.
At low modulation frequency $\omega \ll 1/\tau_{\mathrm{inc}}$, the model transfer function H_1 is clearly a good approximation for H_2. Conversely, using the model H_0 at such low excitation frequencies where energy confinement losses cannot be neglected would yield a

dramatic underestimation of the absorption coefficient η. The transfer function H_0 has a constant phase $\phi_{W_\perp} - \phi_{\mathrm{RF}} = -90°$ and its amplitude approaches $|H_2|$ only in a very narrow angular frequency window $1/\tau_{\mathrm{inc}} \ll \omega \ll 1/\tau_{\mathrm{a}}$ where both the confinement losses and the plasma anisotropy can be neglected.

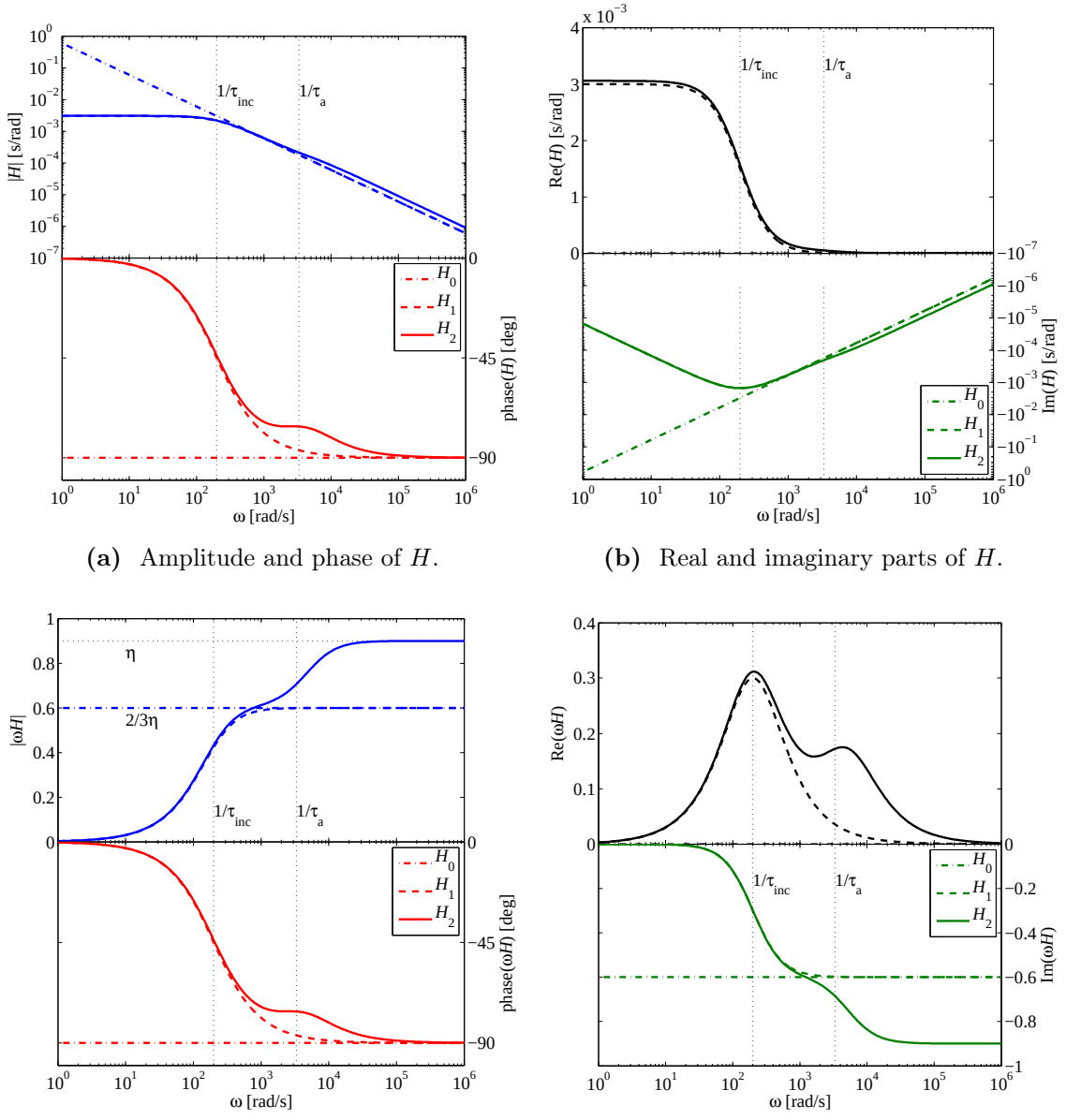

(a) Amplitude and phase of H.

(b) Real and imaginary parts of H.

(c) Amplitude and phase of ωH.

(d) Real and imaginary parts of ωH.

Figure 6.5: Perpendicular kinetic energy transfer function. (a,c) Amplitude and phase, (b,d) real and imaginary parts of the model transfer function H_2 (solid curves) for the perpendicular kinetic energy response to RF heating as a function of the RF power modulation angular frequency ω, calculated for $\eta = 0.9$, $\tau_{\mathrm{inc}} = 5$ ms and $\tau_{\mathrm{a}} = 0.3$ ms. H_1 (dashed curves) is the limit of H_2 for $\tau_{\mathrm{a}}\omega \to 0$ and H_0 (dash-dotted curves) is the additional limit of H_1 for $\tau_{\mathrm{inc}}\omega \to \infty$. The angular frequencies $1/\tau_{\mathrm{inc}}$ and $1/\tau_{\mathrm{a}}$ and the absorption coefficient η are indicated by dotted lines. At high modulation frequency, the amplitude and phase of ωH_2 saturate at η and $-90°$, respectively.

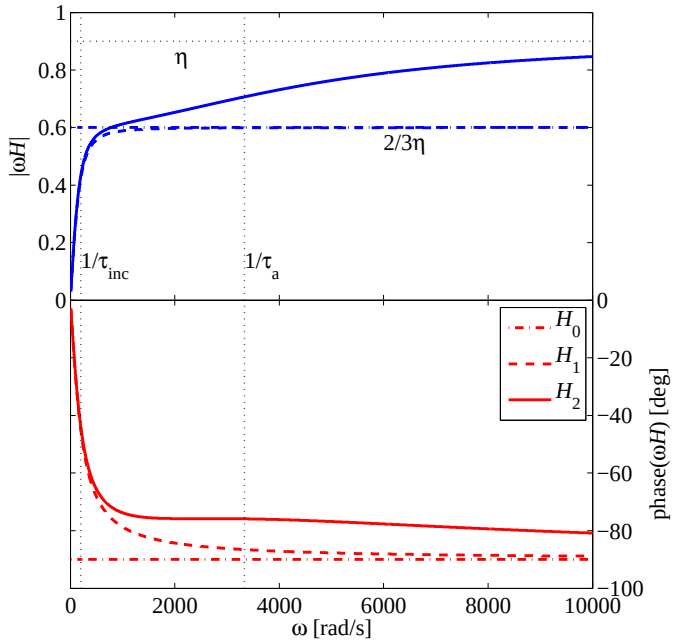

(a) Amplitude and phase of ωH.

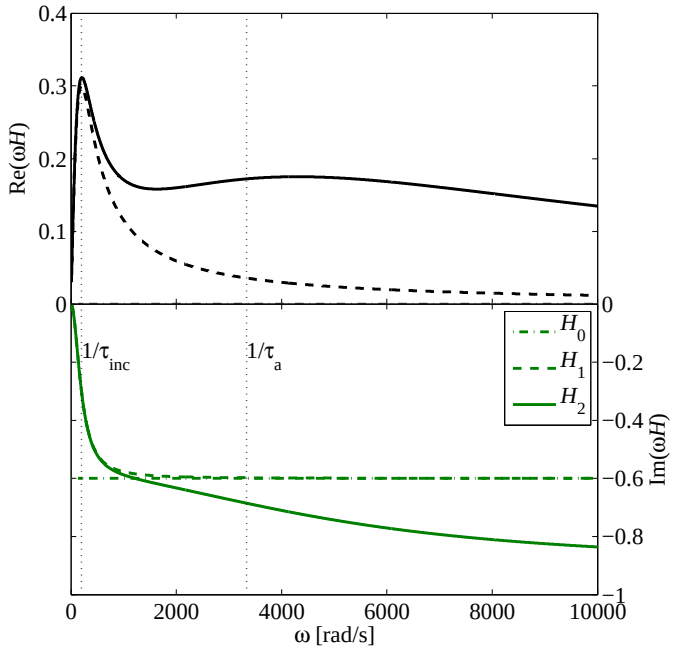

(b) Real and imaginary parts of ωH.

Figure 6.6: Perpendicular kinetic energy transfer function. (a) Amplitude and phase, (b) real and imaginary parts of the model transfer function H_2 (solid curves) for the perpendicular kinetic energy response to RF heating as a function of the RF power modulation angular frequency ω, calculated for $\eta = 0.9$, $\tau_{\rm inc} = 5$ ms and $\tau_{\rm a} = 0.3$ ms. H_1 (dashed curves) is the limit of H_2 for $\tau_{\rm a}\omega \to 0$ and H_0 (dash-dotted curves) is the additional limit of H_1 for $\tau_{\rm inc}\omega \to \infty$. The angular frequencies $1/\tau_{\rm inc}$ and $1/\tau_{\rm a}$ and the absorption coefficient η are indicated by dotted lines. At high modulation frequency, the amplitude and phase of ωH_2 saturate at η and $-90°$, respectively.

6.3.3 Oscillation analysis

Harmonic response identification

In order to evaluate the experimental transfer function (6.3.34) and compare it to the H_2, H_1 and H_0 models, the complex amplitudes of the reference modulated RF power and of the perpendicular kinetic energy need to be extracted from the experimental traces at the RF power modulation frequency. For the perpendicular kinetic energy, the simple relation (6.3.18) is used:

$$\hat{W}_\perp \simeq -\frac{2\pi}{\mu_0}(\widehat{RB_{\varphi \mathrm{v}}\Phi_{\mathrm{pl}}}) \tag{6.3.41}$$

where it is assumed that the modulation of the magnetic equilibrium (that is $\hat{S}_1$ and $\widehat{\delta_R S_2}$) can be neglected in comparison to the plasma toroidal flux modulation. This assumption needs to be checked for each experiment. The complex amplitude $\hat{S}(\omega)$ at the angular frequency ω of any experimental signal $S(t)$ can be estimated by a simple Fourier transform:

$$\hat{S}(\omega) = \int_{-\infty}^{+\infty} S(t)\mathrm{e}^{\mathrm{i}\omega t}\mathrm{d}t. \tag{6.3.42}$$

But in MECH experiments, the number of cycles available for the oscillation analysis is finite and not necessarily integer which will cause truncation problems in a standard Fourier analysis. Moreover, the fast modulation of the plasma toroidal flux induced by the EC power modulation is often superimposed on a slow drift of the signal which will strongly bias the Fourier components of the signal, in particular if the number of modulation cycles is small. A harmonic response identification method (HRIM) accounting for these effects is thus used to extract the complex amplitudes $\hat{W}_\perp$ and $\hat{P}_{\mathrm{RF}}$. The HRIM method is presented in subsection 5.2.1.

Power absorption estimation

Once the complex amplitudes $\hat{W}_\perp$ and $\hat{P}_{\mathrm{RF}}$ are extracted from the DML signal and the RF reference trace, respectively, the experimental transfer function H is calculated with (6.3.34):

$$\boxed{H(\omega) = \frac{\hat{W}_\perp}{\hat{P}_{\mathrm{RF}}} \simeq -\frac{2\pi}{\mu_0}\frac{\widehat{RB_{\varphi \mathrm{v}}\Phi_{\mathrm{pl}}}}{\hat{P}_{\mathrm{RF}}}.} \tag{6.3.43}$$

In the frame of the plasma response model derived in subsection 6.3.2, there are then three ways of estimating the RF power absorption coefficient η from H.

- If the modulation frequency is high enough ($\omega \gg 1/\tau_a$), the phase of the perpendicular kinetic energy response relative to the RF power excitation tends to $\phi_{W_\perp} - \phi_{RF} = -90°$ and the power absorption coefficient can be directly estimated from (6.3.40) using the H_2 model:

$$\eta \simeq \omega|H| = \omega\frac{|\hat{W}_\perp|}{|\hat{P}_{RF}|} \simeq \omega\frac{2\pi}{\mu_0}\frac{|\widehat{RB_{\varphi v}\Phi}_{pl}|}{|\hat{P}_{RF}|} \tag{6.3.44}$$

  However, according to our estimation of the anisotropy relaxation time $\tau_a = 0.3$ ms, this method requires modulation frequencies of the order of $f = 1$ kHz and such experiments may be limited by the DML diagnostic bandwidth and a low signal to noise ratio.

- If the angular frequency window between $1/\tau_{inc}$ and $1/\tau_a$ is broad enough, one can try to find a modulation frequency such that the plasma response phase tends to $-90°$. The power absorption coefficient can then be directly inferred from (6.3.38) using the H_0 model:

$$\eta \simeq \frac{3}{2}\omega|H| \simeq \omega\frac{3\pi}{\mu_0}\frac{|\widehat{RB_{\varphi v}\Phi}_{pl}|}{|\hat{P}_{RF}|} \tag{6.3.45}$$

  In our example, we estimate $\tau_{inc} = 5$ ms and $\tau_a = 0.3$ ms and the corresponding modulation frequency domain is delimited by $1/\tau_{inc} \sim 200$ rad/s $\ll \omega \ll 1/\tau_a \sim 3300$ rad/s, or 30 Hz $\ll f \ll 530$ Hz.

- A robust way to estimate the power absorption coefficient is to repeat the MECH experiment for several modulation angular frequencies ω in order to scan the plasma frequency response $H(\omega)$. A model transfer function (e.g. H_2 or H_1 at low frequency) is then fitted on the experimental $H(\omega)$ to extract the physical parameters τ_{inc}, τ_a and η. This method requires several plasma discharges for the modulation frequency scan but it allows the detection of any singularity in the plasma frequency response to MECH.

Transfer function fitting

A method for the fitting of experimental frequency response measurement is proposed in [95] and in appendix A.2 of referece [81]. The goal of this system transfer identification (STI) is to find a rational function

$$\bar{H}(\omega) = \frac{\sum_{m=0}^{M} b_m(i\omega)^m}{\sum_{n=0}^{N} a_n(i\omega)^n} = \frac{B(i\omega)}{A(i\omega)} \tag{6.3.46}$$

of two polynomials $A(\mathrm{i}\omega)$ and $B(\mathrm{i}\omega)$ with real coefficients a_n and b_n (with $a_N = 1$) such that it minimizes the square of the total error modulus

$$\sigma^2 = \frac{1}{K}\sum_{k=0}^{K} e_k * e_k \tag{6.3.47}$$

where

$$e_k \equiv \bar{H}(\omega_k) - H(\omega_k) \tag{6.3.48}$$

is the error of the fitted transfer function $\bar{H}$ with respect to the experimental transfer function H for the k measurement at ω_k, and e_k* is the complex conjugate of e_k.

6.3.4 Summary

In TCV, the plasma toroidal flux Φ_{pl} is measured using the DML diagnostic. This quantity is linked to the perpendicular kinetic energy $W_\perp$ by the simple relation

$$W_\perp \simeq \frac{1}{2}\left[S_1 + \delta_R S_2\right] - \frac{2\pi}{\mu_0} R B_{\varphi \mathrm{v}} \Phi_{\mathrm{pl}} \tag{6.3.49}$$

where the following assumptions were made and verified for TCV plasmas:

- ✓ Quasi-static plasma: $W_{\mathrm{rot}} \ll W_{\mathrm{kin}\perp}$.
- ✓ Small plasma diamagnetism: $|B_\varphi - B_{\varphi \mathrm{v}}| \ll B_{\varphi \mathrm{v}}$.

In modulated ECH experiments, the experimental kinetic energy frequency response is evaluated by the ratio of complex amplitudes at the modulation angular frequency ω:

$$H(\omega) = \frac{\hat{W}_\perp}{\hat{P}_{\mathrm{RF}}} \simeq -\frac{2\pi}{\mu_0}\frac{\widehat{R B_{\varphi \mathrm{v}} \Phi_{\mathrm{pl}}}}{\hat{P}_{\mathrm{RF}}} \tag{6.3.50}$$

where it is assumed that

- ⊗ the modulation of Shafranov's surface integrals is negligible: $|\hat{S}_1| \ll |\hat{W}_\perp|$ and $|\widehat{\delta_R S_2}| \ll |\hat{W}_\perp|$. This assumption has to be checked for each experiment.

In order to estimate the RF power absorption coefficient η, the experimental transfer function can be fitted with the model H_2 (6.3.35) derived from the linearized evolution equations for the perpendicular and parallel kinetic energies assuming:

- ⊗ A negligible modulation of the Ohmic power : $(|\hat{P}_{\mathrm{OH}}| \ll |\eta \hat{P}_{\mathrm{RF}}|)$. This assumption has to be checked for each experiment.

- A low sensitivity of the absorption coefficient η, the energy incremental confinement time τ_{inc} and the isotropization time τ_{a} on both the RF power level P_{RF} and the modulation frequency ω. This linearity assumption can be tested by repeating the experiment for several power modulation depths and frequencies;

- One final important point: this whole method for the estimation of the RF power absorption is valid if the RF power is the only modulated power source. Plasmas with ELMs or strong sawtooth activity have to be excluded. Indeed, even when the sawtooth oscillation frequency ω_{st} and the power modulation frequency ω_{mod} are far apart, a non-linear harmonic coupling is expected and the component of the energy modulation at ω_{mod} due to the sawtooth activity is not negligible [96]. In this case, the sawtooth power modulation cannot be distinguished from the RF power modulation and yields a distortion of the power absorption estimate.

6.4 X3 MECH experiments

6.4.1 Scan A: X3 modulated ECH frequency scan

Introduction

In this subsection, the perturbative analysis of the plasma toroidal flux described in the previous section is applied to estimate the X3 power absorption coefficient in X2-preheated plasmas. The plasma perpendicular kinetic energy response to X3 modulated ECRH (X3 MECH) is measured using the DML diagnostic for several power modulation frequencies. This X3 MECH frequency scan is called "scan A" in the sequel of this text, whereas "scan B" refers to the X2 pre-heating injection angle scan of subsection 6.4.2. A model transfer function is then fitted on the experimental data to retrieve the physical quantities. Nevertheless, an oscillator-like response of the plasma is observed and no reasonable estimate of the X3 absorption coefficient can be drawn from the best fit.

Experimental setup

The plasma equilibrium is a limited L-mode plasma with medium shaping (edge elongation $\kappa_a \simeq 1.3$ and triangularity $\delta_a \simeq 0.17$) centered at $Z_{\text{axis}} \simeq 0.25$ m and $R_{\text{axis}} \simeq 0.91$ m. The vacuum toroidal magnetic field is $B_{\varphi \text{v}}(R_0) \simeq 1.45$ T and the

plasma current during the ECH phase is $I_\varphi \simeq 132$ kA. With such a low plasma current, the safety factor at the edge is high ($q_a > 7$). As a consequence, the sawtooth activity has a low amplitude (see soft X-ray trace in figure 6.7) with a frequency $f_{\mathrm{st}} \simeq 294 \pm 26$ Hz (evaluated in #19291, $t = [0.6; 0.8]$ s). It is thus not expected to strongly perturb the measurement. The central electron density and temperature are $n_{e0} \simeq 2.5 \cdot 10^{19}$ m^{-3} and $T_{e0} \simeq 2.5$ keV, respectively. Both traces are given in figure 6.7, along with the poloidal beta β_{p} and the diamagnetism parameter μ calculated by the LIUQE equilibrium reconstruction code, as well as the X2 and X3 RF power traces. The LIUQE code is run with a 5 kHz sampling rate in the time interval $t = [0.85, 0.95]$ s, denoted by a high concentration of data points in both β_{p} and μ traces.

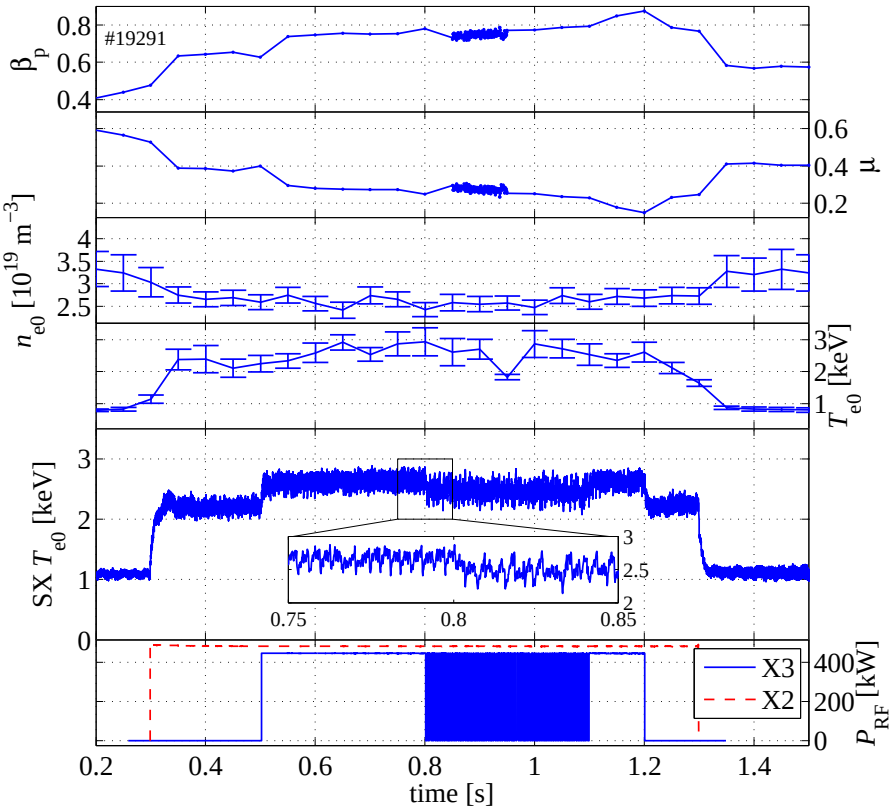

Figure 6.7: X3 MECH experiment. From top to bottom: normalized kinetic energy ("poloidal beta") β_{p}, diamagnetism parameter μ, central electron density n_{e0} and temperature T_{e0} (Thomson scattering, corrected by FIR for the density), central electron temperature determined by the filter method applied to soft X-ray signals, along with a zoom on the trace, X3 (blue) and X2 (red dashed) power traces. Between $t = 0.8$ s and $t = 1.1$ s, the X3 power amplitude is fully (ON/OFF) modulated at $f = 237$ Hz with a 50% duty-cycle square waveform. TCV shot #19291.

In these experiments dating from the 2000 TCV campaign, the X3 gyrotron #7 (G7) is connected to the upper lateral launcher #3 (L3) usually used for X2 power

injection. The X3 power beam ($P_{\mathrm{RF}} \simeq 450$ kW) is injected with launcher angles $(\theta_{\mathrm{L}}, \phi_{\mathrm{L}}) \simeq (39.9°, 0°)$, i.e. in the poloidal plane ($\phi_{\mathrm{inj}} = 0°$) with a downward poloidal angle $\theta_{\mathrm{inj}} = -39.9°$. The X3 power injection starts at $t = 0.5$ s and stops at $t = 1.2$ s and the amplitude is fully (ON/OFF) modulated with a 50% duty-cycle square waveform in the time interval $t = [0.8; 1.1]$ s. The modulation frequency f is varied on a shot to shot basis, e.g. $f = 237$ Hz for the discharge presented in figure 6.7.
The plasma is preheated with 480 kW of continuous X2 power in the time interval $t = [0.3, 1.3]$ s. The X2 beam is injected via the equatorial launcher L1 with launcher angles $(\theta_{\mathrm{L}}, \phi_{\mathrm{L}}) = (38.1°, 161.0°)$, corresponding to a clockwise toroidal injection angle $\phi_{\mathrm{inj}} = 15°$ with an upward poloidal injection angle $\theta_{\mathrm{inj}} = 35.3°$ in the vertical plane of injection. The injection geometry is presented in figure 6.8.

Ray-tracing and Fokker-Planck simulations

Both X2 and X3 beams are simulated with 25-ray bundles for TCV shot #19291 (at $t = 0.7$ s) using the ray-tracing code C3PO [29], with the LIUQE equilibrium and the experimental profiles data from the heated plasma at $t = 0.7$ s. The resulting toroidal and poloidal beam trajectories are given in figures 6.8(a) and 6.8(b), respectively, along with the linear power deposition profiles in figure 6.8(c). The X2 power beam is absorbed at $\rho_\psi \simeq 0.31$ with an efficiency $\eta = 100\%$, whereas the X3 power beam is absorbed closer to the plasma center, at $\rho_\psi \simeq 0.11$, with an efficiency $\eta \simeq 35\%$. According to the power deposition profiles and to the safety factor profile given in figures 6.8(c) and (d) respectively, both power beams are deposited inside the $q = 1$ flux surface located at $\rho_\psi \simeq 0.4$.
As indicated in references [43, 97, 98], the local toroidal angle of the X2 beam is $\phi \simeq 23.0°$ where ϕ is defined as

$$\sin(\phi) \equiv -\frac{\mathbf{k} \cdot \mathbf{B}}{\|\mathbf{k}\| \|\mathbf{B}\|} \tag{6.4.1}$$

such that $\phi = 0°$ for pure ECH with $\mathbf{k} \perp \mathbf{B}$, $\phi > 0°$ for co-ECCD and $\phi < 0°$ for counter-ECCD (by Fisch-Boozer effect). A non-negligible co-ECCD effect is expected. Quasi-linear Fokker-Planck simulations for the X2 beam using the LUKE code [30] yield a co-ECCD current $I_{\mathrm{CD}} = 27$ kA. This is in perfect agreement with the net plasma current increase of ~ 7 kA (from $I_\phi \simeq 125$ kA to $I_\varphi \simeq 132$ kA) observed on the magnetic measurements, since TCV feedback control system reduces the Ohmic part by 20 kA to follow the reference. Nevertheless, the presence of ECCD is expected to generate a fast electrons tail in the distribution function, in turn enhancing the X3 power absorption.

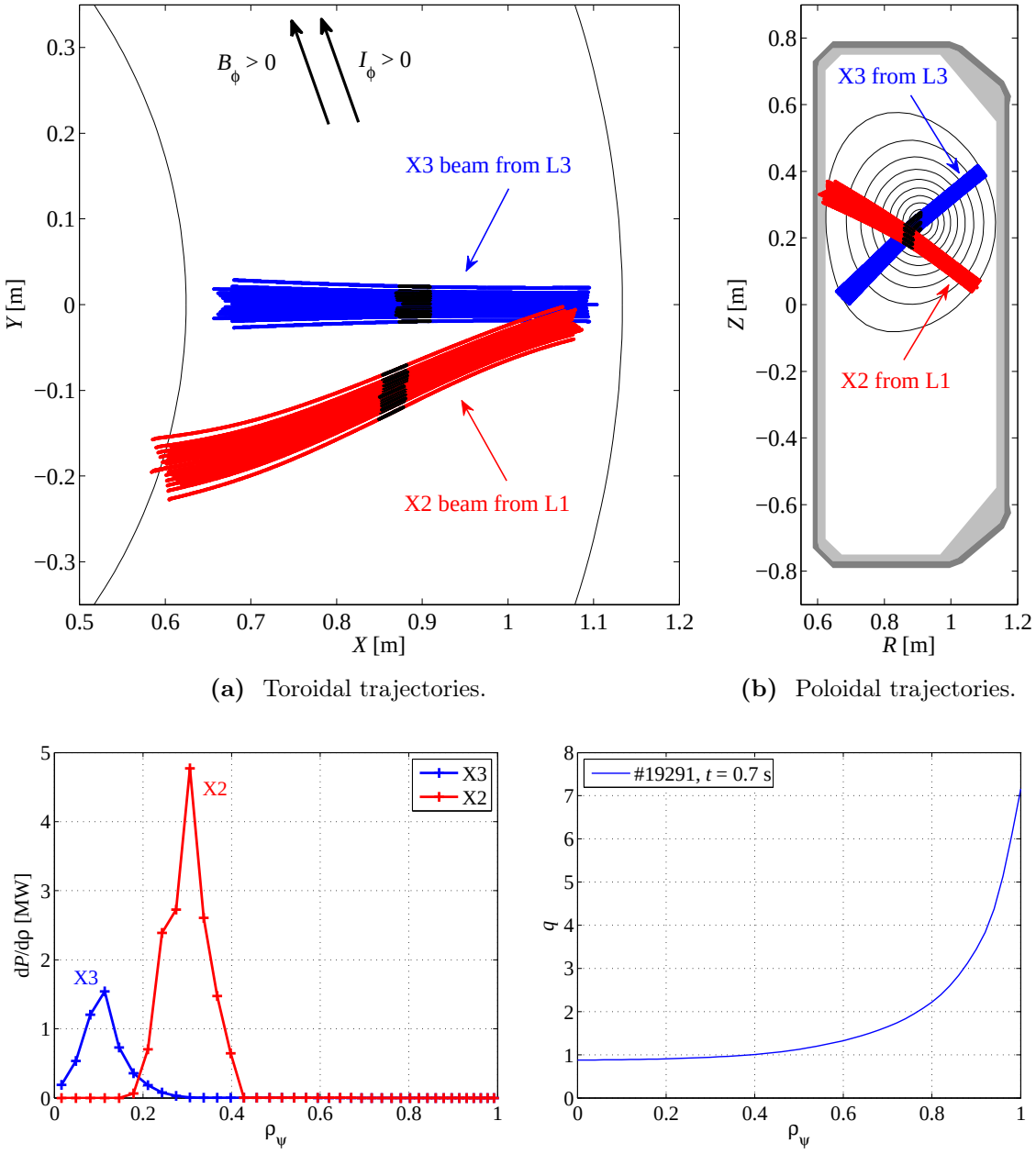

(a) Toroidal trajectories. **(b)** Poloidal trajectories.

(c) Linear power deposition profiles. **(d)** Safety factor profile.

Figure 6.8: X3 and X2 power beams trajectories and deposition profiles. C3PO ray-tracing simulations for the X2 (blue) and X3 (red) power beams. (a) Toroidal trajectories and (b) poloidal trajectories (on ρ_ψ contours). (c) Linear power deposition profiles and (d) safety factor profile. Both beams are deposited inside the $q = 1$ surface. TCV shot#19291 at $t = 0.7$ s.

X3 MECH oscillation analysis

Prior to performing the oscillation analysis of the plasma response to the X3 MECH, one has to check the remaining pending assumptions summarized in subsection 6.3.4. In the time interval of fast LIUQE equilibrium reconstruction, the HRIM analysis

of LIUQE's β, μ and normalized Shafranov integrals is performed to estimate the component of these signals at the MECH frequency. The analysis is presented in figure 6.9 for the case of MECH frequency $f = 237$ Hz. The respective complex amplitude moduli are: $|\hat{\beta}_\mathrm{p}| \simeq (10.7 \pm 0.8) \cdot 10^{-3}$, $|\hat{\mu}| \simeq (9.8 \pm 0.8) \cdot 10^{-3}$ and $|\widehat{s^*}| \simeq (0.47 \pm 0.06) \cdot 10^{-3}$, where s^* denotes the combination of normalized Shafranov integrals $s^* \equiv 1/2[s_1 + \delta R s_2]$. The error interval on the complex amplitude moduli comes from the root mean square difference between the original and the reconstructed signals. In consequence, one has

$$\frac{|\hat{\mu}|}{|\hat{\beta}_\mathrm{p}|} \simeq 92 \pm 14\% \qquad \text{and} \qquad \frac{|\widehat{s^*}|}{|\hat{\beta}_\mathrm{p}|} \simeq 4.4 \pm 0.9\%. \tag{6.4.2}$$

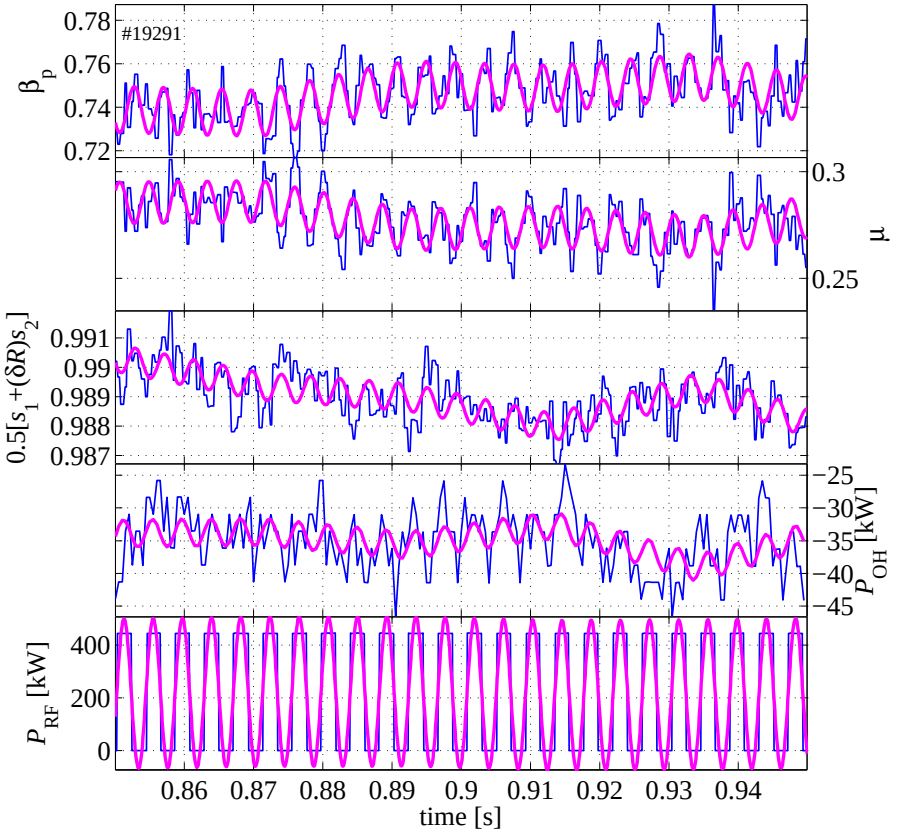

Figure 6.9: Oscillation analysis of the various plasma energies and input powers. From top to bottom: LIUQE normalized kinetic energy β_p, normalized plasma toroidal magnetic energy μ and normalized Shafranov integral combination s^*, as well as Ohmic power and X3 RF power. Superimposed on the time traces (in blue) are the reconstructed signals from the oscillation analysis at $f = 237$ Hz (in thick magenta). TCV shot #19291.

One can thus safely neglect the modulation of the normalized Shafranov integrals combination s^* with respect to the modulation of β_p and μ in equation (6.3.19), which is exactly equivalent to neglecting the modulation of the normalized Shafranov

integrals combination $S^* = 1/2[S_1 + \delta R S_2]$ with respect to the modulation of $W_\perp$ and $\Phi_{\rm pl}$ in equation (6.3.18).

A similar analysis of the Ohmic power oscillation is performed, to be compared with the RF power modulation. As a result, the moduli of the respective complex amplitudes are $|\hat{P}_{\rm OH}| \simeq 2.1 \pm 0.5$ kW and $|\hat{P}_{\rm RF}| \simeq 283 \pm 4$ kW such that $|\hat{P}_{\rm OH}|/|\hat{P}_{\rm RF}| \simeq 0.7 \pm 0.2\%$ and the modulation of the Ohmic power due to the X3 MECH can be safely neglected.

One must also check the level of perturbation caused by the sawtooth activity on the measurement of the plasma toroidal flux $\Phi_{\rm pl}$. The oscillation analysis before and after the onset of X3 MECH is given in figure 6.10 for the uncorrected flux $\Phi_{\rm DML2}$, the total compensation flux $\Phi_{\rm BO}$ and the corrected plasma flux $\Phi_{\rm pl} = \Phi_{\rm DML2} - \Phi_{\rm BO}$, as well as for the central electron temperature $T_{\rm e0}$ calculated from the soft X-ray emission. The corresponding complex amplitude moduli $\hat{\Phi}_{\rm DML2}$, ... are listed in table 6.1. The fast modulation at $f = 1300$ Hz observed on $\Phi_{\rm DML2}$, $\Phi_{\rm pl}$ and $T_{\rm e0}$ is a parasitic perturbation from the fly-wheel generator.

Before the onset of the X3 MECH at $f = 237$ Hz, the f-components of $\Phi_{\rm pl}$ and $T_{\rm e0}$ are of the order of the measurement error. After the X3 MECH onset, the electron temperature modulation amplitude increases by an order of magnitude. As regards the plasma toroidal flux, the modulation amplitude increase is somewhat less than a factor 10. The f-component of $\Phi_{\rm pl}$ which is not induced by the MECH but rather by the sawtooth activity (or other natural oscillations in the plasma) is thus small compared to the MECH perturbation amplitude, but its level must be carefully checked for each experiment. Finally, the modulation in the plasma toroidal flux $\Phi_{\rm pl}$ mainly comes from the uncorrected flux $\Phi_{\rm DML2}$. The total correction flux $\Phi_{\rm BO}$ does not contribute substantially to the modulation of $\Phi_{\rm pl}$.

	Complex amplitude modulus $\|\hat{\Phi}\|$	
Modulated signal	**(a) Before MECH**	**(b) During MECH**
Uncorrected plasma flux $\Phi_{\rm DML2}$	1.1 ± 0.5 μWb	7.7 ± 0.7 μWb
Total correction $\Phi_{\rm BO}$	0.3 ± 0.2 μWb	0.6 ± 0.2 μWb
Corrected plasma flux $\Phi_{\rm pl}$	1.1 ± 0.6 μWb	7.6 ± 0.7 μWb
Electron temperature $T_{\rm e0}$	8.7 ± 4.5 eV	90.5 ± 6.1 eV

Table 6.1: Modulation amplitudes at $f_{\rm mod}$ due to X3 MECH in presence of X2 co-ECCD. Low plasma current L-mode. TCV shot #19291, (a) $t = [0.7; 0.8]$ s and (b) $t = [0.8; 0.9]$ s.

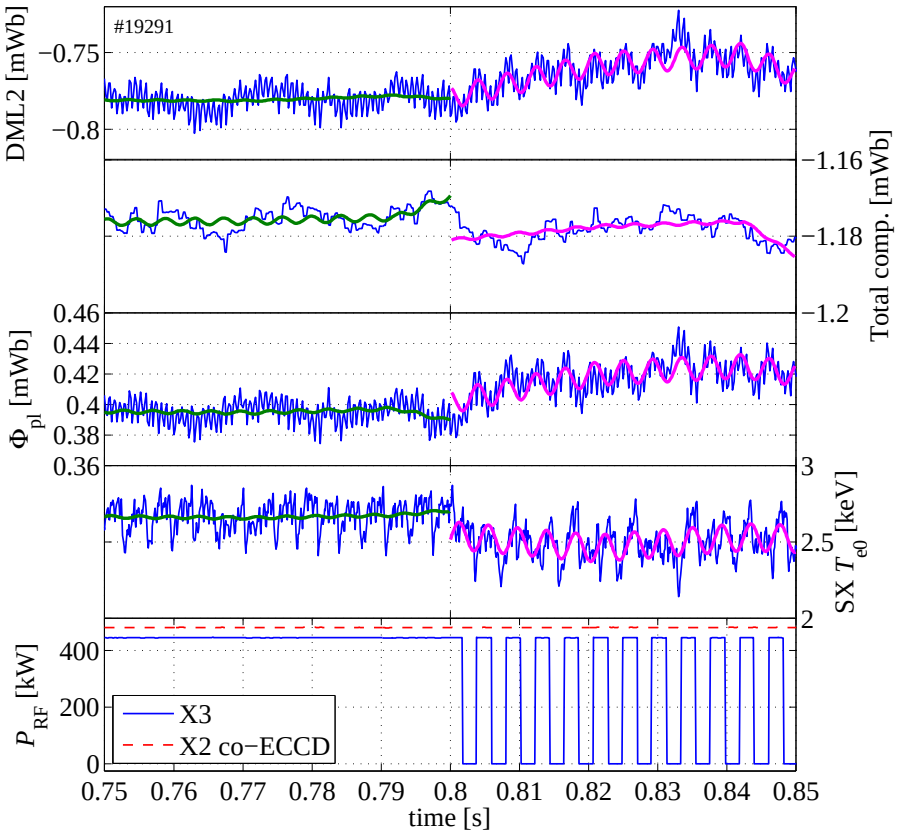

Figure 6.10: Oscillation analysis of the plasma toroidal flux components. From top to bottom: uncorrected plasma toroidal flux Φ_{DML2} from the DML2 loop, total compensation flux Φ_{BO}, corrected plasma toroidal flux Φ_{pl}, central electron temperature from soft X-ray measurements (absorber method), X2 (red dashed) and X3 (blue) power traces. Superimposed on the time traces (blue) are the reconstructed signals from the oscillation analysis at $f = 237$ Hz, before (thick green) and after (thick magenta) the onset of X3 MECH. TCV shot #19291.

Experimental frequency response and transfer function fitting

The X3 MECH experiment is repeated for a series of X3 power modulation frequencies: $f = 19, 73, 123, 163, 213, 237, 343$ and 703 Hz (in TCV shots #19288, 289, 303, 290, 294, 291, 292 and 302, respectively). Oscillation analysis of the RF power trace and the plasma toroidal flux response are performed for each frequency (at the fundamental) and the experimental transfer function is calculated according to equation (6.3.43), repeated here:

$$H(\omega) = \frac{\hat{W}_{\perp}}{\hat{P}_{\mathrm{RF}}} \simeq -\frac{2\pi}{\mu_0} \frac{\widehat{RB_{\varphi \mathrm{v}} \Phi_{\mathrm{pl}}}}{\hat{P}_{\mathrm{RF}}}. \tag{6.4.3}$$

For the two lowest modulation frequencies, the amplitude of the plasma response is high enough to perform the analysis also at the third harmonic of the MECH frequency with a reasonable signal to noise ratio, providing additional measurements

of the experimental transfer function H at $f = 57$ Hz and $f = 219$ Hz.

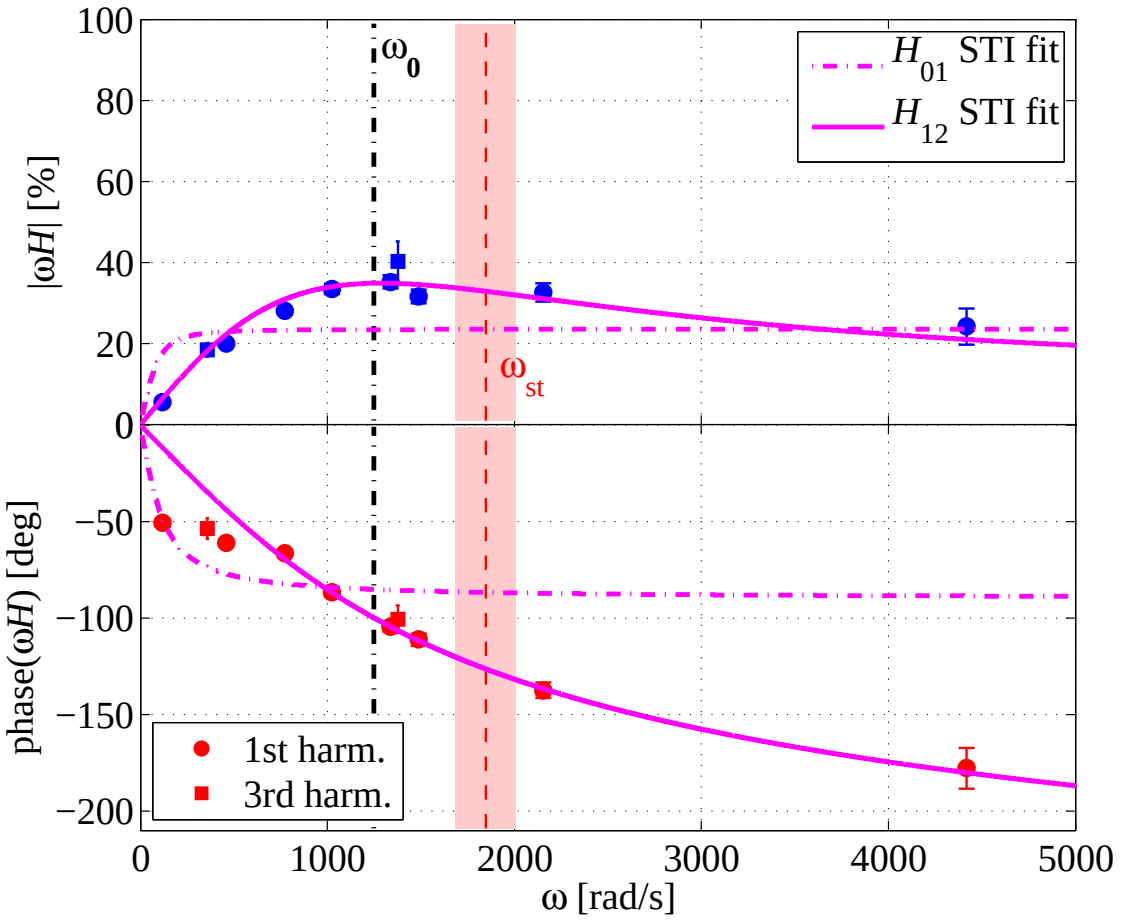

Figure 6.11: Scan A. Plasma frequency response to X3 MECH. Amplitude and phase of the experimental plasma frequency response at the first (•) and third (■) harmonics of the X3 MECH excitation angular frequencies ω, along with the STI fits for $M = 0, N = 1$ (dash-dotted curve) and $M = 1, N = 2$.

The amplitude and the phase of ωH are given in figure 6.11, to be compared with the model transfer functions shown in figure 6.6(a). The transfer function phase $\text{phase}(\omega H) = \Delta\phi = \phi_{W_\perp} - \phi_{\text{RF}}$ increases with increasing frequency but it does not exhibit the expected saturation at $\Delta\phi = -90°$, increasing monotonically towards larger values. The amplitude also shows an unexpected behavior, with a maximum around $f \simeq 1400$ rad/*second*, followed by a clear decrease at higher frequencies.
The system transfer identification (STI) fit is performed on the experimental data for several orders M and N of the numerator and of the denominator of (6.3.46). The best fits are obtained when weighting the rational function numerator with a weight $w = \omega$. Indeed, the transfer function amplitude decreases with increasing excitation frequency, see figure 6.5(a), which makes it difficult to properly determine

the phase at high frequency. A weight proportional to ω forces the fit to account for the phase information at high ω.

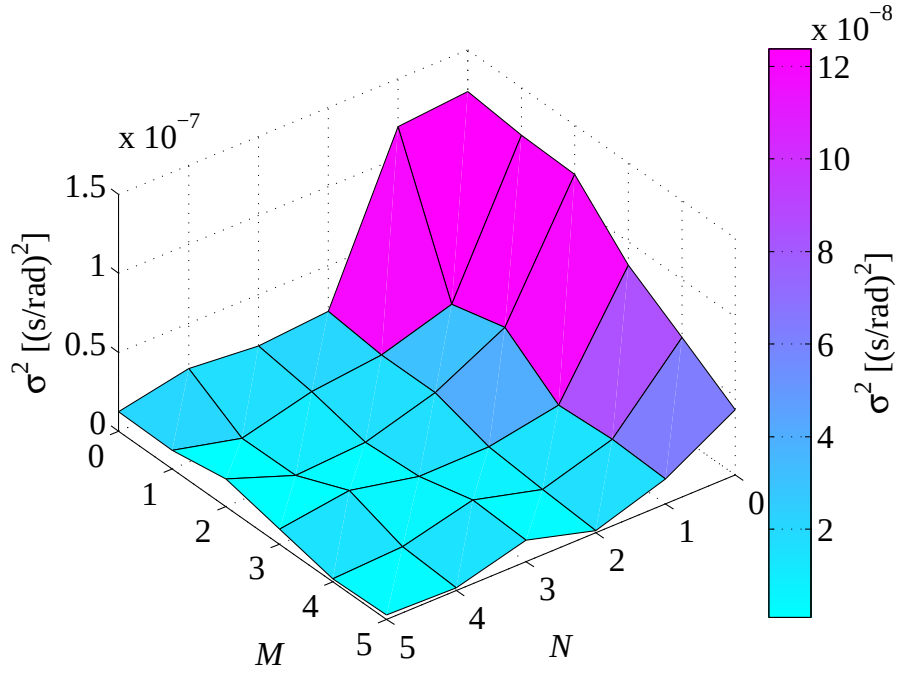

Figure 6.12: X3 MECH. STI optimization. Loss function σ^2 of the STI fitting of the plasma frequency response to X3 MECH for several numerator and denominator orders M and N. The lowest orders corresponding to a model of the system dynamic and yielding an acceptable loss function value are $M = 1, N = 2$.

The resulting values of the cost function (6.3.47) are plotted in figure 6.12. The saturation in the improvement of the fit, i.e. the saturation in the reduction of the cost function σ^2, with increasing M and N is clear. The STI fit is optimized for the minimum orders M and N yielding the saturation value of σ^2 and corresponding to a known model of the system dynamic. For the X3 MECH frequency scan, both conditions are met for a numerator order $M = 1$ and a denominator order $N = 2$, i.e.

$$H_{12} = \frac{b_0 + b_1(\mathrm{i}\omega)}{a_0 + a_1(\mathrm{i}\omega) + a_2(\mathrm{i}\omega)^2} \tag{6.4.4}$$

where $a_2 = 1$. This fit corresponds to the model transfer function H_2 of (6.3.35) and yields $\sigma^2 \simeq 1.7 \cdot 10^{-8}$ s^{2}rad^{-2}. The resulting fit is shown in figures 6.11, 6.13 and 6.14. It reproduces well the trend of the amplitude, the phase and the real and imaginary parts of the experimental transfer function on the whole frequency span. Nevertheless, identifying the fit parameters of (6.4.4) to the coefficients of H_2 gives the following overdetermined equations system for the physical parameters η, τ_{inc}

and τ_a:

$$\eta\frac{\tau_a+\tau_{inc}}{\tau_a\tau_{inc}} = b_0 \simeq 855\ \mathrm{s}^{-1} \tag{6.4.5}$$

$$\eta = b_1 \simeq -0.12 \tag{6.4.6}$$

$$\frac{2\tau_a+3\tau_{inc}}{2\tau_a\tau_{inc}^2} = a_0 \simeq 1.56\cdot 10^6\ \mathrm{s}^{-2} \tag{6.4.7}$$

$$\frac{4\tau_a+3\tau_{inc}}{2\tau_a\tau_{inc}} = a_1 \simeq 2.49\cdot 10^3\ \mathrm{s}^{-1} \tag{6.4.8}$$

which clearly yields non-reasonable physical parameters, in particular a negative absorption coefficient $\eta \simeq -12\%$. Actually, the denominator roots $s_{1,2} = \mathrm{i}\omega_{1,2}$ of H_{12} are complex conjugate and yield pole frequencies with a real part:

$$\omega_{1,2} \simeq \pm 121 + 1243\mathrm{i}\ \mathrm{rad/s}. \tag{6.4.9}$$

The system thus behaves like a forced damped harmonic oscillator with the following parameters:

$$\omega_0 \equiv \sqrt{\Omega^2+\gamma^2} \simeq 1249\ \mathrm{rad/s} \qquad \text{proper angular frequency} \tag{6.4.10}$$

$$Q \equiv \frac{\omega_0}{2\gamma} \simeq 0.50 \qquad \text{quality factor} \tag{6.4.11}$$

where Ω and γ are the real and imaginary parts of $\omega_{1,2}$ respectively. The low quality factor indicates that the oscillator is strongly damped and the system exhibits no resonance. Indeed, for a quality factor $Q < \sqrt{1/2}$, the resonant angular frequency defined as

$$\Omega_r \equiv \omega_0\sqrt{1-\frac{1}{2Q^2}} \tag{6.4.12}$$

is purely imaginary. There is no finite excitation frequency at which the response amplitude is maximum, as indicated by the monotonically decreasing amplitude $|H|$ versus ω in figure 6.13.

Finally, the proper angular frequency ω_0 of the system is of the order of the sawtooth angular frequency $\omega_{st} \equiv 2\pi f_{st} \simeq 1847 \pm 163$ rad/s which makes it a good candidate to explain the intrinsic oscillatory behavior of the system. Note that ω_{st} is evaluated at full ECH power. During the modulation, the average ECH level is twice lower and the sawtooth angular frequency is expected to decrease, thus reducing the discrepancy between ω_0 and ω_{st}.

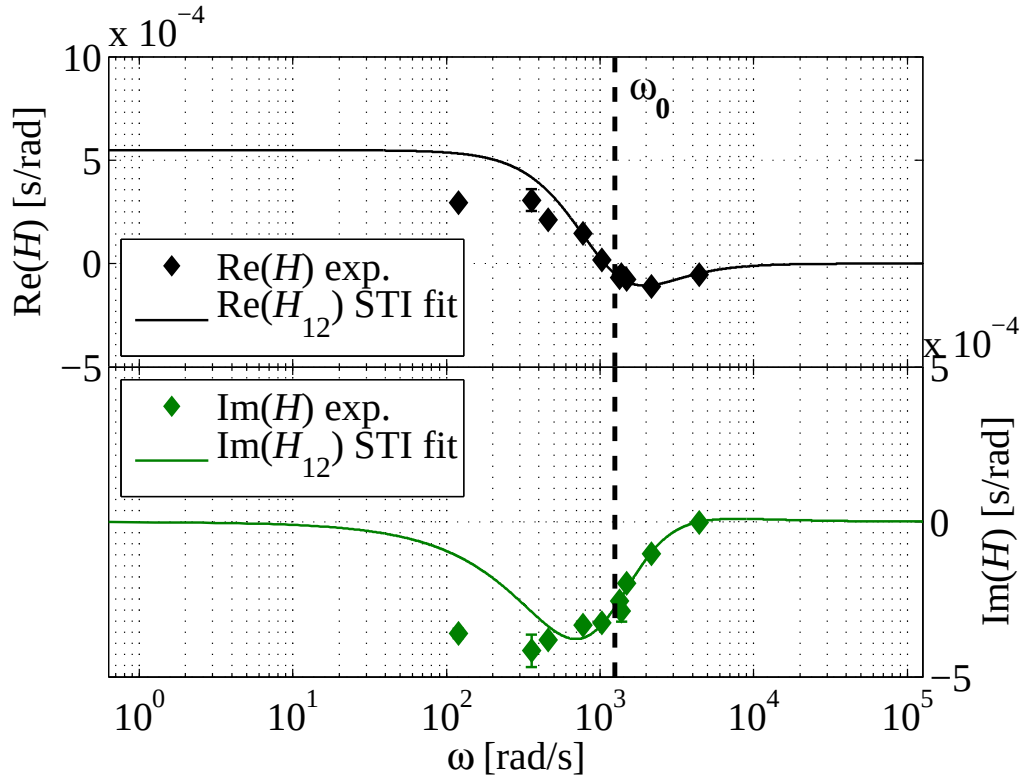

(a) Real and imaginary parts of H.

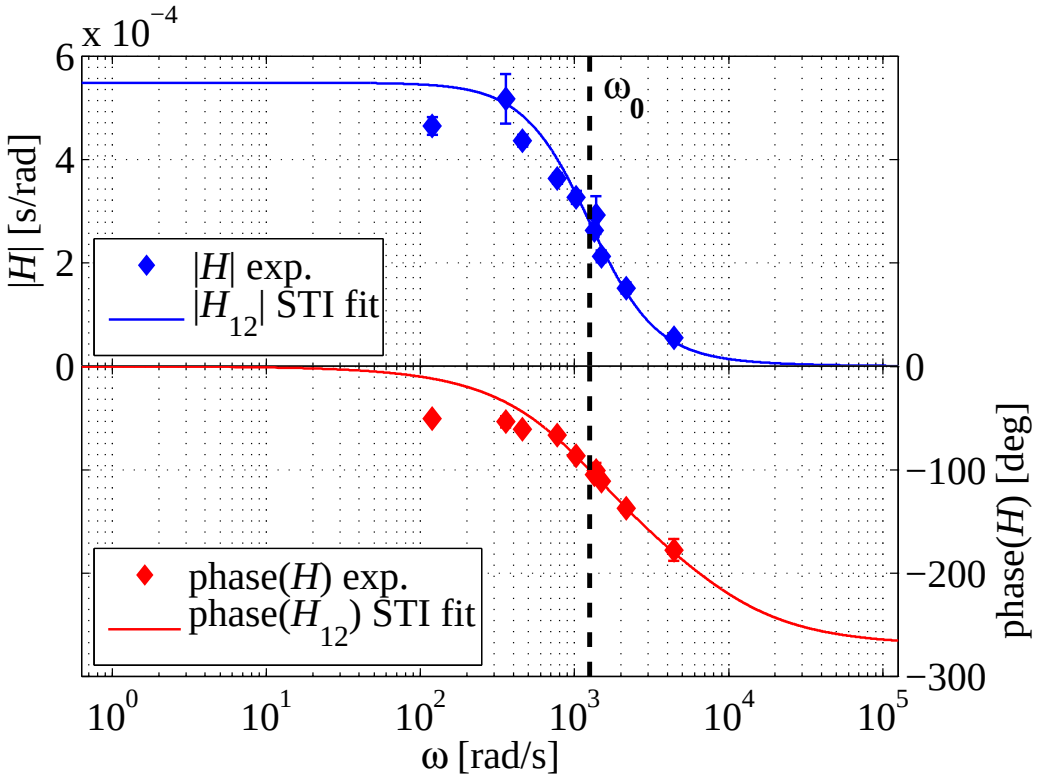

(b) Amplitude and phase of H.

Figure 6.13: X3 MECH frequency scan. Experimental frequency response and STI fit H_{12}.

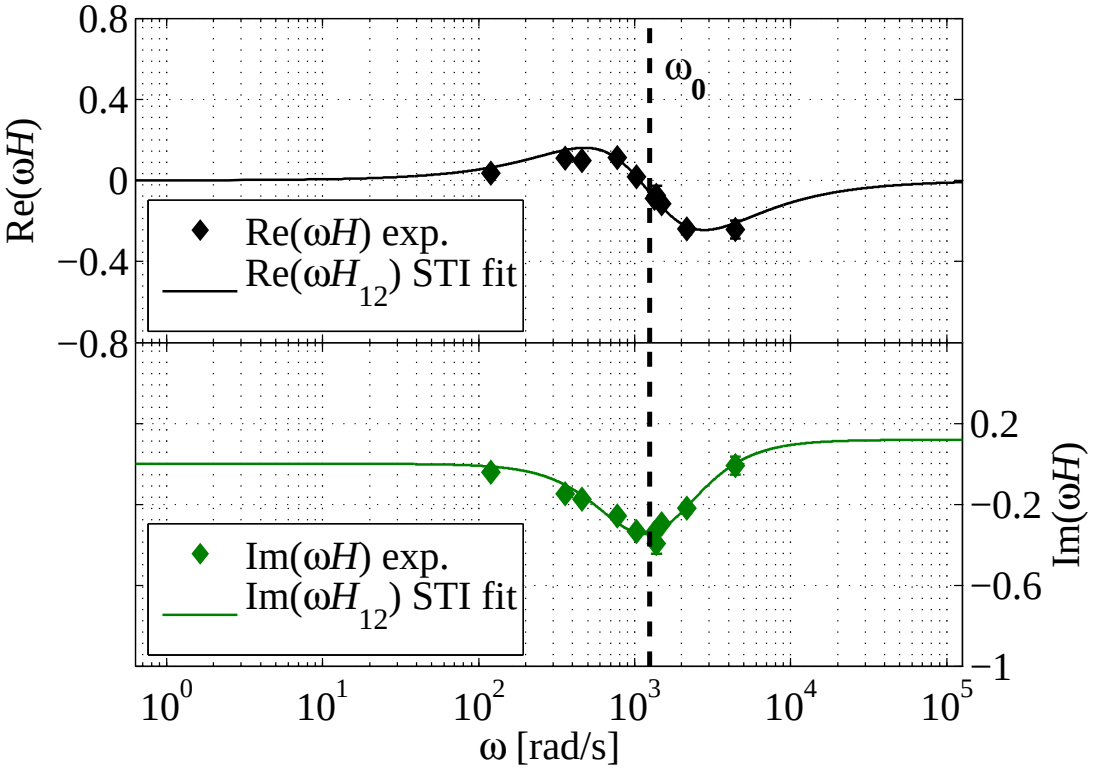

(a) Real and imaginary parts of ωH.

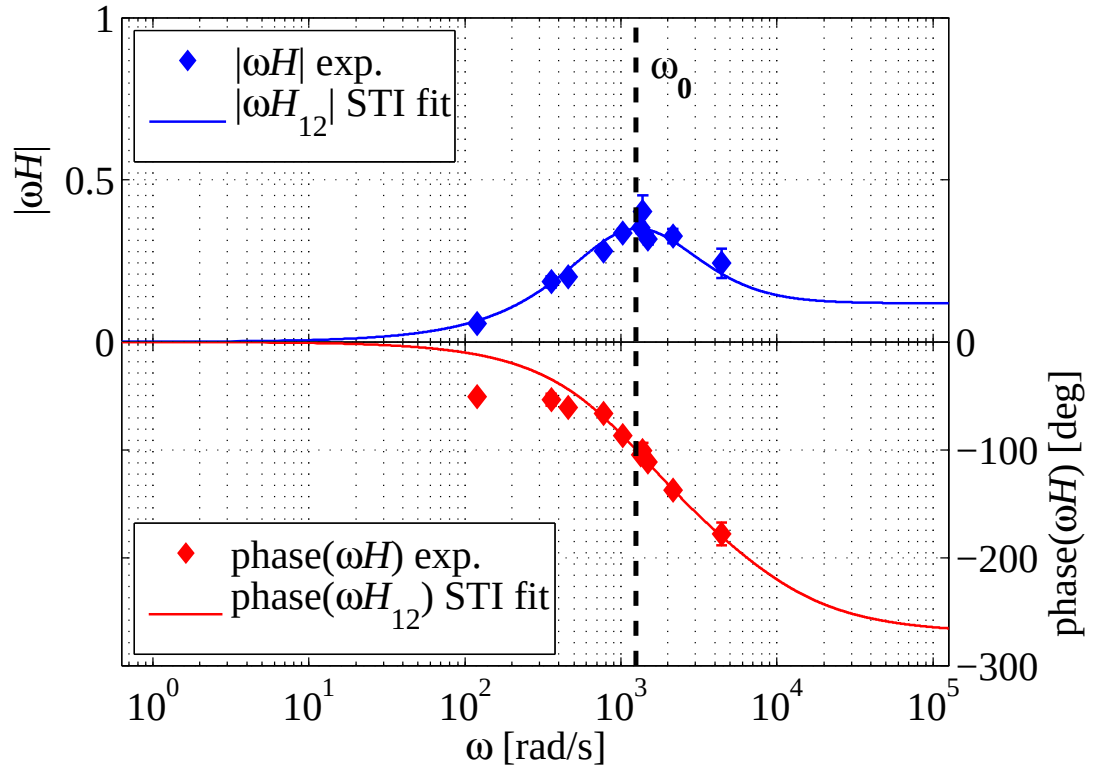

(b) Amplitude and phase of ωH.

Figure 6.14: X3 MECH frequency scan. Experimental frequency response and STI fit H_{12}.

Going back to the STI fitting of the experimental transfer function, one can choose $M = 0$ and $N = 1$, i.e.

$$H_{01} = \frac{b_0}{a_0 + a_1(\mathrm{i}\omega)} \tag{6.4.13}$$

with $a_1 = 1$, which corresponds to the model transfer function H_1 of (6.3.36). The resulting value of the cost function, $\sigma^2 \simeq 12.0 \cdot 10^{-8}$ s^{2}rad^{-2}, is one order of magnitude larger than for H_{12} and the fit is of relatively poor quality, see figures 6.11, 6.15 and 6.16. Comparing the fit parameters of (6.4.13) to the coefficients of H_1 yields

$$\frac{2}{3}\eta = b_0 \simeq 0.24 \qquad \Rightarrow \quad \eta \simeq 35\% \tag{6.4.14}$$

$$\frac{1}{\tau_{\mathrm{inc}}} = a_0 \simeq 105 \text{ s}^{-1} \qquad \Rightarrow \quad \tau_{\mathrm{inc}} \simeq 9.6 \text{ ms} \tag{6.4.15}$$

The X3 power absorption coefficient drawn from the H_{01} fit is in coherent agreement with the C3PO linear calculation. The estimated incremental confinement time is large in comparison to typical values expected for these plasmas but still in a relevant range. On the other hand, this low order model is unable to explain the detailed behavior of the plasma frequency response and the resulting physical parameters, although relevant, should be handled with care.

These shots were previously analyzed in [97,98]. In these references, both the experimental points and the H_{01} fit were normalized to their respective maximum value (thus using different normalization factors) for the sake of comparing the general trend. Doing so, no estimate of the X3 power absorption coefficient could be drawn from the measurements. Moreover, the use of different normalization factors for the experimental data and the fit is misleading: the reader may think that both the experiment and the model agree on 100% X3 power absorption, which is not the case.

Summary

A frequency scan of X3 modulated ECH (MECH) is performed in low-current limited L-mode plasmas in presence of continuous X2 co-ECCD. The plasma frequency response to the X3 MECH exhibits an unexpected damped oscillator behavior preventing a proper estimation of the physical parameters from the comparison of our model to the system transfer identification fitting of the experimental data. Although the sawtooth activity amplitude is not important, it is the best candidate to explain the intrinsic oscillatory behavior of the plasma perpendicular kinetic energy.

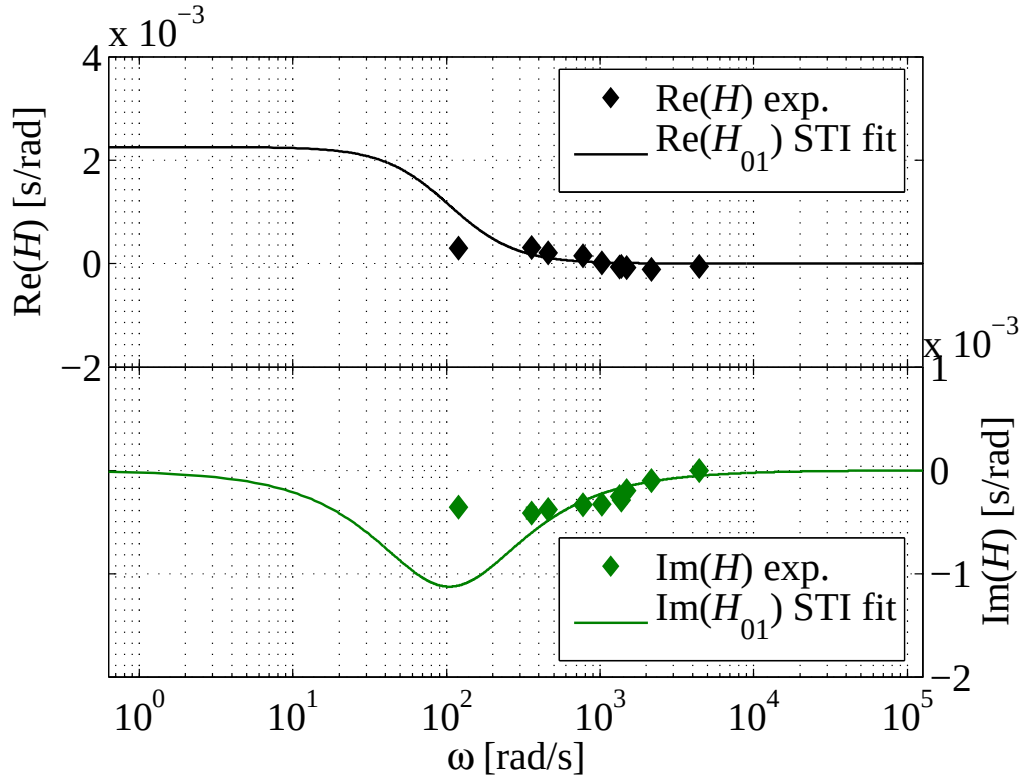

(a) Real and imaginary parts of H.

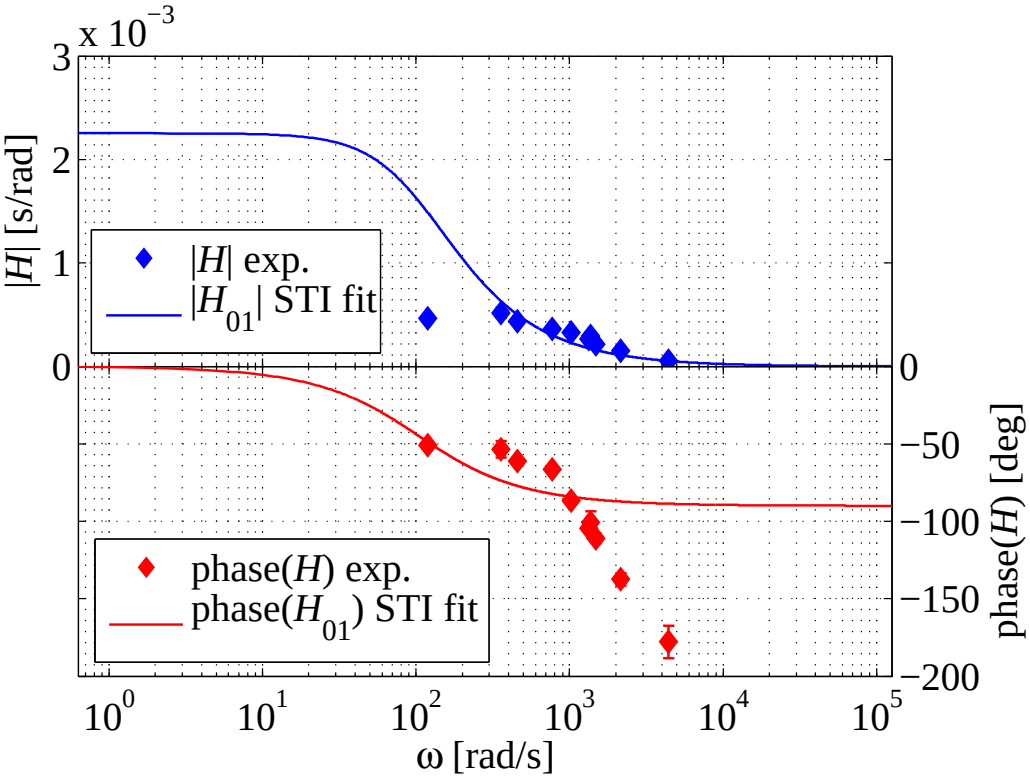

(b) Amplitude and phase of H.

Figure 6.15: X3 MECH frequency scan. Experimental frequency response and STI fit H_{01}.

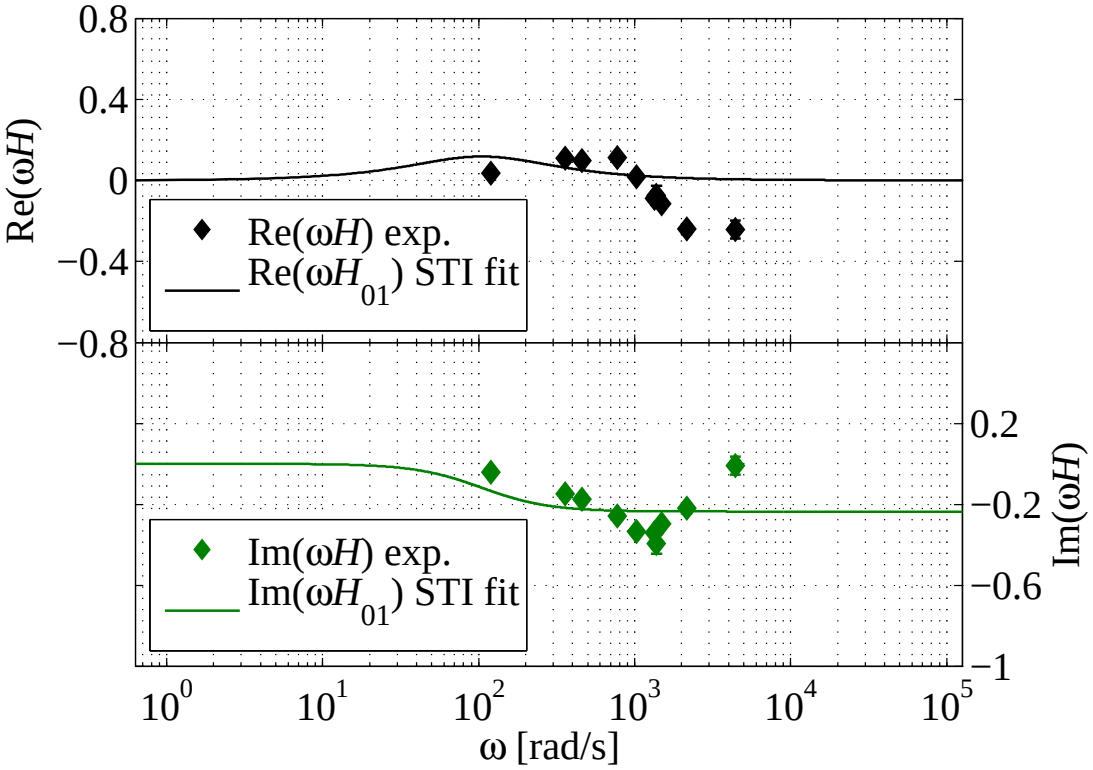

(a) Real and imaginary parts of ωH.

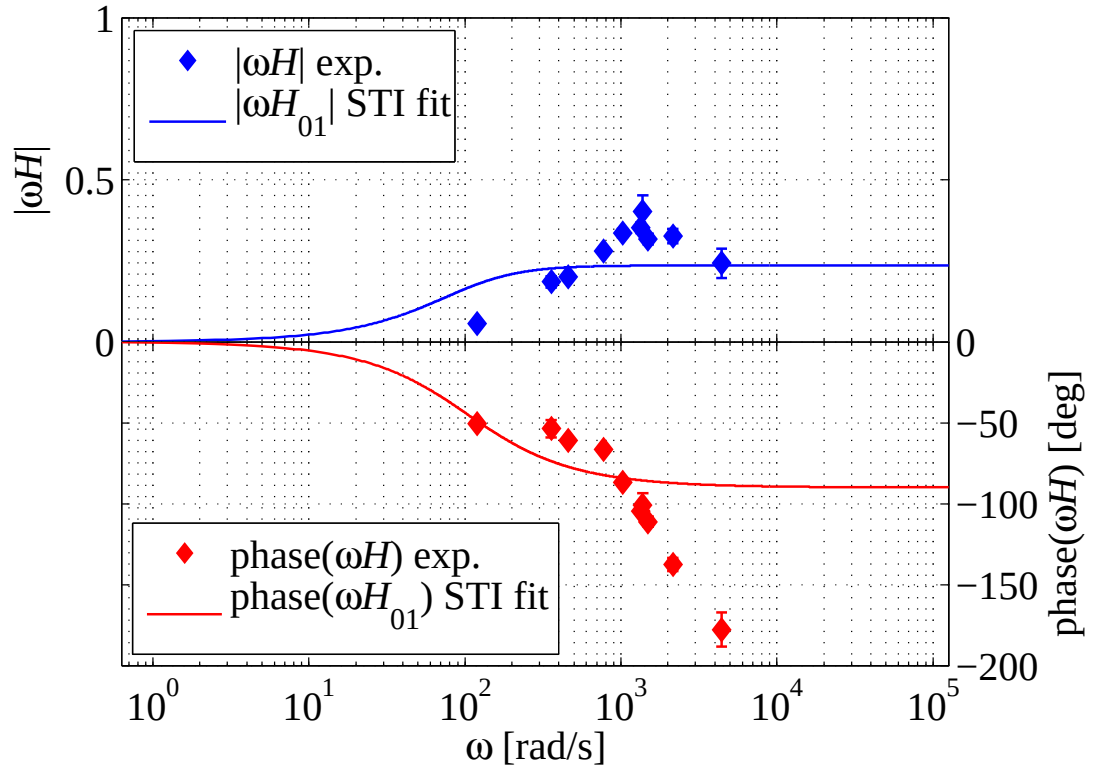

(b) Amplitude and phase of ωH.

Figure 6.16: X3 MECH frequency scan. Experimental frequency response and STI fit H_{01}.

6.4.2 Scan B: X3 absorption versus X2-ECCD

Introduction

The fast electron population generated by the X2 ECCD enhances the X3 power absorption, according to RF power absorption theory [1]. In order to measure this X2/X3 synergy, the X3 MECH experiment described in subsection 6.4.1 is repeated for a fixed modulation frequency, but varying the X2 pre-heating conditions. The local toroidal angle ϕ of the X2 wave is scanned on shot to shot basis from negative to positive values, i.e. from counter-ECCD to co-ECCD. This set of experiments is referred to as "scan B". One expects to observe a variation of the X3 power absorption coefficient with ϕ. But, as it is presented below, the sawtooth activity behavior varies dramatically with ϕ. In particular, it strongly modulates the plasma toroidal flux in the X2 co-ECCD case, which perturbs the measurement of the plasma response to X3 MECH. As a consequence, the X3 power absorption coefficient cannot be safely determined.

Experimental setup

In these experiments, the equilibrium is a limited L-mode plasma very similar to the one of scan A ($\kappa_a \simeq 1.3$, $\delta_a \simeq 0.18$, $Z_{\text{axis}} \simeq 0.24$ m, $R_{\text{axis}} \simeq 0.90$ m, $B_{\varphi \text{v}}(R_0) \simeq 1.45$ T, $n_{e0} \simeq 2.5 \cdot 10^{19}$ m^{-3} and $T_{e0} \simeq 2.6$ keV) apart from the plasma current which is increased from $I_\varphi \simeq 132$ kA to $I_\varphi \simeq 202$ kA, see figure 6.17. As a consequence, the edge safety factor is decreased from $q_a \simeq 7$ to $q_a \simeq 4.5$ leading to a slower ($f_{\text{st}} \simeq 220$ Hz) and stronger sawtooth activity compared to the sawtooth activity observed in the X3 MECH frequency scan experiments. At this lower q_a, each sawtooth crash induces a central electron temperature drop of $\Delta T_{\text{e0}} > 600$ keV (see the soft X-ray traces in figure 6.17), typically twice the temperature drop observed in scan A, see figure 6.7.

The X3 power injection geometry is identical to the geometry used in scan A, see figure 6.8: a downward injection in the poloidal plane from the upper lateral launcher L3, aiming at central power absorption. The X3 power modulation is performed at a fixed frequency $f = 237$ Hz such that the modulation angular frequency is far from typical values of the inverse incremental confinement time and of the inverse anisotropy relaxation time as estimated in subsection 6.3.3:

$$\frac{1}{\tau_{\text{inc}}} \simeq 200 \text{ rad/s} \ll \omega \equiv 2\pi f \simeq 1490 \text{ rad/s} \ll \frac{1}{\tau_{\text{a}}} \simeq 5000 \text{ rad/s}. \tag{6.4.16}$$

In this case, a rough estimate of the X3 absorption efficiency η is obtained directly

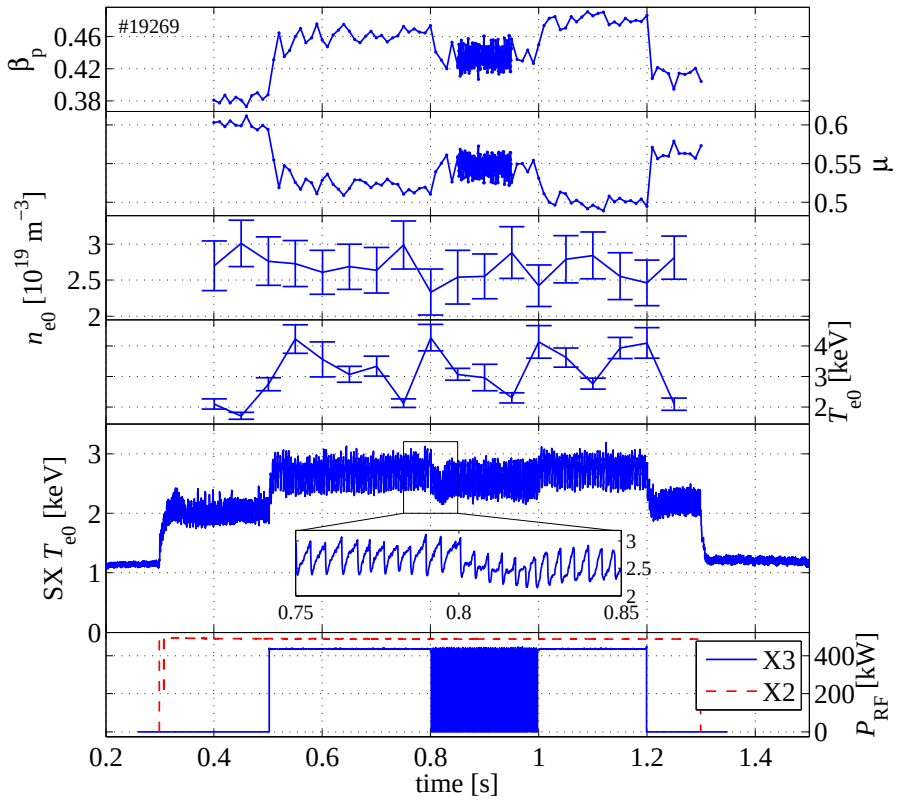

Figure 6.17: X3 MECH experiment. From top to bottom: LIUQE normalized kinetic energy β_p and diamagnetism parameter μ, central electron density $n_{\mathrm{e}0}$ and temperature $T_{\mathrm{e}0}$ (Thomson scattering, corrected by FIR for the density), central electron temperature determined by the filter method applied to soft X-ray signals, along with a zoom on the trace, X3 (blue) and X2 (red dashed) power traces. Between $t = 0.8$ s and $t = 1.0$ s, the X3 power amplitude is fully (ON/OFF) modulated at a fixed frequency $f = 237$ Hz with a 50% duty-cycle square waveform. The X2 local injection angle ϕ is scanned from shot to shot (scan B). In this example, $\phi \simeq 23.0°$ and the X2 power drives $I_{\mathrm{CD}} \simeq 25$ kA of non-inductive plasma current (LUKE simulation). #19269.

from the simple transfer function model H_0, see equation (6.3.45) in subsection 6.3.3:

$$\eta \simeq \frac{3}{2}\omega|H|. \tag{6.4.17}$$

For this estimate to be valid, the phase of the plasma response to the X3 MECH must be close to $-90°$.

Similarly to scan A, the plasma is preheated with ~ 480 kW of continuous central X2 power deposition in the time interval $t = [0.3, 1.3]$ s. The X2 beam is injected via the equatorial launcher L1. In scan B, the launcher angles $(\theta_\mathrm{L}, \phi_\mathrm{L})$ are varied on a shot to shot basis in order to scan the local toroidal angle defined in (6.4.1) at the absorption layer from $\phi = -43°$ to $\phi = +40°$ while keeping a quasi-central deposition within the $q = 1$ flux surface. The fraction of plasma current generated by ECCD effect is thus varied from shot to shot, from counter-ECCD for $\phi < 1$, to

co-ECCD for $\phi > 1$, via pure ECH for $\phi = 0$.

X3 MECH oscillation analysis: X2 co-ECCD central pre-heating

As for the frequency scan A, the oscillation analysis of the normalized kinetic energy β_p, the diamagnetism parameter μ, the normalized Shafranov term $s^* \equiv 1/2[s_1 + \delta R s_2]$, the Ohmic power P_{OH} and the X3 RF power P_{RF} is performed for each experiment in the angle scan B in order to check the validity of the assumptions summarized in subsection 6.3.4.

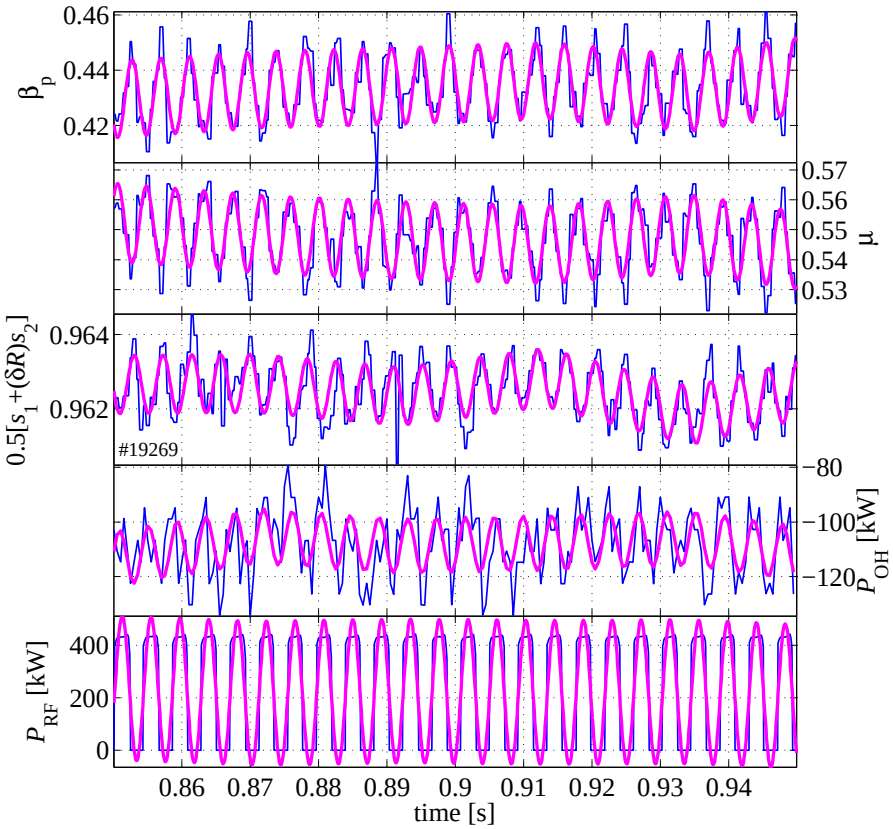

Figure 6.18: Oscillation analysis of the various plasma energies and input powers. X3 MECH experiment with continuous X2 co-ECCD at $\phi \simeq 23.0°$. From top to bottom: LIUQE normalized kinetic energy β_p, plasma toroidal magnetic energy μ and Shafranov term s^*, as well as Ohmic power and X3 RF power. Superimposed on the time traces (in blue) are the reconstructed signals from the oscillation analysis at $f = 237$ Hz (in thick magenta). #19269.

Figure 6.18 presents an example of the X3 MECH oscillation analysis for X2 co-ECCD pre-heating at $\phi \simeq 23.0°$. The corresponding complex amplitude moduli are $|\hat{\beta}_p| \simeq (13.9 \pm 0.5) \cdot 10^{-3}$, $|\hat{\mu}| \simeq (13.1 \pm 0.5) \cdot 10^{-3}$ and $|\widehat{s^*}| \simeq (0.78 \pm 0.04) \cdot 10^{-3}$. As a consequence, one has

$$\frac{|\hat{\mu}|}{|\hat{\beta}_p|} \simeq 94 \pm 6\% \qquad \text{and} \qquad \frac{|\widehat{s^*}|}{|\hat{\beta}_p|} \simeq 5.6 \pm 0.5\%. \tag{6.4.18}$$

One can thus safely neglect the modulation of the normalized Shafranov integrals combination s^* with respect to the modulation of β_p and μ in equation (6.3.19).
A similar analysis of the Ohmic power oscillation is performed, to be compared with the RF power modulation. As a result, the respective complex amplitude moduli are $|\hat{P}_{OH}| \simeq 10.1 \pm 1.4$ kW and $|\hat{P}_{RF}| \simeq 275 \pm 4$ kW such that $|\hat{P}_{OH}|/|\hat{P}_{RF}| \simeq 3.7 \pm 0.6\%$ and the modulation of the Ohmic power due to the X3 MECH can be safely neglected.

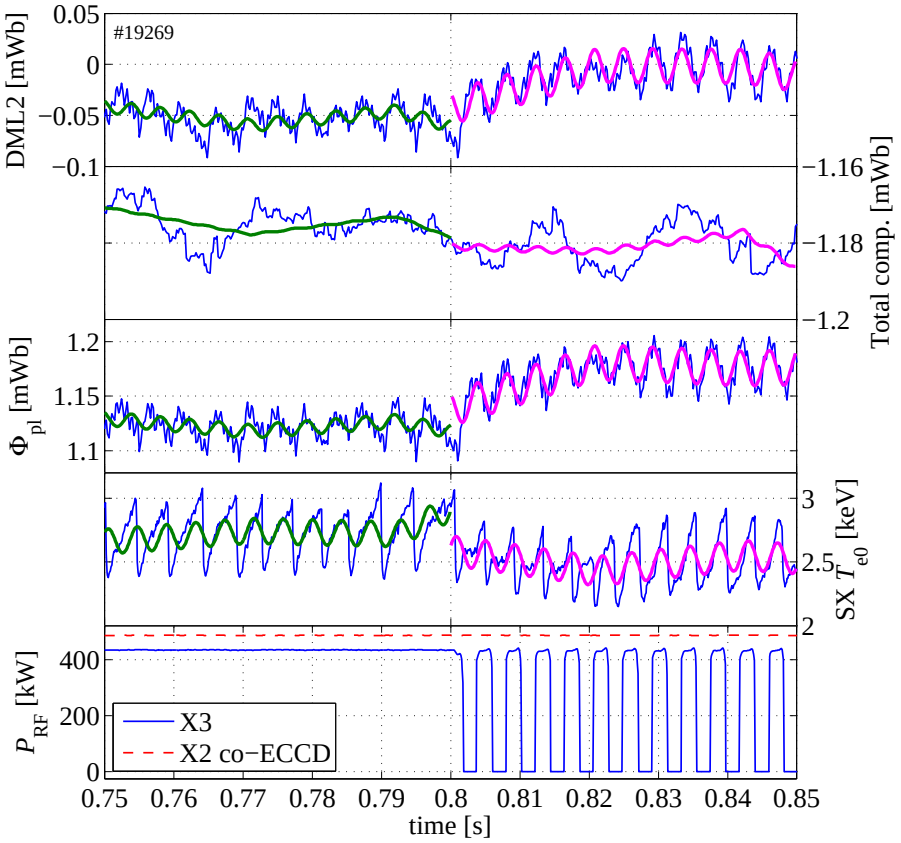

Figure 6.19: Oscillation analysis of the plasma toroidal flux components. X3 MECH experiment with continuous X2 co-ECCD at $\phi \simeq 23.0°$. From top to bottom: uncorrected plasma toroidal flux Φ_{DML2} from the DML2 loop, total compensation flux Φ_{BO}, corrected plasma toroidal flux Φ_{pl}, central electron temperature from soft X-ray measurements (absorber method), X2 (red dashed) and X3 (blue) power traces. Superimposed on the time traces (blue) are the reconstructed signals from the oscillation analysis at $f = 237$ Hz, before (thick green) and after (thick magenta) the onset of X3 MECH. TCV shot #19269.

The oscillation analysis is also performed before and after the onset of X3 MECH for the uncorrected flux Φ_{DML2}, the total compensation flux Φ_{BO} and the corrected plasma flux $\Phi_{pl} = \Phi_{DML2} - \Phi_{BO}$, as well as for the central electron temperature T_{e0} calculated from the soft X-ray emission, see figure 6.19. The resulting complex amplitude moduli $\hat{\Phi}_{DML2}$, ... are listed in table 6.2.

	Complex amplitude modulus $\lvert\hat{\Phi}\rvert$	
Modulated signal	**(a) Before MECH**	**(b) During MECH**
Uncorrected plasma flux Φ_{DML2}	3.8 ± 1.0 μWb	19.6 ± 0.9 μWb
Total correction Φ_{BO}	0.2 ± 0.4 μWb	1.7 ± 0.4 μWb
Corrected plasma flux Φ_{pl}	4.0 ± 0.9 μWb	18.4 ± 0.8 μWb
Electron temperature T_{e0}	60 ± 11 eV	169 ± 8 eV

Table 6.2: Modulation amplitudes due to X3 MECH in presence of X2 co-ECCD. TCV shot #19269, (a) $t = [0.7; 0.8]$ s and (b) $t = [0.8; 0.9]$ s.

First, the modulation in the plasma toroidal flux Φ_{pl} mainly comes from the uncorrected flux Φ_{DML2}. The total correction flux Φ_{BO} does not contribute substantially to the modulation of Φ_{pl}.

Before the onset of the X3 MECH at $f = 237$ Hz, the f-components of Φ_{pl} and T_{e0} are already non-negligible. They increase by less than a factor 5 when the X3 power modulation starts. The f-component of Φ_{pl} induced by the sawtooth activity is thus of the same order than the component due to the MECH and will strongly bias the X3 power absorption estimate. Moreover, since the frequencies of the sawtooth activity (before the MECH) and of the MECH excitation are close ($f = 237$ Hz and $f_{\mathrm{st}} \simeq 220$ Hz), frequency locking is happing between the sawtooth activity and the X3 MECH: after typically 30 ms of transient regime the sawtooth crash always occurs within 1 ms around the X3 power switch-off, as can be seen from the soft X-ray trace in figure 6.19. This locking effect is also revealed by spectrograms of the electron temperature and of the plasma toroidal flux in figure 6.20 for the X2 co-ECCD experiment with $\phi \simeq 20°$: the sawtooth activity frequency smoothly evolves to the MECH excitation frequency after the MECH onset.

Even when the frequencies of the MECH excitation and of the sawtooth activity are not similar, some coupling happens via higher harmonics and the sawtooth contribution at the MECH frequency is not negligible [96]. In other words, the presence of the external excitation itself modify the sawtooth oscillation. The way the sawtooth and MECH complex amplitudes combine in the complex plane is not trivial and both excitations cannot be distinguished from each other: one cannot simply subtract the modulation amplitude evaluated before the MECH onset from the modulation amplitude in presence of the MECH to get rid of the sawtooth contribution.

Finally, it is worth noting that it is only the increase of 70 kA in the plasma cur-

rent with respect to the X3 MECH scan experiments of subsection 6.4.1 which dramatically enhances the impact of the sawtooth activity on the plasma toroidal flux measurement. The power absorption measurement using the DML diagnostic is thus unexpectedly very sensitive to the plasma conditions.

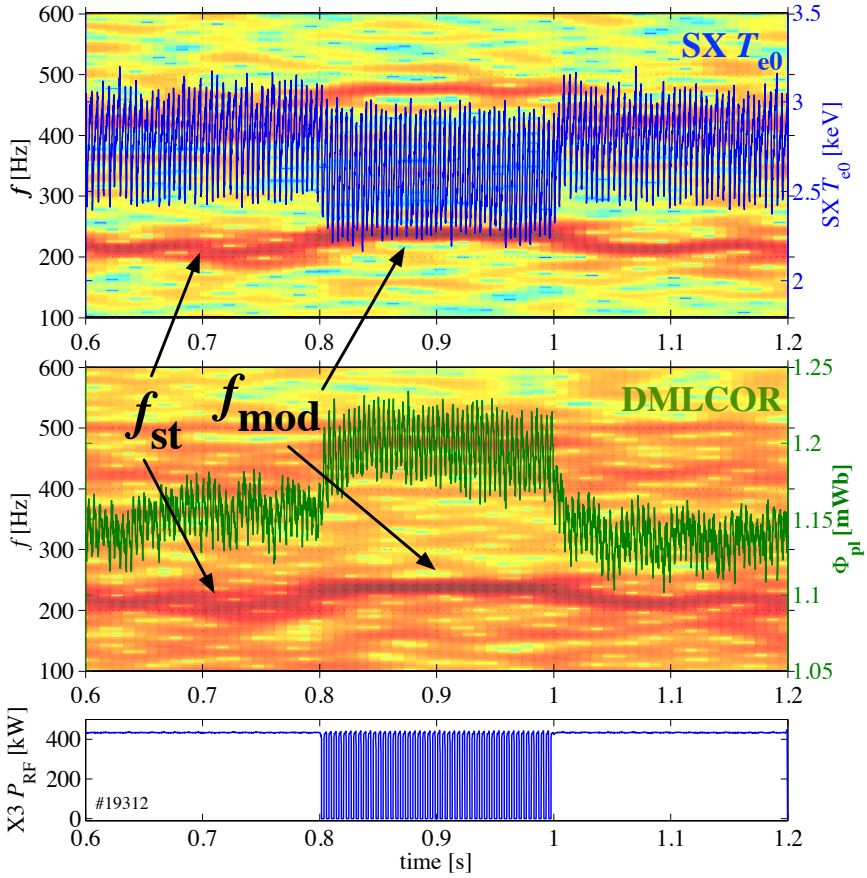

Figure 6.20: Sawtooth frequency locking to X3 MECH in presence of X2 co-ECCD. X3 MECH experiment with continuous X2 co-ECCD at $\phi \simeq 20.0°$. From top to bottom: Spectrograms of the central electron temperature from soft X-ray measurements (absorber method) and of the corrected plasma toroidal flux Φ_{pl} (with superimposed time traces), and X3 power time trace. The sawtooth frequency f_{st} smoothly connects to the X3 modulation frequency f_{mod} when the X3 MECH is turned on at $t = 0.8$ s. TCV shot #19312.

X3 MECH oscillation analysis: X2 counter-ECCD central pre-heating

For the sake of completeness, the detailed oscillation analysis is presented here for a X3 MECH experiment with X2 counter-ECCD, i.e. the case $\phi \simeq -31.5°$. The traces of β_p, μ, the normalized Shafranov term $s^* \equiv 1/2[s_1 + \delta R s_2]$, the Ohmic power P_{OH} and the X3 RF power P_{RF} and their respective components at $f =$

237 Hz are plotted in figure 6.21. The corresponding complex amplitude moduli are $|\hat{\beta}_\mathrm{p}| \simeq (6.2 \pm 0.5) \cdot 10^{-3}$, $|\hat{\mu}| \simeq (5.7 \pm 0.5) \cdot 10^{-3}$, $|\widehat{s^*}| \simeq (0.19 \pm 0.11) \cdot 10^{-3}$, $|\hat{P}_\mathrm{OH}| \simeq 3.6 \pm 1.6$ kW and $|\hat{P}_\mathrm{RF}| \simeq 272 \pm 4$ kW. In consequence, one has

$$\frac{|\hat{\mu}|}{|\hat{\beta}_\mathrm{p}|} \simeq 92 \pm 16\%, \quad \frac{|\widehat{s^*}|}{|\hat{\beta}_\mathrm{p}|} \simeq 3.0 \pm 2.1\% \quad \text{and} \quad \frac{|\hat{P}_\mathrm{OH}|}{|\hat{P}_\mathrm{RF}|} \simeq 1.3 \pm 0.6\%. \tag{6.4.19}$$

The oscillation of the Shafranov term and of the Ohmic power can be safely neglected compared to the oscillation of the diamagnetism and of the RF power, respectively.

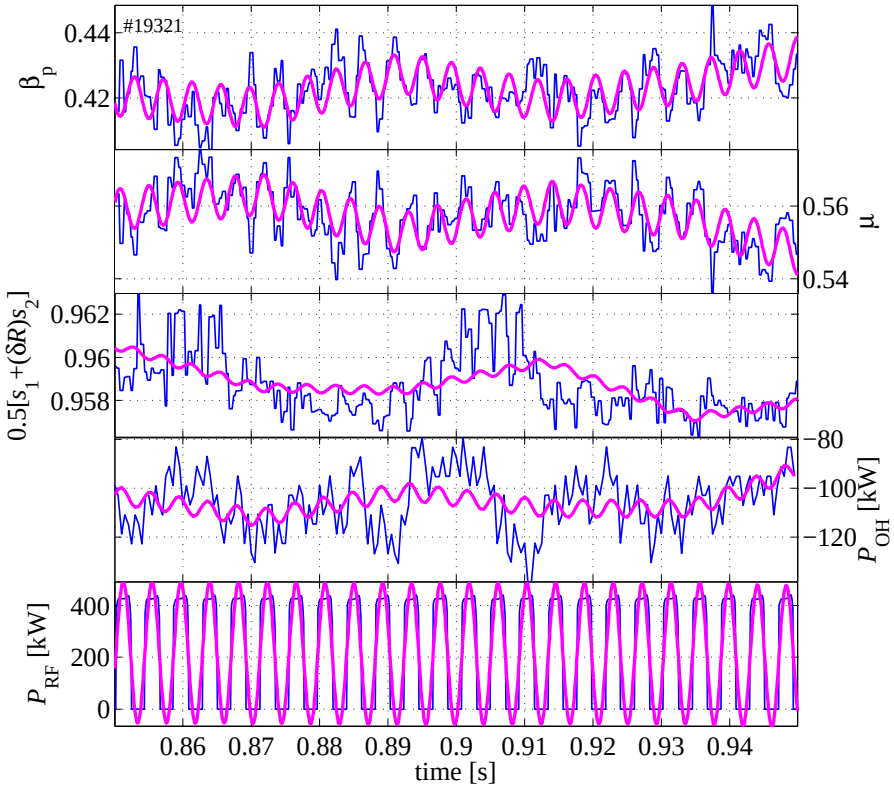

Figure 6.21: Oscillation analysis of the various plasma energies and input powers. From top to bottom: LIUQE normalized kinetic energy β_p, normalized plasma toroidal magnetic energy μ and normalized Shafranov integral combination s^*, as well as Ohmic power and X3 RF power. Superimposed on the time traces (in blue) are the reconstructed signals from the oscillation analysis at $f = 237$ Hz (in thick magenta). TCV shot #19321.

In the case of X2 counter-ECCD pre-heating, the plasma does not exhibit any strong sawtooth activity, but rather irregular oscillations affecting the plasma flux Φ_pl, see figure 6.23. The frequency of this activity is not well determined, as indicated by the spectrograms in figure 6.22. No frequency locking with the X3 MECH is to be expected. A detailed analysis of these different MHD activity regimes as a function of the X2 pre-heating condition is not the scope of this work but it is important for the analysis interpretation to observe their relative impact on the measurements.

Here, the oscillation of the plasma toroidal flux before the X3 MECH onset is less important than in the X2 co-ECCD case (in absolute) but it is still of the order of 20% of the oscillation amplitude in presence of X3 MECH, as indicated in table 6.3. Moreover, the way the presence of modulation in the RF power amplitude itself modifies the MHD regime is not straightforward. In short, the pollution level of the measurements in the case of counter-ECCD pre-heating is expected to be less than in the case of co-ECCD pre-heating but it cannot be neglected.

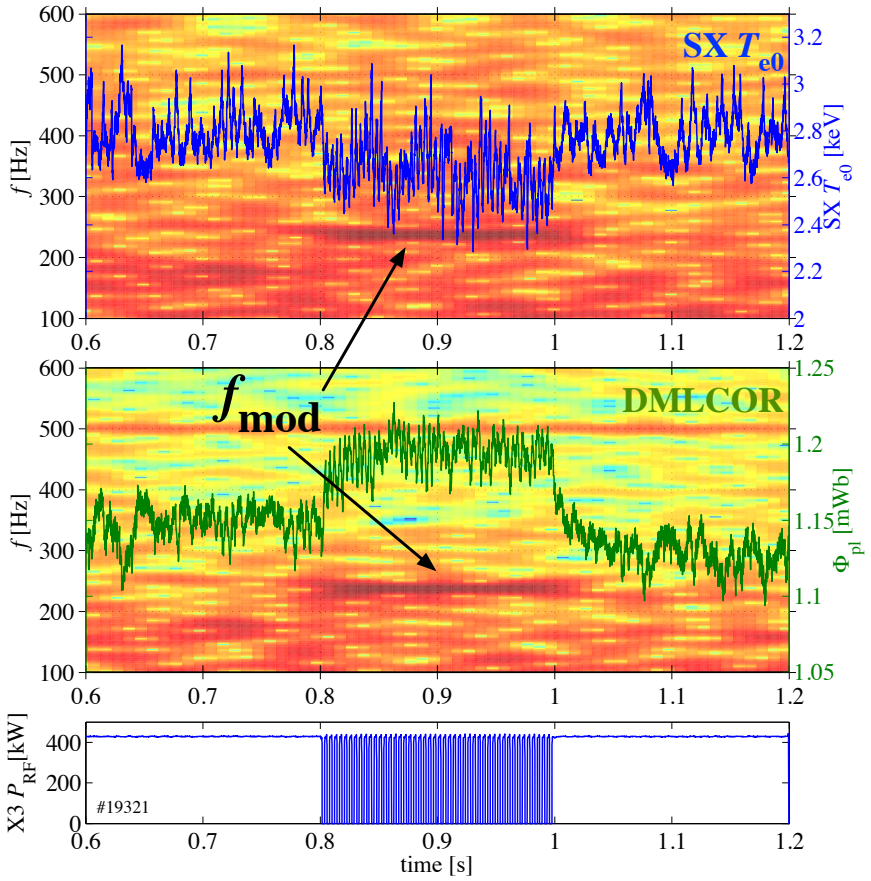

Figure 6.22: Irregular plasma oscillations in presence of X2 counter-ECCD. X3 MECH experiment with continuous X2 counter-ECCD at $\phi \simeq -31.5°$. From top to bottom: Spectrograms of the central electron temperature from soft X-ray measurements (absorber method) and of the corrected plasma toroidal flux Φ_{pl} (with superimposed time traces), and X3 power time trace. An irregular plasma oscillation is observed instead of a fixed-frequency sawtooth oscillation, yielding much less pollution of the DML signal at the X3 MECH modulation frequency f_{mod}. TCV shot #19321.

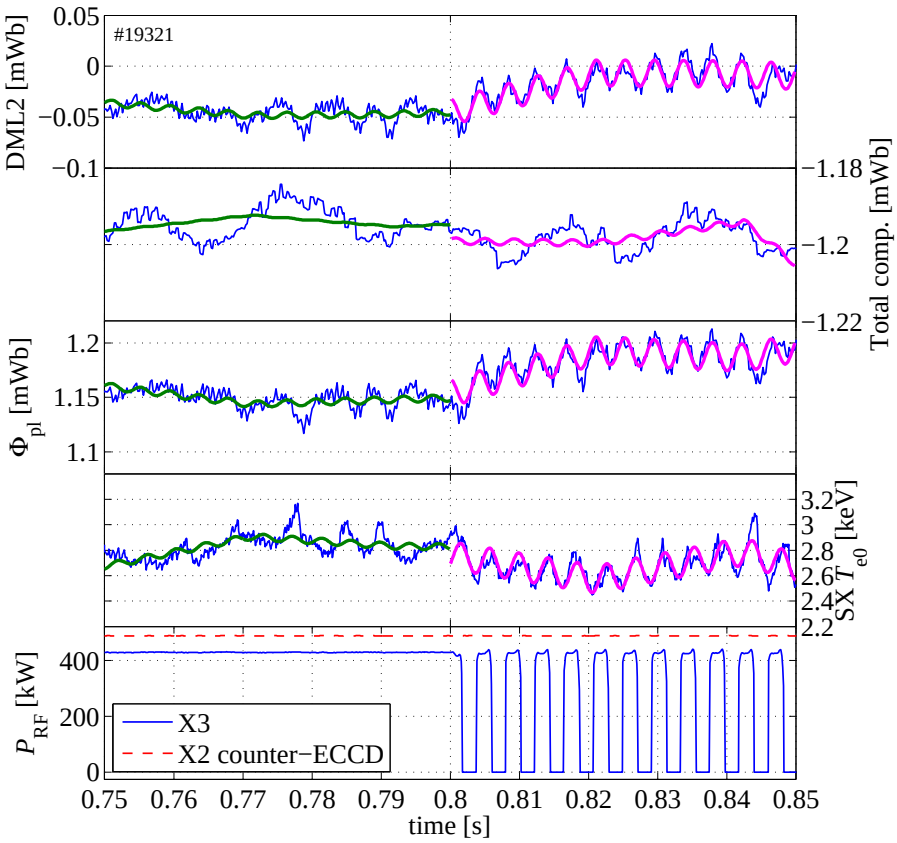

Figure 6.23: Oscillation analysis of the plasma toroidal flux components. X3 MECH experiment with continuous X2 counter-ECCD at $\phi \simeq -31.5°$. From top to bottom: uncorrected plasma toroidal flux Φ_{DML2} from the DML2 loop, total compensation flux Φ_{BO}, corrected plasma toroidal flux Φ_{pl}, central electron temperature from soft X-ray measurements (absorber method), X2 (red dashed) and X3 (blue) power traces. Superimposed on the time traces (blue) are the reconstructed signals from the oscillation analysis at $f = 237$ Hz, before (thick green) and after (thick magenta) the onset of X3 MECH. TCV shot #19321.

	Complex amplitude modulus $\lvert\hat{\Phi}\rvert$	
Modulated signal	**(a) Before MECH**	**(b) During MECH**
Uncorrected plasma flux Φ_{DML2}	2.3 ± 0.6 μWb	12.0 ± 0.7 μWb
Total correction Φ_{BO}	0.3 ± 0.3 μWb	0.8 ± 0.2 μWb
Corrected plasma flux Φ_{pl}	2.2 ± 0.6 μWb	11.6 ± 0.6 μWb
Electron temperature T_{e0}	18 ± 5 eV	111 ± 4 eV

Table 6.3: Modulation amplitudes due to X3 MECH in presence of X2 counter-ECCD. TCV shot #19321, (a) $t = [0.7; 0.8]$ s and (b) $t = [0.8; 0.9]$ s.

X2 ECCD scan

The oscillation analysis at fixed modulation frequency $f = 237$ Hz of the X3 MECH is performed for each experiment in the X2-ECCD scan B. Figure 6.24 shows the

resulting estimates of the X3 power absorption coefficient η and the plasma response phase $\Delta\phi = \phi_{W_\perp} - \phi_{\mathrm{RF}}$ versus the X2 local toroidal angle ϕ. The X3 absorption η seems to improve dramatically in presence of X2 ECCD. But the X3 absorption coefficient dependence on ϕ is asymmetric with respect to the sign of ϕ: in presence of X2 counter-ECCD ($\phi < 0°$) η doubles with respect to the pure X2 ECRH case ($\phi = 0°$), whereas in the experiments with X2 co-ECCD ($\phi > 0°$), η is increased by a factor up to 3 with values above 100%.

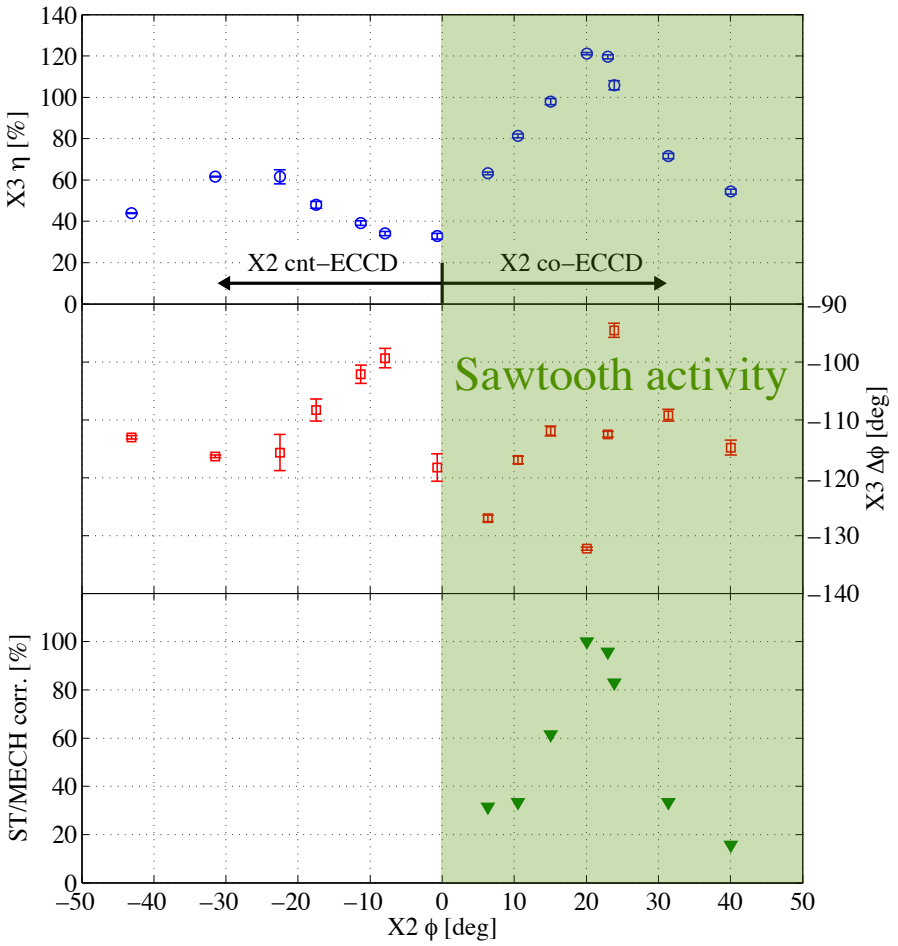

Figure 6.24: X3 absorption versus X2 pre-heating. From top to bottom: X3 absorption estimate from DML measurements, plasma response phase with respect to the X3 MECH excitation and sawtooth/X3 MECH correlation, versus the X2 local toroidal angle ϕ. In the X2 co-ECCD cases, the X3 absorption measurement is strongly polluted by the sawtooth activity, as indicated by the high sawtooth/X3 MECH correlation. Corresponding TCV shot numbers in increasing ϕ order: #19323, 321, 270, 322, 311, 314, 18782 ($\phi = 0°$, pure ECRH), 19284, 274, 286, 312, 269, 285, 278 and 283.

When these experiments were first analyzed and published in [43,97,98], the strong influence of the sawtooth activity on the DML measurements was not noticed. In these references, the experimental results are compared to the absorption calculated

by the linear ray tracing code TORAY-GA. Although the numerical results exhibit a symmetric improvement of the X3 absorption in presence of the X2 co- and counter-ECCD, this is not sufficient to explain the absorption observed in the experiment. This discrepancy was thought to come from the TORAY-GA code assuming an isotropic distribution function and thus neglecting the effect of the hot electrons generated by the X2 ECCD, but the asymmetry versus ϕ and the values above 100% in the X2 co-ECCD cases remained unexplained.

Recent quasi-linear Fokker-Planck simulations of these experiments were performed with the LUKE code [99], but the expected X3 power absorption increase due to the electron distribution function anisotropy was not observed.

From the detailed analysis presented in the previous paragraphs, we now know that the asymmetry of the X3 power absorption with respect to the local toroidal angle ϕ of the X2 pre-heating is due to the adverse effect of sawtooth in the X2 co-ECCD case, yielding erroneous estimate of the X3 absorption coefficient by oscillation analysis of the DML measurements. Moreover, one cannot exclude some pollution from natural plasma oscillations in the results for the X2 counter-ECCD cases too.

A direct estimate of the sawtooth/X3 MECH correlation in the experiments with X2 co-ECCD pre-heating is obtained by counting the numbers $n_{\mathrm{crash,ON}}$ and $n_{\mathrm{crash,OFF}}$ of sawtooth crashes happening when the X3 power is on and off, respectively. With n_{crash} the total number of sawtooth crashes, the observer defined as

$$\mathrm{corr} \equiv \left| \frac{n_{\mathrm{crash,ON}}}{n_{\mathrm{crash}}} - \frac{n_{\mathrm{crash,OFF}}}{n_{\mathrm{crash}}} \right| \tag{6.4.20}$$

is 0% when there is no sawtooth/X3 MECH correlation (50% of crashes when X3 is on, 50% of crashes when X3 is off) and 100% for a perfect sawtooth/X3 MECH correlation (all crashes when X3 is on or off). In the X3 MECH experiments with X2 co-ECCD pre-heating, this correlation measure reaches 100% for $\phi \simeq 20°$, see figure 6.24. The sawtooth activity is perfectly locked to the X3 MECH and the absorption measurement is completely erroneous.

Summary

The sensitivity of the X3 absorption efficiency on the X2 ECCD pre-heating conditions is studied in limited L-mode plasmas using the DML measurements. Detailed analysis of the plasma toroidal flux Φ_{pl} before and after the X3 MECH onset reveals that in the plasmas with X2 co-ECCD pre-heating the amplitude of the unexpected Φ_{pl} modulation caused by the sawtooth activity is of the same order than the amplitude of the modulation produced by the X3 power excitation. A clear frequency

locking of the sawtooth activity on the X3 MECH makes it impossible to distinguish both modulation sources and leads to an overestimation of the X3 power absorbed fraction. The apparent asymmetry of the X3 power absorption with respect to the sign of the X2 RF-driven current is thus caused by different sawtooth activity regimes.

6.5 X2 MECH experiments

6.5.1 MECH frequency scan in presence of sawtooth activity

Introduction

In view of the difficulties met in section 6.4 for the estimation of the X3 power absorption in X3 MECH experiments with X2 ECCD pre-heating using the DML diagnostic, the method is tested in the present section for a simpler scenario, i.e. X2 MECH without ECCD. According to the ray-tracing calculations, the X2 power is fully absorbed, which makes the interpretation of the experimental results easier than in the X3 MECH experiments.

Experimental setup

The equilibrium is a limited L-mode plasma with edge elongation $\kappa_a \simeq 1.5$ and edge triangularity $\delta_a \simeq 0.39$ located close to the machine equator ($Z_{\text{axis}} \simeq 0.03$ m and $R_{\text{axis}} \simeq 0.88$ m). The vacuum toroidal magnetic field at the vessel center is $B_{\varphi \text{v}}(R_0) \simeq -1.44$ T and the plasma current during the ECH phase is $I_\varphi \simeq -250$ kA (where the minus signs indicate that both the magnetic field and the plasma current circulate in the clockwise direction). The safety factor at the edge is $q_a > 5$ and the sawtooth activity has a frequency $f_{\text{st}} \simeq 480 \pm 31$ Hz in the Ohmic phase (#40685, $t = [0.2; 0.3]$ s).The sawtooth frequency drops down to $f_{\text{st}} \simeq 248 \pm 25$ Hz during ECH (#40685, $t = [0.36; 0.46]$ s), as indicated by the spectrograms in figure 6.28. The central electron density and temperature are $n_{e0} \simeq 1.8 \cdot 10^{19}$ m^{-3} and $T_{e0} \simeq 2.6$ keV, respectively. The relevant plasma parameters traces are given in figure 6.25.
The RF power of four second harmonic gyrotrons (G1, G2, G4 and G5) in X-mode polarization (X2) is used in these experiments in order to increase the signal to noise ratio of the plasma response to MECH with an important power modulation depth. The X2 power beams are injected from the equatorial launchers L1 and L4, and from the upper lateral launchers L2 and L5 with launcher angles $(\theta_{\text{L}}, \phi_{\text{L}}) \simeq (14°, 180°)$ and $(\theta_{\text{L}}, \phi_{\text{L}}) \simeq (50°, 0°)$, i.e. the X2 power beams are injected in the poloidal plane

($\phi_{\rm inj} \simeq 0°$) with an upward poloidal angle $\theta_{\rm inj} \simeq 14°$ and a downward poloidal angle $\theta_{\rm inj} \simeq -50°$, respectively. The ECH begins at $t = 0.3$ s with a 200 ms power flattop corresponding to the average level during the modulation in order to start the modulation in stationary conditions and to ensure a continuous heating level. It allows the observation of the MHD activity with the same level of additional heating than during the modulated ECH.

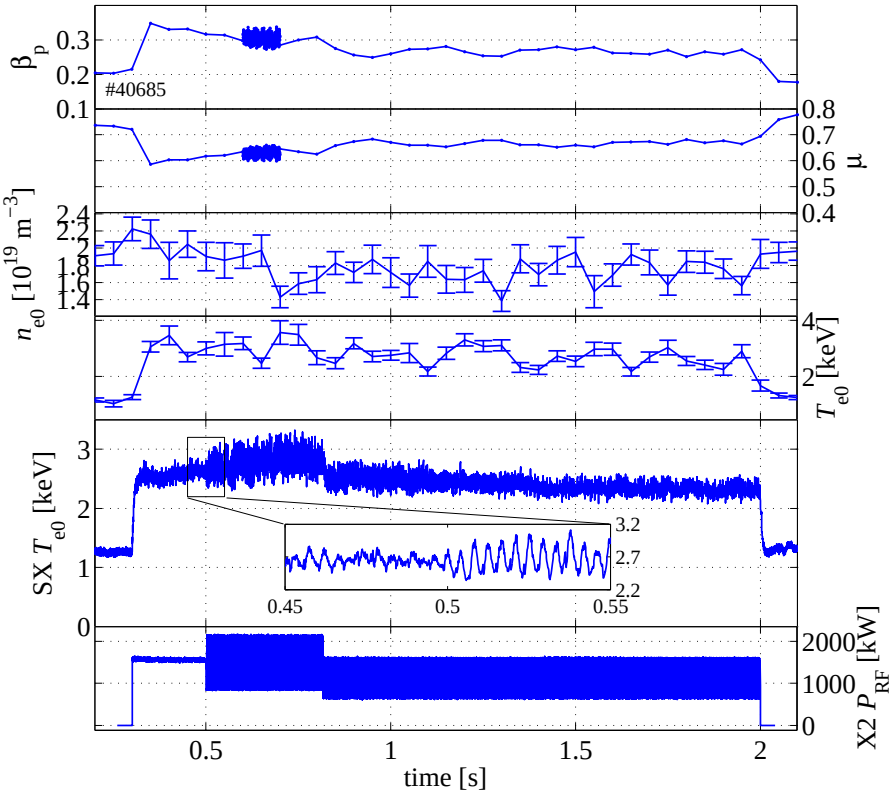

Figure 6.25: X2 MECH experiment in presence of sawtooth activity. From top to bottom: normalized kinetic energy ("poloidal beta") $\beta_{\rm p}$, diamagnetism parameter μ, central electron density $n_{\rm e0}$ and temperature $T_{\rm e0}$ (Thomson scattering, corrected by FIR for the density), central electron temperature determined by the filter method applied to soft X-ray signals, along with a zoom around the X2 MECH onset time at $t = 0.5$ s, X2 total power trace. Between $t = 0.5$ s and $t = 2.0$ s, the X2 power amplitude is modulated with a 50% duty-cycle square waveform and a series of different frequencies. TCV shot #40685.

The power amplitude is then modulated with a 50% duty-cycle square waveform in the time interval $t = [0.5; 2.0]$ s. An identical modulation depth was programmed for all gyrotrons. The actual (measured) modulation depth is slightly different for all gyrotrons due to their individual efficiencies to the applied high voltage. The RF power is modulated between $P_1 \simeq 206$ kW and $P_2 \simeq 522$ kW for G1, $P_1 \simeq 208$ kW and $P_2 \simeq 532$ kW for G2, $P_1 = 210$ kW and $P_2 = 500$ kW for G4 and $P_1 = 245$ kW and $P_2 = 565$ kW for G5. The total modulation depth is $\Delta P \simeq 1250$ kW. Due

to arcs in the gyrotrons resonant cavity or to high stray power levels triggering the ECH safety, gyrotrons have stopped randomly during the experiments (as did G2 at $t \simeq 0.82$ s in figure 6.25). But the resulting various power modulation depths are taken into account in the oscillation analysis and do not affect the experimental results. Finally, the modulation frequency f is scanned in five plasma discharges, with several successive values in each discharge, as summarized in table 6.4.

Shot	**Time**	**Gyrotrons**	**MECH f**	**Comment**
	[s]		[Hz]	
#40683	[0.5; 1.25]	1, 2	19	G4 & 5 stop at $t \simeq 0.31$ s.
	[1.25; 2.0]	1, 2	37	
#40685	[0.5; 0.8]	1, 2, 4, 5	237	
	[0.8; 1.1]	1, 4, 5	277	G2 stops at $t \simeq 0.82$ s.
	[1.1; 1.4]	1, 4, 5	337	
	[1.4; 1.7]	1, 4, 5	377	
	[1.7; 2.0]	1, 4, 5	437	
#40688	[0.5; 0.8]	1, 4, 5	237	G2 stops at $t \simeq 0.51$ s.
	[0.8; 1.1]	1, 4, 5	277	
	[1.1; 1.4]	(1), 4, 5	337	G1 stops at $t \simeq 1.26$ s.
	[1.4; 1.7]	4, 5	377	
	[1.7; 2.0]	4, 5	437	
#40689	[0.5; 0.875]	1, 4, 5	137	G2 not used.
	[0.875; 1.125]	1, 4, 5	169	
	[1.125; 1.625]	1, 4, 5	193	
	[1.625; 1.2]	1, 4, 5	213	
#40690	[0.5; 0.75]	1, 4, 5	467	G2 not used.
	[0.75; 1.0]	1, 4, 5	537	
	[1.0; 1.25]	1, 4, 5	577	
	[1.25; 1.5]	1, 4, 5	637	
	[1.5; 1.75]	1, 4, 5	677	
	[1.75; 2.0]	1, 4, 5	737	

Table 6.4: X2 MECH setup.

Ray-tracing calculation

The trajectory and the linear absorption efficiency of the X2 beams from launchers L1 and L2 are calculated with 25-ray bundles for TCV shot #40685 (at $t = 0.5$ s) using the ray-tracing C3PO code [29]. The simulation results are identical for the X2 beams coming from launchers L4 and L5, respectively.

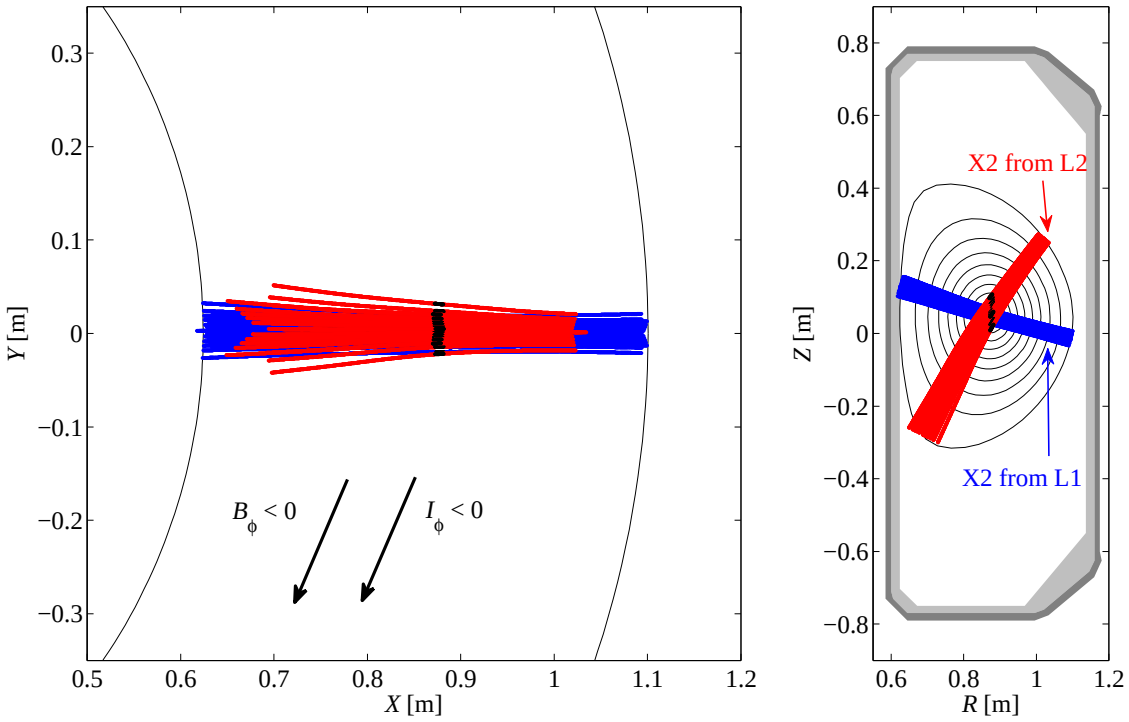

(a) Toroidal trajectories. **(b)** Poloidal trajectories.

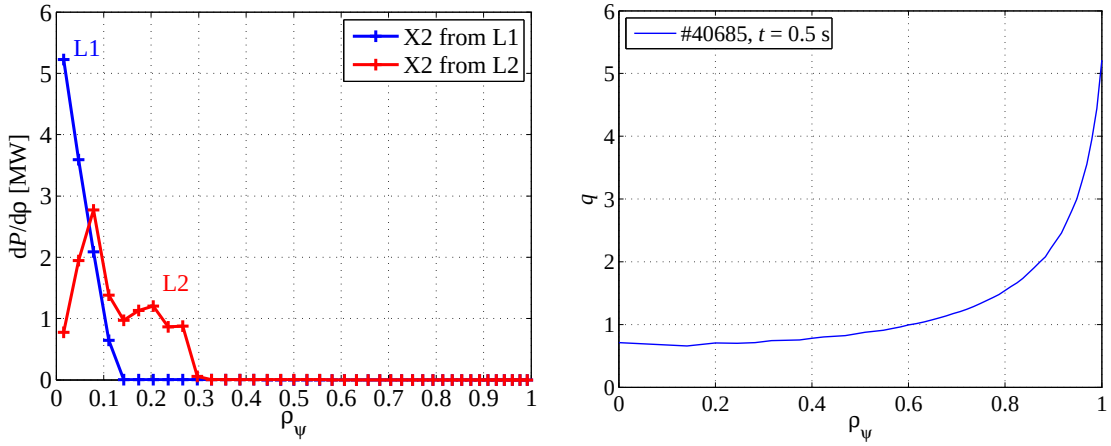

(c) Linear power deposition profiles. **(d)** Safety factor profile.

Figure 6.26: X2 power beams trajectories and deposition profiles. C3PO ray-tracing simulations for the X2 power beams from launchers L1 (blue) and L2 (red). (a) Toroidal trajectories and (b) poloidal trajectories (on ρ_ψ contours). (c) Linear power deposition profiles and (d) safety factor profile. Both beams are deposited inside the $q = 1$ surface. TCV shot#40685 at $t = 0.5$ s.

The resulting toroidal and poloidal beam trajectories are given in figures 6.26(a) and 6.26(b), respectively, along with the linear power deposition profiles in figure 6.26(c). The X2 power beams from launchers L1 and L2 are absorbed with an efficiency $\eta \simeq 100\%$ and deposition profiles centered at $\rho_\psi \simeq 0$ and $\rho_\psi \simeq 0.15$, respectively. According to the power deposition profiles and to the safety factor profile given in figure 6.26(d), all beams are deposited inside the $q = 1$ flux surface located at $\rho_\psi \simeq 0.6$. Simulations with the TORAY code are in perfect agreement with the numerical results of C3PO.

Oscillation analysis

The usual oscillation analysis is performed to check the assumptions summarized in subsection 6.3.4. The figure 6.27 shows an example of this analysis for the case of four gyrotrons modulated at $f = 237$ Hz.

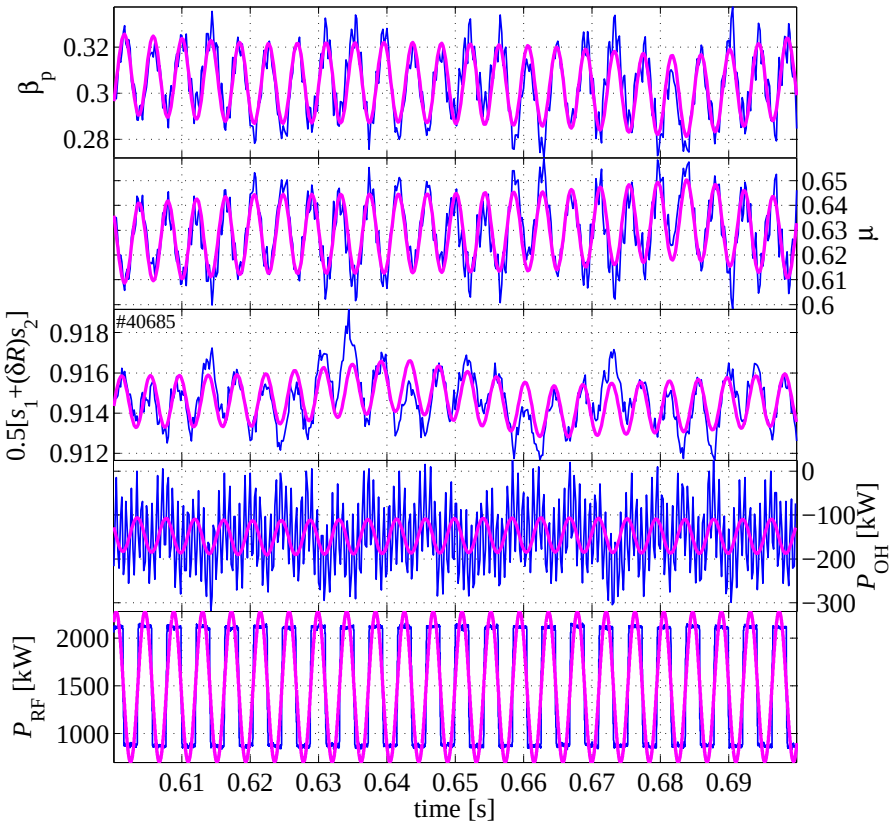

Figure 6.27: Oscillation analysis of the various plasma energies and input powers. From top to bottom: LIUQE normalized kinetic energy β_p, normalized plasma toroidal magnetic energy μ and normalized Shafranov integral combination s^*, as well as Ohmic power and X2 RF power. Superimposed on the time traces (in blue) are the reconstructed signals from the oscillation analysis at $f = 237$ Hz (in thick magenta). TCV shot #40685.

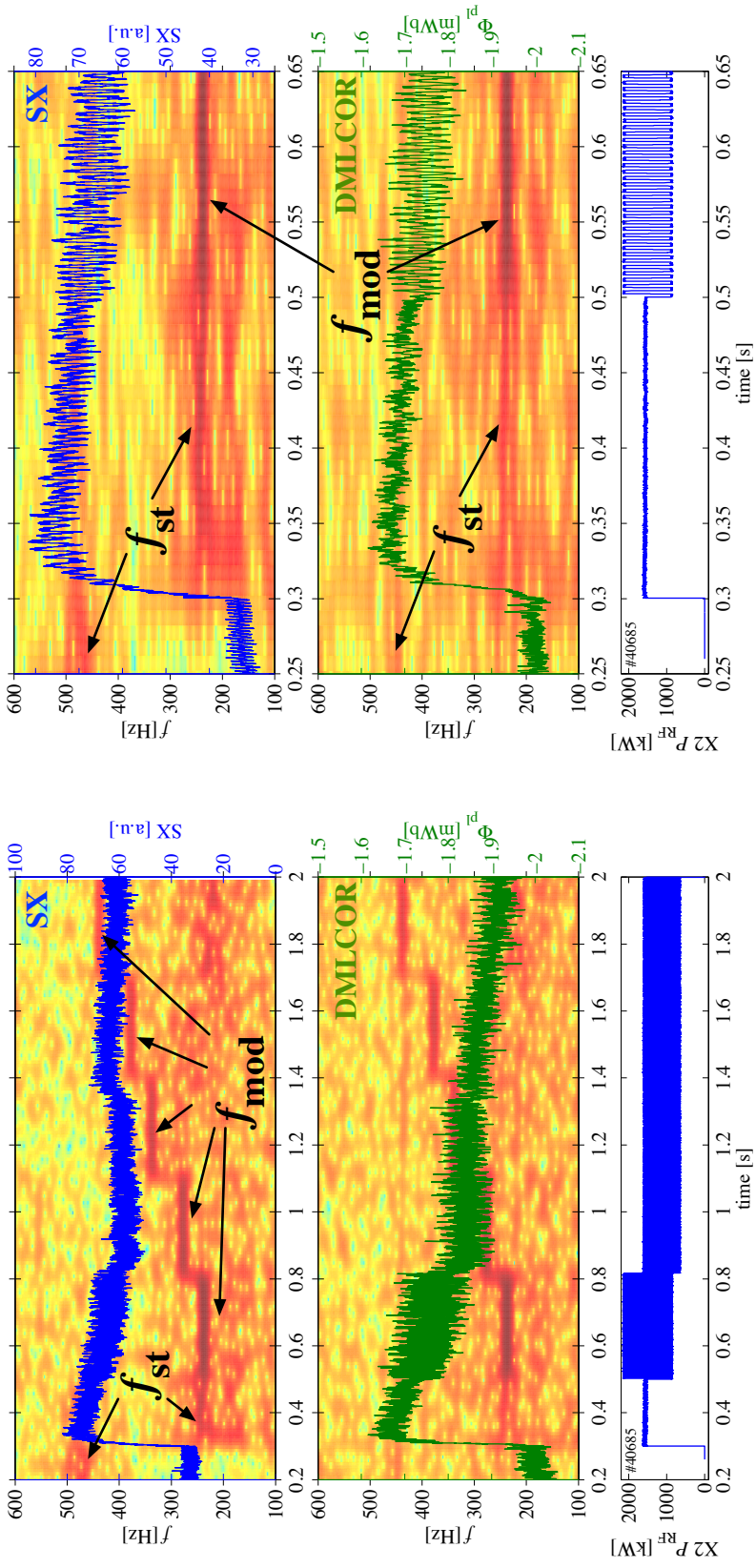

(a) Whole X2 MECH frequency scan.

(b) Zoom on X2 MECH onset.

Figure 6.28: X2 MECH frequency scan in presence of sawtooth activity. From top to bottom: Spectrogram of the soft X-ray signal from a central-viewing channel (DMPX # 32), spectrogram of the corrected plasma toroidal flux Φ_{pl}, and total X2 power time trace (gyrotrons G1, 2, 4 and 5). The signal time traces are superimposed on the spectrograms. (a) Total X2 MECH frequency scan and (b) zoom on the X2 MECH onset. The successive MECH and sawtooth frequencies are indicated by f_{mod} and f_{st}, respectively. The sawtooth frequency drops from $f_{st} \simeq 480$ Hz to $f_{st} \simeq 250$ Hz when the ECH starts at $t = 0.3$ s and the perturbation induced on Φ_{pl} is not negligible. The sawtooth activity will contribute to the Φ_{pl} modulations induced by the MECH starting at $t = 0.5$ s. TCV shot #40685.

The resulting complex amplitude moduli of the poloidal beta, the plasma diamagnetism and the Shafranov integrals are $|\hat{\beta}_{\rm p}| \simeq (17.4 \pm 0.6)\cdot 10^{-3}$, $|\hat{\mu}| \simeq (16.0 \pm 0.5)\cdot 10^{-3}$ and $|\widehat{s^*}| \simeq (1.29 \pm 0.06)\cdot 10^{-3}$, respectively. Accordingly, one has

$$\frac{|\hat{\mu}|}{|\hat{\beta}_{\rm p}|} \simeq 92 \pm 6\% \qquad \text{and} \qquad \frac{|\widehat{s^*}|}{|\hat{\beta}_{\rm p}|} \simeq 7.4 \pm 0.6\% \tag{6.5.1}$$

and the modulation of s^* can be neglected. The complex amplitude moduli of the Ohmic power and the RF power are $|\hat{P}_{\rm OH}| \simeq 39 \pm 5$ kW and $|\hat{P}_{\rm RF}| \simeq 790 \pm 3$ kW such that $|\hat{P}_{\rm OH}|/|\hat{P}_{\rm RF}| \simeq 5.0 \pm 0.7\%$ and the modulation of the Ohmic power can be safely neglected.

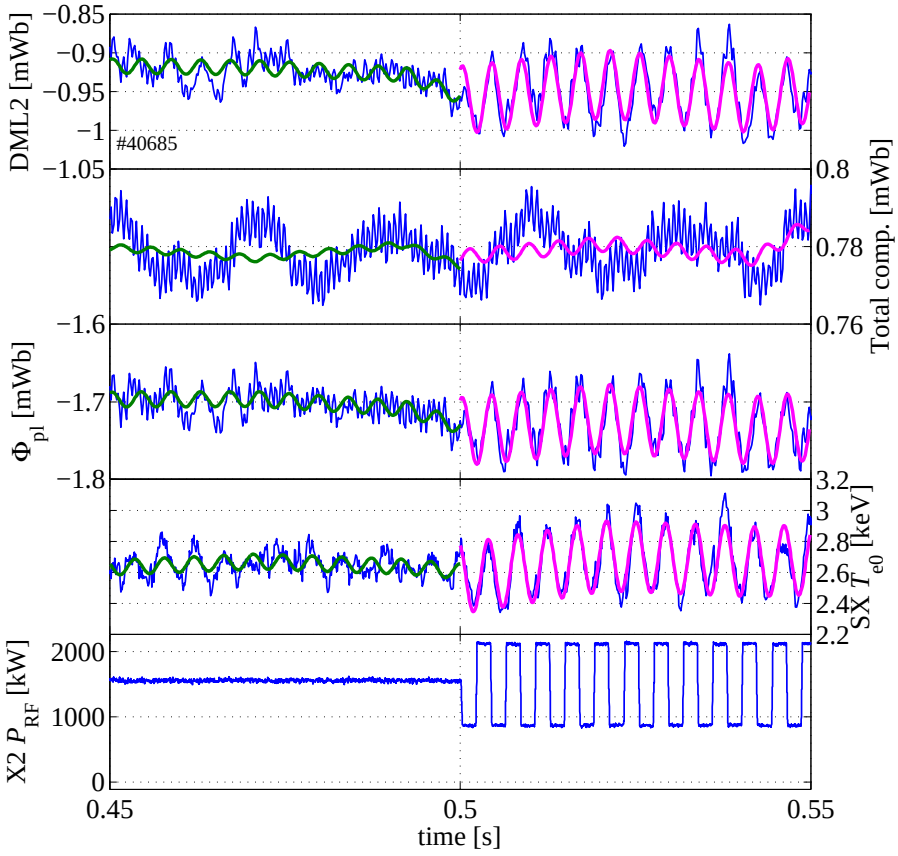

Figure 6.29: Oscillation analysis of the plasma toroidal flux components. From top to bottom: uncorrected plasma toroidal flux $\Phi_{\rm DML2}$ from the DML2 loop, total compensation flux $\Phi_{\rm BO}$, corrected plasma toroidal flux $\Phi_{\rm pl}$, central electron temperature from soft X-ray measurements (absorber method) and X2 power trace. Superimposed on the time traces (blue) are the reconstructed signals from the oscillation analysis at $f = 237$ Hz, before (thick green) and after (thick magenta) the onset of X2 MECH. TCV shot #40685.

The oscillation analysis of the plasma toroidal flux components is performed before and after the MECH onset, see figure 6.29. The respective complex amplitude moduli are given in table 6.5. The sawtooth activity at $f_{\rm st} \simeq 248$ Hz before the X2

MECH onset is clearly visible on the soft X-ray trace. The sawtooth oscillation also affects the plasma toroidal flux and its modulation amplitude before the X2 MECH onset is not negligible, see figure 6.28.

	Complex amplitude modulus $\lvert\hat{\Phi}\rvert$	
Modulated signal	**(a) Before MECH**	**(b) During MECH**
Uncorrected plasma flux Φ_{DML2}	9.3 ± 1.5 μWb	47.9 ± 1.6 μWb
Total correction Φ_{BO}	0.9 ± 0.6 μWb	2.2 ± 0.6 μWb
Corrected plasma flux Φ_{pl}	9.7 ± 1.4 μWb	47.9 ± 1.5 μWb
Electron temperature T_{e0}	51 ± 4 eV	241 ± 5 eV

Table 6.5: Modulation amplitudes due to X2 MECH in presence of sawtooth activity. TCV shot #40685, (a) $t = [0.4; 0.5]$ s and (b) $t = [0.5; 0.6]$ s.

Experimental frequency response and transfer function fitting

The oscillation analysis is performed for each X2 MECH frequency and the experimental transfer function is calculated according to equation (6.3.43). The oscillation analysis at the third and fifth harmonics is also used for the two lowest X2 MECH frequencies. The resulting amplitude and phase are given in figure 6.31 to be compared with the model transfer functions plotted in figure 6.6.

Instead of a saturation at $\Delta\phi = -90°$, the experimental transfer function phase $\Delta\phi$ exhibits jumps to $\Delta\phi = -135°$ and $\Delta\phi = -180°$ occurring at frequencies close to the fundamental and the second harmonics of the sawtooth frequency, respectively. A maximum of the transfer function amplitude is observed at the fundamental of the sawtooth frequency: for X2 MECH frequencies close to the sawtooth frequency, the plasma toroidal flux modulation due to the sawtooth activity adds to the modulation due to the MECH which artificially increases the plasma response to the MECH and subsequently the RF power absorption estimate.

The system transfer identification (STI) fit is performed on the experimental data for several orders M and N of the numerator and of the denominator of (6.3.46), see figure 6.30. The best fit matching with a known model of the plasma response to MECH is obtained for $M = 1$ and $N = 2$, i.e. a transfer function of the type

$$H_{12} = \frac{b_0 + b_1(\mathrm{i}\omega)}{a_0 + a_1(\mathrm{i}\omega) + a_2(\mathrm{i}\omega)^2} \tag{6.5.2}$$

where $a_2 = 1$. This fit corresponds to the the model transfer function H_2 given by (6.3.35). The resulting fit is shown in figures 6.31, 6.32 and 6.33. It reproduces

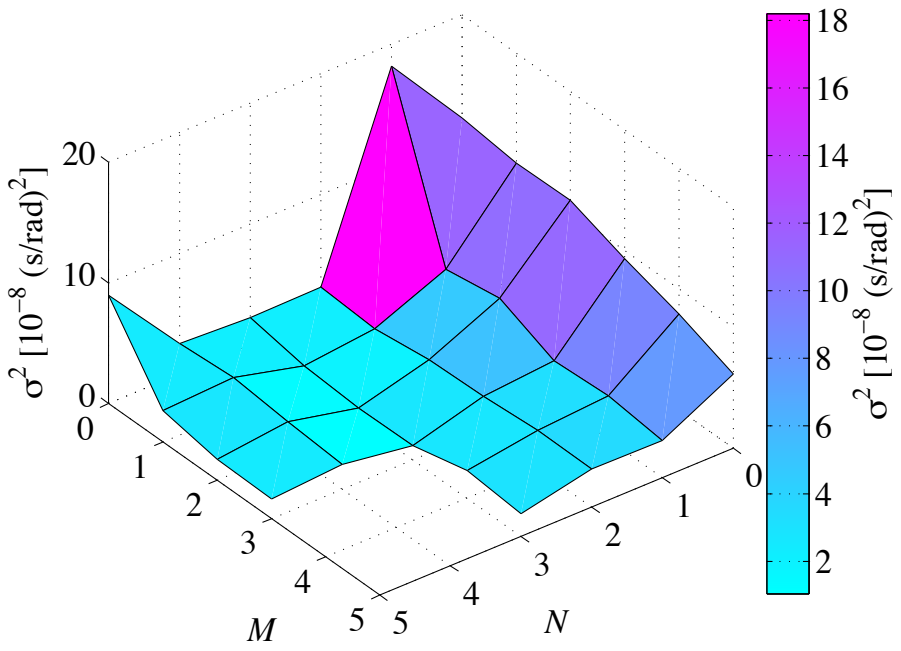

Figure 6.30: X2 MECH. STI optimization. Loss function σ^2 of the STI fitting of the plasma frequency response to X2 MECH for several numerator and denominator orders M and N. The lowest orders corresponding to a model of the system dynamic and yielding an acceptable loss function value are $M = 1, N = 2$. The STI method does not converge for $M = N = 4$.

well the trend of the amplitude, the phase and the real and imaginary parts of the experimental transfer function on the whole frequency span. Identifying the coefficients of H_2 with the fit parameters of H_{12} obtained from the STI gives:

$$\eta \frac{\tau_a + \tau_{inc}}{\tau_a \tau_{inc}} = b_0 \simeq 761 \text{ s}^{-1} \tag{6.5.3}$$

$$\eta = b_1 \simeq -0.06 \tag{6.5.4}$$

$$\frac{2\tau_a + 3\tau_{inc}}{2\tau_a \tau_{inc}^2} = a_0 \simeq 2.05 \cdot 10^6 \text{ s}^{-2} \tag{6.5.5}$$

$$\frac{4\tau_a + 3\tau_{inc}}{2\tau_a \tau_{inc}} = a_1 \simeq 1.25 \cdot 10^3 \text{ s}^{-1} \tag{6.5.6}$$

which clearly yields non-reasonable physical parameters, in particular a negative absorption coefficient $\eta \simeq -6\%$.

As in the X3 MECH frequency scan experiment, the denominator roots $s_{1,2} = \mathrm{i}\omega_{1,2}$ of H_{12} are complex conjugate and yield pole frequencies with a real part

$$\omega_{1,2} \simeq \pm 1288 + 625\mathrm{i} \text{ rad/s}. \tag{6.5.7}$$

This indicates that the system behaves like a forced damped harmonic oscillator

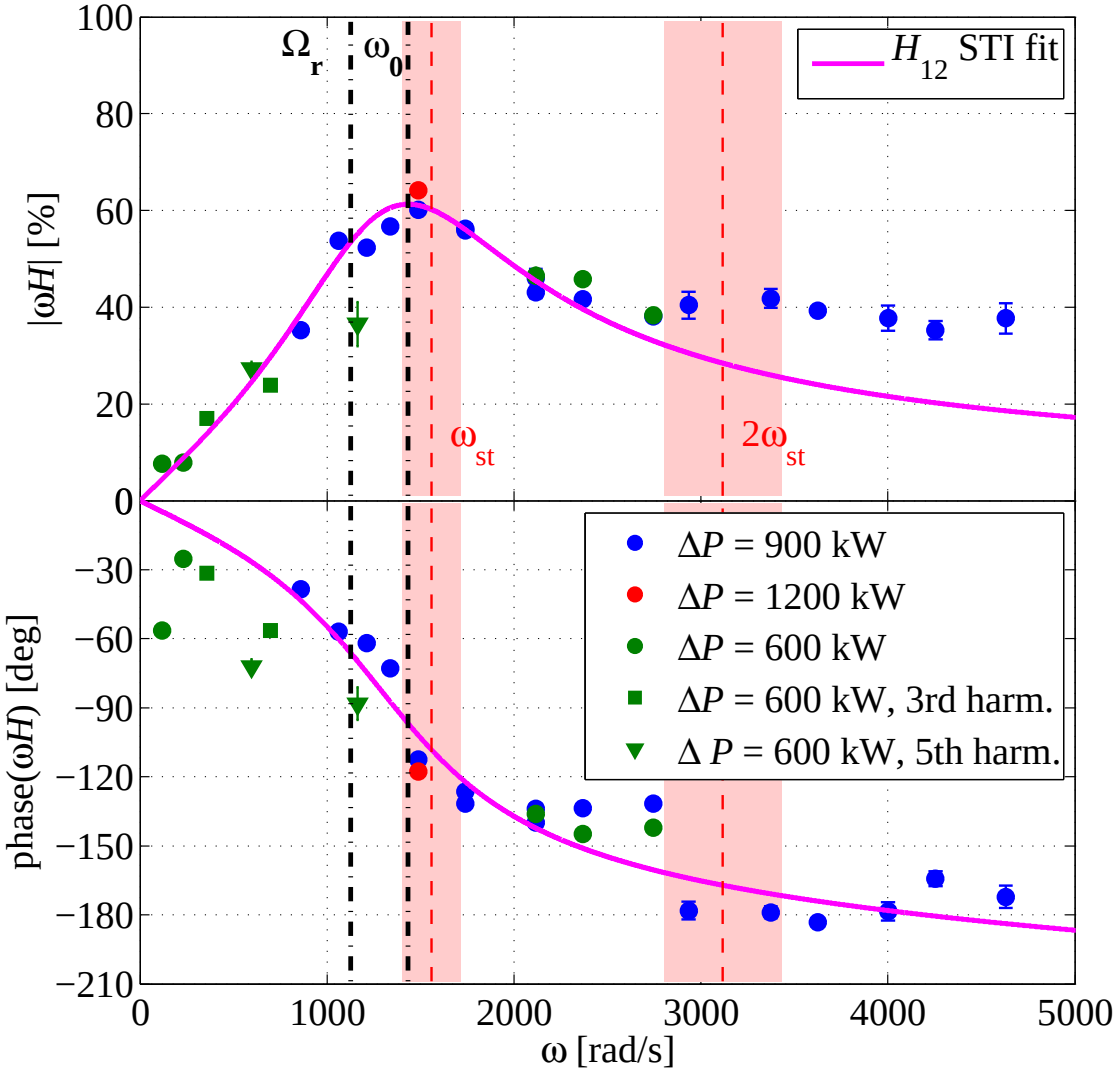

Figure 6.31: Experimental frequency response to X2 MECH in presence of sawtooth activity. Amplitude and phase of the experimental plasma frequency response at the first (•), third (■) and fifth (▼) harmonics of the X2 MECH excitation angular frequencies ω, along with the STI fit for $M = 1, N = 2$. The vertical dashed lines indicate the first and second harmonics of the sawtooth angular frequency. The light red surfaces denote their standard deviations.

with the following parameters:

$$\omega_0 \equiv \sqrt{\Omega^2 + \gamma^2} \simeq 1432 \text{ rad/s} \qquad \text{proper angular frequency} \qquad (6.5.8)$$

$$Q \equiv \frac{\omega_0}{2\gamma} \simeq 1.15 \qquad \text{quality factor} \qquad (6.5.9)$$

$$\Omega_r \equiv \omega_0 \sqrt{1 - \frac{1}{2Q^2}} \simeq 1126 \text{ rad/s} \qquad \text{resonant angular frequency} \qquad (6.5.10)$$

Conversely to the X3 MECH case, the damping is low enough to allow the presence of a resonance in the plasma frequency response to X2 MECH. The resonant behavior

of the experimental transfer function is clear in figures 6.32 and 6.33, with the maximum amplitude $|H|$ reached at the Ω_r. The proper angular frequency coincides with the sawtooth angular frequency $\omega_{st} \simeq 1558 \pm 157$ rad/s estimated prior to the MECH onset but with the same time-averaged ECH level. The sawtooth activity is thus a good candidate to explain the intrinsic oscillatory behavior of the system and the energy transfer mechanism necessary in a resonant effect.

Summary

A frequency scan of X2 MECH is performed in limited L-mode plasmas in presence of sawtooth activity. As suspected from the earlier X3 MECH frequency scan, the plasma response behaves like a forced and damped harmonic oscillator with a resonance at the sawtooth frequency. In such a situation, our transfer function model becomes inadequate and no relevant estimate of the physical parameters can be drawn from the experiment. To do so, a modification of the physical model of the system is necessary. Prior to this, the next subsection is devoted to test the method with X2 MECH experiments in low-current L-mode plasmas without sawtooth activity.

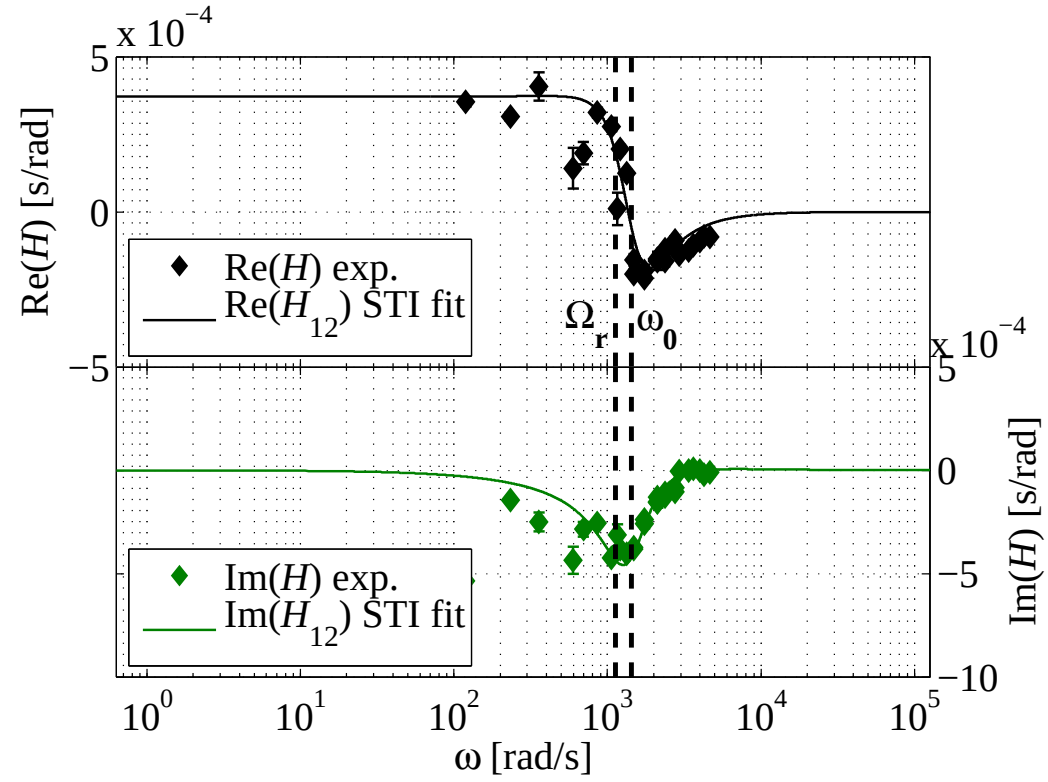

(a) Real and imaginary parts of H.

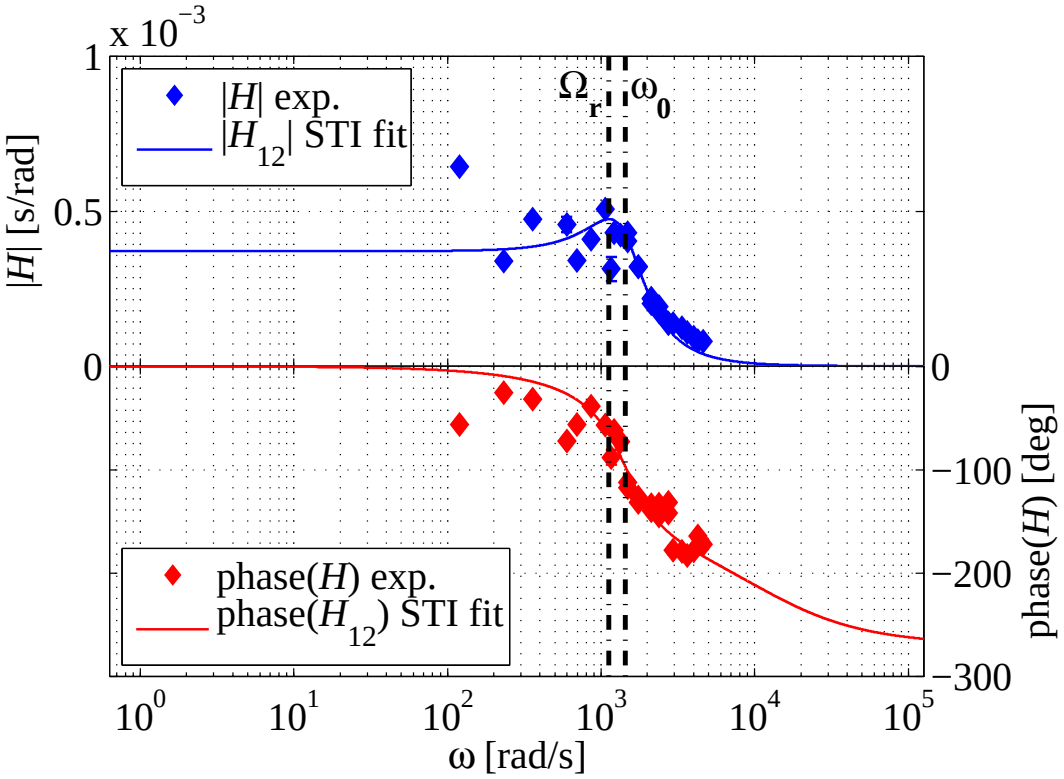

(b) Amplitude and phase of H.

Figure 6.32: Experimental frequency response to X2 MECH in presence of sawtooth activity and STI fit H_{12}.

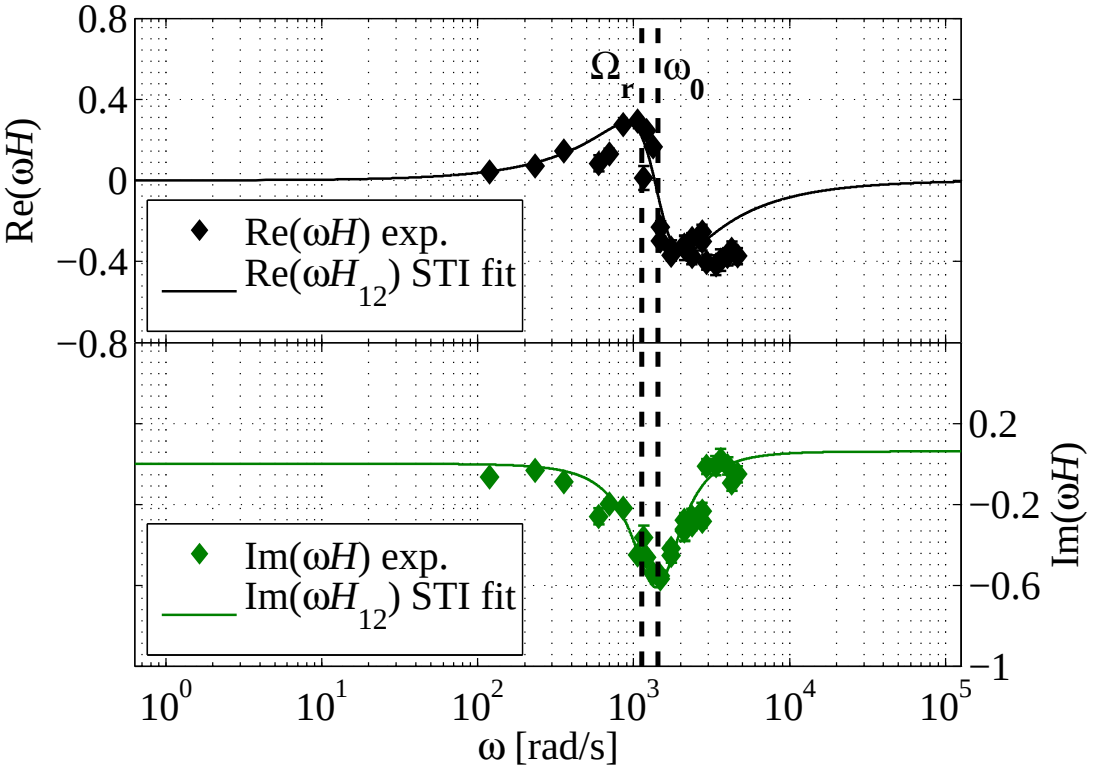

(a) Real and imaginary parts of ωH.

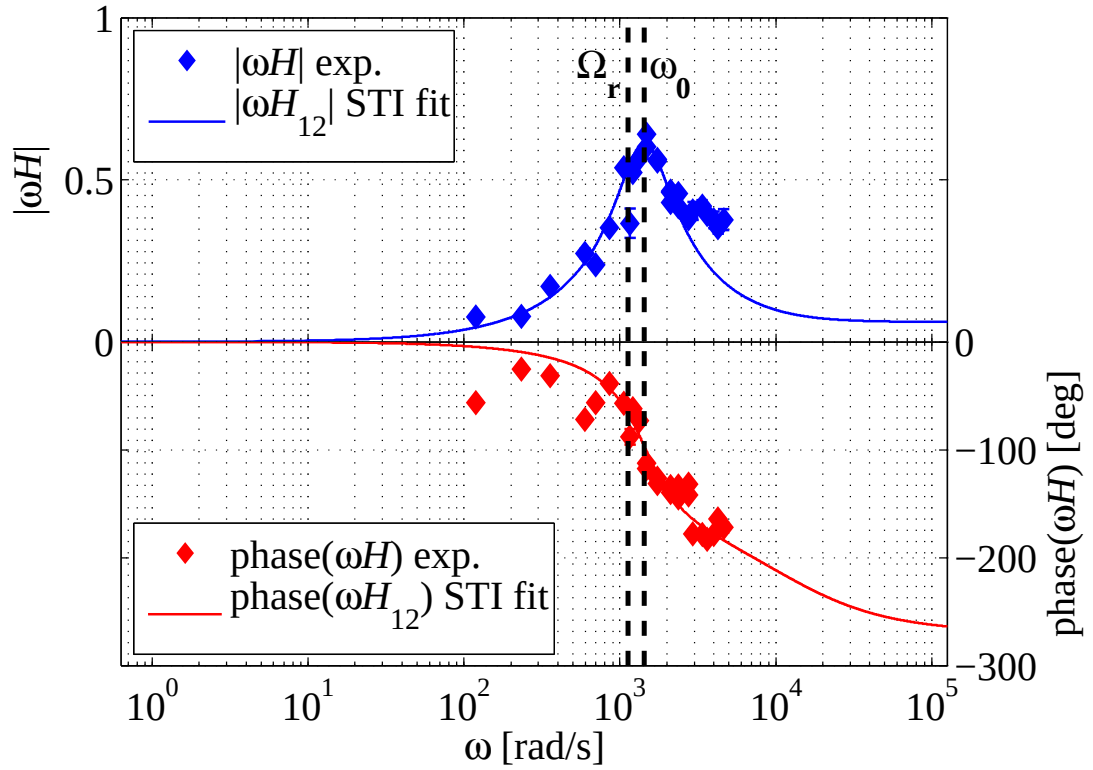

(b) Amplitude and phase of ωH.

Figure 6.33: Experimental frequency response to X2 MECH in presence of sawtooth activity and STI fit H_{12}.

6.5.2 MECH frequency scan in absence of sawtooth activity

Introduction

Since the sawtooth activity has proven to prevent a proper estimate of the RF power absorption in MECH experiments, the X2 MECH frequency scan is repeated in low-current L-mode plasmas without sawtooth activity.

Shot	Time	Gyrotrons	MECH f	Comment
	[s]		[Hz]	
#40928	$[0.7; 1.075]$	1, 2	137	
	$[1.075; 1.45]$	1, 2	169	
	$[1.45; 1.825]$	1, 2	193	
	$[1.825; 2.2]$	(1),(2)	213	G1 & 2 stop at $t \simeq 1.96$ s.
#40931	$[0.7; 1.0]$	1, 2	237	
	$[1.0; 1.3]$	1, 2	277	
	$[1.3; 1.6]$	(1),(2)	337	G1 & 2 stop at $t \simeq 1.4$ s.
#40937	$[0.7; 1.0]$	1, 2	237	
	$[1.0; 1.3]$	1, 2	277	
	$[1.3; 1.6]$	1, 2	337	
	$[1.6; 1.9]$	1, 2	377	
	$[1.9; 2.2]$	1, 2	437	

Table 6.6: X2 MECH setup.

Experimental setup

The equilibrium is a limited L-mode plasma with edge elongation $\kappa_a \simeq 1.3$ and edge triangularity $\delta_a \simeq 0.16$ located close to the machine equator ($Z_{\text{axis}} \simeq 0.04$ m and $R_{\text{axis}} \simeq 0.88$ m). The central electron density and temperature are $n_{e0} \simeq 2.0 \cdot 10^{19}$ m^{-3} and $T_{e0} \simeq 3.0$ keV, respectively. The vacuum toroidal magnetic field at the vessel center is $B_{\varphi v}(R_0) \simeq -1.45$ T. The plasma current during the ECH phase is programmed to be very low, i.e. $I_\varphi \simeq -115$ kA and $I_\varphi \simeq -100$ kA, such that the safety factor is $q_a > 7$ at the edge and barely crosses $q = 1$ at plasma center as indicated by the LIUQE safety factor profile in figure 6.35(d). In consequence, no visible sawtooth activity is observed on the central soft X-ray trace given in figure 6.34.

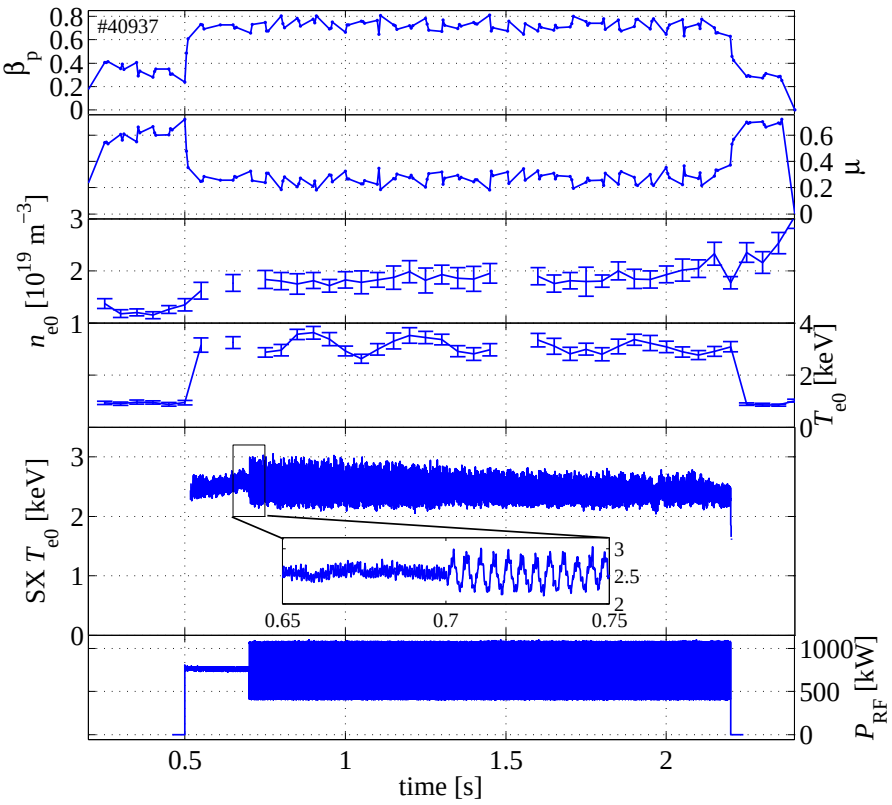

Figure 6.34: X2 MECH experiment in absence of sawtooth activity. From top to bottom: LIUQE β_p and μ, central electron density $n_{\mathrm{e}0}$ and temperature $T_{\mathrm{e}0}$ (Thomson scattering, corrected by FIR for the density), central electron temperature from soft X-ray signals, and X2 total power trace. Between $t = 0.7$ s and $t = 2.2$ s, the X2 power amplitude is modulated with a 50% duty-cycle square waveform and a series of different frequencies. TCV shot #40937.

The RF power of two second harmonic gyrotrons (G1 and G2) in X-mode polarization (X2) is used in these experiments. The X2 power beams are injected from the equatorial launcher L1 and from the upper lateral launcher L2 with launcher angles $(\theta_\mathrm{L}, \phi_\mathrm{L}) \simeq (8°, 0°)$ and $(\theta_\mathrm{L}, \phi_\mathrm{L}) \simeq (49°, 0°)$, i.e. the X2 power beams are injected in the poloidal plane ($\phi_\mathrm{inj} \simeq 0°$) with an downward poloidal angles $\theta_\mathrm{inj} \simeq -8°$ and $\theta_\mathrm{inj} \simeq -49°$, respectively. The ECH begins at $t = 0.5$ s with a 200 ms power flattop corresponding to the average power level during the modulation in order to start the modulation in stationary conditions and to ensure a continuous heating level.

The power amplitude is then modulated with a 50% duty-cycle square waveform in the time interval $t = [0.7; 2.2]$ s. The RF power is modulated between $P_1 \simeq 206$ kW and $P_2 \simeq 522$ kW for G1, and $P_1 \simeq 208$ kW and $P_2 \simeq 532$ kW for G2. The total modulation depth is $\Delta P \simeq 640$ kW. Finally, the modulation frequency f is scanned in three plasma discharges, with several successive values in each discharge, as summarized in table 6.6.

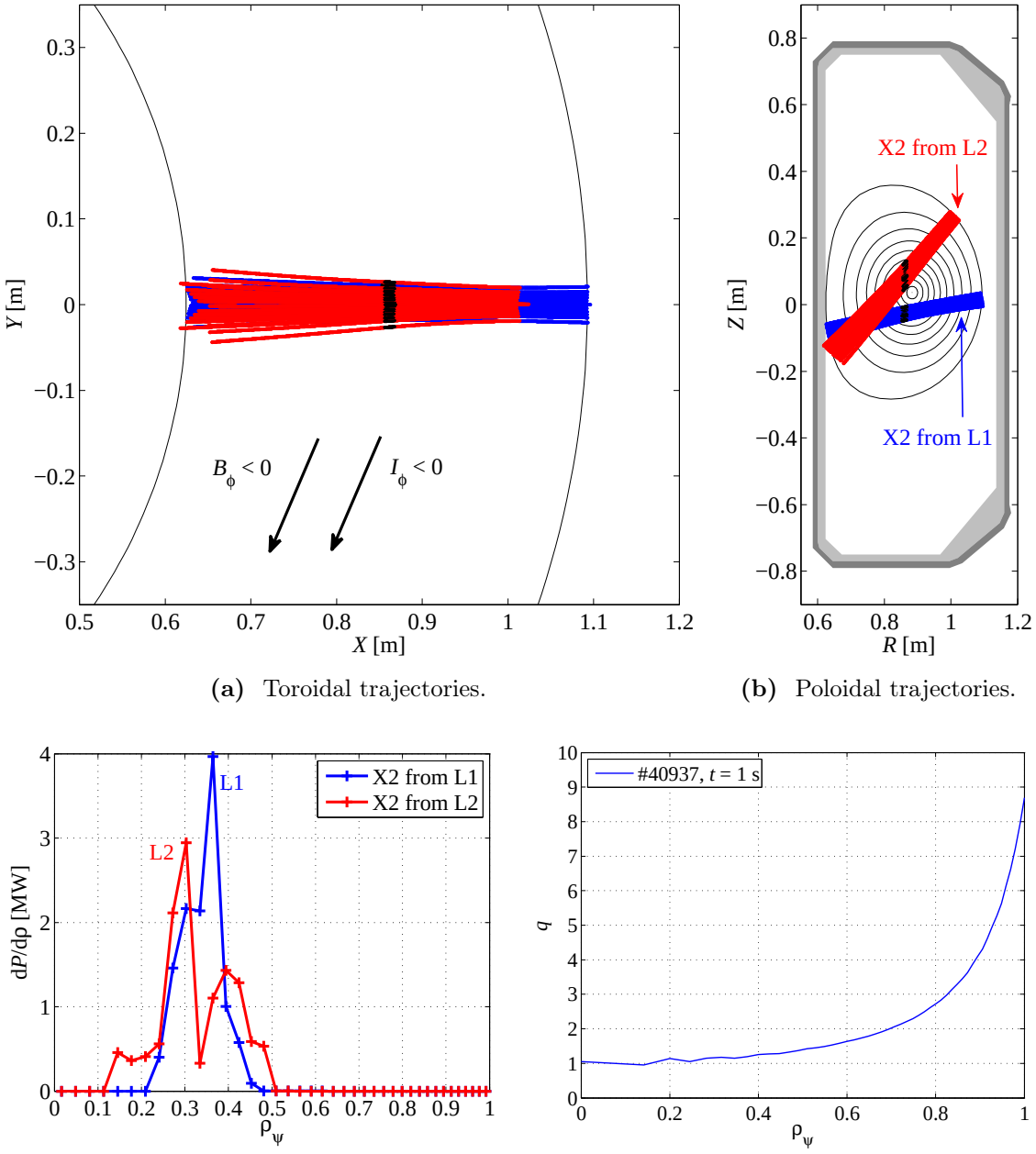

(a) Toroidal trajectories.

(b) Poloidal trajectories.

(c) Linear power deposition profiles.

(d) Safety factor profile.

Figure 6.35: X2 power beams trajectories and deposition profiles. C3PO ray-tracing simulations for the X2 power beams from launchers L1 (blue) and L2 (red). (a) Toroidal trajectories and (b) poloidal trajectories (on ρ_ψ contours). (c) Linear power deposition profiles and (d) safety factor profile. TCV shot#40937 at $t = 1.0$ s.

Ray-tracing calculation

The trajectory and the linear absorption efficiency of the X2 beams from launchers L1 and L2 are calculated with 25-ray bundles for TCV shot #40685 (at $t = 1.0$ s) using the ray-tracing C3PO code [29]. The resulting toroidal and poloidal beam

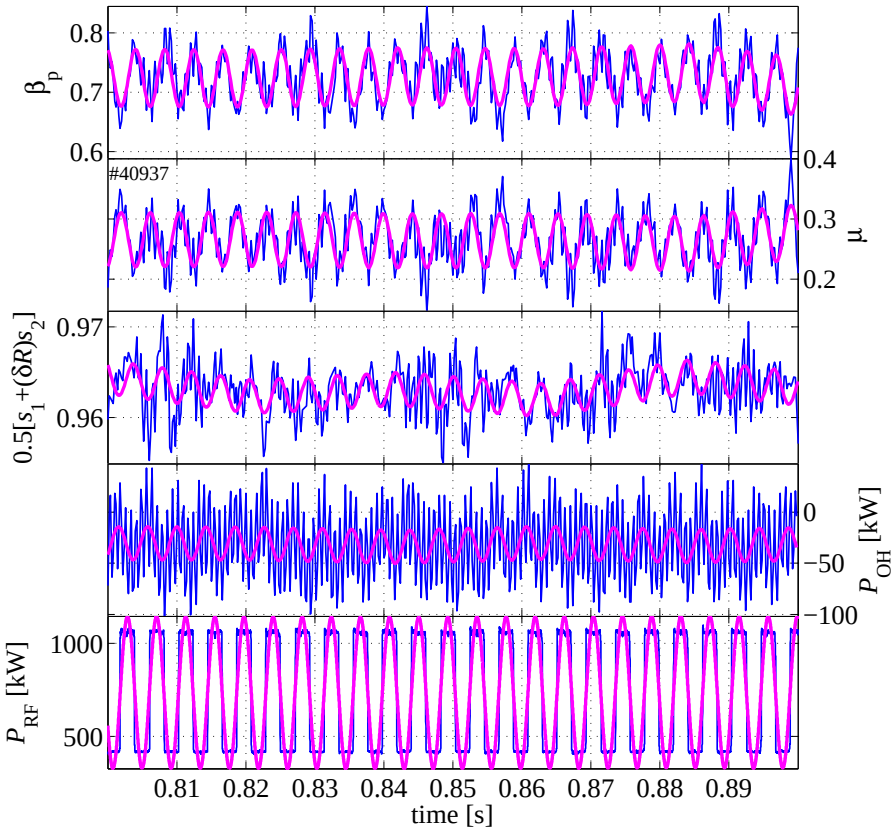

Figure 6.36: Oscillation analysis of the various plasma energies and input powers. From top to bottom: LIUQE normalized kinetic energy β_p, normalized plasma toroidal magnetic energy μ and normalized Shafranov integral combination s^*, as well as Ohmic power and X2 RF power. Superimposed on the time traces (in blue) are the reconstructed signals from the oscillation analysis at $f = 237$ Hz (in thick magenta). TCV shot #40937.

trajectories are given in figures 6.35(a) and 6.35(b), respectively, along with the linear power deposition profiles in figure 6.35(c). The X2 power beams from launchers L1 and L2 are absorbed with an efficiency $\eta \simeq 100\%$ and the deposition profiles are centered at $\rho_\psi \simeq 0.35$ and $\rho_\psi \simeq 0.30$, respectively. According to the safety factor profile given in figure 6.35(d), the RF power is deposited partly inside and partly outside the $q = 1$ flux surface located around $\rho_\psi \simeq 0.2$. Simulations with the TORAY code are in perfect agreement with the numerical results of C3PO.

Oscillation analysis

The usual oscillation analysis is performed to check the assumptions summarized in subsection 6.3.4. The figure 6.36 shows an example of this analysis for the X2 MECH experiment at $f = 237$ Hz. The corresponding complex amplitude moduli are $|\hat{\beta}_p| \simeq (48.4 \pm 2.3) \cdot 10^{-3}$, $|\hat{\mu}| \simeq (45.2 \pm 2.4) \cdot 10^{-3}$ and $|\widehat{s^*}| \simeq (1.86 \pm 0.17) \cdot 10^{-3}$. In consequence, one has

$$\frac{|\hat{\mu}|}{|\hat{\beta}_{\rm p}|} \simeq 93 \pm 9\% \qquad \text{and} \qquad \frac{|\widehat{s^*}|}{|\hat{\beta}_{\rm p}|} \simeq 3.8 \pm 0.5\%. \tag{6.5.11}$$

A similar analysis of the Ohmic power oscillation is performed, to be compared with the RF power modulation. As a result, the moduli of the respective complex amplitudes are $|\hat{P}_{\rm OH}| \simeq 16 \pm 3$ kW and $|\hat{P}_{\rm RF}| \simeq 408 \pm 1$ kW such that $|\hat{P}_{\rm OH}|/|\hat{P}_{\rm RF}| \simeq 4.0 \pm 0.6\%$ and the modulation of the Ohmic power can be safely neglected.

The oscillation analysis of the plasma toroidal flux components is performed before and after the MECH onset, see figure 6.37. The respective complex amplitude moduli are given in table 6.7. As expected for a non-sawtoothing plasma, the modulation amplitude of the plasma toroidal flux $\Phi_{\rm pl}$ before the X2 MECH onset does not exceed the level of the measurement error. The modulation amplitude of $\Phi_{\rm pl}$ is increased by one order of magnitude when the X2 MECH starts. No pollution of the plasma frequency response is thus expected in this case.

	Complex amplitude modulus $\|\hat{\Phi}\|$	
Modulated signal	**(a) Before MECH**	**(b) During MECH**
Uncorrected plasma flux $\Phi_{\rm DML2}$	1.5 ± 1.2 μWb	21.5 ± 1.3 μWb
Total correction $\Phi_{\rm BO}$	0.1 ± 0.7 μWb	1.5 ± 0.7 μWb
Corrected plasma flux $\Phi_{\rm pl}$	1.5 ± 1.1 μWb	21.6 ± 1.3 μWb
Electron temperature $T_{\rm e0}$	8.4 ± 3.8 eV	267 ± 5 eV

Table 6.7: Modulation amplitudes due to X2 MECH in absence of sawtooth activity. TCV shot #40937, (a) $t = [0.6; 0.7]$ s and (b) $t = [0.7; 0.8]$ s.

As in the previous X3 and X2 MECH experiments, the contribution of the plasma toroidal flux correction $\Phi_{\rm BO}$ to the total flux modulation is very small ($< 10\%$).

Experimental frequency response and transfer function fitting

The oscillation analysis is performed for each X2 MECH frequency and the experimental transfer function is calculated according to equation (6.3.43). The resulting amplitude and phase are given in figure 6.38 to be compared with the model transfer functions in figure 6.6.

The maximum in the amplitude of ωH observed in presence of sawtooth activity in the previous subsection (see figure 6.31) does not exist in non-sawtoothing plasmas. Conversely, the amplitude saturates at $|\omega H| \simeq 0.6$ for angular frequencies which are

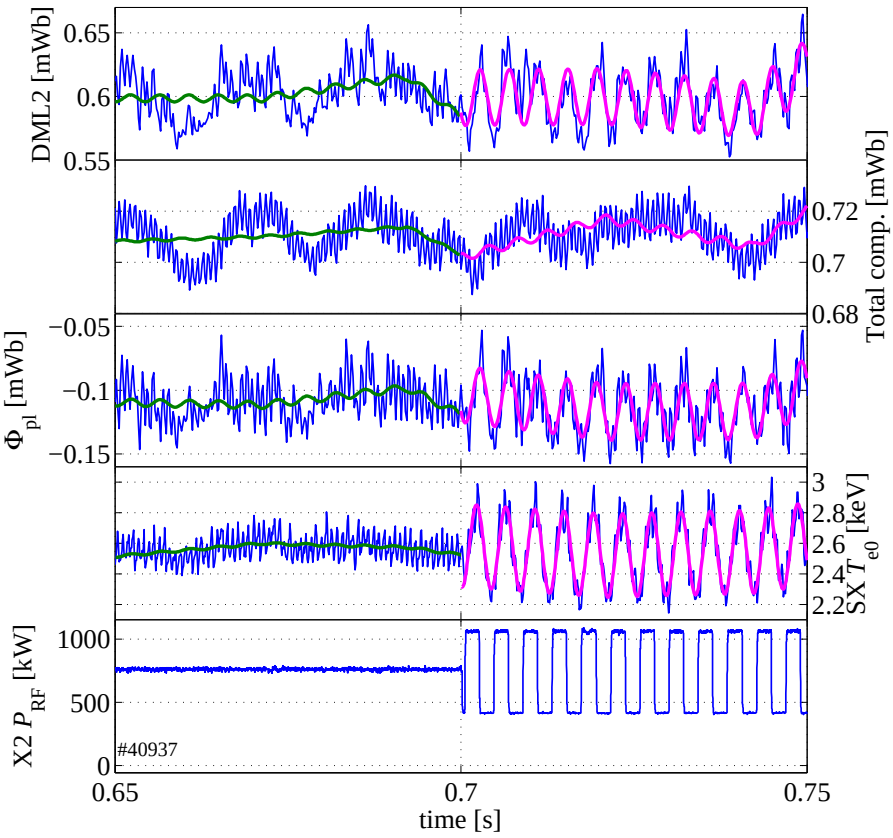

Figure 6.37: Oscillation analysis of the plasma toroidal flux components. From top to bottom: uncorrected plasma toroidal flux Φ_{DML2} from the DML2 loop, total compensation flux Φ_{BO}, corrected plasma toroidal flux Φ_{pl}, central electron temperature from soft X-ray measurements (absorber method), X2 power trace. Superimposed on the time traces (blue) are the reconstructed signals from the oscillation analysis at $f = 237$ Hz, before (thick green) and after (thick magenta) the onset of X2 MECH. TCV shot #40937.

far from both typical confinement and anisotropy relaxation times

$$\frac{1}{\tau_{\mathrm{inc}}} \simeq 200 \text{ rad/s} \ll \omega \simeq 1000 \text{ rad/s} \ll \frac{1}{\tau_{\mathrm{a}}} \simeq 5000 \text{ rad/s} \tag{6.5.12}$$

as expected from the model transfer function. In this case, the absorption coefficient of the X2 power can be estimated from the model transfer function H_0 using equation (6.3.45)

$$\eta \simeq \frac{3}{2}\omega|H| \simeq 100\%. \tag{6.5.13}$$

This estimation is valid if the phase of the transfer function saturates at $\Delta\phi = -90°$ in the same time, which is still not the case here in spite of the absence of sawtooth activity.

The system transfer identification (STI) fit is performed on the experimental data for several orders M and N of the numerator and of the denominator of (6.3.46), see figure 6.39. As in the case of sawtoothing plasmas, the best fit matching with a

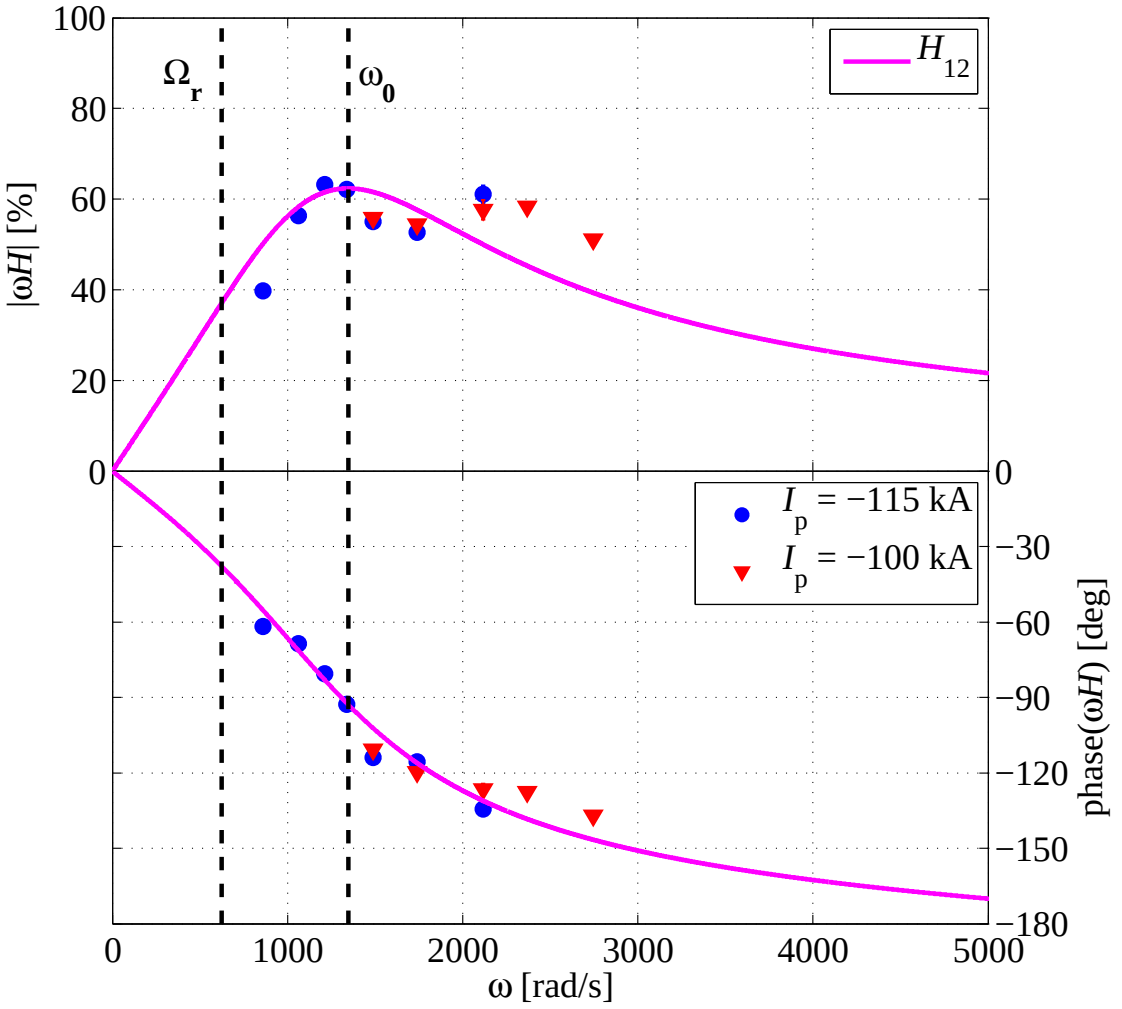

Figure 6.38: Experimental frequency response to X2 MECH in absence of sawtooth activity. Amplitude and phase of the experimental plasma frequency response to X2 MECH excitation at angular frequencies ω, along with the STI fit for $M = 1, N = 2$.

known model of the plasma response to MECH is obtained for $M = 1$ and $N = 2$, i.e. a transfer function of the type

$$H_{12} = \frac{b_0 + b_1(\mathrm{i}\omega)}{a_0 + a_1(\mathrm{i}\omega) + a_2(\mathrm{i}\omega)^2} \tag{6.5.14}$$

where $a_2 = 1$. This fit corresponds to the the model transfer function H_2 given by (6.3.35).

The resulting fit is shown in figures 6.38, 6.40 and 6.41. It reproduces well the trend of the amplitude, the phase and the real and imaginary parts of the experimental transfer function on the whole frequency span. Identifying the coefficients of H_2 with the fit parameters of H_{12} obtained from the STI gives:

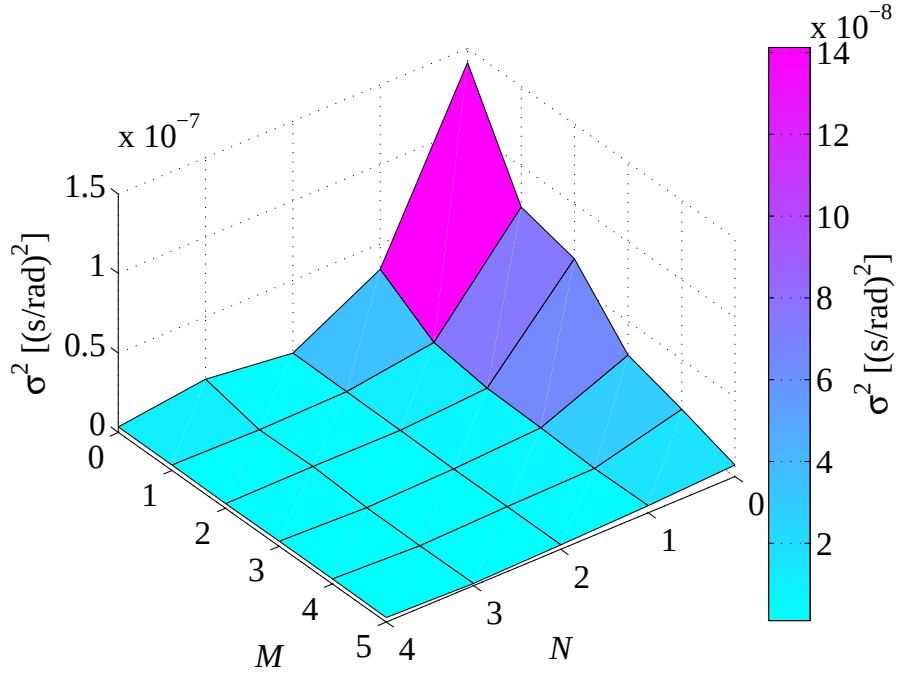

Figure 6.39: X2 MECH. STI optimization. Loss function σ^2 of the STI fitting of the plasma frequency response to X2 MECH for several numerator and denominator orders M and N. The lowest orders corresponding to a model of the system dynamic and yielding an acceptable loss function value are $M = 1, N = 2$. The STI method does not converge for $M = N = 4$.

$$\eta \frac{\tau_a + \tau_{inc}}{\tau_a \tau_{inc}} = b_0 \simeq 1050 \text{ s}^{-1} \tag{6.5.15}$$

$$\eta = b_1 \simeq -0.04 \tag{6.5.16}$$

$$\frac{2\tau_a + 3\tau_{inc}}{2\tau_a \tau_{inc}^2} = a_0 \simeq 1.81 \cdot 10^6 \text{ s}^{-2} \tag{6.5.17}$$

$$\frac{4\tau_a + 3\tau_{inc}}{2\tau_a \tau_{inc}} = a_1 \simeq 1.68 \cdot 10^3 \text{ s}^{-1} \tag{6.5.18}$$

which clearly yields non-reasonable physical parameters, in particular a negative absorption coefficient $\eta \simeq -4\%$. As in the previous X3 and X2 MECH experiments, the denominator roots $s_{1,2} = \mathrm{i}\omega_{1,2}$ of H_{12} are complex conjugate and yield pole frequencies with a real part

$$\omega_{1,2} \simeq \pm 1049 + 843\mathrm{i} \text{ rad/s}. \tag{6.5.19}$$

This indicates that the system behaves like a forced damped harmonic oscillator with the following parameters:

$$\omega_0 \equiv \sqrt{\Omega^2 + \gamma^2} \simeq 1346 \text{ rad/s} \qquad \text{proper angular frequency} \qquad (6.5.20)$$

$$Q \equiv \frac{\omega_0}{2\gamma} \simeq 0.80 \qquad \text{quality factor} \qquad (6.5.21)$$

$$\Omega_\text{r} \equiv \omega_0 \sqrt{1 - \frac{1}{2Q^2}} \simeq 623 \text{ rad/s} \qquad \text{resonant angular frequency} \qquad (6.5.22)$$

In spite of the absence of sawtooth activity, the frequency response of the perpendicular plasma kinetic energy exhibits a resonance when it is excited by modulated ECH. The presence of the MECH thus destabilizes an eigen mode in the plasma, maybe a temperature profile relaxation inside the $q = 2$ flux surface instead of the sawtooth activity inside the $q = 1$ flux surface.
The resonant behavior of the experimental transfer function is clear in figures 6.40 and 6.41, with the maximum amplitude $|H|$ reached at the resonant angular frequency Ω_r. A very high damping explains the low quality factor Q and the large difference between the resonant angular frequency Ω_r and the proper angular frequency ω_0. The strong damping also implies that the presence of this plasma mode affects the phase rather than the amplitude of the plasma response.

Summary

The X2 MECH frequency scan experiment is repeated in low-current L-modes. Despite the fact that no sawtooth activity is observed during the continuous ECH phase, the frequency response to MECH of the plasma perpendicular kinetic energy behaves like a forced harmonic oscillator with a strongly damped resonance. This affects in particular the phase of the transfer function which takes values far beyond $\Delta\phi = -90°$. The mechanism responsible for the observed behavior is still to be identified.

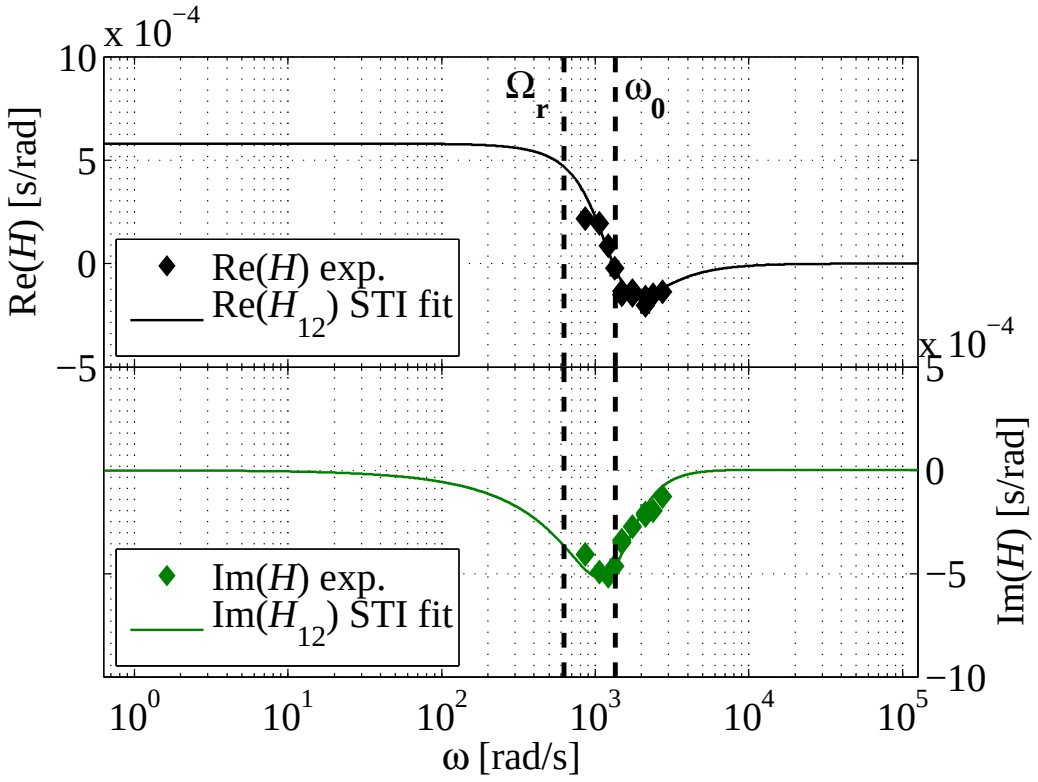

(a) Real and imaginary parts of H.

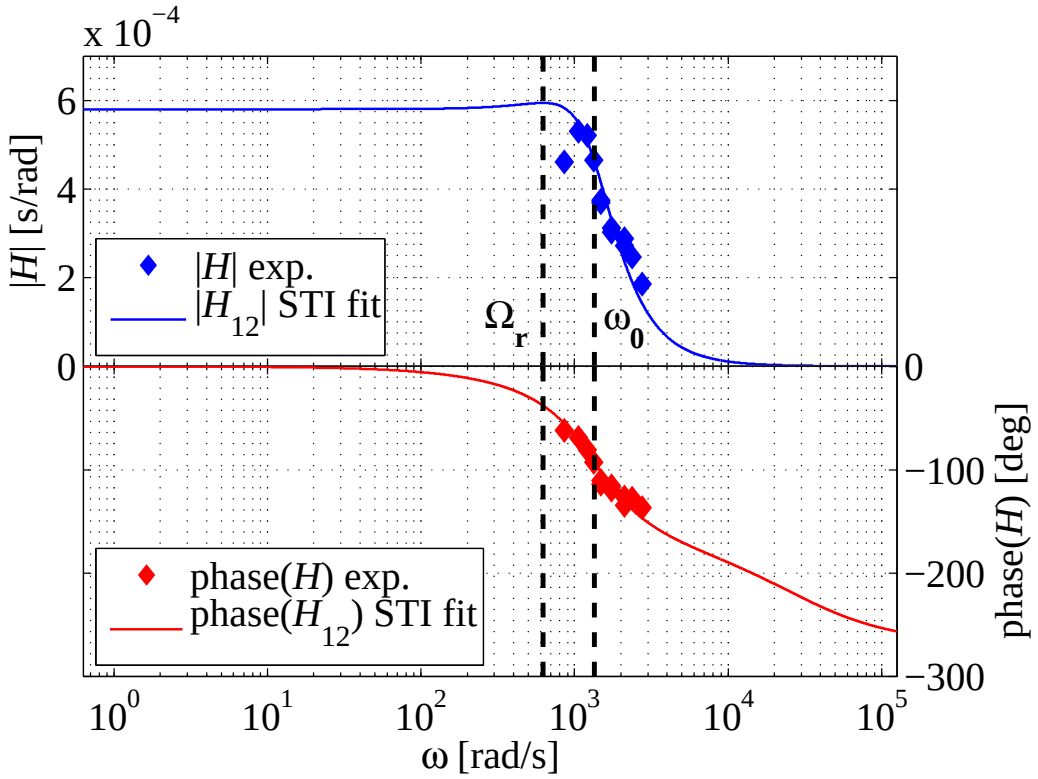

(b) Amplitude and phase of H.

Figure 6.40: Experimental frequency response to X2 MECH in absence of sawtooth activity and STI fit H_{12}.

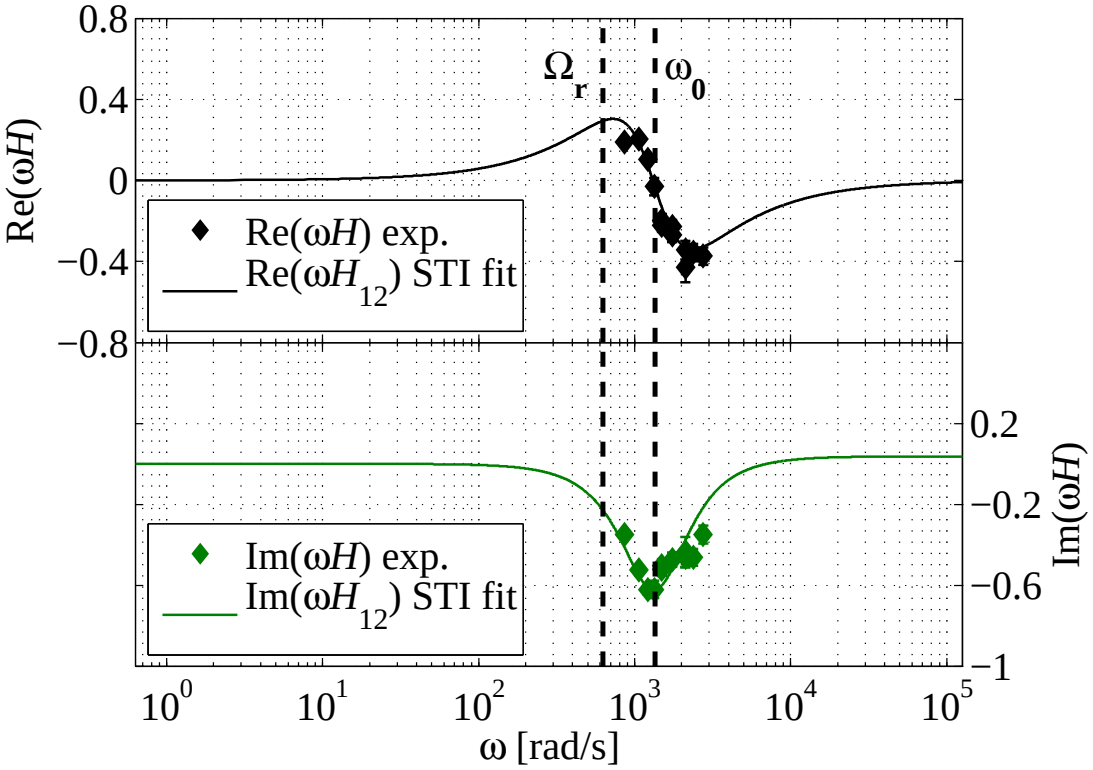

(a) Real and imaginary parts of ωH.

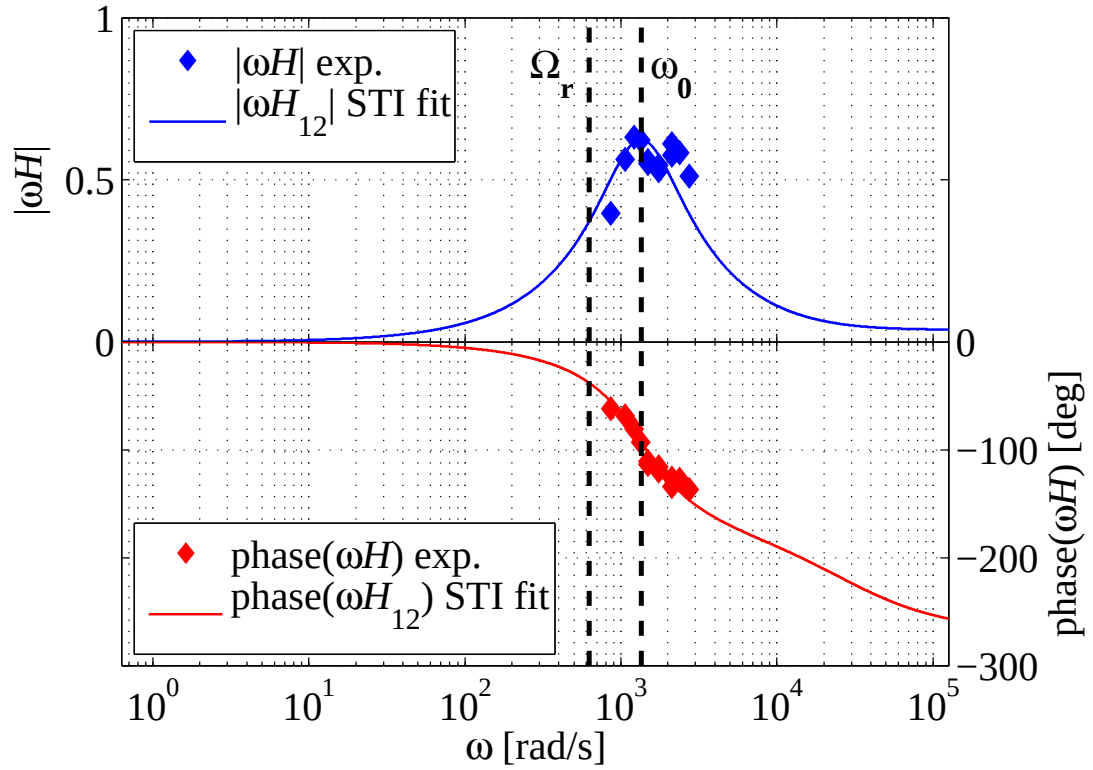

(b) Amplitude and phase of ωH.

Figure 6.41: Experimental frequency response to X2 MECH in absence of sawtooth activity and STI fit H_{12}.

6.6 Modulated EBW experiments

Introduction

For the sake of completeness, a case of modulated electron Bernstein wave heating (MEBH) is treated in this section, in spite of the major drawbacks suffered by the oscillation analysis of the DML signal in presence of sawtooth activity, as observed in the previous sections. Here, modulated second harmonic RF power in O-mode (O2) is coupled to an overdense H-mode plasma via O-X-B mode conversion.
The first EBW absorption measurements using the DML diagnostic in TCV are presented in [22–24]. In these references, the analysis is based on the uncorrected plasma toroidal flux Φ_{DLM2} from the DML2 loop. But it is shown in the following that, conversely to the X2 and X3 MECH experiments, the modulation of the compensation flux Φ_{BO} is not negligible and must be accounted for by using the corrected toroidal plasma flux Φ_{pl}. Similarly, the modulation of the plasma magnetic equilibrium is not negligible either and must be taken into account via the Shafranov integrals for a proper analysis of the plasma perpendicular kinetic energy response to modulated EBH.

Experimental setup

In order to couple second harmonic O-mode (O2) power to the Bernstein mode via O-X-B mode-conversion, an O2-overdense plasma with steep density gradient at the cutoff is obtained in a diverted ELM-free H-mode with strong shaping (elongation and triangularity at 95% of the normalized poloidal flux $\kappa_{95} \simeq 1.70$ and $\delta_{95} \simeq 0.40$) and located in the upper half of the machine at $Z_{\mathrm{axis}} \simeq 0.19$ m and $R_{\mathrm{axis}} \simeq 0.90$ m. The vacuum toroidal magnetic field flattop at $B_{\varphi \mathrm{v}}(R_0) \simeq 1.44$ T lasts until $t = 0.6$ s and is followed by a slow sweep down to $B_{\varphi \mathrm{v}}(R_0) \simeq 1.42$ T at $t = 0.7$ s. A high plasma current, i.e. $I_\varphi \simeq 420$ kA, is necessary to reach the L-H transition in Ohmic regime. The safety factor at 95% of the normalized poloidal flux is low, i.e. $q_{95} \simeq 2.4$. In consequence, the sawtooth activity has a broad inversion radius up to $\rho_{\psi,\mathrm{inv}} \simeq 0.43 \pm 0.04$ ($\rho_{\psi,\mathrm{vol}} = 0.35 \pm 0.03$) as measured from the 64-point soft X-ray profiles of the DMPX diagnostic, see figure 6.42.
In absence of ELMs, the H-mode electron density is not regulated and increases monotonically from $n_{e0} \simeq (8.5 \pm 1.7) \cdot 10^{19}$ m^{-3} after the L-H transition ($t = 0.38$ s) to $n_{e0} \simeq (24.1 \pm 5.2) \cdot 10^{19}$ m^{-3} before the discharge disruption ($t = 0.70$ s). In the meanwhile, the central electron temperature remains approximately constant at $T_{e0} \simeq 654 \pm 38$ eV. The relevant plasma parameters traces are given in figure 6.42.

The O2 power from gyrotron G2 is injected via the upper lateral launcher L2. The optimum injection angles for the O-X-B mode conversion were pre-calculated with the ART code. The measured launcher angles are $(\theta_L, \phi_L) \simeq (43.1 \pm 0.1°, -40.7 \pm 0.2°)$, corresponding to a downward poloidal injection angle $\theta_{inj} \simeq -31.2°$ and a counter-clockwise toroidal injection angle $\phi_{inj} \simeq 31.4°$. The power injection is programmed to start at $t = 0.5$ s, after the plasma L-H transition happening at $t \simeq 0.36$ s. The power amplitude is fully modulated (between $P_1 = 0$ kW and $P_2 \simeq 450$ kW) with a 50% duty-cycle square waveform with frequency $f = 181$ Hz. The modulation is visible on the soft X-ray emission coming from the edge, where the EBW is absorbed with a strong Doppler shift, see figure 6.42.

Oscillation analysis

The usual oscillation analysis is performed to check the assumptions summarized in subsection 6.3.4. Figure 6.43(a) shows the oscillation analysis of the normalized plasma kinetic energy β_p, the normalized plasma toroidal magnetic energy μ and the normalized Shafranov term $s^* \equiv 1/2[s_1 + \delta R s_2]$ from 5 kHz LIUQE calculation, along with the Ohmic power and the RF power. The corresponding complex amplitude moduli are $|\hat{\beta}_p| \simeq (0.81 \pm 0.12) \cdot 10^{-3}$, $|\hat{\mu}| \simeq (1.37 \pm 0.13) \cdot 10^{-3}$, $|\widehat{s^*}| \simeq (1.79 \pm 0.05) \cdot 10^{-3}$, $|\hat{P}_{OH}| \simeq 33 \pm 6$ kW and $|\hat{P}_{RF}| \simeq 284 \pm 1$ kW. In consequence, one has

$$\frac{|\hat{\mu}|}{|\hat{\beta}_p|} \simeq 170 \pm 42\%, \qquad \frac{|\widehat{s^*}|}{|\hat{\beta}_p|} \simeq 222 \pm 39\% \tag{6.6.1}$$

and

$$\frac{|\hat{P}_{OH}|}{|\hat{P}_{RF}|} \simeq 11.6 \pm 2.3\%. \tag{6.6.2}$$

In this case, the modulation of the Shafranov term $S^* \equiv 1/2[S_1 + \delta R S_2]$ in the relation (6.3.49) is not negligible and must be accounted for in the analysis.
The oscillation analysis of the plasma toroidal flux components is performed before and after the modulated EBH onset, see figures 6.44(a) and 6.44(b). The respective complex amplitude moduli are given in table 6.8. Before the MEBH onset, the modulation amplitude at $f = 181$ Hz of all the plasma toroidal flux components and of the central electron density is of the order of the measurement error. The sawtooth activity is thus not expected to perturb the measurement, especially since the RF power is absorbed far off-axis.

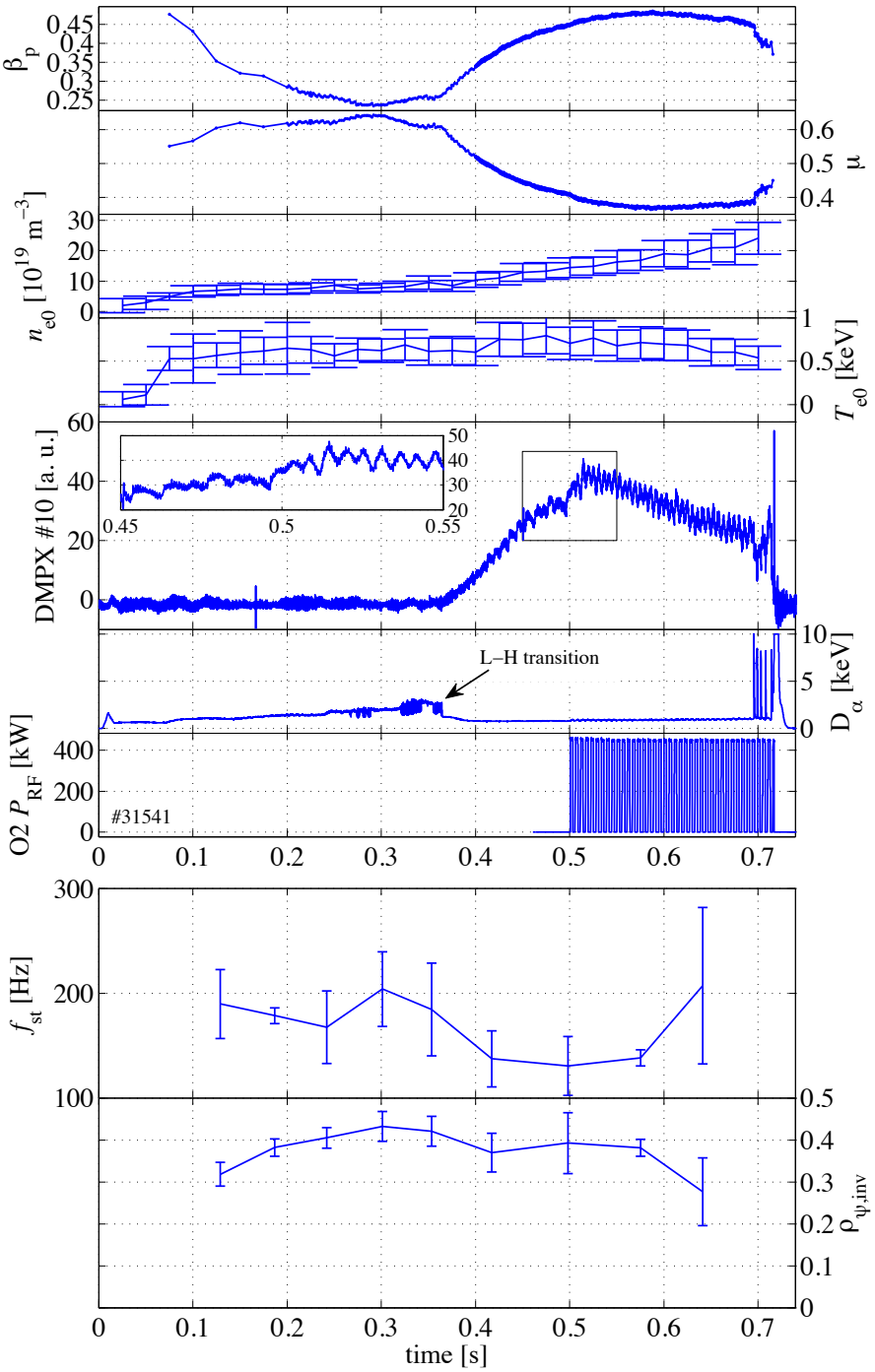

Figure 6.42: Modulated EBH experiment in overdense H-mode plasma. From top to bottom: LIUQE β_p and μ, central electron density $n_{\mathrm{e}0}$ and temperature $T_{\mathrm{e}0}$ (Thomson scattering, corrected by FIR for the density), soft X-ray signal from an edge-viewing line-of-sight with a zoom around the MEBH onset, deuterium recombination light D_α, O2 RF power trace, sawtooth frequency and inversion radius from the analysis of soft X-ray profiles (DMPX). The L-H transition at $t \simeq 0.36$ s is indicated by an abrupt drop of the D_α light. Between $t = 0.5$ s and the plasma disruption after $t = 0.7$ s, the O2 power amplitude is modulated with a 50% duty-cycle square waveform at $f = 181$ Hz. The modulation is clearly visible on the edge soft X-ray signal. TCV shot #31541.

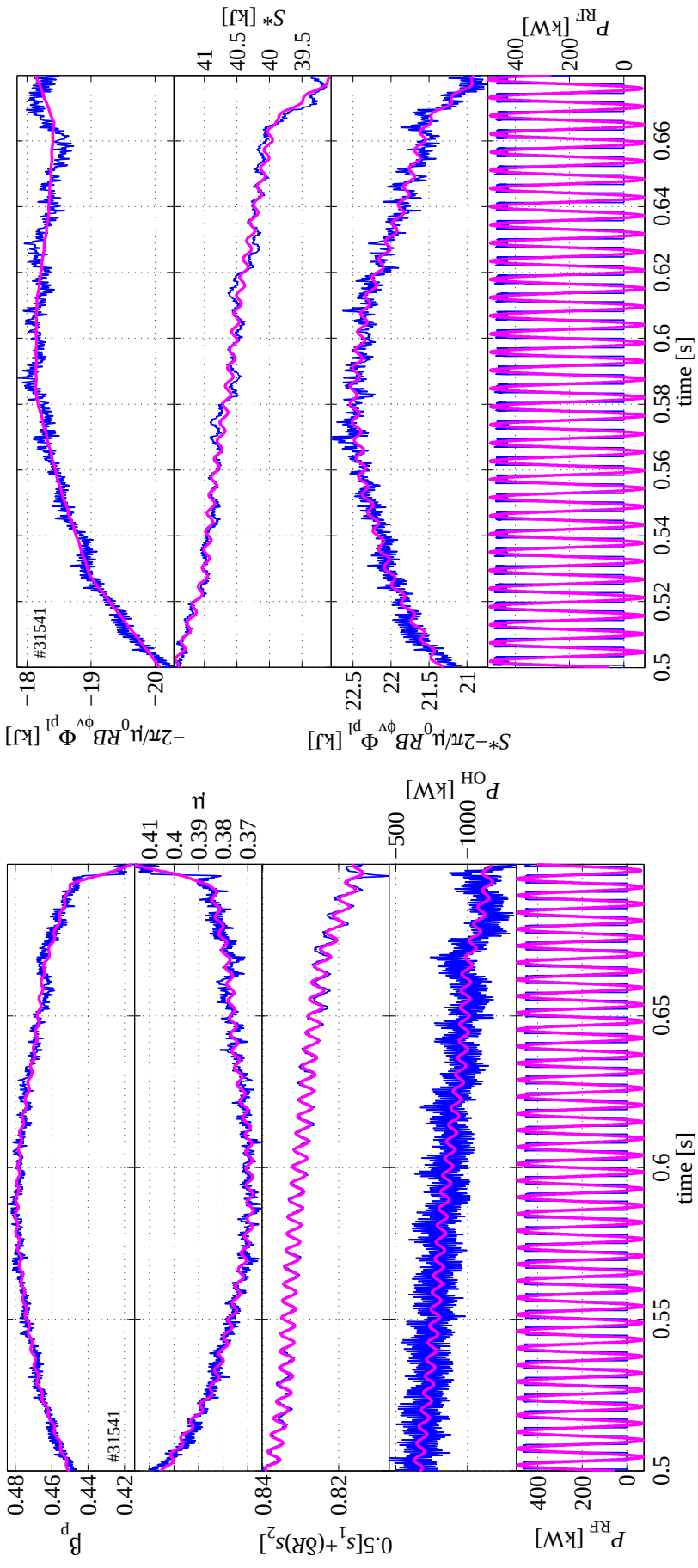

(a) Oscillation of the plasma energies and input powers.

(b) Oscillation of the perpendicular kinetic energy components.

Figure 6.43: Oscillation analysis of the plasma energies, input powers and perpendicular kinetic energy components. (a) From top to bottom: LIUQE normalized kinetic energy β_p, normalized plasma toroidal magnetic energy μ and normalized Shafranov integral combination s^*, as well as Ohmic power and O2 RF power. (b) From top to bottom: components of the perpendicular kinetic energy $-2\pi/\mu_0 RB_{\varphi\mathrm{v}}$ and S^*, perpendicular kinetic energy $W_{\mathrm{kin}\perp} = S^* - 2\pi/\mu_0 RB_{\varphi\mathrm{v}}$ and O2 RF power. Superimposed on the time traces (in blue) are the reconstructed signals from the oscillation analysis at $f = 181$ Hz (in thick magenta). TCV shot #31541.

During the MEBH, the modulation of the compensation flux Φ_{BO} is as important as the modulation of the uncorrected plasma toroidal flux Φ_{DML2} from the DML2 loop and must be accounted for. As a consequence, the modulation of the corrected plasma toroidal flux $\Phi_{\mathrm{pl}} \equiv \Phi_{\mathrm{DML2}} - \Phi_{\mathrm{BO}}$ is totally cancelled, as indicated in figure 6.44(b). A detailed analysis of the nine separate back-off components shows that the modulation comes mainly from the compensation flux FIX-POL-VESSEL for the toroidal vessel currents.

	Complex amplitude modulus $\lvert\hat{\Phi}\rvert$	
Modulated signal	**(a) Before MEBH**	**(b) During MEBH**
Uncorrected plasma flux Φ_{DML2}	0.7 ± 1.4 μWb	17.9 ± 1.3 μWb
Total correction Φ_{BO}	0.5 ± 0.6 μWb	17.7 ± 0.7 μWb
Corrected plasma flux Φ_{pl}	0.4 ± 1.5 μWb	0.7 ± 1.2 μWb
Electron temperature T_{e0}	1.1 ± 0.8 eV	0.3 ± 0.4 eV

Table 6.8: Modulation amplitudes due to modulated EBH. TCV shot #31541, (a) $t = [0.4; 0.5]$ s and (b) $t = [0.5; 0.6]$ s.

In summary, after compensation of an important contribution coming from modulated image currents in TCV vessel, the plasma toroidal flux is not modulated and the oscillation of the plasma perpendicular kinetic energy is fully determined by the oscillation of the plasma equilibrium via the Shafranov integrals. This effects were not observed in the X2 and X3 MECH experiments. This may be explained by a lesser stiffness of the diverted magnetic equilibrium used here with respect to the limited equilibrium used in the previous experiments. Moreover, EBW always have a finite $k_{\|}$ at the absorption and drive some current. Since this modulated current is generated close to the plasma edge, it may generate important image current in the tokamak vessel. The full relation (6.3.49) must be used with the corrected plasma toroidal flux:

$$W_{\perp} \simeq S^* - \frac{2\pi}{\mu_0} R B_{\varphi \mathrm{v}} \Phi_{\mathrm{pl}} \qquad \text{with} \qquad S^* \equiv \frac{1}{2}\left[S_1 + \delta_R S_2\right]. \tag{6.6.3}$$

In order to obtain S^*, the normalized s^* from the LIUQE calculation at 5 kHz is multiplied by the LIUQE normalization factor $N = 4/(R_0 \mu_0 I_{\varphi}^2)$ where $R_0 = 0.88$ m and $I_{\varphi}(t)$ is also calculated by LIUQE. The oscillation analysis of the three terms in equation (6.6.3) is given in figure 6.43(b) and yields:

$$|\omega H| \equiv \left| \frac{\omega \hat{W}_{\perp}}{\hat{P}_{\mathrm{RF}}} \right| \simeq 0.22 \qquad \text{and} \qquad \Delta\Phi \simeq -49^{\circ}. \tag{6.6.4}$$

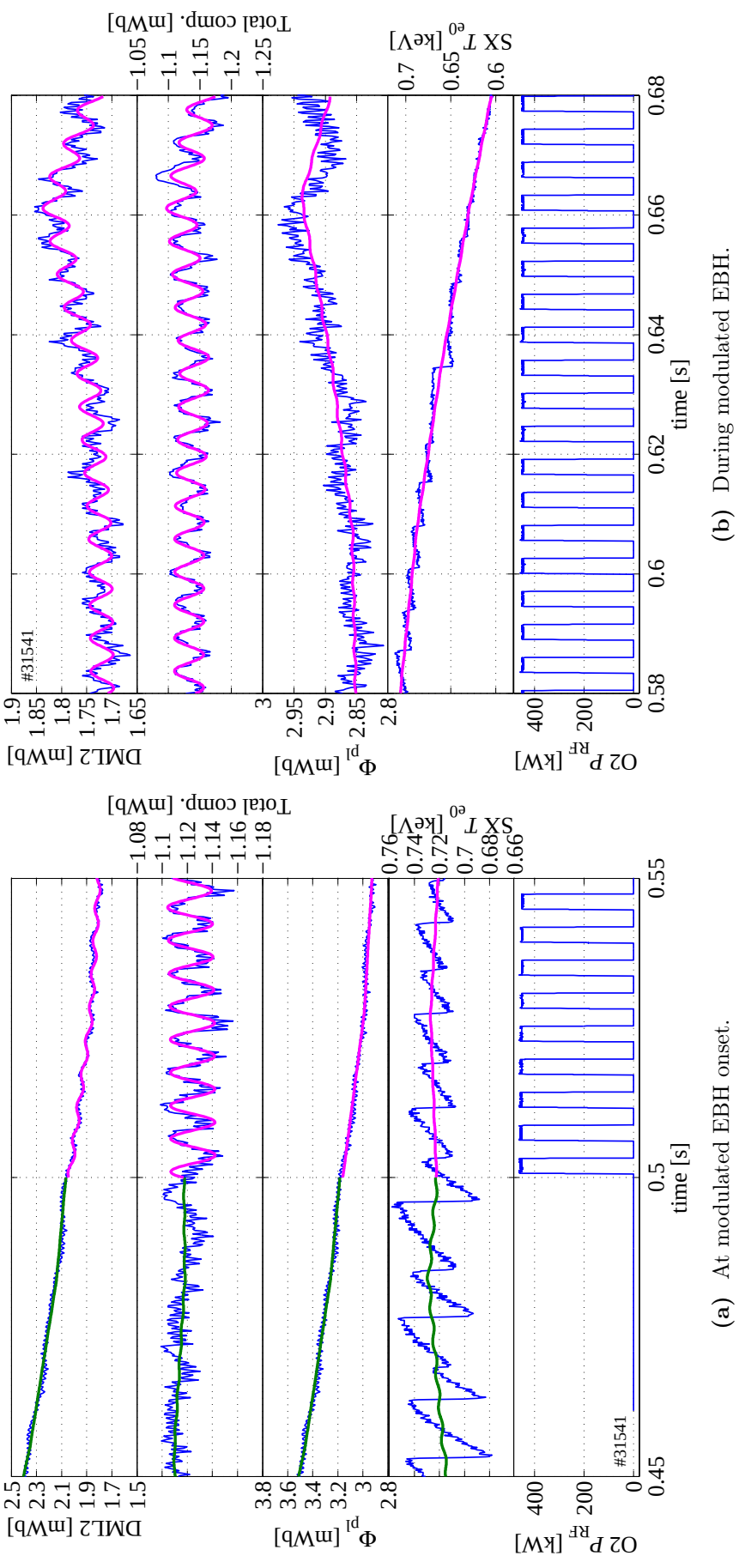

(a) At modulated EBH onset.

(b) During modulated EBH.

Figure 6.44: Oscillation analysis of the plasma toroidal flux components. From top to bottom: uncorrected plasma toroidal flux Φ_{DML2} from the DML2 loop, total compensation flux Φ_{BO}, corrected plasma toroidal flux Φ_{pl}, central electron temperature from soft X-ray measurements (absorber method), O2 power trace. Superimposed on the time traces (blue) are the reconstructed signals from the oscillation analysis at $f = 181$ Hz, before (thick green) and after (thick magenta) the onset of O2 MECH. The compensation signal exactly cancels the modulation of the uncorrected plasma toroidal flux, and the modulation amplitude of the corrected flux is quasi-null. TCV shot #31541.

Assuming that the modulation frequency is far from both the energy confinement and relaxation times, one can estimate the power absorption with the relation (6.3.45):

$$\eta \simeq \frac{3}{2}|\omega H| \simeq 33\%. \tag{6.6.5}$$

Summary

In the case of modulated EBH in an overdense diverted H-mode plasma, the modulation of the compensation flux and of the magnetic equilibrium must be taken into account.

6.7 Conclusions and outlooks

Experiments with modulated RF power injection aiming at the power absorption estimation are analyzed. The plasma perpendicular kinetic energy response to the modulated ECH (MECH) is measured using TCV DML diagnostic.

Modulation frequency scans are performed for X3 and X2 MECH. In both cases, the plasma frequency response exhibits an unexpected forced harmonic oscillator behavior with proper frequency at the sawtooth frequency and a strongly damped resonance. A proper estimate of the power absorption coefficient from either the fit of the plasma frequency response or a single frequency measurement thus necessitates a modification of the response modeling in order to account for the sawtooth dynamic. This behavior is still observed in non-sawtoothing plasmas, suggesting that another natural plasma oscillation is at play.

An unexplained asymmetry in the improvement of the X3 ECH absorption in presence of X2 ECCD pre-heating with respect to the sign of the driven current was previously observed [43, 97, 98]. It is now clear that this asymmetry is due to different regimes of sawtooth activity. Indeed, with X2 counter-ECCD, the sawtooth oscillation is irregular and a low pollution level is expected. Conversely, X2 co-ECCD enhances the sawtooth oscillation at a frequency close to the X3 MECH frequency. Frequency locking happens between the two perturbations and the sawtooth activity artificially increases the X3 power absorption estimate, yielding erroneous values up to 120%.

In EBH experiments, the finite current-drive effect induces a modulation of the magnetic equilibrium. In consequence, the modulation of the perpendicular kinetic energy comes from the Shafranov terms rather than from the diamagnetic term.

These results are not in favor of a routine use of the DML diagnostic for the estimation of ECH absorption coefficients in modulation experiments, in particular due to the plasma toroidal flux sensitivity to the sawtooth activity. All earlier analyses of central X2 and X3 MECH are potentially erroneous and must be reconsidered. Further experiments are proposed on this subject:

- **A scan of the sawtooth frequency.** In order to test whether the sawtooth activity is actually the source of the resonance observed in the plasma kinetic energy frequency response to MECH, one should repeat the X2 MECH frequency scan in plasmas with different and well defined sawtooth frequencies. One expects a shift of the resonance frequency in coherence with the shift in the sawtooth frequency.

- **Influence of the RF power deposition location.** X2 MECH frequency scans at different deposition radii inside and outside the sawtooth inversion radius will allow us to test the sensitivity of the sawtooth activity pollution to the power deposition location.

- **Influence of the magnetic configuration.** X2 MECH frequency scans in diverted and limited plasmas will allow to test the sensitivity of the plasma response to the magnetic configuration, in particular the relative importance of the Shafranov and diamagnetic terms.

- **Influence of the ECCD fraction.** X2 MECH frequency scans at different toroidal injection angles will allow to test the sensitivity of the plasma response to the ECCD fraction, in particular the relative importance of the Shafranov and diamagnetic terms.

The last two proposals aim at distinguishing which of the diverted equilibrium and the finite current drive fraction is responsible for the modulated equilibrium and vessel currents in the EBH experiment of section 6.6.

Chapter 7

On the possibility of electron Bernstein wave current drive in TCV

7.1 Introduction

Electron Bernstein waves offer the possibility to drive non-inductive current in plasmas which are overdense to the standard electron cyclotron current drive (ECCD). Electron Bernstein wave current drive (EBCD) in an overdense plasma was demonstrated for the first time in "current-free" plasmas at the W7-AS stellarator [17, 18]. In this chapter, the performance of the electron Bernstein wave current drive (EBCD) in TCV is investigated using a ray-tracing code and a Fokker-Planck code.

7.2 Fokker-Planck simulation of EBCD in TCV

A systematic analysis of the EBW current drive performance in TCV is carried out using the Antenna-Mode-conversion-Ray-tracing code (AMR) [26, 27] coupled to the Fokker-Planck solver LUKE [30]. In this study, the main parameters influencing the EBW trajectory and absorption are scanned, i.e. the poloidal position of the EBW injection and the toroidal magnetic field value. In this work, only the poloidal scan at fixed toroidal magnetic field $B_\varphi = -1.44$ T is presented. Scans at lower magnetic fields are in progress.

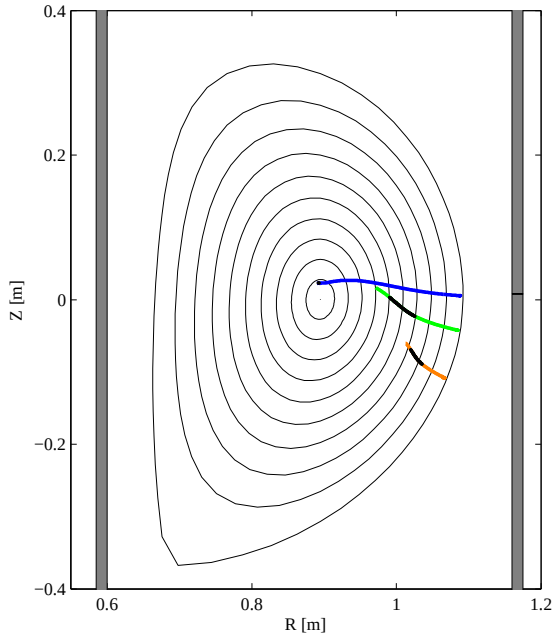

(a) Poloidal trajectory of rays injected from different poloidal positions.

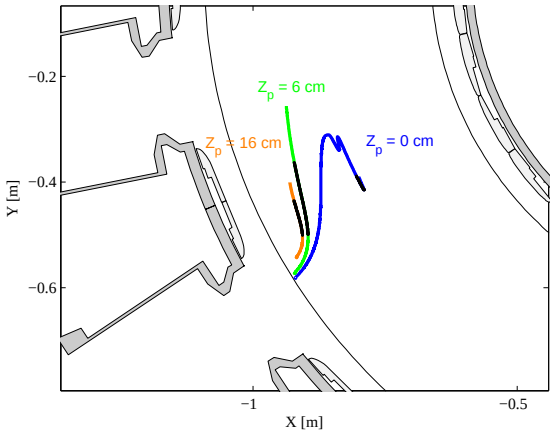

(b) Corresponding toroidal trajectories.

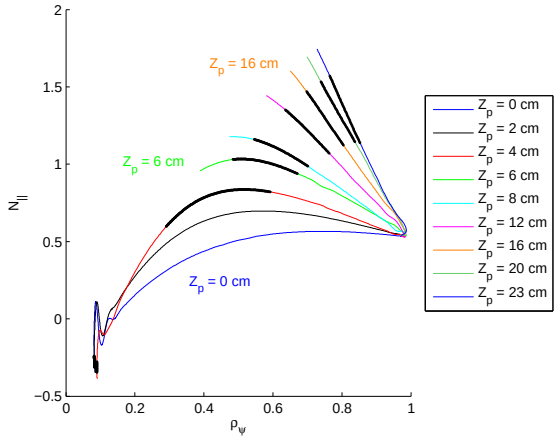

(c) Parallel refractive index $N_{\|}$ evolution along the rays path.

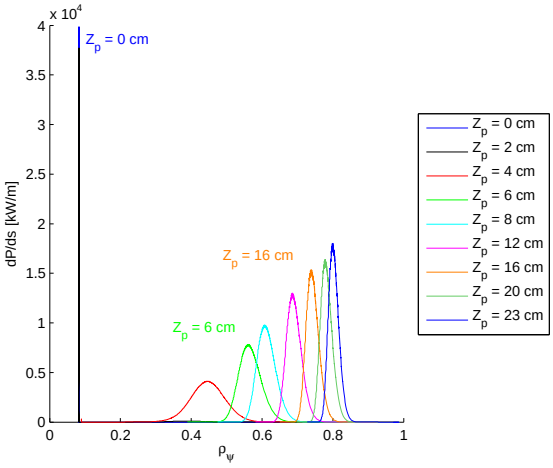

(d) Corresponding linear power deposition profiles.

Figure 7.1: Scan of the poloidal position of EBW injection. (a) Poloidal trajectories, (b) toroidal trajectories, (c) parallel refractive index evolution and (d) power deposition profiles calculated in AMR ray tracing simulations of single rays injected with positive initial refractive index $N_{\|,\mathrm{inj}} > 0$ in a plasma with $B_\varphi = -1.44$ T. The different poloidal positions of the EBW injection are obtained by scanning the plasma vertical position Z_p in front of the equatorial power launcher located at $Z = 0$ cm. The absorption location defined as $\frac{\mathrm{d}P}{\mathrm{d}s} / \max(\frac{\mathrm{d}P}{\mathrm{d}s}) > 1\%$ is indicated by black dots. The closer to the plasma midplane is the EBW injection, the less important is the $N_{\|}$-upshift and the more central is the Doppler-shifted resonant absorption. The case with $Z_\mathrm{p} = +4$cm shows two deposition locations, around $\rho_\psi = 0.4$ and at $\rho_\psi = 0.1$, with opposite $N_{\|}$ signs thus driving current in opposite directions.

The different poloidal positions of the EBW injection are obtained by artificial shifting the plasma magnetic axis vertical position Z_p in front of the EBW power launcher located at the equator of TCV vacuum vessel ($Z = 0$ cm). For each configuration in the scan, the optimum injection angles are determined, the EBW ray-tracing is performed and the quasi-linear wave-plasma interaction is calculated. Full absorption is achieved in all cases.

The simulations are performed using the experimental magnetic equilibrium and profiles data of an overdense ELM-free H-mode plasma ($I_\mathrm{p} = 350$ kA, $q_{95} = 2.3$, $\kappa_a = 1.62$, $\delta_a = 0.53$). The profiles given in input to the simulations are shown in figure 4.1. Figure 7.1 presents the simulation results for single rays of 500 kW injected in the clockwise toroidal direction (i.e. $N_{\parallel,\mathrm{inj}} > 0$). For all poloidal positions of the EBW injection, the sign of the driven current I_CD is opposite to that of the parallel refractive index at the absorption $N_{\parallel,\mathrm{abs}}$, which indicates that the Fisch-Boozer effect is dominating the Ohkawa effect in the EBCD generation at all absorption radii achieved in the scan.

When the EBW is injected close to the plasma midplane ($Z_\mathrm{p} \leq 4$cm), the parallel refractive index $N_\parallel$ remains small, thus allowing low-Doppler-shifted resonant absorption at the plasma center ($\rho_\psi \simeq 0.1$) where the electron temperature is the highest. However the parallel refractive index oscillates around $N_\parallel = 0$ when approaching the plasma center, which may reduce the net driven current I_CD and thus the current drive efficiency by cancelation of co- and counter-current drive. This effect is observed for the case at $Z_\mathrm{p} = 4$ cm: the $N_\parallel$ upshift along the ray is strong enough for the wave to be partly absorbed with $N_\parallel > 0$ generating a current $I_\mathrm{CD} = -3.9$ kA. The remaining power in the wave is deposited with $N_\parallel < 0$, thus decreasing the net driven current to $I_\mathrm{CD} = -2.6$ kA. This effect may be stronger in the experiment due to the finite beam size and the spread in N-spectrum of the injected EC wave.

When the EBW is injected far above the plasma midplane, only one wave-plasma interaction location remains with positive $N_\parallel$. As indicated in figure 7.2, the maximum counter-current $I_\mathrm{CD} = -3.8$ kA is obtained for $Z_\mathrm{p} = 6$ cm with high normalized current drive efficiency [3]:

$$\xi_\mathrm{CD} = 32.7 \frac{n_\mathrm{e} I_\mathrm{CD} R_\mathrm{p}}{P_\mathrm{RF} T_\mathrm{e}} = -0.45 \tag{7.2.1}$$

where n_e is the electron density in [10^{20} m^{-3}], I_CD is the driven current in [A], R_p is the plasma major radius in [m], P_RF is the absorbed RF power in [W] and T_e is the electron temperature at the absorption in [keV]. Despite the high normalized

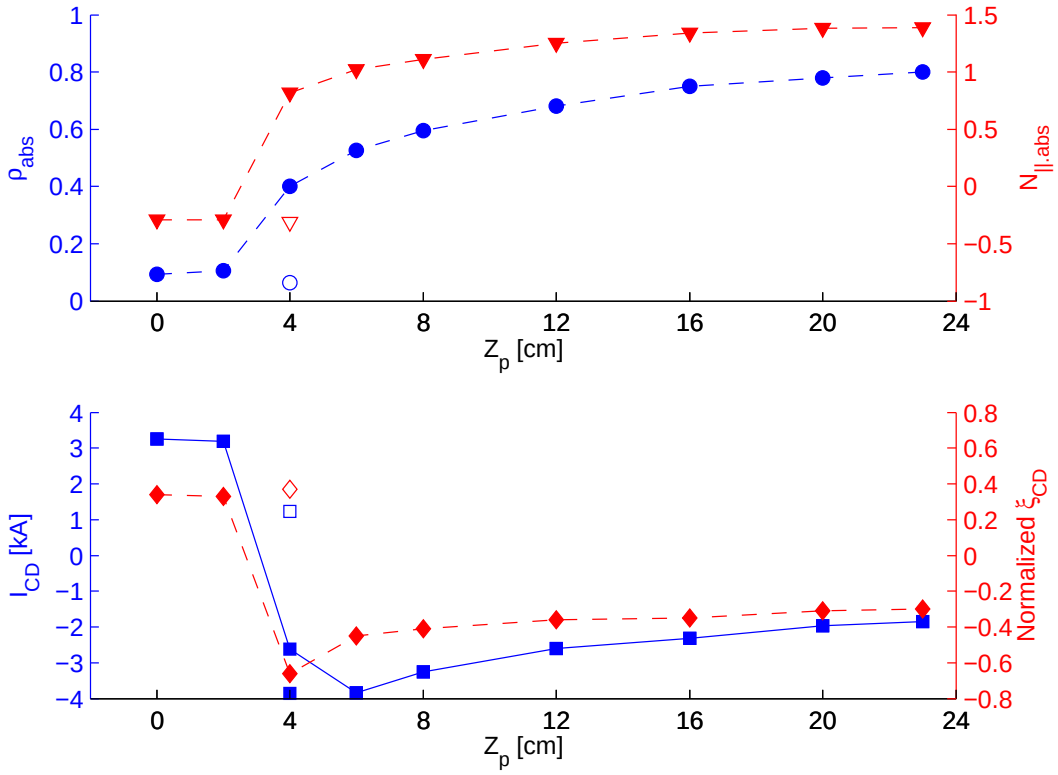

Figure 7.2: EBCD efficiency in TCV Quasi-linear Fokker-Planck calculations for the plasma vertical position scan. Top: normalized radius $\rho_{\psi,\mathrm{abs}}$ and parallel refractive index $N_{\parallel,\mathrm{abs}}$ at the absorption peaks. Bottom: driven current I_{CD} and normalized current drive efficiency ξ_{CD}. The empty symbols correspond to the secondary absorption peak along the ray path. For the driven current I_{CD} only, the values at both absorption peaks is summed and the net current drive is indicated.

current drive efficiency ξ_{CD}, the absolute driven current is small due to the very unfavorable $T_{\mathrm{e}}/n_{\mathrm{e}}$ ratio. Indeed, it is only of the order of 1% of the Ohmic current (for 500 kW of injected power).

If the increase of the driven current I_{CD} when scanning the absorption location from $\rho_{\mathrm{abs}} = 0.8$ to 0.5 (when scanning Z_{p} from 23 cm to 6 cm) was only due to the variation of the local electron density and temperature at ρ_{abs}, the normalized current drive efficiency ξ_{CD} would remain constant. However, ξ_{CD} increases by typically a factor 2, which indicates that an effect which is not accounted for in ξ_{CD} is at play. This effect cannot be due to $N_{\parallel}$ since it decreases with decreasing ρ_{abs}. It may certainly be attributed to the increasingly dominant Fisch-Boozer current drive effect when moving the absorption location away from the trapped particle region at the LFS edge of the plasma. This is in good accordance with a study of the relative importance of the Ohkawa and Fisch-Boozer effects in EBCD as a function of the local inverse aspect-ratio published in [100].

Tentative counter- and co-EBCD experiments in TCV have been performed with 500 kW of O-mode power injected in plasmas located respectively at $Z_p = +6$ cm above and $Z_p = -10$ cm below the launching antenna located at the vessel equator. In both cases, plasma current modulation of typically 3 kA in the "co-EBCD" direction are observed, thus indicating that the effect of plasma heating on the resistivity is dominating the current drive effect. Thus no clear evidence of EBCD effect has been observed yet.

Note that a driven current of 1% of the Ohmic current is sufficiently large to change the sawtooth activity when deposited around the sawtooth inversion radius [78]. However, many difficulties will be met when designing an experiment to sweep the EBCD generation location through the sawtooth inversion radius. Indeed, in order to sweep the radial location of the EBW power deposition, one needs to vary the position of the H-mode plasma with respect to the launching antenna. As a result, the optimum injection angle for the O-X mode conversion also varies and must be tracked in real time with the steerable antenna. Moreover, the ELM-free H-mode plasmas have a strongly non-stationary density and thus naturally time-varying sawtooth frequency and amplitude, an effect which one has to distinguish from the EBCD effect.

7.3 Conclusions

Ray-tracing and Fokker-Planck simulations of the EBCD performances in TCV overdense H-mode plasmas are performed with the AMR-LUKE codes. According to a scan of the poloidal position of the EBW power injection, the variation of the EBCD efficiency when varying the radial location of absorption is predominantly due to trapped-particles effects. In future work, a detailed analysis of the distribution functions calculated by LUKE should confirm this interpretation.

When injected far above the plasma midplane, the EBW undergoes a strong upshift of its parallel refractive index $N_\parallel$ and the strongly Doppler-shifted resonant absorption takes place at the plasma edge where the Ohkawa effect is in competition with the Fisch-Boozer effect. As a result, the current drive efficiency is low. When injected at the plasma midplane, the EBW reaches the plasma center but oscillations of the wave parallel refractive index around $N_\parallel = 0$ induce driven currents with opposite signs, thus reducing the net EBCD efficiency. The maximum EBCD effect is observed for an intermediate power injection geometry, yielding mid-radius absorption where the Ohkawa effect is reduced and a high normalized current drive

efficiency $\xi_{CD} = 0.45$ is achieved. However, the absolute driven current remains small ($\lesssim 1\%$ of the Ohmic current) due to the unfavorable temperature to density ratio in these H-mode plasmas. In the experiment, such small EBCD currents will be hardly distinguishable from variations of the Ohmic current due to a modification of the plasma resistivity by EBH.

Chapter 8

Lower-hybrid parametric instability

8.1 Introduction

In electron Bernstein wave heating via the O-X-B double-mode conversion process, the O-mode wave converted into a X-mode wave at the O-mode cutoff propagates back towards the plasma edge where it reaches the upper hybrid (UH) resonance and conflues with the Bernstein mode in a wave-wave interaction. Approaching the UH resonance (UHR) layer, the wave electric field grows to large values which may cause nonlinear effects like the loss of a fraction of the power in a lower-hybrid wave.

This phenomenon is called the lower-hybrid parametric instability (LHPI) and was observed in EBH experiments via X-B mode conversion from the high-field side in the Versator II tokamak [9] and in the FT-1 tokamak [10], as well as in EBH experiments via O-X-B double mode conversion from the low-field side of H-mode plasmas in the W7-AS stellarator [15] and in the MAST spherical tokamak [20, 101].

In the present work, the LHPI is studied for the first time in EBH experiments via O-X-B double mode conversion in a standard aspect-ratio medium-size tokamak, i.e. TCV, with a high level of injected RF power ($P_{\mathrm{RF}} = 500$ kW).

Non-linear wave theory elements for the parametric instability are reviewed in section 8.2. Section 8.3 presents the design, the construction and the vessel implementation of TCV new loop-antenna for the detection of the LH waves. The experimental results obtained with the LHPI-antenna are discussed in section 8.4, in particular the detailed LHPI spectrum dynamic with the discharge evolution and the detection of the LHPI threshold power. Conclusions and outlooks are given in section 8.5.

8.2 Theory elements of parametric instabilities

8.2.1 Physical mechanism

Nonlinear wave effects in plasmas can be classified into two families [102]: weak and strong turbulence. In the case of weak turbulence, both the turbulence fluctuations and the wave have small amplitudes. The strong turbulence regime is characterized by either large-amplitude turbulence fluctuations, or a large-amplitude wave, or both altogether. Conversely to strong turbulence effects, weak turbulence effects can be analyzed with perturbation theory.

Parametric instabilities (PI) belong to the strong turbulence family. In a PI, a large-amplitude incoming electromagnetic (EM) wave with high frequency ω_0 (called "pump wave") beats with a plasma background mode with low frequency ω_1, thus generating additional waves at frequencies $\omega_2 = \omega_0 - \omega_1$ and $\omega_3 = \omega_0 + \omega_1$ (called "decay waves"). The energy and momentum conservation implies the following selection rules for the wave vectors and frequencies:

$$\omega_0(\mathbf{k}_0) = \omega_1(\mathbf{k}_1) + \omega_2(\mathbf{k}_2) \qquad \text{and} \qquad \mathbf{k}_0 = \mathbf{k}_1 + \mathbf{k}_2, \tag{8.2.1}$$

$$\omega_0(\mathbf{k}_0) = -\omega_1(\mathbf{k}_1) + \omega_3(\mathbf{k}_3) \qquad \text{and} \qquad \mathbf{k}_0 = -\mathbf{k}_1 + \mathbf{k}_3. \tag{8.2.2}$$

The wave triplet must satisfy these rules for the PI to happen. In turn, the incoming pump wave can beat with the generated decay waves, thus enhancing the low frequency mode, which increases the initial beating effect and the amplitude of the decay waves, etc... In consequence of this non-linear three-wave coupling, both the low frequency mode and the decay waves grow exponentially at the expense of the pump wave. On a longer time scale, the decay waves themselves may undergo parametric instabilities, generating new decay waves. This induces a cascade of the pump wave sideband into lower frequency waves and of the low-frequency mode into higher frequency waves. A broad spectrum is produced and saturates at large amplitude.

For the initial exponential growth to happen, the pump wave amplitude must be large enough to overcome the linear damping of the low-frequency mode and of the decay waves. Hence a minimum pump wave threshold power exists below which the PI does not occur.

In a parametric instability, the modes are coupled via the particles dynamic response to the oscillating fields of the various waves in presence. This coupling mechanism and thus the type of parametric instability (i.e. the triplet of waves involved in the process) which may arise vary according to the plasma conditions, in particular the

plasma density and the presence of a background magnetic field.

8.2.2 Zoo of parametric instabilities in magnetized plasmas

In this work, we will deal with only parametric instabilities in magnetized plasmas. In such an environment, parametric instabilities may imply various types of waves triplets [102], classified here into two categories:

- A high-frequency long-wavelength EM pump wave $\mathbf{k}_0$ decaying into short-wavelength electrostatic ion and electron modes $\mathbf{k}_1$ and $\mathbf{k}_2$. In this case, $k_0 \simeq 0$ and $\mathbf{k}_1 \simeq -\mathbf{k}_2$. The pump wave can also be a long-wavelength electrostatic mode. Decay into two short-wavelength electrostatic ion modes is possible in multi-ion species plasmas.

- A high-frequency long-wavelength EM pump wave $\mathbf{k}_0$ decaying into another EM wave $\mathbf{k}_1$ and a short-wavelength electrostatic ion or electron mode $\mathbf{k}_2$. In this case, the pump wave number cannot be ignored in comparison to the wave number of the decay waves. Generally, these parametric instabilities are backscattering processes with $\mathbf{k}_1 = -\mathbf{k}_0$ and $\mathbf{k}_2 = 2\mathbf{k}_0$. In this category of PI, one finds the decay

  - of a Whistler wave into an ion acoustic wave and an electron plasma wave;
  - of an ordinary wave into an ion acoustic wave and an electron plasma wave;
  - of an extraordinary wave into an upper-hybrid wave and an ion acoustic wave;
  - of an extraordinary wave into an upper-hybrid wave and a lower-hybrid wave.

  The corresponding pump wave threshold powers are given in [102] for the case of homogeneous plasmas. A solution is also proposed to account for the plasma density inhomogeneity in the WKB limit, which may increase the threshold power for the backscattering instability by several orders of magnitude [9].

8.2.3 Lower-hybrid parametric instability (LHPI) in EBH experiments

The last parametric instability listed here above is the lower-hybrid parametric instability (LHPI). It is observed in RF-heated plasmas via X-B or O-X-B mode

conversion. The LHPI in O-X-B mode conversion is described schematically in figure 8.1 for the 2nd harmonic EBH experiments in TCV overdense plasmas. After conversion to the slow X-mode at the plasma cutoff, the EC wave electric field increases while approaching the upper-hybrid resonance (UHR) and the slow X-mode becomes akin to an UH wave. A lower-hybrid parametric instability is then expected to arise if the usual selection rules are satisfied:

$$\omega_X = \omega_{LH} + \omega_{UH}, \tag{8.2.3}$$

$$\mathbf{k}_X = \mathbf{k}_{LH} + \mathbf{k}_{UH}. \tag{8.2.4}$$

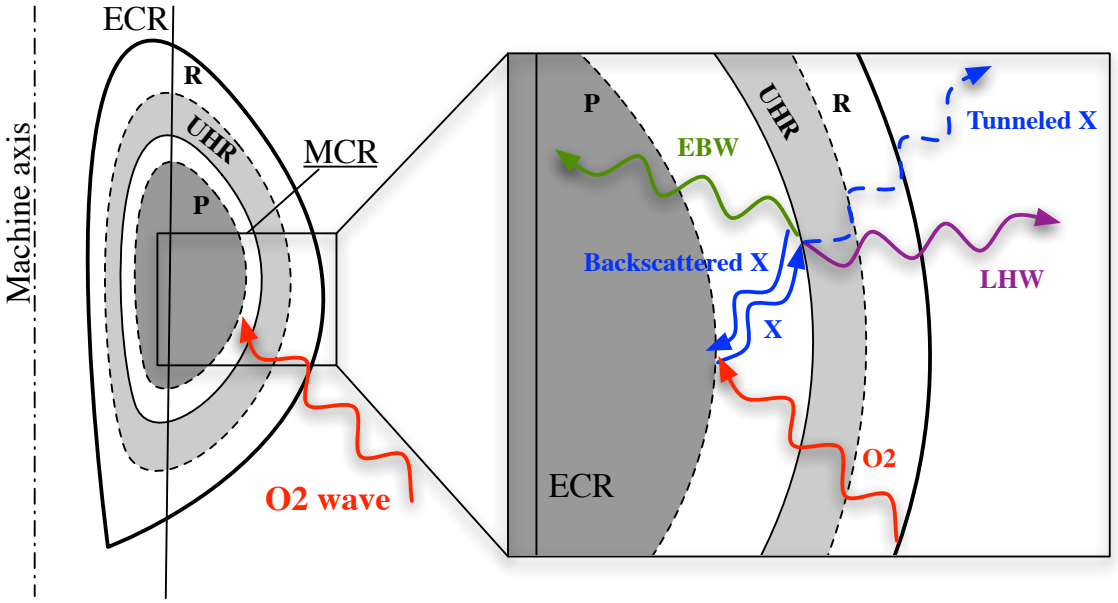

Figure 8.1: Schematic of LHPI in TCV high-density 2nd harmonic O-X-B experiments. Left: poloidal cross-section of diverted plasma with typical O-mode plasma cutoff (P), X-mode R-cutoff and UH resonance for the second harmonic. The light and dark grey regions are evanescent for X-mode and O-mode waves, respectively. Right: zoom on the mode conversion region (MCR). At the P-cutoff, the incoming O2 wave converts into a X2 wave propagating back towards the UHR where some power is decaying into a backscattered X-wave and a LH-wave leaving the plasma. The remaining EC power couples to the EBW with some additional losses by tunneling effect outwards through the thin evanescent layer between the UHR and R-cutoff.

The incoming EC wave decays into a LH wave leaving the plasma and a backscattered UH wave. The remaining slow X-wave power then couples to the Bernstein mode in a linear wave-wave interaction at the UHR, with additional losses by tunneling of the slow X-wave to the fast X-wave leaving the plasma through the evanescent layer between the UHR and the R-cutoff. The steeper the density gradient at the mode conversion region, the thiner the evanescent layer and the larger the tunneling losses.

The study of the LHPI is of special interest for the EBW-heated plasmas for several reasons:

- In O-X-B experiments, the presence of a LHPI is a clear signature that an efficient O-X mode conversion is at play, thus allowing some EC power in X-mode to reach the UHR layer where the X-B mode conversion and incidentally the LHPI happen. The LHPI signal can thus be used as an additional monitoring diagnostic for the optimization of the O-mode injection angles.

- On the other hand, the EC power passed into the LH wave is lost for the EBW heating of electrons. Similarly to LH heating, the decay LH waves may generate a fast ion tail [10]. But in most EBH experiments, the mode conversion region is located close to the plasma edge where the fast ion confinement is poor. The energetic ions are thus lost before they can give their energy to bulk ions and participate to the overall plasma heating. A detailed analysis of the LHPI may help to quantify and perhaps to prevent this loss channel.

- Finally, there is a debate as to know whether the backscattered decay UH wave will convert back to EC waves and leave the plasma thus enhancing the damaging effect of the LHPI on the EBH efficiency [28], or propagate towards the EC resonance where it is absorbed by electrons in the form of a Bernstein wave thus participating in the overall EBH efficiency [9]. A better understanding of the LHPI phenomenon should help to sort out this question.

LHPI observations in fusion devices

As mentioned in the chapter introduction, the LHPI was observed in past EBH experiments carried out in various fusion devices. These experiments are briefly reviewed here and the corresponding physical parameters and experimental results are given in tables 8.1 and 8.2, respectively, along with the typical TCV parameters for the LHPI experiments presented in this chapter.
In the Versator II [9] and FT-1 [10] tokamaks, as well as in the W7-AS stellarator [15] and in the MAST spherical tokamak [20, 101], the low-frequency (LF) part of the LHPI spectrum (corresponding to the LH wave itself) was detected with either an electrostatic probe (Versator II) or a loop probe (FT-1, W7-AS) installed at the edge of the plasma, or with both (MAST). During EBH, the LF spectra exhibit peaks matching with the fundamental, second and third (MAST) harmonics of the LH frequency f_{LH} calculated from measured profiles in the mode conversion region,

thus identifying the detected radiation as decay waves from the LHPI of the X-wave at the UHR.

Machine	R_0 [m]	a [m]	I_p [kA]	B_{φ_v} [T]	P_{RF} [kW]	f_{RF} [GHz]	ℓ	EBH
Versator II tokamak [9]	0.4	0.13	50	1.25	120	35.08	1	X-B
FT-1 tokamak [10]	0.625	0.2	30	1.06	150	30.6	1	X-B
W7-AS stellarator [15]	2	0.2	-	1.25	110	70	2	O-X-B
MAST spher. tok. [20, 101]	0.85	0.65	1350	0.52	800	60	5	O-X-B
TCV tokamak	0.88	0.25	400	1.45	500	82.7	2	O-X-B

Table 8.1: Physical parameters of various LHPI experiments. Major radius R_0, minor radius a, Ohmic plasma current I_p, central vacuum magnetic field $B_{\varphi v}$, maximum injected RF power P_{RF}, RF power frequency f_{RF} and resonant harmonic number ℓ. The last column gives the type of mode conversion used in the EBH process: X-B from HFS or O-X-B from LFS.

Machine	B_φ [T]	n_e [10^{19} m^3]	T_e [eV]	f_{LH} [MHz]	P_{th} [kW]	LHPI measurements
Versator II	1.14	0.26	100	400	50	HF and LF spectra Threshold power (vs n_e)
FT-1*	1.06	0.6	800	300	20	HF and LF spectra Threshold power Amplitude vs n_e
W7-AS*	1.25	10	500	900	-	HF and LF spectra Non-linearity vs P_{RF}
MAST	0.38	4.5	140	134	-	LF spectrum Non-linearity vs P_{RF}

Table 8.2: Measured LHPI frequencies and threshold powers. Physical parameters B_φ, n_e and T_e are measured close to the UHR layer. For the experiments marked with *, the central B_φ and T_e are given, and n_e is line-averaged. Here, f_{LH} and P_{th} are respectively the experimental LH decay wave frequency and threshold power, if measured. In the last column, HF and LF denote high-frequency and low-frequency spectra, respectively

The high-frequency (HF) part of the LHPI spectrum (i.e. the intermediate-frequency backscattered waves) was also observed with horn antennas connected to microwave receivers in Versator II, FT-1 and W7-AS. Several satellite peaks of the HF spectrum,

down- and up-shifted by f_{LH} from the pump wave frequency and from each other are observed, in good correlation with the LF spectra.
In W7-AS and MAST, a clear non-linear increase of the LHPI signal amplitude is observed with increasing power coupled to the plasma. In Versator II and FT-1, the experimental LHPI threshold power determined in scans of the injected RF power is in reasonable agreement with theoretical predictions.
Finally, the generation of a fast ion tail is observed in the FT-1 tokamak in correlation with the appearance of the LHPI during EBH, suggesting efficient ion heating by the LH waves coming from the pump wave decay.

LHPI threshold power

As mentioned earlier, all parametric instabilities are subject to a minimum pump wave threshold power below which the linear damping of the decay waves prevents the exponential growth of the instability. In reference [28], the pump wave threshold power for the LHPI of an upper-hybrid wave incoming on the UHR from the HFS and decaying into a lower-hybrid wave and a backscattered upper-hybrid wave is derived for a cold inhomogeneous magnetized plasma slab. The waves electric fields are described by Maxwell's equations with the cold dielectric tensor. The charge density perturbations caused by the waves are the source of the nonlinearity. They are described by special forms of the Poisson equation. Assuming that the pump wave frequency is more than twice the EC frequency at the UHR layer ($\omega_0 > 2\Omega_{\mathrm{ce}}$), which is verified for all 2$^{\mathrm{nd}}$ harmonic EBH experiments in TCV, the solution of the system of equation yields the threshold power per unit surface

$$\frac{P_{\mathrm{th}}}{\pi\rho^2} = 2\cdot 10^{-3}\,\frac{f_0^{1/3}\,\tilde{T}^{11/12}\,T_{\mathrm{e}}^{5/4}\,B_\varphi^{1/3}}{L^{4/3}} \tag{8.2.5}$$

where P_{th} [W] is the pump wave threshold power, ρ [cm] is the e-fold Gaussian beam radius of the pump wave, f_0 [GHz] is the pump frequency, $\tilde{T} \equiv T_{\mathrm{e}} + 4T_{\mathrm{i}}$ with T_{e} [eV] and T_{i} [eV] the electron and ion temperatures, B_φ [T] is the toroidal magnetic field and L [cm] is a combined density and magnetic field scale length along the inhomogeneity direction x:

$$L = \left[\frac{\mathrm{d}\,\ln(n(x))}{\mathrm{d}x} + \frac{2\Omega_{\mathrm{ce}}^2}{\omega_{\mathrm{pe}}^2}\frac{\mathrm{d}\,\ln(B(x))}{\mathrm{d}x}\right]^{-1}. \tag{8.2.6}$$

The physical parameters in 8.2.5 must be evaluated at the UHR where the LHPI takes place. Actually, the minimum injected EC power yielding an LHPI effect must be higher than the threshold 8.2.5 since both O-X and X-B linear conversions have efficiencies less than 100% due to partial wave reflexion and tunneling, respectively.

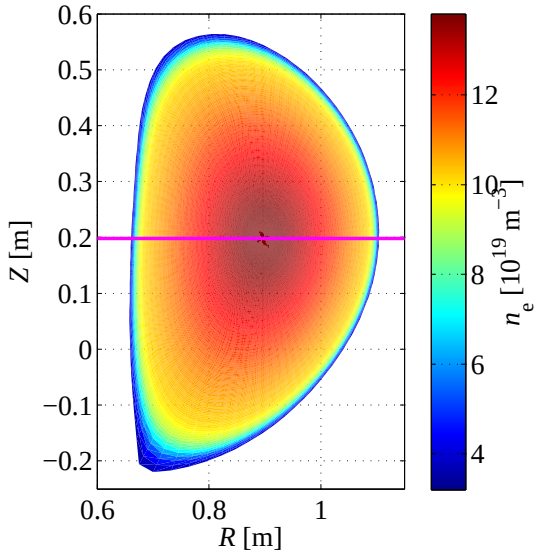

(a) H-mode electron density.

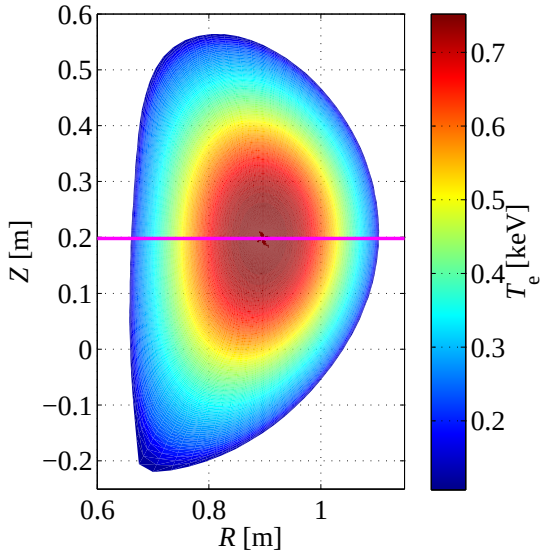

(b) H-mode electron temperature.

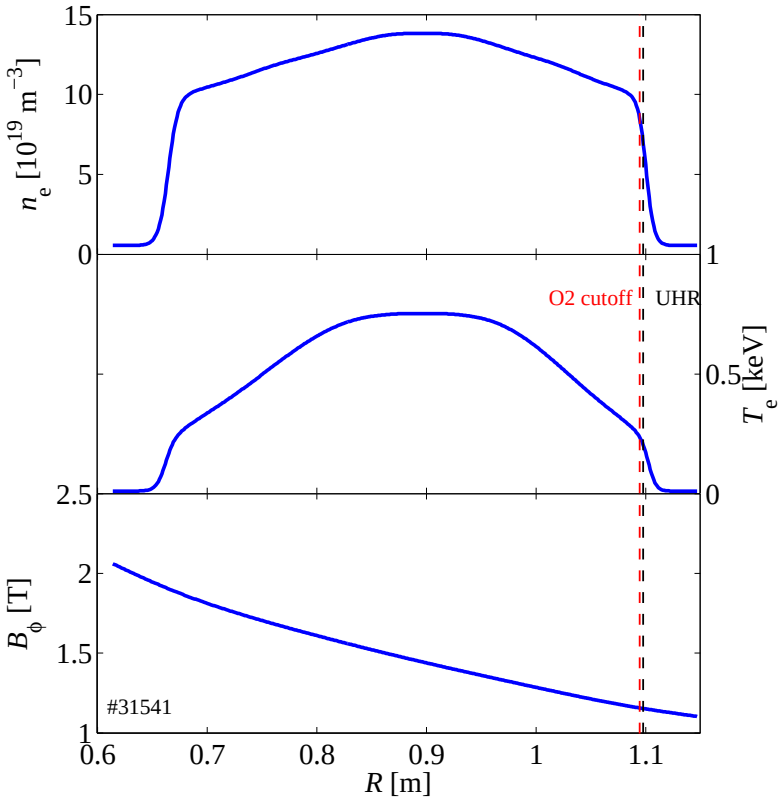

(c) H-mode profiles mapped on equilibrium midplane $Z = Z_{\text{axis}}$.

Figure 8.2: Typical electron density and temperature profiles in TCV overdense ELM-free H-modes. Poloidal maps of the electron (a) density and (b) temperature. The thick magenta line indicates the equilibrium midplane at $Z = Z_{\text{axis}}$. (c) Corresponding profiles mapped on the equilibrium midplane, along with the profile of total toroidal magnetic field. The red and black dashed vertical lines indicate the LFS positions of the O2 plasma cutoff and UH resonance, respectively. #31541, $t = 0.5$ s.

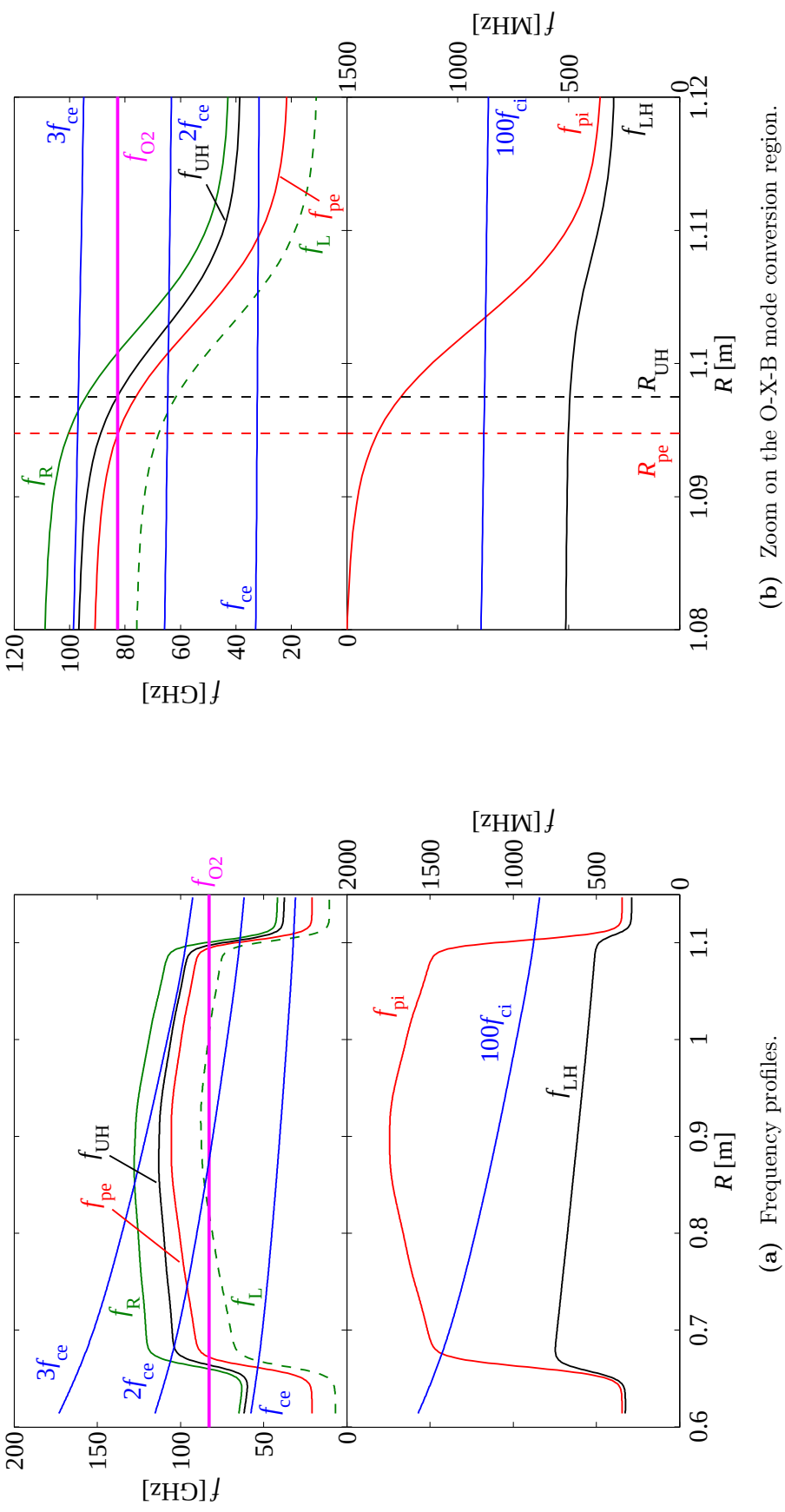

(a) Frequency profiles.

(b) Zoom on the O-X-B mode conversion region.

Figure 8.3: Typical frequency profiles in TCV overdense ELM-free H-modes. (a) Frequency profiles corresponding to the electron density and magnetic field profiles shown in figure 8.2. The ion and hybrid frequencies are calculated for Deuterium. The O2 power frequency is in cutoff ($f_{O2} \leq f_{pe}$) on most of the profile. The cutoff is located at the very edge of the plasma, in the steep density gradient region. (b) Detailed view of the O-X-B mode conversion between the O2 cutoff at R_{pe} and the UH resonance at R_{UH}. #31541, $t = 0.5$ s.

LHPI in TCV

The expected LHPI threshold power and LH decay wave frequency are evaluated for TCV second harmonic O-X-B experiments using typical ELM-free H-mode plasma density, temperature and magnetic field profiles, as shown in figure 8.2. The corresponding frequency profiles for a deuterium plasma are given in figure 8.3.
Here, the upper-hybrid and lower hybrid frequencies are defined from the resonance condition 3.2.52 for the cold plasma model, equivalent to the condition $A = 0$ in the cold plasma dispersion relation 3.3.24. Accounting for both electron and ion dynamics, i.e. for both high and low frequency waves, and solving for the wave angular frequency yields

$$\omega_{\mathrm{UH/LH}}^2 \equiv \left(\frac{\omega_\mathrm{p}^2 + \Omega_\mathrm{ci}^2 + \Omega_\mathrm{ce}^2}{2}\right)\left[1 \pm \left(1 + \frac{4\Omega_\mathrm{ci}\Omega_\mathrm{ce}\left(\omega_\mathrm{p}^2 - \Omega_\mathrm{ci}\Omega_\mathrm{ce}\right)}{\left(\omega_\mathrm{p}^2 + \Omega_\mathrm{ci}^2 + \Omega_\mathrm{ce}^2\right)^2}\right)^{1/2}\right] \tag{8.2.7}$$

where the upper and lower signs are for the upper- and lower-hybrid angular frequencies, respectively. Here, we use the definition

$$\omega_\mathrm{p}^2 \equiv \omega_\mathrm{pe}^2 + \omega_\mathrm{pi}^2. \tag{8.2.8}$$

The H-mode pedestal implies a steep edge density gradient and a relatively flat central profile increasing up to $n_{\mathrm{e}0} = 13.8 \cdot 10^{19}$ m^{-3} at the plasma center. As a consequence, most of the plasma volume is overdense to second harmonic O-mode (O2). Indeed, the O2 frequency $f_{\mathrm{O2}} = 82.7$ GHz meets its cutoff $f_\mathrm{pe} = f_{\mathrm{O2}}$ and the UH resonance $f_\mathrm{UH} = f_{\mathrm{O2}}$ in the high-gradient region at the very edge of the plasma, i.e. at $R_\mathrm{pe} \simeq 1.095$ m and $R_\mathrm{UH} \simeq 1.097$ m, respectively. The O-X-B mode conversion layer is thus only 2 mm thick. In this region of the plasma, the expected frequency of the decay LH waves generated by LHPI is $f_\mathrm{LH} \simeq 500$ MHz.
Figure 8.4 shows the scale-length L and threshold power density $P_\mathrm{th}/\pi\rho^2$ resulting from the profiles of plasma parameters and frequencies given in figures 8.2 and 8.3. The threshold power is calculated on the whole profile although the LHPI selection rules (8.2.3) and (8.2.4) may not be fulfilled everywhere. Due to the rather flat density profile with steep edge gradients, the mixed scale-length L varies by several orders of magnitude with R, from $L \simeq 1$ cm at the edge to $L \lesssim 10$ m in the center. Hence, the P_th profile shape dependence is dominated by the $1/L^{4/3}$ factor in equation 8.2.5. The inhomogeneity at the plasma edge dramatically increases the LHPI threshold power in the O-X-B mode-conversion region. Assuming $T_\mathrm{i} \simeq T_\mathrm{e}$, one gets $P_\mathrm{th}/\pi\rho^2 = 2.7$ kW/cm^2 for the plasma parameters at the UHR ($f_\mathrm{pe} \simeq 77.9$ GHz, $f_\mathrm{ce} \simeq 32.3$ GHz, $T_\mathrm{e} \simeq 214$ eV, $n_\mathrm{e} \simeq 7.5 \cdot 10^{19}$ m^{-3}, $B_\varphi \simeq 1.15$ T, $L_n \simeq 14.8$ mm,

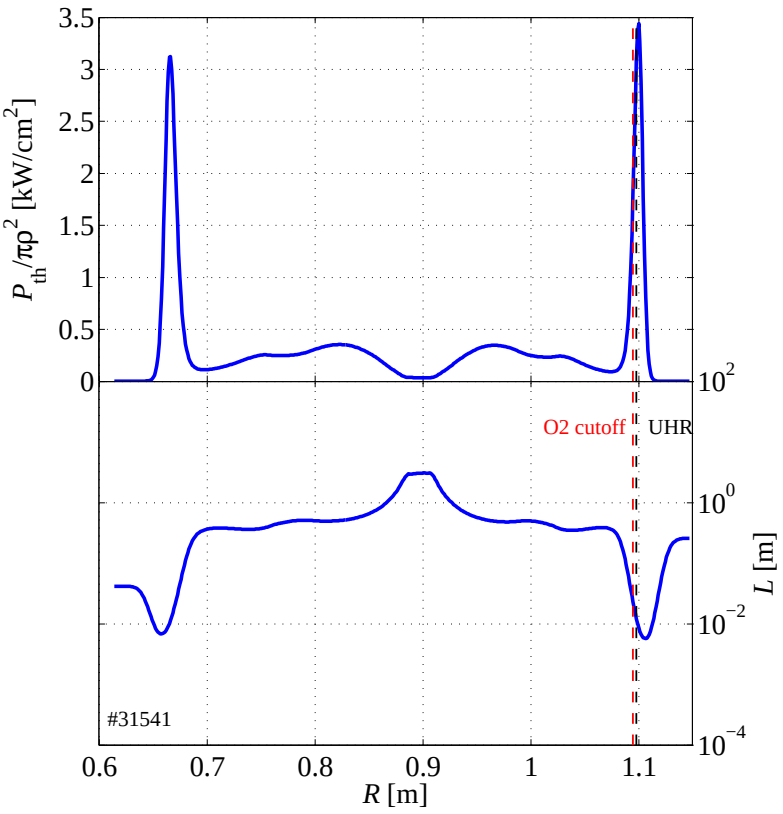

Figure 8.4: LHPI threshold power profile. LHPI threshold power density $P_{\mathrm{th}/\pi\rho^2}$ and mixed scale length L calculated from equations (8.2.5) and (8.2.6) for the profiles of plasma parameters and frequencies given in figures 8.2 and 8.3. The red and black dashed vertical lines indicate the LFS positions of the O2 plasma cutoff and UH resonance, respectively. #31541, $t = 0.5$ s.

$L_B \simeq 1.058$ m and $L = 14.7$ mm). In TCV, the radius of the EC power beams is approximately $\rho \simeq 2$ cm (as indicated in section 2.2). The LHPI is thus expected to be observed above $P_{\mathrm{th}} \simeq 34$ kW of injected O2 power in TCV EBH experiments. Due to the strong radial variation of the P_{th} profile at the plasma edge, the actual value of the LHPI threshold power strongly depends on the plasma cutoff position, i.e. on the density pedestal height and on the pump wave frequency f_0. For a slightly lower density pedestal height (or a higher pump wave frequency) such that the O2 cutoff is located on the flat part of the density profile rather than in the thin high density gradient region, the threshold power would drop by one order of magnitude, which is in favor of LHPI. On the other hand, the O-X conversion efficiency would be reduced due to the lower density gradient and less power is expected to reach the X-B mode-conversion region where the LHPI takes place, which is not in favor of LHPI. There are thus two competing phenomena at play for the intensity of the LHPI. Finally, note that the LH wave frequency is not a rapidly varying function of R.

The threshold power $P_{\rm th}$ is very sensitive to the scale length at the mode conversion region (MCR), which strongly depends on the MCR position in the H-mode density profile. The latter is mainly regulated by the density pedestal height. When the pedestal height is larger than the plasma cutoff density, the MCR is located in the steep density gradient region and $P_{\rm th}$ is high. Otherwise, the MCR is located in the much flatter central part of the profile where $P_{\rm th}$ is lower.

8.3 TCV LHPI antenna

This section presents TCV's new LHPI-antenna whose design, construction, vessel implementation and initial exploitation is part of this thesis work.

8.3.1 Antenna design and construction

The loop-antenna is designed to detect the oscillating magnetic field of waves in the $f = 0.2 - 2$ GHz frequency range, in particular the low-frequency part of the LHPI decay spectrum expected in O-X-B EBH experiments. The corresponding vacuum wavelength range is $\lambda \equiv c/f = 0.15 - 1.5$ m. The different parts of the antenna and its implementation in TCV port are illustrated in figures 8.5, 8.6 and 8.7. Unless stated, all parts are made in non-magnetic stainless steel.

- The waves are detected by a 60 mm $\times$ 60 mm square **loop-probe**. The loop dimensions are chosen to be twice smaller than the shortest wavelength to be measured. In order to have a low self-inductance, the loop is made of a folded 1.5-millimeter-thick 5-millimeter-wide plate.

- The loop-probe is connected to a **coaxial conductor** of length $L = 401.5$ mm. One end of the probe is screwed on the internal conductor, the other end is welded on the edge of the external conductor. The internal conductor is a solid rod of radius $r_1 = 2.5$ mm and the external conductor is a tube of internal radius $r_2 = 6$ mm and wall thickness $\Delta r = 2$ mm. The impedance of this coaxial conductor is thus $Z = 60 \ln(r_2/r_1) \simeq 53\ \Omega$. Holes are drilled in the tube to ensure a good vacuum quality in the whole antenna system. The internal rod is held in place thanks to two PEEK (thermoplastic resine) insulating rings.

- A **symmetry coupler** is welded on the outer of the coaxial conductor, next to the loop probe. This piece is also called **"balun"** since it is meant to *bal*ance

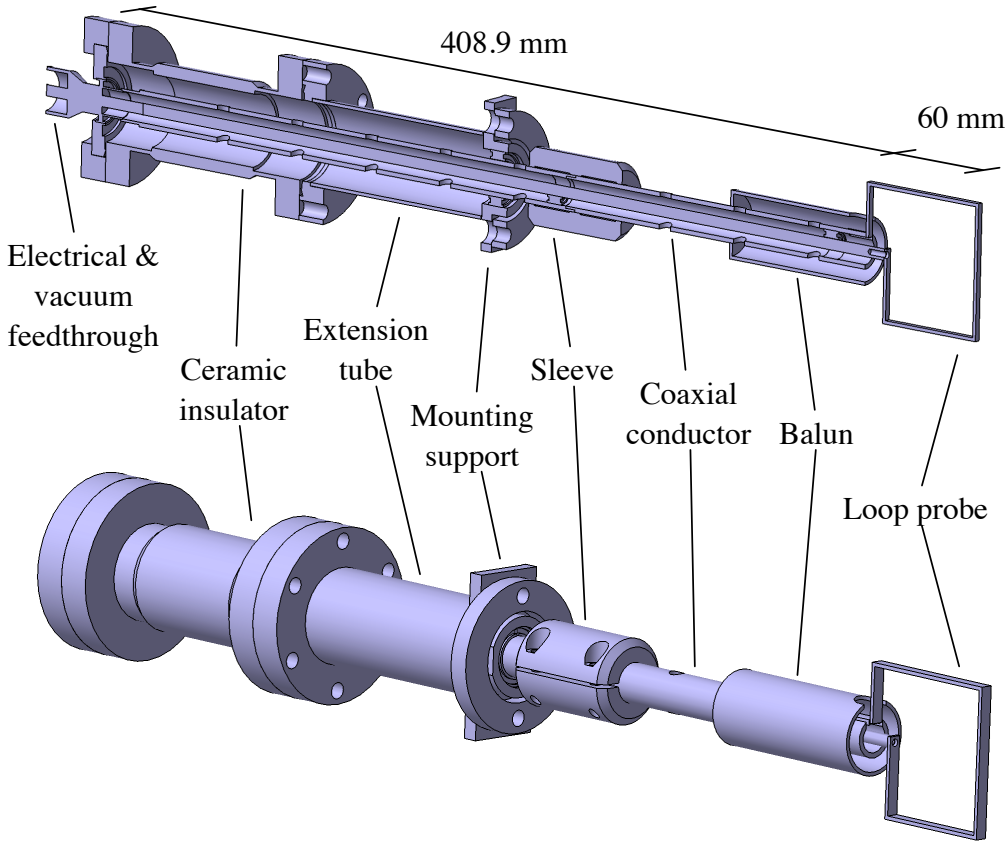

Figure 8.5: TCV new LHPI-antenna. The top figure is a cut view along the antenna coaxial conductor.

the *un*balanced impedance between the loop probe and the coaxial conductor. It is made of a tube of 13.5 mm internal radius and 1.5 mm wall thickness. For an efficient balancing effect, the balun length must be equal to a quarter of the wavelength, i.e. $\lambda/4 = 7.5$ cm for the middle-range frequency $f = 1$ GHz.

- The other end of the coaxial conductor is welded on a type-N **electrical feedthrough** mounted on a flange.

- During the EBH experiments, the LHPI-antenna will be directly connected to a spectrum analyzer which is at the same ground than the data acquisition system and the other diagnostics in this region of TCV. This ground is independent from TCV vessel ground. Hence, the LHPI-antenna must be electrically isolated from the vacuum vessel. A 104.5-millimeter-long **ceramic insulator** is thus inserted between the antenna flange and the port flange.

- The port is shared with a previously installed "sniffer" detector for the EC stray power, as illustrated in figures 8.6 and 8.7. As a consequence, there

is not enough room on the port flange for a direct connexion of the ceramic insulator. The port is thus extended with a 92-millimeter-long **extension tube** (35 mm internal diameter, 1.5 mm wall thickness) such that the LHPI-antenna is installed as close to the port center as possible.

- In order to mount the antenna on the port flange, the coaxial conductor is divided in two parts which are connected with the help of a **sleeve**.
- To prevent any bending of the antenna due to its own mass, the coaxial conductor is held in place by a **mounting support** on the port flange. A PEEK ring around the external conductor isolates it from the port flange.

8.3.2 Implementation on TCV

The LHPI-antenna is installed in the upper-lateral port of TCV sector 10 located at $Z = 455$ mm above the machine midplane. It is located 180° toroidally away from the EC power launcher L1 (in sector 2) used in the LHPI experiments presented here, as indicated in the toroidal view of figure 8.9(a). The port is shared with the wave guide of an EC stray power "sniffer" detector. The antenna dimensions were chosen such that the tip of the loop-probe is ≈ 2.5 cm back in the shadow of the graphite tiles screwed on the inner wall of TCV vacuum vessel. The antenna is thus not directly exposed to the plasma.

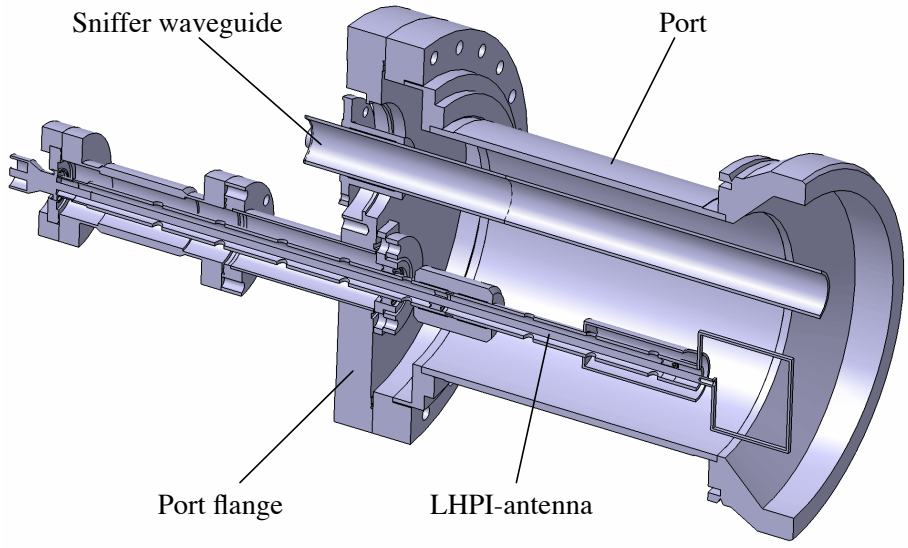

Figure 8.6: LHPI-antenna port implementation. Cut view of the TCV upper-lateral port in sector 10, showing the waveguide of the sniffer EC stray power detector and the LHPI-antenna. In fact, the probe is oriented at 45° and not vertically as in the drawing.

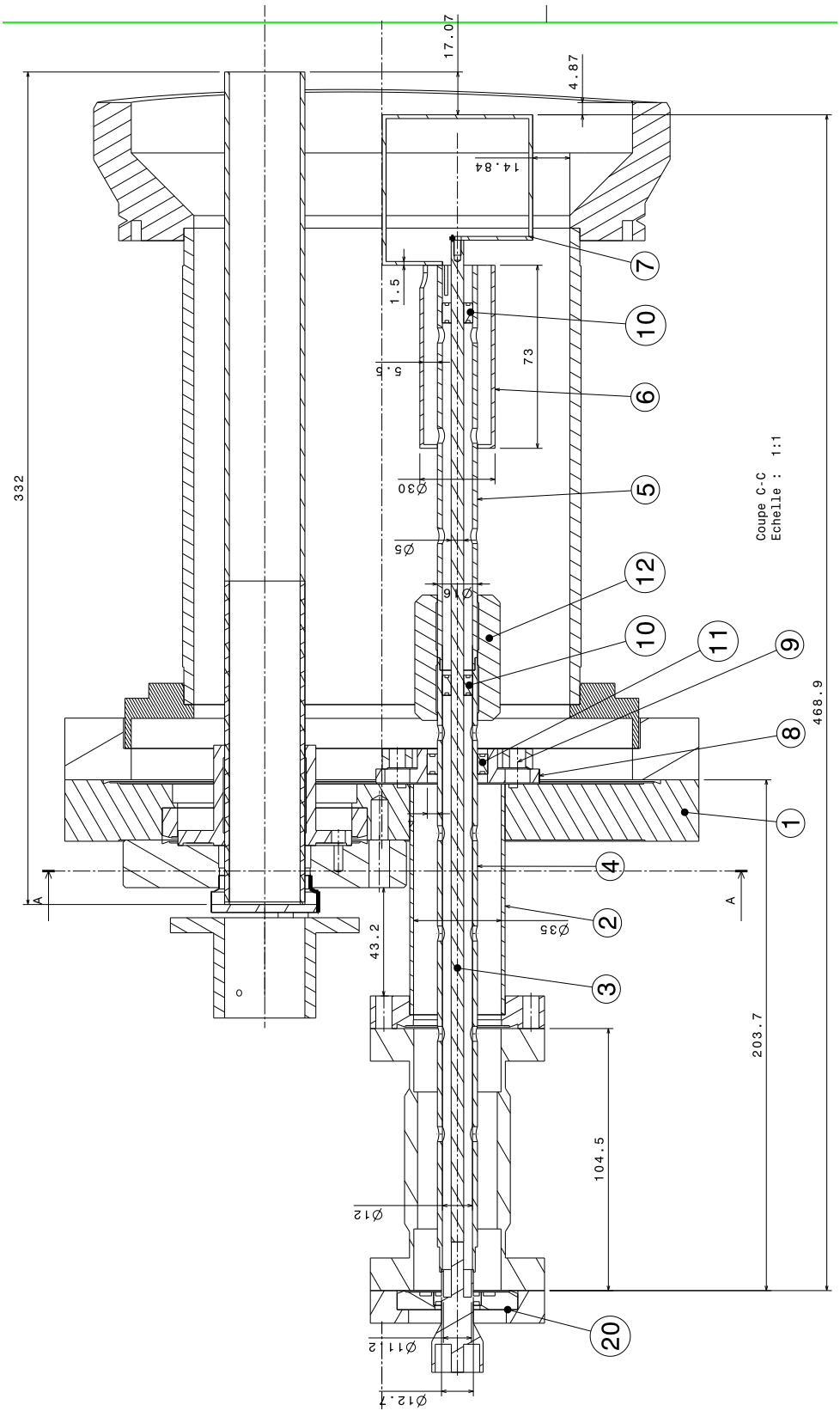

Figure 8.7: LHPI-antenna plan. (1) Port flange, (2) extension tube, (3) internal conductor (rod), (4) and (5) external conductors (tubes), (6) balun, (7) 6 cm × 6 cm loop probe, (8) and (9) elements of the mounting support for the coaxial conductor, (10) and (11) insulating rings, (12) sleeve for the external conductors connexion, (20) electrical and vacuum feedthrough.

8.4 Experimental results in TCV

8.4.1 LHPI spectrum evolution with H-mode conditions

Introduction

EBH experiments with the newly installed loop-antenna are performed aiming at the detection of the LH decay waves. The time-evolution of the LH spectrum is monitored while the non-stationary H-mode is evolving, revealing a high sensitivity of the LHPI signal intensity on the H-mode plasma conditions.

Experimental setup

In this experiment, the equilibrium is the usual high-current ($I_\varphi \simeq -400$ kA) over-dense ELM-free H-mode diverted and strongly shaped ($\kappa_a \simeq 1.76$, $\delta_a \simeq 0.54$) plasma necessary for the O-X-B mode conversion in TCV. The vacuum magnetic field at the vessel center is $B_{\varphi v}(R_0) \simeq -1.44$ T. The plasma is located in the upper half of TCV vacuum vessel ($Z_{\text{axis}} \simeq 0.23$ m and $R_{\text{axis}} \simeq 0.89$ m), i.e. close to the LHPI-antenna and in front of the Thomson scattering system for optimum measurements of the electron density and temperature profiles, in particular the pedestal profiles measured by the Thomson-edge system.
Given the high plasma density achieved in H-mode regime, the three lasers of the Thomson scattering system don't need to be trigged simultaneously. Each laser produces enough scattered light to measure n_e and T_e with a high signal-to-noise ratio. The lasers are thus trigged independently, separated by 1 ms, producing triple light pulses every 50 ms. The number of experimental data points per profile is tripled, which allows high-quality fits of the steep edge profiles as illustrated in figure 8.8 and by the small errorbars on the measured pedestal parameters shown in figure 8.11.
The O2 power is injected from the equatorial launcher L1. It is programmed to start after the expected L-H transition time. The RF power amplitude is constant at 350 kW, i.e. high above the calculated LHPI threshold power. The optimum launcher angles for the O-X mode conversion are pre-calculated by the AMR code using the equilibrium and profiles data from a similar H-mode plasma, yielding $(\theta_L, \phi_L) \simeq (+44.8°, +138.3°)$: the wave is injected from below the plasma with an upward injection angle $\theta_{\text{inj}} \simeq 31.7°$. Figure 8.9 shows a post-shot 7-ray simulation performed with the AMR code using the experimental equilibrium and the profiles data of figure 8.8. Since the plasma equilibrium is located above the EC power injec-

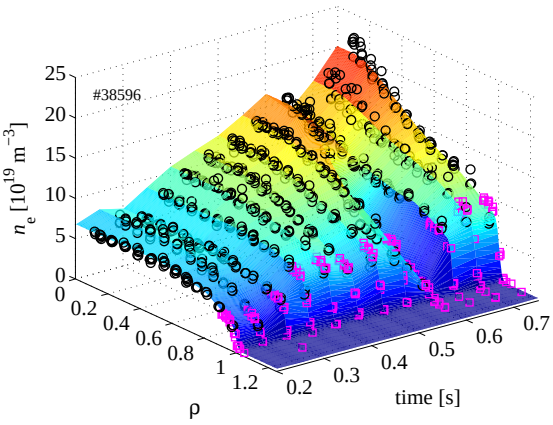

(a) Electron density profile evolution.

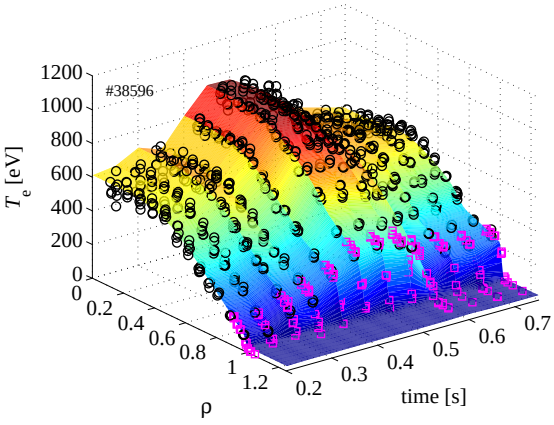

(b) Electron temperature profile evolution.

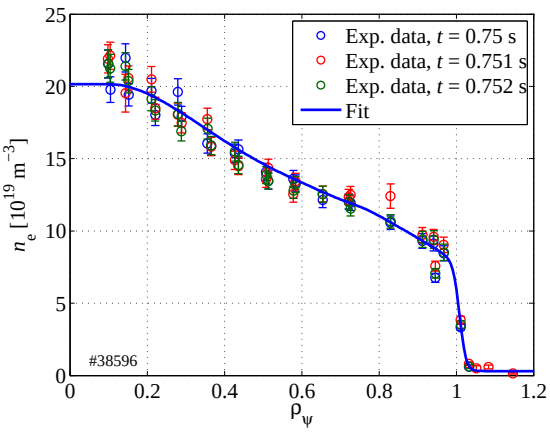

(c) Electron density profile at $t = 0.75$ s.

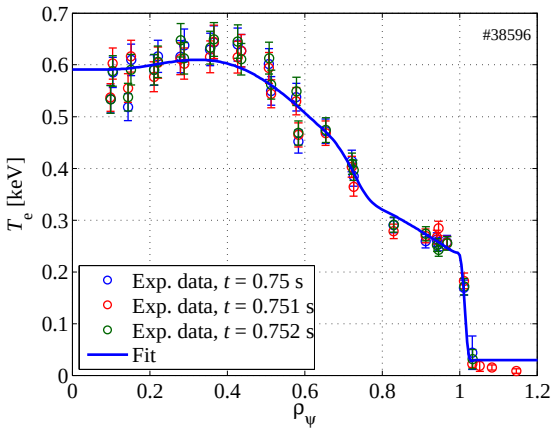

(d) Electron temperature profile at $t = 0.75$ s.

Figure 8.8: High-quality H-mode profiles measurements. (a) Electron density and (b) electron temperature profiles versus time. The colour surfaces are the fits on the experimental data from the Thomson scattering central (○) and edge (□) lines-of-sight. (c)-(d) Fitted profiles used in the ray-tracing simulation presented in figure 8.9 and the threshold power calculation of figure 8.13. #38596.

tion point, the wave penetrates the plasma below its midplane. As a consequence, the wavenumber undergoes a strong upshift along the Bernstein wave propagation up to $N_\parallel \simeq 1.5$ at the absorption location. Hence the Doppler-shifted absorption takes place far off-axis on the LFS of the plasma at $\rho_\psi \simeq 0.81$, as indicated in figure 8.10.

The fraction of non-absorbed power is detected by two EC stray power detectors. Detector S1 is located in TCV sector 1 next to the EC power launcher. Detector S2 is located five sectors away from the launcher, but it has a higher sensitivity.

In this experiment, the LHPI antenna is connected to a spectrum analyzer of the HP-8500 series allowing a fast frequency sweeping with a high repetition rate. The

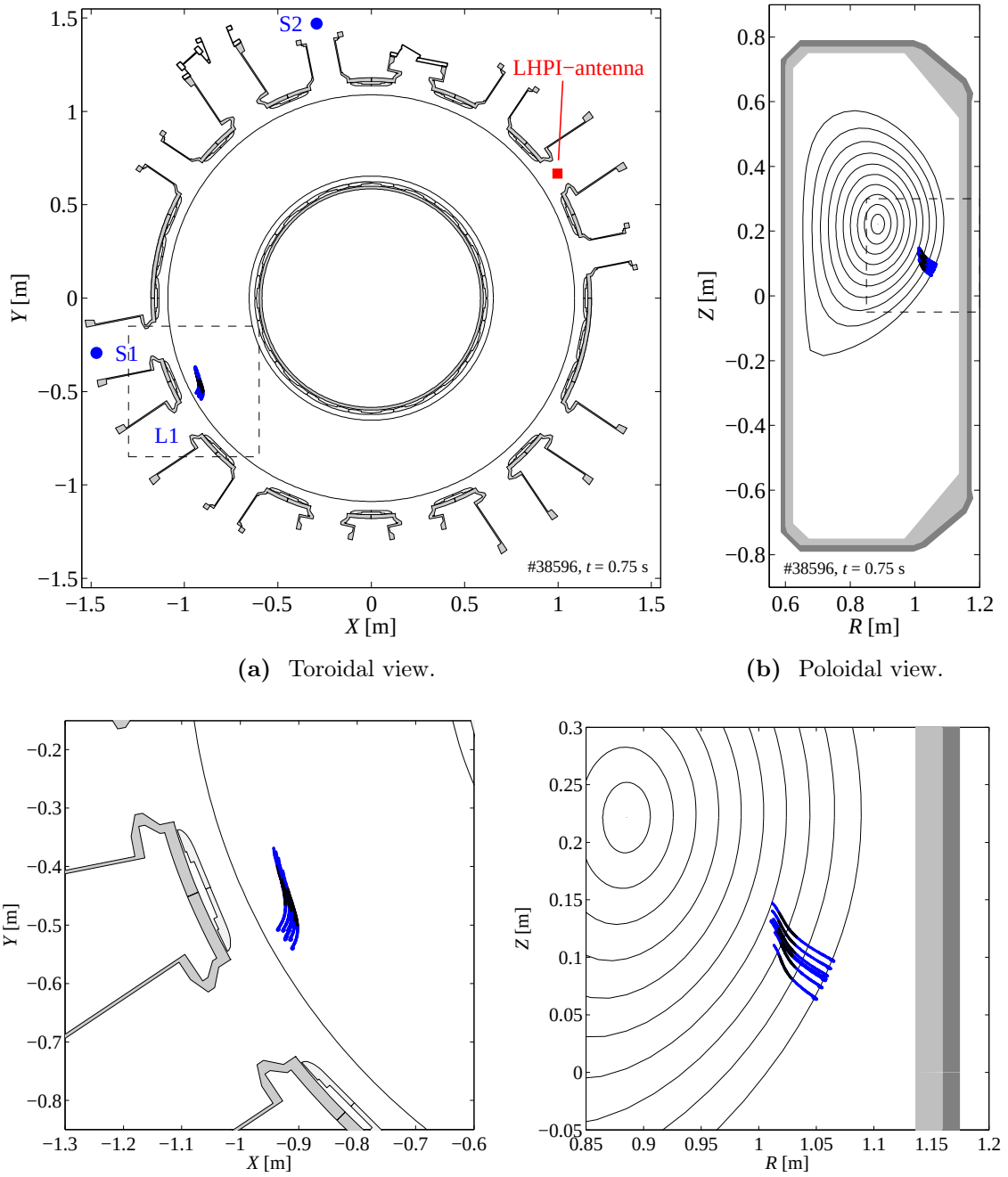

(a) Toroidal view. **(b)** Poloidal view.

(c) Details of the toroidal view. **(d)** Details of the poloidal view.

Figure 8.9: AMR ray-tracing trajectories. (a) Toroidal and (b) poloidal views of the 7-ray EBW trajectory calculated by the AMR ray-tracing code. The LHPI-antenna (denoted by a red ■) is located at 180° toroidally from the EBW power injected from launcher L1. The position of the stray diodes S1 and S2 is denoted by two blue •. The dashed frames define the detail views on the ray trajectories given in (c) and (d). Black dots along the rays indicate the power absorption location. The corresponding deposition profile and refractive index evolution are given in figures 8.10. #38596 at $t = 0.75$ s using experimental profiles data shown in figures 8.8(c)-(d).

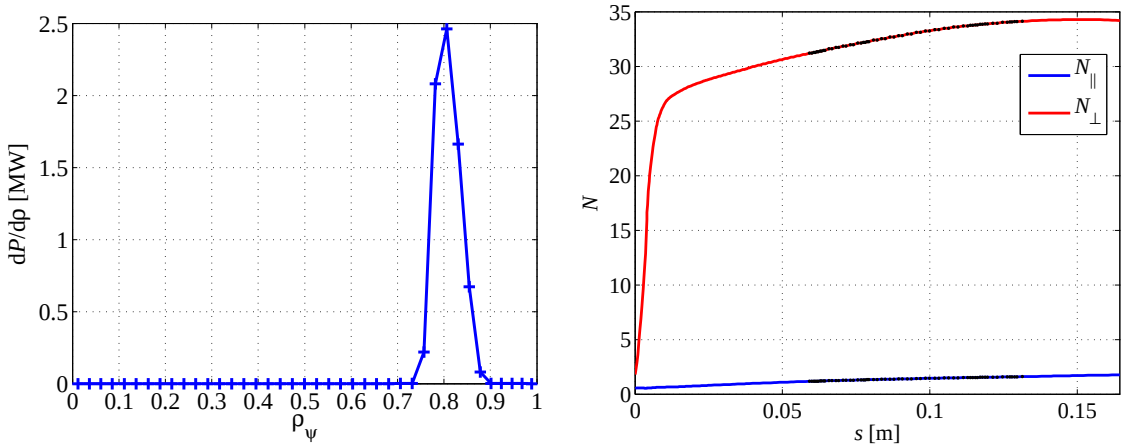

(a) Power deposition profile. **(b)** Central ray refraction indices.

Figure 8.10: Power deposition profile and refraction indices. (a) Power deposition profile and (b) refraction indices along the central ray propagation, corresponding to the ray-tracing simulation of figure 8.9. The EBW power deposition location is strongly Doppler-shifted at $\rho_\psi \simeq 0.81$ due to a $N_\parallel$-upshift. #38596 at $t = 0.75$ s.

spectrum analyzer is setup to continuously sweep the $300-800$ MHz range in ~ 2 ms with only ~ 0.3 ms blank time between the sweeps. The LHPI spectrum is thus monitored at a rate of 435 Hz.

LHPI spectrum evolution

Figure 8.11 shows the time-evolution of the LHPI-antenna signal spectrum, the plasma parameters and the density pedestal parameters drawn from the modified tanh fit of the edge density profile shown in figure 8.8.

The plasma L-H transition occurs shortly before $t = 0.3$ s as indicated by the characteristic drop in the emission of D_α recombination light. An ELM-free H-mode follows, which is sequenced in three parts (numbered (I) to (III) thereafter) due to a large isolated ELM at $t \simeq 0.42$ s and a short back-transition to L-mode in the time interval $t = 0.59 - 0.61$ s. The plasma termination occurs at $t \simeq 0.79$ s.

When the O2 power injection starts at $t = 0.35$ s, the plasma cutoff is just established. The low EC stray power measured by the detector S1 is the signature that an efficient O-X-B mode conversion is at play, which should be accompanied by a LHPI. Indeed, signal from the LHPI-antenna is detected as soon as the EBH starts. No LHPI-antenna signal is detected when the EC power coupling with the plasma is lost due to ELMs, as indicated by high stray power level, which confirms that the LHPI-antenna signal is generated by O-X-B mode-converted EC power.

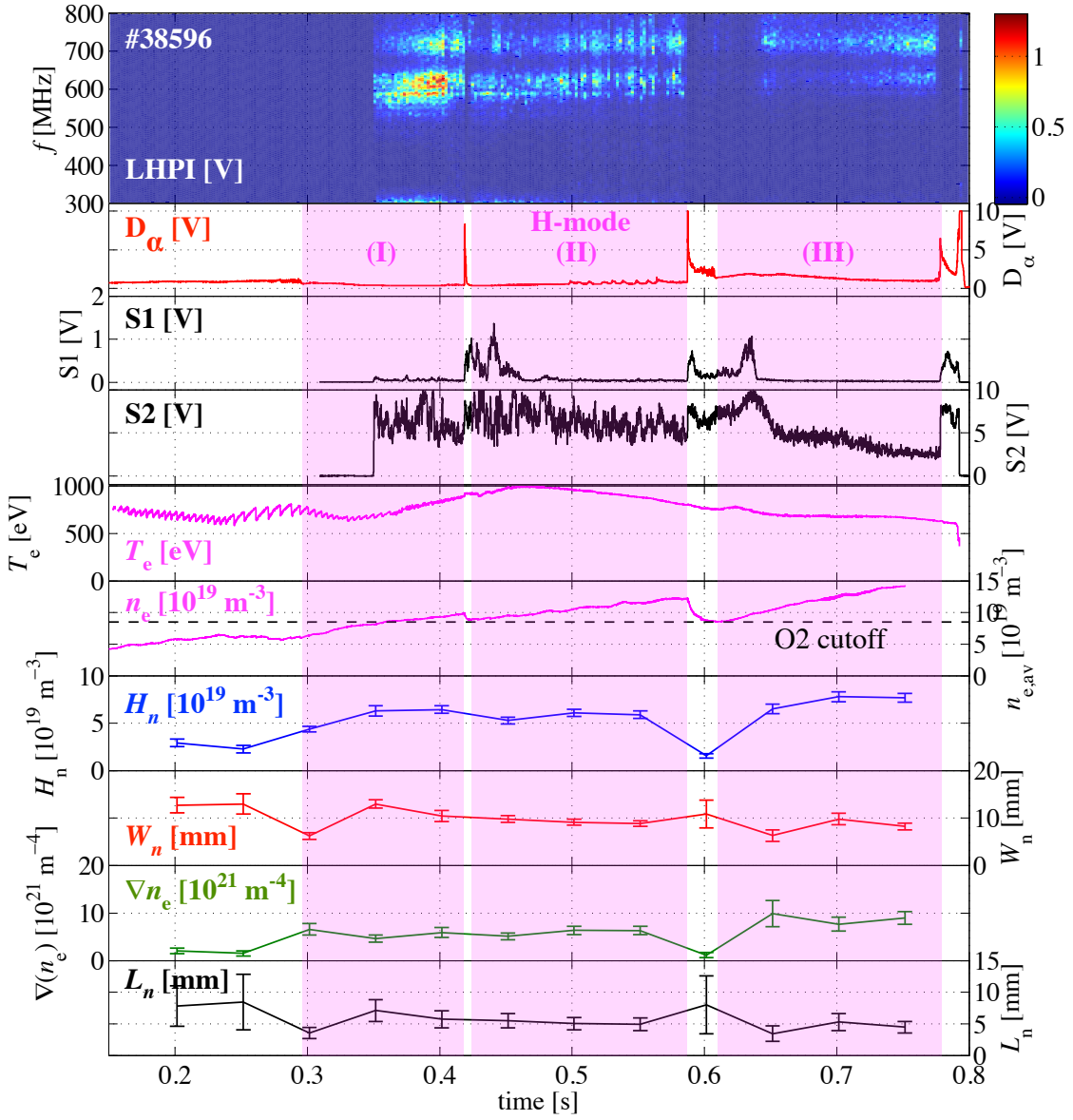

Figure 8.11: LHPI spectrum monitoring. From top to bottom: Time evolution of the LHPI spectrum, the D_α recombination light, the EC stray power measured by S1 and S2 detectors, the central electron temperature T_e (soft X-ray), the line-averaged electron density n_e (FIR) and the electron density pedestal parameters from the profiles fitted on Thomson data in figure 8.8: height H_n, width W_n, maximum gradient ∇n_e and scale length at maximum gradient $L_n = n_e/\nabla n_e$. The LHPI signal amplitude shows a strong sensitivity on the H-mode conditions. The H-mode phases are indicated by magenta backgrounds. The ELM-free H-mode regime implies a steepening of the edge electron density gradient and a rise of the central electron density reaching the second-harmonic O-mode plasma cutoff with $n_e > 8.5 \cdot 10^{19} \mathrm{m}^{-3}$ shortly before the O2 power injection starts at $t = 0.35$ s. #38596.

Figure 8.12 shows two LHPI spectra measured at the beginning and at the end of

the EBH experiment. Two broad peaks are observed in the range of the expected LH wave frequency. They remain essentially centered on $f_1 \simeq 620$ MHz and $f_2 \simeq 710$ MHz during the whole EBH experiment.

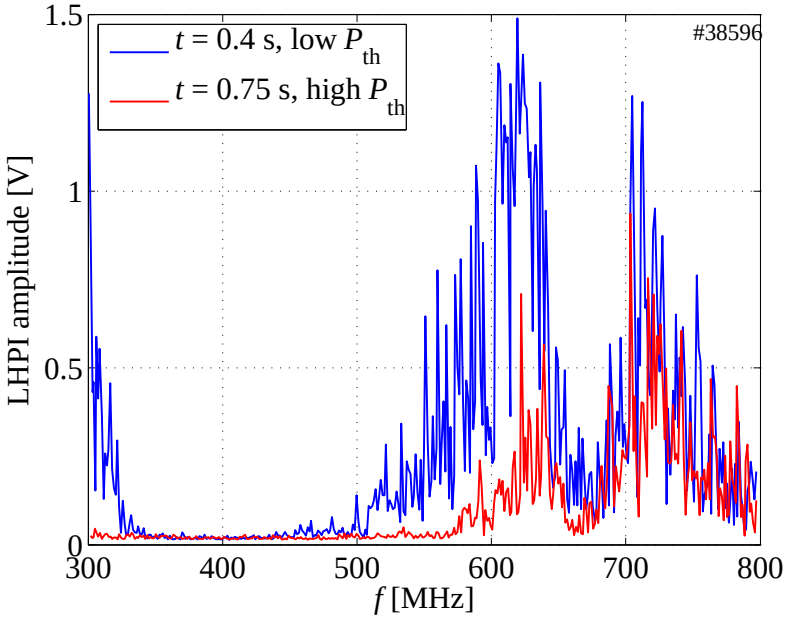

Figure 8.12: LHPI spectra at low and high PI threshold power levels. LHPI spectra measured by the loop-antenna in EBH experiment at fixed injected O2 power, at times $t \simeq 0.4$ s (blue) and $t \simeq 0.75$ s (red) when the LHPI threshold power P_{th} is low and high, respectively. #38596.

Conversely to the waves frequency, the amplitude of the LHPI signal and the width of the peak both vary with the H-mode conditions. Indeed, as mentioned earlier, a steepening of the density gradient at the mode conversion region has three effects: a more efficient O-X mode conversion, a larger probability of X-mode tunneling loss through the evanescent layer and a higher LHPI threshold power. These effects are in competition for the generation of LHPI: at fixed injected O2 power, the first effect increases LHPI emission whereas the last two tend to diminish the LHPI. The evolution of the LHPI signal amplitude with the H-mode conditions is thus not trivial to interpret. The discussion of this point is split according to the three H-mode sequences (I), (II) and (III).

H-mode sequence (I). In H-mode phase (I), the LHPI emission signal is the most intense of the discharge. It is of higher amplitude than in H-mode (III) although the EC power-plasma coupling is less efficient, as indicated by EC stray power signals of higher amplitude in H-mode (I) than in H-mode (III) for both S1 and S2 detectors.

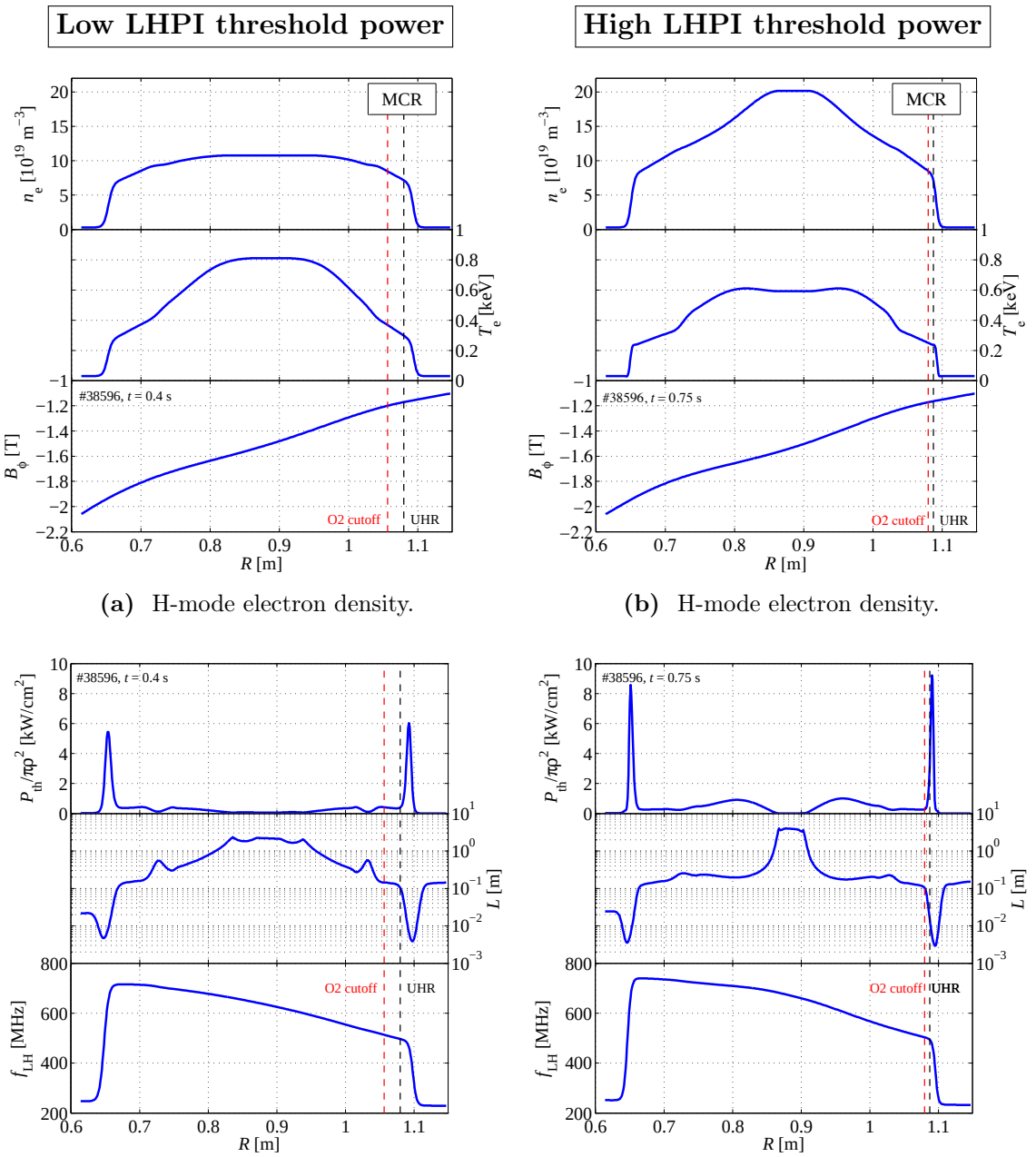

(a) H-mode electron density.

(b) H-mode electron density.

(c) H-mode electron temperature.

(d) H-mode electron temperature.

Figure 8.13: Low and high LHPI threshold power. (a)-(b) Midplane profiles of electron density, electron temperature and toroidal magnetic field for low and high pedestal height, respectively. (c)-(d) Corresponding profiles of LHPI threshold power density $P_{\rm th}/\pi\rho^2$ calculated using equation (8.2.5), mixed scale length L and LH frequency $f_{\rm LH}$. The red and black dashed vertical lines indicate the LFS positions of the O2 plasma cutoff and UH resonance, respectively. When the H-mode pedestal height is low (left column), the mode conversion region (MCR) is located between the steep edge gradient and the flat central profile regions. As a consequence, the scale length is large and the LHPI threshold power is low. At larger pedestal height when the H-mode profiles have developed (right column), the MCR is located in the steep edge gradient region where the LHPI threshold power is a factor ~ 8 times higher. #38596 at $t \simeq 0.4$ s and $t \simeq 0.75$ s, see figures 8.8 and 8.11.

The high LHPI signal amplitude is due to the low density pedestal height H_n in H-mode (I) compared to H-mode (III). As a consequence, the O-X-B mode conversion region (MCR) is not located at the plasma edge where the density gradient is steep, but in a slightly more central and flatter profile region, as indicated by detailed profiles analysis in figure 8.13(a). The resulting local scale length is large and the LHPI threshold power calculated from equation (8.2.5) is dramatically lower than in the edge region, as indicated in figure 8.13(c), thus allowing the generation of a strong LHPI by the incoming EC wave. The H-mode parameters at the UHR and the calculated LHPI threshold power are given in table 8.3. For an EC beam of radius $\rho = 2$ cm, the LHPI threshold power is $P_{\rm th} \simeq 5$ kW $\ll P_{\rm inj} \simeq 350$ kW.
The same analysis is performed for each electron density and temperature profile measured by the Thomson scattering system every 50 ms. The resulting time-evolution of the MCR position, the mixed field and density scale length, the LHPI threshold power and the LH frequency at the UHR is given in figure 8.14.

			LHPI threshold power at the UHR						
t [s]	$R_{\rm pe}$ [m]	$R_{\rm UH}$ [m]	$n_{\rm e}$ [10^{19} m^{-3}]	$T_{\rm e}$ [eV]	B_φ [T]	L [m]	$P_{\rm th}/\pi\rho^2$ [kW/cm^2]	$P_{\rm th}$ [kW]	$f_{\rm LH}$ [MHz]
0.40	1.056	1.080	7.16	298	-1.17	0.105	0.40	5	497
0.75	1.080	1.087	7.13	238	-1.16	0.015	3.15	40	494

Table 8.3: Low and high LHPI threshold powers at the UHR. Corresponding to figure 8.13. The LHPI threshold power $P_{\rm th}$ is calculated for an EC beam of radius $\rho = 2$ cm.

H-mode sequence (II). After the isolated ELM at $t \simeq 0.42$ s which briefly deteriorates the O-X-B mode conversion efficiency, the ELM-free H-mode exhibits a dithering activity characterized by short pulses of D_α light emission. Each of theses pulses is correlated by a loss of the coupling efficiency, as indicated by the S2 detector, and of LHPI signal. As a result of this oscillating transition between H-mode and L-mode confinements, the density pedestal development saturates gradient $\nabla(n_{\rm e})$ and scale length L_n at marginally higher values than in the H-mode (I), see figure 8.11. This rather small difference nonetheless yields a twice higher LHPI threshold power as indicated by figure 8.14. This effect and the H-mode dithering together lead to a lower LHPI signal amplitude in H-mode (II) than in H-mode (I).

H-mode sequence (III). After a short L-mode regime, the H-mode reestablishes without the oscillating confinement observed in H-mode (II). As a consequence, the

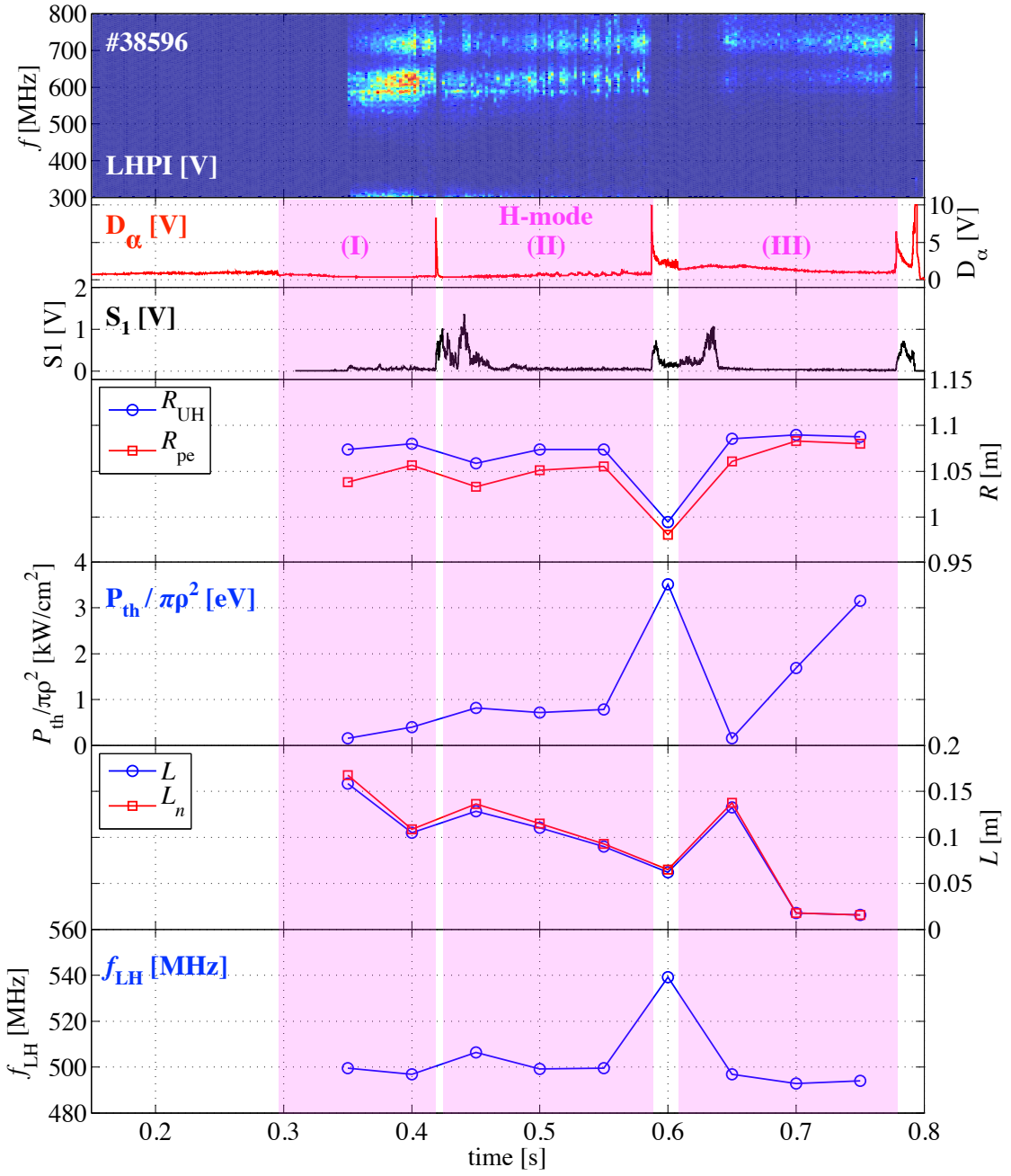

Figure 8.14: LHPI threshold power evolution. From top to bottom: Time evolution of the LHPI spectrum, D_α recombination light, EC stray power from S1 detector, O2 cutoff and UHR major radius coordinates $R_{\rm pe}$ and $R_{\rm UH}$, and LHPI evaluated at the UHR: LHPI threshold power density, electron density scale lenght L_n and mixed scale lengths L, LH frequency. #38596.

density profile develops a large pedestal height and the steepest gradient achieved in this discharge, see figure 8.11. As a consequence, the mode conversion region is located in the steep edge density region, as indicated by the profile analysis in figure **??**. This yields a very short mixed scale length and a high LHPI threshold power $P_{\rm th} \simeq 40$ kW at the UHR, as indicated by figures 8.13(d) and 8.14. Moreover,

a steep density gradient at the mode conversion region favors the X-mode tunneling through the evanescent between the UHR and the R-cutoff. Both the high instability threshold and the X-mode tunneling effect combine such that the LHPI signal observed in H-mode (III) is low compared to H-mode (I), as indicated the spectra in figure 8.12, despite the excellent profile conditions for the O-X mode-conversion as indicated by the close to zero stray level measured by the S1 detector.
The slow increase of the LHPI signal amplitude with time in H-mode (III) is caused by a slightly improving O-X coupling efficiency, as indicated by the diminishing EC stray power measured by detector S2.

Summary

In TCV EBH experiments, LH waves coming from a parametric instability at the O-X-B mode conversion are detected with the newly installed LHPI-antenna. The detected waves are in the expected frequency range. Thanks to a fast sweeping spectrum analyzer, the LHPI spectra is monitored at a high time rate. As expected, the LHPI signal amplitude is highly sensitive to the H-mode conditions, in particular the density pedestal height which regulates the position of the mode conversion region and thus the local value of the density gradient. The LHPI signal evolution is in good correlation with the evolution of the LHPI threshold power calculated from Thomson scattering profiles measurements.

8.4.2 LHPI threshold power and frequency cascading.

Introduction

In order to determine the LHPI threshold power in TCV EBH experiments, a scan of the injected O2 power is performed on a shot to shot basis.

Experimental setup

In this set of experiments, the magnetic equilibrium and the RF power injection geometry are similar to the experiment presented in the previous section. Continuous O2 power is injected from launcher 1 in the H-mode plasma located in front of the LHPI-antenna. The H-mode plasma is repeated and the power amplitude is scanned on a shot to shot basis.
In standard operation regime, the power output of TCV second harmonic gyrotrons can be varied between typically $P_{\mathrm{RF}} \simeq 200$ kW and $P_{\mathrm{RF}} \simeq 500$ kW by changing the high voltage applied to the cathode between $V_{\mathrm{k}} \simeq 60$ kV and $V_{\mathrm{k}} \simeq 70$kV with fixed

electron beam current $I_b \simeq 22$ A and gyrotron magnet current. Since the LHPI threshold power is expected at a typical value of $P_{th} \simeq 30$ kW, the gyrotron output power is scanned at lower values down to $P_{RF} \simeq 100$ kW by decreasing the electron beam current to $I_b \simeq 10$ A. The magnet current is corrected such that the gyrotron cavity produces the optimum electromagnetic mode. Further lower RF power levels are achieved down to $P_{RF} \simeq 27$ kW by detuning the magnet current. For each gyrotron setup, the actual level of injected O2 power is assessed by calorimetric measurement of a 2-second power pulse launched in a water load.
The LHPI-antenna is connected to a spectrum analyzer of the HP-71000 series. This apparatus allows the measurement of the LHPI spectrum on a broader frequency band, i.e. from 200 MHz to 2 GHz, but has a much lower repetition rate than the spectrum analyzer used in the previous experiment (sweep time $\simeq 50$ ms, blank time $\simeq 75$ ms). As a consequence, only 2-3 full sweeps are achieved in each H-mode plasma. A resolution bandwidth of 3 MHz and a video bandwidth of 100 kHz are chosen.

Experimental estimate of LHPI threshold power

As in the previous experiment, the H-mode plasmas present sporadic isolated ELMs briefly deteriorating the density profile pedestal and the O-X-B mode conversion efficiency. For each level of injected RF power, one LHPI spectrum is collected in an ELM-free phase of the plasma with high density pedestal and efficient wave-plasma coupling. In all cases, these conditions are met at the end of the discharge, just before the plasma disruption, similarly to the H-mode (III) presented in figure 8.11. As a consequence, all LHPI spectra presented here are measured in plasmas with similar parameters whose averages over the frequency sweeps are $n_{e0} \simeq (14.4 \pm 0.1) \cdot 10^{19}$ m^{-3}, $T_{e0} \simeq 786 \pm 4$ eV (Thomson, corrected by FIR), $Z_{axis} \simeq 0.23 \pm 0$ cm and $(\theta_L, \phi_L) \simeq (43.9°, 137.6°)$.
Figure 8.15 shows several LHPI spectra for increasing levels of injected O2 power. For the sake of clarity, only five of the spectra measured in the power range $P_{RF} \simeq 25 - 220$ kW are given here. The complete power scan is visible in figure 8.17. The peaks at $f_1 \simeq 650$ MHz and $f_2 \simeq 740$ MHz detected in the spectrum monitoring experiment of subsection 8.4.1 are recovered here. Three additional peaks are observed above $f = 1$ GHz, centered at $f_3 \simeq 1050$ MHz, $f_4 \simeq 1200$ MHz, $f_5 \simeq 1320$ MHz and $f_6 \simeq 1600$ MHz, the last two frequencies being close to the second harmonic of f_1 and f_2, respectively. The presence of the peaks at f_3 and f_4 remains unexplained.

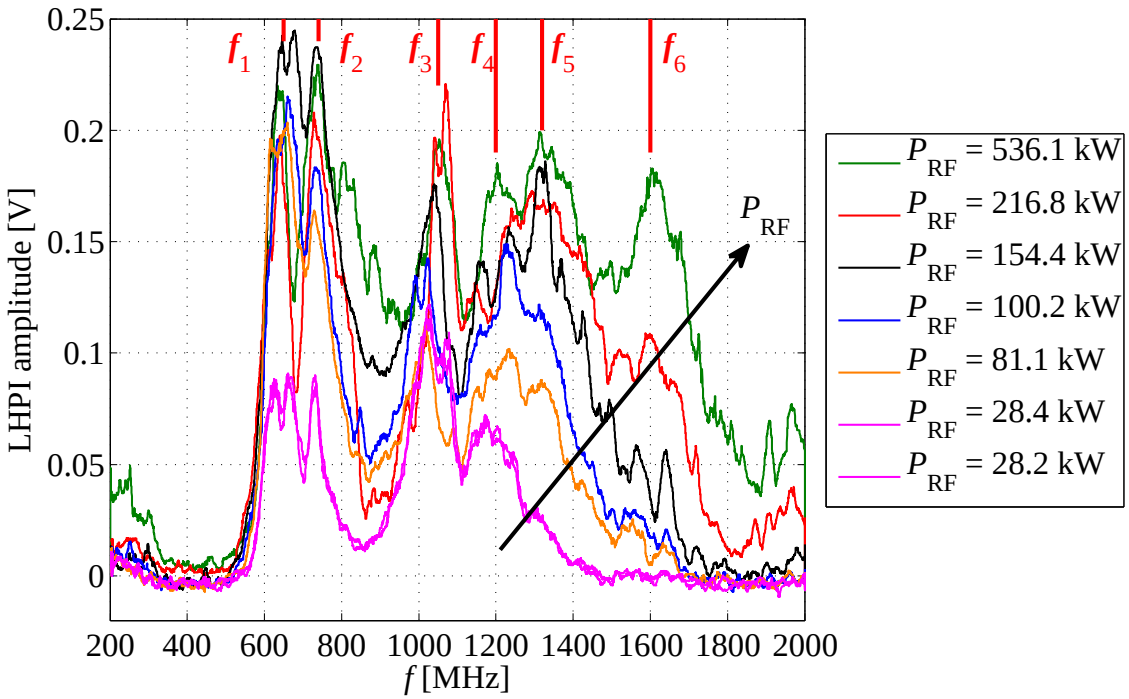

Figure 8.15: EBH power scan. LHPI spectra for increasing injected O2 power P_{RF}. Increasing the pump wave power yields three effects: the amplitude rise of the whole spectrum, a slight shift towards higher frequencies and a broadening of the spectrum towards higher frequencies with a fifth peak appearing above 1.5 GHz. The perfectly overlapping magenta spectra at low P_{RF} are measured in separate plasmas, thus demonstrating a high reproducibility of the LHPI signal. Shot numbers in decreasing P_{RF} order: #38706, 38708, 41875, 77, 88, 86 and 87.

The low power experiment was repeated, demonstrating a very high reproducibility of the spectrum shape and amplitude, as indicated by the perfectly overlapping magenta spectra in figure 8.15.
Several effects are observed with increasing pump wave power:

- An average rise of the amplitude of the whole spectrum is observed.
- The peaks are slightly shifted of ~ 20 MHz towards higher frequencies.
- The LHPI spectrum broadens towards higher frequencies with fifth and sixth peaks appearing above $P_{\mathrm{RF}} \simeq 80$ kW and $P_{\mathrm{RF}} \simeq 215$ kW respectively. This broadening is the signature of a further decay of the decay waves themselves at high pump wave power.

The spectrum energy E is proportional to the expression:

$$E \propto \int S(f) f \, \mathrm{d}f \tag{8.4.1}$$

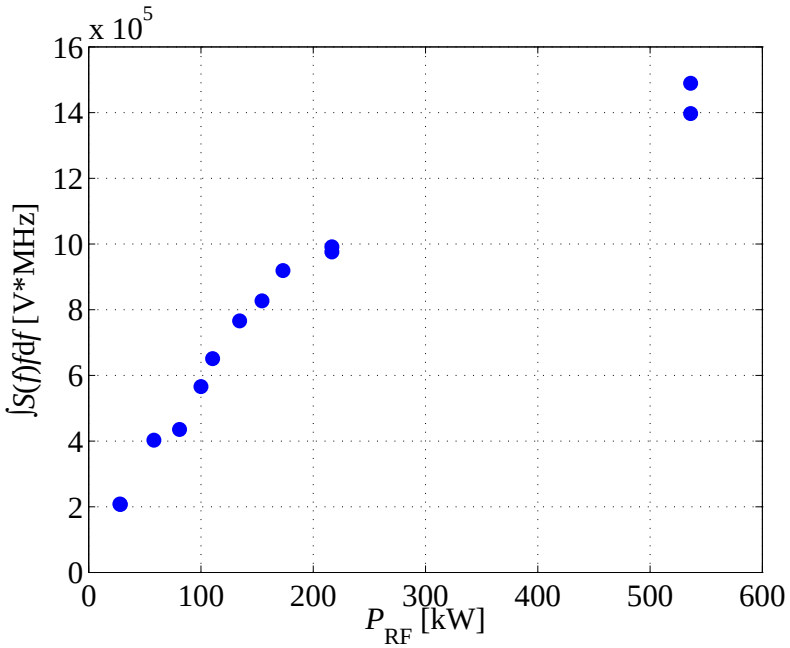

Figure 8.16: LHPI threshold power. Integrated spectrum energy $\int S(f) f \, \mathrm{d}f$ on the whole measured frequency band. The threshold injected power for the LHPI to arise is $P_{\mathrm{th}} \simeq 50$ kW. TCV shots in decreasing P_{RF} order: #38705 to 38708, #41880, 79, 78, 85, 77, 88, 89, 86 and 87.

where $S(f)$ is the amplitude at frequency f. As expected for the LHPI, the spectrum energy on the whole frequency range $200 - 2000$ MHz increases non-linearly with increasing P_{RF}, as indicated by figure 8.16. The LHPI threshold power is clearly below $P_{\mathrm{RF}} = 100$ kW, typically around $P_{\mathrm{RF}} \simeq 50$ kW. Since both the O-X and the X-B mode conversions have efficiencies below 100%, the actual value of the LHPI threshold power is lower than the injected P_{RF}, i.e. $P_{\mathrm{th}} \lesssim 50$ kW, in good agreement with the typical threshold power values $P_{\mathrm{th}} \lesssim 30 - 40$ kW estimated from the experimental profiles in subsection 8.4.1. Additional measurements at further lower pump wave power would be necessary for more precise determination of the LHPI threshold power.

LHPI energy cascading

The broadening of the LHPI spectrum towards larger frequencies is accompanied by a saturation and a decrease of the signal amplitude at lower frequencies, as indicated in figure 8.17. The cascading of the energy from the low-frequency bands to the high frequency bands as the pump wave power is increased is revealed when the spectrum energy (8.4.1) is evaluated for successive frequency bands, as in figure 8.18. Clearly, the energy in the band $600 - 800$ MHz reaches a maximum for $P_{\mathrm{RF}} \simeq 130$ kW, and then starts to decrease. The next frequency bands exhibit the same trend, but

saturates at increasing pump wave power for increasing frequency. The energy of the two highest frequency bands increases dramatically above $P_{\mathrm{RF}} \simeq 150$ kW, at the expense of the lower bands. This cascading effect is a clear signature that a nonlinear coupling of multiple waves with constantly increasing frequencies is at play.

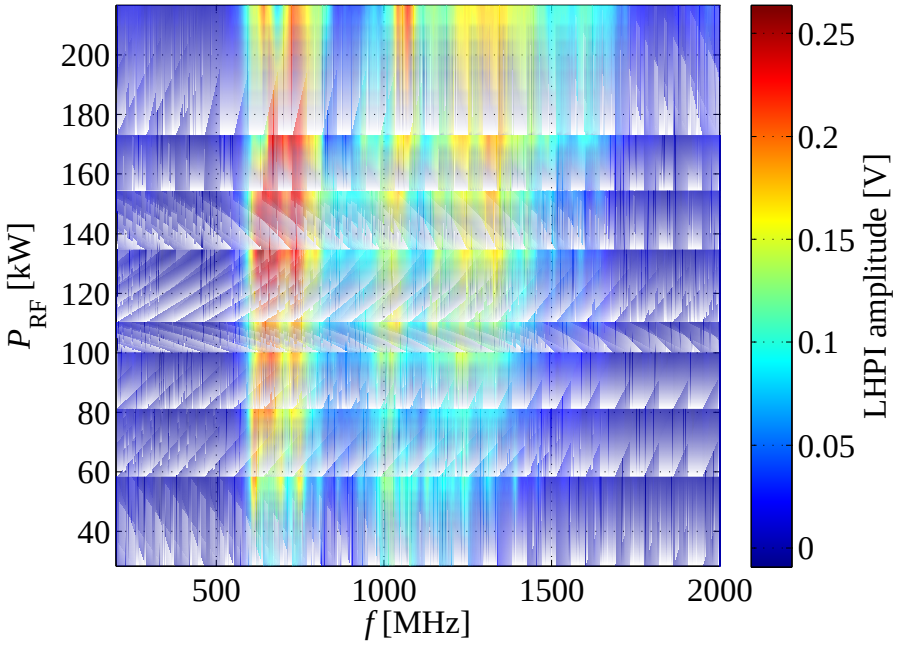

Figure 8.17: LHPI spectrum broadening. LHPI spectrum versus frequency and injected O2 power P_{RF}. With increasing pump wave power, the measured LHPI spectrum broadens towards higher frequencies while the low frequency amplitude saturates. TCV shots in decreasing P_{RF} order: #38708, 41880, 79, 78, 85, 77, 88, 89 and 86.

Summary

An O2 power scan is performed in order to estimate the LHPI threshold power when the mode conversion region is located in the region of steep edge density gradient, yielding a value in the expected range ($P_{\mathrm{RF}} \simeq 20$ kW) but lower than the threshold calculated from the experimental profiles. A broadening of the LHPI spectrum towards higher frequencies is observed with increasing pump wave power. The generation of these higher-frequency decay waves occurs at the expense of the lower band energy, a cascading effect typical of these non-linear wave interactions [102].

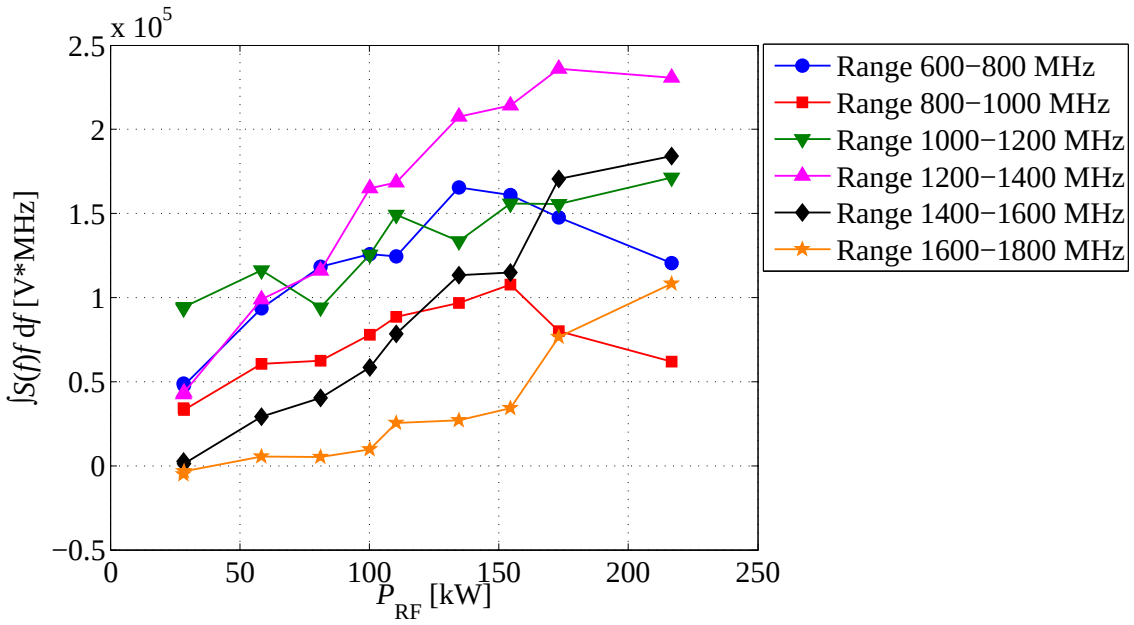

Figure 8.18: LHPI energy cascading. Integrated spectrum energy $\int S(f)f \, \mathrm{d}f$ in successive frequency bands versus the injected O2 power P_{RF}. The energy content at low frequency (bands up to 1400 MHz) saturates at high O2 injected power. Further increasing the pump wave power, the low frequency bands amplitude decreases in favor of higher frequency waves (bands above 1400 MHz). The higher is the frequency band, the higher is the P_{RF} power of saturation. TCV shots in decreasing P_{RF} order: #38708, 41880, 79, 78, 85, 77, 88, 89 86 and 87.

8.5 Conclusions and outlooks

A lower-hybrid parametric instability is expected to arise during the X-B mode conversion at the UHR in EBH experiments. It may be damaging for the wave-plasma coupling efficiency since it induces power losses by partial reflexion of the pump wave and generation of LH waves. The LHPI is subject to a pump wave threshold power, mainly regulated by the density gradient at the mode conversion region (MCR). As a consequence, three effects are in competition for an efficient wave-plasma coupling via O-X-B mode conversion: at high density gradient, the O-X transmission is good, the LHPI threshold power is high but the tunneling losses at the X-B mode conversion may be large. The net effect is thus not trivial and it is of high importance to study the LHPI as a function of the plasma conditions and of the O-X-B efficiency.

A new loop-antenna (called LHPI-antenna) for the detection of electromagnetic waves in the range $0.2 - 2$ GHz was designed, built and installed on TCV. Initial experiments were performed and low frequency waves were detected in the expected LH frequency range. The waves are present only when the conditions for an efficient

O-X-B mode conversion are gathered. Hence, the generation of these waves can be safely attributed to a LHPI.

Fast monitoring of the LHPI spectrum allowed to us show for the first time the correlation of the amplitude of the detected waves with the local LHPI threshold power at the mode conversion region estimated from the experimental profiles data. Conditions for both low and high LHPI threshold powers (i.e. flat and steep density gradients) were achieved in the same plasma discharge (at different times). The most efficient O-X-B coupling (low EC stray power) is observed in the steep density gradient case. A steep density gradient at the MCR has thus a net beneficial effect on the overall O-X-B mode conversion efficiency.

The LHPI threshold power is determined experimentally with an EBH power scan, yielding $P_{\mathrm{th}} \lesssim 50$ kW in good agreement with the calculated value from the experimental profiles data. At high pump wave power, a broadening of the LHPI spectrum towards higher frequencies is observed. The LHPI energy cascade from the low frequency LH bands to higher frequency bands, expected in high power EBH experiments, is demonstrated for the first time in the TCV measurements.

Some further effort is also required to interpret the many peaks observed in the LHPI spectrum at high EBH power.

In the future, EBH experiments at very low power will allow a better determination of the experimental LHPI threshold power. A check measurement of the LHPI-antenna frequency response is still planned in order to diagnose possible cut-off frequencies of the system. Finally, the exploration of the high frequency part of the LHPI spectrum (i.e. the pump wave sideband around 82.7 GHz $\pm f_{\mathrm{LH}}$) will help to identify the waves participating in the parametric instability, but requires a high frequency resolution ECE channels.

This part of the thesis work is in preparation for publication.

Chapter 9

Summary and conclusions

This thesis work focuses on the study of radio frequency (RF) power heating of low and high density plasmas in the *Tokamak à Configuration Variable* (TCV). TCV is a medium size fusion device offering the unique ability to vary the magnetic equilibrium over a wide range of plasma positions and shape parameters. TCV is equipped with a highly flexible ECH and ECCD system consisting of six gyrotrons of 500 kW nominal power, delivering second-harmonic electron cyclotron (EC) power of ordinary (O2) or extraordinary (X2) polarization. X2/O2 power is injected into the plasma though six independently steerable launchers from TCV's low-field side. In addition, three third-harmonic (X3) 500 kW gyrotrons can inject RF power vertically along the EC resonance from one steerable launcher from the top of TCV vacuum vessel.

At high density, standard electron cyclotron heating (ECH) and current drive (ECCD) are precluded by the appearance of a cutoff layer screening the access to the EC resonance at the plasma center. As a consequence, X2 ECH is possible over typically less than 15% of TCV's operational domain in density. O2 waves can access the resonance at twice the X2 cutoff but absorption is poor. X3 extends the domain of TCV ECH-heated plasmas up to typically 45% of the Greenwald empirical density limit, and so provides heating in particular in high-confinement (H-mode) plasmas whose density is controlled by an edge-localized mode (ELM) activity. At higher densities, the plasma can be heated by electron Bernstein waves (EBW) branch in which an electrostatic wave propagates beyond the plasma cutoff with no upper density limit. In TCV, this mode is excited by O-X-B double mode conversion of O2 power injected. This mode conversion process is most efficient at an optimum incident angle from the LFS. The conditions for an efficient mode conversion (i.e. a steep density gradient at the O2 plasma cutoff) are met at the

edge of ELM-free H-mode plasmas, a high confinement regime characterized by the appearance of a pedestal in the electron temperature and density profiles.

The existence of an optimum injection angle for the O-X-B mode conversion in TCV was examined by scanning the O2 power injection angles in the range of that obtained from an analytical solution to the mode-conversion equation. A clear minimum in the measured level of stray EC power was observed, confirming that an efficient O-X-B mode conversion is indeed present. The experimental angle is in excellent agreement with those calculated by the AMR code solving the full wave equations in a 1D plasma slab using the experimental equilibrium and plasma profile data. The numerical simulations confirm that the width of the mode conversion angular window is sensitive to the pedestal density gradient, whereas the optimum injection direction strongly depends on the plasma vertical position relative to the antenna injecting the O2 power.

The location of the RF power deposition was determined by analyzing the plasma response to modulated ECH (MECH) using the break-in-slope (BIS) method based on an estimation of the instantaneous change in the time derivative of the plasma kinetic energy at the RF power switch-on/off times. For the first time, the unique ability of the BIS analysis to retrieve an estimated power deposition profile is successfully used to track time-varying X2 power deposition location when either the toroidal magnetic field or the plasma position relative to the antenna is swept during the plasma discharge.

In a modulated EBH experiment, BIS analysis of local soft X-ray emission profiles was used to detect the power absorption well inside the O2 cutoff of a strongly sawtoothing H-mode plasma, in excellent agreement with a harmonic response identification (HRIM) analysis of the same data. This represents the first demonstration of resonant EBW absorption in an overdense plasma of a standard aspect-ratio tokamak. All experimental RF power deposition locations are in agreement within 10% of the normalized radius coordinate ρ_{vol} with the results of the C3PO and AMR ray-tracing codes for the propagation of ECWs and the EBWs, respectively. Both codes are coupled to the LUKE Fokker-Planck solver code. The implementation in the AMR code of TCV RF power launchers geometry and the coupling of AMR to LUKE for the TCV environment were part of this thesis, in close collaboration with J. Urban (IPP, Prague) and J. Decker (CEA, Cadarache).

In TCV, the diamagnetic loop (DML) diagnostic has been extensively used since 2002 to determine the global RF power absorption efficiency by oscillation analysis of the toroidal plasma flux response to modulated ECH. It was shown that the

plasma perpendicular kinetic energy is linked to the sum of the plasma toroidal flux with a combination of Shafranov integrals. In this thesis, a careful re-analysis of previously published X3 absorption experiments [43, 98] showed that a strong perturbation of the analysis due to modulations of the toroidal plasma flux from sawtooth activity was neglected.

To investigate this question, a verification of the model derivation and new X2 MECH experiments was performed. The experimental frequency transfer functions of the perpendicular kinetic energy, in response to X2 and X3 MECH, indicate that the plasma behaves like a damped oscillator forced by the modulated ECH, with a resonance at the sawtooth frequency. Since modeling of the plasma response to MECH does not account for the sawtooth oscillation, this procedure yields erroneous estimates of the power absorption coefficient that may be artificially increased by the sawtooth perturbation. This effect is, unsurprisingly, especially strong when the RF power modulation frequency is close to the sawtooth frequency. In particular, an asymmetric improvement of the X3 power absorption in X2 pre-heated plasmas with respect to the sign of the X2 ECCD was reported from previous TCV experiments. This effect remained unexplained, in spite of extensive Fokker-Planck simulations to investigate the effect of the fast electrons. From this thesis work, this asymmetry can be now unequivocally attributed to the strong sawtooth activity destabilized in the case of central X2 co-ECCD and locking in phase and frequency to the X3 RF power modulation.

In non-sawtoothing plasmas, the perturbation on the amplitude of the experimental transfer function is considerably reduced and a 100% X2 power absorption efficiency is obtained, in agreement with numerical modeling. However, this result must be dealt with with caution since the transfer function phase behavior indicates that a periodic relaxation of the plasma perpendicular kinetic energy is still at play. Finally, in the case of modulated EBH, the plasma toroidal flux response is dominated by the oscillation of the Shafranov integrals which were previously neglected in the analysis. Further experiments will be required to determine whether this effect results from the small modulated EBCD fraction predicted by the Fokker-Planck simulations or a modulation of the diverted equilibrium (X2 and X3 MECH experiments are instead performed in limited plasmas). In conclusion, these observation argue against the routine use of the DML diagnostic for the estimation of ECH absorption coefficients in modulation experiments, unless the kinetic energy response model is successfully modified to account for the sawtooth perturbation.

A systematic study of the electron Bernstein wave current drive (EBCD) perfor-

mances in TCV is carried out using the AMR-LUKE codes. The poloidal position of the EBW injection is scanned. For each configuration in the scan, the optimal injection angles for the O-X-B mode conversion are determined, the EBW ray-tracing performed and the quasi-linear wave-plasma interaction calculated. The variation of the EBCD efficiency when varying the radial location of absorption is predominantly due to trapped-particles effects.

With injection far above the plasma midplane, the EBW undergoes a strong upshift of its parallel refractive index $N_\parallel$ and the strongly Doppler-shifted resonant absorption takes place at the plasma edge where the Ohkawa effect is in competition with the Fisch-Boozer effect. As a result, the current drive efficiency is low.

When injected at the plasma midplane, the EBW reaches the plasma center but oscillations of the wave parallel refractive index around $N_\parallel = 0$ induce driven currents of opposite sign, thus reducing the *net* EBCD efficiency. The maximum EBCD effect is observed for an intermediate power-injection-geometry, yielding mid-radius absorption where the Ohkawa effect is reduced and a high normalized current drive efficiency $\xi_{\mathrm{CD}} = 0.45$ is achieved. However, the absolute driven current remains small ($\lesssim 1\%$ of the Ohmic current for 500 kW of injected RF power) due to the unfavorable temperature to density ratio in these H-mode plasmas. Experimentally, such small EBCD currents cannot be safely distinguished from variations of the Ohmic current due to a modification of the plasma resistivity by EBH.

In the framework of this thesis, a new loop-antenna for the detection of electromagnetic waves in the $0.2 - 2$ GHz frequency range was designed, built and installed on TCV. This antenna is designed for the study of the lower-hybrid (LH) waves generated by a parametric instability (PI) expected to arise during the X-B mode conversion at the upper-hybrid resonance in EBH experiments. This LHPI may cause substantial power losses, decreasing the global EBH efficiency. In initial experiments, low frequency waves were detected in the expected LH frequency range. The waves are present only when the conditions for an efficient O-X-B mode conversion are fulfilled so the generation of these waves can be attributed to a LHPI. Fast monitoring of the LHPI spectrum showed, for the first time, the correlation of the amplitude of the detected waves with the local LHPI threshold power at the mode conversion region, estimated from the experimental profiles data. Conditions for both low and high LHPI threshold powers (i.e. flat and steep density gradients, respectively) were achieved in the same plasma. The most efficient O-X-B coupling (low EC stray power) is observed in the second case. A steep density gradient at the mode conversion region was thus found to have a net beneficial effect on the overall

O-X-B mode conversion efficiency.
The LHPI threshold power is determined to be $\lesssim 50$ kW based on an EBW power scan, which is in good agreement with the value calculated using the experimental plasma parameter profiles. At high pump wave power, a broadening of the LHPI spectrum towards higher frequencies is observed. The LHPI energy cascade from the low frequency LH bands to higher frequency bands, expected in high power EBH experiments, is demonstrated for the first time in TCV.

Appendix A

Coordinate systems, sign conventions and EC power injection angles

A.1 TCV coordinate systems and sign conventions

A.1.1 Cylindrical coordinates

TCV cylindrical coordinate system is defined by the right-handed orthogonal triplet (R, φ, Z) where the Z-axis is aligned with TCV revolution axis, see figure A.1:

- R is the major radius coordinate, positive towards the outside of TCV, with $R = 0$ on TCV vertical revolution axis.
- φ is the toroidal angle coordinate, positive **counter-clockwise** seen from the top, with $\varphi = 0$ between TCV sector 1 and sector 16.
- Z is the vertical coordinate, positive upward, with $Z = 0$ on the equatorial plane of TCV.

Historically, the positive φ toroidal direction in TCV was chosen to coincide with the counter-clockwise numbering of the 16 sectors, starting on the west side of TCV.

A.1.2 Toroidal coordinates

TCV toroidal coordinate system is defined by the right-handed orthogonal triplet (r, θ, φ), see figure A.1(b)

- r is the minor radius coordinate, positive towards the outside of the plasma, with $r = 0$ on the plasma magnetic axis whose position is given by $(R_{\text{axis}}, Z_{\text{axis}})$ in cylindrical coordinates.

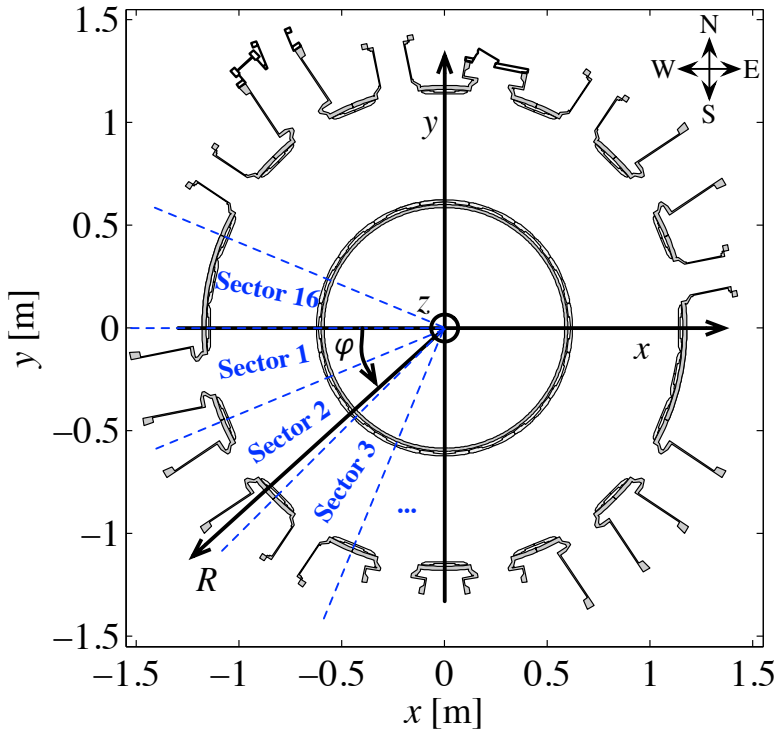

(a) Toroidal view (from the top) of TCV cartesian and cylindrical coordinate systems (x, y, z) and (R, φ, Z).

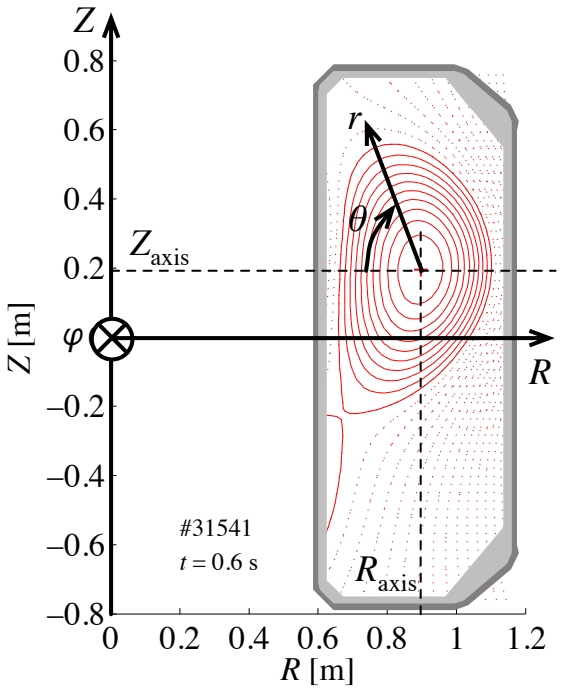

(b) Poloidal view of TCV toroidal and cylindrical coordinate systems (r, θ, φ) and (R, φ, Z).

Figure A.1: TCV coordinate systems.

- θ is the poloidal angle coordinate, positive clockwise seen with TCV vertical axis on the left, with $\theta = 0$ on the high-field side midplane.
- φ is the toroidal angle coordinate, positive **counter-clockwise** seen from the top, with $\varphi = 0$ between TCV sector 1 and sector 16.

The toroidal coordinate angle φ is the same for both TCV cylindrical and toroidal coordinate systems.

A.1.3 Cartesian coordinates

TCV cartesian coordinate system is defined by the right-handed orthogonal triplet (x, y, z) where the z-axis is aligned with TCV revolution axis and (x, y) is the TCV equatorial plane, see figure A.1(a):

- The x axis points towards the outside of TCV between sectors 8 and 9 (approximately towards the east), with $x = 0$ on TCV vertical axis.
- The y axis points towards the outside of TCV between sectors 12 and 13 (approximately towards the north), with $y = 0$ on TCV vertical axis.
- The z axis is positive upward, with $z = 0$ on the equatorial plane of TCV.

N.B. When dealing with magnetic diagnostics, one often choose the x and y axes pointing between sectors 16-1 and 4-5, i.e. toward the west and the south directions, respectively, for a better consistency with the choice of $\varphi = 0$.

A.1.4 Magnetic field, plasma current and poloidal flux

Since φ is positive in the **counter-clockwise** direction, TCV toroidal magnetic field B_φ and plasma current I_p are defined to be

- **positive** (or "reverse" in TCV vocabulary) when directed counter-clockwise (trigonometric direction) seen from the top.
- **negative** (or "forward" in TCV vocabulary) when directed clockwise (anti-trigonometric direction) seen from the top.

This implies that a positive plasma current creates a positive B_θ magnetic field component which, in turn, creates a positive contribution to the poloidal flux

$$\psi_\mathrm{p} = \int \mathbf{B}_\theta \cdot \mathrm{d}\mathbf{A} \tag{A.1.1}$$

on the HFS of the plasma magnetic axis. On the LFS of the plasma magnetic axis, both B_θ and the resulting poloidal flux contribution are negative. The integration surface d$\mathbf{A}$ is directed in the positive Z direction [103]. In other words:

- For positive currents, ψ_p grows from TCV vertical axis towards the magnetic axis of the plasma, is maximum on the magnetic axis and then decreases towards the LFS.

- For negative currents, ψ_p decreases from TCV vertical axis towards the magnetic axis of the plasma, is minimum on the magnetic axis and then increases towards the LFS.

To get proper signs for the radial and vertical magnetic field components, we thus have to chose the following relative signs:

$$B_R = -\frac{1}{R}\frac{\partial\psi}{\partial Z} \tag{A.1.2}$$

$$B_Z = +\frac{1}{R}\frac{\partial\psi}{\partial R} \tag{A.1.3}$$

where

$$\psi = \frac{1}{2\pi}\psi_\mathrm{p} \tag{A.1.4}$$

is the poloidal magnetic flux function. These equations can as well be written

$$\mathbf{B} = B_\varphi\hat{\boldsymbol{\varphi}} + \frac{1}{R}\nabla\psi\times\hat{\boldsymbol{\varphi}} \tag{A.1.5}$$

with $\hat{\boldsymbol{\varphi}}$ the unit vector in the positive φ direction.

A.2 AMR coordinate systems and sign conventions

The AMR code uses the same coordinate systems and conventions as for TCV, defined in the section above.

A.3 LUKE coordinate systems and sign conventions

In the LUKE code, the toroidal angle coordinate is positive in the **clockwise** direction. The cylindrical and toroidal coordinate systems are thus defined by the right-handed orthogonal triplets (R, Z, φ) and (r, φ, θ), respectively.

A.4 EC power injection angles

A.4.1 Launcher angles

The six launchers of TCV X2/O2 ECH system are cylindrical, with their revolution axes lying on a major radius of TCV torus. The last mirror of the launchers has two degrees of freedom, as indicated on figure 2.6:

- The so-called **toroidal launcher angle** ϕ_{L}: The whole antenna can rotate of an angle $-180^\circ < \phi_{\mathrm{L}} < +180^\circ$ around its axis, with $\phi_{\mathrm{L}} > 0$ clockwise when looking towards the plasma.

- The so-called **poloidal launcher angle** θ_{L}: The last mirror can be tilted and θ_{L} is defined as the angle between the beam center wave vector and the launcher axis. By definition, θ_{L} is always positive with $7^\circ < \theta_{\mathrm{L}} < 55^\circ$.

When $\phi_{\mathrm{L}} = 0^\circ$ or $\pm 180^\circ$, the beam is injected in the poloidal plane containing the launcher axis, with no toroidal component. When $\phi_{\mathrm{L}} > 0$, the beam is injected in the negative φ (clockwise) direction, and vice versa.

A.4.2 Effective injection angles

Both launcher angles contain toroidal and poloidal direction informations. They can thus be combined to get an effective geometry with independent poloidal and toroidal injection angles $(\theta_{\mathrm{inj}}, \phi_{\mathrm{inj}})$, see figure A.2:

- The poloidal angle θ_{inj} is the angle between the wave vector and the horizontal plane containing the launcher axis. It is defined positive upward.

- The toroidal angle ϕ_{inj} is the angle between the launcher axis and the wave vector projection on the horizontal plane containing the launcher axis. It is defined positive towards the right when viewing at the plasma from the LFS.

In function of the launcher angles, the injection angles write:

$$\theta_{\mathrm{inj}} = -\arcsin\left(\frac{f}{a}\right) = -\arcsin\left(\frac{c}{a}\frac{f}{c}\right) = -\arcsin\left(\sin(\theta_{\mathrm{L}})\cos(\phi_{\mathrm{L}})\right), \tag{A.4.1}$$

$$\phi_{\mathrm{inj}} = -\arctan\left(\frac{d}{b}\right) = -\arctan\left(\frac{c}{b}\frac{d}{c}\right) = -\arctan\left(\tan(\theta_{\mathrm{L}})\sin(\phi_{\mathrm{L}})\right). \tag{A.4.2}$$

Since $\theta_{\mathrm{L}} > 0$, $\sin(\theta_{\mathrm{L}}) > 0$ and $\tan(\theta_{\mathrm{L}}) > 0$ always. This leads to

- $\theta_{\mathrm{inj}} > 0$ for $-180^\circ < \phi_{\mathrm{L}} < -90^\circ$ and $+90^\circ < \phi_{\mathrm{L}} < +180^\circ$,

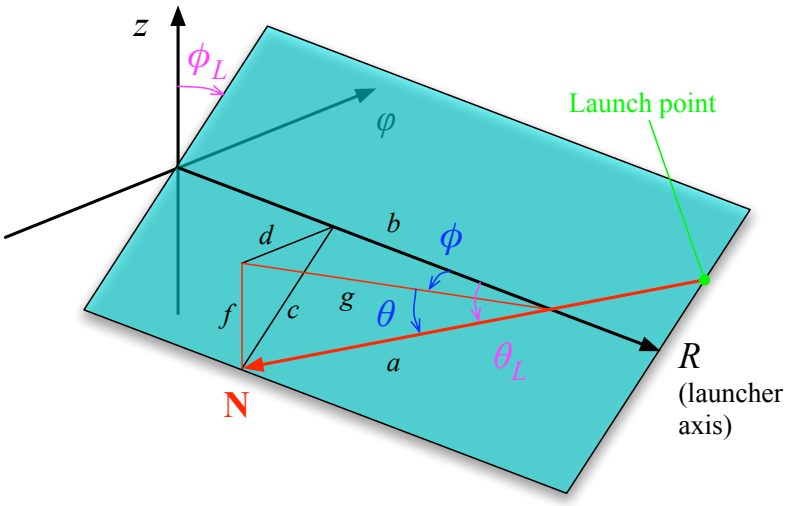

Figure A.2: Injection angles. Effective poloidal and toroidal injection angles $(\theta_{\rm inj}, \phi_{\rm inj})$ versus the poloidal and toroidal launcher angles $(\theta_{\rm L}, \phi_{\rm L})$. The semi-transparent blue plane is defined by the launcher axis (lying along TCV major radius R) and the normalized wave vector $\mathbf{N}$. The φ-axis indicates the local toroidal direction. $\theta_{\rm L}$ is the angle between the launcher axis and the wave vector. $\phi_{\rm L}$ is the angle between the vertical z axis and the blue plane. $\theta_{\rm inj}$ is the angle between the horizontal plane containing the launcher axis and the wave vector. $\phi_{\rm inj}$ is the angle between the launcher axis and the wave vector projection on the horizontal plane containing the launcher axis. We also define the following quantities: a is the length of $\mathbf{N}$ after it crosses the launcher axis, b and c are the projections of a on R and on the (φ, z) plane respectively, g is the projection of a on the horizontal plane, d and f are respectively the horizontal and vertical projections of c.

- $\phi_{\rm inj} > 0$ for $\phi_{\rm L} < 0$.

The inverse formulas are:

$$\theta_{\rm L} = \arccos\left(\frac{b}{a}\right) = \arccos\left(\frac{b}{g}\frac{g}{a}\right) = \arccos\left(\cos(\phi_{\rm inj})\cos(\theta_{\rm inj})\right), \tag{A.4.3}$$

$$\begin{aligned}\phi_{\rm L} &= \arctan\left(\frac{d}{f}\right) = \arctan\left(\frac{d}{g}\frac{g}{f}\right) \\ &= -180^\circ \times \text{sign}\left(\phi_{\rm inj}\right) \text{H}(\theta_{\rm inj}) + \arctan\left(\frac{\sin(\phi_{\rm inj})}{\tan(\theta_{\rm inj})}\right).\end{aligned} \tag{A.4.4}$$

Since $-90^\circ < \theta_{\rm inj}, \phi_{\rm inj} < +90^\circ$, it is clear that $0^\circ < \theta_{\rm L} < +90^\circ$ as needed (the negative solution is neglected). The first term in the expression for $\phi_{\rm L}$ (with $\text{H}(\theta_{\rm inj})$ the Heaviside function) was added to ensure $-180^\circ < \phi_{\rm L} < +180^\circ$ and $\phi_{\rm L} > 0$ when $\phi_{\rm inj} < 0$.

A.4.3 AMR injection angles

In the AMR code, the injection geometry is defined in terms of effective injection angles $(\theta_{\rm AMR}, \phi_{\rm AMR})$ **defined around the major radius axis R' going through**

the beam waist center, instead of the major radius axis R of the launcher, as indicated in figure A.3. The axis R and R' are located at toroidal angles φ and φ', respectively. The effective toroidal angle of injection ϕ_{inj} must then be corrected by $\Delta\varphi = \varphi' - \varphi$. On the other hand, the poloidal angle of injection θ_{inj} does not need any correction: the angle between the horizontal plane containing the launcher axis and the wave vector is equal to the angle between any horizontal plane and the wave vector, as indicated in figure A.4.

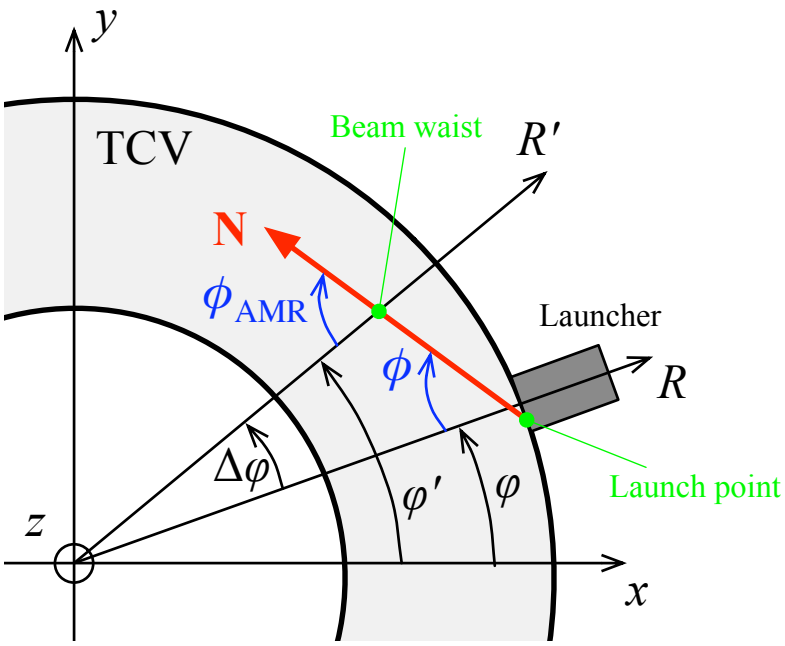

Figure A.3: AMR toroidal injection angle. Toroidal top view of the normalized wave vector **N** and its angles ϕ_{inj} with respect to the launcher axis (R, φ) and ϕ_{AMR} with respect to the radial axis (R', φ') going through the beam waist center. Clearly, $\phi_{\text{AMR}} = \phi_{\text{inj}} + \Delta\varphi$.

Finally, the actual AMR injection expressed in terms of the launcher angles are:

$$\theta_{\text{AMR}} = -\arcsin\left(\sin(\theta_{\text{L}})\cos(\phi_{\text{L}})\right), \tag{A.4.5}$$

$$\phi_{\text{AMR}} = -\arctan\left(\tan(\theta_{\text{L}})\sin(\phi_{\text{L}})\right) + \Delta\varphi. \tag{A.4.6}$$

A.4.4 Refractive index

According to the angles definition in the previous section, the refractive index components in the AMR toroidal coordinate system (R, φ, Z) are given by:

$$N_R = -\cos(\theta_{\text{AMR}})\cos(\phi_{\text{AMR}}), \tag{A.4.7}$$

$$N_\varphi = \cos(\theta_{\text{AMR}})\sin(\phi_{\text{AMR}}), \tag{A.4.8}$$

$$N_Z = \sin(\theta_{\text{AMR}}). \tag{A.4.9}$$

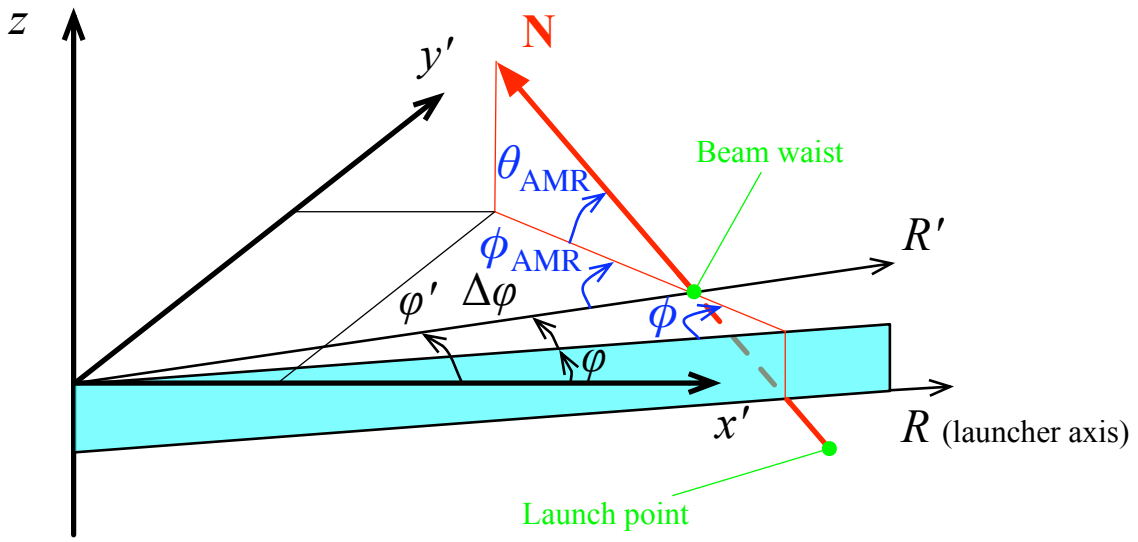

Figure A.4: AMR poloidal injection angle. 3D view of the normalized wave vector **N**. In the situation represented here, the launcher angles are typically $(\theta_L, \phi_L) = (-120°, +20°)$ and the launch point is slightly below the launcher axis R, whereas the radial axis R' going through the beam waist center is above the launcher axis. The blue plane is the vertical plane containing R and shows the toroidal angle difference $\Delta\varphi$ between R and R'.

And in the AMR cartesian coordinate system (x, y, z):

$$\begin{aligned} N_x &= N_R \cos(\varphi') - N_\varphi \sin(\varphi') \\ &= \cos(\theta_{\text{AMR}})[-\cos(\phi_{\text{AMR}})\cos(\varphi') - \sin(\phi_{\text{AMR}})\sin(\varphi')] \\ &= -\cos(\theta_{\text{AMR}})\cos(\phi_{\text{AMR}} - \varphi'), \end{aligned} \tag{A.4.10}$$

$$\begin{aligned} N_y &= N_R \sin(\varphi') + N_\varphi \cos(\varphi') \\ &= \cos(\theta_{\text{AMR}})[-\cos(\phi_{\text{AMR}})\sin(\varphi') + \sin(\phi_{\text{AMR}})\cos(\varphi')] \\ &= \cos(\theta_{\text{AMR}})\sin(\phi_{\text{AMR}} - \varphi'), \end{aligned} \tag{A.4.11}$$

$$N_z = N_Z = \sin(\theta_{\text{AMR}}) \tag{A.4.12}$$

where φ' is the toroidal position of the beam waist center.

Appendix B

MHD integral relations

B.1 Introduction

The plasma contribution to the toroidal magnetic flux is defined as

$$\Phi_{\mathrm{pl}} \equiv \int_S (B_\varphi - B_{\varphi \mathrm{v}})\ \mathrm{d}S. \tag{B.1.1}$$

where B_φ is the total toroidal magnetic field, $B_{\varphi \mathrm{v}}$ is the vacuum toroidal magnetic field produced by the tokamak toroidal coils system and S is a poloidal surface encompassing the plasma cross-section. The plasma toroidal flux is generated by the plasma poloidal currents which in turn are mainly due to the cyclotron gyration of the charged particles (always diamagnetic) and the particles trajectory along the helicoidal field lines (always paramagnetic). These combined effects yield a net diamagnetic flux (respectively a net paramagnetic flux), i.e. a net decrease (respectively a net increase) of the toroidal field, when $\beta_{\mathrm{p}} > 1$ (respectively $\beta_{\mathrm{p}} < 1$). This can be seen from the simplified balance equation (B.5.19).

In TCV, Φ_{pl} is measured by the diamagnetic loop (DML) diagnostic [91]. The DML system consists in a single-turn coil closely wound on the external surface of the vacuum vessel and a set of compensation coils in the poloidal plane to compensate for the vacuum field contribution and the many parasitic toroidal and poloidal fluxes.

The goal of this appendix is to show how the toroidal plasma flux Φ_{pl} is linked to the total plasma kinetic energy

$$W_{\mathrm{kin}} \equiv \frac{3}{2} \int_V \frac{2p_\perp + p_\parallel}{3}\ \mathrm{d}V = W_{\mathrm{kin}\perp} + W_{\mathrm{kin}\parallel}. \tag{B.1.2}$$

In the sequel of this text, the conventions described in table B.1 are used.

Subscript	Signification
pl / v	plasma / vacuum quantity
p / t (or φ)	poloidal / toroidal component
$\parallel$ / $\perp$	component parallel / perpendicular to the total magnetic field $\mathbf{B}$

Table B.1: Subscript conventions used in this appendix.

B.2 Force balance equation

B.2.1 Ideal MHD model

The ideal single-fluid MHD model for a fully ionized plasma of two particles species, electron and singly charged ions ($\alpha = \mathrm{e}, \mathrm{i}$), confined in a magnetic field is given by:

$$\frac{\partial \rho_\mathrm{m}}{\partial t} + \nabla \cdot (\rho_\mathrm{m} \mathbf{u}) = 0 \qquad \text{mass evolution} \qquad \text{(B.2.1)}$$

$$\rho_\mathrm{m} \frac{\mathrm{d}\mathbf{u}}{\mathrm{d}t} = \rho_\mathrm{m} \frac{\partial \mathbf{u}}{\partial t} + \rho_\mathrm{m} \mathbf{u} \cdot \nabla \mathbf{u} = \mathbf{J} \times \mathbf{B} - \nabla \cdot \mathbb{P} \qquad \text{momentum evolution} \qquad \text{(B.2.2)}$$

$$\frac{\mathrm{d}}{\mathrm{d}t} \left(\frac{p}{\rho_\mathrm{m}^\gamma} \right) = 0 \qquad \text{energy evolution} \qquad \text{(B.2.3)}$$

$$\mathbf{E} + \mathbf{u} \times \mathbf{B} = 0 \qquad \text{Ohm's law} \qquad \text{(B.2.4)}$$

$$\nabla \times \mathbf{E} = -\frac{\partial \mathbf{B}}{\partial t} \qquad \text{Faraday's law} \qquad \text{(B.2.5)}$$

$$\nabla \times \mathbf{B} = \mu_0 \mathbf{J} \qquad \text{Ampère's law} \qquad \text{(B.2.6)}$$

$$\nabla \cdot \mathbf{B} = 0 \qquad \text{(B.2.7)}$$

$$\nabla \cdot \mathbf{E} = 0 \qquad \text{Gauss's law} \qquad \text{(B.2.8)}$$

where $\rho_\mathrm{m} \equiv m_\mathrm{i} n$ is the mass density with the particle density $n \equiv n_\mathrm{i} = n_\mathrm{e}$, $\mathbf{u} \equiv \mathbf{u}_\mathrm{i}$ is the fluid velocity, $\mathbf{J} \equiv en\,(\mathbf{u}_\mathrm{i} - \mathbf{u}_\mathrm{e})$ is the current density, $\mathbb{P} = \mathbb{P}_\mathrm{i} + \mathbb{P}_\mathrm{e}$ is the total pressure tensor, $p \equiv \mathrm{Tr}(\mathbb{P})/3$ is the scalar pressure and $\gamma = 5/3$ is the ratio of specific heats. The ideal MHD model is derived from the full Maxwell's equations coupled with a kinetic model of the plasma described by a Boltzmann equation for each species distribution function f_α. Equation (B.2.4) is the Ohm's law for a perfect conductor. Equations (B.2.6) and (B.2.8) are the low-frequency Ampère's and Gauss's laws, respectively, where both the displacement current and the net charge are neglected.

B.2.2 Momentum conservation

Inserting the current density from Ampère's law in the momentum time evolution equation and adding the mass time evolution equation multiplied by the fluid velocity $\mathbf{u}$ gives

$$\frac{\partial \rho_\mathrm{m}\mathbf{u}}{\partial t} + \mathbf{u}\left[\nabla\cdot(\rho_\mathrm{m}\mathbf{u})\right] + \rho_\mathrm{m}\mathbf{u}\cdot\nabla\mathbf{u} = \frac{1}{\mu_0}(\nabla\times\mathbf{B})\times\mathbf{B} - \nabla\cdot\mathbb{P}. \tag{B.2.9}$$

The second and third terms can be written as

$$\mathbf{u}\left[\nabla\cdot(\rho_\mathrm{m}\mathbf{u})\right] + \rho_\mathrm{m}\mathbf{u}\cdot\nabla\mathbf{u} = u_j\nabla_i(\rho_\mathrm{m}u_i) + \rho_\mathrm{m}u_i\nabla_i u_j = \nabla_i\left(\rho_\mathrm{m}u_iu_j\right) = \nabla\cdot\left(\rho_\mathrm{m}\mathbf{u}\mathbf{u}\right). \tag{B.2.10}$$

Using the following vector identity

$$\nabla(\mathbf{A}\cdot\mathbf{B}) = \mathbf{A}\times(\nabla\times\mathbf{B}) + \mathbf{B}\times(\nabla\times\mathbf{A}) + (\mathbf{A}\cdot\nabla)\mathbf{B} + (\mathbf{B}\cdot\nabla)\mathbf{A} \tag{B.2.11}$$

with $\mathbf{A} = \mathbf{B}$, the magnetic field term can be written as:

$$\begin{aligned}(\nabla\times\mathbf{B})\times\mathbf{B} &= (\mathbf{B}\cdot\nabla)\mathbf{B} - \frac{1}{2}\nabla(B^2)\\ &= B_i\nabla_i B_j + \underbrace{(\nabla_i B_i)}_{\nabla\cdot\mathbf{B}=0}B_j - \frac{1}{2}\nabla_i(B_jB_j)\\ &= \nabla_i\left(B_iB_j - \frac{1}{2}\delta_{ij}B_kB_k\right) = \nabla\cdot\left(\mathbf{B}\mathbf{B} - \frac{1}{2}B^2\mathbb{I}\right).\end{aligned} \tag{B.2.12}$$

The momentum conservation equation then becomes

$$\frac{\partial \rho_\mathrm{m}\mathbf{u}}{\partial t} + \nabla\cdot\left[\rho_\mathrm{m}\mathbf{u}\mathbf{u} + \frac{B^2}{2\mu_0}\mathbb{I} - \frac{\mathbf{B}\mathbf{B}}{\mu_0} + \mathbb{P}\right] = \frac{\partial \rho_\mathrm{m}\mathbf{u}}{\partial t} + \nabla\cdot\mathbb{T} = 0 \tag{B.2.13}$$

with the stress tensor defined as

$$\mathbb{T} \equiv \rho_\mathrm{m}\mathbf{u}\mathbf{u} + \frac{B^2}{2\mu_0}\mathbb{I} - \frac{\mathbf{B}\mathbf{B}}{\mu_0} + \mathbb{P}. \tag{B.2.14}$$

It is convenient to split the pressure tensor $\mathbb{P}$ into its components perpendicular and parallel to the total magnetic field $\mathbf{B}$:

$$\mathbb{P} = p_\perp\mathbb{I} + \left(p_\parallel - p_\perp\right)\frac{\mathbf{B}\mathbf{B}}{B^2}. \tag{B.2.15}$$

The stress tensor (B.2.14) takes then the following form:

$$\boxed{\mathbb{T} = \rho_\mathrm{m}\mathbf{u}\mathbf{u} + \left(p_\perp + \frac{B^2}{2\mu_0}\right)\mathbb{I} - \sigma\frac{\mathbf{B}\mathbf{B}}{\mu_0} \qquad \text{with} \qquad \sigma \equiv 1 - \frac{\mu_0\left(p_\parallel - p_\perp\right)}{B^2}} \tag{B.2.16}$$

where σ is the pressure anisotropy parameter. Choosing a local orthonormal coordinate system with the third direction along $\mathbf{B}$, the stress tensor (B.2.16) can be expressed as

$$\mathbb{T} = \rho_\mathrm{m}\mathbf{u}\mathbf{u} + \begin{pmatrix} p_\perp + \frac{B^2}{2\mu_0} & 0 & 0 \\ 0 & p_\perp + \frac{B^2}{2\mu_0} & 0 \\ 0 & 0 & p_\parallel - \frac{B^2}{2\mu_0} \end{pmatrix}. \tag{B.2.17}$$

The magnetic field exerts an additional pressure in the transverse direction and a tension in the longitudinal direction. The stress tensor $\mathbb{T}$ is symmetric, i.e.

$$T_{ij} = T_{ji}. \tag{B.2.18}$$

B.2.3 Equilibrium

Describing an stationary equilibrium, we have $\frac{\partial}{\partial t} = 0$, and the force balance equation can be written as

$$\boxed{\nabla \cdot \mathbb{T} = 0.} \tag{B.2.19}$$

B.3 Integral relations

B.3.1 General case: anisotropic flowing plasma

In this section, the derivation of the MHD integral relations followed in [104] is extended to the case of an anisotropic plasma with non-zero fluid velocity, recovering the results of [105] obtained by similar extension of the derivation in [92]. In the latter references, the derivation starts from the virial theorem from [106] and the force balance equation (B.2.19) averaged on a volume enclosing the plasma. Here, the more general approach of [104] is followed by first projecting the force balance equation (B.2.19) on an arbitrary vector field $\mathbf{Q}$ before the volume integration:

$$\begin{aligned} 0 = \int_V (\nabla \cdot \mathbb{T}) \cdot \mathbf{Q} \, \mathrm{d}V &= \int_V \left[\nabla \cdot (\mathbb{T} \cdot \mathbf{Q}) - \mathbb{T} : \nabla \mathbf{Q})\right] \, \mathrm{d}V \\ &= \oint_{\partial V} \hat{\mathbf{n}} \cdot \mathbb{T} \cdot \mathbf{Q} \, \mathrm{d}A - \int_V \mathbb{T} : \nabla \mathbf{Q} \, \mathrm{d}V \end{aligned} \tag{B.3.1}$$

where the second equality comes from

$$\nabla \cdot (\mathbb{T} \cdot \mathbf{Q}) = \nabla_i (T_{ij} Q_j) = (\nabla_i T_{ij}) Q_j + \underbrace{T_{ij}}_{=T_{ji}} (\nabla_i Q_j) = (\nabla \cdot \mathbb{T}) \cdot \mathbf{Q} + \mathbb{T} : \nabla \mathbf{Q} \tag{B.3.2}$$

and the third equality stands from the divergence theorem with $\hat{\mathbf{n}}$ the unit vector normal to ∂V. Here, the colon symbol represents the matrix multiplication with

sum on both indices:

$$\mathbf{A} : \mathbf{B} = \sum_{i,j} A_{ij} B_{ji}. \tag{B.3.3}$$

In the integral relation (B.3.1), V is a toroidal volume of arbitrary poloidal cross section encompassing the plasma (i.e. $V_{\mathrm{pl}} \subseteq V$), ∂V is the boundary of V, $\mathrm{d}V$ is the volume element on V and $\mathrm{d}A$ is the surface element on ∂V. The poloidal cross section of the volume V has a surface S and a boundary ∂S. The plasma has also an arbitrary poloidal cross section, see figure B.1. Equation (B.3.1) leads the following integral relation:

$$\int_V \mathbb{T} : \nabla \mathbf{Q} \, \mathrm{d}V = \oint_{\partial V} \hat{\mathbf{n}} \cdot \mathbb{T} \cdot \mathbf{Q} \, \mathrm{d}A. \tag{B.3.4}$$

Inserting the stress tensor (B.2.16) in the integral relation (B.3.4), and assuming that $\mathbb{P} = 0$ (i.e. $p_\perp = p_\parallel = 0$ and $\sigma = 1$) and $\mathbf{u} = 0$ outside the plasma and thus on ∂V yields:

$$\int_V \left[\rho_{\mathrm{m}} \mathbf{u}\mathbf{u} + \left(p_\perp + \frac{B^2}{2\mu_0} \right) \mathbb{I} - \sigma \frac{\mathbf{B}\mathbf{B}}{\mu_0} \right] : \nabla \mathbf{Q} \, \mathrm{d}V = \oint_{\partial V} \hat{\mathbf{n}} \cdot \left[\frac{B^2}{2\mu_0} \mathbb{I} - \frac{\mathbf{B}\mathbf{B}}{\mu_0} \right] \cdot \mathbf{Q} \, \mathrm{d}A. \tag{B.3.5}$$

Standard manipulations on the terms of equation (B.3.5) are performed as follows:

- The term $\mathbb{I} : \nabla \mathbf{Q}$ becomes

$$\mathbb{I} : \nabla \mathbf{Q} = \delta_{ij} \nabla_i Q_j = \nabla_j Q_j = \nabla \cdot \mathbf{Q}. \tag{B.3.6}$$

- The terms of the form $\hat{\mathbf{n}} : \mathbf{v}\mathbf{v} : \mathbf{Q}$ with $\mathbf{v}$ a vector field become

$$\hat{\mathbf{n}} : \mathbf{v}\mathbf{v} : \mathbf{Q} = \hat{n}_i v_i v_j Q_j = (\hat{\mathbf{n}} \cdot \mathbf{v})(\mathbf{v} \cdot \mathbf{Q}). \tag{B.3.7}$$

The equation (B.3.5) thus writes

$$\begin{aligned} &\int_V \left[\rho_{\mathrm{m}} \mathbf{u}\mathbf{u} : \nabla \mathbf{Q} + \left(p_\perp + \frac{B^2}{2\mu_0} \right) \nabla \cdot \mathbf{Q} - \frac{\sigma}{\mu_0} \mathbf{B}\mathbf{B} : \nabla \mathbf{Q} \right] \mathrm{d}V \\ &= \oint_{\partial V} \left[\frac{B^2}{2\mu_0} \hat{\mathbf{n}} \cdot \mathbf{Q} - \frac{1}{\mu_0} (\hat{\mathbf{n}} \cdot \mathbf{B})(\mathbf{B} \cdot \mathbf{Q}) \right] \mathrm{d}A. \end{aligned} \tag{B.3.8}$$

This last relation is valid independent of axisymmetry. If $\mathbf{Q}$ is an axisymmetric vector field without toroidal component, one has

$$\mathbf{Q} = Q_R \hat{\mathbf{R}} + Q_Z \hat{\mathbf{Z}} \quad \text{and} \quad \frac{\partial Q_R}{\partial \varphi} = \frac{\partial Q_Z}{\partial \varphi} = 0, \tag{B.3.9}$$

where, $\hat{\mathbf{R}}$ and $\hat{\mathbf{Z}}$ are the unitary vectors in the major radius and vertical directions, respectively. Equation (B.3.8) thus conveniently splits into toroidal and poloidal components. In particular, the total magnetic field $\mathbf{B}$ writes

$$\mathbf{B} = \mathbf{B}_\varphi + \mathbf{B}_{\mathrm{p}} \quad \text{with} \quad \mathbf{B}_\varphi = \frac{F}{R} \hat{\boldsymbol{\varphi}} \quad \text{and} \quad \mathbf{B}_{\mathrm{p}} = \frac{\nabla \psi}{R} \times \hat{\boldsymbol{\varphi}} \tag{B.3.10}$$

where $\hat{\boldsymbol{\varphi}}$ is the unitary vector in the toroidal direction and ψ is the poloidal stream function closely related to the poloidal flux ψ_p. The flux surface quantity F is defined as

$$F \equiv RB_\varphi = F_\mathrm{v} + F_\mathrm{pl} \tag{B.3.11}$$

where F is divided into its plasma and vacuum contributions

$$F_\mathrm{pl} \equiv RB_{\varphi\mathrm{pl}} \quad \text{and} \quad F_\mathrm{v} \equiv RB_{\varphi\mathrm{v}} = \text{const} \tag{B.3.12}$$

with $B_{\varphi\mathrm{pl}}$ and $B_{\varphi\mathrm{v}}$ the plasma and vacuum contributions to the toroidal magnetic field, respectively. The fluid velocity can as well be split into its toroidal and poloidal components:

$$\mathbf{u} = u_\varphi \hat{\boldsymbol{\varphi}} + \mathbf{u}_\mathrm{p}. \tag{B.3.13}$$

Noting that $\partial_\varphi \hat{\mathbf{R}} = \hat{\boldsymbol{\varphi}}$, the non-trivial dyadic product $\nabla\mathbf{Q}$ in equation (B.3.8) explicitly writes

$$\begin{aligned}
\nabla\mathbf{Q} &= \left[\hat{\mathbf{R}}\partial_R + \hat{\boldsymbol{\varphi}}\frac{1}{R}\partial_\varphi + \hat{\mathbf{Z}}\partial_Z\right]\left[Q_R\hat{\mathbf{R}} + Q_Z\hat{\mathbf{Z}}\right] \\
&= \partial_R(Q_R)\hat{\mathbf{R}}\hat{\mathbf{R}} + \partial_R(Q_Z)\hat{\mathbf{R}}\hat{\mathbf{Z}} + \frac{1}{R}\underbrace{\partial_\varphi(Q_R)}_{=0}\hat{\boldsymbol{\varphi}}\hat{\mathbf{R}} \\
&\quad + \frac{1}{R}Q_R\hat{\boldsymbol{\varphi}}\underbrace{\partial_\varphi(\hat{\mathbf{R}})}_{\hat{\boldsymbol{\varphi}}} + \frac{1}{R}\underbrace{\partial_\varphi(Q_Z)}_{=0}\hat{\boldsymbol{\varphi}}\hat{\mathbf{Z}} + \partial_Z(Q_R)\hat{\mathbf{Z}}\hat{\mathbf{R}} + \partial_Z(Q_Z)\hat{\mathbf{Z}}\hat{\mathbf{Z}} \\
&= \begin{pmatrix} \partial_R Q_R & 0 & \partial_R Q_Z \\ 0 & Q_R/R & 0 \\ \partial_Z Q_R & 0 & \partial_Z Q_Z \end{pmatrix}.
\end{aligned} \tag{B.3.14}$$

Thus the first and third terms in the left-hand side of equation (B.3.8) read

$$\mathbf{uu} : \nabla\mathbf{Q} = \left[\mathbf{u}_\mathrm{p}\mathbf{u}_\mathrm{p} + \underbrace{\mathbf{u}_\mathrm{p}\mathbf{u}_\varphi}_{=0} + \underbrace{\mathbf{u}_\varphi\mathbf{u}_\mathrm{p}}_{=0} + \mathbf{u}_\varphi\mathbf{u}_\varphi\right] : \nabla\mathbf{Q} = \mathbf{u}_\mathrm{p}\mathbf{u}_\mathrm{p} : \nabla\mathbf{Q} + u_\varphi^2\frac{Q_R}{R} \tag{B.3.15}$$

and

$$\mathbf{BB} : \nabla\mathbf{Q} = \left[\mathbf{B}_\mathrm{p}\mathbf{B}_\mathrm{p} + \underbrace{\mathbf{B}_\mathrm{p}\mathbf{B}_\varphi}_{=0} + \underbrace{\mathbf{B}_\varphi\mathbf{B}_\mathrm{p}}_{=0} + \mathbf{B}_\varphi\mathbf{B}_\varphi\right] : \nabla\mathbf{Q} = \mathbf{B}_\mathrm{p}\mathbf{B}_\mathrm{p} : \nabla\mathbf{Q} + B_\varphi^2\frac{Q_R}{R}. \tag{B.3.16}$$

Assuming $B_{\varphi\mathrm{pl}} = 0$ outside the plasma volume and in particular on ∂V, one uses $\mathbf{B} = \mathbf{B}_\mathrm{p} + \mathbf{B}_{\varphi\mathrm{v}}$ on the right-hand side of equation (B.3.8) and $\mathbf{B}_\varphi \cdot \mathbf{Q} = 0$ due to the poloidal nature of $\mathbf{Q}$. Moreover, the following relation is derived using the

divergence theorem:

$$\oint_{\partial V} \frac{B_{\varphi \mathrm{v}}^2}{2\mu_0} \hat{\mathbf{n}} \cdot \mathbf{Q} \, \mathrm{d}A = \int_V \nabla \cdot \left(\frac{B_{\varphi \mathrm{v}}^2}{2\mu_0} \mathbf{Q} \right) \, \mathrm{d}V = \int_V \left[\frac{B_{\varphi \mathrm{v}}^2}{2\mu_0} \nabla \cdot \mathbf{Q} + \mathbf{Q} \cdot \nabla \left(\frac{B_{\varphi \mathrm{v}}^2}{2\mu_0} \right) \right] \, \mathrm{d}V. \tag{B.3.17}$$

Reminding that the vacuum field is $B_{\varphi \mathrm{v}} \propto R^{-1}$, one writes

$$\nabla B_{\varphi \mathrm{v}}^2 = -2 \frac{B_{\varphi \mathrm{v}}^2}{R} \hat{\mathbf{R}} \tag{B.3.18}$$

and

$$\oint_{\partial V} \frac{B_{\varphi \mathrm{v}}^2}{2\mu_0} \hat{\mathbf{n}} \cdot \mathbf{Q} \, \mathrm{d}A = \int_V \frac{B_{\varphi \mathrm{v}}^2}{2\mu_0} \left[\nabla \cdot \mathbf{Q} - 2 \frac{Q_R}{R} \right] \, \mathrm{d}V. \tag{B.3.19}$$

Finally, inserting (B.3.15) and (B.3.16) in equation (B.3.8) and subtracting equation (B.3.19) gives:

$$\boxed{\begin{aligned} &\int_V \left[\left(\rho_{\mathrm{m}} \mathbf{u}_{\mathrm{p}} \mathbf{u}_{\mathrm{p}} - \frac{\sigma}{\mu_0} \mathbf{B}_{\mathrm{p}} \mathbf{B}_{\mathrm{p}} \right) : \nabla \mathbf{Q} + \rho_{\mathrm{m}} u_\varphi^2 \frac{Q_R}{R} + \left(p_\perp + \frac{B_{\mathrm{p}}^2}{2\mu_0} \right) \nabla \cdot \mathbf{Q} \right. \\ &\qquad \left. + \frac{B_\varphi^2 \left(p_\parallel - p_\perp \right)}{B^2} \frac{Q_R}{R} + \frac{B_\varphi^2 - B_{\varphi \mathrm{v}}^2}{2\mu_0} \left(\nabla \cdot \mathbf{Q} - 2 \frac{Q_R}{R} \right) \right] \, \mathrm{d}V \\ &= \frac{1}{\mu_0} \oint_{\partial V} \left[\frac{B_{\mathrm{p}}^2}{2} \hat{\mathbf{n}} \cdot \mathbf{Q} - (\hat{\mathbf{n}} \cdot \mathbf{B}_{\mathrm{p}})(\mathbf{B}_{\mathrm{p}} \cdot \mathbf{Q}) \right] \, \mathrm{d}A \end{aligned}} \tag{B.3.20}$$

with $\sigma \equiv 1 - \frac{\mu_0 \left(p_\parallel - p_\perp \right)}{B^2}$. The relation (B.3.20) is the force balance equation for an ideal MHD equilibrium $\nabla \cdot \mathbb{T} = 0$ with fluid flow and pressure anisotropy, in integral form and projected on an arbitrary poloidal axisymmetric vector field $\mathbf{Q}$. Equations (7) and (8) in [105] are together equivalent to equation (B.3.20).

The relation (B.3.20) can be linked to different yet equivalent expressions found in the literature. Introducing the unit vector $\hat{\boldsymbol{\tau}}$ tangential to ∂V (and thus perpendicular to the normal vector $\hat{\mathbf{n}}$), $\mathbf{Q}$ and $\mathbf{B}_{\mathrm{p}}$ separate into normal and tangential components:

$$\mathbf{Q} = (\mathbf{Q} \cdot \hat{\mathbf{n}}) \hat{\mathbf{n}} + (\mathbf{Q} \cdot \hat{\boldsymbol{\tau}}) \hat{\boldsymbol{\tau}} = Q_n \hat{\mathbf{n}} + Q_\tau \hat{\boldsymbol{\tau}}, \tag{B.3.21}$$

$$\mathbf{B}_{\mathrm{p}} = (\mathbf{B}_{\mathrm{p}} \cdot \hat{\mathbf{n}}) \hat{\mathbf{n}} + (\mathbf{B}_{\mathrm{p}} \cdot \hat{\boldsymbol{\tau}}) \hat{\boldsymbol{\tau}} = B_n \hat{\mathbf{n}} + B_\tau \hat{\boldsymbol{\tau}}. \tag{B.3.22}$$

The right-hand side of equation (B.3.20) then writes

$$\frac{B_{\mathrm{p}}^2}{2} \hat{\mathbf{n}} \cdot \mathbf{Q} - (\hat{\mathbf{n}} \cdot \mathbf{B}_{\mathrm{p}})(\mathbf{B}_{\mathrm{p}} \cdot \mathbf{Q}) = \frac{B_\tau^2 - B_n^2}{2} Q_n - B_n B_\tau Q_\tau. \tag{B.3.23}$$

The relation (B.3.20) is thus identical to equation (1) in [94]. Similarly, noting that

$$\nabla \cdot \mathbf{Q} - 2 \frac{Q_R}{R} = -\frac{Q_R}{R} + \frac{\partial Q_R}{\partial R} + \frac{\partial Q_Z}{\partial Z} = R^2 \nabla \cdot (R^{-2} \mathbf{Q}), \tag{B.3.24}$$

it is clear that equation (B.3.20) is identical to equation (32) in [107].

B.3.2 Special case: Static isotropic plasma

In the limit of static isotropic plasma, $\mathbf{u} = 0$ and the pressure tensor reduces to the scalar pressure: $p_\perp = p_\parallel = p$. Thus $\sigma = 1$ and equation (B.3.20) reduces to

$$\boxed{\begin{aligned}\int_V \Bigg[-\frac{1}{\mu_0}\mathbf{B}_\mathrm{p}\mathbf{B}_\mathrm{p} : \nabla\mathbf{Q} + \left(p + \frac{B_\mathrm{p}^2}{2\mu_0}\right)\nabla\cdot\mathbf{Q} \\ + \frac{B_\varphi^2 - B_{\varphi\mathrm{v}}^2}{2\mu_0}\left(\nabla\cdot\mathbf{Q} - 2\frac{Q_R}{R}\right)\Bigg]\ \mathrm{d}V \\ = \frac{1}{\mu_0}\oint_{\partial V}\left[\frac{B_\mathrm{p}^2}{2}\hat{\mathbf{n}}\cdot\mathbf{Q} - (\hat{\mathbf{n}}\cdot\mathbf{B}_\mathrm{p})(\mathbf{B}_\mathrm{p}\cdot\mathbf{Q})\right]\ \mathrm{d}A,\end{aligned}} \tag{B.3.25}$$

which is exactly identical to equation (15) in [104] taking $\mathbf{B}_2 = 0$ and assuming $p = 0$ on the boundary ∂V (called S in the reference [104]). The result is also quoted as equation (31) in [107]. Finally, equations (11) and (12) in [92] (i.e. the static isotropic version of equations (7) and (8) in [105]) are together equivalent to equation (B.3.25).

B.4 Specific moments

B.4.1 Moments in integral form

The freedom in the choice of the axisymmetric poloidal vector field $\mathbf{Q}$ is now exploited to derive a set of linearly independent moments of the integral force balance equation. The choices of $\mathbf{Q}$ made in [107] are followed here (see equations (36)-(38) in this reference). In the next subsection, these choices are linked to other choices found in the literature. The following notation is defined for the surface integral on the right-hand side of equation (B.3.20):

$$\boxed{\begin{aligned}I(\mathbf{Q}) &\equiv \frac{1}{\mu_0}\oint_{\partial V}\left[\frac{B_\mathrm{p}^2}{2}\hat{\mathbf{n}}\cdot\mathbf{Q} - (\hat{\mathbf{n}}\cdot\mathbf{B}_\mathrm{p})(\mathbf{B}_\mathrm{p}\cdot\mathbf{Q})\right]\ \mathrm{d}A \\ &= \frac{1}{\mu_0}\oint_{\partial V}\left[\frac{B_\tau^2 - B_n^2}{2}Q_n - B_n B_\tau Q_\tau\right]\ \mathrm{d}A.\end{aligned}} \tag{B.4.1}$$

Moment #1

Choosing $\mathbf{Q}_1 \equiv R\hat{\mathbf{R}} + Z\hat{\mathbf{Z}}$, one gets

$$\nabla\cdot\mathbf{Q}_1 = \frac{1}{R}\frac{\partial(RQ_{1R})}{\partial R} + \frac{\partial Q_{1Z}}{\partial Z} = 3 \tag{B.4.2}$$

and

$$\nabla \mathbf{Q}_1 = \begin{pmatrix} \partial_R Q_{1R} & 0 & \partial_R Q_{1Z} \\ 0 & Q_{1R}/R & 0 \\ \partial_Z Q_{1R} & 0 & \partial_Z Q_{1Z} \end{pmatrix} = \begin{pmatrix} 1 & 0 & 0 \\ 0 & 1 & 0 \\ 0 & 0 & 1 \end{pmatrix}. \tag{B.4.3}$$

Inserting in equation (B.3.20) leads

$$\begin{aligned} I_1 &= \int_V \left[\rho_\mathrm{m} u_\mathrm{p}^2 - \frac{\sigma}{\mu_0} B_\mathrm{p}^2 + \rho_\mathrm{m} u_\varphi^2 + 3\left(p_\perp + \frac{B_\mathrm{p}^2}{2\mu_0}\right) + \frac{B_\varphi^2 \left(p_\parallel - p_\perp\right)}{B^2} + \frac{B_\varphi^2 - B_{\varphi\mathrm{v}}^2}{2\mu_0} \right] \mathrm{d}V \\ &= \int_V \left[\rho_\mathrm{m} u^2 + \frac{B_\mathrm{p}^2}{2\mu_0} + 2p_\perp + p_\parallel + \frac{B_\varphi^2 - B_{\varphi\mathrm{v}}^2}{2\mu_0} \right] \mathrm{d}V \end{aligned} \tag{B.4.4}$$

where $I_1 \equiv I(\mathbf{Q}_1)$.

Generalized virial theorem:

Equation (B.4.4) is the generalized virial theorem [106] for plasmas with fluid flow and pressure anisotropy

$$\boxed{\begin{aligned} &\int_V \left[\rho_\mathrm{m} u^2 + \frac{B_\mathrm{p}^2}{2\mu_0} + 2p_\perp + p_\parallel + \frac{B_\varphi^2 - B_{\varphi\mathrm{v}}^2}{2\mu_0} \right] \mathrm{d}V \\ &= \frac{1}{\mu_0} \oint_{\partial V} \left[\frac{B_\mathrm{p}^2}{2} \hat{\mathbf{n}} \cdot \mathbf{r} - (\hat{\mathbf{n}} \cdot \mathbf{B}_\mathrm{p})(\mathbf{B}_\mathrm{p} \cdot \mathbf{r}) \right] \mathrm{d}A \end{aligned}} \tag{B.4.5}$$

where it is assumed that $p_\parallel = p_\perp = 0$ and $B_\varphi = B_{\varphi\mathrm{v}}$ on ∂V, and $\mathbf{r} \equiv R\hat{\mathbf{R}} + Z\hat{\mathbf{Z}}$ is the position vector in the poloidal plane.

Moment #2

Choosing $\mathbf{Q}_2 = \hat{\mathbf{R}}$, one gets

$$\nabla \cdot \mathbf{Q}_2 = \frac{1}{R}\frac{\partial (R Q_{2R})}{\partial R} + \frac{\partial Q_{2Z}}{\partial Z} = \frac{1}{R} \tag{B.4.6}$$

and

$$\nabla \mathbf{Q}_2 = \begin{pmatrix} \partial_R Q_{2R} & 0 & \partial_R Q_{2Z} \\ 0 & Q_{2R}/R & 0 \\ \partial_Z Q_{2R} & 0 & \partial_Z Q_{2Z} \end{pmatrix} = \begin{pmatrix} 0 & 0 & 0 \\ 0 & 1/R & 0 \\ 0 & 0 & 0 \end{pmatrix}. \tag{B.4.7}$$

Inserting in equation (B.3.20) and using the relation $\mathrm{d}V = 2\pi R \mathrm{d}S$ between the toroidal volume element $\mathrm{d}V$ and the surface element $\mathrm{d}S$ of the poloidal cross section

yields

$$\begin{aligned} I_2 &= \int_V \left[\frac{\rho_\mathrm{m} u_\varphi^2}{R} + \frac{1}{R}\left(p_\perp + \frac{B_\mathrm{p}^2}{2\mu_0} \right) + \frac{1}{R}\frac{B_\varphi^2 \left(p_\parallel - p_\perp \right)}{B^2} - \frac{1}{R}\left(\frac{B_\varphi^2 - B_{\varphi\mathrm{v}}^2}{2\mu_0} \right) \right] \mathrm{d}V \\ &= 2\pi \int_S \left[\rho_\mathrm{m} u_\varphi^2 + p_\parallel + \frac{B_\mathrm{p}^2}{2\mu_0} - \frac{B_\mathrm{p}^2 \left(p_\parallel - p_\perp \right)}{B^2} - \frac{B_\varphi^2 - B_{\varphi\mathrm{v}}^2}{2\mu_0} \right] \mathrm{d}S \end{aligned} \tag{B.4.8}$$

where $I_2 \equiv I(\mathbf{Q}_2)$. Note that in a tokamak plasma, the second-but-last term on the right-hand side of (B.4.8) associated to the pressure anisotropy can be neglected since [105]

$$\frac{B_\mathrm{p}^2 \left(p_\parallel - p_\perp \right)}{B^2} \ll \frac{B_\mathrm{p}^2}{2\mu_0} \qquad \text{near the plasma edge,} \tag{B.4.9}$$

$$\frac{B_\mathrm{p}^2 \left(p_\parallel - p_\perp \right)}{B^2} \ll p_\parallel \qquad \text{close to the plasma center.} \tag{B.4.10}$$

Moment #3

Choosing $\mathbf{Q}_3 = Z\hat{\mathbf{Z}}$, one gets

$$\nabla \cdot \mathbf{Q}_3 = \frac{1}{R}\frac{\partial (R Q_{3R})}{\partial R} + \frac{\partial Q_{3Z}}{\partial Z} = 1 \tag{B.4.11}$$

and

$$\nabla \mathbf{Q}_3 = \begin{pmatrix} \partial_R Q_{3R} & 0 & \partial_R Q_{3Z} \\ 0 & Q_{3R}/R & 0 \\ \partial_Z Q_{3R} & 0 & \partial_Z Q_{3Z} \end{pmatrix} = \begin{pmatrix} 0 & 0 & 0 \\ 0 & 0 & 0 \\ 0 & 0 & 1 \end{pmatrix}. \tag{B.4.12}$$

Inserting in equation (B.3.20) yields

$$\begin{aligned} I_3 &= \int_V \left[\rho_\mathrm{m} u_Z^2 - \frac{\sigma B_Z^2}{\mu_0} + p_\perp + \frac{B_\mathrm{p}^2}{2\mu_0} + \frac{B_\varphi^2 - B_{\varphi\mathrm{v}}^2}{2\mu_0} \right] \mathrm{d}V \\ &= \int_V \left[\rho_\mathrm{m} u_Z^2 - \frac{B_Z^2}{\mu_0} + \frac{B_Z^2 \left(p_\parallel - p_\perp \right)}{B^2} + p_\perp + \frac{B_\mathrm{p}^2}{2\mu_0} + \frac{B_\varphi^2 - B_{\varphi\mathrm{v}}^2}{2\mu_0} \right] \mathrm{d}V \end{aligned} \tag{B.4.13}$$

where $I_3 \equiv I(\mathbf{Q}_3)$.

Moment #4

For the sake of completeness, the integral for $\mathbf{Q}_4 = R\hat{\mathbf{R}}$ is also calculated but it will not be used further on since it is not linearly independent with respect to I_1 and I_3: $I_4 = I_1 - I_3$. One has

$$\nabla \cdot \mathbf{Q}_4 = \frac{1}{R}\frac{\partial (R Q_{4R})}{\partial R} + \frac{\partial Q_{4Z}}{\partial Z} = 2 \tag{B.4.14}$$

and

$$\nabla\mathbf{Q}_4 = \begin{pmatrix} \partial_R Q_{4R} & 0 & \partial_R Q_{4Z} \\ 0 & Q_{4R}/R & 0 \\ \partial_Z Q_{4R} & 0 & \partial_Z Q_{4Z} \end{pmatrix} = \begin{pmatrix} 1 & 0 & 0 \\ 0 & 1 & 0 \\ 0 & 0 & 0 \end{pmatrix}. \tag{B.4.15}$$

Inserting in equation (B.3.20) yields

$$\begin{aligned} I_4 &= \int_V \left[\rho_\mathrm{m} u_R^2 - \frac{\sigma B_R^2}{\mu_0} + \rho_\mathrm{m} u_\varphi^2 + 2\left(p_\perp + \frac{B_\mathrm{p}^2}{2\mu_0}\right) + \frac{B_\varphi^2\left(p_\parallel - p_\perp\right)}{B^2} \right] \mathrm{d}V \\ &= \int_V \left[\rho_\mathrm{m} u^2 - \rho_\mathrm{m} u_Z^2 + \frac{B_Z^2}{\mu_0} + p_\perp + p_\parallel - \frac{B_Z^2\left(p_\parallel - p_\perp\right)}{B^2} \right] \mathrm{d}V. \end{aligned} \tag{B.4.16}$$

where $I_4 \equiv I(\mathbf{Q}_4)$.

B.4.2 Link with Shafranov integrals

In the present work, we use the right-handed cylindrical coordinate system (R, φ, Z), where $R = 0$ on the system toroidal revolution axis and $Z = 0$ on the system mid-plane. This cylindrical coordinate system reduces to a cartesian coordinate system (R, Z) in the poloidal plane. In the reference [92], Shafranov uses a polar coordinate system (ρ, θ) in the poloidal plane (called (ρ, ω) in the reference). This polar coordinate system is centered on an arbitrarily chosen point (R', Z'), see figure B.1. The choice of the vertical position Z' has no influence on the Shafranov integrals. It appears explicitly only when one wants to express Shafranov integrals from polar coordinates to cartesian coordinates. In the sequel of this text, we chose $Z' = 0$. The arbitrary major radius R' is called R in reference [92].
As a choice for R', one can use

- the magnetic axis major radius R_axis;
- the machine major radius R_0;
- the center of the toroidal current density distribution as in [107]:

$$\left[R_\mathrm{c}^2, Z_\mathrm{c}\right] = \frac{1}{I_\varphi}\int_S \left[R^2, Z\right] j_\varphi \,\mathrm{d}S \quad \text{and} \quad I_\varphi = \int_S j_\varphi \,\mathrm{d}S; \tag{B.4.17}$$

- any major radius R_T averaged over the plasma configuration.

In this appendix, the general notation R' will be kept.
Shafranov defines the following surface integrals (equations (24) and (25) in [92]):

$$S_1 \equiv I(\rho\hat{\boldsymbol{\rho}}) \tag{B.4.18}$$

$$S_2 \equiv I(R'\hat{\mathbf{R}}) \tag{B.4.19}$$

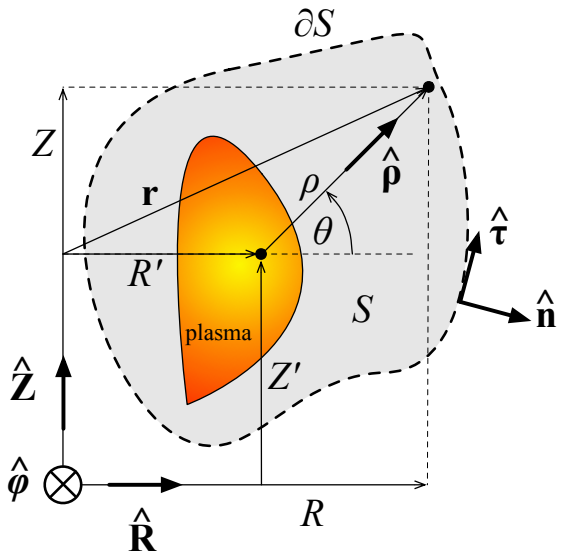

Figure B.1: Poloidal coordinate systems. Any position $\mathbf{r}$ in the poloidal plane can be described using either the cartesian coordinates (R, Z) or the polar coordinates (ρ, θ) centered on the arbitrary position (R', Z'). S is the poloidal cross-section of the axisymmetric volume V and ∂S is the boundary of S. The unitary vectors $\hat{\boldsymbol{\tau}}$ and $\hat{\mathbf{n}}$ are respectively tangential and normal to the surface δS.

where $I(\mathbf{Q})$ is defined in (B.4.1). Here, a capital S_i is used to emphasize that S_1 and S_2 are the unnormalized Shafranov integrals, unlike s_1 and s_2 in Shafranov's text. Noting that

$$\rho\hat{\boldsymbol{\rho}} = (R - R')\hat{\mathbf{R}} + (Z - Z')\hat{\mathbf{Z}} \tag{B.4.20}$$

where we chose $Z' = 0$. Shafranov's integrals are easily linked with the integrals defined in the previous subsection:

$$\boxed{\begin{aligned} S_1 &\equiv I(\rho\hat{\boldsymbol{\rho}}) = I\left((R - R')\hat{\mathbf{R}} + Z\hat{\mathbf{Z}}\right) = I_1 - R'I_2, && \text{(B.4.21)} \\ S_2 &\equiv I(R'\hat{\mathbf{R}}) = R'I(\hat{\mathbf{R}}) = R'I_2. && \text{(B.4.22)} \end{aligned}}$$

Normalized versions of integrals S_1 and S_2 are given as equations (9) and (10) in [105] and as equations (6) to (8) in [94] along with a definition of a normalized I_3. Both references use different normalization than Shafranov's in [92] (and use the symbol R_0 for the arbitrary polar coordinates center R'). Moreover, V is chosen to be the plasma volume in [94]. As a consequence, $\hat{\mathbf{n}} \cdot \mathbf{B}_\mathrm{p} = 0$ everywhere on the boundary surface ∂V. The $(\hat{\mathbf{n}} \cdot \mathbf{B}_\mathrm{p})(\mathbf{B}_\mathrm{p} \cdot \mathbf{Q})$ terms thus vanish in the Shafranov integrals. A summary of the different conventions met in the literature is given in table B.2.

Reference	Shafranov integrals			Normalization
Shafranov [92]	$s_1 \equiv i(\rho\hat{\boldsymbol{\rho}})$	$s_2 \equiv i(R'\hat{\mathbf{R}})$	-	$N_\mathrm{q} = \frac{4}{R'\mu_0 I_\varphi^2}$, $N_\mathrm{i} = \frac{N_\mathrm{q}}{2}$
Cooper and Wooton [105]	$s_1 \equiv i(\rho\hat{\boldsymbol{\rho}})$	$s_2 \equiv i(R'\hat{\mathbf{R}})$	-	$N_\mathrm{q} = \frac{2\mu_0}{V\langle B_\mathrm{p}^2\rangle}$, $N_\mathrm{i} = \frac{N_\mathrm{q}}{2}$
Lao et al. [94]	$S_1 \equiv i(\rho\hat{\boldsymbol{\rho}})$	$S_2 \equiv i(R'\hat{\mathbf{R}})$	$S_3 \equiv i(Z\hat{\mathbf{Z}})$	$N_\mathrm{q} = \frac{2\mu_0}{V\bar{B}_\mathrm{p}^2}$, $N_\mathrm{i} = N_\mathrm{q}$, $V = V_\mathrm{pl}$
LIUQE code	Same as in [94]			$N_\mathrm{q} = \frac{4}{R'\mu_0 I_\varphi^2}$, $N_\mathrm{i} = N_\mathrm{q}$, $V = V_\mathrm{pl}$, $R' = R_0 = 0.88$ m
Braams [107]	$s_1 \equiv i(R\hat{\mathbf{R}} + Z\hat{\mathbf{Z}})$	$s_2 \equiv i(\hat{\mathbf{R}})$	$s_3 \equiv i(R\hat{\mathbf{R}})$	$N_\mathrm{q} = \frac{4}{R'\mu_0 I_\varphi^2}$, $(N_\mathrm{i} = N_\mathrm{q})$, $R' = R_\mathrm{c}$
This work	$i_1 \equiv i(R\hat{\mathbf{R}} + Z\hat{\mathbf{Z}})$	$i_2 \equiv i(\hat{\mathbf{R}})$	$i_3 \equiv i(Z\hat{\mathbf{Z}})$	$N_\mathrm{q} = \frac{2\mu_0}{V\bar{B}_\mathrm{p}^2}$, $N_\mathrm{i} = N_\mathrm{q}$
This work	$s_1 \equiv i(\rho\hat{\boldsymbol{\rho}})$	$s_2 \equiv i(R'\hat{\mathbf{R}})$	-	$N_\mathrm{q} = \frac{2\mu_0}{V\bar{B}_\mathrm{p}^2}$, $N_\mathrm{i} = N_\mathrm{q}$

Table B.2: Shafranov integrals in the literature. $\bar{B}_\mathrm{p}$ and $\langle B_\mathrm{p}^2\rangle$ are the contour-averaged poloidal field and the flux-surface average square poloidal field defined in (B.4.42) and (B.4.23), respectively. R_c^2 is the average current density distribution center defined in (B.4.17). The TCV equilibrium reconstruction code LIUQE uses the same definitions as in reference [94], except for the normalization factor, which is evaluated in the limit of circular cross-section for both the plasma and the volume V. In LIUQE, the arbitrary center R' of the polar coordinate system is chosen to be TCV vacuum vessel major radius $R_0 = 0.88$ m. Finally, in the present work and in the LIUQE code, the plasma toroidal magnetic energy W_M is defined as in equation (B.4.27), whereas in references [92, 94, 104, 105] W_M is defined with an opposite sign.

$$\langle B_\mathrm{p}^2\rangle \equiv \frac{\oint_{\partial S} B_\mathrm{p}^2 \dfrac{\mathrm{d}\ell}{B_\mathrm{p}}}{\oint_{\partial S} \dfrac{\mathrm{d}\ell}{B_\mathrm{p}}}. \tag{B.4.23}$$

B.4.3 Moments in terms of plasma quantities

Plasma quantities

The following plasma quantities are defined:

$$W_{\mathrm{kin}\parallel} \equiv \frac{1}{2}\int_V p_\parallel \,\mathrm{d}V \quad \text{parallel kinetic energy} \tag{B.4.24}$$

$$W_{\mathrm{kin}\perp} \equiv \frac{1}{2}\int_V 2p_\perp \,\mathrm{d}V \quad \text{perpendicular kinetic energy} \tag{B.4.25}$$

$$W_{\mathrm{kin}} \equiv \frac{3}{2}\int_V \frac{2p_\perp + p_\parallel}{3}\,\mathrm{d}V = W_{\mathrm{kin}\perp} + W_{\mathrm{kin}\parallel} \quad \text{total kinetic energy} \tag{B.4.26}$$

$$W_{\mathrm{M}} \equiv \int_V \frac{B_\varphi^2 - B_{\varphi\mathrm{v}}^2}{2\mu_0}\,\mathrm{d}V \quad \text{plasma toroidal magnetic energy} \tag{B.4.27}$$

$$W_{\mathrm{L}} \equiv \int_V \frac{B_{\mathrm{p}}^2}{2\mu_0}\,\mathrm{d}V \quad \text{poloidal magnetic energy} \tag{B.4.28}$$

$$W_{\mathrm{rot}} \equiv \int_V \frac{1}{2}\rho_{\mathrm{m}} u^2 \,\mathrm{d}V = W_{\mathrm{rot}\varphi} + W_{\mathrm{rot,p}} \quad \text{fluid rotation energy} \tag{B.4.29}$$

The plasma toroidal magnetic energy W_{M} is defined with the opposite sign in [92,94, 104,105]. All quantities are independent of R'. Only the plasma volume V_{pl} (enclosed by the toroidal volume V) contributes to W_{kin}, W_{M} and W_{rot} since $p_\parallel = p_\perp = 0$, $B_\varphi^2 - B_{\varphi\mathrm{v}}^2 = 0$ and $\mathbf{u} = 0$ outside the plasma. In consequence, only W_{L} depends on the choice of the volume V. Similarly to [94, 105] (and to [92, 104] for the case of isotropic static plasmas), one defines a major radius R_T averaged on the plasma configuration:

$$R_T \equiv \frac{\displaystyle\int_S g 2\pi R \,\mathrm{d}S}{\displaystyle\int_S g 2\pi \,\mathrm{d}S} = \frac{\int_V g \,\mathrm{d}V}{I_2} \tag{B.4.30}$$

where the weighting factor g is

$$g = \rho_{\mathrm{m}} u_\varphi^2 + p_\parallel + \frac{B_{\mathrm{p}}^2}{2\mu_0} - \frac{B_{\mathrm{p}}^2\left(p_\parallel - p_\perp\right)}{B^2} - \frac{B_\varphi^2 - B_{\varphi\mathrm{v}}^2}{2\mu_0} \tag{B.4.31}$$

Moments

In terms of the plasma quantities, the equations (B.4.4), (B.4.8) and (B.4.13) write

$$I_1 = S_1 + S_2 = 2W_{\mathrm{rot}} + W_{\mathrm{L}} + 2W_{\mathrm{kin}\perp} + 2W_{\mathrm{kin}\parallel} + W_{\mathrm{M}}, \tag{B.4.32}$$

$$I_2 = \frac{S_2}{R'} = \frac{1}{R_T}\left[2W_{\mathrm{rot}\varphi} + 2W_{\mathrm{kin}\parallel} + W_{\mathrm{L}} - W_{\mathrm{M}} - \int_V \frac{B_{\mathrm{p}}^2\left(p_\parallel - p_\perp\right)}{B^2}\,\mathrm{d}V\right], \tag{B.4.33}$$

$$I_3 = 2W_{\mathrm{rot}Z} + W_{\mathrm{kin}\perp} + W_{\mathrm{L}} + W_{\mathrm{M}} + \int_V \left[-\frac{B_Z^2}{\mu_0} + \frac{B_Z^2\left(p_\parallel - p_\perp\right)}{B^2}\right]\mathrm{d}V. \tag{B.4.34}$$

B.4.4 Moments in terms of normalized plasma quantities

Normalized plasma quantities

Similarly to [94, 105] (and to [92, 104] for the case of isotropic static plasmas), the normalized dimensionless plasma quantities corresponding to $W_{\rm kin}$, $W_{\rm M}$, $W_{\rm L}$ and $W_{\rm rot}$ are introduced as follows

$$\beta_{\rm p\parallel} \equiv N_{\rm q}\int_V p_\parallel \,\mathrm{d}V = N_{\rm q} 2W_{\rm kin\parallel} \quad \text{normalized parallel pressure} \tag{B.4.35}$$

$$\beta_{\rm p\perp} \equiv N_{\rm q}\int_V p_\perp \,\mathrm{d}V = N_{\rm q} W_{\rm kin\perp} \quad \text{norm. perpendicular pressure} \tag{B.4.36}$$

$$\beta_{\rm p} \equiv \frac{2\beta_{\rm p\perp}+\beta_{\rm p\parallel}}{3} = N_{\rm q}\int_V \frac{2p_\perp+p_\parallel}{3}\,\mathrm{d}V = N_{\rm q}\frac{2}{3}W_{\rm kin} \tag{B.4.37}$$

$$\mu \equiv N_{\rm q}\int_V \frac{B_\varphi^2 - B_{\varphi\rm v}^2}{2\mu_0}\,\mathrm{d}V = N_{\rm q}W_{\rm M} \quad \text{plasma diamagnetism} \tag{B.4.38}$$

$$\ell \equiv N_{\rm q}\int_V \frac{B_{\rm p}^2}{2\mu_0}\,\mathrm{d}V = N_{\rm q}W_{\rm L} \quad \text{plasma inductance} \tag{B.4.39}$$

$$w \equiv N_{\rm q}\int_V \frac{1}{2}\rho_{\rm m}u^2\,\mathrm{d}V = N_{\rm q}W_{\rm rot} \quad \text{norm. rotation energy density} \tag{B.4.40}$$

where the normalization factor $N_{\rm q}$ for the plasma quantities is chosen to be

$$N_{\rm q} \equiv \frac{2\mu_0}{V\bar{B}_{\rm p}^2} \tag{B.4.41}$$

with the average poloidal field $\bar{B}_{\rm p}$ evaluated on the contour ∂S bounding the poloidal surface S:

$$\bar{B}_{\rm p} = \frac{\oint_{\partial S} B_{\rm p}\,\mathrm{d}s}{\oint_{\partial S}\mathrm{d}s}. \tag{B.4.42}$$

Different choices of $N_{\rm q}$ are met in the literature, see table B.2. All normalized quantities now depend on the choice of the volume V, but only the plasma volume contribute to $\beta_{\rm p}$, $\beta_{\rm p\perp}$, $\beta_{\rm p\parallel}$, μ and w since $\mathbb{P}=0$, $\mathbf{u}=0$ and $B_\varphi - B_{\varphi\rm v}=0$ outside the plasma. Conversely, both the plasma volume $V_{\rm pl}$ and the remaining volume $V\setminus V_{\rm pl}$ of V contribute to the inductance ℓ. The inductance ℓ can thus be split into its internal contribution ℓ_i and external contribution ℓ_e:

$$\ell \equiv \ell_i + \ell_e, \tag{B.4.43}$$

$$\ell_i \equiv \frac{2\mu_0}{V\bar{B}_{\rm p}^2}\int_{V_{\rm pl}}\frac{B_{\rm p}^2}{2\mu_0}\,\mathrm{d}V, \tag{B.4.44}$$

$$\ell_e \equiv \frac{2\mu_0}{V\bar{B}_{\rm p}^2}\int_{V\setminus V_{\rm pl}}\frac{B_{\rm p}^2}{2\mu_0}\,\mathrm{d}V. \tag{B.4.45}$$

Normalized integrals

The surface integrals defined by (B.4.1) are normalized using a normalization factor $N_\mathrm{i} = N_\mathrm{q}$:

$$i(\mathbf{Q}) \equiv N_\mathrm{i} I(\mathbf{Q}) = N_\mathrm{i} \frac{1}{\mu_0} \oint_{\partial V} \left[\frac{B_\mathrm{p}^2}{2} \hat{\mathbf{n}} \cdot \mathbf{Q} - (\hat{\mathbf{n}} \cdot \mathbf{B}_\mathrm{p})(\mathbf{B}_\mathrm{p} \cdot \mathbf{Q}) \right] \mathrm{d}A. \tag{B.4.46}$$

In particular, one defines the normalized integrals for the different choices of $\mathbf{Q}$:

$$[i_m, s_n] \equiv N_\mathrm{i} \, [I_m, S_n] \quad \text{for} \quad m = 1, 2, 3 \quad \text{and} \quad n = 1, 2. \tag{B.4.47}$$

Integrals s_1, s_2 and i_3 are exactly equivalent to equations (6), (7) and (8) in [94]. Different choices of N_i are met in the other references, see table B.2.

Moments

Equations (B.4.32), (B.4.33) and (B.4.34) then read

$$\boxed{
\begin{aligned}
i_1 &= s_1 + s_2 = 2w + \ell + 2\beta_{\mathrm{p}\perp} + \beta_{\mathrm{p}\parallel} + \mu, && \text{(B.4.48)} \\
i_2 &= \frac{s_2}{R'} = \frac{1}{R_T} \left[2w_\varphi + \beta_{\mathrm{p}\parallel} + \ell - \mu - \frac{2\mu_0}{V \bar{B}_\mathrm{p}^2} \int_V \frac{B_\mathrm{p}^2 \left(p_\parallel - p_\perp \right)}{B^2} \, \mathrm{d}V \right], && \text{(B.4.49)} \\
i_3 &= 2w_Z + \beta_{\mathrm{p}\perp} + \ell + \mu - \frac{2\mu_0}{V \bar{B}_\mathrm{p}^2} \int_V \frac{B_Z^2}{\mu_0} \, \mathrm{d}V + \frac{2\mu_0}{V \bar{B}_\mathrm{p}^2} \int_V \frac{B_Z^2 \left(p_\parallel - p_\perp \right)}{B^2} \, \mathrm{d}V. && \text{(B.4.50)}
\end{aligned}
}$$

Equation (B.4.50) can be somewhat simplified by introducing the normalized vertical field α like equation (11) in [94]:

$$\alpha \equiv \frac{2 \displaystyle\int_V B_Z^2 \, \mathrm{d}V}{\displaystyle\int_V B_\mathrm{p}^2 \, \mathrm{d}V} = \frac{\dfrac{2\mu_0}{V \bar{B}_\mathrm{p}^2} \displaystyle\int_V \frac{B_Z^2}{\mu_0} \, \mathrm{d}V}{\ell} \tag{B.4.51}$$

such that

$$\boxed{i_3 = 2w_Z + \beta_{\mathrm{p}\perp} + \ell \left(1 - \alpha \right) + \mu + \frac{2\mu_0}{V \bar{B}_\mathrm{p}^2} \int_V \frac{B_Z^2 \left(p_\parallel - p_\perp \right)}{B^2} \, \mathrm{d}V.} \tag{B.4.52}$$

Equations (B.4.48), (B.4.49) and (B.4.52) are exactly equal to equations (2), (3) and (4) in [94] where the poloidal rotation and the anisotropy term $\int_V \frac{B_\mathrm{p}^2 \left(p_\parallel - p_\perp \right)}{B^2} \, \mathrm{d}V$ have been neglected.

These relations can now be combined to obtained expressions for specific physical quantities of interest like W_kin or W_L (i.e. β_p or ℓ).

B.5 Pressure balance equation

As previously noticed, the poloidal magnetic energy W_{L} is the only plasma quantity appearing in the integral relations (B.4.32)-(B.4.34) which depends on the choice for the toroidal volume V. It is thus convenient to combine the integral relations such as to get a pressure balance equation independent of W_{L}.

B.5.1 General case

In terms of plasma quantities

An expression for $W_{\mathrm{kin}\perp}$ is retrieved by inserting W_{L} from (B.4.33) into (B.4.32):

$$W_{\mathrm{L}} = \frac{R_T}{R'} S_2 - 2W_{\mathrm{rot}\varphi} - 2W_{\mathrm{kin}\parallel} + W_{\mathrm{M}} + \int_V \frac{B_{\mathrm{p}}^2 \left(p_\parallel - p_\perp\right)}{B^2} \,\mathrm{d}V \tag{B.5.1}$$

and thus

$$W_{\mathrm{kin}\perp} = \frac{1}{2}\left[S_1 + \left(1 - \frac{R_T}{R'}\right) S_2\right] - W_{\mathrm{rot}} + W_{\mathrm{rot}\varphi} - W_{\mathrm{M}} - \frac{1}{2}\int_V \frac{B_{\mathrm{p}}^2 \left(p_\parallel - p_\perp\right)}{B^2} \,\mathrm{d}V. \tag{B.5.2}$$

It is convenient to introduce the relative difference δ_R between the arbitrary major radius R' of the polar coordinate system and the mean radius R_T:

$$\delta_R \equiv \frac{R' - R_T}{R'}. \tag{B.5.3}$$

The pressure balance equation becomes

$$\boxed{W_{\mathrm{kin}\perp} = \frac{1}{2}\left[S_1 + \delta_R S_2\right] - W_{\mathrm{rot}} + W_{\mathrm{rot}\varphi} - W_{\mathrm{M}} - \frac{1}{2}\int_V \frac{B_{\mathrm{p}}^2 \left(p_\parallel - p_\perp\right)}{B^2} \,\mathrm{d}V} \tag{B.5.4}$$

or in terms of I_1 and I_2

$$\boxed{W_{\mathrm{kin}\perp} = \frac{1}{2}\left[I_1 - R_T I_2\right] - W_{\mathrm{rot}} + W_{\mathrm{rot}\varphi} - W_{\mathrm{M}} - \frac{1}{2}\int_V \frac{B_{\mathrm{p}}^2 \left(p_\parallel - p_\perp\right)}{B^2} \,\mathrm{d}V.} \tag{B.5.5}$$

In terms of normalized plasma quantities

Similarly, a normalized version of the pressure balance equation is retrieved by inserting ℓ from (B.4.49) into (B.4.48):

$$\ell = \frac{R_T}{R'} s_2 - 2w_\varphi - \beta_{\mathrm{p}\parallel} + \mu + \frac{2\mu_0}{V\bar{B}_{\mathrm{p}}^2}\int_V \frac{B_{\mathrm{p}}^2 \left(p_\parallel - p_\perp\right)}{B^2} \,\mathrm{d}V \tag{B.5.6}$$

$$\Rightarrow \beta_{\mathrm{p}\perp} = \frac{1}{2}\left[s_1 + \left(1 - \frac{R_T}{R'}\right) s_2\right] - w + w_\varphi - \mu - \frac{1}{2}\frac{2\mu_0}{V\bar{B}_{\mathrm{p}}^2}\int_V \frac{B_{\mathrm{p}}^2 \left(p_\parallel - p_\perp\right)}{B^2} \,\mathrm{d}V. \tag{B.5.7}$$

Using the definition of the radial shift δ_R introduced previously, the pressure balance equation becomes

$$\boxed{\beta_{\mathrm{p}\perp} = \frac{1}{2}\left[s_1 + \delta_R s_2\right] - w + w_\varphi - \mu - \frac{1}{2}\frac{2\mu_0}{V\bar{B}_{\mathrm{p}}^2}\int_V \frac{B_{\mathrm{p}}^2\left(p_\parallel - p_\perp\right)}{B^2}\,\mathrm{d}V} \tag{B.5.8}$$

or in terms of i_1 and i_2

$$\boxed{\beta_{\mathrm{p}\perp} = \frac{1}{2}\left[i_1 - R_T i_2\right] - w + w_\varphi - \mu - \frac{1}{2}\frac{2\mu_0}{V\bar{B}_{\mathrm{p}}^2}\int_V \frac{B_{\mathrm{p}}^2\left(p_\parallel - p_\perp\right)}{B^2}\,\mathrm{d}V.} \tag{B.5.9}$$

B.5.2 Small diamagnetism approximation

In standard tokamak conditions, the plasma contribution to the toroidal field (i.e. the so-called diamagnetic effect) is small:

$$|B_\varphi - B_{\varphi\mathrm{v}}| \ll B_{\varphi\mathrm{v}}. \tag{B.5.10}$$

The plasma toroidal magnetic energy W_{M} can thus be directly expressed in terms of the plasma toroidal flux Φ_{pl} defined in (B.1.1):

$$W_{\mathrm{M}} \equiv \int_V \frac{B_\varphi^2 - B_{\varphi\mathrm{v}}^2}{2\mu_0}\,\mathrm{d}V \approx \int_S \frac{2B_{\varphi\mathrm{v}}\left(B_\varphi - B_{\varphi\mathrm{v}}\right)}{2\mu_0} 2\pi R\,\mathrm{d}S = \frac{2\pi}{\mu_0} R B_{\varphi\mathrm{v}} \Phi_{\mathrm{pl}}. \tag{B.5.11}$$

where the fact that $RB_{\varphi\mathrm{v}} = \text{const}$ was used. It is then direct to link the normalized diamagnetism parameter μ to the plasma toroidal flux Φ_{pl}:

$$\mu \equiv \frac{2\mu_0}{V\bar{B}_{\mathrm{p}}^2} W_{\mathrm{M}} \simeq \frac{2\mu_0}{V\bar{B}_{\mathrm{p}}^2}\frac{2\pi}{\mu_0} R B_{\varphi\mathrm{v}} \Phi_{\mathrm{pl}} = \frac{4\pi}{V\bar{B}_{\mathrm{p}}^2} R B_{\varphi\mathrm{v}} \Phi_{\mathrm{pl}}. \tag{B.5.12}$$

In terms of plasma quantities

Inserting the approximate expression for W_{M} in the pressure balance equation (B.5.4), one gets

$$\boxed{W_{\mathrm{kin}\perp} = \frac{1}{2}\left[S_1 + \delta_R S_2\right] - W_{\mathrm{rot}} + W_{\mathrm{rot}\varphi} - \frac{2\pi}{\mu_0} R B_{\varphi\mathrm{v}} \Phi_{\mathrm{pl}} - \frac{1}{2}\int_V \frac{B_{\mathrm{p}}^2\left(p_\parallel - p_\perp\right)}{B^2}\,\mathrm{d}V} \tag{B.5.13}$$

or in terms of I_1 and I_2

$$\boxed{W_{\mathrm{kin}\perp} = \frac{1}{2}\left[I_1 - R_T I_2\right] - W_{\mathrm{rot}} + W_{\mathrm{rot}\varphi} - \frac{2\pi}{\mu_0} R B_{\varphi\mathrm{v}} \Phi_{\mathrm{pl}} - \frac{1}{2}\int_V \frac{B_{\mathrm{p}}^2\left(p_\parallel - p_\perp\right)}{B^2}\,\mathrm{d}V.} \tag{B.5.14}$$

In terms of normalized plasma quantities

Inserting the approximate expression for μ in the pressure balance equation (B.5.8), one gets

$$\boxed{\beta_{\mathrm{p}\perp} = \frac{1}{2}\left[s_1 + \delta_R s_2\right] - w + w_\varphi - \frac{4\pi}{V\bar{B}_{\mathrm{p}}^2} R B_{\varphi \mathrm{v}} \Phi_{\mathrm{pl}} - \frac{1}{2}\frac{2\mu_0}{V\bar{B}_{\mathrm{p}}^2}\int_V \frac{B_{\mathrm{p}}^2\left(p_\parallel - p_\perp\right)}{B^2}\,\mathrm{d}V} \tag{B.5.15}$$

or in terms of i_1 and i_2

$$\boxed{\beta_{\mathrm{p}\perp} = \frac{1}{2}\left[i_1 - R_T i_2\right] - w + w_\varphi - \frac{4\pi}{V\bar{B}_{\mathrm{p}}^2} R B_{\varphi \mathrm{v}} \Phi_{\mathrm{pl}} - \frac{1}{2}\frac{2\mu_0}{V\bar{B}_{\mathrm{p}}^2}\int_V \frac{B_{\mathrm{p}}^2\left(p_\parallel - p_\perp\right)}{B^2}\,\mathrm{d}V.} \tag{B.5.16}$$

B.5.3 Small diamagnetism and cylindrical limit

In the cylindrical limit, one has $\delta_R = 0$ and $s_1 = 2$ [94]. If one neglects the rotation energy w and the small last term in equation (B.5.15), the relation writes:

$$\beta_{\mathrm{p}\perp} = 1 - \frac{4\pi}{V\bar{B}_{\mathrm{p}}^2} R B_{\varphi \mathrm{v}} \Phi_{\mathrm{pl}}. \tag{B.5.17}$$

In the cylindrical limit, the contour-averaged poloidal field is evaluated directly from Ampère's law:

$$\bar{B}_{\mathrm{p}} = \frac{\mu_0 I_\varphi}{2\pi a} \tag{B.5.18}$$

where a is the plasma minor radius. Moreover, one has $2\pi R_0 = L$ and $V = L\pi a^2$ where L is the plasma column length. The simplified pressure balance equation in the cylindrical limit and for small plasma diamagnetism thus writes

$$\beta_{\mathrm{p}\perp} = 1 - \frac{8\pi B_{\varphi \mathrm{v}}}{\mu_0^2 I_\varphi^2}\Phi_{\mathrm{pl}} \tag{B.5.19}$$

which can also be seen as a relation for the plasma diamagnetic flux Φ_{pl} as a function of the plasma physical parameters I_φ, $B_{\varphi \mathrm{v}}$ and $\beta_{\mathrm{p}\perp}$.

B.6 Equations for the inductance

B.6.1 In terms of plasma quantities

$W_{\mathbf{L}} + 2W_{\mathbf{kin}\parallel}$ as a function of $W_{\mathbf{M}}$

An expression for $W_{\mathrm{L}} + 2W_{\mathrm{kin}\parallel}$ is directly obtained from equation (B.4.33):

$$\boxed{W_{\mathrm{L}} + 2W_{\mathrm{kin}\parallel} = \frac{R_T}{R'} S_2 - 2W_{\mathrm{rot}\varphi} + W_{\mathrm{M}} + \int_V \frac{B_{\mathrm{p}}^2\left(p_\parallel - p_\perp\right)}{B^2}\,\mathrm{d}V} \tag{B.6.1}$$

or in terms of I_1 and I_2

$$\boxed{W_\mathrm{L} + 2W_{\mathrm{kin}\parallel} = R_T I_2 - 2W_{\mathrm{rot}\varphi} + W_\mathrm{M} + \int_V \frac{B_\mathrm{p}^2 \left(p_\parallel - p_\perp\right)}{B^2} \,\mathrm{d}V.} \tag{B.6.2}$$

$W_\mathbf{L} + 2W_{\mathbf{kin}\parallel}$ as a function of $W_{\mathbf{kin}\perp}$

Extracting W_M from (B.4.32)

$$W_\mathrm{M} = S_1 + S_2 - 2W_\mathrm{rot} - W_\mathrm{L} - 2W_{\mathrm{kin}\perp} - 2W_{\mathrm{kin}\parallel} \tag{B.6.3}$$

and inserting in (B.4.33) gives

$$\begin{aligned} W_\mathrm{L} + 2W_{\mathrm{kin}\parallel} = \frac{1}{2}\left[S_1 + \left(1 + \frac{R_T}{R'}\right) S_2\right] - W_\mathrm{rot} - W_{\mathrm{rot}\varphi} \\ - W_{\mathrm{kin}\perp} + \frac{1}{2}\int_V \frac{B_\mathrm{p}^2 \left(p_\parallel - p_\perp\right)}{B^2} \,\mathrm{d}V. \end{aligned} \tag{B.6.4}$$

Using the definition of δ_R, we get

$$\boxed{\begin{aligned} W_\mathrm{L} + 2W_{\mathrm{kin}\parallel} = \frac{1}{2}\left[S_1 + (2 - \delta_R) S_2\right] - W_\mathrm{rot} - W_{\mathrm{rot}\varphi} \\ - W_{\mathrm{kin}\perp} + \frac{1}{2}\int_V \frac{B_\mathrm{p}^2 \left(p_\parallel - p_\perp\right)}{B^2} \,\mathrm{d}V \end{aligned}} \tag{B.6.5}$$

or in terms of I_1 and I_2:

$$\boxed{\begin{aligned} W_\mathrm{L} + 2W_{\mathrm{kin}\parallel} = \frac{1}{2}\left[I_1 + R_T I_2\right] - W_\mathrm{rot} - W_{\mathrm{rot}\varphi} \\ - W_{\mathrm{kin}\perp} + \frac{1}{2}\int_V \frac{B_\mathrm{p}^2 \left(p_\parallel - p_\perp\right)}{B^2} \,\mathrm{d}V. \end{aligned}} \tag{B.6.6}$$

$W_\mathbf{L}$ as a function of Shafranov integrals only

To get rid of W_M, $W_{\mathrm{kin}\parallel}$ and $W_{\mathrm{kin}\perp}$, one substracts twice the equation (B.4.34) and R_T times the equation (B.4.33) from equation (B.4.32):

$$\begin{aligned} S_1 + S_2 - 2I_3 - \frac{R_T S_2}{R'} = &- 2W_{\mathrm{rot}Z} + 2W_{\mathrm{rot}R} - 2W_\mathrm{L} \\ &+ 2\int_V \frac{B_Z^2}{\mu_0} \,\mathrm{d}V + \int_V \frac{\left(B_\mathrm{p}^2 - 2B_Z^2\right)\left(p_\parallel - p_\perp\right)}{B^2} \,\mathrm{d}V \end{aligned} \tag{B.6.7}$$

thus leading to an expression for W_L

$$\begin{aligned} W_\mathrm{L} = W_{\mathrm{rot}R} - W_{\mathrm{rot}Z} - \frac{S_1}{2} + I_3 - \frac{S_2}{2}\left(1 - \frac{R_T}{R'}\right) \\ + \int_V \frac{B_Z^2}{\mu_0} \,\mathrm{d}V + \frac{1}{2}\int_V \frac{\left(B_\mathrm{p}^2 - 2B_Z^2\right)\left(p_\parallel - p_\perp\right)}{B^2} \,\mathrm{d}V. \end{aligned} \tag{B.6.8}$$

Using the definition of δ_R, one gets

$$\boxed{W_{\mathrm{L}} = W_{\mathrm{rot}R} - W_{\mathrm{rot}Z} - \frac{S_1}{2} + I_3 - \delta_R \frac{S_2}{2} + \int_V \frac{B_Z^2}{\mu_0}\,\mathrm{d}V + \frac{1}{2}\int_V \frac{\left(B_{\mathrm{p}}^2 - 2B_Z^2\right)\left(p_\parallel - p_\perp\right)}{B^2}\,\mathrm{d}V} \tag{B.6.9}$$

or in terms of I_1 and I_2

$$\boxed{W_{\mathrm{L}} = W_{\mathrm{rot}R} - W_{\mathrm{rot}Z} - \frac{I_1}{2} + I_3 - R_T \frac{I_2}{2} + \int_V \frac{B_Z^2}{\mu_0}\,\mathrm{d}V + \frac{1}{2}\int_V \frac{\left(B_{\mathrm{p}}^2 - 2B_Z^2\right)\left(p_\parallel - p_\perp\right)}{B^2}\,\mathrm{d}V.} \tag{B.6.10}$$

B.6.2 In terms of normalized plasma quantities

$\ell + \beta_{\mathrm{p}\parallel}$ as a function of μ

An expression for $\ell + \beta_{\mathrm{p}\parallel}$ is obtained directly from equation (B.4.49):

$$\boxed{\ell + \beta_{\mathrm{p}\parallel} = \frac{R_T}{R'} s_2 - 2w_\varphi + \mu + \frac{2\mu_0}{V\bar{B}_{\mathrm{p}}^2}\int_V \frac{B_{\mathrm{p}}^2\left(p_\parallel - p_\perp\right)}{B^2}\,\mathrm{d}V} \tag{B.6.11}$$

or in terms of i_1 and i_2

$$\boxed{\ell + \beta_{\mathrm{p}\parallel} = R_T i_2 - 2w_\varphi + \mu + \frac{2\mu_0}{V\bar{B}_{\mathrm{p}}^2}\int_V \frac{B_{\mathrm{p}}^2\left(p_\parallel - p_\perp\right)}{B^2}\,\mathrm{d}V.} \tag{B.6.12}$$

$\ell + \beta_{\mathrm{p}\parallel}$ as a function of $\beta_{\mathrm{p}\perp}$

Extracting μ from (B.4.48)

$$\mu = s_1 + s_2 - 2w - \ell - 2\beta_{\mathrm{p}\perp} - \beta_{\mathrm{p}\parallel} \tag{B.6.13}$$

and inserting in (B.4.49) gives

$$\ell + \beta_{\mathrm{p}\parallel} = \frac{1}{2}\left[s_1 + \left(1 + \frac{R_T}{R'}\right) s_2\right] - w - w_\varphi - \beta_{\mathrm{p}\perp} + \frac{1}{2}\frac{2\mu_0}{V\bar{B}_{\mathrm{p}}^2}\int_V \frac{B_{\mathrm{p}}^2\left(p_\parallel - p_\perp\right)}{B^2}\,\mathrm{d}V \tag{B.6.14}$$

which is identical to equation (12) in [94]. Using the definition of δ_R, one gets

$$\boxed{\ell + \beta_{\mathrm{p}\parallel} = \frac{1}{2}\left[s_1 + (2 - \delta_R)\, s_2\right] - w - w_\varphi - \beta_{\mathrm{p}\perp} + \frac{1}{2}\frac{2\mu_0}{V\bar{B}_{\mathrm{p}}^2}\int_V \frac{B_{\mathrm{p}}^2\left(p_\parallel - p_\perp\right)}{B^2}\,\mathrm{d}V} \tag{B.6.15}$$

or in terms of i_1 and i_2

$$\boxed{\ell + \beta_{\mathrm{p}\parallel} = \frac{1}{2}\left[i_1 + R_T i_2\right] - w - w_\varphi - \beta_{\mathrm{p}\perp} + \frac{1}{2}\frac{2\mu_0}{V\bar{B}_{\mathrm{p}}^2}\int_V \frac{B_{\mathrm{p}}^2\left(p_\parallel - p_\perp\right)}{B^2}\,\mathrm{d}V.} \tag{B.6.16}$$

ℓ as a function of Shafranov integrals only

To get rid of μ, $\beta_{\mathrm{p}\parallel}$ and $\beta_{\mathrm{p}\perp}$, one subtracts twice the equation (B.4.52) and R_T times the equation (B.4.49) from equation (B.4.48):

$$s_1+s_2-2i_3-\frac{R_T s_2}{R'}=-2w_Z+2w_R-2\ell(1-\alpha)+\frac{2\mu_0}{V\bar{B}_{\mathrm{p}}^2}\int_V\frac{\left(B_{\mathrm{p}}^2-2B_Z^2\right)\left(p_\parallel-p_\perp\right)}{B^2}\,\mathrm{d}V \tag{B.6.17}$$

Thus, one gets an expression for ℓ:

$$\ell=\frac{1}{1-\alpha}\left[w_R-w_Z-\frac{s_1}{2}+i_3-\frac{s_2}{2}\left(1-\frac{R_T}{R'}\right)+\frac{1}{2}\frac{2\mu_0}{V\bar{B}_{\mathrm{p}}^2}\int_V\frac{\left(B_{\mathrm{p}}^2-2B_Z^2\right)\left(p_\parallel-p_\perp\right)}{B^2}\,\mathrm{d}V\right] \tag{B.6.18}$$

which is identical to equation (18) in [94]. Using the definition of δ_R, one gets

$$\boxed{\ell=\frac{1}{1-\alpha}\left[w_R-w_Z-\frac{s_1}{2}+i_3-\delta_R\frac{s_2}{2}+\frac{1}{2}\frac{2\mu_0}{V\bar{B}_{\mathrm{p}}^2}\int_V\frac{\left(B_{\mathrm{p}}^2-2B_Z^2\right)\left(p_\parallel-p_\perp\right)}{B^2}\,\mathrm{d}V\right]} \tag{B.6.19}$$

or in terms of i_1 and i_2

$$\boxed{\ell=\frac{1}{1-\alpha}\left[w_R-w_Z-\frac{i_1}{2}+i_3+R_T\frac{i_2}{2}+\frac{1}{2}\frac{2\mu_0}{V\bar{B}_{\mathrm{p}}^2}\int_V\frac{\left(B_{\mathrm{p}}^2-2B_Z^2\right)\left(p_\parallel-p_\perp\right)}{B^2}\,\mathrm{d}V\right].} \tag{B.6.20}$$

B.7 Isotropic static plasma

In the case of a static isotropic plasma, one has

$$u=0 \quad\Rightarrow\quad W_{\mathrm{rot}}=0 \qquad \text{and} \qquad w=0; \tag{B.7.1}$$

$$p_\perp=p_\parallel\equiv p \quad\Rightarrow\quad W_{\mathrm{kin}}=\frac{3}{2}W_{\mathrm{kin}\perp}=3W_{\mathrm{kin}\parallel} \qquad \text{and} \qquad \beta_{\mathrm{p}\perp}=\beta_{\mathrm{p}\parallel}=\beta_{\mathrm{p}}. \tag{B.7.2}$$

B.7.1 Pressure balance equation

The general pressure balance equation (B.5.4) becomes

$$\boxed{W_{\mathrm{kin}}=\frac{3}{4}\left[S_1+\delta_R S_2\right]-\frac{3}{2}W_{\mathrm{M}}\approx\frac{3}{4}S^*-\frac{3\pi}{\mu_0}RB_{\varphi\mathrm{v}}\Phi_{\mathrm{pl}}} \tag{B.7.3}$$

or in terms of I_1 and I_2

$$\boxed{W_{\mathrm{kin}}=\frac{3}{4}\left[I_1-R_T I_2\right]-\frac{3}{2}W_{\mathrm{M}}\approx\frac{3}{4}I^*-\frac{3\pi}{\mu_0}RB_{\varphi\mathrm{v}}\Phi_{\mathrm{pl}}} \tag{B.7.4}$$

where the small diamagnetism assumption is used for the last equality and the following definitions are introduced:

$$\Phi_{\rm pl} \equiv \int_S (B_\varphi - B_{\varphi {\rm v}})\ {\rm d}S \quad , \quad S^* \equiv S_1 + \delta_R S_2 \quad \text{and} \quad I^* \equiv I_1 - R_T I_2. \tag{B.7.5}$$

In terms of normalized plasma quantities, the pressure balance equation (B.5.8) becomes

$$\boxed{\beta_{\rm p} = \frac{1}{2}\left[s_1 + \delta_R s_2\right] - \mu \approx \frac{1}{2}s^* - \frac{2\mu_0}{V\bar{B}_{\rm p}^2}\frac{2\pi}{\mu_0} R B_{\varphi {\rm v}} \Phi_{\rm pl}} \tag{B.7.6}$$

or in terms of i_1 and i_2

$$\boxed{\beta_{\rm p} = \frac{1}{2}\left[i_1 - R_T i_2\right] - \mu \approx \frac{1}{2}i^* - \frac{2\mu_0}{V\bar{B}_{\rm p}^2}\frac{2\pi}{\mu_0} R B_{\varphi {\rm v}} \Phi_{\rm pl}} \tag{B.7.7}$$

where

$$\Phi_{\rm pl} \equiv \int_S (B_\varphi - B_{\varphi {\rm v}})\ {\rm d}S \quad , \quad s^* \equiv s_1 + \delta_R s_2 \quad \text{and} \quad i^* \equiv i_1 - R_T i_2. \tag{B.7.8}$$

B.7.2 Equations for the inductance

In case of a static isotropic plasma, the equation (B.6.1) for $W_{\rm L} + 2W_{\rm kin\|}$ as a function of the $W_{\rm M}$ becomes

$$\boxed{W_{\rm L} + \frac{2}{3}W_{\rm kin} = \frac{R_T}{R'}S_2 + W_{\rm M} \approx \frac{R_T}{R'}S_2 + \frac{2\pi}{\mu_0} R B_{\varphi {\rm v}} \Phi_{\rm pl}} \tag{B.7.9}$$

or in terms of I_1 and I_2

$$\boxed{W_{\rm L} + \frac{2}{3}W_{\rm kin} = R_T I_2 + W_{\rm M} \approx R_T I_2 + \frac{2\pi}{\mu_0} R B_{\varphi {\rm v}} \Phi_{\rm pl}.} \tag{B.7.10}$$

In terms of normalized plasma quantities, the inductance equation (B.6.11) becomes

$$\boxed{\ell + \beta_{\rm p} = \frac{R_T}{R'}s_2 + \mu \approx \frac{R_T}{R'}s_2 + \frac{4\pi}{V\bar{B}_{\rm p}^2} R B_{\varphi {\rm v}} \Phi_{\rm pl}} \tag{B.7.11}$$

or in terms of i_1 and i_2

$$\boxed{\ell + \beta_{\rm p} = R_T i_2 + \mu \approx R_T i_2 + \frac{4\pi}{V\bar{B}_{\rm p}^2} R B_{\varphi {\rm v}} \Phi_{\rm pl}.} \tag{B.7.12}$$

Appendix C

Energy anisotropy relaxation

Electron cyclotron heating (ECH) increases the electron kinetic energy in the direction perpendicular to the magnetic field, thus generating an anisotropy in the electron distribution function. In order to analyze the response of the perpendicular energy to modulated ECH (MECH), one needs a model for its time evolution, indicating how fast the anisotropy is relaxed by the restoring Coulomb collisions.
In this appendix, separate equations for the evolution of the perpendicular and the parallel temperatures due to binary Coulomb collisions are derived for two anisotropic distribution functions f_α and f_β, yielding an expression for the net anisotropy-dependent energy exchange rate.

C.1 Anisotropy separation

As mentioned above, one needs separate equations for the perpendicular and parallel plasma kinetic energies in order to describe accurately the plasma response to ECH

$$\frac{\mathrm{d}W_\perp}{\mathrm{d}t} = -\frac{W_\perp}{\tau_{\mathrm{inc}}} + \eta P_{\mathrm{RF}} + \left.\frac{\partial W_\perp}{\partial t}\right|_{\mathrm{coll}} \tag{C.1.1}$$

$$\frac{\mathrm{d}W_\parallel}{\mathrm{d}t} = -\frac{W_\parallel}{\tau_{\mathrm{inc}}} + P_{\mathrm{OH}} + \left.\frac{\partial W_\parallel}{\partial t}\right|_{\mathrm{coll}}. \tag{C.1.2}$$

Here, $W_\perp$ and $W_\parallel$ represent the sum over all species of the perpendicular and parallel kinetic energies, respectively:

$$W_\perp = \sum_\alpha W_{\alpha\perp} \qquad \text{with} \qquad W_{\alpha\perp} = \frac{1}{2}\int 2p_{\alpha\perp}\mathrm{d}V \tag{C.1.3}$$

$$W_\parallel = \sum_\alpha W_{\alpha\parallel} \qquad \text{with} \qquad W_{\alpha\parallel} = \frac{1}{2}\int p_{\alpha\parallel}\mathrm{d}V \tag{C.1.4}$$

and the pressures defined as

$$p_{\alpha\perp} = \int m_\alpha w_{\alpha\perp}^2 f_\alpha(t,\mathbf{x},\mathbf{v}_\alpha)\mathrm{d}^3 v_\alpha \tag{C.1.5}$$

$$p_{\alpha\parallel} = \int m_a w_{\alpha\parallel}^2 f_\alpha(t,\mathbf{x},\mathbf{v}_\alpha)\mathrm{d}^3 v_\alpha \tag{C.1.6}$$

where $f_\alpha(t,\mathbf{x},\mathbf{v}_\alpha)$ is the α particles time and space dependent velocity distribution function, and $\mathbf{w}_\alpha \equiv \mathbf{v}_\alpha - \mathbf{u}_\alpha$ is the particle microscopic velocity independent from the fluid drift $\mathbf{u}_\alpha$. In equations (C.1.1) and (C.1.2), it is assumed that the Ohmic power P_{OH} and the absorbed RF power P_{RF} increase mainly the parallel and perpendicular energies, respectively, with η the RF power absorption efficiency. The first term on the right-hand side of both equations is an effective loss term accounting for transport and radiation losses. The incremental confinement time τ_{inc} is assumed to be identical in both directions. The last term treats of the perpendicular and parallel kinetic energies evolution due to the restoring collisions. This term can be expressed in a convenient form by separating out the energy anisotropy A_α from the total energy W_α, for each species α [90]:

$$W_\alpha \equiv W_{\alpha\perp} + W_{\alpha\parallel} \tag{C.1.7}$$

$$A_\alpha \equiv \frac{1}{2}W_{\alpha\perp} - W_{\alpha\parallel} \tag{C.1.8}$$

such that

$$W_{\alpha\perp} = \frac{2}{3}W_\alpha + \frac{2}{3}A_\alpha \tag{C.1.9}$$

$$W_{\alpha\parallel} = \frac{1}{3}W_\alpha - \frac{2}{3}A_\alpha. \tag{C.1.10}$$

The variation of the perpendicular and parallel kinetic energies of the species α due to collisions on all field particles $\beta \neq \alpha$ and to self-interactions $\beta = \alpha$ write:

$$\left.\frac{\partial W_{\alpha\perp}}{\partial t}\right|_{\mathrm{col}} = \sum_\beta \left.\frac{\partial W_{\alpha\perp}}{\partial t}\right|_{\alpha\beta} = \frac{2}{3}\sum_\beta \left.\frac{\partial W_\alpha}{\partial t}\right|_{\alpha\beta} + \frac{2}{3}\sum_\beta \left.\frac{\partial A_\alpha}{\partial t}\right|_{\alpha\beta} \tag{C.1.11}$$

$$\left.\frac{\partial W_{\alpha\parallel}}{\partial t}\right|_{\mathrm{col}} = \sum_\beta \left.\frac{\partial W_{\alpha\parallel}}{\partial t}\right|_{\alpha\beta} = \frac{1}{3}\sum_\beta \left.\frac{\partial W_\alpha}{\partial t}\right|_{\alpha\beta} - \frac{2}{3}\sum_\beta \left.\frac{\partial A_\alpha}{\partial t}\right|_{\alpha\beta} \tag{C.1.12}$$

where the variation of the total kinetic energy of the species α is given by the volume integration of the energy exchange rate density $Q_{\alpha\beta}$:

$$\left.\frac{\partial W_\alpha}{\partial t}\right|_{\alpha\beta} = \int Q_{\alpha\beta}\mathrm{d}V \qquad \text{with} \qquad Q_{\alpha\beta} \equiv \int C_{\alpha\beta}\frac{m_\alpha w_\alpha^2}{2}\mathrm{d}^3 v_\alpha. \tag{C.1.13}$$

Here, $C_{\alpha\beta}$ is the collision operator for the species α on the field particles of species β:

$$C_{\alpha\beta} \equiv \left.\frac{\partial f_\alpha(\mathbf{v}_\alpha)}{\partial t}\right|_{\alpha\beta}. \tag{C.1.14}$$

We will consider only the case of fully ionized plasmas and binary collisions between charged particles. Choosing $C_{\alpha\beta}$ to be the Fokker-Planck collision operator for two-particle Coulomb collisions (neglecting collective effects), the total plasma kinetic energy is conserved by collisions

$$\left.\frac{\partial W}{\partial t}\right|_{\text{col}} = \sum_{\alpha} \left.\frac{\partial W_\alpha}{\partial t}\right|_{\text{col}} = \sum_{\alpha,\beta} \left.\frac{\partial W_\alpha}{\partial t}\right|_{\alpha\beta} = \int \sum_{\alpha,\beta} Q_{\alpha\beta} \mathrm{d}V = 0. \tag{C.1.15}$$

where we have used the total plasma energy conservation property of the Fokker-Planck collision operator:

$$\sum_{\alpha,\beta} Q_{\alpha\beta} = 0. \tag{C.1.16}$$

Summing equations (C.1.11) and (C.1.12) over all species α thus yields

$$\left.\frac{\partial W_\perp}{\partial t}\right|_{\text{col}} = \frac{2}{3} \sum_{\alpha,\beta} \left.\frac{\partial A_\alpha}{\partial t}\right|_{\alpha\beta} \tag{C.1.17}$$

$$\left.\frac{\partial W_\parallel}{\partial t}\right|_{\text{col}} = -\frac{2}{3} \sum_{\alpha,\beta} \left.\frac{\partial A_\alpha}{\partial t}\right|_{\alpha\beta}. \tag{C.1.18}$$

As expected from the plasma energy conservation, the variation of the perpendicular and parallel kinetic energies are equal but with opposite signs, i.e. any energy lost from the perpendicular part in a collision is gained by the parallel part and vice versa. The variation of the α species anisotropy due to collisions on the species β writes

$$\left.\frac{\partial A_\alpha}{\partial t}\right|_{\alpha\beta} = \left.\frac{\partial\left(\frac{1}{2}W_{\alpha\perp} - W_{\alpha\parallel}\right)}{\partial t}\right|_{\alpha\beta} = \frac{1}{2}\int n_\alpha \left.\frac{\partial\left(T_{\alpha\perp} - T_{\alpha\parallel}\right)}{\partial t}\right|_{\alpha\beta} \mathrm{d}V \tag{C.1.19}$$

where we used $p_{\alpha\perp,\parallel} = n_\alpha T_{\alpha\perp,\parallel}$ and the particle number conservation property of the Fokker-Planck collision operator:

$$\left.\frac{\partial n_\alpha}{\partial t}\right|_{\alpha\beta} = n_a \int C_{\alpha\beta} \mathrm{d}^3 v_\alpha = 0. \tag{C.1.20}$$

C.2 Non-linear solution

The problem is now to find separate expressions for the evolution of the perpendicular and parallel temperatures of the anisotropic species α due to collisions on the species β. From the temperature and pressure definitions (C.1.5) and (C.1.6), one writes

$$\left.\frac{\partial T_{\alpha\perp}}{\partial t}\right|_{\alpha\beta} = \frac{1}{n_\alpha}\int m_\alpha w_{\alpha\perp}^2 \left.\frac{\partial f_\alpha(\mathbf{v}_\alpha)}{\partial t}\right|_{\alpha\beta} \mathrm{d}^3 v_\alpha \tag{C.2.1}$$

$$\left.\frac{\partial T_{\alpha\parallel}}{\partial t}\right|_{\alpha\beta} = \frac{1}{n_\alpha}\int m_\alpha w_{\alpha\parallel}^2 \left.\frac{\partial f_\alpha(\mathbf{v}_\alpha)}{\partial t}\right|_{\alpha\beta} \mathrm{d}^3 v_\alpha. \tag{C.2.2}$$

For small deflection binary Coulomb collisions, the Fokker-Planck collision operator writes

$$C_{\alpha\beta} = \left.\frac{\partial f_\alpha(\mathbf{v}_\alpha)}{\partial t}\right|_{\alpha\beta} = -\frac{\partial}{\partial \mathbf{v}_\alpha}\cdot \mathbf{j}_{\alpha\beta} \tag{C.2.3}$$

where $\mathbf{j}_{\alpha\beta}$ is the velocity space collisional current in Landau's form [108]

$$\mathbf{j}_{\alpha\beta} \equiv \frac{c_{\alpha\beta}}{m_\alpha}\int \frac{v^2\mathbb{I}-\mathbf{vv}}{v^3}\cdot\left(\frac{f_\alpha}{m_\beta}\frac{\partial f_\beta}{\partial \mathbf{v}_\beta} - \frac{f_\beta}{m_\alpha}\frac{\partial f_\alpha}{\partial \mathbf{v}_\alpha}\right)\mathrm{d}^3 v_\beta \tag{C.2.4}$$

with $\mathbf{v} \equiv \mathbf{v}_\alpha - \mathbf{v}_\beta$ the relative velocity and

$$c_{\alpha\beta} \equiv \frac{q_\alpha^2 q_\beta^2 \ln(\Lambda_{\alpha\beta})}{8\pi\varepsilon_0^2}. \tag{C.2.5}$$

Here, m_α and $q_\alpha \equiv eZ_\alpha$ are respectively the mass and the electric charge of a particle α, with Z_α the ionization level and $\ln(\Lambda_{\alpha\beta})$ the Coulomb logarithm. Clearly, equation (C.2.3) is nonlinear for the case of self-interactions (i.e. $\beta = \alpha$). The set of equations (C.2.3)-(C.2.5) is valid for time-varying, inhomogeneous but unmagnetized plasmas. As reviewed in [109], the only effect of a strong magnetic field is to modify the Coulomb logarithm by replacing the Debye length by the Larmor radius as the maximum collision impact parameter. One wants to solve the general problem for initially two anisotropic bi-Maxwellian elliptic distribution functions

$$f_\alpha(t,\mathbf{x},\mathbf{v}_\alpha) = n_\alpha(t,\mathbf{x})\left(\frac{b_{\alpha\perp}}{\sqrt{\pi}}\right)^2\left(\frac{b_{\alpha\parallel}}{\sqrt{\pi}}\right)\mathrm{e}^{-b_{\alpha\perp}^2(\mathbf{v}_{\alpha\perp}-\mathbf{u}_{\alpha\perp})^2 - b_{\alpha\parallel}^2(\mathbf{v}_{\alpha\parallel}-\mathbf{u}_{\alpha\parallel})^2} \tag{C.2.6}$$

$$f_\beta(t,\mathbf{x},\mathbf{v}_\beta) = n_\beta(t,\mathbf{x})\left(\frac{b_{\beta\perp}}{\sqrt{\pi}}\right)^2\left(\frac{b_{\beta\parallel}}{\sqrt{\pi}}\right)\mathrm{e}^{-b_{\beta\perp}^2(\mathbf{v}_{\beta\perp}-\mathbf{u}_{\beta\perp})^2 - b_{\beta\parallel}^2(\mathbf{v}_{\beta\parallel}-\mathbf{u}_{\beta\parallel})^2} \tag{C.2.7}$$

normalized to the particle number densities n_α and n_β, respectively, with the inverse thermal velocities defined as

$$b_{\alpha\perp} \equiv \sqrt{\frac{m_\alpha}{2T_{\alpha\perp}(t,\mathbf{x})}} \qquad \text{and} \qquad b_{\alpha\parallel} \equiv \sqrt{\frac{m_\alpha}{2T_{\alpha\parallel}(t,\mathbf{x})}}. \tag{C.2.8}$$

Note that both densities and temperatures are time and space dependent functions. Distribution functions (C.2.6) and (C.2.7) are assumed to remain bi-Maxwellian throughout the relaxation process, with time-dependent densities and temperatures. For the case of self-interactions ($\beta = \alpha$), the time evolution of the anisotropy described by the non-linear analytical solution of this bi-Maxwellian model (see equations (C.2.20) and (C.2.21)) is compared in [109] to the numerical solution of a nonlinear Fokker-Planck code allowing distortions of the distribution function. This results in a perfect agreement of the bi-Maxwellian model with the numerical solution in the case of perpendicular relaxation (i.e. $T_{\alpha\perp} > T_{\alpha\parallel}$ initially), but not in the

case of parallel relaxation (i.e. $T_{\alpha\parallel} > T_{\alpha\perp}$ initially). Since the goal here is to describe the plasma response to perpendicular RF heating, we are mainly concerned by the perpendicular relaxation which is very well described by the bi-Maxwellian model. Due to the separation of the perpendicular and parallel components, the integration over $\mathbf{v}_\beta$ in (C.2.4) is not trivial and involves integrals of the form

$$\int \mathrm{e}^{-b_{\beta\perp}^2(\mathbf{v}_{\beta\perp}-\mathbf{u}_{\beta\perp})^2-b_{\beta\parallel}^2(\mathbf{v}_{\beta\parallel}-\mathbf{u}_{\beta\parallel})^2}\frac{\left(\mathbf{v}_{\alpha\perp}-\mathbf{v}_{\beta\perp}\right)^2}{\left|\mathbf{v}_\alpha-\mathbf{v}_\beta\right|^3}\mathrm{d}^3v_\beta. \tag{C.2.9}$$

With the only restriction of zero perpendicular fluid velocity (i.e. $\mathbf{u}_{\alpha\perp} = \mathbf{u}_{\beta\perp} = 0$), a closed non-linear solution to this problem is given in [110] in terms of generalized double hypergeometric Kampé de Fériet functions. Further restricting the problem to two populations α and β with no relative parallel fluid flow, i.e. $\mathbf{u}_{\alpha\parallel} = \mathbf{u}_{\beta\parallel}$, the solution takes a much simpler form:

$$\left.\frac{\partial T_{\alpha\perp}}{\partial t}\right|_{\alpha\beta} = \frac{3}{4}\frac{\nu_{\alpha\beta}}{A_{\alpha\beta}}\frac{1}{m_\alpha+m_\beta}\frac{1}{\xi}\left\{A-\phi(\xi)\left[B\xi+A\right]\right\} \tag{C.2.10}$$

$$\left.\frac{\partial T_{\alpha\parallel}}{\partial t}\right|_{\alpha\beta} = \frac{3}{2}\nu_{\alpha\beta}\frac{1}{m_\alpha+m_\beta}\frac{1}{\xi}\left\{-C+\phi(\xi)\left[D\xi+C\right]\right\} \tag{C.2.11}$$

with the coefficients

$$A = 2m_\alpha T_{\alpha\perp} + 3m_\beta T_{\alpha\perp} + m_\alpha T_{\beta\perp}, \tag{C.2.12}$$

$$B = 2m_\alpha T_{\alpha\perp} + m_\beta T_{\alpha\perp} - m_\alpha T_{\beta\perp}, \tag{C.2.13}$$

$$C = 2m_\alpha T_{\alpha\parallel} + 3m_\beta T_{\alpha\parallel} + m_\alpha T_{\beta\parallel}, \tag{C.2.14}$$

$$D = m_\beta T_{\alpha\parallel} + m_\alpha T_{\beta\parallel}, \tag{C.2.15}$$

the ratio $A_{\alpha\beta}$ defined as

$$A_{\alpha\beta} \equiv \frac{m_\beta T_{\alpha\perp} + m_\alpha T_{\beta\perp}}{m_\beta T_{\alpha\parallel} + m_\alpha T_{\beta\parallel}} \tag{C.2.16}$$

and a collision frequency $\nu_{\alpha\beta}$ defined as

$$\nu_{\alpha\beta} = \frac{q_\alpha^2 q_\beta^2 n_\beta \ln(\Lambda_{\alpha\beta})\sqrt{2m_\alpha m_\beta}(m_\alpha+m_\beta)}{6\pi^{3/2}\varepsilon_0^2 m_\alpha\left[m_\beta T_{\alpha\parallel}+m_\alpha T_{\beta\parallel}\right]^{3/2}}. \tag{C.2.17}$$

The function $\phi(x)$ is

$$\phi(x) \equiv \frac{\arctan(\sqrt{x})}{\sqrt{x}} \tag{C.2.18}$$

with the anisotropy parameter ξ

$$\xi \equiv A_{\alpha\beta} - 1 = \frac{m_\beta(T_{\alpha\perp}-T_{\alpha\parallel}) + m_\alpha(T_{\beta\perp}-T_{\beta\parallel})}{m_\beta T_{\alpha\parallel} + m_\alpha T_{\beta\parallel}}. \tag{C.2.19}$$

This result was previously derived by Lehner in [111] for the case of isotropic field particles β. For the special case of the relaxation of the particles α on themselves ($\beta = \alpha$), the solution reduces to

$$\left.\frac{\partial T_{\alpha\perp}}{\partial t}\right|_{\alpha\alpha} = -\frac{3}{4}\nu_{\alpha\alpha}T_{\alpha\parallel}\frac{1}{\xi}\left\{[3+\xi]\phi(\xi) - 3\right\} \tag{C.2.20}$$

$$\left.\frac{\partial T_{\alpha\parallel}}{\partial t}\right|_{\alpha\alpha} = -2\left.\frac{\partial T_{\alpha\perp}}{\partial t}\right|_{\alpha\alpha} \tag{C.2.21}$$

with $\xi = (T_{\alpha\perp} - T_{\alpha\parallel})/T_{\alpha\parallel}$. This particular result was first derived by Kogan in [112] and quoted by Trubnikov in [113].

C.3 Anisotropy-dependent relaxation time

Following the example of [109] for self-collisions, one can derive an anisotropy-dependent frequency for the energy transfer from the perpendicular direction to the parallel direction. Assuming isotropic field particles β, the anisotropy parameter reduces to

$$\xi = \frac{m_\beta(T_{\alpha\perp} - T_{\alpha\parallel})}{m_\beta T_{\alpha\parallel} + m_\alpha T_\beta}. \tag{C.3.1}$$

The rate of temperature anisotropy relaxation then writes

$$\left.\frac{\partial(T_{\alpha\perp} - T_{\alpha\parallel})}{\partial t}\right|_{\alpha\beta} \equiv \left.\frac{\partial T_{\alpha\perp}}{\partial t}\right|_{\alpha\beta} - \left.\frac{\partial T_{\alpha\parallel}}{\partial t}\right|_{\alpha\beta} = -\nu_{\mathrm{a}}^{\alpha/\beta}(\xi)(T_{\alpha\perp} - T_{\alpha\parallel}) \tag{C.3.2}$$

where the anisotropy-dependent relaxation frequency for the collisions of the α particles on the β particles is defined as

$$\begin{aligned}\nu_{\mathrm{a}}^{\alpha/\beta}(\xi) \equiv & \frac{3}{4}\nu_{\alpha\beta}\frac{1}{\xi^2}\frac{m_\beta}{(m_\beta T_{\alpha\parallel} + m_\alpha T_\beta)(m_\alpha + m_\beta)} \\ & \left[\frac{-1}{\xi+1}\left\{A - \phi(\xi)[B\xi + A]\right\} + 2\left\{-C + \phi(\xi)[D\xi + C]\right\}\right].\end{aligned} \tag{C.3.3}$$

Similarly for the α particles self-interactions, one writes

$$\left.\frac{\partial(T_{\alpha\perp} - T_{\alpha\parallel})}{\partial t}\right|_{\alpha\alpha} \equiv \left.\frac{\partial T_{\alpha\perp}}{\partial t}\right|_{\alpha\alpha} - \left.\frac{\partial T_{\alpha\parallel}}{\partial t}\right|_{\alpha\alpha} = -\nu_{\mathrm{a}}^{\alpha/\alpha}(\xi)(T_{\alpha\perp} - T_{\alpha\parallel}) \tag{C.3.4}$$

where

$$\nu_{\mathrm{a}}^{\alpha/\alpha}(\xi) \equiv \frac{9}{4}\nu_{\alpha\alpha}\frac{1}{\xi^2}\left\{[3+\xi]\phi(\xi) - 3\right\}. \tag{C.3.5}$$

This formulation is of special interest for RF-heated plasmas where the temperature anisotropy is maintained by the power absorbed in the direction perpendicular to the magnetic field. The anisotropy relaxation frequencies are thus maintained at

the same level and the energy transfer rate from the perpendicular direction to the parallel direction is constant.

Inserting the expressions (C.3.2) and (C.3.4) in the relation (C.1.19), the effective (total) energy transfer frequency of the species α due to collision on all species is defined by

$$\left.\frac{\partial A_\alpha}{\partial t}\right|_{\text{col}} = \sum_\beta \left.\frac{\partial A_\alpha}{\partial t}\right|_{\alpha\beta} = -\nu_{\text{a}}^{\alpha} A_\alpha \tag{C.3.6}$$

and writes

$$\nu_{\text{a}}^{\alpha} = \nu_{\text{a}}^{\alpha/\alpha} + \sum_{\beta\neq\alpha} \nu_{\text{a}}^{\alpha/\beta}. \tag{C.3.7}$$

Here, the plasma was assumed to be homogeneous such that

$$\left.\frac{\partial A_\alpha}{\partial t}\right|_{\alpha\beta} = -\frac{1}{2}\int n_\alpha \nu_{\text{a}}^{\alpha/\beta}(T_{\alpha\perp} - T_{\alpha\parallel})\text{d}V = -\nu_{\text{a}}^{\alpha/\beta} A_\alpha. \tag{C.3.8}$$

For X2 EC-heated L-mode plasmas in TCV, typical densities and temperatures values are $n_{\text{e}} = n_{\text{e}^*} = n_{\text{i}} = 1\cdot 10^{19}$ m^{-3}, $T_{\text{e}} = 2$ keV, $T_{\text{i}} = 1$ keV and $T_{\text{e}^*\perp} = 10$ keV, $T_{\text{e}^*\parallel} = T_{\text{e}}$, and the energy transfer frequencies are:

$$\nu_{\text{a}}^{\text{e}^*/\text{e}} \simeq 2300 \text{ Hz} \tag{C.3.9}$$

$$\nu_{\text{a}}^{\text{e}^*/\text{i}} \simeq 1700 \text{ Hz} \tag{C.3.10}$$

$$\nu_{\text{a}}^{\text{e}^*/\text{e}^*} \simeq 1200 \text{ Hz} \tag{C.3.11}$$

$$\Rightarrow \quad \nu_{\text{a}}^{\text{e}^*} \simeq 5200 \text{ Hz} \qquad \text{and} \qquad \tau_{\text{a}}^{\text{e}^*} \simeq 190 \text{ µs}. \tag{C.3.12}$$

where the anisotropy relaxation time is defined as

$$\tau_{\text{a}}^{\text{e}^*} \equiv \frac{1}{\nu_{\text{a}}^{\text{e}^*}} = \left[\nu_{\text{a}}^{\text{e}^*/\text{e}^*} + \nu_{\text{a}}^{\text{e}^*/\text{e}} + \nu_{\text{a}}^{\text{e}^*/\text{i}}\right]^{-1}. \tag{C.3.13}$$

The isotropization rate of the heated electrons is thus much faster than the plasma incremental confinement time. In all experiments using modulated RF power presented in this work, the modulation frequency applied to the RF power source does not exceed $f = 800$ Hz and is thus much slower than the typical isotropization rate.

C.4 Energy evolution equations

Inserting the expressions (C.1.17), (C.1.18) and (C.3.6) in (C.1.1) and (C.1.2), and using the definition $A_\alpha \equiv \frac{1}{2}W_{\alpha\perp} - W_{\alpha\parallel}$, the plasma perpendicular and parallel energy

evolution equations write

$$\frac{\mathrm{d}W_\perp}{\mathrm{d}t} = -\frac{W_\perp}{\tau_{\mathrm{inc}}} + \eta P_{\mathrm{RF}} - \frac{2}{3}\sum_\alpha \nu_{\mathrm{a}}^\alpha \left(\frac{1}{2}W_{\alpha\perp} - W_{\alpha\parallel}\right) \tag{C.4.1}$$

$$\frac{\mathrm{d}W_\parallel}{\mathrm{d}t} = -\frac{W_\parallel}{\tau_{\mathrm{inc}}} + P_{\mathrm{OH}} + \frac{2}{3}\sum_\alpha \nu_{\mathrm{a}}^\alpha \left(\frac{1}{2}W_{\alpha\perp} - W_{\alpha\parallel}\right). \tag{C.4.2}$$

where ν_{a}^α is a function of the energy anisotropy. Of course, only the species α with anisotropic temperatures contribute with an anisotropy relaxation term to the energy evolution.

In the case of EC heated plasmas, one can consider three populations: the bulk ions with $T_{\mathrm{i}\perp} = T_{\mathrm{i}\parallel} = T_{\mathrm{i}}$, the bulk electron with $T_{\mathrm{e}\perp} = T_{\mathrm{e}\parallel} = T_{\mathrm{e}}$ and the anisotropic heated electrons with $T_{\mathrm{e}^*\perp} > T_{\mathrm{e}^*\parallel} \approx T_{\mathrm{e}}$. The total plasma anisotropy is due only to the hot electrons, i.e.

$$\frac{1}{2}W_\perp - W_\parallel = \frac{1}{2}W_{\mathrm{e}^*\perp} - W_{\mathrm{e}^*\parallel}, \tag{C.4.3}$$

and the energy evolution equations write

$$\frac{\mathrm{d}W_\perp}{\mathrm{d}t} = -\frac{W_\perp}{\tau_{\mathrm{inc}}} + \eta P_{\mathrm{RF}} - \frac{2}{3}\frac{1}{\tau_{\mathrm{a}}^{\mathrm{e}^*}}\left(\frac{1}{2}W_\perp - W_\parallel\right) \tag{C.4.4}$$

$$\frac{\mathrm{d}W_\parallel}{\mathrm{d}t} = -\frac{W_\parallel}{\tau_{\mathrm{inc}}} + P_{\mathrm{OH}} + \frac{2}{3}\frac{1}{\tau_{\mathrm{a}}^{\mathrm{e}^*}}\left(\frac{1}{2}W_\perp - W_\parallel\right). \tag{C.4.5}$$

C.5 Small anisotropy limit

A linear expression for the energy isotropization rate is obtained assuming an isotropic distribution function for the field particles β, i.e. $T_{\beta\perp} = T_{\beta\parallel} \equiv T_\beta$ and a small anisotropy of the α species, i.e. $T_{\alpha\perp} \approx T_{\alpha\parallel} \approx T_\alpha$, where T_α is the equilibrium temperature

$$T_\alpha \equiv \frac{2T_{\alpha\perp} + T_{\alpha\parallel}}{3}, \tag{C.5.1}$$

such that

$$\xi = \frac{m_\beta(T_{\alpha\perp} - T_{\alpha\parallel})}{m_\beta T_{\alpha\parallel} + m_\alpha T_\beta} \ll 1. \tag{C.5.2}$$

The function $\phi(\xi)$ can be developed for a small argument

$$\phi(\xi) \approx 1 - \frac{\xi}{3} + \frac{\xi^2}{5} + \mathcal{O}(\xi^3). \tag{C.5.3}$$

Inserting $\phi(\xi)$ in equations (C.2.10) and (C.2.11) and keeping only the first order in ξ yields

$$\begin{aligned}\left.\frac{\partial T_{\alpha\perp}}{\partial t}\right|_{\alpha\beta} &= \nu_{\alpha\beta}\frac{m_\alpha}{m_\alpha + m_\beta}(T_\beta - T_{\alpha\perp}) \\ &+ \frac{1}{5}\nu_{\alpha\beta}\frac{m_\beta}{m_\alpha + m_\beta}\left(\frac{(m_\alpha - m_\beta)T_{\alpha\perp} - 2m_\alpha T_\beta}{m_\beta T_{\alpha\perp} + m_\alpha T_\beta}\right)(T_{\alpha\perp} - T_{\alpha\parallel})\end{aligned} \tag{C.5.4}$$

$$\left.\frac{\partial T_{\alpha\parallel}}{\partial t}\right|_{\alpha\beta} = \nu_{\alpha\beta}\frac{m_\alpha}{m_\alpha+m_\beta}(T_\beta - T_{\alpha\parallel}) + \frac{1}{5}\nu_{\alpha\beta}\frac{m_\beta}{m_\alpha+m_\beta}\left(\frac{(3m_\alpha+2m_\beta)T_{\alpha\parallel}-2m_\alpha T_\beta}{m_\beta T_{\alpha\parallel}+m_\alpha T_\beta}\right)(T_{\alpha\perp}-T_{\alpha\parallel}). \tag{C.5.5}$$

In these expressions, the first term represents the energy exchange from the α particles to the β particles during the collisions. Obviously, it is negative and yields an energy loss for the α particles if $T_{\alpha\perp} \approx T_{\alpha\parallel} > T_\beta$. The second term represents the energy transfer between the perpendicular and the parallel parts due to the deflection of the α particles momentum during the collisions on the β particles. For the case of the α self-interactions, inserting (C.5.3) in (C.2.20) and (C.2.21) leads to

$$\left.\frac{\partial T_{\alpha\perp}}{\partial t}\right|_{\alpha\alpha} = -\frac{1}{5}\nu_{\alpha\alpha}(T_{\alpha\perp}-T_{\alpha\parallel}) \tag{C.5.6}$$

$$\left.\frac{\partial T_{\alpha\parallel}}{\partial t}\right|_{\alpha\alpha} = -2\left.\frac{\partial T_{\alpha\perp}}{\partial t}\right|_{\alpha\alpha}. \tag{C.5.7}$$

Finally, the net temperature isotropization rates of the α species by collisions on the β particle and on themselves write

$$\left.\frac{\partial (T_{\alpha\perp}-T_{\alpha\parallel})}{\partial t}\right|_{\alpha\beta} = -\frac{1}{5}\nu_{\alpha\beta}\frac{m_\beta}{m_\alpha+m_\beta}\left(\frac{(2m_\alpha+3m_\beta)T_\alpha+3m_\alpha T_\beta}{m_\beta T_\alpha+m_\alpha T_\beta}\right)(T_{\alpha\perp}-T_{\alpha\parallel}) \tag{C.5.8}$$

$$\left.\frac{\partial (T_{\alpha\perp}-T_{\alpha\parallel})}{\partial t}\right|_{\alpha\alpha} = 3\left.\frac{\partial T_{\alpha\perp}}{\partial t}\right|_{\alpha\alpha} = -\frac{3}{5}\nu_{\alpha\alpha}(T_{\alpha\perp}-T_{\alpha\parallel}) \tag{C.5.9}$$

where we used the fact that $T_{\alpha\perp} \approx T_{\alpha\parallel} \approx T_\alpha$. We note that collisions always reduce the temperature anisotropy. One can define isotropization frequencies with

$$\left.\frac{\partial (T_{\alpha\perp}-T_{\alpha\parallel})}{\partial t}\right|_{\alpha\beta} = -\nu_{\mathrm{a}}^{\alpha/\beta}(T_{\alpha\perp}-T_{\alpha\parallel}) \tag{C.5.10}$$

$$\left.\frac{\partial (T_{\alpha\perp}-T_{\alpha\parallel})}{\partial t}\right|_{\alpha\alpha} = -\nu_{\mathrm{a}}^{\alpha/\alpha}(T_{\alpha\perp}-T_{\alpha\parallel}) \tag{C.5.11}$$

such that

$$\nu_{\mathrm{a}}^{\alpha/\beta} = \frac{1}{5}\nu_{\alpha\beta}\frac{m_\beta}{m_\alpha+m_\beta}\left(\frac{(2m_\alpha+3m_\beta)T_\alpha+3m_\alpha T_\beta}{m_\beta T_\alpha+m_\alpha T_\beta}\right) \tag{C.5.12}$$

$$\nu_{\mathrm{a}}^{\alpha/\alpha} = \frac{3}{5}\nu_{\alpha\alpha}. \tag{C.5.13}$$

The small anisotropy assumption thus yields isotropization frequencies which are constant throughout the relaxation process.

Bibliography

[1] M. Bornatici, R. Cano, O. De Barbieri *et al.*, ***Electron cyclotron emission and absorption in fusion plasmas***, *Nuclear Fusion*, vol. 23, no. 9, pp. 1153–1257, 1983. (Cited on pages 1 and 151.)

[2] V. Erckmann and U. Gasparino, ***Electron cyclotron resonance heating and current drive in toroidal fusion plasmas***, *Plasma Physics and Controlled Fusion*, vol. 36, no. 12, pp. 1869–1962, 1994. (Cited on page 1.)

[3] R. Prater, ***Heating and current drive by electron cyclotron waves***, *Physics of Plasmas*, vol. 11, no. 5, pp. 2349–2376, 2004. (Cited on pages 1, 2, 127 and 197.)

[4] M. Lennholm, L.-G. Eriksson, F. Turco *et al.*, ***Demonstration of Effective Control of Fast-Ion-Stabilized Sawteeth by Electron-Cyclotron Current Drive***, *Physical Review Letters*, vol. 102, no. 11, p. 115004, 2009. (Cited on pages 1 and 77.)

[5] H. Zohm, G. Gantenbein, F. Leuterer *et al.*, ***Control of MHD instabilities by ECCD: ASDEX Upgrade results and implications for ITER***, *Nuclear Fusion*, vol. 47, no. 3, pp. 228–232, 2007. (Cited on pages 1 and 77.)

[6] I. B. Bernstein, ***Waves in a Plasma in a Magnetic Field***, *Physical Review*, vol. 109, no. 1, pp. 10–21, 1958. (Cited on pages 2 and 50.)

[7] T. H. Stix, ***Radiation and absorption via mode conversion in an inhomogeneous collision-free plasma***, *Physical Review Letters*, vol. 15, no. 23, pp. 878–882, 1969. (Cited on page 3.)

[8] V. Kopecký, J. Preinhaelter, and J. Václavík, ***Transformation of waves and electron heating in a radially inhomogeneous plasma***, *Journal of Plasma Physics*, vol. 3, no. 2, pp. 179–188, 1969. (Cited on page 3.)

[9] F. S. McDermott, G. Bekefi, K. E. Hackett *et al.*, ***Observation of the parametric decay instability during electron cyclotron resonance heating on the Versator II tokamak***, *Physics of Fluids*, vol. 25, no. 9, pp. 1488–1490, 1982. (Cited on pages 3, 201, 203, 205 and 206.)

[10] D. G. Bulyginskii, V. V. D'yachenko, M. A. Irzak *et al.*, ***Nonlinear phenomena during electron cyclotron heating in the FT-1 tokamak***, *Soviet Journal of Plasma Physics*, vol. 12, no. 2, pp. 77–80, 1986. (Cited on pages 3, 201, 205 and 206.)

[11] V. Shevchenko, Y. Baranov, M. O?Brien *et al.*, ***Generation of Noninductive Current by Electron-Bernstein Waves on the COMPASS-D Tokamak***, *Physical Review Letters*, vol. 89, no. 26, p. 265005, 2002. (Cited on page 3.)

[12] S. Shiraiwa, K. Hanada, M. Hasegawa *et al.*, ***Heating by an Electron Bernstein Wave in a Spherical Tokamak Plasma via Mode Conversion***, *Physical Review Letters*, vol. 96, no. 18, p. 185003, 2006. (Cited on page 3.)

[13] J. Preinhaelter and V. Kopecký, ***Penetration of high-frequency waves into a weakly inhomogeneous magnetized plasma at oblique incidence and their transformation to Bernstein modes***, *Journal of Plasma Physics*, vol. 10, part 1, pp. 1–12, 1973. (Cited on pages 3 and 59.)

[14] J. Preinhaelter, ***Penetration of an ordinary wave into a weakly inhomogeneous magnetoplasma at oblique incidence***, *Czechoslovak Journal of Physics*, vol. B 25, pp. 39–50, 1975. (Cited on pages 3 and 59.)

[15] H. P. Laqua, V. Erckmann, H. J. Hartfuss *et al.*, ***Resonant and Nonresonant Electron Cyclotron Heating at Densities above the Plasma Cutoff by O-X-B Mode Conversion at the W7-AS Stellarator***, *Physical Review Letters*, vol. 78, no. 18, pp. 3467–3470, 1997. (Cited on pages 3, 201, 205 and 206.)

[16] H. P. Laqua, the W7-AS Team, and the ECRH Group, ***Electron Bernstein wave heating and emission via the OXB process in W7-AS***, *Plasma Physics and Controlled Fusion*, vol. 41, no. 3A, pp. A273–A284, 1999. (Cited on page 3.)

[17] H. P. Laqua, H. Maassberg, F. Volpe *et al.*, ***Electron Bernstein wave heating and current drive in overdense plasmas at the W7-AS stellarator***, *Nuclear Fusion*, vol. 43, no. 11, pp. 1324–1328, 2003. (Cited on pages 3 and 195.)

[18] H. P. Laqua, H. Maassberg, N. B. Marushchenko *et al.*, ***Electron-Bernstein-Wave Current Drive in an Overdense Plasma at the Wendelstein 7-AS Stellarator***, *Physical Review Letters*, vol. 90, no. 7, p. 075003, 2003. (Cited on pages 3 and 195.)

[19] F. Volpe, H. P. Laqua, and the W7-AS Team, ***BXO mode-converted electron Bernstein emission diagnostic***, *Review of Scientific Instruments*, vol. 74, no. 3, pp. 1409–1413, 2003. (Cited on pages 3 and 69.)

[20] V. Shevchenko, G. Cunningham, A. Gurchenko *et al.*, ***Development of electron Bernstein wave research in MAST***, *Fusion Science and Technology*, vol. 52, no. 2, pp. 202–215, 2007. (Cited on pages 3, 201, 205 and 206.)

[21] H. P. Laqua, ***Electron Bernstein wave heating and diagnostic***, *Plasma Physics and Controlled Fusion*, vol. 49, no. 4, pp. R1–R42, 2007. (Cited on page 3.)

[22] A. Mueck, L. Curchod, Y. Camenen *et al.*, ***Demonstration of Electron-Bernstein-Wave Heating in a Tokamak via O-X-B Double-Mode Conversion***, *Physical Review Letters*, vol. 98, no. 17, p. 175004, 2007. (Cited on pages 4, 69, 75, 77 and 186.)

[23] A. Mueck, Y. Camenen, S. Coda *et al.*, ***Electron Bernstein wave heating and emission in the TCV tokamak***, *Fusion Science and Technology*, vol. 52, no. 2, pp. 221–229, 2007. (Cited on pages 4, 69, 75 and 186.)

[24] A. Pochelon, A. Mueck, L. Curchod *et al.*, ***Electron Bernstein wave heating of over-dense H-mode plasmas in the TCV tokamak via O-X-B double mode conversion***, *Nuclear Fusion*, vol. 47, no. 11, pp. 1552–1558, 2007. (Cited on pages 4, 69, 75 and 186.)

[25] J. Urban and J. Preinhaelter, ***Adaptive finite elements method for the solution of the Maxwell equations in inhomogeneous magnetized plasma***, *Czechoslovak Journal of Physics*, vol. 54, pp. C109–C115, 2004. (Cited on pages 5 and 60.)

[26] J. Urban and J. Preinhaelter, ***Adaptive finite elements for a set of second-order ODEs***, *Journal of Plasma Physics*, vol. 72, part 6, pp. 1041–1044, 2006. (Cited on pages 5, 60 and 195.)

[27] J. Urban, J. Preinhaelter, S. J. Diem *et al.*, ***EBW Simulations in an Experimental Context***, *Journal of Plasma and Fusion Research SERIES*, vol. 8, pp. 1153–1157, 2009. (Cited on pages 5, 60 and 195.)

[28] E. Z. Gusakov and A. V. Surkov, ***Induced backscattering in an inhomogeneous plasma at the upper hybrid resonance***, *Plasma Physics and Controlled Fusion*, vol. 49, no. 5, pp. 631–639, 2007. (Cited on pages 5, 205 and 207.)

[29] Y. Peysson and J. Decker, ***C3PO, a ray-tracing code for arbitrary axisymmetric magnetic equilibrium***, *EURATOM-CEA report EUR-CEA-FC-1739*, 2008. (Cited on pages 5, 61, 94, 103, 138, 165 and 177.)

[30] J. Decker and Y. Peysson, ***DKE: a fast numerical solver for the 3-D relativistic bounce-averaged electron Drift Kinetic Equation***, *EURATOM-CEA report EUR-CEA-FC-1736*, 2004. (Cited on pages 6, 60, 94, 138 and 195.)

[31] J. Wesson, ***Tokamaks*, 2nd ed.**, ser. *Oxford Engineering Science*. Clarendon Press, Oxford, 1997. (Cited on page 9.)

[32] C. Schlatter, ***Turbulent ion heating in TCV tokamak plasmas***, Ph.D. thesis, no. 4479, Ecole Polytechnique Fédérale de Lausanne (EPFL), CH-1015 Lausanne, Switzerland, July 2009. (Cited on pages 9 and 64.)

[33] J. P. Freidberg, ***Ideal Magnetohydrodynamics***, ser. *Modern Perspectives in Energy*. Plenum Press, New York, 1987. (Cited on page 9.)

[34] R. D. Hazeltine and J. D. Meiss, ***Plasma Confinement***. Dover Publications, Mineola, 2003. (Cited on page 9.)

[35] F. Hofmann, J. B. Lister, M. Anton *et al.*, ***Creation and Control of Variably Shaped Plasmas in TCV***, *Plasma Phys. Control. Fusion*, vol. 12B, pp. B277–B288, 1994. (Cited on pages 9 and 92.)

[36] F. Troyon, R. Gruber, H. Saurenmann *et al.*, ***MHD-limits to plasma confinement***, *Plasma Physics and Controlled Fusion*, vol. 26, no. 1A, pp. 209–215, 1984. (Cited on page 15.)

[37] M. Greenwald, J. L. Terry, S. M. Wolfe *et al.*, ***A new look at density limits in tokamaks***, *Nuclear Fusion*, vol. 28, no. 12, pp. 2199–2207, 1988. (Cited on pages 15, 27 and 51.)

[38] A. Scarabosio, A. Pochelon, and Y. Martin, ***Plasma shape stabilization of current rise MHD instabilities in TCV***, *Plasma Physics and Controlled Fusion*, vol. 49, no. 7, pp. 1041–1060, 2007. (Cited on page 15.)

[39] H. Weisen, J.-M. Moret, S. Franke *et al.*, ***Effect of plasma shape on confinement and MHD behaviour in the TCV tokamak***, *Nuclear Fusion*, vol. 37, no. 12, pp. 1741–1758, 1997. (Cited on page 15.)

[40] Y. Camenen, A. Pochelon, R. Behn *et al.*, ***Impact of plasma triangularity and collisionality on electron heat transport in TCV L-mode plasmas***, *Nuclear Fusion*, vol. 47, no. 7, pp. 510–516, 2007. (Cited on page 15.)

[41] T. P. Goodman and the TCV team, ***Experience in integrated control of the multi-megawatt electron cyclotron heating system on the TCV tokamak: the first decade***, *Nuclear Fusion*, vol. 48, no. 5, p. 054011, 2008. (Cited on page 15.)

[42] T. P. Goodman, S. Alberti, M. A. Henderson *et al.*, ***Design and installation of the electron cyclotron wave system for the TCV tokamak***, in *Proceedings of the 19th Symposium On Fusion Technology (SOFT), Lisbon, Portugal, 16 – 20 September 1996*, vol. 1, 1996, p. 565. (Cited on pages 17 and 92.)

[43] S. Alberti, T. P. Goodman, M. A. Henderson *et al.*, ***Full absorption of third harmonic ECH in TCV tokamak plasmas in the presence of second harmonic ECCD***, *Nuclear Fusion*, vol. 42, no. 1, pp. 42–45, 2002. (Cited on pages 19, 138, 160, 192 and 235.)

[44] J.-P. Hogge, S. Alberti, L. Porte *et al.*, ***Preliminary results of top launch third harmonic X-mode electron cyclotron heating in the TCV tokamak***, *Nuclear Fusion*, vol. 43, no. 11, p. 1353?1360, 2003. (Cited on page 19.)

[45] G. Arnoux, S. Alberti, L. Porte *et al.*, ***Third harmonic X-mode absorption in a top-launch configuration on the TCV tokamak***, *Plasma Physics and Controlled Fusion*, vol. 47, no. 2, pp. 295–314, 2005. (Cited on page 19.)

[46] G. Bekefi, ***Radiation processes in plasmas*, 2nd ed.**, ser. *Wiley series in plasma physics*. John Wiley and Sons, New York-London-Sidney, 1966. (Cited on page 20.)

[47] I. H. Hutchinson, ***Principles of plasma diagnostics*, 2nd ed.** Cambridge University Press, Cambridge, United Kingdom, 2002. (Cited on pages 20, 21, 22 and 26.)

[48] A. Sushkov, V. Andreev, Y. Camenen *et al.*, ***High-resolution multiwire proportional soft X-ray diagnostic measurements on TCV***, *Review of Scientific Instruments*, vol. 79, no. 2, p. 023506, 2008. (Cited on page 22.)

[49] Y. Camenen, ***Etude du transport d'énergie thermique dans les plasmas du Tokamak à Configuration Variable au moyen de chauffage électronique cyclotronique***, Ph.D. thesis, no. 3618, Ecole Polytechnique Fédérale de Lausanne (EPFL), CH-1015 Lausanne, Switzerland, November 2006. (Cited on page 22.)

[50] G. Charpak, R. Bouclier, T. Bressani *et al.*, ***The use of multiwire proportional counters to select and localize charged particles***, *Nuclear Instruments and Methods*, vol. 62, no. 3, pp. 262–268, 1968. (Cited on page 22.)

[51] R. Behn, S. Franke, and Z. A. Pietrzyk, ***The Thomson scattering diagnostic on the TCV tokamak***, in *Proceedings of the 21st EPS Conference on Controlled Fusion and Plasma Physics, Montpellier, France, 27 June – 1 July 1994*, ser. *Europhysics Conference Abstracts (ECA)*, vol. 18B. European Physical Society (EPS), 1994, pp. 1251–1255. (Cited on page 24.)

[52] R. Behn, S. Franke, Z. A. Pietrzyk *et al.*, ***The Thomson Scattering Diagnostic on TCV***, in *Proceedings of the 7th International Symposium on Laser-aided Plasma Diagnostics (LAPD), Fukuoka, Japan, 5 – 8 December 1995*, M. Muruoka, Ed., Fukuoka, Japan, 1995, pp. 392–397. (Cited on page 24.)

[53] S. Franke, ***Application of Thomson scattering at 1.06 μm as a diagnostic for spatial profile measurements of electron temperature and density on the TCV tokamak***, Ph.D. thesis, no. 1654, Ecole Polytechnique Fédérale de Lausanne (EPFL), CH-1015 Lausanne, Switzerland, 1997. (Cited on page 24.)

[54] R. Behn, J. H. Rommers, R. A. Pitts *et al.*, ***A Thomson scattering diagnostic for measurements in the divertor region of TCV***, *Review of Scientific Instruments*, vol. 70, no. 1, pp. 768–771, 1999. (Cited on page 24.)

[55] R. Behn, A. Alfier, S. Y. Medvedev *et al.*, ***Edge profiles of electron temperature and density during ELMy H-mode in ohmically heated TCV plasmas***, *Plasma Physics and Controlled Fusion*, vol. 49, no. 8, pp. 1289–1308, 2007. (Cited on pages 24 and 27.)

[56] S. Barry, C. Nieswand, and S. L. Prunty, ***Far-infrared polarimetry on the TCV tokamak***, in *Proceedings of the 8th International Symposium on Laser-aided Plasma Diagnostics (LAPD), Doorwerth, The Netherlands, 22 – 26 September 1997*, 1997, pp. 313–318. (Cited on page 25.)

[57] S. Barry, ***The extension of the FIR interferometer of TCV to a polarimeter and measurements of the Faraday rotation caused by the poloidal magnetic field***, Ph.D. thesis, National University of Ireland, Cork, Ireland, 1999, also as Lausanne Plasma Report LRP 638/99. (Cited on page 25.)

[58] F. Wagner, G. Becker, K. Behringer *et al.*, ***Regime of Improved Confinement and High Beta in Neutral-Beam-Heated Divertor Discharges of the ASDEX Tokamak***, *Physical Review Letter*, vol. 49, no. 19, pp. 1408–1412, 1982. (Cited on page 26.)

[59] F. Wagner, ***A quarter-century of H-mode studies***, *Plasma Physics and Controlled Fusion*, vol. 49, no. 12B, pp. B1–B33, 2007. (Cited on page 26.)

[60] J. W. Hughes, D. A. Mossessian, A. E. Hubbard *et al.*, ***Observations and empirical scalings of the high-confinement mode pedestal on Alcator C-Mod***, *Physics of Plasmas*, vol. 9, no. 7, pp. 3019–3030, 2002. (Cited on page 26.)

[61] H. Zohm, ***Edge localized modes (ELMs)***, *Plasma Physics and Controlled Fusion*, vol. 38, no. 2, pp. 105–128, 1996. (Cited on page 26.)

[62] J. W. Connor, ***Edge-localized modes – physics and theory***, *Plasma Physics and Controlled Fusion*, vol. 40, no. 5, pp. 531–542, 1998. (Cited on page 26.)

[63] H. Weisen, F. Hofmann, M. J. Dutch *et al.*, ***Ohmic H-modes in the TCV tokamak***, *Plasma Physics and Controlled Fusion*, vol. 38, no. 8, pp. 1137–1148, 1996. (Cited on pages 26 and 27.)

[64] Y. R. Martin, L. Porte, and S. Alberti, ***Third harmonic EC heating of ELMy H-mode in TCV***, *Plasma Physics and Controlled Fusion*, vol. 48, no. 5A, pp. A163–A169, 2006. (Cited on page 27.)

[65] A. Pitzschke, ***Pedestal Characteristics and MHD Stability of H-Mode Plasmas in TCV***, Ph.D. thesis, no. 4917, Ecole Polytechnique Fédérale de Lausanne (EPFL), CH-1015 Lausanne, Switzerland, December 2010. (Cited on page 27.)

[66] M. Brambilla, ***Kinetic Theory of Plasma Waves: Homogeneous Plasmas***, ser. *International series of monographs on physics*, vol. 96. Oxford Science Publications, Oxford, 1998. (Cited on pages 33, 36, 38, 41, 42, 50 and 60.)

[67] T. H. Stix, ***Waves in Plasmas***. American Institute of Physics, Springer-Verlag, New York, 1992. (Cited on pages 33, 46 and 50.)

[68] D. G. Swanson, ***Plasma Waves***. Academic Press, San Diego, 1989. (Cited on page 33.)

[69] P. C. Clemmow and J. P. Dougherty, ***Electrodynamics of Particles and Plasmas***, ser. *Advanced Physics*. Addison-Wesley, London, 1969. (Cited on pages 43 and 46.)

[70] J. D. Jackson, ***Classical Electrodynamics*, 3rd ed.** John Wiley & Sons, New York, 1999. (Cited on page 53.)

[71] F. R. Hansen, J. P. Lynov, and P. Michelsen, ***The O-X-B mode conversion scheme for ECRH of a high-density tokamak plasma***, *Plasma Physics and Controlled Fusion*, vol. 27, no. 10, pp. 1077–1100, 1985. (Cited on page 56.)

[72] F. R. Hansen, J. P. Lynov, C. Maroli *et al.*, ***Full-wave calculations of the O-X mode conversion process***, *Journal of Plasma Physics*, vol. 39, part 2, pp. 319–337, 1988. (Cited on pages 59 and 60.)

[73] E. Mjølhus, ***Coupling to Z mode near critical angle***, *Journal of Plasma Physics*, vol. 31, part 1, pp. 7–28, 1984. (Cited on page 59.)

[74] P. Pavlo, L. Krlín, and Z. Tlučhoř, ***Effects of magnetized alpha particles on lower hybrid heating and current drive in a reactor grade plasma***, *Nuclear Fusion*, vol. 31, no. 4, pp. 711–727, 1991. (Cited on page 61.)

[75] J. Decker and A. K. Ram, ***Relativistic description of electron Bernstein waves***, *Physics of Plasmas*, vol. 13, no. 11, p. 112503, 2006. (Cited on page 61.)

[76] A. N. Karpushov, B. P. Duval, R. Chavan *et al.*, ***On the possibility of neutral beam heating on the TCV tokamak***, *Fusion Engineering and Design*, 2010, proceedings of the 26th Symposium on Fusion Technology (SOFT), Porto, Portugal, 27 September – 1 October 2010, poster P1-54. To be published. (Cited on page 64.)

[77] F. Volpe, ***Electron Bernstein emission diagnostic of electron temperature profile at W7-AS Stellarator***, Ph.D. thesis, Ernst Moritz Arndt Universität, D-17487 Greifswald, Germany, March 2003, [Report 13/1, Max-Planck-Institut für Plasmaphysik, D-85748 Garching, Germany]. (Cited on page 69.)

[78] C. Angioni, T. P. Goodman, M. A. Henderson *et al.*, ***Effects of localized electron heating and current drive on the sawtooth period***, *Nuclear Fusion*, vol. 43, no. 6, pp. 455–468, 2003. (Cited on pages 77 and 199.)

[79] R. J. La Haye, A. Isayama, and M. Maraschek, ***Prospects for stabilization of neoclassical tearing modes by electron cyclotron current drive in ITER***, *Nuclear Fusion*, vol. 49, no. 4, p. 045005, 2009. (Cited on page 77.)

[80] A. Manini, J.-M. Moret, F. Ryter *et al.*, ***Signal processing techniques based on singular value decomposition applied to modulated ECH experiments***, *Nuclear Fusion*, vol. 43, no. 6, pp. 490–511, 2003. (Cited on page 77.)

[81] J.-M. Moret, T. Dudok de Wit, B. Joye *et al.*, ***Investigation of plasma transport processes using the dynamical response of soft X ray emission***, *Nuclear Fusion*, vol. 33, no. 8, pp. 1185–1200, 1993. (Cited on pages 77, 80 and 134.)

[82] J. Berrino, S. Cirant, F. Gandini *et al.*, ***Automatic Real-Time Tracking and Stabilization of Magnetic Islands in a Tokamak Using Tem-***

perature Fluctuations and ECW Power, *IEEE Transactions on Nuclear Science*, vol. 53, no. 3, pp. 1009–1014, 2006. (Cited on page 77.)

[83] J. I. Paley, F. Felici, S. Coda *et al.*, ***Real time control of the sawtooth period using EC launchers***, *Plasma Physics and Controlled Fusion*, vol. 51, no. 5, p. 055010, 2009. (Cited on page 77.)

[84] D. J. Gambier, M. P. Evrard, J. Adam *et al.*, ***ICRF power deposition profile and determination of the electron thermal diffusivity by modulation experiments in JET***, *Nuclear Fusion*, vol. 30, no. 1, pp. 23–34, 1990. (Cited on page 78.)

[85] J.-M. Moret, ***Etude de la réponse dynamique du plasma de TCA et ses conséquences sur la compréhension du confinement et du chauffage***, Ph.D. thesis, no. 758, Ecole Polytechnique Fédérale de Lausanne (EPFL), CH-1015 Lausanne, Switzerland, 1988. (Cited on page 80.)

[86] D. Van Eester, ***A minimization procedure for estimating the power deposition and heat transport from the temperature response to auxiliary power modulation***, *Plasma Physics and Controlled Fusion*, vol. 46, no. 11, pp. 1675–1697, 2004. (Cited on page 81.)

[87] E. A. Lerche, D. Van Eester, and JET EFDA contributors, ***Improved break-in-slope analysis of the plasma energy response in tokamaks***, *Plasma Physics and Controlled Fusion*, vol. 50, no. 3, p. 035003, 2008. (Cited on page 82.)

[88] S. Gnesin, J. Decker, T. P. Goodman *et al.*, ***Synergy of 2nd and 3rd harmonic electron cyclotron absorption mediated by suprathermal electrons in the TCV tokamak***, in *Proceedings of the 36th EPS Conference on Controlled Fusion and Plasma Physics, Sofia, Bulgaria, 29 June – 3 July 2009*, ser. *Europhysics Conference Abstracts (ECA)*, M. Mateev and E. Benova, Eds., vol. 33E. European Physical Society (EPS), 2009, pp. P.2–139. (Cited on page 83.)

[89] C. W. Simm, ***Etude comparative des disruptions internes avec chauffage additionnel par ondes d'Alfvén, dans le plasma du tokamak TCA***, Ph.D. thesis, no. 696, Ecole Polytechnique Fédérale de Lausanne (EPFL), CH-1015 Lausanne, Switzerland, 1987. (Cited on page 98.)

[90] D. Lebeau, R. Koch, A. M. Messiaen *et al.*, ***ICRH power absorption measurements from analysis of RF sinusoidal low-frequency modulation experiments in TEXTOR***, *Plasma Physics and Controlled Fusion*, vol. 37, no. 10, pp. 1141–1168, 1995. (Cited on pages 116, 127, 128 and 272.)

[91] J.-M. Moret, F. Buhlmann, and G. Tonetti, ***Fast single loop diamagnetic measurements on the TCV tokamak***, *Review of Scientific Instruments*, vol. 74, no. 11, pp. 4634–4643, 2003. (Cited on pages 117, 119 and 247.)

[92] V. D. Shafranov, ***Determination of the parameters β_I and ℓ_i in a tokamak for arbitrary shape of plasma pinch cross-section***, *Plasma Physics*, vol. 13, no. 9, pp. 757–762, 1971. (Cited on pages 122, 250, 254, 257, 258, 259, 260 and 261.)

[93] B. P. Duval, A. Bortolon, A. Karpushov *et al.*, ***Bulk plasma rotation in the TCV tokamak in the absence of external momentum input***, *Plasma Physics and Controlled Fusion*, vol. 49, no. 12B, pp. B195–B209, 2007. (Cited on page 123.)

[94] L. L. Lao, H. S. John, R. D. Stambaugh *et al.*, ***Separation of $\bar{\beta}_p$ and ℓ_i in tokamaks of non-circular cross-section***, *Nuclear Fusion*, vol. 25, no. 10, pp. 1421–1436, 1985. (Cited on pages 124, 253, 258, 259, 260, 261, 262, 265, 267 and 268.)

[95] J.-M. Moret, ***Fitting of transfer functions to frequency response measurements***, CRPP/EPFL, CH-1015 Lausanne, LRP 498, December 1994. (Cited on page 134.)

[96] A. Jacchia, F. de Luca, G. M. D. Hogeweij *et al.*, ***Simultaneous analysis of ECH modulation and sawtooth activity in the plasma core of the RTP tokamak***, *Nuclear Fusion*, vol. 34, no. 12, pp. 1629–1639, 1994. (Cited on pages 136 and 155.)

[97] A. Manini, ***Analysis and interpretation of the plasma dynamic response to additional heating power using different diagnostics***, Ph.D. thesis, no. 2599, Ecole Polytechnique Fédérale de Lausanne (EPFL), CH-1015 Lausanne, Switzerland, July 2002. (Cited on pages 138, 148, 160 and 192.)

[98] A. Manini, J.-M. Moret, S. Alberti *et al.*, ***Modulated ECH power absorption measurements using a diamagnetic loop in the TCV tokamak***,

Plasma Physics and Controlled Fusion, vol. 44, no. 2, pp. 139–157, 2002. (Cited on pages 138, 148, 160, 192 and 235.)

[99] J. Decker, S. Coda, Y. Peysson *et al.*, ***Modeling of third harmonic ECRH experiments in TCV***, in *Proceedings of the 37th EPS Conference on Controlled Fusion and Plasma Physics, Dublin, Ireland, 21 – 25 June 2010*, ser. *Europhysics Conference Abstracts (ECA)*, C. McKenna, Ed., vol. 34A. European Physical Society (EPS), 2010, p. P5.149. (Cited on page 161.)

[100] J. Decker, A. K. Ram, Y. Peysson *et al.*, ***Electron Bernstein Wave Heating and Current Drive in Axisymmetric Toroidal Plasmas***, in *Proceedings of the 35th EPS Conference on Controlled Fusion and Plasma Physics, Hersonissos, Crete, Greece, 9 – 13 June, 2008*, ser. *Europhysics Conference Abstracts (ECA)*, P. Lalousis and S. Moustaizis, Eds., vol. 32D. European Physical Society (EPS), 2008, p. P1.099. (Cited on page 198.)

[101] A. Surkov, G. Cunningham, A. Gurchenko *et al.*, ***Parametric decay instability accompanying electron Bernstein wave heating in MAST***, in *Proceedings of the 32th EPS Conference on Controlled Fusion and Plasma Physics, Tarragona, Spain, 21 – 25 June 2010*, ser. *Europhysics Conference Abstracts (ECA)*, C. Hidalgo and B. P. van Milligen, Eds., vol. 29C. European Physical Society (EPS), 2005, p. P5.103. (Cited on pages 201, 205 and 206.)

[102] M. Porkolab and R. P. H. Chang, ***Nonlinear wave effects in laboratory plasmas: A comparison between theory and experiment***, *Review of Modern Physics*, vol. 50, no. 4, pp. 745–795, 1978. (Cited on pages 202, 203 and 229.)

[103] J.-M. Moret, F. Buhlmann, D. Fasel *et al.*, ***Magnetic measurements on the TCV Tokamak***, *Review of Scientific Instruments*, vol. 69, no. 6, pp. 2333–2348, 1998. (Cited on page 242.)

[104] L. E. Zakharov and V. D. Shafranov, ***Equilibrium of a toroidal plasma with noncircular cross section***, *Soviet Physics Technical Physics*, vol. 18, no. 2, pp. 151–156, 1973. (Cited on pages 250, 254, 259, 260 and 261.)

[105] W. A. Cooper and A. J. Wootton, ***β_p Analysis for Tokamak Plasma With Anisotropic Pressure and Mass Flow***, *Plasma Physics*, vol. 24, no. 9, pp. 1183–1185, 1982. (Cited on pages 250, 253, 254, 256, 258, 259, 260 and 261.)

[106] V. D. Shafranov, ***Plasma equilibrium in a magnetic field***, ser. *Reviews of Plasma Physics*, vol. 2, M. A. Leontovich, Ed. Consultants Bureau, New York, 1966. (Cited on pages 250 and 255.)

[107] B. J. Braams, ***The interpretation of tokamak magnetic diagnostics***, *Plasma Physics and Controlled Fusion*, vol. 33, no. 7, pp. 715–748, 1991. (Cited on pages 253, 254, 257 and 259.)

[108] J.-M. Moret, ***Relaxation et transport dans un plasma*, 3rd ed.**, EPFL, Lausanne, 2008, course notes given in the frame of the Physics Doctoral School. (Cited on page 274.)

[109] H. Schamel, H. Hamnén, D. F. Düchs *et al.*, ***Nonlinear analysis of Coulomb relaxation of anisotropic distributions***, *Physics of Fluids B*, vol. 1, no. 1, pp. 76–86, 1989. (Cited on pages 274 and 276.)

[110] P. Hellinger and P. M. Trávníček, ***On Coulomb collisions in bi-Maxwellian plasmas***, *Physics of Plasmas*, vol. 16, no. 5, p. 054501, 2009. (Cited on page 275.)

[111] G. Lehner, ***On the Relaxation of Anisotropic Plasmas***, *Zeitschrift für Physik*, vol. 206, pp. 284–292, 1967. (Cited on page 276.)

[112] V. I. Kogan, ***The rate of equalization of the temperatures of charged particles in a plasma***, ser. *Plasma physics and the problem of controlled thermonuclear reactions*, vol. 1, M. A. Leontovich, Ed. Pergamon Press, New York, 1961. (Cited on page 276.)

[113] B. A. Trubnikov, ***Particle interactions in a fully ionized plasma***, ser. *Reviews of Plasma Physics*, vol. 1, M. A. Leontovich, Ed. Consultants Bureau, New York, 1965. (Cited on page 276.)

Remerciements

Mes premiers remerciements vont bien sûr à mon superviseur, Antoine Pochelon, dont la curiosité et l'enthousiasme inébranlables ont toujours été sources d'inspiration malgré nos occasionnelles divergences de vue. Il a su ouvrir de nouvelles voies lorsque la route semblait bloquée. Et la grande liberté dont j'ai joui m'a permis de gagner en indépendance, qualité dont je manquais cruellement au début de cette aventure. Merci aussi pour ces précieuses digressions extra-physiques, musicales et littéraires : les râgas envoûtants de Sheila Dhar et les périples de Nicolas Bouvier m'ont accompagné tout au long de l'écriture de la thèse.

Un travail de thèse ne se réalise pas sans l'apport inestimable des collègues, en particulier lorsque l'étude porte sur une machine aussi importante que TCV. Au CRPP, les chercheurs "seniors" gardent leur porte ouverte en permanence et sont prêts à donner beaucoup de leur temps pour aider les étudiants. Ma gratitude va tout particulièrement à Basil Duval. Toujours clairvoyant, il a su comprendre lorsque je me sentais perdu, lorsque la motivation me quittait, et trouver les mots justes pour me remettre sur les rails. Merci, car j'ai beaucoup appris sur moi-même... et sur l'humour britannique !

Merci aussi à Jean-Marc Moret avec qui j'ai partagé de longues et nombreuses discussions au sujet de la DML... et des couleurs chez Messiaen. Il fallait beaucoup de patience pour répondre à toutes mes questions. Et je regretterai longtemps nos conversations musicales.

Mes remerciements vont ensuite à l'équipe "ECH" de TCV : Laurie Porte, Stefano Alberti, Mark Henderson et en particulier Timothy Goodman qui m'a donné beaucoup de son précieux temps. Merci de m'avoir toujours accueilli avec un réel intérêt et beaucoup d'humour. Merci aussi à Miguel Silva, "gyrotroniste" en or, toujours calme, disponible et prêt à résoudre les problèmes. Mes dernières sessions expérimentales n'auraient pas été réussies sans son aide inestimable.

Merci encore aux autres membres de l'équipe du tokamak, en particulier à Stefano Coda, qui font que TCV est une expérience vivante, malgré des temps parfois diffi-

ciles.

J'aimerais ensuite remercier les ateliers de dessin, de mécanique, d'électricité et d'électronique pour leur travail et leur aide lors de la conception et de l'installation du nouveau diagnostique LHPI présenté dans cette thèse. Merci en particulier à René Chavan, Guy Pochon, William Matthey-Doret, Christian Moura, Jean-Pierre Baertschi, Pascal Conti, Frédéric Dolizy, Damien Fasel et Philippe Marmillod.

Merci ensuite à tous mes collègues doctorants en général, et à mes collègues de bureau en particulier : Andreas, Theo, Federico, Silvano, Yann, Gilles, Andrea, Gustavo, Joseph, Gaël, Sun Hee, Gennady, Alexander. Que serait la vie sociale du CRPP sans les apéros endiablés, les tournois de pétanques (merci Benoît !), les séminaires doctorants et les pauses café ? Un merci spécial à Anja Mueck et Yann Camenen pour tout le temps qu'ils m'ont donné pendant ma première année de thèse, ainsi qu'à Christian Schlatter pour l'aide qu'il m'a généreusement offerte pour le diagnostique LHPI et bien d'autres choses.

I would like then to thank my international collaborators and friends, Joan Decker and Jakub Urban, for their wonderful work to provide the TCV team with a reliable EBW simulation tool. Their continuous help and patience with my many questions made this project possible.

Many thanks to Prabal Chattopadhyay whose visits at CRPP have been highlights of my thesis project. His always friendly and wise advices have been of a special value to me. I have learned a lot while working with him on the LHPI project. And I will never forget our long tea-chats and the wonderful indian meals we have cooked together and shared!

I express my sincerest gratitude to the thesis jury members for their interest in my work, in particular to Heinrich Laqua for the precious advices he gave me since the very beginning of this work. I also would like to specially acknowledge Stefan Brunner for his detailed reading of the manuscript and his priceless comments!

Merci à Henri Weisen, Minh Quang Tran et en particulier Ambrogio Fasoli pour la reconnaissance dont ils ont fait preuve à l'égard de mon travail d'assistant, ainsi que pour m'avoir offert de les remplacer en cours ex-cathedra lors des leurs absences. Les séances d'exercice passées avec les étudiants font partie de mes meilleurs souvenirs professionnels à l'EPFL.

Mes remerciements vont aussi à la direction du CRPP et tout spécialement à Yves Martin pour la confiance qu'il m'a donnée dans le cadre de la "Fusion Energy Conference" organisée par le CRPP dans les murs de l'ONU à Genève en octobre 2008. La responsabilité du catering et du repas de gala n'était pas une mince affaire, mais

assurément une expérience professionnelle de grande valeur.
Un immense merci à toute l'équipe du secrétariat du CRPP, avec une mention particulière pour Edith Grueter qui sait écouter les doctorants et leur faciliter les tâches administratives. Merci à Anh Eymann-Nguyen qui suit les doctorants en physique tout au long de leur cursus, avec une bienveillance quasi maternelle.
Je pense aussi à tous mes amis qui m'ont apporté leur soutien inconditionnel, surtout dans les périodes de doute : Guillaume et Verena, Guillaume et Véronique, Pierre-Yves et Marc-Henri, Pierre Macquat, Micaël et Laura, Sébastien, Philippe et Gabriela, Laurent et Raphaël, Olivier et Vincent, Florian, Didier, Eric et Serge, David et Marin, et l'équipe des repas du mardi : Martin, Mathias, Géraldine, Claude et Daniel. Et bien sûr mon équipe de volley ABFAB ainsi que mon professeur de violoncelle Pascal Desarzens qui m'ont prodigué les bouffées d'oxygène nécessaires pour avancer sereinement.
Je ne remercierai jamais assez ma famille, en particulier ma soeur, mon frère et mes parents qui ont toujours cru en moi et ont montré un intérêt constant dans mon travail. Je vous aime !
Finalement, le plus grand des MERCIS à ma tendre moitié, Nicolas, qui m'a accompagné tout au long de ces cinq années parfois difficiles et sans qui je n'aurais pas terminé ce travail. Avec sa patience d'ange (il en fallait !), il a su me guider dans les moments de doutes, m'imposer des vacances quand j'en avais besoin, être ma deuxième tête lorsque j'oubliais tout et m'entourer de tout son amour, quoiqu'il arrive. J'espère que les cinq prochaines années seront aussi belles que les premières !

Publications and contributions

Refereed journal articles

- L. Curchod, P. K. Chattopadhyay, A. Pochelon *et al.*, ***Observations of the lower-hybrid parametric instability in high power EBH experiments in the TCV tokamak***, in preparation for submission.

- L. Curchod, F. Felici, A. Pochelon *et al.*, ***Multiple EC power deposition locations tracking by break-in-slope analysis in TCV plasmas***, submitted for publication in *Plasma Physics and Controlled Fusion*.

- N. A. Kirneva, K. A. Razumova, A. Pochelon *et al.* (including L. Curchod), ***Dependence of L-mode confinement on the EC power deposition profile in the TCV tokamak***, submitted for publication in *Plasma Physics and Controlled Fusion*.

- A. Mueck, L. Curchod, Y. Camenen *et al.*, ***Demonstration of Electron-Bernstein-Wave Heating in a Tokamak via O-X-B Double-Mode Conversion***, *Physical Review Letters*, vol. 98, no. 17, p. 175004, 2007.

- A. Mueck, Y. Camenen, S. Coda *et al.* (including L. Curchod), ***Electron Bernstein wave heating and emission in the TCV tokamak***, *Fusion Science and Technology*, vol. 52, no. 2, pp. 221–229, 2007.

- A. Pochelon, A. Mueck, L. Curchod *et al.*, ***Electron Bernstein wave heating of over-dense H-mode plasmas in the TCV tokamak via O-X-B double mode conversion***, *Nuclear Fusion*, vol. 47, no. 11, pp. 1552–1558, 2007.

Conference proceedings

- M. G. Sevillano, I. Garrido, A. Garrido *et al.* (including L. Curchod), ***Observer-based real-time control for the poloidal beta of the plasma using diamagnetic measurements in tokamak fusion reactors***, contributed paper 168 presented at the 50th IEEE Conference on Decision and Control and European Control Conference, Orlando, Florida, USA, 12 – 15 December 2011.

- J. Decker, Y. Peysson, S. Coda, L. Curchod *et al.*, ***Fast electrons physics in tokamak plasmas***, contributed paper I-2 presented at the 20th International Toki Conference (ITC-20), Ceratopia Toki, Toki-City, Gifu, Japan, 7 – 10 December 2010.

- J. Decker, S. Coda, Y. Peysson *et al.* (including L. Curchod), ***Modeling of third harmonic ECRH experiments in TCV***, in *Proceedings of the 37th EPS Conference on Controlled Fusion and Plasma Physics, Dublin, Ireland, 21 – 25 June 2010*, ser. *Europhysics Conference Abstracts (ECA)*, C. McKenna, Ed., vol. 34A. European Physical Society (EPS), 2010, p. P5.149.

- L. Curchod, A. Pochelon, J. Decker *et al.*, ***Simultaneous Power Deposition Detection of Two EC Beams with the BIS Analysis in Moving TCV Plasmas***, in *Proceedings of the 18th Topical Conference on Radio Frequency Power in Plasmas, Gent, Belgium, 24 – 26 June 2009*, ser. *American Institute of Physics (AIP) Conference Proceedings*, V. Bobkov and J.-M. Noterdaeme, Eds., vol. 1187. American Institute of Physics (AIP), 2009, pp. 515-518.

- J. I. Paley, F. Felici, L. Curchod *et al.*, ***Real Time Control of EC Heating and Current Drive Systems on TCV***, contributed paper presented at the 5th IAEA Technical meeting on ECRH Physics and Technology for Large Fusion Devices, Gandhinagar, India, 18 – 20 February 2009.

- L. Curchod, A. Pochelon, S. Coda *et al.*, ***Electron Bernstein Wave Core Deposition via O-X-B double mode conversion in the TCV tokamak***, contributed paper presented at the Swiss Physical Society Annual Meeting, Geneva, Switzerland, 26 – 27 March, 2008.

- J. Decker, A. K. Ram, Y. Peysson *et al.* (including L. Curchod), ***Electron Bernstein Wave Heating and Current Drive in Axisymmetric Toroidal Plasmas***, in *Proceedings of the 35th EPS Conference on Controlled Fusion and Plasma Physics, Hersonissos, Crete, Greece, 9 – 13 June, 2008*, ser. *Europhysics Conference Abstracts (ECA)*, P. Lalousis and S. Moustaizis Eds., vol. 32D. European Physical Society (EPS), 2008, p. P1.099.

- A. Pochelon, Y. Camenen, A. Marinoni *et al.* (including L. Curchod), ***Physics Insight and Performance Benefit from Plasma Shaping Experiments in MHD and Energy Transport in the TCV Tokamak***, contributed paper EX/P5.15 presented at the 22nd IAEA Fusion Energy Conference, Geneva, Switzerland, 13 – 18 October 2008.

- L. Curchod, A. Mueck, A. Pochelon *et al.*, ***Optimizing Central Electron Bernstein Wave Deposition via O-X-B Double Mode Conversion in the TCV Tokamak***, in *Proceedings of the 34th EPS Conference on Controlled Fusion and Plasma Physics, Warsaw, Poland, 2 – 6 July, 2007*, ser. *Europhysics Conference Abstracts (ECA)*, P. Gąsior and J. Wołowski Eds., vol. 31F. European Physical Society (EPS), 2007, p. P5.052.

- A. Mueck, Y. Camenen, S. Coda, L. Curchod *et al.*, ***Electron Bernstein Wave Heating and Emission in the TCV Tokamak***, in *Proceedings of the 33th EPS Conference on Controlled Fusion and Plasma Physics, Rome, Italy, 19 – 23 June, 2006*, ser. *Europhysics Conference Abstracts (ECA)*, F. De Marco and G. Vlad Eds., vol. 30I. European Physical Society (EPS), 2006, p. P1.153.

- A. Mueck, Y. Camenen, S. Coda, L. Curchod *et al.*, ***Electron Bernstein Wave Heating in the TCV Tokamak***, in *Proceedings of the 14th Joint Workshop on Electron Cyclotron Emission and Electron Cyclotron Resonance Heating, Santorini Island, Greece, 9 – 12 May, 2006*, A. Lazaros Ed., Heliotopos Conferences, 2006.

- A. Pochelon, A. Mueck, Y. Camenen *et al.* (including L. Curchod), ***Electron Bernstein Wave Heating of High Density H-modes in the TCV Tokamak***, contributed paper EX/P6.2 presented at the 21st IAEA Fusion Energy Conference, Chengdu, China, 16 – 21 October 2006.

Loïc Curchod

Graduate physicist

EPFL CRPP
Station 13
CH-1015 Lausanne
Switzerland
✉ *loic.curchod@epfl.ch*
Born 23rd January 1983
Swiss

Education

05/2006 – 04/2011 **Ph.D. thesis in Physics**, *École Polytechnique Fédérale de Lausanne (EPFL)*, Switzerland.

09/2001 – 04/2006 **Master of Science in Physics**, *École Polytechnique Fédérale de Lausanne (EPFL)*, Switzerland.

08/2003 – 06/2004 **Academic exchange year**, *Carnegie Mellon University (CMU)*, Pittsburgh, USA.

Ph.D. thesis

Institute: Centre de Recherches en Physique des Plasmas, EPFL, Switzerland

Title: *High density plasma heating in the Tokamak à Configuration Variable*

Description: Demonstration of microwave power coupling to over-dense plasmas in an experimental thermonuclear fusion device.

- Development of methods for the measurement of the microwave power absorption.
- Development of data analysis tools in MATLAB©.
- Numerical simulations of the coupling, the propagation and the absorption of the microwaves in the plasma.
- Design, construction and initial exploitation of an antenna for the detection of non-linear wave effects.

Publications

L. Curchod et al., *Plasma Physics and Controlled Fusion*, (2011), submitted for publication

A. Mueck, L. Curchod et al., *Physical Review Letter* **98**, 175004 (2007)

A. Mueck, Y. Camenen, S. Coda, L. Curchod et al., *Fusion Science and Technology* **52**, 221 (2007)

A. Pochelon, A. Mueck, L. Curchod et al., *Nuclear Fusion* **47**, 1552 (2007)

Professional experience

05/2006 – 03/2011 **Assistantship and teaching**, *EPFL*, Switzerland.
First assistant: organization and support of physics exercise sessions for undergraduate students (mechanical engineering, computer sciences, mathematics and life sciences). Web site manager. Professor substitute (ex-cathedra lectures in front of 150 students).
Competences involved: teaching, communication, altruism, leadership

summers 2005 – 2009 **Music festival**, *Verbier Festival and Academy*, Verbier, Switzerland.
Staff member in one of Europe's major classical music festivals. Responsible officer of the *Windows on the Orchestra* concerts: stage management, organization of artists and instruments transport, audience welcoming, programs preparation.
Competences involved: dynamism, logistic, flexibility, endurance

10/2008 **Conference organization**, *22nd IAEA Fusion Energy Conference*, United Nations Organization, Geneva, Switzerland.
Member of the local organization committee, responsible officer for the catering (1 week, 800 participants). Organization of the welcome reception, the gala dinner (300 guests) and a piano concert
Competences involved: communication, logistic, creativity

06 – 09/2004 **Industry internship**, *idQuantique S.A.*, Carouge (Geneva), Switzerland.
Design and realization of a test bench for single photon detectors. Automatized test procedure using LabView©.
Competences involved: fast learning, creativity

Languages

French	**Native**	
English	**Fluent**	*One academic year in the USA. Work in an English speaking institute and scientific domain.*
German	**Elementary**	*8 years of school and high school education.*

Computer skills

Operating system	*MacOSX, Windows, UNIX*	Programming	*Basic skills in C/C++, Fortran*
Scientific	*Matlab, LabView, Mathematica*	Typography and graphics	*LaTeX, Microsoft Office, iWork, OmniGraffle, basic skills in Wiki and HTML*

Interests

Culture Music: playing cello, classical and jazz concerts, recordings collector. Reading: French and English novels.

Sports Volleyball, badminton.